frontiers | Research Topics

Bioinorganic chemistry of metals in cell function and disease

Edited by
Kourosh Honarmand Ebrahimi, Simone Ciofi Baffoni
and Peter-Leon Hagedoorn

Published in
Frontiers in Cell and Developmental Biology
Frontiers in Molecular Biosciences

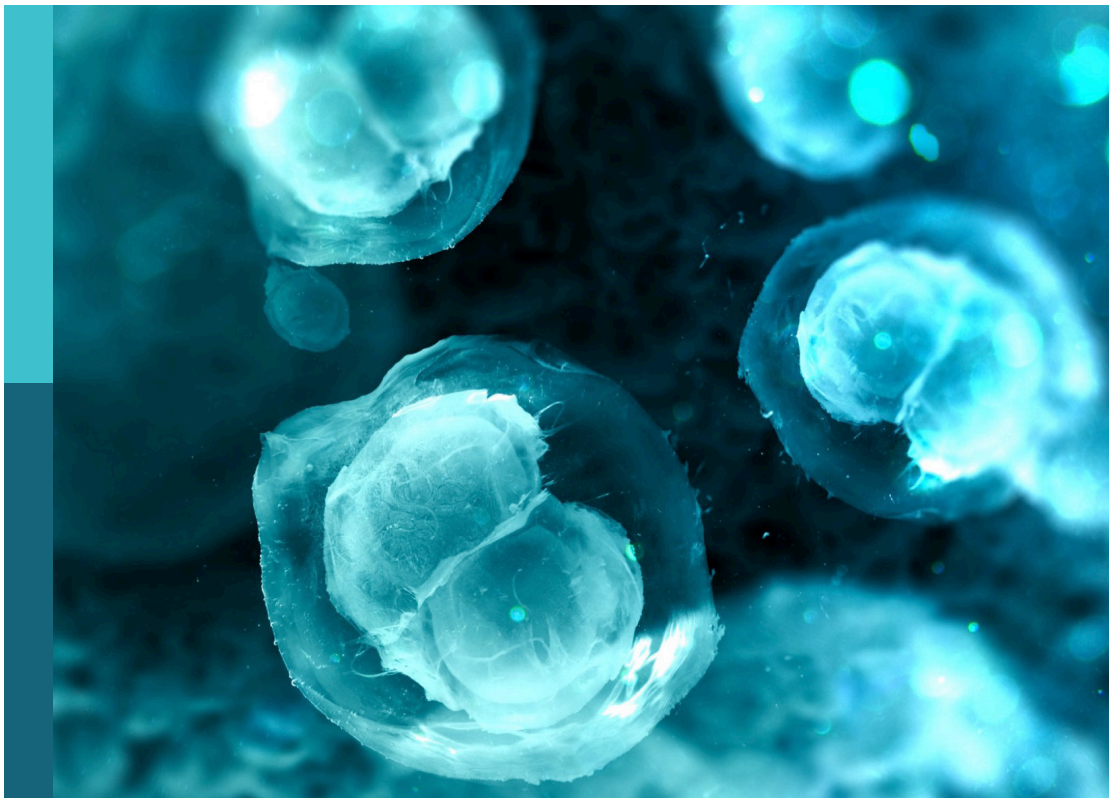

ISSN 1664-8714
ISBN 978-2-8325-2420-6
DOI 10.3389/978-2-8325-2420-6

About Frontiers

Frontiers is more than just an open access publisher of scholarly articles: it is a pioneering approach to the world of academia, radically improving the way scholarly research is managed. The grand vision of Frontiers is a world where all people have an equal opportunity to seek, share and generate knowledge. Frontiers provides immediate and permanent online open access to all its publications, but this alone is not enough to realize our grand goals.

Frontiers journal series

The Frontiers journal series is a multi-tier and interdisciplinary set of open-access, online journals, promising a paradigm shift from the current review, selection and dissemination processes in academic publishing. All Frontiers journals are driven by researchers for researchers; therefore, they constitute a service to the scholarly community. At the same time, the *Frontiers journal series* operates on a revolutionary invention, the tiered publishing system, initially addressing specific communities of scholars, and gradually climbing up to broader public understanding, thus serving the interests of the lay society, too.

Dedication to quality

Each Frontiers article is a landmark of the highest quality, thanks to genuinely collaborative interactions between authors and review editors, who include some of the world's best academicians. Research must be certified by peers before entering a stream of knowledge that may eventually reach the public - and shape society; therefore, Frontiers only applies the most rigorous and unbiased reviews. Frontiers revolutionizes research publishing by freely delivering the most outstanding research, evaluated with no bias from both the academic and social point of view. By applying the most advanced information technologies, Frontiers is catapulting scholarly publishing into a new generation.

What are Frontiers Research Topics?

Frontiers Research Topics are very popular trademarks of the *Frontiers journals series*: they are collections of at least ten articles, all centered on a particular subject. With their unique mix of varied contributions from Original Research to Review Articles, Frontiers Research Topics unify the most influential researchers, the latest key findings and historical advances in a hot research area.

Find out more on how to host your own Frontiers Research Topic or contribute to one as an author by contacting the Frontiers editorial office: frontiersin.org/about/contact

Bioinorganic chemistry of metals in cell function and disease

Topic editors

Kourosh Honarmand Ebrahimi — King's College London, United Kingdom

Simone Ciofi Baffoni — University of Florence, Italy

Peter-Leon Hagedoorn — Delft University of Technology, Netherlands

Citation

Ebrahimi, K. H., Baffoni, S. C., Hagedoorn, P.-L., eds. (2023). *Bioinorganic chemistry of metals in cell function and disease*. Lausanne: Frontiers Media SA. doi: 10.3389/978-2-8325-2420-6

Table of contents

frontiers in Cell and Developmental Biology

OPINION
published: 04 March 2022
doi: 10.3389/fcell.2022.864830

Metals Are Integral to Life as We Know It

Daniele Rossetto[1] *and Sheref S. Mansy*[1,2]*

[1]D-CIBIO, University of Trento, Povo, Italy, [2]Department of Chemistry, University of Alberta, Edmonton, AB, Canada

Investigations of biology and the origins of life regularly focus on the components of the central dogma and thus the elements that compose nucleic acids and peptides. Less attention is given to the inorganic components of a biological cell, which are required for biological polymers to function. The Earth was and continues to be rich in metals, and so investigations of the emergence and evolution of life must account for the role that metal ions play. Evolution is shaped by what is present, and not all elements of the periodic table are equally accessible. The presence of metals, the solubility of their ions, and their intrinsic reactivity all impacted the composition of the cells that emerged. Geological and bioinformatic analyses clearly show that the suite of accessible metal ions changed over the history of the Earth; however, such analyses tend to be interpreted in comparison to average oceanic conditions, which do not represent well the many niche environments present on the Earth. While there is still debate concerning the sequence of events that led to extant biology, what is clear is that life as we know it requires metals, and that past and current metal-dependent events remain, at least partially, imprinted in the chemistry of the cell.

Keywords: origins of life, prebiotic chemistry, metal ions, bioinorganic chemistry, metallopeptides

OPEN ACCESS

Edited by:
Simone Ciofi Baffoni,
University of Florence, Italy

Reviewed by:
Terence Phillip Kee,
University of Leeds, United Kingdom
Michael Assfalg,
University of Verona, Italy

***Correspondence:**
Sheref S. Mansy
sheref.mansy@ualberta.ca

Specialty section:
This article was submitted to Cellular Biochemistry, a section of the journal Frontiers in Cell and Developmental Biology

Received: *28 January 2022*
Accepted: *18 February 2022*
Published: *04 March 2022*

Citation:
Rossetto D and Mansy SS (2022) Metals Are Integral to Life as We Know It. Front. Cell Dev. Biol. 10:864830. doi: 10.3389/fcell.2022.864830

The elements necessary for extant biology are frequently referred to as CHNOPS for carbon, hydrogen, nitrogen, oxygen, phosphorous, and sulfur. While undoubtedly necessary for the synthesis of biological molecules, such as nucleic acids, proteins, and lipids, CHNOPS alone is incapable of supporting life as we know it (**Figure 1**). Nothing alive today or in the past on this planet can be adequately understood without invoking metals. In extant biology, metal ions aid the folding of biological polymers, catalyze the reactions of metabolism, form gradients across membranes that serve as energy reserves, and mediate signal transduction events. Every class of molecules in biology, from nucleic acids to proteins and antibiotics are impacted by metal ions, which is why living cells put so much effort in regulating the concentrations of intracellular free metal ions (Capdevila et al., 2017). What perhaps goes less frequently noticed is the impact of the environment on the distribution and exploitation of metal ions in biology. We are accustomed to viewing biology in the light of evolution and how environmental conditions shape emergent phenotypes. The role of metal ions in biology is no different. Our planet has always been rich in metals, so Darwinian evolution must be thought of in the context of these conditions. Metal ions affect ionic polymers, such as nucleic acids and the soluble domains of proteins, by neutralizing charges and thus facilitating the formation of the tertiary folds necessary for activity. Further, metals themselves intrinsically possess catalytic activity. Since it is easier to scavenge existing parts (i.e. metal ions) for needed function rather than to build from scratch, it is not surprising that metal ions are frequently found within the active sites of enzymes. We see this in both biology and *in vitro* evolution experiments (Bartel and Szostak, 1993; Monreal Santiago et al., 2020), where selected polymers frequently rely on the activity of a coordinated metal ion, even if metal-dependent function was not

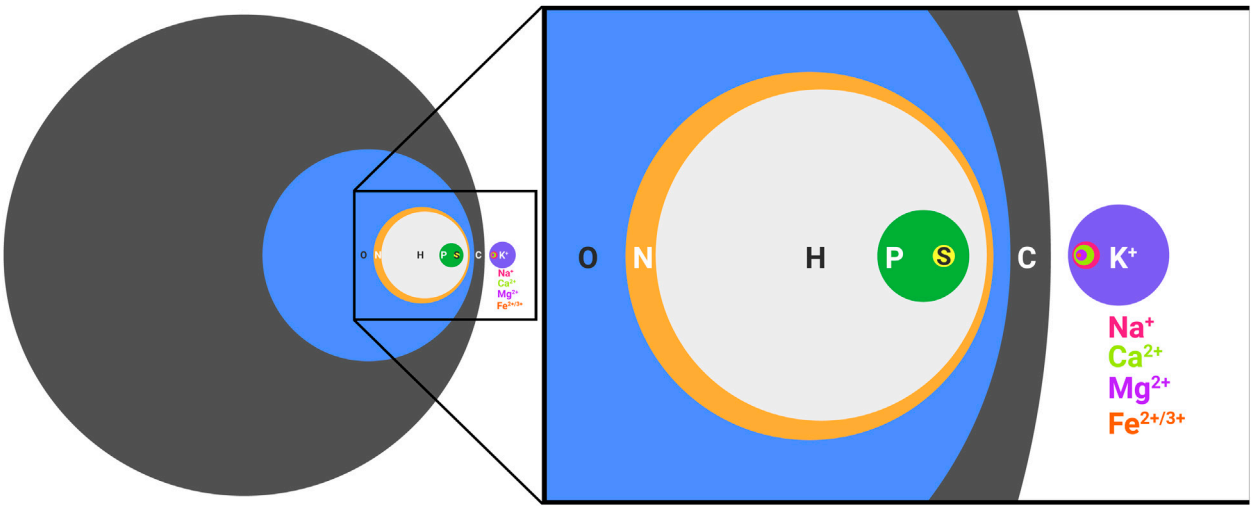

FIGURE 1 | CHNOPS and the most abundant metal ions of a biological cell. Diameters are proportional to percent dry weight. Data are of an average bacterial composition and taken from Lawford and Rousseau, 1996; Tchobanoglous Burton, Franklin L., Stensel, H. David, Metcalf and Eddy, 2003.

intentionally sought (Seelig and Szostak, 2007). We know that in many instances metal-independent activity is possible, because the natural metal-dependent activity of some enzymes can be used as a starting point to engineer metal-independent activity (Casareno et al., 1995), and when environments change, metal reliant pathways can evolve to exploit the use of organic cofactors in place of metal ions (Daniel and Danson, 1995). However, metal-dependent catalysis does not require the formation of a stable complex. Instead, metal ions can enter and exit an active site, as needed, to mediate turnover. Such a scenario is observed for *Bacillus halodurans* RNase H, which exploits for catalysis a transient Mg^{2+} and two transient K^+ that do not make direct contact with the protein (Samara and Yang, 2018). Such dynamics are possible because the intracellular concentrations of Mg^{2+} and K^+ are high, so high affinity, static binding is not necessary.

If biology exploits what is accessible, then it is reasonable to ask which metal ions were present. Relative abundancies throughout the universe roughly correlate with atomic number, with smaller elements of even atomic number found in greater abundance than larger elements of odd atomic number (Da Silva and Williams, 2001). However, planetary compositions, unsurprisingly, are different from each other due to the impact of gravity and heat from the sun, leading to smaller, metal-rich planets closer to the sun, such as the Earth, and larger, more gaseous planets with lower metal abundancies further away. Further deviations result from meteoritic impacts. The metals of greatest abundance on the Earth are the alkali and alkaline Earth metals of periods two to four and the first-row transition metals. Trivalent and higher valent metal cations are not typically encountered, because of their precipitation as hydroxides and oxides. Therefore, solubility limits the accessible options to mono- and di-valent cations. A clear example of this is the change in concentration of oceanic iron before ($\sim 10^{-7}$ mM Fe^{2+}) and after ($\sim 10^{-19}$ mM Fe^{3+}) the great oxidation event. The appearance of oxygen also altered the ratios of sulfate to sulfide, which in turn affected the solubility of metal ions. Metal sulfates are highly soluble in comparison to metal sulfides, and so the concentrations of some metal ions, such those of copper and zinc, increased after the Earth became aerobic. In fact, copper and zinc-dependent enzymes are found much more frequently in higher organisms that emerged after the great oxidation event. While loss of a specific metal ion could be detrimental, that was likely not always the case. Some enzymes retain function with different metal ions. For example, some forms of superoxide dismutase (SOD) are functional as Fe^{2+}- or Mn^{2+}-bound protein (Meier et al., 1982). Similar promiscuity was likely common in the past, particularly with Fe^{2+}, which could have been used in place of Mg^{2+} (Moore et al., 2017; Okafor et al., 2017). The common binding motifs between iron-sulfur clusters and Zn^{2+} also suggest that more ancient scaffolds may have been used for the coordination of newly available metal ions (Belmonte and Mansy, 2017; Shimberg et al., 2018). Although oceanic concentrations of metal ions fluctuated over the history of the Earth, some metal ions, such as Na^+, K^+, Mg^{2+}, and Ca^{2+}, are soluble as sulfides and oxides, and thus may not have changed much.

While it is instructive to assess the compositional evolution of the ocean, oceanic conditions are not where all life evolved. The planet is highly varied in composition and conditions, and so care must be taken when inferring past events based on average conditions of the ocean. For example, despite the much lower abundance of molybdenum (~100-fold lower concentration) in the sea of the anaerobic Earth in comparison to iron, evolutionary analysis indicates that Mo-dependent nitrogenase predates Fe-dependent nitrogenase (Kacar et al., 2021). This suggests that such enzymes emerged from organisms in niche environments not well represented by average oceanic conditions. The same is likely true for the emergence of the Earth's first cells, which likely did not occur under the average conditions of the Earth. Several competing theories exist, with prebiotic chemistry of surface lake conditions being the most intensely investigated (Sasselov et al.,

2020). Lake conditions are attractive since lakes can harness the energy of the sun and can keep molecules necessary for life, such as phosphate, soluble. Lakes rich in carbonate would have led to the precipitation of complexes with Mg^{2+} and Ca^{2+}, thus decreasing the concentrations of these metal ions, which would have facilitated the formation of protocellular structures (Toparlak et al., 2020) and allowed for phosphate concentrations higher than one molal (Toner and Catling, 2020). While decreasing the concentration of Mg^{2+} may have been helpful for some chemical steps, Mg^{2+} would have facilitated other necessary reactions. Mg^{2+}-binding sites are postulated to be older than the last universal common ancestor (LUCA), and at least 18% of extant gene products are thought to bind Mg^{2+} (Shalaeva et al., 2018).

Since the enzymes that mediate metabolism are heavily reliant on metal cofactors, many suspect that prebiotic analogues of extant metabolism may have operated on the prebiotic Earth in a metal-dependent fashion. The degree of involvement of metal ions is debated, with some advocating for a strong role in catalyzing glycolysis (Keller et al., 2014) and the citric acid cycle (Muchowska et al., 2019), and others advocating for a diminished role (Stubbs et al., 2020). Nevertheless, metal ions must have impacted prebiotic chemistry, as it is difficult to imagine environments completely devoid of metals. Copper (Patel et al., 2015) and iron (Xu et al., 2018) ions have been invoked in cyanosulfidic protometabolic pathways that synthesize RNA, amino acids, and lipid precursors. The prebiotic synthesis of phosphoenol pyruvate exploits manganese (Coggins and Powner, 2017), and the non-enzymatic copying and ligation of RNA strands relies on Mg^{2+} (Adamala and Szostak, 2013). More complex metallocofactors, such as iron-sulfur clusters, can be synthesized prebiotically (Bonfio et al., 2017), retain redox activity when bound to small peptides (Scintilla et al., 2016; Kim et al., 2018), and can engage in electron transfer reactions that generate a proton gradient across a lipid membrane (Bonfio et al., 2018).

Billions of years of evolution have given rise to organisms that are supported by finely tuned chemistry, which can be seen by how metals are used in biology. Signal transduction makes use of metal ions with fast ligand exchange rates, such as Na^{+}, K^{+}, and Ca^{2+} (Cowan, 1997). Enzymes exploit the Lewis acidity of metal ions, e.g. Zn^{2+}, to mediate reactions with small substrates that would be difficult to achieve with only protein sidechains (Da Silva and Williams, 2001). However, the origins of the observed metal dependencies reflect what is or was readily accessible. An instructive example of how metal dependence can become embedded is seen by the lengths that modern organisms, including pathogenic bacteria (Capdevila et al., 2017), go to acquire Fe^{2+}. Ultimately, life relies on a conserved set of metal ions in a way that is not too dissimilar from the well-recognized dependencies on a shared genetic code and a common central metabolism. What is less clear is the extent that each of these central pillars of biology rely on each other, and similarly, if life must be constructed from these same parts. It is easy to propose that different planetary conditions could give rise to life completely orthogonal to ours today, but it is more difficult to imagine when considering the limits of availability and accessible chemistry (Pace, 2001). To date, few have attempted to define the metal requirements for the emergence of life (Zerkle et al., 2005; McKay, 2014; Barge et al., 2021). Although evolution suggests that there is unlikely to be a requirement for one specific metal, the probability of prebiotic chemistry advancing towards cell-like activity may be significantly lower in the absence of the intrinsic catalytic activity of metal ions in general. As the search for extraterrestrial life focuses on rocky planets, there is already a presumption to the importance of metals. The variable, instead, is accessibility.

AUTHOR CONTRIBUTIONS

Both authors wrote the manuscript together.

FUNDING

We thank the Simons Foundation (290358FY18 and 290358FY19) and the Natural Sciences and Engineering Research Council of Canada (NSERC) (RGPIN-2020-04375) for funding.

REFERENCES

Adamala, K., and Szostak, J. W. (2013). Nonenzymatic Template-Directed RNA Synthesis inside Model Protocells. *Science* 342, 1098–1100. doi:10.1126/science.1241888

Barge, L. M., Rodriguez, L. E., Weber, J. M., and Theiling, B. P. (2021). Determining the "Biosignature Threshold" for Life Detection on Biotic, Abiotic, or Prebiotic Worlds. *Astrobiology* [Epub ahead of print]. doi:10.1089/ast.2021.0079

Bartel, D., and Szostak, J. (1993). Isolation of New Ribozymes from a Large Pool of Random Sequences [see Comment]. *Science* 261, 1411–1418. doi:10.1126/science.7690155

Belmonte, L., and Mansy, S. S. (2017). Patterns of Ligands Coordinated to Metallocofactors Extracted from the Protein Data Bank. *J. Chem. Inf. Model.* 57, 3162–3171. doi:10.1021/acs.jcim.7b00468

Bonfio, C., Godino, E., Corsini, M., Fabrizi de Biani, F., Guella, G., and Mansy, S. S. (2018). Prebiotic Iron-Sulfur Peptide Catalysts Generate a pH Gradient across Model Membranes of Late Protocells. *Nat. Catal.* 1, 616–623. doi:10.1038/s41929-018-0116-3

Bonfio, C., Valer, L., Scintilla, S., Shah, S., Evans, D. J., Jin, L., et al. (2017). UV-light-driven Prebiotic Synthesis of Iron-Sulfur Clusters. *Nat. Chem* 9, 1229–1234. doi:10.1038/nchem.2817

Capdevila, D. A., Edmonds, K. A., and Giedroc, D. P. (2017). Metallochaperones and Metalloregulation in Bacteria. *Essays Biochem.* 61, 177–200. doi:10.1042/EBC20160076

Casareno, R., Li, D., and Cowan, J. A. (1995). Rational Redesign of a Metal-dependent Nuclease. Engineering the Active Site of Magnesium-dependent Ribonuclease H to Form an Active "Metal-independent" Enzyme. *J. Am. Chem. Soc.* 117, 11011–11012. doi:10.1021/ja00149a026

Coggins, A. J., and Powner, M. W. (2017). Prebiotic Synthesis of Phosphoenol Pyruvate by α-phosphorylation-controlled Triose Glycolysis. *Nat. Chem* 9, 310–317. doi:10.1038/nchem.2624

Cowan, J. A. (1997). *Inorganic Biochemistry: An Introduction*. Wiley.

Da Silva, F. J. J. R., and Williams, R. J. P. (2001). *The Biological Chemistry of the Elements : The Inorganic Chemistry of Life*. 2nd ed. Oxford; New York: Oxford University Press.

Daniel, R. M., and Danson, M. J. (1995). Did Primitive Microorganisms Use Nonhem Iron Proteins in Place of NAD/P? *J. Mol. Evol.* 40, 559–563. doi:10.1007/BF00160501

Kacar, B., Garcia, A. K., and Anbar, A. D. (2021). Evolutionary History of Bioessential Elements Can Guide the Search for Life in the Universe. *ChemBioChem* 22, 114–119. doi:10.1002/cbic.202000500

Keller, M. A., Turchyn, A. V., and Ralser, M. (2014). Non-enzymatic Glycolysis and Pentose Phosphate Pathway-like Reactions in a Plausible Archean Ocean. *Mol. Syst. Biol.* 10, 725. doi:10.1002/msb.20145228

Kim, J. D., Pike, D. H., Tyryshkin, A. M., Swapna, G. V. T., Raanan, H., Montelione, G. T., et al. (2018). Minimal Heterochiral De Novo Designed 4Fe-4S Binding Peptide Capable of Robust Electron Transfer. *J. Am. Chem. Soc.* 140, 11210–11213. doi:10.1021/jacs.8b07553

McKay, C. P. (2014). Requirements and Limits for Life in the Context of Exoplanets. *Proc. Natl. Acad. Sci.* 111, 12628–12633. doi:10.1073/pnas.1304212111

Meier, B., Barra, D., Bossa, F., Calabrese, L., and Rotilio, G. (1982). Synthesis of Either Fe- or Mn-Superoxide Dismutase with an Apparently Identical Protein Moiety by an Anaerobic Bacterium Dependent on the Metal Supplied. *J. Biol. Chem.* 257, 13977–13980. doi:10.1016/s0021-9258(19)45329-5

Monreal Santiago, G., Liu, K., Browne, W. R., and Otto, S. (2020). Emergence of Light-Driven Protometabolism on Recruitment of a Photocatalytic Cofactor by a Self-Replicator. *Nat. Chem.* 12, 603–607. doi:10.1038/s41557-020-0494-4

Moore, E. K., Jelen, B. I., Giovannelli, D., Raanan, H., and Falkowski, P. G. (2017). Metal Availability and the Expanding Network of Microbial Metabolisms in the Archaean Eon. *Nat. Geosci.* 10, 629–636. doi:10.1038/ngeo3006

Muchowska, K. B., Varma, S. J., and Moran, J. (2019). Synthesis and Breakdown of Universal Metabolic Precursors Promoted by Iron. *Nature* 569, 104–107. doi:10.1038/s41586-019-1151-1

Okafor, C. D., Lanier, K. A., Petrov, A. S., Athavale, S. S., Bowman, J. C., Hud, N. V., et al. (2017). Iron Mediates Catalysis of Nucleic Acid Processing Enzymes: Support for Fe(II) as a Cofactor Before the Great Oxidation Event. *Nucleic Acids Res.* 45, 3634–3642. doi:10.1093/nar/gkx171

Pace, N. R. (2001). The Universal Nature of Biochemistry. *Proc. Natl. Acad. Sci.* 98, 805–808. doi:10.1097/00000441-196304000-0001410.1073/pnas.98.3.805

Patel, B. H., Percivalle, C., Ritson, D. J. D., and Duffy, J. D. (2015). Common Origins of RNA, Protein and Lipid Precursors in a Cyanosulfidic Protometabolism. *Nat. Chem* 7, 301–307. doi:10.1038/nchem.2202

Samara, N. L., and Yang, W. (2018). Cation Trafficking Propels RNA Hydrolysis. *Nat. Struct. Mol. Biol.* 25, 715–721. doi:10.1038/s41594-018-0099-4

Sasselov, D. D., Grotzinger, J. P., and Sutherland, J. D. (2020). The Origin of Life as a Planetary Phenomenon. *Sci. Adv.* 6, 1–9. doi:10.1126/sciadv.aax3419

Scintilla, S., Bonfio, C., Belmonte, L., Forlin, M., Rossetto, D., Li, J., et al. (2016). Duplications of an Iron-sulphur Tripeptide Leads to the Formation of a Protoferredoxin. *Chem. Commun.* 52, 13456–13459. doi:10.1039/c6cc07912a

Seelig, B., and Szostak, J. W. (2007). Selection and Evolution of Enzymes from a Partially Randomized Non-catalytic Scaffold. *Nature* 448, 828–831. doi:10.1038/nature06032

Shalaeva, D. N., Cherepanov, D. A., Galperin, M. Y., Golovin, A. V., and Mulkidjanian, A. Y. (2018). Evolution of Cation Binding in the Active Sites of P-Loop Nucleoside Triphosphatases in Relation to the Basic Catalytic Mechanism. *Elife* 7, 1–35. doi:10.7554/eLife.37373

Shimberg, G. D., Pritts, J. D., and Michel, S. L. J. (2018). *Iron–Sulfur Clusters in Zinc Finger Proteins*. 1st ed. Elsevier, 101–137. doi:10.1016/bs.mie.2017.09.005Iron-Sulfur Clusters in Zinc Finger Proteins

Stubbs, R. T., Yadav, M., Krishnamurthy, R., and Springsteen, G. (2020). A Plausible Metal-free Ancestral Analogue of the Krebs Cycle Composed Entirely of α-ketoacids. *Nat. Chem.* 12, 1016–1022. doi:10.1038/s41557-020-00560-7

Toner, J. D., and Catling, D. C. (2020). A Carbonate-Rich lake Solution to the Phosphate Problem of the Origin of Life. *Proc. Natl. Acad. Sci. USA* 117, 883–888. doi:10.1073/pnas.1916109117

Toparlak, Ö. D., Karki, M., Egas Ortuno, V., Krishnamurthy, R., and Mansy, S. S. (2020). Cyclophospholipids Increase Protocellular Stability to Metal Ions. *Small* 16, 1903381–1903388. doi:10.1002/smll.201903381

Xu, J., Ritson, D. J., Ranjan, S., Todd, Z. R., Sasselov, D. D., and Sutherland, J. D. (2018). Photochemical Reductive Homologation of Hydrogen Cyanide Using Sulfite and Ferrocyanide. *Chem. Commun.* 54, 5566–5569. doi:10.1039/c8cc01499j

Zerkle, A. L., House, C. H., and Brantley, S. L. (2005). Biogeochemical Signatures through Time as Inferred from Whole Microbial Genomes. *Am. J. Sci.* 305, 467–502. doi:10.2475/ajs.305.6-8.467

Conflict of Interest: The authors declare that the research was conducted in the absence of any commercial or financial relationships that could be construed as a potential conflict of interest.

Publisher's Note: All claims expressed in this article are solely those of the authors and do not necessarily represent those of their affiliated organizations, or those of the publisher, the editors and the reviewers. Any product that may be evaluated in this article, or claim that may be made by its manufacturer, is not guaranteed or endorsed by the publisher.

frontiers in Molecular Biosciences

ORIGINAL RESEARCH
published: 10 March 2022
doi: 10.3389/fmolb.2022.828674

Ni^{2+}-Assisted Hydrolysis May Affect the Human Proteome; Filaggrin Degradation *Ex Vivo* as an Example of Possible Consequences

Ewa Izabela Podobas[1,2,3], Danuta Gutowska-Owsiak[2,4], Sébastien Moretti[5], Jarosław Poznański[1], Mariusz Kulińczak[6], Marcin Grynberg[1]*, Aleksandra Gruca[7], Arkadiusz Bonna[8], Dawid Płonka[1], Tomasz Frączyk[1], Graham Ogg[2] and Wojciech Bal[1]*

[1]*Institute of Biochemistry and Biophysics, Polish Academy of Sciences, Warsaw, Poland,* [2]*Medical Research Council Human Immunology Unit, National Institute for Health Research Oxford Biomedical Research Centre, Medical Research Council Weatherall Institute of Molecular Medicine, University of Oxford, Oxford, United Kingdom,* [3]*Institute of Genetics and Biotechnology, University of Warsaw, Warsaw, Poland,* [4]*University of Gdansk, Intercollegiate Faculty of Biotechnology of University of Gdansk and Medical University of Gdansk, Gdansk, Poland,* [5]*SIB Swiss Institute of Bioinformatics, Vital-IT Team, Lausanne, Switzerland,* [6]*The Maria Sklodowska-Curie National Research Institute of Oncology, Warsaw, Poland,* [7]*Institute of Informatics, Faculty of Automatic Control, Electronics and Computer Science, Silesian University of Technology, Gliwice, Poland,* [8]*Department of Biochemistry, University of Cambridge, Cambridge, United Kingdom*

OPEN ACCESS

Edited by:
Kourosh Honarmand Ebrahimi, King's College London, United Kingdom

Reviewed by:
Michel Simon, Université de Toulouse, France
Leonid Breydo, West Pharmaceutical Services, United States

***Correspondence:**
Ewa Izabela Podobas
ei.podobas@uw.edu.pl
Marcin Grynberg
mr.cingg@gmail.com

Specialty section:
This article was submitted to Cellular Biochemistry, a section of the journal Frontiers in Molecular Biosciences

Received: *03 December 2021*
Accepted: *31 January 2022*
Published: *10 March 2022*

Citation:
Podobas EI, Gutowska-Owsiak D, Moretti S, Poznański J, Kulińczak M, Grynberg M, Gruca A, Bonna A, Płonka D, Frączyk T, Ogg G and Bal W (2022) Ni^{2+}-Assisted Hydrolysis May Affect the Human Proteome; Filaggrin Degradation Ex Vivo as an Example of Possible Consequences. Front. Mol. Biosci. 9:828674. doi: 10.3389/fmolb.2022.828674

Deficiency in a principal epidermal barrier protein, filaggrin (FLG), is associated with multiple allergic manifestations, including atopic dermatitis and contact allergy to nickel. Toxicity caused by dermal and respiratory exposures of the general population to nickel-containing objects and particles is a deleterious side effect of modern technologies. Its molecular mechanism may include the peptide bond hydrolysis in X_1-S/T-c/p-H-c-X_2 motifs by released Ni^{2+} ions. The goal of the study was to analyse the distribution of such cleavable motifs in the human proteome and examine FLG vulnerability of nickel hydrolysis. We performed a general bioinformatic study followed by biochemical and biological analysis of a single case, the FLG protein. FLG model peptides, the recombinant monomer domain human keratinocytes *in vitro* and human epidermis *ex vivo* were used. We also investigated if the products of filaggrin Ni^{2+}-hydrolysis affect the activation profile of Langerhans cells. We found X_1-S/T-c/p-H-c-X_2 motifs in 40% of human proteins, with the highest abundance in those involved in the epidermal barrier function, including FLG. We confirmed the hydrolytic vulnerability and pH-dependent Ni^{2+}-assisted cleavage of FLG-derived peptides and FLG monomer, using *in vitro* cell culture and *ex-vivo* epidermal sheets; the hydrolysis contributed to the pronounced reduction in FLG in all of the models studied. We also postulated that Ni-hydrolysis might dysregulate important immune responses. Ni^{2+}-assisted cleavage of barrier proteins, including FLG, may contribute to clinical disease associated with nickel exposure.

Keywords: filaggrin, human proteome, protein degradation, Ni^{2+}-assisted hydrolysis, nickel toxicity, nickel allergy

INTRODUCTION

Prevalence of nickel alloys in the industry and daily use items is inadvertently associated with the occupational and environmental exposure to airborne particles containing nickel oxides and salts, and to Ni^{2+} ions present in water and food and released from nickel alloys (by dermal contact) (World Health Organization, 2000; Kasprzak et al., 2003; Nieminen et al., 2007; Zambelli et al., 2016; Ahlström et al., 2019). While medicinal aspects of the resulting nickel toxicity have been thoroughly described, the underlying molecular mechanisms remain the subject of research (Ahlström et al., 2019; Genchi et al., 2020). The Ni^{2+}-assisted peptide bond hydrolysis (Ni-hydrolysis) is one such reaction, occurring selectively before S/T in proteins bearing X_1-S/T-c/p-H-c-X_2 motifs (Ni-hydrolytic motifs, excluding P at the third and reduced C at the first, third and fifth residues within the motif) exposed to Ni^{2+} ions in solution (Kopera et al., 2010; Krezel et al., 2010; Podobas et al., 2014). It proceeds via the N-O acyl shift in the X_1-S/T moiety, followed by ester hydrolysis (**Figure 1A**). The reaction rate depends on pH, temperature and the bulkiness of the first, third and fifth residues, being significantly faster for X_1 = G (fast motifs) (Ariani et al., 2013). The effectiveness this process was proven for Cu^{2+} (Bal et al., 2000) and Pd^{2+} ions (Wezynfeld et al., 2016), but Ni-hydrolysis was investigated to the largest extent, due to its higher efficiency. On the other hand, Co^{2+} and Zn^{2+} ions were proven to be non-reactive in this respect (Bal et al., 2000).

Filaggrin (FLG) plays key roles in maintaining skin homeostasis, epidermal structure and the barrier function (Candi et al., 2005; Sandilands et al., 2009; Brown and McLean, 2012). It is expressed as a large >400 kDa precursor (profilaggrin; proFLG), forming the bulk of keratohyalin granules (KHGs). ProFLG consists of 10–12 nearly identical FLG repeats, subsequently released from KHGs into the cytoplasm during post-translational processing (Matoltsy and Matoltsy, 1970). These monomers are essential in aggregating keratin filaments in *stratum corneum* while the proFLG N-terminal domain plays an important role during epidermal terminal differentiation process. Further FLG proteolysis proceeds down to amino acids, which contribute to the epidermal hydration, acidic *stratum corneum* pH maintenance, and protection against UV radiation (Gibbs et al., 2008; Kezic et al., 2008; Fluhr et al., 2010). FLG release from the KHGs (Gutowska-Owsiak et al., 2018) and processing is precisely controlled spatially and temporally, and the FLG deficiency results in abnormal epidermal architecture and barrier insufficiency, promoting skin inflammation and allergic sensitisation by allergens penetrating the defective epidermis (Gruber et al., 2011). Finally, FLG loss-of-function mutations might also increase dermal absorption of chemicals (Rietz Liljedahl et al., 2021) and increase the risk for allergic sensitization against nickel (Novak et al., 2008; Thyssen et al., 2010).

The key role of FLG in the skin barrier formation and its enrichment in Ni-hydrolytic motifs inspired us to study its interaction with Ni^{2+} ions in cell-free and biological systems.

Here we present the hydrolytic cleavage pattern search tool which allowed us to analyse the distribution of such cleavable motifs in the human proteome and catalogued them according to their physiological function. Fast G-motifs are generally abundant, but particularly highly enriched in proteins supporting the epidermal barrier of the human body, e.g. FLG, expressed predominantly in keratinocytes.

MATERIALS AND METHODS

Database Creation

For our *in silico* research the UniProt database—release 2017_05—was used. We decided to leave all protein isomers as a full representation of functional proteome. But we keep only a non-redundant protein set to avoid duplicates after clustering with the cd-hit tool version 4.6.8 and these parameters: "-c 0.98 -d 0 -aS 0.98 -p 1 -g 1". Two patterns—following the PROSITE Pattern syntax (https://prosite.expasy.org/prosuser.html)—were searched with the/Pattern Search/ tool version 1 from MyHits (https://www.ncbi.nlm.nih.gov/pubmed/17545200): "x-[ST]-{CP}-H-{C}-x" or "G-[ST]-{CP}-H-{C}-x". Perl 5.18.2 (script get_motif_stat.pl) was used to parse results. Additionally results containing proteins with those words in their description were discarded: "(Fragment)" or "Truncated". Here a correction has been made. In the case of overlapping motives, we counted them as one. The following research tasks were considered: estimation of the number of motifs per protein, estimation of the number of motifs normalized by the length of proteins, estimation of the number of motifs by type (specific amino acids at specific positions). On the base of such prepared data, further statistical analyses were performed.

Amino Acid Enrichment

Experimental amino acid occurrences on position X_1 of X_1-S/T-c/p-H-c-X_2 motif were corrected for the abundance of each amino acid in the whole proteome. Positive value indicates that a particular residue type is found on X-position more frequently than in the whole proteome.

Cumulative Distribution Function (CDF)

Cumulative distribution functions were obtained according to the standard approach (Montgomery and Runger, 2007) and visualized using Origin software (version 9.7, www.originlab.com).

Quantitative Analysis of Hydrolytic Motifs Frequency Within the Human Proteome

The number of X_1-S/T-c/p-H-c-X_2 motifs was determined for each individual protein. The distribution of these numbers was then analysed assuming Poisson distribution, which assumes no correlations between particular motifs. The analysis was performed using Origin software (version 9.7, www.originlab.com).

Single-Term GO Functional Enrichment Analysis

Gene Ontology functional enrichment analysis was performed using topGO R package with custom GO mapping files based on Gene Ontology human annotations files from April 2018. Only

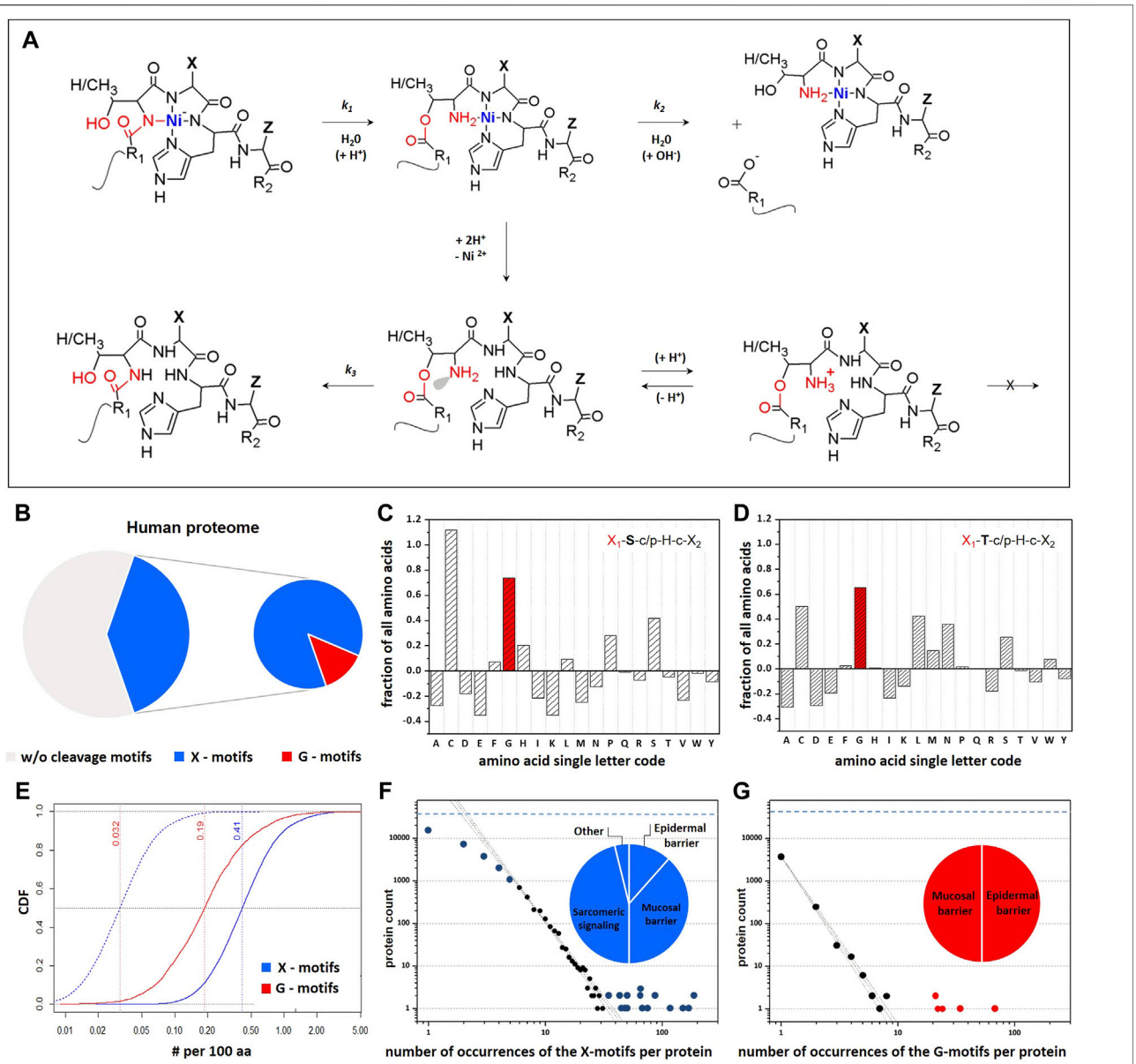

FIGURE 1 | Frequency of Ni-hydrolysis-susceptible X_1-ST-cp-H-c-X_2 motifs (Kopera et al., 2010; Krezel et al., 2010; Podobas et al., 2014) within the human proteome. **(A)** Ni-hydrolysis is enabled through formation of a square-planar 4N Ni^{2+} complex involving the imidazole nitrogen of the participating histine and three preceding amide nitrogens. The N–O acyl shift from the carbonyl group of S/T peptide bond to the hydroxyl group, follows an apparent first order kinetic regime **(k_1)**. The resulting ester hydrolyzes spontaneously into two peptides, also according to the apparent first order kinetics **(k_2)**. Protonation of metal ion binding to the amine group prevents the O–N acyl shift by engaging the nitrogen's lone electron pair (grey). The Ni^{2+} ion facilitates the acyl shift and prevents its reversal, by stabilization of the reaction products. **(B)** Schematic percentage representation of the Ni-assisted hydrolysis-susceptible motifs within human proteome. **(C,D)** Propensities of each of the 20 canonical amino acids on X_1-position within S and T containing motifs. Frequencies of individual amino acids on X_1-positon were corrected for their occurrence in the whole proteome. Positive values identify amino acids that are more likely to occur in this position than in the total proteome. **(E)** Cumulative distribution function (CDFs) of G occurrences on the X_1 position within hydrolytic motifs (red). Distribution is normalized per 100 residues in protein sequences. Chopped blue line follows the CDF expected for G-motif, which was obtained from the CDF observed for X-motif (blue line) after correction for 7.07% of glycine content. Each individual protein is contributing to the CDF curves as a single step of the same height. Dotted vertical lines denote the median of the distribution. **(F,G)** Quantitative analysis of the number of hydrolytic motifs in each protein. Thick lines follow the general trend expected according to the Poisson distribution used for statistical analysis, while dashed lines indicate the associated 95% confidence bands. Blue and red symbols mark data substantially deviated from Poisson distributions. The total number of proteins with X-motifs in the database (31099, dashed horizontal line) stands the upper limit for the number of proteins with hydrolytic motifs, thus explaining the deviation observed for proteins with small number of cleavage motifs occurrences.

Gene Ontology terms from Biological Process were used for annotation. Initial datasets G-S/T-c/p-H-c-X_2 and X_1-S/T-c/p-H-c-X_2 included 4111 and 31099 proteins denoted with UniProt accession numbers. As GO annotations are provided for UniProtKB identifier, the first step involved translation UniProt accession numbers to Uniprot KB identifiers and

filtering out isoforms. After the filtering step, the datasets G-S/T-c/p-H-c-X_2 and X_1-S/T-c/p-H-c-X_2 2938 and 23120 protein identifiers respectively. To assess the statistical significance of GO terms enrichment in both datasets, Fisher Exact test was used with Benjamin-Hochberg adjustment for multiple testing corrections.

Analysis of Hydrolytic Motifs Within Filaggrins From Various Species

In order to create the list of proteins from diverse organisms we used the ScanProSite Tool which allows to scan a protein database against a motif. We used the X_1-S/T-c/p-H-c-X_2 motif for this purpose. We then normalized the number of cleavage sites dividing it by the total sequence length (# of motifs * 100/seq length). Dataset has been used to create a circular phylogenetic tree in NCBI CommonTree (https://www.ncbi.nlm.nih.gov/Taxonomy/CommonTree/wwwcmt.cgi) and visualized in iTOL https://itol.embl.de/(Letunic and Bork, 2021).

In Silico Analysis of proFLG Sequence and Selection of Peptides

In silico analysis of proFLG sequence was performed on the base available in NCBI database human proFLG amino acid sequence (Ref. NP_002007.1) and information about FLG repeats (Sandilands et al., 2009). The FLG domains separation was proposed and compared using WebLogo 3 application (Schneider and Stephens, 1990; Crooks et al., 2004).

Peptide Synthesis

All peptides were synthesized in the solid phase according to the Fmoc protocol (Chan and White, 2000) using the Prelude automatic synthesizer (Protein Technologies). The syntheses were accomplished using N-α-9-Fluorenylmethyloxycarbonyl (F-moc) amino acids (Novabiochem) on a TentaGel® S RAM resin (Rapp Polymere), using O-(Benzotriazol-1-yl)-N,N,N′,N′-tetramethyluronium hexafluorophosphate (HBTU, Sigma-Aldrich) as a coupling reagent, in the presence of N,N-diisopropylethylamine (DIEA, Sigma-Aldrich). The acetylation of the N-terminus was carried out in 10% acetic anhydride in DCM. The cleavage was done manually by the cleavage mixture composed of 95% trifluoroacetic acid (TFA, Sigma-Aldrich), 2.5% triisopropylsilane (TIS, Sigma-Aldrich) and 2.5% water. Peptides were isolated from cleavage mixtures by the addition of ice-cold diethyl ether and centrifugation. Following precipitation, peptides were dissolved in water and lyophilized. Peptides were purified by HPLC (Waters) using an analytical C18 column (ACE 250 × 4.6 mm) monitored at 220 and 280 nm. The eluting solvent A was 0.1% (v/v) TFA in water, and solvent B was 0.1% (v/v) TFA in 90% (v/v) HPLC grade acetonitrile (Rathburn Chemicals). The correctness of molecular masses and purities of the peptides was confirmed using Premier Q-Tof ESI-MS spectrometer (Waters). After this step, peptide solutions were frozen in liquid nitrogen and lyophilized.

Ni^{2+}-Assisted FLG Peptides Hydrolysis

The hydrolysis experiments were performed in a 20 mM HEPES buffer (Sigma-Aldrich), using 0.5 mM peptide and 2 mM $Ni(NO_3)_2$ (Sigma-Aldrich). The samples were incubated in pH 8.2, at 50°C and pH 7.4, at 37°C. The aliquots were periodically collected from the samples and acidified by addition 2% (v/v) TFA. Control samples, containing peptide and buffer, but without Ni^{2+}, were gathered at the same time points. For analysis, reaction mixtures were diluted by water 4 to 1 and injected into the HPLC system (Waters), equipped with an analytical C18 column. The eluting solvent A was 0.1% (v/v) TFA in water, and solvent B was 0.1% (v/v) TFA in 90% (v/v) acetonitrile. The chromatograms were obtained at 220 and 280 nm. After separation, the products of hydrolysis were identified using electrospray ionization mass spectrometry (ESI-MS). The relative amounts of these fractions in each chromatogram were calculated by peak integration using data analysis software Origin 8.1 or Origin Pro 2017 (OriginLab Corporation).

Kinetic Analysis

To calculate the rate constants of the acyl shift step (k_1) and the ester hydrolysis step (k_2) of the hydrolysis reaction the set of three equations (Kinet A, Kinet B, and Kinet C) was used, similarly to previous studies (Kopera et al., 2010; Ariani et al., 2013; Protas et al., 2013).

Kinet A $$y = A_0 \times \exp(-k_1 \times x)$$

Kinet B $$y = \left(\frac{k_1 \times A_0}{k_2 - k_1}\right) \times \left(\exp(-k_1 \times x) - \exp(-k_2 \times x)\right)$$

Kinet C $$y = A_0 \times \left(1 + \left(\frac{1}{k_1 - k_2}\right)\right) \times \left(k_2 \exp(-k_1 \times x) - \exp(k_2 \times x)\right)$$

In these equations y is a molar fraction of a given species, x is the time axis, and A_0 denotes the initial concentration of the substrate.

UV–Visible and Circular Dichroism Spectroscopies

The UV-visible spectra were recorded in the range of 850–330 nm, on a LAMBDA 950 UV/vis/NIR spectrophotometer (PerkinElmer). The path length was 1 cm. Complexometric titrations were performed for the samples containing 0.95 mM peptide and 0.9 mM $Ni(NO_3)_2$ dissolved in H_2O. The pH of the solution was adjusted manually in the range of 3–11.5 by titrating with small amounts of concentrated NaOH. Circular dichroism (CD) spectra of Ni^{2+} complexes with peptides were recorded in the range of 270–800 nm, on a Jasco J-815 spectropolarimeter, using the same samples as for UV-vis experiments. The pK_a values for the complex formation were obtained by fitting the absorption value at the band maximum to the Hill equation (Acerenza and Mizraji, 1997).

Molecular Modeling of Ni^{2+} Complexes

All molecular mechanics simulations were performed using YASARA2 force-field (Krieger et al., 2004) extended for the Ni^{2+} coordination by adding the *ab initio* derived topology and charge distributions. The N-Ni distances were constrained as a pseudo-bond of the appropriate length, and the geometry was forced according to the expected square planar coordination of Ni^{2+} by additional constrains for N-Ni-N angles (90°) and N-Ni-N-N pseudo-dihedrals (180°). Additional pseudo-dihedral constrains were introduced to mimic sp^2 hybridisation of the Nitrogen (C-N-Cα-N = 180°). Model peptides were built in extended conformation and the structure of their complexes with Ni was initially optimised using implemented in Yasara algorithm that combines simulated annealing and energy minimisation. The further ten cycles of high temperature molecular dynamics (250 ps at 1,000 K) followed by stepwise cooling and final energy minimization were done to assess conformational flexibility of a given Ni-peptide complex. Molecular graphics were created with YASARA (www.yasara.org) and POVRay (www.povray.org).

FLG Recombinant Protein: Plasmid Construction

Plasmids were constructed using a sequence- and ligation-independent cloning (SLIC) method (Li and Elledge, 2007). Nucleotide sequence encoding 10th FLG repeat domain were encloned in pET28 vector using BamHI and XhoI restrictions sites. The FLG 10th construct contained a C-terminal His6-tag. As a control, a construct for maize protein kinase CK2α was obtained in similar conditions. The CK2α protein has a molecular weight similar to FLG and contains no X_1-S/T-c/p-H-c-X_2 motifs. The maize protein kinase CK2α construct contained a C-terminal His6-tag. The constructs were verified by sequencing.

Protein Production and Purification

The constructs were transformed into *E. coli* BL21-CodonPlus-RIL and propagated overnight in LB liquid media containing kanamycin and chloramphenicol at 37°C. The bacterial cultures were diluted 1: 100 in LB liquid media supplemented by antibiotics and incubated at 37°C until the culture has reached the mid-log phase of growth. Protein expression was induced by IPTG (1 mM) for 2 h at 37°C. The cells were harvested by centrifugation (10 min, 5,000 × *g*, 4°C). The pellets were mixed with lysis buffer (10 mM Tris pH 8, 150 mM NaCl, 10 mM imidazole) supplemented with protease inhibitors cocktail and lysed by sonication. The cell lysate was clarified by centrifugation (60 min, 24,000 × *g*, 4°C) and used for affinity purification on a HisPur™ Cobalt Resin (Thermo Fisher). Pure protein was eluted by an elution buffer (10 mM Tris pH 8, 150 mM NaCl, 300 mM imidazole). Samples were dialysed (10 mM Tris pH 8.5, 150 mM NaCl, MWCO: 12–14000 Da) and analyzed on SDS-PAGE. Bands of interest were cut out and identified by MALDI-TOF MS after trypsin digestion.

Ni^{2+}-Assisted FLG Monomer Hydrolysis

FLG protein domains (30 μM) were incubated in 10 mM TRIS/150 mM NaCl buffer with or without nickel ions [1 mM $Ni(NO_3)_2$] under optimal (pH 8.2, 50°C) and physiological (pH 7.4, 37°C) conditions. The reactions were stopped by freezing the collected samples in liquid nitrogen. Samples from different time points were separated using the Tricine-SDS page technique and Bio-Rad system. The experiment was repeated for CK2α control protein. Gels after electrophoresis were scanned (E-gel imager Camera, Life Technologies) and the scans used for densitometric analyses (ImageJ program).

Cell Proliferation Assay

In order to find out the toxic concentration of $Ni(NO_3)_2$ for keratinocytes, the cell proliferation assay (MTT) was performed. Cells were cultured in a 96-well plate and after 24 h of exposure to a gradient of $Ni(NO_3)_2$ concentrations (10^{-2} to 10^{-7} M final concentration) the test was performed according to manufacturer's protocol (CellTiter 96® Non-Radioactive Cell Proliferation Assay, Promega). The assay determined the half maximal inhibitory concentration value IC_{50} as approximately 1 mM $Ni(NO_3)_2$.

Normal Human Epidermal Keratinocyte Culture

Normal human epidermal keratinocytes (NHEKs) (purchased from Lonza) were cultured in monolayers in a dedicated medium (Lonza, KBM-2) at the Ca^{2+} level of 0.06 mM. To stimulate differentiation and FLG expression, a calcium switch was conducted over a period of 24 h by replacing the culture media with fresh media adjusted to a 1.5 mM final calcium concentration. A $Ni(NO_3)_2$ (Sigma) solution was added to achieve various final concentrations (10 μM, 100 μM and 1 mM). Doses were chosen based on MTT test results (**Supplementary Figure S1**). After 24 h of incubation, the cells were fixed, permeabilized and immunostained with anti-FLG antibodies (Anti-FLG goat G20 (Santa Cruz), and secondary anti-goat Alexa-488 and anti-rabbit Alexa-568 (Life Technologies) antibodies were used. Staining was carried out in PBS and nuclei were visualized by Hoechst (NucBlue, Life Technologies). The slides were coversliped with Mowiol 4-88 (Sigma). Data acquisition was carried out on the Zeiss 780 inverted confocal microscope. Images from three separate experiments were analysed; KHG diameter and integrated intensity from the signal were measured using Fiji: ImageJ program (Abramoff, 2007). For the statistical analysis the Mann–Whitney *U* test was used.

Exposure of Epidermal Sheets to Nickel

Skin samples were obtained from healthy donors undergoing surgery under ethical approval from the UK National Research Ethics Service (14.NW.1153). Epidermal sheets were separated from dermal tissues by overnight incubation in dispase (5 U/ml; Sigma Aldrich) and cultured up to 48 h in KGM-2 keratinocyte medium (Lonza) adjusted with $CaCl_2$ to a 1.5 mM final calcium concentration. The $Ni(NO_3)_2$ solution was added at the 1 mM final concentration. Experiments were repeated on skin explants from 10 donors. For fluorescent antibody staining epidermal sheets were fixed with 4% formaldehyde (Sigma), followed by

0.1% Triton X-100 (Sigma Aldrich) and incubated in a blocking buffer (5% FCS, 2% BSA in PBS) for 1 h. Anti-FLG goat G20 (Santa Cruz), and the secondary anti-goat Alexa488 (Life Technologies) antibody staining was carried out in PBS for 1 h. The nuclei were visualized by Hoechst (NucBlue, Life Technologies). The sheets were mounted on microscope coverslides with Mowiol 4-88 (Sigma) for imaging. Data acquisition was carried out on the Zeiss 780 inverted confocal microscope by recording z-stacks of 2D images (at 0.38 μM intervals) and images taken using inverted confocal microscope (Zeiss 780) by recording 2D images in a 3D z-stack.

Western Blot Analysis

Isolated epidermal sheets were washed in PBS and incubated in an 8M urea buffer (ReadyPrep™ Sequential Extraction Kit, Reagent 2 with reducing reagent; Bio-Rad) and sonicated in a water bath for 30 min. Lysates were spun at 4°C (13,000 rpm, 15 min). Proteins from supernatants were fractionated 7% Tris-Acetate NuPage gels (Life Technologies). Proteins were transferred onto PVDF membranes (iBlot Dry Blot system stacks and iBlot transfer device; LifeTechnologies). Membranes were blocked in a 5% solution of non-fat milk powder in PBS and incubated overnight with desired primary antibodies (anti-FLG goat G-20 (Santa Cruz). Li-Cor infrared secondary antibodies and Li-Cor scanning system (Li-Cor Biosciences) were used for detection.

RNA Isolation and the Assessment of RNA Integrity

Isolation of total RNA from N-HEK cells was performed using the PureLink® RNA Mini Kit (Ambion) according to the manufacturer's protocol. The RNA concentration and purity was estimated using NanoDrop 2000 (Thermo). The assessment of RNA quality was carried out on the Agilent 2100 Bioanalyzer System and Eukaryote Total RNA Nano Assay kit (Agilent) was used, according to the manufacturer's protocol.

Reverse Transcription

Isolated RNA was used as a template for the reverse transcription. The reaction was performed in a S1000™ Thermal Cycler (Bio-Rad) in 20 μl using the High-Capacity cDNA Reverse Transcription Kit (Applied Biosystem) according to the manufacturer's protocol. The ingredients contained: 1,000 ng RNA per sample, reaction buffer, random primers, mix of dNTPs, RNase inhibitor (1.0 U/μl) and MultiScribe™ reverse transcriptase (2.5 U/μl). Conditions of RT reaction are presented in the table below.

Quantitative Real-Time PCR

Gene expression assay was counducted using the StepOne™ Real-Time PCR System and the TaqMan® Gene Expression Assay (Applied Biosystems). Briefly the reaction (holding stage I: 2 min, 50°C; holding stage II: 5 min, 95°C; Cycling stage (40x): 15 s, 95°C and 1 min, 60°C) was performed in 10 μl total volume with 12.5 ng of cDNA (or water as a negative control) addition. TaqMan® Universal Master Mix II with the AmpErase® UNG (uracil-N-glycosylase) (Applied Biosystems) was used. The primers (forward: 5′–GGAAAAGGAATTTCGGCAAAT–3′, reverse: 5′–TCCATGAAGACATCAACCATATCTG–3′) and the TaqMan® MGB probe (5′–FAM CTGAAGAATCCAGATGAC-NFQ-MGB–3′, Applied Biosystems) set for *FLG* gene was designed using Primer Express software (Applied Biosystems) and the specificity was checked using PrimerBLAST tool (NCBI). The specificity of the primers and probe set was confirmed by adequate negative controls. Results were calculated based on a ΔC_T method and *TBP1* (TATA-box binding protein 1) gene (commercially available primer and probe set, accession number: Hs00427620, Applied Biosystems) was used as a reference. For statistical analyses the *t*-test was used.

Langerhans Cell-like Cells

Peripheral blood mononuclear cells (PBMCs) were isolated from blood collected from healthy adult donors under local ethics approval (09/H0606/71). Samples were diluted and centrifuged in a density gradient using a Lymphoprep™ reagent (STEMCELL Technologies Inc.). The $CD14^+$ cells were separated with a MACS MicroBead (Miltenyi Biotec) magnetic separation system according to the manufacturer's protocol. Subsequently, the monocytes were cultured in a 1×10^6/ml density in the RPMI medium supplemented with 10% fetal calf serum, penicillin/streptomycin mix and 2 mM L-glutamine, with addition of cytokines: 250 ng/ml GM-CSF, 100 ng/ml IL-4, 10 ng/ml TGF-β1, all obtained from Pepro-Tech. After 5 days of culture, the cells were exposed to a $Ni(NO_3)_2$ solution (1 mM), peptides (50 μM) or Ni^{2+}-peptide complexes with the same concentrations of peptides and of the nickel salt. After 48 h the cells were harvested for the flow cytometry analysis.

Flow Cytometry

The cells were harvested by decantation into a conical tube and centrifuged (10 min, 1,400 rpm, 4°C). Supernatants were collected and frozen until further analysis. Next, the cells were washed in ice cold 10% FCS in PBS and stained. All staining was carried out on ice and protected from light. Conjugated primary antibodies: anti-human CD86 (APC) and HLA DR (PE), CD80 (FITC) were added in 0.1–10 μg/ml concentration range and incubated for 1 h in the dark at 4°C. The cells were washed three times in PBS and centrifuged (5 min, 1,400 rpm, 4°C), and resuspended in 1 ml of ice cold PBS, containing 10% FCS and 1% sodium azide. The cells were fixed in 1% paraformaldehyde solution and kept in the dark on ice until the analysis. The cytometric analysis was performed on CyAn™ ADP (Beckman Coulter). First, using unstained cells and compensation beads (Anti-Mouse Ig, κ/Negative Control Compensation Particles Set, BD), the compensation procedure was performed. The FCS Express 7 Flow Cytometry Software—RUO, DeNovo Software were used for the final analysis. The results were analysed with the *t*-test.

Analysis of Cytokine Secretion

Cytokine levels (TNFa, IFNa2, IL1b, IL-6, IL-8, IL-10) in the cultures medium was measured by the Luminex 200™ System (Merck Millipore) and Milliplex HCYTOMAG-60K-07 Human

Cytokine MAGNETIC Kit (Merck Millipore). The assay was performed according to the manufacturer's protocol. The results were analysed with the *t*-test.

RESULTS

Ni-Hydrolytic Motifs Are Common in the Human Proteome and Enriched Within Sequences of the Epidermal Barrier Proteins

Our first goal was to characterize and catalogue the distribution of Ni-cleavable motifs within amino acid sequences of human proteins. To this end, the initial UniProt data were cleaned by suitable word filters to eliminate duplicates (partial, truncated or fragmented proteins), while all protein isomers were included to obtain full representation of the functional proteome. This initial data set of 79,077 proteins was searched for the general X_1-S/T-c/p-H-c-X_2 motifs and for the particularly interesting G-S/T-c/p-H-c-X_2 motifs, obtaining 31,099 (**Supplementary Table S1**) and 4,111 (**Supplementary Table S2**) records, respectively. We also prepared complementary lists of proteins without X- (**Supplementary Table S3**) and G- (**Supplementary Table S4**) motifs. We then determined the absolute number of motifs per protein, their frequency (the count normalized by the length of a given protein, **Supplementary Table S1, S2**) and the number of motifs by the type (**Supplementary Tables S5, S6**).

Overall, we determined that as many as 40% of human proteins contain at least one Ni-hydrolytic motif, and 5% of all human proteins contain at least one fast motif (**Figure 1B**). The analysis of amino acid frequencies in these motifs revealed a significant overrepresentation of X_1 = G in both S and T motif variants (**Figures 1C,D**). The cumulative distribution function (CDF) of X_1 = G illustrates this finding (**Figure 1E**).

Notably, we obtained 13 statistically significant gene ontology (GO) terms for the proteins containing the G-motifs (p-value ≤ 0.05 after multiple testing correction); these relate mainly to organ development, organization and morphogenesis (**Supplementary Tables S7, S8**). For general Ni-hydrolytic motifs the number of statistically significant GO terms after correction was 145, with 56 related to the mechanisms of regulation of biological processes. We also distinguished a group of 27 GO terms related to the nervous system development, such as regulation of neuron projection development, axon guidance, brain development, neurogenesis and synapse assembly. Further 11 GO terms are related to transcription and gene expression. Detailed classifications of GO terms are provided in **Supplementary Tables S9, S10**. Overall, the quantitation of occurrence of the Ni-hydrolytic motifs suggests a significant coincidence with the developmental and neuronal functions. Using our database we have also selected immune-related proteins potentially susceptible to Ni-hydrolysis including tumor necrosis factor superfamily, interleukins and interleukin receptors, toll-like receptors and cluster of differentiation proteins (**Supplementary Table S11**).

The occurrence of hydrolytic motifs in the individual human proteins was compared quantitatively with the expected frequencies of the amino acids (**Figures 1F,G**). Central portions of those occurrences adhered to the Poisson distributions for both general and G-motifs. However, in both cases there were groups of proteins which substantially deviated from the Poisson distributions, especially those with more than 34 occurrences of the general motifs and 20 occurrences of the G-motifs. Strikingly, proteins with the higher than expected number of these motifs are mostly involved in the epidermal (filaggrin, filaggrin-2, hornerin) and mucosal (mucins) barrier functions (**Supplementary Tables S12, S13**) which could be important, given that the skin and airway mucosa provide the first line of defence against toxic nickel materials.

Ni-Hydrolysis Occurs in Filaggrin Model Peptides and the Recombinant Filaggrin Monomer Domain

The barrier proteins abundant in the Ni-hydrolytic motifs are potential targets for Ni^{2+} ions and their concomitant hydrolysis might compromise their function. We chose FLG for the *in vitro* and *ex vivo* experimental verification of this hypothesis due to its largest number of G-motifs (67 in proFLG) and its importance in protection from allergic sensitization, including to nickel (Novak et al., 2008). We also searched our database for other proteins related to keratinocyte differentiation. Interestingly, lorricin, involucrin, trichohyalin and elafin do not contain any hydrolytic motifs, while the previously mentioned filaggrin, filaggrin-2 and hornerin are enriched with such motifs (**Supplementary Table S14**).

The FLG monomer domains were identified on the basis of the amino acid sequence of human proFLG, (NCBI database Ref. NP_002007.1) and a prior study on the proFLG component domains (Sandilands et al., 2009). The resulting domains were compared using the WebLogo 3 application. A typical FLG monomer domain contains 17 potential Ni-hydrolytic sites including 7G-motifs with a high degree of conservation, as shown in **Figure 2A**. Next, we chose eight oligopeptides containing Ni-hydrolytic motifs best representing the cleavage sites, taking into account the variability of third and fifth positions in the X_1-S/T-c/p-H-c-X_2 sequence (**Supplementary Table S15**). The abbreviation numbers of filaggrin peptides (FP) denote the order of their occurrence in the monomer (**Figure 2A**). Molecular modelling of ten structures of Ni^{2+} complexes with these peptides characterised by the lowest calculated energy levels repeatedly showed square-planar structures with Ni^{2+} chelate ring conformations very similar to each other (**Figure 2B**, **Supplementary Figure S2**). Next, comparative CD and UV-vis spectroscopic pH titrations were performed in a broad pH range, yielding the pH dependence of complexation (**Figure 2C**, **Supplementary Figure S3**). The calculated pK values showed the absence of stable square-planar complexes below pH 7 for all peptides. Since the Ni^{2+} binding at the individual hydrolytic motifs depends solely on the local sequence, and most of these sites are sufficiently separated from each other, this property of model peptides could be extrapolated over the entire protein (Kopera et al., 2010; Krezel et al., 2010).

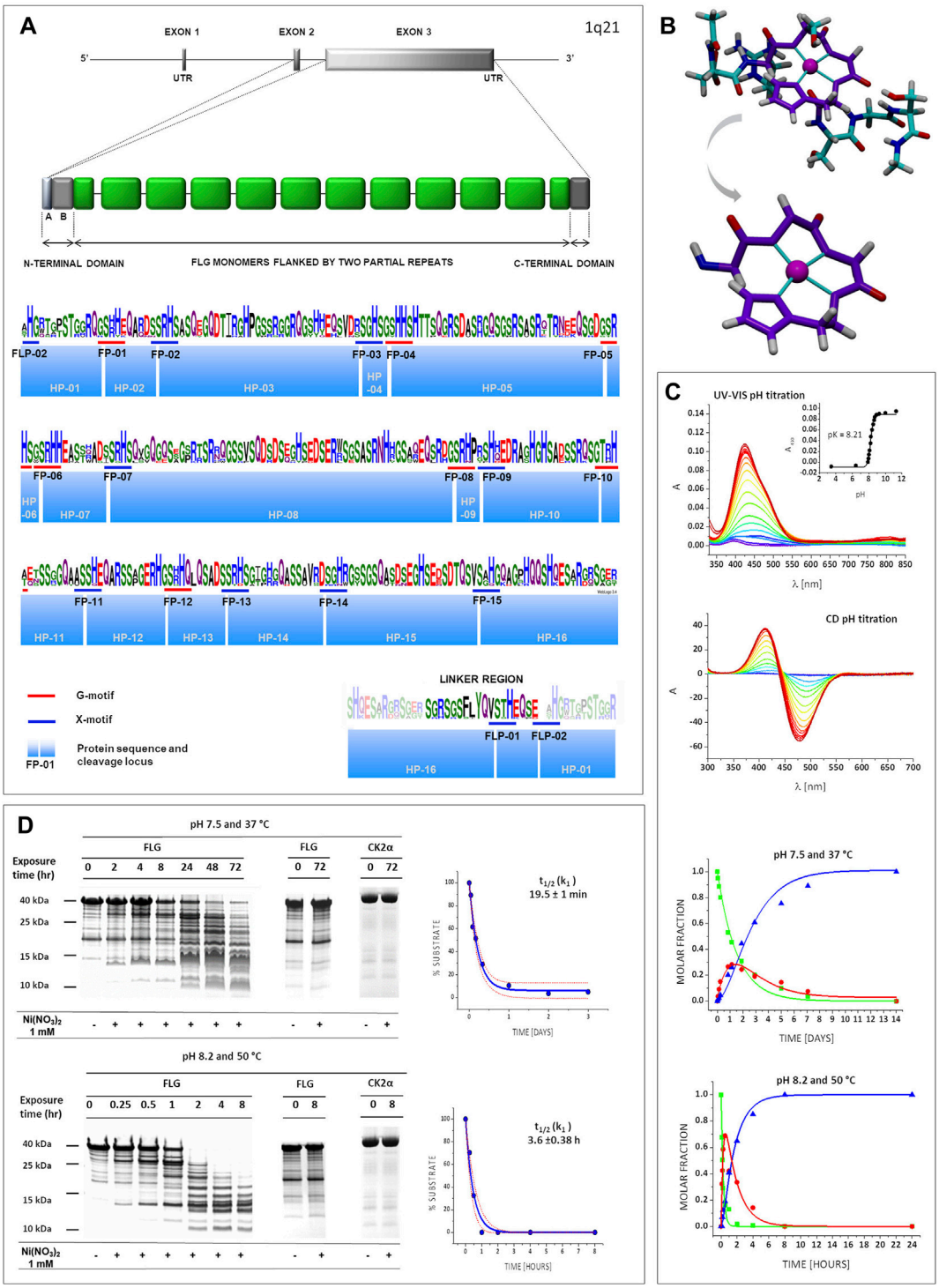

FIGURE 2 | FLG structure and susceptibility to Ni-hydrolysis. **(A)** The *FLG* gene, located on chromosome 1q21, consists of three exons and two introns. ProFLG protein contains several nearly identical FLG monomer units (green) flanked by partial monomer repeats and the N- and a C-terminal domains (dark grey). Each FLG monomer unit is separated from the other repeats by a linker region that is proteolytically cleaved during processing of proFLG into monomers [adapted from Sandilands et al. (2009)]. A graphical representation of an amino acid multiple sequence alignment is shown; the height of a stack indicates the sequence conservation, while the height of symbols within the stack indicates the relative frequency of each amino acid at that position. Colours of amino acids according to chemical properties: polar (green), neutral (purple), basic (blue), acidic (red), hydrophobic (black). Blue and red bars symbolize Ni-hydrolytic motifs; blue boxes symbolize oligopeptides, predicted products of Ni-hydrolysis (HPs). FPs (FLG peptides) and FLP (FLG linker peptide) means consecutive cleavage motifs within the FLG sequence. **(B)** Molecular model of a representative complex (Ni-FP-05). Atoms are marked as: cyan (C), red (O), white (H), indigo (N) and magenta (Ni). 4N square planar structure is highlighted in purple. **(C)**

(*Continued*)

FIGURE 2 | Complexometric and kinetic studies for the Ni-FP-05 complex. CD and UV-VIS pH titration: The pH values marked with colour gradient from dark blue (the lowest pH, 3.5) to red (the highest pH, 11.5). Kinetic studies for the hydrolysis: green squares (substrate), red circles (intermediate product), indigo triangles (final products). **(D)** Ni-hydrolysis of a FLG monomer. Representative gels (left panel) and $t_{1/2}$ (k_1)graphs (right panel). showing results of cleavage The experimental points are present within the $p = 0.05$ confidence bands, calculated on the basis of the fitted kinetic curve with its standard deviation (red, dotted line).

Subsequently, we studied the kinetics of FPs hydrolysis as in our previous work (Kopera et al., 2010), using both harsh (50°C, pH 8.2) and physiological (37°C, pH 7.4) conditions. The peptides were hydrolysed in all cases (**Figure 2C**, **Supplementary Figure S4**). The kinetic parameters were calculated according to the model of the two sequential first order processes of the intermediate ester formation and decay into final products, as stipulated by the reaction mechanism (Krezel et al., 2010; Podobas et al., 2014). The values of k_1 and k_2 rate constants, describing these reaction steps, are presented in **Supplementary Table S16**. The reaction rates varied depending on the peptide sequence, and the hydrolysis was much faster in harsh conditions, as expected (Kopera et al., 2010).

Next, we confirmed the occurrence of Ni-hydrolysis for the FLG monomer domain, using the recombinant 10th FLG monomer domain (FLG-10, full sequence in **Supplementary Table S17**). The nickel concentration differed from that used in the peptide model experiments (2 and 1 mM respectively). Nickel hydrolysis has been the subject of extensive investigations in our research group. The conditions chosen for model oligopeptide studies corresponded to previously described experiments on similar peptides (Protas et al., 2013; Podobas et al., 2014; Wezynfeld et al., 2014). The conditions used for FLG domain had lower total Ni^{2+}, but higher Ni^{2+}/peptide ratio and were aimed at more accurate mirroring of the skin conditions. We would like to note that the Ni^{2+}/peptide ratio is more relevant for the reaction rate than the absolute Ni^{2+} concentration, but the rate is ultimately controlled by the cleavage site saturation (Kopera et al., 2010). Recombinant maize protein kinase CK2α which has no Ni-hydrolytic sites (full sequence in **Supplementary Table S18**) served as a negative control (**Figure 2D**). Therefore, FLG cleavage resulted specifically from the Ni^{2+} presence rather than a residual protease activity. In order to compare the kinetics of the hydrolysis of FLG-10 vs. the FPs, the rate constants for the latter were recalculated by fitting the first order rate law to the final reaction product formation, as described previously (Krezel et al., 2010) (**Supplementary Figure S5** and **Supplementary Table S16**). This was done since only the final reaction products could be quantified in protein gels, while the separate k_1 and k_2 values could be determined for the peptides for an excellent separation of the respective reaction products by HPLC approach (Podobas et al., 2014). The FLG-10 hydrolysis products showed a reproducible pattern of bands, i.e., initially, the two dominant masses (around 25 and 12 kDa) appeared, followed by subsequent hydrolysis of the 25 kDa fragment. The final hydrolysis products had masses within the range of 9–12 kDa, correlating with the cleavage primarily within FP-05 followed by FP-09 and FP-10. As presented in **Figure 2D**, the $t_{½}$ for the final product formation at harsh conditions (pH 8.2, 50°C) was ca. 20 min vs. 3.6 h at physiological conditions (pH 7.4, 37°C), both reactions proceeded according to the pseudo-first order rate law. The similar time evolution of gel band patterns at these two conditions indicated that the relative reaction rates at individual cleavage sites were maintained in FLG-10. The comparison of fragment sizes at the shortest incubation times with the pattern predicted from the sequence analysis and reactions of peptides confirmed FP-05 and FP-13 as initial reaction sites, followed rapidly by other sites; the entire protein was cleaved into small fragments within hours. Under harsh conditions the rate constant for the FLG domain decay is roughly equal to the sum of rates at the individual hydrolysis sites (**Supplementary Figure S6A**), while for the physiological conditions the FLG decay is several fold faster than one might expect from the model peptide data **Supplementary Figure S6B** (note that according to the reaction mechanism the rate constants for cleavages at different FLG sites add up to the overall rate of the domain decay). Altogether, we noticed that at physiological conditions the domain decayed ca. 10 times slower in comparison to the harsh conditions. The multiplicative effect of lowering the reaction temperature and pH on the reaction rate can be estimated as ca. 60–70, stemming from the temperature factor, ca. 2–2.5 and the pH factor, ca. 20–50 (Kopera et al., 2010); here we estimated ca. 40–50 for the most active peptides (**Supplementary Figure S6C**).

Ni-Hydrolysis of Filaggrin Occurs in Human Keratinocytes *In Vitro* and in Human Epidermis *Ex Vivo*

Having determined that the recombinant FLG monomer domain and its model peptides are cleaved by Ni-hydrolysis, we went on to investigate the biological meaning of this phenomenon at both the cellular and tissue levels. Since FLG is expressed predominantly in keratinocytes which are well differentiated, for the cellular study we used normal human epidermal keratinocytes, NHEKs, cultured in the differentiation-promoting medium, i.e. previously well-established calcium-switch model (Gutowska-Owsiak et al., 2018; Gutowska-Owsiak et al., 2020) (**Figure 3A**). These experiments determined that both the number and sizes of KHGs in NHEKs were reduced upon the Ni^{2+} treatment. Interestingly, some positive staining with anti-FLG antibodies could be observed as KHG-unrestricted cytoplasmic or filamentous signal, suggesting the release of the antibody-reactive FLG-derived peptides into the cytoplasm and potentially binding of those to the intermediate keratin filaments in accordance to the native function of FLG monomers.

To investigate the effect of Ni^{2+} on the abundance of FLG in the stratified epidermis, we used *ex vivo* epidermal sheets obtained from skin samples collected from healthy donors (**Figures 3B,C**). The exposure to Ni^{2+} resulted in pronounced reduction in the abundance of FLG^+ KHGs compared to the control samples incubated in the absence of Ni^{2+}, as seen in

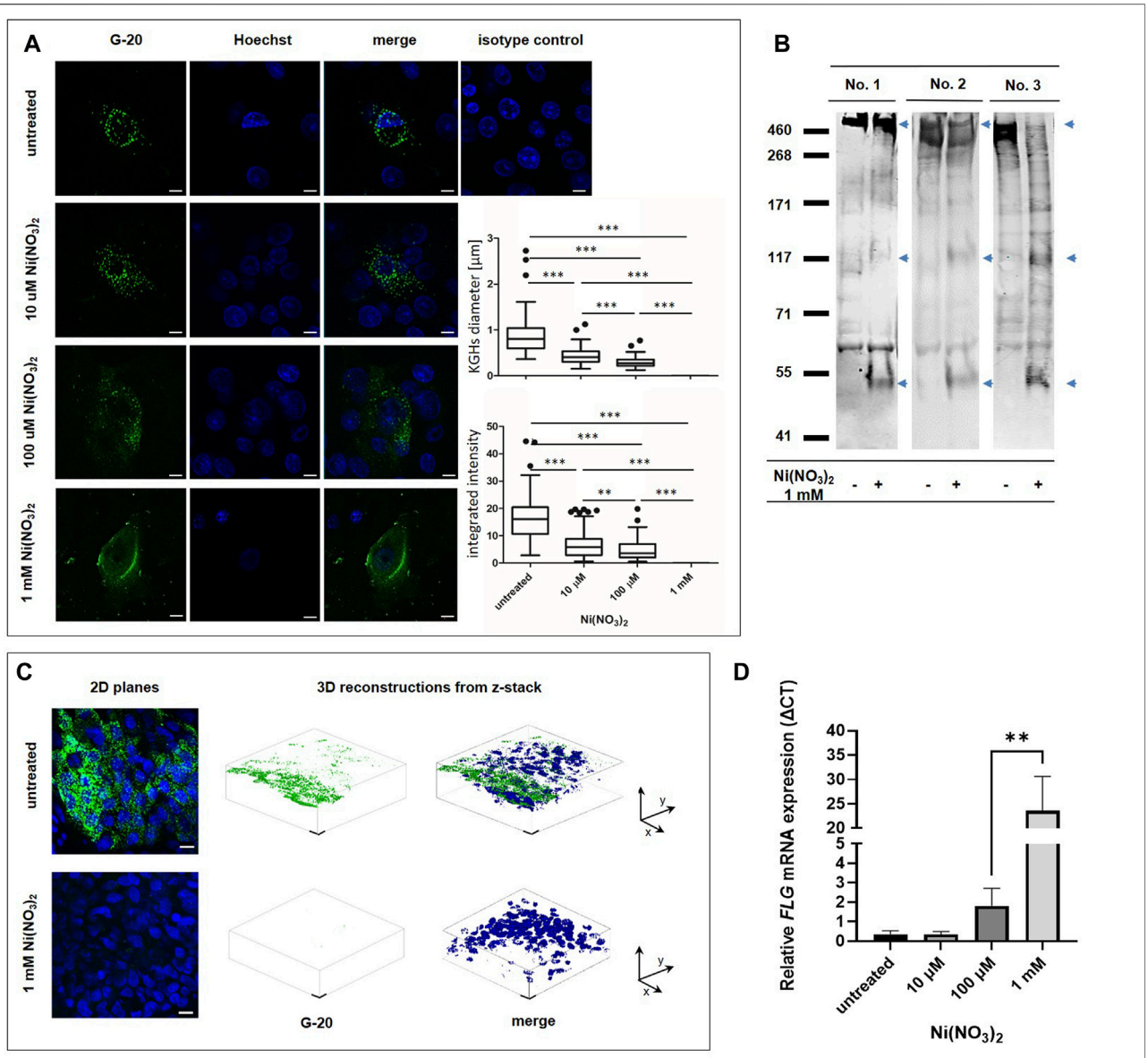

FIGURE 3 | FLG hydrolysis in human keratinocytes *in vitro* and human epidermis *ex vivo*. **(A)** 2D scanning confocal images of fixed NHEK cells immunostained for FLG (green)) and nucleus (blue) after 24 h of treatment with $Ni(NO_3)_2$. Scale bar (10 µM). Diameter of KHGs and integrated intensity from the signal are presented on the Tukey box plots (n~100 pooled counts from images from 3 independent experiments). In 1 mM nickel concentration it was not possible to observe granules. Error bars represent standard deviation. *p*-value = 0.031 (*t*-test). The main body of the boxplot indicates the interquartile ranges (IQR). Whiskers represent 1.5 x IQR. The median is marked by horizontal lines. Statistical significance is marked with asterisks: (**) *p*-value = 0.0012, (***) *p*-value < 0.0001 (Mann–Whitney *U* test). **(B)** Western blot analysis of FLG level in human epidermal sheets *ex vivo* after treatment 1 mM $Ni(NO_3)_2$ for 36 h, using internal G-20 anti-FLG antibody. Arrows mark the appearance of additional bands due to the cleavage. **(C)** Immunostaining of epidermal sheets with anti-FLG antibodies (green and nucleus (blue). 2D planes and 3D reconstructions from z-stack are presented. Scale bar (10 µM). **(D)** Changes in *FLG* mRNA expression in NHEK cells upon treatment with $Ni(NO_3)_2$ for 24 h. The graph presents ΔCT values with relative to the *TBP1* housekeeping gene expression. Error bars represent standard deviation. *p*-value = 0.031 (*t*-test).

confocal microscope 2D- and Z-stack images. Incubation with 1 mM of Ni^{2+} resulted in a complete disappearance of KGHs. Western blot assessment confirmed this reduction at the protein level in the epidermal sheets exposed to the Ni^{2+} salt. The reduction in the signal coming from the proFLG band (the highest band above 400 kDa) was accompanied by disappearance of the signal of lower molecular weight bands and appearance of unusual bands (marked by arrows on **Figure 3B**); this was confirmed for the epidermis obtained from three different donors.

The observed reduction in the FLG-related signal was due to the protein degradation and not to the mRNA level suppression, as demonstrated by the quantitative real time PCR performed on NHEKs, where we observed FLG mRNA upregulation with the increasing Ni^{2+} concentration (**Figure 3D**), likely as a compensatory mechanism.

Products of Filaggrin Ni-Hydrolysis Affect Langerhans Cells Activation Profile

Finally, we evaluated the impact of Ni-assisted FLG hydrolysis on the phenotype of antigen presenting cells. Here, monocyte derived Langerhans cells (MDLCs) were used to investigate the activation potential of Ni^{2+} complexed to products of hydrolysis of ex-FLG peptides (HP, **Figure 2A**). Their full amino acid sequences are presented in **Supplementary Table S15**. For comparative purposes the CD and UV-vis spectroscopic pH titrations of these complexes were performed in a broad pH range. The spectra and titration curves are presented in **Supplementary Figure S7**. The complex formation process was monophasic, and spectral parameters could be readily assigned to 4N complexes in all cases. In the CD spectra the alternate pattern of d-d bands was observed, typical for the ATCUN motifs (Ariani et al., 2013). All pK values fall in the range of 5.4–5.8, which corresponds to the conditional dissociation constants at pH 7.4 in the range of 1 to 0.1 μM (Sokolowska et al., 2002). We also calculated ten lowest energy structures for all the HPs. The examples of calculated structures of the complexes with Ni^{2+} are presented in **Supplementary Figure S8**. In every structural variant, the nickel chelate ring conformations with imposed square planar structure are very similar to each other while the N-terminal and C-terminal parts are much more diverse and adopt many conformations in the simulated structures.

MDLCs were incubated with mixed peptides (HP-02, HP-06, HP-07, HP-12, HP-13, HP-14) and the Ni^{2+}-complexes (Ni-HPs) formed in molar nickel excess; $NiSO_4$ serving as a control; the MDLCs activation was assessed using flow cytometry. In order to gain deeper insights into possible immune pathways that may be affected by the HPs, we also quantified the release of six cytokines from MDLCs, five of which are pro-inflammatory (IFN-α, TNF-α, IL-1β, IL-6, IL-8) and one anti-inflammatory (IL-10). The Luminex assay was performed for HP-06, HP-07 and HP-12.

We noted statistically significant changes between the experimental conditions in results obtained from the same monocyte donor. However, the analysis of pooled results from different biological experiments (between different donors) did not show statistical significance, possibly due to the interindividual variation or relatively low sample number (**Supplementary Table S19, S20**). Observed trends showed that while the presence of FLG-derived peptides alone did not affect the MDLCs profile in a substantial way, the addition of Ni-HPs resulted in an upregulation of the activation markers (CD86 and HLA-DR) on the cells and a parallel complete loss of the CD80-positivity (**Supplementary Figure S9**). Ni^{2+} and Ni-HPs conditions are correlated with the increased percentage of $CD86^+$ and $HLA\text{-}DR^+$ cells and loss of the CD80-positivity. As far as the cytokine responses are concerned, we noticed a trend of increased levels of TNFa, IL-6, IL-8 in Ni-HPs in comparison to the nickel only condition (**Supplementary Figure S10**).

Analysis of Hydrolytic Motifs Within Filaggrins From Various Species

Comparison of numbers of cleavage motifs between species shows a number of details. The full list of motif counts is presented in **Supplementary Table S21** and visualised by the tree of life annotated with hydrolytic motifs datasets (**Figure 4**). Filaggrin, filaggrin-2 and filaggrin-like proteins were taken into consideration. Analysed species are assigned to the following orders: *Primates* (23), *Artiodactyla* (15), *Carnivora* (11), *Rodentia* (8), *Perissodactyla* (3), *Chiroptera* (2), *Lagomorpha* (2), *Tubulidentata* (1), *Pholidota* (1), *Proboscidea* (1), *Dermopter*a (1), *Scandentia* (1), *Afrosoricida* (1), *Sirenia* (1), *Eulipotyphla* (1), *Macroscelidea* (1), *Didelphimorphia* (1), *Cingulata* (1), *Dasyuromorphia* (1). Filaggrin-like proteins from *Cichliformes* and *Cyprinodontiformes* (*Pisces*) were also included. In all groups of more than 2 species, one can notice differentiation in terms of the number of motifs. In Primates however, filaggrins seem to be enriched; count at least 40 motifs per protein in most cases. Filaggrin in *H.sapiens* is at the top of the list here. Interesting outcome is the startling difference between the number of sites between humans and rodents. Since mice and rats are experimental species this difference shows possible issues when comparing human and rodent data.

DISCUSSION

The dermal contact with nickel mostly results from surface corrosion of metal objects of daily use by human sweat (Midander et al., 2007). While the dissolved Ni^{2+} ions enter cells adventitiously *via* a divalent metal transporter (DMT) (Chen et al., 2005) or calcium channels (Funakoshi et al., 1997), the highest load results from the phagocytosis of nickel-containing particles, e.g., intracellular concentrations up to 4.75 M Ni^{2+} were calculated for nickel sulphide (Cangul et al., 2002) https://paperpile.com/c/I6dnK0/jWy7l. It is not a typical scenario for skin exposures, but nevertheless possible after contact with nanoparticles from the polluted air in the industrial environment or after contact with nickel particles scratched from the metal surface. Nickel deposition and *stratum corneum* penetration seems to be significant after relatively short exposure (Ahlström et al., 2018). It is known that nickel is accumulated mostly in a bound state in *stratum corneum*; in contrast, only minor concentrations were found below this layer in healthy skin (Fullerton and Hoelgaard, 1988; Hagvall et al., 2021). Ahlström et al. quantified metallic nickel penetration into the *stratum corneum*; nickel deposition was found to be in the range between 10.1 and 23.5 $\mu g/cm^2$ after three 10-min exposures. (Ahlström et al., 2018). Simultaneously range 0.45–12 ug/g of nickel was confirmed in tattooed skin (Kluger, 2021).

The Ni-hydrolysis of specific susceptible protein motifs is a candidate molecular mechanism of nickel allergy and additional adverse effects of nickel exposure in humans (Wezynfeld et al., 2016). We show that such motifs are present in as many as 40% of human proteins. Among them, the glycine-containing motifs are significantly overrepresented.

The gene ontology analysis revealed that proteins containing those Ni-hydrolytic motifs take part in diverse biological processes including transcription and gene expression; thus, we propose that unspecific proteome degradation may lead to a disturbance of cell homeostasis, contributing to both the known mechanisms of nickel toxicity as well as additional underlying adverse processes not yet ascribed to the nickel exposure. Strikingly, at the organism level, FLG and other barrier proteins known for their role in maintaining the

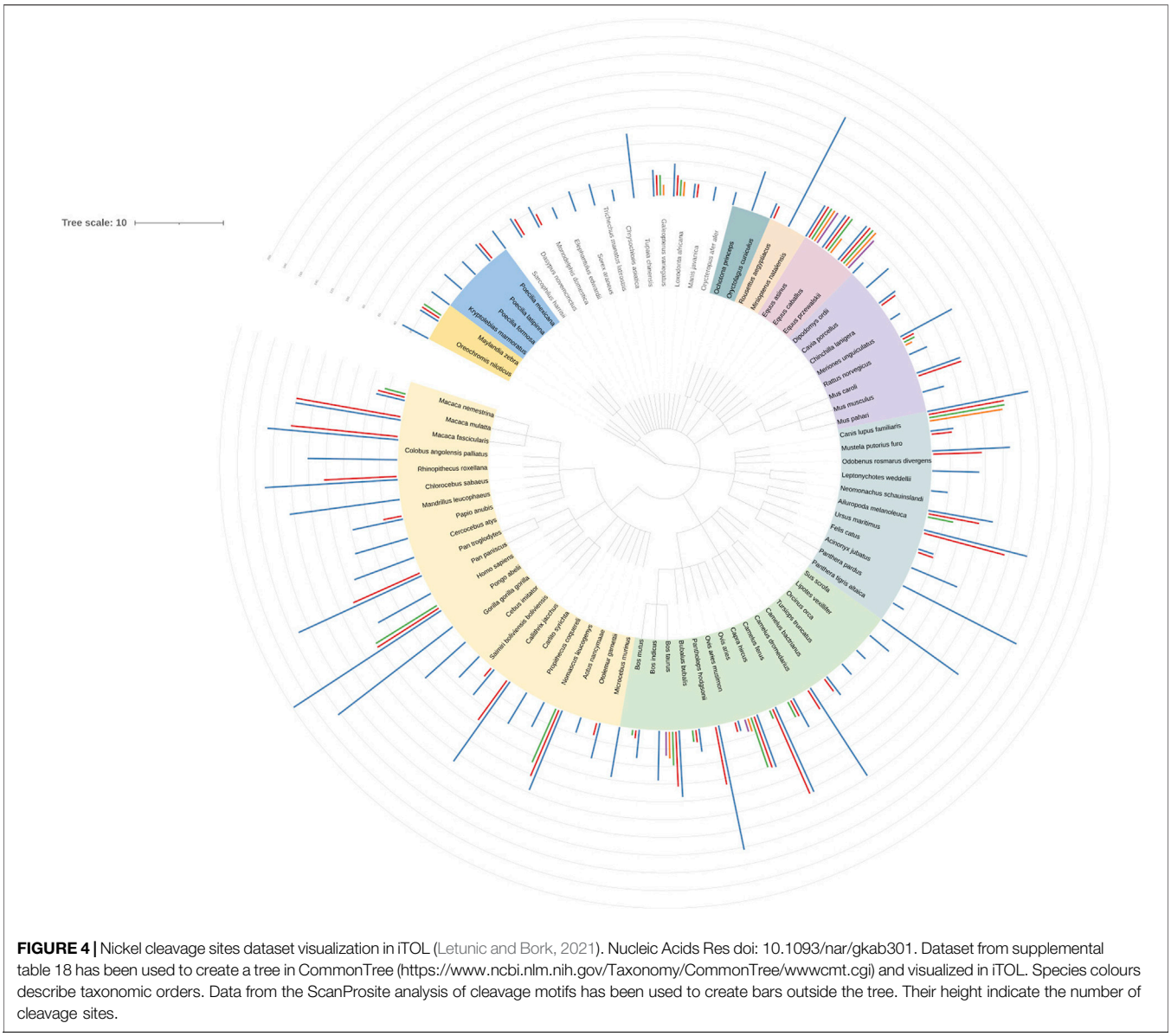

FIGURE 4 | Nickel cleavage sites dataset visualization in iTOL (Letunic and Bork, 2021). Nucleic Acids Res doi: 10.1093/nar/gkab301. Dataset from supplemental table 18 has been used to create a tree in CommonTree (https://www.ncbi.nlm.nih.gov/Taxonomy/CommonTree/wwwcmt.cgi) and visualized in iTOL. Species colours describe taxonomic orders. Data from the ScanProsite analysis of cleavage motifs has been used to create bars outside the tree. Their height indicate the number of cleavage sites.

integrity of the epidermal barrier and the mucosa, exhibit high incidence of Ni-hydrolytic motifs, making them susceptible to nickel-induced degradation. FLG seems to be especially susceptible, since a single FLG domain contains 17 individual hydrolytic motifs in a repetitive pattern, conserved within all the monomer domains; this results in nearly 200 potential cleavage sites in a single proFLG molecule.

Information about FLG evolution in vertebrate is limited. Comparison nucleotide diversity between FLG repeat regions in primates showed that FLG repeats evolved under the birth-and-death model probably as a consequence of species-specific divergence and expansion (Romero et al., 2017). Skin interacts with the environment what potentially expose it to many adaptive factors. However, because of living in modern and industrialised environment, the character of those factor changed comparing to the natural environment. The purely anthropogenic character of the nickel exposure, related to the industrial revolution and lasting for not more than 250 years (8–10 generations, mine production of nickel began in Norway in 1848) is too short for an evolutionary adaptation to a mildly lethal agent (Kasprzak et al., 2003). The amino acids frequencies within hydrolytic motifs indicate the absence of evolutionary pressures to eliminate them. On the other hand, hydrolytic motifs are present in other non-human species. This suggest that the mutations responsible for the formation of hydrolytic motifs were independent and repetitive. Thus, we should to consider non-anthropogenic factors rather including a possible role of skin microbiome. There has been evidenced of the coevolution between skin microbiota and their corresponding host species (Ross et al., 2018). There are also evidences of the coevolution between skin microbiota and their corresponding host species (Ross et al., 2018). We should not than exclude a possible role of skin microbiome on the filaggrin composition.

Based on our results, we could expect rapid degradation of FLG domains. Interestingly, the hydrolytic sequence present in the inter-domain linker was very poorly reactive, indicating that Ni^{2+} ions would not assist the release of FLG monomers from proFLG with and only the intradomain cleavage resulting in abnormal FLG fragments is likely. The pK values for the complex formation obtained from spectroscopic titrations indicate that hydrolytically productive complexes can form only above pH 7. Due to the locality of Ni^{2+} binding to FLG this feature can be extrapolated over the entire protein. However, the hydrolysis is extremely slow below the pH of 7, as it is enabled by a pH-dependent square-planar Ni^{2+} complex (Kopera et al., 2010). This suggests that in healthy skin, characterised by the surface pH ranging from 4.1 to 5.8 (Segger et al., 2008), Ni-hydrolysis is unlikely. We cannot exclude a possible beneficial effect of the high number of Ni-hydrolysis motifs in FLG. In fact, the repetitive nature of the proFLG structure could possibly point to this. In the case of nickel, there is certainly a strong possibility given the importance of FLG gene null mutations associated with nickel contact sensitization (Novak et al., 2008; Thyssen et al., 2010). It is postulated that FLG chelate Ni^{2+} ions by its numerous histidine side chains and prevent their penetration into deeper layers where interaction with the immune system can promote nickel sensitization (Fullerton and Hoelgaard, 1988; Sigel et al., 1990; Thyssen et al., 2010; Hagvall et al., 2021). It should be first noted that the Ni^{2+}-related FLG hydrolytic degradation yields specific oligopeptide complexes in which Ni^{2+} ions are bound more strongly than the original substrate. Moreover, the Ni^{2+} binding should be expected to protect the local sequence S/T-X-H from further proteolysis, by shielding the peptide bonds. Then, the formation of these complexes could potentially facilitate Ni^{2+} penetration of the organism, depending on the properties of these peptides, e.g. the hydrophobicity for membrane penetration. Altogether, the binding of Ni^{2+} to FLG without hydrolysis (possible at low pH) will be protective against Ni^{2+} penetration, but the hydrolysis products may not be as efficient.

However, skin inflammation and keratinocyte differentiation defects lead to a reduction in the content of acidic FLG breakdown products constituting the natural moisturising factor (NMF, i.e., urocanic acid, UA and pyrrolidone carboxylic acid, PCA) within *stratum corneum*. This may result in the elevation of pH up to 9 locally (Schreml et al., 2011) with consequential activation of serine proteases and excessive desquamation. Exposure to Ni^{2+} causing abnormal FLG cleavage could impair NMF generation and further compound the barrier deficiency. On the other hand, Ni-hydrolysis of FLG could also take place intracellularly (pH 7.0–7.4) (Madshus, 1988), as it was demonstrated previously for histone H2A for several cell lines incubated with a $NiCl_2$ solution (Karaczyn et al., 2003; Schreml et al., 2011).

We have indeed shown a decrease in KHGs-concentrated proFLG levels compared to controls incubated without $Ni(NO_3)_2$ both at the cellular and tissue levels. However, there are some limitations to this study that could be addressed in future research. First, the work focused on estimating changes in FLG concentration mainly on the basis of immunolocalization and immunodetection techniques. We performed RT-qPCR experiments on *Flg* mRNA levels. This should also be repeated on the epidermal sheets. We could possibly use an additional method to measure the detrimental effect of nickel on the FLG. Quantification of the NMF compartments such as PCA or UCA NMF might be a solution (Koppes et al., 2017). The second limitation that should be discussed here is relatively high nickel concentration used in experiments on the epidermal model. Our aim was to fully saturate all hydrolytic motifs within proFLG with nickel; nickel ions may be chelated by other histidine-rich proteins what might significantly reduce the exact Ni^{2+} concentration and possibly mask the effects of hydrolysis. The IC_{50} value of $Ni(NO_3)_2$ was 1 mM for the monolayer keratinocytes cultures (**Supplementary Figure S1**). Thus, some not directly related with nickel-hydrolysis toxic effects might occur. However, the data gathered from a Western blot indicated a repetitive pattern of proFLG degradation (**Figure 3B**). This can be explained by the diverse hydrolysis rates for different motifs. Nevertheless, additional analysis related to FLG monomers in the epidermis would be supplemental.

While the rate constant for the FLG domain decay is roughly equal to the sum of rates at individual hydrolysis sites under harsh reaction conditions, it is several fold higher than expected from these data for the physiological conditions. This can be tentatively interpreted as follows: at harsh conditions all His side chains have lost their positive charges, which may result in the loss of prestructuring of Ni^{2+} binding sites enabled by ionic interactions and H-bonds. Such prestructuring was shown to accelerate the hydrolysis (Wezynfeld et al., 2014), but is absent from short model peptides studied here, thus explaining the 5-fold acceleration of FLG hydrolysis at physiological conditions over the expectations.

The studied process yields C-terminal reaction products of FLG cleavage in the Ni^{2+}-complexed form. Dissociation constants of these complexes at pH 7.4 are in the range of 0.1–1 μM (Sokolowska et al., 2002); these complexes are slow to release Ni^{2+} ions by dissociation even if the pH is decreased or the complex gets diluted in the body fluids or makes contact with a stronger chelator (Bal et al., 1996; Sokolowska et al., 2002). This makes them potential candidate Ni^{2+} carriers. A hypothetical protein playing a similar role and activating antigen presenting cells was proposed previously in the literature (Thierse et al., 2004, 2005) The synthetic peptides modelling the products of Ni-hydrolysis might thus be used as a potential tool in nickel allergy research.

In this context, we may propose that the similarity of effects on dendritic cells between free vs complexed Ni^{2+} results from the ability of added Ni^{2+} ions to recruit ligands in the vicinity or on the cell surface which may provide chemical environment for Ni^{2+} similar to that present in FLG peptides. Not only the abundance of such "*prêt-à-porter*" ligands in the extracellular space of the skin may be high, e.g., the serum albumin is present in the extracellular fluid at sub millimolar concentrations. The formation of Ni^{2+} 4N complex with this sequence is a spontaneous process that takes about an hour at neutral pH (Bal et al., 1998). Ni^{2+}-albumin complexes were previously shown to stimulate Ni-reactive T cells in the presence of antigen presenting cells (Thierse et al., 2005) which may partially explain the activation of MDDCs exposed to nickel control in our experiments.

On the other hand, the presence of 50 μM Ni^{2+}-complexed HPs seemingly caused a stronger effect, which should be however confirmed with more biological replicates. Furthermore, it is important to stress that the database of human proteins

highlighted many more targets potentially susceptible to Ni-hydrolysis, including some immune-related. Those include cytokines produced by dendritic cells upon the Ni^{2+} exposure (such TNF-α, IL-6), cluster of differentiation markers playing an important role in T-cell activation (CD80, CD86) and innate recognition receptors such as TLRs; these induce proinflammatory cytokine production and antigen presentation to T-cells. Thus, Ni-hydrolysis might dysregulate important immune responses. On the other hand we cannot exclude a possibility of spontaneous nickel-assisted degradation of those protein compartments similar to that observed for FLG; this factor could hinder the interpretation and should be taken into account. An interesting extension of our research work would be to study cytokine levels after keratinocyte exposure to nickel. Keratinocytes may act as instigators of cutaneous inflammation (Gutowska-Owsiak and Ogg, 2012) through inflammatory cytokine secretion, having an influence on Langerhans cell migration to the draining lymph nodes and T cell trafficking (Barker et al., 1991; Nestle et al., 2009). On the other hand, elevated levels of inflammation markers after keratinocyte exposure to nickel were already reported (Sainte-Marie et al., 1998).

The results presented above indicate that Ni^{2+} ions can cause FLG degradation *via* direct, non-enzymatic hydrolysis within minutes, and suggest that the hydrolysis products may trigger activation of Langerhans cells with accompanied proinflammatory *milieu* in the skin during nickel contact skin allergy. Indeed, Ni^{2+} ions have been previously shown to modulate intracellular pathways in dendritic cells via NF-κB activity and p38 MAPK regulation (Boisleve et al., 2005; Ade et al., 2007). Ni^{2+} was also documented as a regulator of the IL-12 production, important in Th1-driven immune responses (Antonios et al., 2010). Moreover, $NiSO_4$ was already shown to induce the expression of HLA-DR, CD83, CD86, and CD40 and production of IL-8, IL-6, and IL-12p40 in human dendritic cells (Ade et al., 2007).

Proteomic studies with human monocytes identified protein species linked to distinct molecular processes including cell death, that are specifically regulated by Ni^{2+}; the regulation mechanism was not clarified (Jakob et al., 2017). Interestingly, almost half of the aforementioned proteins contain the Ni^{2+} hydrolytic motifs; underscoring the plausibility of the mechanism identified in this study. These findings are applicable to the known occupational hazards of inhalatory nickel exposure (Kasprzak et al., 2003), and to postulated relevance of lower-level exposure of the general population to nickel present in particles generated by combustion of fossil fuels, tobacco smoke and corrosion of metal objects (Vouk and Piver, 1983; Pappas, 2011). Specifically, small particles suspended in the polluted air appear to be particularly toxic; those sized 2.5 µm or less (PM 2.5) and classified as carcinogens by IARC (IARC Working Group on the Evaluation of Carcinogenic Risks to Humans and International Agency for Research on Cancer, 2016) can penetrate through the alveolar epithelium and enter the bloodstream, leading to the secondary tissue accumulation (Li et al., 2015) and, possibly, induction of inflammation (Wang et al., 2017). Recently, the smallest metal nanoparticles were also found to penetrate into the brain via the olfactory bulb (Tallkvist et al., 1998; Oberdörster et al., 2009; Maher et al., 2016); carrying a danger of Ni-hydrolysis directly in the brain. In summary, our results propose a novel, broadly applicable mechanism which could contribute to multiple known nickel-related pathologies and could help identify the relationships of nickel exposure with additional toxic effects.

Ni^{2+}-assisted cleavage of barrier proteins, including FLG, may contribute to clinical disease associated with nickel exposure.

DATA AVAILABILITY STATEMENT

The original contributions presented in the study are included in the article/**Supplementary Material**, further inquiries can be directed to the corresponding authors.

AUTHOR CONTRIBUTIONS

This project was conceived and designed by EIP, DG-O, MG, and WB. GO supervised the work. All of the experimental work was performed by EIP, DG-O, MK, AB, and DP. Selection of some FLG model peptides (QAASSHEQA, YQVSTHEQS, ADSSRHSGI) at the initial stage of the project was performed by TF. Computational analyses were performed by SM, AG, and JP. The manuscript was written and prepared by EIP, DG-O, and WB.

FUNDING

The study was funded in part by the project carried out as part of the Foundation for Polish Science program (TEAM/2009-4/1) co-financed from European Regional Development Fund resources within the framework of Operational Program Innovative Economy. The equipment used was sponsored in part by the Centre for Preclinical Research and Technology (CePT), a project co-sponsored by European Regional Development Fund and Innovative Economy, The National Cohesion Strategy of Poland. EIP is a scholar of the Mazovia Scholarship Program for Innovative Mazovian District co-financed by the European Union under the European Social Fund (No. 493/ES/ZS-III/W-POKL/14), Preludium 5 (No. DEC-2013/09/N/NZ6/02405) and the ETIUDA 2 (No. DEC-2014/12/T/NZ6/00505) projects, funded by the National Science Centre. DG-O and GO are grateful for the support from the Medical Research Council (UK) and the NIHR Oxford Biomedical Research Centre. DG-O also acknowledged funding from the British Skin Foundation.

ACKNOWLEDGMENTS

We thank MSc Małgorzata Orłowska for her help with the iTOL visualization.

SUPPLEMENTARY MATERIAL

The Supplementary Material for this article can be found online at: https://www.frontiersin.org/articles/10.3389/fmolb.2022.828674/full#supplementary-material

REFERENCES

Abramoff, M. (2007). ImageJ as an Image Processing Tool and Library. *Micros. Microanal.* 13 (S02), 1672–1673. doi:10.1017/s1431927607079652

Acerenza, L., and Mizraji, E. (1997). Cooperativity: a Unified View. *Biochim. Biophys. Acta (Bba) - Protein Struct. Mol. Enzymol.* 1339, 155–166. doi:10.1016/s0167-4838(96)00228-2

Ade, N., Antonios, D., Kerdine-Romer, S., Boisleve, F., Rousset, F., and Pallardy, M. (2007). NF-κB Plays a Major Role in the Maturation of Human Dendritic Cells Induced by NiSO4 but Not by DNCB. *Toxicol. Sci.* 99, 488–501. doi:10.1093/toxsci/kfm178

Ahlström, M. G., Thyssen, J. P., Menné, T., Midander, K., Julander, A., Lidén, C., et al. (2018). Short Contact with Nickel Causes Allergic Contact Dermatitis: an Experimental Study. *Br. J. Dermatol.* 179, 1127–1134. doi:10.1111/bjd.16935

Ahlström, M. G., Thyssen, J. P., Wennervaldt, M., Menné, T., and Johansen, J. D. (2019). Nickel Allergy and Allergic Contact Dermatitis: A Clinical Review of Immunology, Epidemiology, Exposure, and Treatment. *Contact Dermatitis* 81, 227–241. doi:10.1111/cod.13327

Antonios, D., Rousseau, P., Larangé, A., Kerdine-Römer, S., and Pallardy, M. (2010). Mechanisms of IL-12 Synthesis by Human Dendritic Cells Treated with the Chemical Sensitizer NiSO4. *J.I.* 185, 89–98. doi:10.4049/jimmunol.0901992

Ariani, H. H., Polkowska-Nowakowska, A., and Bal, W. (2013). Effect of D-Amino Acid Substitutions on Ni(II)-assisted Peptide Bond Hydrolysis. *Inorg. Chem.* 52, 2422–2431. doi:10.1021/ic3022672

Bal, W., Chmurny, G. N., Hilton, B. D., Sadler, P. J., and Tucker, A. (1996). Axial Hydrophobic Fence in Highly-Stable Ni(II) Complex of Des-Angiotensinogen N-Terminal Peptide. *J. Am. Chem. Soc.* 118, 4727–4728. doi:10.1021/ja953988j

Bal, W., Christodoulou, J., Sadler, P. J., and Tucker, A. (1998). Multi-metal Binding Site of Serum Albumin. *J. Inorg. Biochem.* 70, 33–39. doi:10.1016/s0162-0134(98)00010-5

Bal, W., Liang, R., Lukszo, J., Lee, S.-H., Dizdaroglu, M., and Kasprzak, K. S. (2000). Ni(II) Specifically Cleaves the C-Terminal Tail of the Major Variant of Histone H2A and Forms an Oxidative Damage-Mediating Complex with the Cleaved-Off Octapeptide. *Chem. Res. Toxicol.* 13, 616–624. doi:10.1021/tx000044l

Barker, J. N. W. N., Griffiths, C. E. M., Nickoloff, B. J., Mitra, R. S., Dixit, V. M., Nickoloff, B. J., et al. (1991). Keratinocytes as Initiators of Inflammation. *Lancet* 337, 211–214. doi:10.1016/0140-6736(91)92168-2

Boisleve, F., Kerdineromer, S., and Pallardy, M. (2005). Implication of the MAPK Pathways in the Maturation of Human Dendritic Cells Induced by Nickel and TNF-? *Toxicology* 206, 233–244. doi:10.1016/j.tox.2004.08.015

Brown, S. J., and Irwin McLean, W. H. (2012). One Remarkable Molecule: Filaggrin. *J. Invest. Dermatol.* 132, 751–762. doi:10.1038/jid.2011.393

Candi, E., Schmidt, R., and Melino, G. (2005). The Cornified Envelope: a Model of Cell Death in the Skin. *Nat. Rev. Mol. Cel. Biol.* 6, 328–340. doi:10.1038/nrm1619

Cangul, H., Broday, L., Salnikow, K., Sutherland, J., Peng, W., Zhang, Q., et al. (2002). Molecular Mechanisms of Nickel Carcinogenesis. *Toxicol. Lett.* 127, 69–75. doi:10.1016/s0378-4274(01)00485-4

Chan, W., and White, P. (2000). *Fmoc Solid Phase Peptide Synthesis: A Practical Approach*. Oxford, United Kingdom: Peterson's.

Chen, H., Davidson, T., Singleton, S., Garrick, M. D., and Costa, M. (2005). Nickel Decreases Cellular Iron Level and Converts Cytosolic Aconitase to Iron-Regulatory Protein 1 in A549 Cells. *Toxicol. Appl. Pharmacol.* 206, 275–287. doi:10.1016/j.taap.2004.11.011

Crooks, G. E., Hon, G., Chandonia, J.-M., and Brenner, S. E. (2004). WebLogo: a Sequence Logo Generator. *Genome Res.* 14, 1188–1190. doi:10.1101/gr.849004

Fluhr, J. W., Elias, P. M., Man, M.-Q., Hupe, M., Selden, C., Sundberg, J. P., et al. (2010). Is the Filaggrin-Histidine-Urocanic Acid Pathway Essential for Stratum Corneum Acidification? *J. Invest. Dermatol.* 130, 2141–2144. doi:10.1038/jid.2010.74

Fullerton, A., and Hoelgaard, A. (1988). Binding of Nickel to Human Epidermis *In Vitro*. *Br. J. Dermatol.* 119, 675–682. doi:10.1111/j.1365-2133.1988.tb03482.x

Funakoshi, T., Inoue, T., Shimada, H., and Kojima, S. (1997). The Mechanisms of Nickel Uptake by Rat Primary Hepatocyte Cultures: Role of Calcium Channels. *Toxicology* 124, 21–26. doi:10.1016/s0300-483x(97)00131-5

Genchi, G., Carocci, A., Lauria, G., Sinicropi, M. S., and Catalano, A. (2020). Nickel: Human Health and Environmental Toxicology. *Int. J. Environ. Res. Public Health* 17, 679. doi:10.3390/ijerph17030679

Gibbs, N. K., Tye, J., and Norval, M. (2008). Recent Advances in Urocanic Acid Photochemistry, Photobiology and Photoimmunology. *Photochem. Photobiol. Sci.* 7, 655–667. doi:10.1039/b717398a

Gruber, R., Elias, P. M., Crumrine, D., Lin, T.-K., Brandner, J. M., Hachem, J.-P., et al. (2011). Filaggrin Genotype in Ichthyosis Vulgaris Predicts Abnormalities in Epidermal Structure and Function. *Am. J. Pathol.* 178, 2252–2263. doi:10.1016/j.ajpath.2011.01.053

Gutowska-Owsiak, D., and Ogg, G. S. (2012). The Epidermis as an Adjuvant. *J. Invest. Dermatol.* 132, 940–948. doi:10.1038/jid.2011.398

Gutowska-Owsiak, D., de La Serna, J. B., Fritzsche, M., Naeem, A., Podobas, E. I., Leeming, M., et al. (2018). Orchestrated Control of Filaggrin–Actin Scaffolds Underpins Cornification. *Cel. Death Dis.* 9, 412. doi:10.1038/s41419-018-0407-2

Gutowska-Owsiak, D., Podobas, E. I., Eggeling, C., Ogg, G. S., and de la Serna, J. B. (2020). Addressing Differentiation in Live Human Keratinocytes by Assessment of Membrane Packing Order. *Front. Cel. Dev. Biol.* 8, 573230. doi:10.3389/fcell.2020.573230

Hagvall, L., Pour, M. D., Feng, J., Karma, M., Hedberg, Y., and Malmberg, P. (2021). Skin Permeation of Nickel, Cobalt and Chromium Salts in *Ex Vivo* Human Skin, Visualized Using Mass Spectrometry Imaging. *Toxicol. Vitro* 76, 105232. doi:10.1016/j.tiv.2021.105232

IARC Working Group on the Evaluation of Carcinogenic Risks to Humans, and International Agency for Research on Cancer (2016). *Outdoor Air Pollution*. Lyon, France: International Agency for Research on Cancer, World Health Organization.

Jakob, A., Mussotter, F., Ohnesorge, S., Dietz, L., Pardo, J., Haidl, I. D., et al. (2017). Immunoproteomic Identification and Characterization of Ni-Regulated Proteins Implicates Ni in the Induction of Monocyte Cell Death. *Cell Death Dis.* 8, e2684. doi:10.1038/cddis.2017.112

Karaczyn, A. A., Bal, W., North, S. L., Bare, R. M., Hoang, V. M., Fisher, R. J., et al. (2003). The Octapeptidic End of the C-Terminal Tail of Histone H2A Is Cleaved off in Cells Exposed to Carcinogenic Nickel(II). *Chem. Res. Toxicol.* 16, 1555–1559. doi:10.1021/tx0300277

Kasprzak, K. S., Sunderman, F. W., Jr, and Salnikow, K. (2003). Nickel Carcinogenesis. *Mutat. Res.* 533, 67–97. doi:10.1016/j.mrfmmm.2003.08.021

Kezic, S., Kemperman, P. M. J. H., Koster, E. S., de Jongh, C. M., Thio, H. B., Campbell, L. E., et al. (2008). Loss-of-function Mutations in the Filaggrin Gene lead to Reduced Level of Natural Moisturizing Factor in the Stratum Corneum. *J. Invest. Dermatol.* 128, 2117–2119. doi:10.1038/jid.2008.29

Kluger, N. (2021). Nickel and Tattoos: Where Are We? *Contact Dermatitis*. doi:10.1111/cod.13869

Kopera, E., Krezel, A., Protas, A. M., Belczyk, A., Bonna, A., Wysłouch-Cieszyńska, A., et al. (2010). Sequence-specific Ni(II)-dependent Peptide Bond Hydrolysis for Protein Engineering: Reaction Conditions and Molecular Mechanism. *Inorg. Chem.* 49, 6636–6645. doi:10.1021/ic1005709

Koppes, S. A., Kemperman, P., Van Tilburg, I., Calkoen-Kwa, F., Engebretsen, K. A., Puppels, G. J., et al. (2017). Determination of Natural Moisturizing Factors in the Skin: Raman Microspectroscopy versus HPLC. *Biomarkers* 22, 502–507. doi:10.1080/1354750x.2016.1256428

Krezel, A., Kopera, E., Protas, A. M., Poznański, J., Wysłouch-Cieszyńska, A., and Bal, W. (2010). Sequence-specific Ni(II)-dependent Peptide Bond Hydrolysis for Protein Engineering. Combinatorial Library Determination of Optimal Sequences. *J. Am. Chem. Soc.* 132, 3355–3366. doi:10.1021/ja907567r

Krieger, E., Darden, T., Nabuurs, S. B., Finkelstein, A., and Vriend, G. (2004). Making Optimal Use of Empirical Energy Functions: Force-Field Parameterization in crystal Space. *Proteins* 57, 678–683. doi:10.1002/prot.20251

Letunic, I., and Bork, P. (2021). Interactive Tree of Life (iTOL) V5: an Online Tool for Phylogenetic Tree Display and Annotation. *Nucleic Acids Res.* 49, W293–W296. doi:10.1093/nar/gkab301

Li, M. Z., and Elledge, S. J. (2007). Harnessing Homologous Recombination *In Vitro* to Generate Recombinant DNA via SLIC. *Nat. Methods* 4, 251–256. doi:10.1038/nmeth1010

Li, Q., Liu, H., Alattar, M., Jiang, S., Han, J., Ma, Y., et al. (2015). The Preferential Accumulation of Heavy Metals in Different Tissues Following Frequent Respiratory Exposure to PM2.5 in Rats. *Sci. Rep.* 5, 16936. doi:10.1038/srep16936

Madshus, I. H. (1988). Regulation of Intracellular pH in Eukaryotic Cells. *Biochem. J.* 250, 1–8. doi:10.1042/bj2500001

Maher, B. A., Ahmed, I. A. M., Karloukovski, V., MacLaren, D. A., Foulds, P. G., Allsop, D., et al. (2016). Magnetite Pollution Nanoparticles in the Human Brain. *Proc. Natl. Acad. Sci. U. S. A.* 113, 10797–10801. doi:10.1073/pnas.1605941113

Matoltsy, A. G., and Matoltsy, M. N. (1970). The Chemical Nature of Keratohyalin Granules of the Epidermis. *J. Cel Biol.* 47, 593–603. doi:10.1083/jcb.47.3.593

Midander, K., Pan, J., Wallinder, I. O., Heim, K., and Leygraf, C. (2007). Nickel Release from Nickel Particles in Artificial Sweat. *Contact Dermatitis* 56, 325–330. doi:10.1111/j.1600-0536.2007.01115.x

Montgomery, D. C., and Runger, G. C. (2007). *Applied Statistics and Probability for Engineers*. 3RD ED. United States of America: John Wiley & Sons. With CD.

Nestle, F. O., Di Meglio, P., Qin, J.-Z., and Nickoloff, B. J. (2009). Skin Immune Sentinels in Health and Disease. *Nat. Rev. Immunol.* 9, 679–691. doi:10.1038/nri2622

Nieminen, T. M., Ukonmaanaho, L., Rausch, N., and Shotyk, W. (2007). Biogeochemistry of Nickel and its Release into the Environment. *Nickel Its Surprising Impact Nat.*, 1–29. doi:10.1002/9780470028131.ch1

Novak, N., Baurecht, H., Schäfer, T., Rodriguez, E., Wagenpfeil, S., Klopp, N., et al. (2008). Loss-of-function Mutations in the Filaggrin Gene and Allergic Contact Sensitization to Nickel. *J. Invest. Dermatol.* 128, 1430–1435. doi:10.1038/sj.jid.5701190

Oberdörster, G., Elder, A., and Rinderknecht, A. (2009). Nanoparticles and the Brain: Cause for Concern? *J. Nanosci. Nanotechnol.* 9, 4996–5007. doi:10.1166/jnn.2009.gr02

Pappas, R. S. (2011). Toxic Elements in Tobacco and in Cigarette Smoke: Inflammation and Sensitization. *Metallomics* 3, 1181–1198. doi:10.1039/c1mt00066g

Podobas, E. I., Bonna, A., Polkowska-Nowakowska, A., and Bal, W. (2014). Dual Catalytic Role of the Metal Ion in Nickel-Assisted Peptide Bond Hydrolysis. *J. Inorg. Biochem.* 136, 107–114. doi:10.1016/j.jinorgbio.2014.03.008

Protas, A. M., Ariani, H. H. N., Bonna, A., Polkowska-Nowakowska, A., Poznański, J., and Bal, W. (2013). Sequence-specific Ni(II)-dependent Peptide Bond Hydrolysis for Protein Engineering: Active Sequence Optimization. *J. Inorg. Biochem.* 127, 99–106. doi:10.1016/j.jinorgbio.2013.07.037

Rietz Liljedahl, E., Johanson, G., Korres de Paula, H., Faniband, M., Assarsson, E., Littorin, M., et al. (2021). Filaggrin Polymorphisms and the Uptake of Chemicals through the Skin-A Human Experimental Study. *Environ. Health Perspect.* 129, 17002. doi:10.1289/EHP7310

Romero, V., Hosomichi, K., Nakaoka, H., Shibata, H., and Inoue, I. (2017). Structure and Evolution of the Filaggrin Gene Repeated Region in Primates. *BMC Evol. Biol.* 17, 10. doi:10.1186/s12862-016-0851-5

Ross, A. A., Müller, K. M., Weese, J. S., and Neufeld, J. D. (2018). Comprehensive Skin Microbiome Analysis Reveals the Uniqueness of Human Skin and Evidence for Phylosymbiosis within the Class Mammalia. *Proc. Natl. Acad. Sci. U. S. A.* 115, E5786–E5795. doi:10.1073/pnas.1801302115

Sainte-Marie, I., Jumbou, O., Tenaud, I., and Dreno, B. (1998). Comparative Study of the *In Vitro* Inflammatory Activity of Three Nickel Salts on Keratinocytes. *Acta Derm. Venereol.* 78, 169–172. doi:10.1080/000155598441459

Sandilands, A., Sutherland, C., Irvine, A. D., and McLean, W. H. I. (2009). Filaggrin in the Frontline: Role in Skin Barrier Function and Disease. *J. Cel Sci.* 122, 1285–1294. doi:10.1242/jcs.033969

Schneider, T. D., and Stephens, R. M. (1990). Sequence Logos: a New Way to Display Consensus Sequences. *Nucleic Acids Res.* 18, 6097–6100. doi:10.1093/nar/18.20.6097

Schreml, S., Meier, R. J., Wolfbeis, O. S., Landthaler, M., Szeimies, R.-M., and Babilas, P. (2011). 2D Luminescence Imaging of pH *In Vivo*. *Proc. Natl. Acad. Sci.* 108, 2432–2437. doi:10.1073/pnas.1006945108

Segger, D., Aßmus, U., Brock, M., Erasmy, J., Finkel, P., Fitzner, A., et al. (2008). Multicenter Study on Measurement of the Natural pH of the Skin Surface. *Int. J. Cosmet. Sci.* 30, 75. doi:10.1111/j.1468-2494.2007.00403_1.x

Sigel, H., Tribolet, R., and Yamauchi, O. (1990). The Imidazole Group and its Stacking Properties in Mixed Ligand Metal Ion Complexes. *Comments Inorg. Chem.* 9, 305–330. doi:10.1080/02603599008035813

Sokolowska, M., Krezel, A., Dyba, M., Szewczuk, Z., and Bal, W. (2002). Short Peptides Are Not Reliable Models of Thermodynamic and Kinetic Properties of the N-Terminal Metal Binding Site in Serum Albumin. *Eur. J. Biochem.* 269, 1323–1331. doi:10.1046/j.1432-1033.2002.02772.x

Tallkvist, J., Henriksson, J., d'Argy, R., and Tjälve, H. (1998). Transport and Subcellular Distribution of Nickel in the Olfactory System of Pikes and Rats. *Toxicol. Sci.* 43, 196–203. doi:10.1093/toxsci/43.2.196

Thierse, H.-J., Moulon, C., Allespach, Y., Zimmermann, B., Doetze, A., Kuppig, S., et al. (2004). Metal-Protein Complex-Mediated Transport and Delivery of Ni2 to TCR/MHC Contact Sites in Nickel-Specific Human T Cell Activation. *J. Immunol.* 172, 1926–1934. doi:10.4049/jimmunol.172.3.1926

Thierse, H.-J., Gamerdinger, K., Junkes, C., Guerreiro, N., and Weltzien, H. U. (2005). T Cell Receptor (TCR) Interaction with Haptens: Metal Ions as Non-classical Haptens. *Toxicology* 209, 101–107. doi:10.1016/j.tox.2004.12.015

Thyssen, J. P., Johansen, J. D., Linneberg, A., Menné, T., Nielsen, N. H., Meldgaard, M., et al. (2010). The Association between Null Mutations in the Filaggrin Gene and Contact Sensitization to Nickel and Other Chemicals in the General Population. *Br. J. Dermatol.* 162, 1278–1285. doi:10.1111/j.1365-2133.2010.09708.x

Vouk, V. B., and Piver, W. T. (1983). Metallic Elements in Fossil Fuel Combustion Products: Amounts and Form of Emissions and Evaluation of Carcinogenicity and Mutagenicity. *Environ. Health Perspect.* 47, 201–225. doi:10.1289/ehp.8347201

Wang, H., Song, L., Ju, W., Wang, X., Dong, L., Zhang, Y., et al. (2017). The Acute Airway Inflammation Induced by PM2.5 Exposure and the Treatment of Essential Oils in Balb/c Mice. *Sci. Rep.* 7, 44256. doi:10.1038/srep44256

Wezynfeld, N. E., Bossak, K., Goch, W., Bonna, A., Bal, W., and Frączyk, T. (2014). Human Annexins A1, A2, and A8 as Potential Molecular Targets for Ni(II) Ions. *Chem. Res. Toxicol.* 27, 1996–2009. doi:10.1021/tx500337w

Wezynfeld, N. E., Frączyk, T., and Bal, W. (2016). Metal Assisted Peptide Bond Hydrolysis: Chemistry, Biotechnology and Toxicological Implications. *Coord. Chem. Rev.* 327-328, 166–187. doi:10.1016/j.ccr.2016.02.009

World Health Organization (2000). Air Quality Guidelines for Europe. *WHO Reg. Publ. Eur. Ser.* V–X, 1–273.

Zambelli, B., Uversky, V. N., and Ciurli, S. (2016). Nickel Impact on Human Health: An Intrinsic Disorder Perspective. *Biochim. Biophys. Acta* 1864, 1714–1731. doi:10.1016/j.bbapap.2016.09.008

Conflict of Interest: The authors declare that the research was conducted in the absence of any commercial or financial relationships that could be construed as a potential conflict of interest.

Publisher's Note: All claims expressed in this article are solely those of the authors and do not necessarily represent those of their affiliated organizations, or those of the publisher, the editors and the reviewers. Any product that may be evaluated in this article, or claim that may be made by its manufacturer, is not guaranteed or endorsed by the publisher.

frontiers in Cell and Developmental Biology

MINI REVIEW
published: 24 March 2022
doi: 10.3389/fcell.2022.857237

The Role of Iron in *Staphylococcus aureus* Infection and Human Disease: A Metal Tug of War at the Host—Microbe Interface

Madeleine C. van Dijk[1,2], *Robin M. de Kruijff*[2]* *and Peter-Leon Hagedoorn*[1]*

[1]Department of Biotechnology, Delft University of Technology, Delft, Netherlands, [2]Department of Radiation Science and Technology, Delft University of Technology, Delft, Netherlands

Iron deficiency anemia can be treated with oral or intravenous Fe supplementation. Such supplementation has considerable effects on the human microbiome, and on opportunistic pathogenic micro-organisms. Molecular understanding of the control and regulation of Fe availability at the host-microbe interface is crucial to interpreting the side effects of Fe supplementation. Here, we provide a concise overview of the regulation of Fe by the opportunistic pathogen *Staphylococcus aureus*. Ferric uptake regulator (Fur) plays a central role in controlling Fe uptake, utilization and storage in order to maintain a required value. The micro-organism has a strong preference for heme iron as an Fe source, which is enabled by the Iron-regulated surface determinant (Isd) system. The strategies it employs to overcome Fe restriction imposed by the host include: hijacking host proteins, replacing metal cofactors, and replacing functions by non-metal dependent enzymes. We propose that integrated omics approaches, which include metalloproteomics, are necessary to provide a comprehensive understanding of the metal tug of war at the host-microbe interface down to the molecular level.

Keywords: *Staphylococcus aureus*, MRSA, iron homeostasis, nutritional immunity, iron deficiency anemia, ferric uptake regulator, iron-regulated surface determinant system, heme

OPEN ACCESS

Edited by:
Fernando Antunes, University of Lisbon, Portugal

Reviewed by:
Guenter Weiss, Innsbruck Medical University, Austria

***Correspondence:**
Robin M. de Kruijff
r.m.dekruijff@tudelft.nl
Peter-Leon Hagedoorn
p.l.hagedoorn@tudelft.nl

Specialty section:
This article was submitted to Cellular Biochemistry, a section of the journal Frontiers in Cell and Developmental Biology

Received: *18 January 2022*
Accepted: *24 February 2022*
Published: *24 March 2022*

Citation:
van Dijk MC, de Kruijff RM and Hagedoorn P-L (2022) The Role of Iron in Staphylococcus aureus Infection and Human Disease: A Metal Tug of War at the Host—Microbe Interface. Front. Cell Dev. Biol. 10:857237. doi: 10.3389/fcell.2022.857237

INTRODUCTION

Iron deficiency is a major health concern worldwide, resulting in over one billion cases of iron-deficiency anemia (Gardner and Kassebaum 2020; Pasricha et al., 2021). Currently, the first-line treatment for iron deficiency anemia is the use of oral iron supplements. However, many side effects have been reported following their use: e.g., 30–70% of the patients report gastrointestinal problems (DeLoughery 2019). The supplemented iron is only partially absorbed by the human body, resulting in a significantly increased amount of iron available to the human gut microbiome (DeLoughery 2019; Finlayson-Trick et al., 2020). The microbiome of an individual plays an important role in human health, and metal compounds are known to affect the survival and reproduction of bacteria (Sheldon and Skaar 2019). Recognition of these side effects and the discovery that intravenously administered iron causes only minor adverse effects, after having been (incorrectly) considered more dangerous for decades, has sparked the use of intravenous Fe supplementation (Auerbach, Gafter-Gvili, and Macdougall 2020; Schaefer et al., 2020). However, following intravenous iron administration, blood borne pathogens will be exposed to excess iron. One of these pathogens, responsible for a wide variety of clinical diseases, is *Staphylococcus aureus* of which the methicillin

resistant (MRSA) strain represents a global human health challenge (David and Daum 2010; DeLeo et al., 2010; Ganz et al., 2020).

The effect of supplemented iron on *S. aureus* proliferation has been investigated in a few patient studies only, where bacterial growth assays were performed on serum samples taken from the subjects following iron supplementation. In this way, Cross et al. (2015) found supplemented oral iron to significantly increase transferrin saturation (TSAT) in the serum samples. However, while gram-negative bacteria, including *E. coli*, and the gram-positive *Staphylococcus epidermis,* showed elevated growth rates, *S. aureus* appeared unaffected (Cross et al., 2015). The authors suggested this to be caused by a preference of *S. aureus* for heme iron over transferrin-bound iron (Cross et al., 2015), which is consistent with other studies (Barton Pai et al., 2006; Suffredini et al., 2017; Skaar et al., 2004). In fact, in hemodialysis patients, which have significantly lower transferrin levels, intravenous iron sucrose administration was found to correlate with increased non-transferrin-bound iron (NTBI) levels in the patients' serum. Significantly increased *S. aureus* growth was observed on the serum samples of these patients, compared to the NTBI-negative subjects (Barton Pai et al., 2006). This indicates that the molecular form of iron in the blood influences its uptake by *S. aureus*, which seems to prefer NTBI and heme iron, but is less responsive to transferrin-bound iron.

While multiple reviews have recently been published on the interaction of supplemented iron and enteric pathogens on a molecular level (Yilmaz and Li 2018; Finlayson-Trick et al., 2020; Qi et al., 2020), investigations focusing on the impact of supplemented intravenous iron on blood borne pathogens such as *S. aureus* are lacking. Therefore, in this mini-review, we aim to give an overview of recent insights into iron and *S. aureus* in the context of excess iron and iron-limiting conditions imposed by the host (nutritional immunity) during *S. aureus* infections. Here, we will first look in detail at the regulation systems *S. aureus* uses to control uptake of both free and heme iron, and to regulate the intracellular Fe levels, and then describe how the pathogen is able to survive under iron starvation conditions.

REGULATION OF IRON HOMEOSTASIS IN *S. AUREUS* AT THE MICROBE-HOST INTERFACE

Control Systems

In engineering, control systems regulate the operation of devices and their processes using control loops. For a functioning control loop, you need to measure a process value which can be either below or above a target set point. The device or process then needs to be adjusted to attain the desired process value. In a similar manner, bacteria have evolved to control the intracellular concentrations of nutrients and metabolites, including iron, to pre-set conditions required for growth and/or maintenance. For this process, called homeostasis, bacteria produce sensors that measure the amount of intracellular iron, and a control system (or systems) that can change the expression of proteins and the functionality of enzymes in order to reach the target value. This control occurs at: transcriptional (DNA→ mRNA), post-transcriptional (stabilizing or degradation of mRNA), translational (mRNA→ protein) or post-translational level (protein degradation, modification, and allosteric interaction). These four levels allow very precise tuning and distribution of iron, depending on necessity and environmental conditions. Precise tuning is important because Fe is essential for life, while at the same time Fe^{2+} can generate toxic reactive oxygen species (ROS) with O_2, and Fe^{3+} is insoluble under neutral aqueous conditions.

Regulation of Free Iron

In *Staphylococcus aureus,* Fur (ferric uptake regulator) is the major control system for iron (**Figure 1**). The Fur protein is homodimeric, with each monomer consisting of an N-terminal DNA binding domain and a C-terminal dimerization domain (Price and Boyd 2020). Between the two domains is a metal ion binding site, which was recently shown to bind a [2Fe-2S] cluster in *E. coli* (Fontenot et al., 2020). *S. aureus* Fur has been described as binding two separate Fe^{2+} ions in the hinge regions between the N- and C-terminal domains. *E. coli* and *S. aureus* Fur share 30% sequence identity and 49% sequence similarity, which includes three conserved Cysteines (**Supplementary Material**). The precise nature of the Fe-bound form of *S. aureus* Fur remains to be established. Upon dimerization, the DNA binding part of Fe-bound Fur is a transcriptional repressor of a range of genes related to iron homeostasis. It functions by binding to a so-called Fur-box upstream of the coding genes. These genes involve Fe transporters and many other genes, as discussed below. Some are established virulence factors, which means they are involved in disease processes. Related proteins, called Fur family proteins, with affinity to other metal ions or compounds have been discovered, such as Zur (zinc uptake regulator) for Zn^{2+} and PerR (peroxide operon regulator) which is a metal-dependent regulator for hydrogen peroxide. The Fe^{2+} and Mn^{2+} dependence of PerR highlights crosslinks between the different control systems (Horsburgh, Ingham, and Foster 2001).

Ferrous iron uptake by transporter FeoB is still poorly characterized, although recently inhibitors have been identified that may have important medical implications as novel antibiotics against MRSA and other multidrug resistant Gram-positive bacteria (Shin et al., 2021). Fur and PerR differentially regulate the *S. aureus* ferritin gene (FtnA), which encodes the Fe-storage protein ferritin (Morrissey et al., 2004). Ferritin can take up circa 4,000 Fe atoms in the form of a ferrihydrite mineral nanoparticle inside a 24-meric protein sphere (Honarmand Ebrahimi, Hagedoorn, and Hagen 2015). Iron storage by ferritin involves oxidation of Fe^{2+} to Fe^{3+} and concerted incorporation into a growing ferrihydrite mineral core. Upon reduction, by a mechanism that has not yet been established, Fe can also be released from ferritin as Fe^{2+}.

Another Fur controlled Fe uptake system is the FepABC (Fe dependent peroxidase) transporter. The transporter has not been well characterized, but it has been implicated in Fe and possibly heme uptake. The transporter consists of FepA, a predicted membrane anchored lipoprotein that may act as an Fe

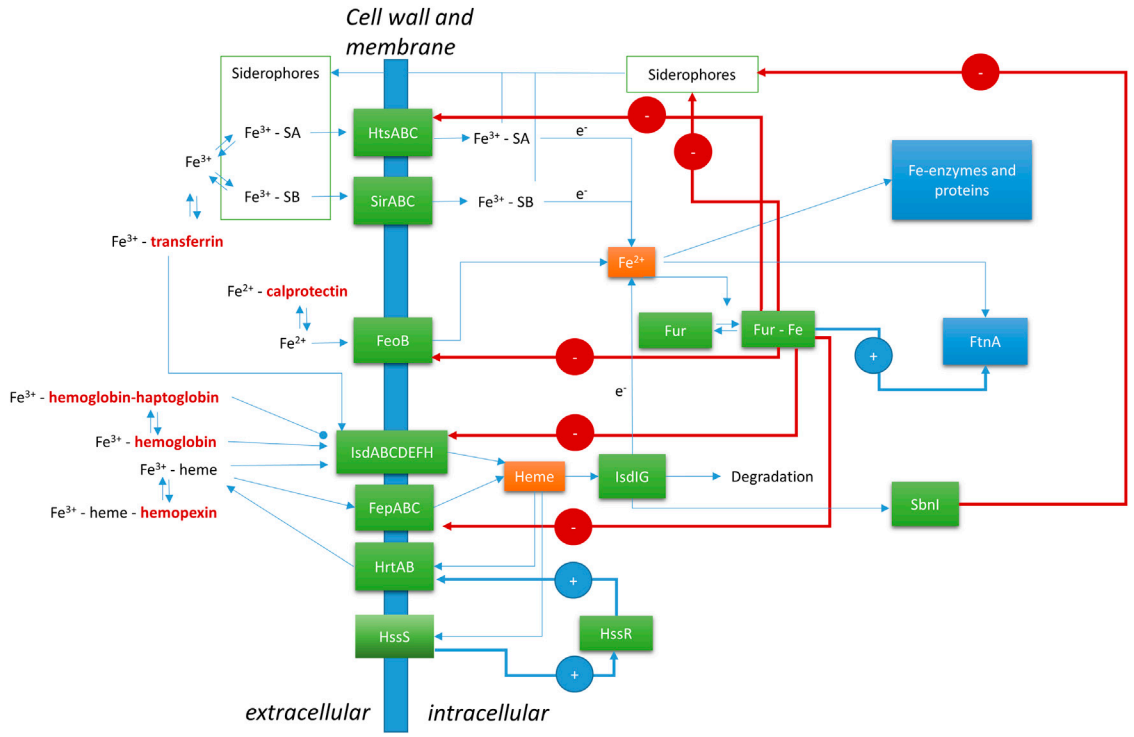

FIGURE 1 | Regulation of Fe by *Staphylococcus aureus* at the host-microbe interface. FeoB, ferrous Fe transporter; FepABC, Fe dependent peroxidase transporter; FtnA, ferritin; Fur, ferric uptake regulator; HrtAB, heme regulator transporter efflux pump; HssR, heme sensing two-component regulator regulatory protein; HssS, heme sensing two-component regulator sensor protein; HtsABC, heme transport system involved in Fe-SA uptake; IsdABCDEFGHI, iron-regulated surface determinant system; SA, Staphyloferrin A; SB, Staphyloferrin B; SbnI, L-serine kinase and heme responsive regulator of SB biosynthesis. Human (host) proteins are in bold and dark red font.

(compound) binding protein, peroxidase FepB, and integral membrane protein FepC (Biswas et al., 2009). FepB can bind heme and protoporphyrin IX (heme without Fe) and has a low peroxidase activity (Turlin et al., 2013). FepB is a substrate of the Twin-Arginine Translocation pathway, which allows membrane translocation of fully folded cofactor bound proteins (Biswas et al., 2009). Heterologous expression of the *S. aureus* FepAB in *E. coli* allowed heme utilization in this organism (Turlin et al., 2013).

Siderophores are small, extracellular, peptide-derived compounds with a high affinity for Fe^{3+}. *S. aureus* produces two siderophores: Staphyloferrin A (SA) and Staphyloferrin B (SB). SA is produced using the gene cluster *sfa*, and SB is produced using the *sbn* gene cluster (Marchetti et al., 2020). The gene clusters are both transcriptionally repressed by Fur. Recently, a heme sensitive regulator of siderophore production was identified: SbnI (Laakso et al., 2016; Verstraete et al., 2019). The gene product of SbnI is an enzyme producing a precursor to the siderophore. Furthermore, the protein can bind DNA and upon dimerization contains a heme binding domain. Heme transfer from IsdI to SnbI has been suggested to help control the production of siderophores, thereby shifting focus to heme utilization rather than free iron uptake. Fe^{3+} bound SA is taken up using the ABC transporter HtsABC (heme transport system). Despite the name, it is unclear if the Hts transporter is involved in heme uptake, and if so by which mechanism (Price and Boyd 2020). Hts transcription is regulated by Fur. SB is taken up by the ABC transporter SirABC (Grigg et al., 2010a).

Siderophores play a very important role in *Staphylococcus* biofilm formation to ensure Fe availability (Johnson et al., 2005; Oliveira et al., 2021). Fe chelators that compete with siderophores can disturb biofilm formation and may therefore be of medical importance (Richter et al., 2017; Coraça-Huber et al., 2018).

Regulation of Heme Iron

Heme obtained from red blood cells is a major source of iron for *Staphylococcus aureus* during infections (Skaar et al., 2004). There is evidence that *S. aureus* has evolved a specificity towards human hemoglobin versus other mammalian orthologs that is unique among pathogenic bacteria (Pishchany et al., 2010). However, a high level of intracellular heme is dangerous due to its potential to form reactive oxygen species (ROS). *S. aureus* uses the two-component regulator HssRS (**Figure 1**) (Heme sensing two-component system) to control the intracellular level of free heme (Price and Boyd 2020; Stauff, Torres, and Skaar 2007; Stauff and Skaar 2009). HssS is a transmembrane protein, which responds to the heme level by an unknown mechanism. Upon activation, HssS acts as a histine kinase to phosphorylate the histidine of HssR, thereby activating the protein as a transcriptional activator of the heme efflux transporter HrtAB

(Heme regulator transporter efflux pump). Whether the precise compound that is expelled by HrtAB is heme or a heme metabolite is unknown (Price and Boyd 2020). Additional targets of HssR have not been identified to date.

The cell wall of *S. aureus* contains a unique system to acquire heme, which is called Isd (Iron-regulated surface determinant system) (Skaar and Schneewind 2004; Grigg et al., 2010b; Mazmanian et al., 2003). Similar systems are present in other Gram-positive pathogenic bacteria, such as *Listeria monocystogenes* and *Clostridium tetani*. This system takes up heme from human (host) hemoproteins. The Isd system involves nine different proteins, of which four are bound to the cell wall: IsdA, IsdB, IsdC, and IsdH. Two proteins, IsdE and IsdF, constitute an ABC-transporter for the heme cofactor. IsdD is a transmembrane protein of unknown function. And the final two proteins, IsdI and IsdG, are soluble intracellular heme degrading enzymes. The outer cell wall proteins IsdB and IsdH bind free heme, methemoglobin and hemoglobin-haptoglobin complexes from the host. The cell wall proteins IsdC and IsdA are involved in heme transport through the 15–30 nm thick cell wall to the ligand binding component of the ABC-transporter IsdE. After translocation of the heme to the cytoplasm, the cofactor is degraded by the heme degrading enzymes IsdI and IsdG. These enzymes are distantly related to well-characterized heme oxygenases and have been found to release Fe from the cofactor, yet the precise reaction mechanism remains to be solved (Grigg et al., 2010b). Fur regulates the expression of the genes for IsdA, IsdB, IsdC and IsdH. The gene for the enzyme sortase B (SrtB) is part of the same transcriptional unit as IsdC, and therefore also regulated by Fur. Sortase B is involved in the cell wall anchoring of the Isd components.

OVERCOMING REDUCED IRON AVAILABILITY

Strategies

Upon infection, the host starts the immune response. Macrophages are activated by interaction with *S. aureus via* Toll-like receptors (TLRs) (Pidwill et al., 2021). This starts signal transduction cascades which include mechanisms to limit the availability of iron in blood (Pandur et al., 2021). Central in the regulation of these processes is the hormone hepcidin. Hepcidin interacts with the host Fe efflux protein ferroportin, thereby limiting Fe export from macrophages (Theurl et al., 2008). Interestingly the same exposed *S. aureus* lipoproteins that support Fe acquisition, for example, *via* the Isd system, are also recognized by the TLRs, thereby evoking inflammation responses in the host (Schmaler et al., 2009; Sheldon and Heinrichs 2012). One of the cellular host responses involved is the endocytosis and degradation of erythrocytes by the macrophages in a process called erythrophagocytosis (Knutson et al., 2005). The Fe retained by the host cells is also put to good use, as Fe^{2+} enabled production of ROS is used to kill bacteria taken up by these cells (Rosen et al., 1995; Haschka, Hoffmann, and Weiss 2021). Interestingly. ROS also induce antibiotic resistance in *S. aureus*, indicating a negative side-effect of our innate immune response (Rowe et al., 2020).

In the context of sepsis, *S. aureus* is capable of lysing erythrocytes by secreting hemolytic toxins to free hemoglobin and obtain it through the Isd system (Torres et al., 2010). The *S. aureus* heme-oxygenases IsdG and IsdI have been shown to be important for full virulence with heme as the primary iron source (Reniere and Skaar 2008). Host heme oxygenase 1 (HO1) catalyzes the rate-limiting step in heme degradation, producing biliverdin, Fe^{2+} and CO (carbon monoxide) (Singh et al., 2018). CO can act as a messenger in various protective cascades. Links between HO1 and protective effects on *S. aureus* infection have been shown (MacGarvey et al., 2012; Gahlot et al., 2017).

The host restricts the availability of iron in its different forms further by producing the hemoglobin binding protein haptoglobin, the heme binding protein hemopexin, the free Fe^{3+} binding proteins transferrin and lactoferrin, and the free Fe^{2+} binding protein calprotectin (Nakashige et al., 2015; Marchetti et al., 2020). Haptoglobin binding to hemoglobin inhibits uptake of heme by the Isd system of *S. aureus*, although the protein still binds to IsdH (Mikkelsen, Runager, and Andersen 2020). Calprotectin (CP) was originally identified to be involved in Mn^{2+} limitation by the host, but was more recently found to bind Fe^{2+} efficiently in the presence of Ca^{2+} (Nakashige et al., 2015). It has been demonstrated that CP induces Fe starvation in *S. aureus* cultures (Obisesan, Zygiel, and Nolan 2021; Zygiel et al., 2021). The ability of *S. aureus* to efficiently incorporate heme affords protection against CP induced Fe starvation (Zygiel et al., 2021). In the preceding sections we have described the mechanisms through which *S. aureus* controls intracellular Fe levels in response to iron sources in the human host. However, these control systems may be insufficient when Fe availability is strongly reduced. Pathogenic bacteria such as *S. aureus* have evolved several strategies to tackle the metal restrictions imposed through nutritional immunity: 1) hijacking host proteins, 2) replacing metal cofactors, and 3) replacing functions by non-metal dependent enzymes. We will discuss examples of each strategy below.

Hijacking Host Proteins

S. aureus cannot use hemopexin as a heme source using the Isd system. However, it has been reported to take up iron from host transferrin using a transferrin receptor. The nature of the transferrin receptor of *S. aureus* is convoluted in literature. This cell-wall associated protein was first identified as a functional glyceraldehyde-3-phosphate dehydrogenase (GAPDH) (Modun, Morrissey, and Williams 2000). However, this was shown to be incorrect, and the protein was identified as staphylococcal transferrin-binding protein StbA (Taylor and Heinrichs 2002). Later, it was shown that StbA is the same protein as IsdA, part of the Isd system for heme uptake described above (Clarke, Wiltshire, and Foster 2004; Maresso and Schneewind 2006). The ongoing tug of war for Fe between host transferrin and bacterial transferrin receptors has caused rapid evolutionary development of the involved proteins (Barber and Elde 2014). The presence of a transferrin receptor indicates that *S. aureus* can take up Fe from transferrin, at least to some extent, although the major Fe source from the host is heme.

Replacing Metal Cofactors

A well-established example of replacing metal cofactors by *S. aureus* are the Mn-dependent superoxide dismutases (SODs). Neutrophils, and other host immune cells, can induce oxidative bursts as a defensive strategy against *S. aureus* (Rigby and DeLeo 2012). This process generates high levels of damaging ROS, including superoxide (Forrester et al., 2018; Jakubczyk et al., 2020). The expression of SODs is one way in which *S. aureus* can combat ROS. *S. aureus* has two superoxide dismutases, SodA and SodM. SodA can incorporate only Mn as metal cofactor while SodM can use either Fe or Mn depending on the conditions (Garcia et al., 2017). As part of the host immune response, the neutrophil protein CP sequesters trace metals, including Mn. The action of CP disturbs the correct metalation of SodA (Kehl-Fie et al., 2013). However, *S. aureus* encodes an additional Mn-dependent SOD, SodM, which can substitute its metal cofactor for Fe under Mn-limiting conditions (Garcia et al., 2017; Treffon et al., 2020). In this way, *S. aureus* can retain sufficient SOD activity despite CP activity and maintain virulence. Small non-coding regulatory RNA molecule RsaC (co-transcribed with Mn transporter MntABC) represses the translation of the SodA coding mRNA under Mn limiting conditions. So, if there is a shortage of Mn (Mn uptake by MntABC needed), the Mn SOD is suppressed in favor of the Fe containing SOD. A clinically relevant example of a highly oxidative stressful environment with strong CP presence are the airways of cystic fibrosis patients, where *S. aureus* can cause persistent infections for years. Investigation of gene expression demonstrated significantly elevated SodM expression levels in clinical isolates compared to laboratory strains (Treffon et al., 2020).

Replacing Functions by Non-metal Dependent Enzymes

An alternative strategy of *S. aureus* to respond to nutritional immunity is to use a protein variant that lacks a metal cofactor altogether. The consumption of glucose through glycolysis is a process fundamental to many life forms. For bacteria, some of the enzymes involved are Mn-dependent. Yet even under Mn-limited conditions, *S. aureus* was shown to prefer glucose as main carbon source despite its burden on cellular Mn demand (Radin et al., 2019b). It has recently been demonstrated that *S. aureus* can express a Mn-independent variant of phosphoglycerate mutase to maintain glucose consumption under Mn-stress (Radin et al., 2019a). The discovery of metal-independent variants is not unique to *S. aureus* and may indicate a broader pattern among bacteria.

CONCLUSION AND PERSPECTIVES

Despite the wealth of knowledge on metal homeostasis in *S. aureus* at the host-microbe interface, a comprehensive overview of the complex interactions between different metal control systems is currently lacking. Many individual proteins and pathways have been identified. However, in most cases, the molecular mechanisms of action of all these different proteins are not fully established. We envision that an integrated omics approach to determine the changes in the proteome, metabolome and metalloproteome will offer a comprehensive view of the pathogen response to nutritional immunity as well as Fe overload. Recently, integrated omics approaches have been successfully used to explore the molecular action of metallodrugs such as platinum and ruthenium anticancer drugs (Wang, Li, and Sun 2019; Steel and Hartinger 2020). Of key importance will be metalloproteomics, which will provide information on the changing intracellular metal distribution among *S. aureus*' proteins. Such experiments have been performed for Fe in *E. coli* using the metalloproteomic approach Metal Isotope Radio Autography in Gel Electrophoresis (MIRAGE), which showed substantial changes in Fe distribution among proteins under normal and high Fe conditions (Sevcenco et al., 2011; 2009). It will be especially interesting to focus on the complex interplay between Fe and Mn homeostasis in this respect, as described above for SOD. A comprehensive understanding down to the molecular level will provide a new basis for the development of treatments against pathogenic bacteria, including MRSA. At the same time, it will allow clinicians to take pathogen response into account when treating iron-deficient patients, paving the way towards personalized treatment. This new understanding is crucial, especially considering the continuous increase of multidrug-resistant bacteria and their far-reaching impact on human health globally.

AUTHOR CONTRIBUTIONS

MCD, RMK, and P-LH conceptualized, wrote and edited the manuscript and approved the submitted version of the manuscript.

SUPPLEMENTARY MATERIAL

The Supplementary Material for this article can be found online at: https://www.frontiersin.org/articles/10.3389/fcell.2022.857237/full#supplementary-material

REFERENCES

Auerbach, M., Gafter-Gvili, A., and Macdougall, I. C. (2020). Intravenous Iron: A Framework for Changing the Management of Iron Deficiency. *Lancet Haematol.* 7, e342. doi:10.1016/S2352-3026(19)30264-9

Barber, M. F., and Elde, N. C. (2014). Escape from Bacterial Iron Piracy through Rapid Evolution of Transferrin. *Science* 346 (6215), 1362–1366. doi:10.1126/science.1259329

Barton Pai, A., Pai, M. P., Depczynski, J., McQuade, C. R., and Mercier, R.-C. (2006). Non-Transferrin-Bound Iron Is Associated with Enhanced *Staphylococcus aureus* Growth in Hemodialysis Patients Receiving Intravenous Iron Sucrose. *Am. J. Nephrol.* 26 (3), 304–309. doi:10.1159/000094343

Biswas, L., Biswas, R., Nerz, C., Ohlsen, K., Schlag, M., Schafer, T., et al. (2009). Role of the Twin-Arginine Translocation Pathway in *Staphylococcus*. *J. Bacteriol.* 191 (19), 5921–5929. doi:10.1128/JB.00642-09

Clarke, S. R., Wiltshire, M. D., and Foster, S. J. (2004). IsdA of *Staphylococcus aureus* Is a Broad Spectrum, Iron-Regulated Adhesin. *Mol. Microbiol.* 51 (5), 1509–1519. doi:10.1111/j.1365-2958.2003.03938.x

Coraça-Huber, D. C., Dichtl, S., Steixner, S., Nogler, M., and Weiss, G. (2018). Iron Chelation Destabilizes Bacterial Biofilms and Potentiates the Antimicrobial

Activity of Antibiotics against Coagulase-Negative Staphylococci. *Pathog. Dis.* 76 (5), 52. doi:10.1093/femspd/fty052

Cross, J. H., Bradbury, R. S., Fulford, A. J., Jallow, A. T., Wegmüller, R., Prentice, A. M., et al. (2015). Oral Iron Acutely Elevates Bacterial Growth in Human Serum. *Sci. Rep.* 5 (1), 1–7. doi:10.1038/srep16670

David, M. Z., and Daum, R. S. (2010). Community-Associated Methicillin-Resistant *Staphylococcus Aureus* : Epidemiology and Clinical Consequences of an Emerging Epidemic. *Clin. Microbiol. Rev.* 23 (3), 616–687. doi:10.1128/CMR.00081-09

DeLeo, F. R., Otto, M., Kreiswirth, B. N., and Chambers, H. F. (2010). Community-Associated Meticillin-Resistant *Staphylococcus aureus*. *The Lancet* 375 (9725), 1557–1568. doi:10.1016/S0140-6736(09)61999-1

DeLoughery, T. G. (2019). Safety of Oral and Intravenous Iron. *Acta Haematol.* 142 (1), 8–12. doi:10.1159/000496966

Finlayson-Trick, E. C. L., Fischer, J. A., Goldfarb, D. M., and Karakochuk, C. D. (2020). The Effects of Iron Supplementation and Fortification on the Gut Microbiota: A Review. *Gastrointest. Disord.* 2 (4), 327–340. doi:10.3390/gidisord2040030

Fontenot, C. R., Tasnim, H., Valdes, K. A., Popescu, C. V., and Ding, H. (2020). Ferric Uptake Regulator (Fur) Reversibly Binds a [2Fe-2S] Cluster to Sense Intracellular Iron Homeostasis in *Escherichia Coli*. *J. Biol. Chem.* 295 (46), 15454–15463. doi:10.1074/jbc.RA120.014814

Forrester, S. J., Kikuchi, D. S., Hernandes, M. S., Xu, Q., and Griendling, K. K. (2018). Reactive Oxygen Species in Metabolic and Inflammatory Signaling. *Circ. Res.* 122 (6), 877–902. doi:10.1161/CIRCRESAHA.117.311401

Gahlot, S., Nasreen, N., Johnson, J. A., Sahn, S. A., and Mohammed, K. A. (2017). Heme Oxygenase-1 Deficiency Diminishes Methicillin-Resistant *Staphylococcus aureus* Clearance Due to Reduced TLR9 Expression in Pleural Mesothelial Cells. *PLOS ONE* 12 (1), e0169245. doi:10.1371/journal.pone.0169245

Ganz, T., Aronoff, G. R., Goodnough, L. T., Macdougall, I. C., Mayer, G., Porto, G., et al. (2020). Iron Administration, Infection, and Anemia Management in CKD: Untangling the Effects of Intravenous Iron Therapy on Immunity and Infection Risk. *Kidney Med.* 2, 341–353. doi:10.1016/j.xkme.2020.01.006

Garcia, Y. M., Barwinska-Sendra, A., Tarrant, E., Skaar, E. P., Waldron, K. J., and Kehl-Fie, T. E. (2017). A Superoxide Dismutase Capable of Functioning with Iron or Manganese Promotes the Resistance of *Staphylococcus aureus* to Calprotectin and Nutritional Immunity. *Plos Pathog.* 13 (1), e1006125–19. doi:10.1371/journal.ppat.1006125

Gardner, W., and Kassebaum, N. (2020). Global, Regional, and National Prevalence of Anemia and its Causes in 204 Countries and Territories, 1990-2019. *Curr. Dev. Nutr.* 4 (Supplement_2), 830. doi:10.1093/cdn/nzaa053_035

Grigg, J. C., Cheung, J., Heinrichs, D. E., and Murphy, M. E. P. (2010a). Specificity of Staphyloferrin B Recognition by the SirA Receptor from *Staphylococcus aureus*. *J. Biol. Chem.* 285 (45), 34579–34588. doi:10.1074/jbc.M110.172924

Grigg, J. C., Ukpabi, G., Gaudin, C. F. M., and Murphy, M. E. P. 2010b. "Structural Biology of Heme Binding in the *Staphylococcus aureus* Isd System." *J. Inorg. Biochem.* 104 (3): 341–348. doi:10.1016/j.jinorgbio.2009.09.012

Haschka, D., Hoffmann, A., and Weiss, G. (2021). Iron in Immune Cell Function and Host Defense. *Semin. Cel Develop. Biol.* 115 (July), 27–36. doi:10.1016/j.semcdb.2020.12.005

Honarmand Ebrahimi, K., Hagedoorn, P.-L., and Hagen, W. R. (2015). Unity in the Biochemistry of the Iron-Storage Proteins Ferritin and Bacterioferritin. *Chem. Rev.* 115 (1), 295–326. doi:10.1021/cr5004908

Horsburgh, M. J., Ingham, E., and Foster, S. J. 2001, In *Staphylococcus aureus* , Fur Is an Interactive Regulator with PerR, Contributes to Virulence, and Is Necessary for Oxidative Stress Resistance through Positive Regulation of Catalase and Iron Homeostasis, *J. Bacteriol.*, 183 (2): 468–475. doi:10.1128/JB.183.2.468-475.2001

Jakubczyk, K., Dec, K., Kałduńska, J., Kawczuga, D., Kochman, J., and Janda, K. (2020). Reactive Oxygen Species - Sources, Functions, Oxidative Damage. *Pol. Merkur Lekarski* 48 (284), 124–127.

Johnson, M., Cockayne, A., Williams, P. H., and Morrissey, J. A. 2005. "Iron-Responsive Regulation of Biofilm Formation in *Staphylococcus Aureus* Involves Fur-Dependent and Fur-Independent Mechanisms." *J. Bacteriol.* 187 (23): 8211–8215. doi:10.1128/JB.187.23.8211-8215.2005

Kehl-Fie, T. E., Chitayat, S., Hood, M. I., Damo, S., Restrepo, N., Garcia, C., et al. (2011). Nutrient Metal Sequestration by Calprotectin Inhibits Bacterial Superoxide Defense, Enhancing Neutrophil Killing of *Staphylococcus aureus*. *Cell Host & Microbe* 10 (2), 158–164. doi:10.1016/j.chom.2011.07.004

Knutson, M. D., Oukka, M., Koss, L. M., Aydemir, F., and Wessling-Resnick, M. (2005). Iron Release from Macrophages after Erythrophagocytosis Is Up-Regulated by Ferroportin 1 Overexpression and Down-Regulated by Hepcidin. *Proc. Natl. Acad. Sci.* 102 (5), 1324–1328. doi:10.1073/pnas.0409409102

Laakso, H. A., Marolda, C. L., Pinter, T. B., Stillman, M. J., and Heinrichs, D. E. (2016). A Heme-Responsive Regulator Controls Synthesis of Staphyloferrin B in *Staphylococcus aureus*. *J. Biol. Chem.* 291 (1), 29–40. doi:10.1074/jbc.M115.696625

MacGarvey, N. C., Suliman, H. B., Bartz, R. R., Fu, P., Withers, C. M., Welty-Wolf, K. E., et al. (2012). Activation of Mitochondrial Biogenesis by Heme Oxygenase-1-Mediated NF-E2-Related Factor-2 Induction Rescues Mice from Lethal *Staphylococcus aureus* Sepsis. *Am. J. Respir. Crit. Care Med.* 185 (8), 851–861. doi:10.1164/rccm.201106-1152OC

Marchetti, M., de Bei, O., Bettati, S., Campanini, B., Kovachka, S., Gianquinto, E., et al. (2020). Iron Metabolism at the Interface between Host and Pathogen: From Nutritional Immunity to Antibacterial Development. *Int. J. Mol. Sci.* 21 (6), 2145. doi:10.3390/ijms21062145

Maresso, A. W., and Schneewind., O. (2006). Iron Acquisition and Transport in *Staphylococcus aureus*. *BioMetals* 19 (2), 193–203. doi:10.1007/s10534-005-4863-7

Mazmanian, S. K., Skaar, E. P., Gaspar, A. H., Humayun, M., Gornicki, P., Jelenska, J., et al. (2003). Passage of Heme-Iron across the Envelope of *Staphylococcus Aureus*. *Science* 299 (5608), 906–909. doi:10.1126/science.1081147

Mikkelsen, J. H., Runager, K., and Andersen, C. B. F. (2020). The Human Protein Haptoglobin Inhibits IsdH-Mediated Heme-Sequestering by *Staphylococcus aureus*. *J. Biol. Chem.* 295 (7), 1781–1791. doi:10.1074/jbc.RA119.011612

Modun, B., Morrissey, J., and Williams, P. (2000). The Staphylococcal Transferrin Receptor: A Glycolytic Enzyme with Novel Functions. *Trends Microbiol.* 8 (5), 231–237. doi:10.1016/S0966-842X(00)01728-5

Morrissey, J. A., Cockayne, A., Brummell, K., and Williams, P. 2004. "The Staphylococcal Ferritins Are Differentially Regulated in Response to Iron and Manganese and via PerR and Fur." *Infect. Immun.* 72 (2): 972–979. doi:10.1128/IAI.72.2.972-979.2004

Nakashige, T. G., Zhang, B., Krebs, C., and Nolan, E. M. (2015). Human Calprotectin Is an Iron-Sequestering Host-Defense Protein. *Nat. Chem. Biol.* 11 (10), 765–771. doi:10.1038/nchembio.1891

Obisesan, A. O., Zygiel, E. M., and Nolan, E. M. (2021). Bacterial Responses to Iron Withholding by Calprotectin. *Biochemistry* 60 (45), 3337–3346. doi:10.1021/acs.biochem.1c00572

Oliveira, F., Rohde, H., Vilanova, M., and Cerca, N. (2021). Fighting *Staphylococcus epidermidis* Biofilm-Associated Infections: Can Iron Be the Key to Success? *Front. Cel. Infect. Microbiol.* 11 563. doi:10.3389/fcimb.2021.798563

Pandur, E., Tamási, K., Pap, R., Jánosa, G., and Sipos, K. (2021). Distinct Effects of *Escherichia coli*, *Pseudomonas aeruginosa* and *Staphylococcus aureus* Cell Wall Component-Induced Inflammation on the Iron Metabolism of THP-1 Cells. *Int. J. Mol. Sci.* 22 (3), 1497. doi:10.3390/ijms22031497

Pasricha, Sant. Rayn., Tye-Din, Jason., Muckenthaler, Martina. U., and Swinkels, Dorine. W. (2021). Iron Deficiency. *The Lancet* 397, 233. doi:10.1016/S0140-6736(20)32594-0

Pidwill, G. R., Gibson, J. F., Cole, J., Renshaw, S. A., and Foster, S. J. (2021). The Role of Macrophages in *Staphylococcus aureus* Infection. *Front. Immunol.* 11 (January). doi:10.3389/fimmu.2020.620339

Pishchany, G., McCoy, A. L., Torres, V. J., Krause, J. C., Crowe, J. E., Fabry, M. E., et al. (2010). Specificity for Human Hemoglobin Enhances *Staphylococcus aureus* Infection. *Cell Host & Microbe* 8 (6), 544–550. doi:10.1016/j.chom.2010.11.002

Price, E. E., and Boyd, J. M. (2020). Genetic Regulation of Metal Ion Homeostasis in *Staphylococcus aureus*. *Trends Microbiol.* 28 (10), 821–831. doi:10.1016/j.tim.2020.04.004

P. Skaar, E., and Schneewind, O. 2004. "Iron-Regulated Surface Determinants (Isd) of *Staphylococcus aureus*: Stealing Iron from Heme." *Microbes Infect.* 6 (4): 390–397. doi:10.1016/j.micinf.2003.12.008

Qi, X., Zhang, Y., Guo, H., Hai, Y., Luo, Y., and Yue, T. (2020). Mechanism and Intervention Measures of Iron Side Effects on the Intestine. *Crit. Rev. Food Sci. Nutr.* 60 (12), 2113–2125. doi:10.1080/10408398.2019.1630599

Radin, J. N., Kelliher, J. L., Párraga Solórzano, P. K., Grim, K. P., Ramezanifard, R., Slauch, J. M., et al. (2019a). Metal-Independent Variants of Phosphoglycerate Mutase Promote Resistance to Nutritional Immunity and Retention of Glycolysis during Infection. *Plos Pathog.* 15 (7), e1007971–21. doi:10.1371/journal.ppat.1007971

Radin, J. N., Zhu, J., Brazel, E. B., McDevitt, C. A., and Kehl-Fie, T. E. (2019b). Synergy between Nutritional Immunity and Independent Host Defenses Contributes to the Importance of the MntABC Manganese Transporter during *Staphylococcus aureus* Infection. *Infect. Immun.* 87 (1). doi:10.1128/IAI.00642-18

Reniere, M. L., and Skaar, E. P. (2008). *Staphylococcus aureus* Haem Oxygenases Are Differentially Regulated by Iron and Haem. *Mol. Microbiol.* 69 (5), 1304–1315. doi:10.1111/j.1365-2958.2008.06363.x

Richter, K., Thomas, N., Claeys, J., McGuane, J., Prestidge, C. A., Coenye, T., et al. (2017). A Topical Hydrogel with Deferiprone and Gallium-Protoporphyrin Targets Bacterial Iron Metabolism and Has Antibiofilm Activity. *Antimicrob. Agents Chemother.* 61 (6). doi:10.1128/AAC.00481-17

Rigby, K. M., and DeLeo, F. R. (2012). Neutrophils in Innate Host Defense against *Staphylococcus aureus* Infections. *Semin. Immunopathol* 34 (2), 237–259. doi:10.1007/s00281-011-0295-3

Rosen, G. M., Pou, S., RamosCohen, C. L. Myron. S., Cohen, M. S., and Britigan, B. E. (1995). Free Radicals and Phagocytic Cells. *FASEB J.* 9 (2), 200–209. doi:10.1096/fasebj.9.2.7540156

Rowe, S. E., Wagner, N. J., Li, L., Beam, J. E., Wilkinson, A. D., Radlinski, L. C., et al. (2020). Reactive Oxygen Species Induce Antibiotic Tolerance during Systemic *Staphylococcus aureus* Infection. *Nat. Microbiol.* 5 (2), 282–290. doi:10.1038/s41564-019-0627-y

Schaefer, B., Meindl, E., Wagner, S., Tilg, H., and Zoller, H. (2020). Intravenous Iron Supplementation Therapy. *Mol. Aspects Med.* 75, 100862. doi:10.1016/j.mam.2020.100862

Schmaler, M., Jann, N. J., Ferracin, F., Landolt, L. Z., Biswas, L., Götz, F., et al. (2009). Lipoproteins in *Staphylococcus aureus* Mediate Inflammation by TLR2 and Iron-dependent Growth *In Vivo*. *J. Immunol.* 182 (11), 7110–7118. doi:10.4049/jimmunol.0804292

Sevcenco, A.-M., Krijger, G. C., Pinkse, M. W. H., Verhaert, P. D. E. M., Hagen, W. R., and Hagedoorn, P.-L. (2009). Development of a Generic Approach to Native Metalloproteomics: Application to the Quantitative Identification of Soluble Copper Proteins in *Escherichia coli*. *J. Biol. Inorg. Chem.* 14, 631–640. doi:10.1007/s00775-009-0477-9

Sevcenco, A.-M., Pinkse, M. W. H., Wolterbeek, H. T., Verhaert, P. D. E. M., Hagen, W. R., and Hagedoorn, P.-L. 2011. "Exploring the Microbial Metalloproteome Using MIRAGE." *Metallomics* 3: 1324–1330. doi:10.1039/C1MT00154J

Sheldon, J. R., and Heinrichs, D. E. (2012). The Iron-Regulated Staphylococcal Lipoproteins. *Front. Cel. Inf. Microbio.* 2. doi:10.3389/fcimb.2012.00041

Sheldon, J. R., and Skaar, E. P. (2019). Metals as Phagocyte Antimicrobial Effectors. *Curr. Opin. Immunol.* 60 (October), 1–9. doi:10.1016/j.coi.2019.04.002

Shin, M., Jin, Y., Park, J., Mun, D., Kim, S. R., Payne, S. M., et al. (2021). Characterization of an Antibacterial Agent Targeting Ferrous Iron Transport Protein FeoB against *Staphylococcus aureus* and Gram-Positive Bacteria. *ACS Chem. Biol.* 16 (1), 136–149. doi:10.1021/acschembio.0c00842

Singh, N., Ahmad, Z., Baid, N., and Kumar, A. (2018). Host Heme Oxygenase-1: Friend or Foe in Tackling Pathogens? *IUBMB Life* 70 (9), 869–880. doi:10.1002/iub.1868

Skaar, E. P., Humayun, M., Bae, T., DeBord, K. L., and Schneewind., O. (2004). Iron-Source Preference of *Staphylococcus aureus* Infections. *Science* 305 (5690), 1626–1628. doi:10.1126/science.1099930

Stauff, D. L., and Skaar, E. P. (2009). The Heme Sensor System of *Staphylococcus aureus*. *Contrib. Microbiol.* 16, 120–135. doi:10.1159/000219376

Stauff, D. L., Torres, V. J., and Skaar, E. P. (2007). Signaling and DNA-Binding Activities of the *Staphylococcus aureus* HssR-HssS Two-Component System Required for Heme Sensing. *J. Biol. Chem.* 282 (36), 26111–26121. doi:10.1074/jbc.M703797200

Steel, T. R., and Hartinger, C. G. (2020). Metalloproteomics for Molecular Target Identification of Protein-Binding Anticancer Metallodrugs. *Metallomics* 12 (11), 1627–1636. doi:10.1039/d0mt00196a

Suffredini, D. A., Xu, W., Sun, J., Barea-Mendoza, J., Solomon, S. B., Brashears, S. L., et al. (2017). Parenteral Irons versus Transfused Red Blood Cells for Treatment of Anemia during Canine Experimental Bacterial Pneumonia. *Transfusion* 57 (10), 2338–2347. doi:10.1111/trf.14214

Taylor, J. M., and Heinrichs, D. E. (2002). Transferrin Binding in *Staphylococcus aureus*: Involvement of a Cell Wall-Anchored Protein. *Mol. Microbiol.* 43 (6), 1603–1614. doi:10.1046/j.1365-2958.2002.02850.x

Theurl, I., Theurl, M., Seifert, M., Mair, S., Nairz, M., Rumpold, H., et al. (2008). Autocrine Formation of Hepcidin Induces Iron Retention in Human Monocytes. *Blood* 111 (4), 2392–2399. doi:10.1182/blood-2007-05-090019

Torres, V. J., Attia, A. S., Mason, W. J., Hood, M. I., Corbin, B. D., Beasley, F. C., et al. (2010). *Staphylococcus aureus* Fur Regulates the Expression of Virulence Factors that Contribute to the Pathogenesis of Pneumonia. *Infect. Immun.* 78 (4), 1618–1628. doi:10.1128/IAI.01423-09

Treffon, J., Chaves-Moreno, D., Niemann, S., Pieper, D. H., Vogl, T., Roth, J., et al. (2020). Importance of Superoxide Dismutases A and M for Protection of *Staphylococcus aureus* in the Oxidative Stressful Environment of Cystic Fibrosis Airways. *Cell Microbiol.* 22, 1–14. doi:10.1111/cmi.13158

Turlin, E., Débarbouillé, M., Augustyniak, K., Gilles, A.-M., and Wandersman, C. (2013). *Staphylococcus aureus* FepA and FepB Proteins Drive Heme Iron Utilization in *Escherichia coli*. *PLoS ONE* 8 (2), e56529. doi:10.1371/journal.pone.0056529

Verstraete, M. M., Morales, L. D., Kobylarz, M. J., Loutet, S. A., Laakso, H. A., Pinter, T. B., et al. (2019). The Heme-Sensitive Regulator SbnI Has a Bifunctional Role in Staphyloferrin B Production by *Staphylococcus aureus*. *J. Biol. Chem.* 294 (30), 11622–11636. doi:10.1074/jbc.RA119.007757

Wang, Y., Li, H., and Sun, H. (2019). Metalloproteomics for Unveiling the Mechanism of Action of Metallodrugs. *Inorg. Chem.* 58 (20), 13673–13685. doi:10.1021/acs.inorgchem.9b01199

Yilmaz, B., and Li, H. (2018). Gut Microbiota and Iron: The Crucial Actors in Health and Disease. *Pharmaceuticals* 11 (4), 98. doi:10.3390/PH11040098

Zygiel, E. M., Obisesan, A. O., Nelson, C. E., Oglesby, A. G., and Nolan, E. M. (2021). Heme Protects *Pseudomonas aeruginosa* and *Staphylococcus aureus* from Calprotectin-Induced Iron Starvation. *J. Biol. Chem.* 296 (January), 100160. doi:10.1074/jbc.RA120.015975

Conflict of Interest: The authors declare that the research was conducted in the absence of any commercial or financial relationships that could be construed as a potential conflict of interest.

Publisher's Note: All claims expressed in this article are solely those of the authors and do not necessarily represent those of their affiliated organizations, or those of the publisher, the editors and the reviewers. Any product that may be evaluated in this article, or claim that may be made by its manufacturer, is not guaranteed or endorsed by the publisher.

frontiers | Frontiers in Cell and Developmental Biology

BRIEF RESEARCH REPORT
published: 01 April 2022
doi: 10.3389/fcell.2022.856300

Oral Elesclomol Treatment Alleviates Copper Deficiency in Animal Models

Sai Yuan[1†], *Tamara Korolnek*[1] *and Byung-Eun Kim*[1,2*]

[1]*Department of Animal and Avian Sciences, University of Maryland, College Park, MD, United States,* [2]*Biological Sciences Graduate Program, College Park, MD, United States*

Copper (Cu) is an essential trace element for key biochemical reactions. Dietary or genetic copper deficiencies are associated with anemia, cardiomyopathy, and neurodegeneration. The essential requirement for copper in humans is illustrated by Menkes disease, a fatal neurodegenerative disorder of early childhood caused by mutations in the ATP7A copper transporter. Recent groundbreaking studies have demonstrated that a copper delivery small molecule compound, elesclomol (ES), is able to substantially ameliorate pathology and lethality in a mouse model of Menkes disease when injected as an ES-Cu^{2+} complex. It is well appreciated that drugs administered through oral means are more convenient with better efficacy than injection methods. Here we show, using genetic models of copper-deficient *C. elegans* and mice, that dietary ES supplementation fully rescues copper deficiency phenotypes. Worms lacking either the homolog of the CTR1 copper importer or the ATP7 copper exporter showed normal development when fed ES. Oral gavage with ES rescued intestine-specific *Ctr1* knockout mice from early postnatal lethality without additional copper supplementation. Our findings reveal that ES facilitates copper delivery from dietary sources independent of the intestinal copper transporter CTR1 and provide insight into oral administration of ES as an optimal therapeutic for Menkes disease and possibly other disorders of copper insufficiency.

Keywords: copper transport, copper defficiency, intestine, Menkes disease, elesclomol, ATP7A copper exporter, CTR1 copper importer, *C. elegans*

OPEN ACCESS

Edited by:
Kourosh Honarmand Ebrahimi, King's College London, United Kingdom

Reviewed by:
Paul Cobine, Auburn University, United States
Daniel N. Cox, Georgia State University, United States
Richard Burke, Monash University, Australia

***Correspondence:**
Byung-Eun Kim
bekim@umd.edu

[†]***Present address** :*
Sai Yuan, Division of Vascular Surgery, University of California, San Francisco, CA, United States

Specialty section:
This article was submitted to Cellular Biochemistry, a section of the journal Frontiers in Cell and Developmental Biology

Received: *17 January 2022*
Accepted: *03 March 2022*
Published: *01 April 2022*

Citation:
Yuan S, Korolnek T and Kim B-E (2022) Oral Elesclomol Treatment Alleviates Copper Deficiency in Animal Models. Front. Cell Dev. Biol. 10:856300. doi: 10.3389/fcell.2022.856300

INTRODUCTION

Copper (Cu) is an essential micronutrient required as a catalytic cofactor for a wide range of biochemical processes, including ATP generation in mitochondria, maturation of hormones, iron mobilization, and disproportionation of toxic superoxide (Kim et al., 2008). The essential nature of copper in humans is underscored by Menkes disease, an X-linked copper deficiency disorder caused by mutations in the ATP7A copper exporter (Kaler, 2011). Defects in Menkes patients are attributed primarily to impaired copper transport from intestinal epithelial cells (IECs) to the circulation, resulting in a systemic copper deficiency (Petris et al., 1996; Wang et al., 2012a). Clinical symptoms of Menkes include severe neurodegeneration, connective tissue defects, hypothermia, and impaired pigmentation. Most cases of Menkes disease typically lead to death within a few years after birth. Some individual patients harboring mild forms of ATP7A mutations exhibit extended life spans; nevertheless, profound neurodevelopmental delays are observed in these patients (Madsen and Gitlin, 2007; Kaler, 2011).

Yeast, fruit flies, zebrafish, and mice have all been used as model organisms to understand the role of ATP7A in copper metabolism and evaluate potential treatments for Menkes disease (Nose et al.,

2006; Turski and Thiele, 2007; Madsen and Gitlin, 2008; Smith et al., 2017). Our recent studies in *C. elegans* models revealed that tight control of copper homeostasis is required for normal growth and development of worms, and that this regulation is in part controlled by the functions of a CTR1 copper importer ortholog, CHCA-1, and an ATP7A ortholog, CUA-1, in the intestine (Chun et al., 2017a; Yuan et al., 2018). Given the conservation of the pathway for the import and distribution of dietary copper in *C. elegans*, this animal is well-poised to serve as a model organism for therapeutic approaches for Menkes disease treatments.

The copper-binding molecule elesclomol (ES) was identified in a yeast-based screen as an efficient copper delivery agent for cellular copper-dependent proteins. ES is especially efficient at delivering copper to mitochondrial cuproenzymes such as cytochrome c oxidase (CcO), which is essential for energy generation (Soma et al., 2018). We have recently shown that subcutaneous injections of an ES-Cu^{2+} complex in the *mottled-brindled* (*mo-br*) mouse, a model for classical Menkes disease (Rossi et al., 2001), resulted in profound improvement of Menkes-like pathology including neonatal lethality and neurodegeneration (Guthrie et al., 2020). The ES-Cu^{2+} complex injections rescued systemic copper levels in multiple tissues including the brain, which is highly susceptible to copper-deficiency, and restored activities of essential cuproenzymes to the point where catastrophic outcomes were prevented. However, it is not known whether orally supplied ES can escort copper through polarized enterocytes to be effective in treating the severe systemic copper deficiency found in animal models of Menkes disease or under conditions of complete *Atp7a* ablation.

In this study, we use genetic models of copper-deficient *C. elegans* to demonstrate that supplementation with ES alone in the diet fully rescues developmental defects found in *chca-1*- and *cua-1*-deleted worms. We further demonstrate that oral gavage with ES alone can rescue intestine specific *Ctr1* knockout mice from neonatal mortality without additional copper supplementation. These results suggest that ES can facilitate copper delivery from dietary sources independent of the intestinal copper transporting system and offers efficient administration options in treating Menkes and other copper-deficiency patients.

RESULTS

ES Rescues Developmental Phenotypes and Copper Levels in *Chca-1*-Mutants in *C. elegans*

We recently demonstrated that nematodes expressing a non-functional copy of intestinal CHCA-1, the nematode homolog of the mammalian copper transporter *Ctr1,* fail to accumulate wild-type levels of copper in their body and arrest during larval development when grown under copper deficient conditions (Yuan et al., 2018). Given the functional conservation between nematode CHCA-1 and mammalian *Ctr1,* its facile manipulation and genetic tractability, we set out to determine if *C. elegans* is a suitable animal model to explore ES as a potential therapeutic for copper deficiency disorders. To that end, we first asked if ES can rescue the copper deficiency phenotypes of the *chca-1(tm6506)* mutant strain that we previously characterized (Yuan et al., 2018). Synchronized L1 cultures of *chca-1(tm6506)*) mutants and wild-type (WT) worms were grown on standard growth media in the absence (Basal) or presence of 100 μM bathocuproinedisulfonic acid (BCS)—a membrane-impermeable copper chelator—or BCS-containing media supplemented with 10 μM copper chloride ($CuCl_2$) or various concentrations of ES (from 1 to 50 μM). As shown in **Figure 1A** (panel d), *chca-1* mutants grown on BCS-containing plates have a dramatic larval arrest phenotype when compared to mutants grown on control plates (**Figures 1A,C**) and WT worms grown under either condition. As expected, this larval arrest phenotype is fully rescued by copper supplementation, and importantly, by supplementation with ES in a dose dependent matter (**Figure 1A**, e-h).

We used COPAS sorting to quantitatively examine the larval phenotype of the *chca-1(tm6506)* mutant. As shown in **Figure 1B**, rescue of the larval arrest phenotype—as determined by an increase in body size—is observed at doses as low as 5 μM ES with full rescue observed at 50 μM ES supplementation. Moreover, the ability of ES to rescue the larval phenotype is comparable to rescue observed by copper supplementation. Furthermore, ICP-MS analysis of worms grown under the same conditions demonstrated that whole animal copper levels in the *chca-1(tm6506)* are fully rescued by ES supplementation (**Figure 1C**). These results strongly suggest that ES can efficiently restore copper levels and reverse phenotypes caused by copper deficiency even in the presence of the high-affinity copper chelator, BCS. Importantly, these data suggest that *C. elegans* represents a viable experimental animal model to interrogate the biology of ES and its potential as a therapeutic for copper deficiency disorders.

ES Supplementation Rescues the Developmental Phenotypes of a *C. elegans* Model of Menkes Disease

Our previous studies identified *cua-1*, the *C. elegans* homolog of ATP7A/B, as a key regulator of systemic copper homeostasis in the worm (Chun et al., 2017a). While CUA-1 is expressed in the intestine, hypodermis, pharynx, and neurons in *C. elegans, cua-1* primarily functions as a copper exporter at the basolateral membrane of the intestine, delivering dietary copper to extraintestinal tissues as needed. Notably, *cua-1* mutant model Menkes disease in that they exhibit systemic copper deficiency (Chun et al., 2017a). *cua-1* RNAi in the presence of 100 μM BCS results in a severe developmental arrest phenotype (**Figures 2A,D**). Importantly, this phenotype is rescued by treatment with 5 μM ES even in the absence of

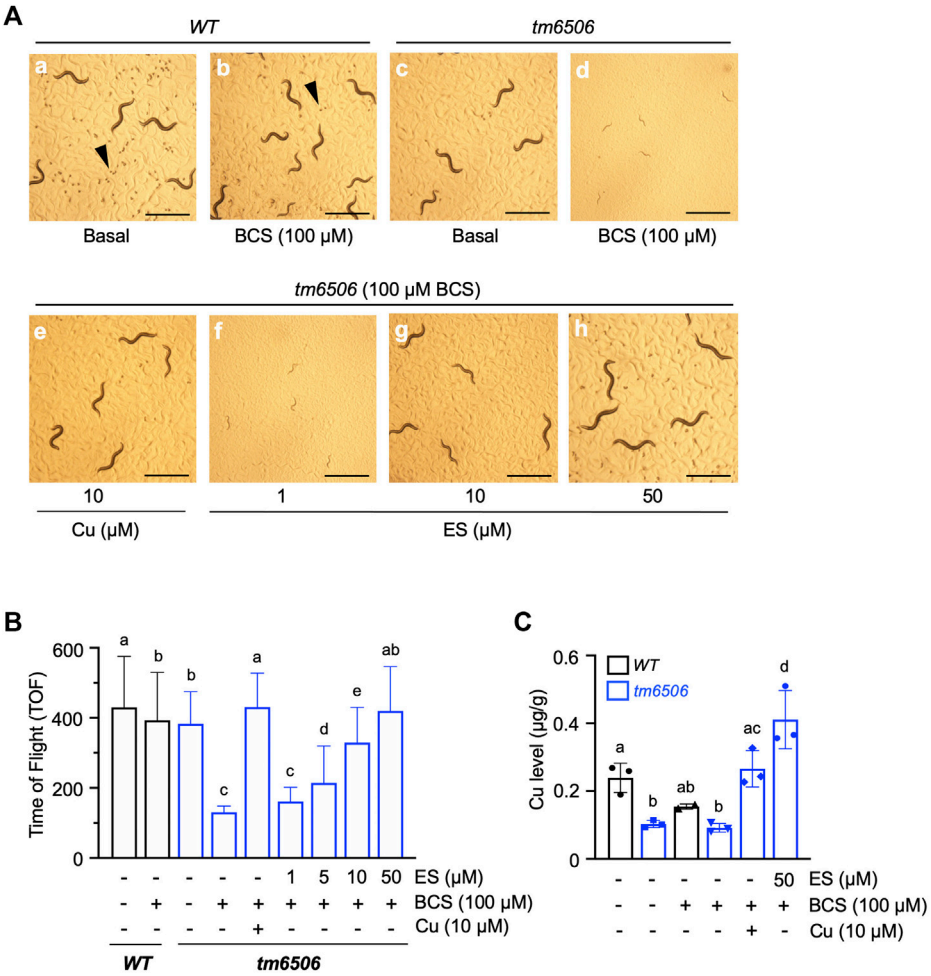

FIGURE 1 | Dietary ES rescues larval arrest phenotypes associated with copper deficiency in *chca-1* mutants in *C. elegans*. **(A)**, Representative images of *C. elegans* nematodes grown under copper-deficient conditions. Synchronized L1 larval cultures of WT and *chca-1(tm6506)* mutant worms were seeded onto control plates, plates containing 100 μM of the copper chelator BCS or BCS-containing plates supplemented with $CuCl_2$ (10 μM) or ES (from 1 to 50 μM). Images taken 72 h after seeding worms. Arrowheads indicate eggs. Egg numbers in the representative fields are a: ~110, b: ~20, c:~10, d: none, e: ~10, f: none, g: none, h:~50. Scale bar, 1 mm. **(B)**, Body length quantification as a measure of larval development. Worms were grown as in A. and body length was determined using a COPAS BioSort system. Number of worms tested for each condition: 88-269. Groups with different letters are statistically significantly different from each other at $p = 0.05$ (one-way ANOVA, Sidak post hoc test). **(C)**, Total worm copper levels measured by ICP-MS. Different letters indicate statistically significant differences as determined by a two-way ANOVA, Tukey post hoc test. Error bars represent mean ± SD.

exogenous copper supplementation (**Figures 2A,H**). Worms simultaneously grown in *cua-1(RNAi)* and in the presence 100 μM BCS that manage to escape arrest and reach reproductive age were interrogated for their ability to produce viable embryos as measured by the hatching rate. As shown in **Figure 2B**, *cua-1* RNAi in the presence of 100 μM BCS results in a severe defect in hatching rate. However, this phenotype can be partially rescued by treatment with 5 μM ES.

A number of groups have shown that *cua-1* is expressed in multiple tissues in the worm (Wakabayashi et al., 1998; Chun et al., 2017a). To specifically demonstrate ES rescue of copper transport across the intestinal membrane, we made use of the BK015 worm line [$P_{vha\text{-}6}$*::CUA-1.1::GFP::unc-54 3′UTR; cua-1*(*ok904*)] which ectopically expresses a GFP-tagged version of CUA-1 driven by an intestine-specific promoter in a *cua-1*-null mutant background (Chun et al., 2017a). BK015 worms require added dietary copper for optimal growth but can be maintained with about 50% survival on standard OP50 bacteria without dietary copper amendments (**Figure 2C**, a-b and D). This morbidity is presumably caused by the lack of CUA-1 in extraintestinal tissues such as pharynx and neurons. Knockdown of *cua-1* in BK015 worms results in complete larval lethality (**Figures 2C,D**). However, this lethality can be rescued almost fully in a dose-dependent manner by 500 nM ES supplementation (**Figure 2D**). Thus, ES is specifically capable of rescuing defective intestinal copper export, the major hallmark of Menkes disease, in a whole animal model. Notably, 5 μM ES also rescues suboptimal growth of BK015 under basal media

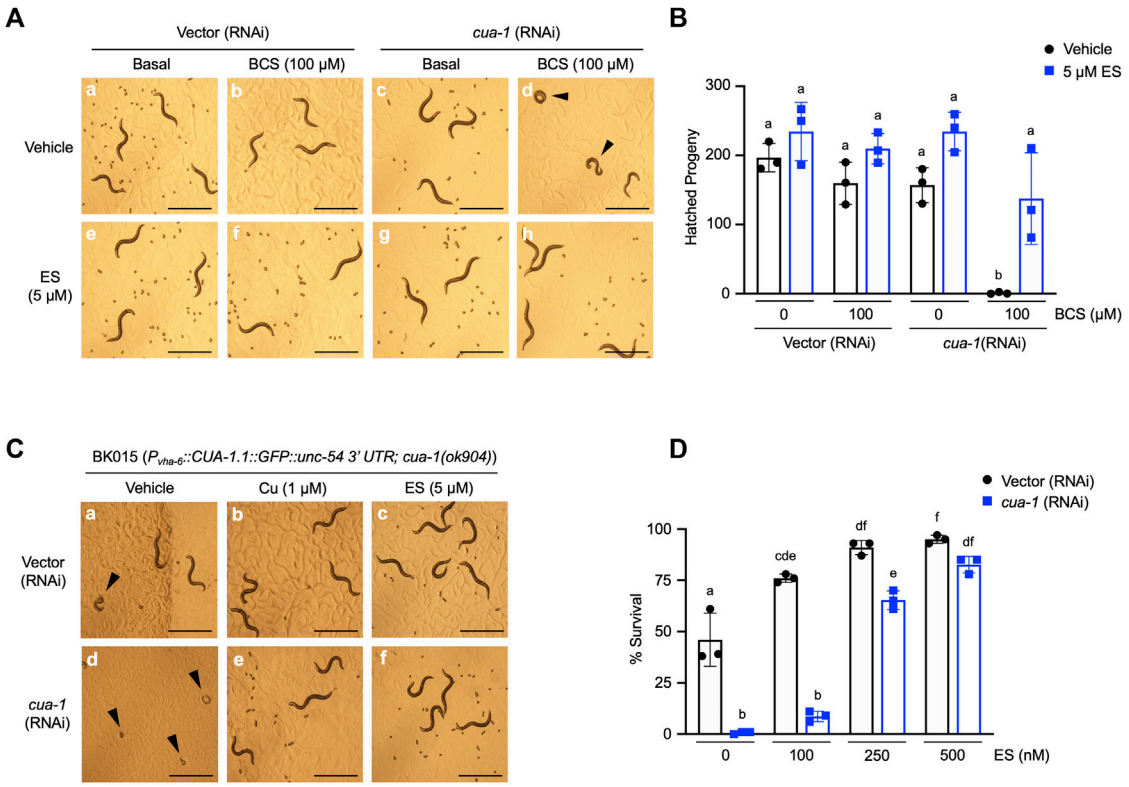

FIGURE 2 | Dietary ES supplementation rescues developmental phenotypes in a *C. elegans* model of Menkes disease. **(A)**, (top row) WT worms were exposed to RNAi from the L1 stage for 4 days with or without 100 μM BCS treatment in the presence of vehicle (DMSO); (bottom row) worms grown under identical conditions as above supplemented with 5 μM ES. Representative microscope images from three independent replicates are shown; arrowheads show representative arrested worms. Scale bar, 1 mm. **(B)**, WT worms grown under varying RNAi and BCS conditions supplemented with vehicle (DMSO) or 5 μM ES were picked to individual plates at the L4 stage in triplicate, allowed to lay eggs, and transferred to fresh plates every 24 h for 3 days. Eggs were incubated overnight to allow hatching and progeny number was determined as the total hatched larvae, $n = 3$ biological replicates (different letters indicate statistical significance at $p = 0.05$, by two-way ANOVA, Tukey's post hoc test). Error bars represent mean ± SEM. **(C)**, Transgenic worms expressing CUA-1 in the intestine [BK015 strain, $P_{vha\text{-}6}$*::CUA-1.1::GFP::unc-54 3′UTR; cua-1(ok904)*] were cultured on RNAi plates supplemented with either vehicle (DMSO), 1 μM copper, or 5 μM ES from the L1 stage for 4 days. Representative microscope images from three independent replicates are shown; arrowheads point at arrested larvae that eventually die. Scale bar, 1 mm. **(D)**, BK015 strain worms were cultured on RNAi plates supplemented with either vehicle (DMSO) or indicated amounts of ES from the L1 stage for 4 days and then scored for their ability to survive larval lethality and make it to the adult stage (% survival on *y*-axis). $n = 3$ biological replicates (different letters indicate statistical significance by two-way ANOVA, Tukey's post hoc test). Error bars represent mean ± SEM.

conditions (**Figures 2C,F**), indicating that ES is capable of restoring copper homeostasis defects further downstream of intestinal copper export.

Effects of ES on CUA-1 Localization in the Intestine

To further assess the effect of ES on organismal copper homeostasis in *C. elegans*, we analyzed the subcellular localization of CUA-1.1, which is encoded by one of two splice isoforms of *cua-1*. We have previously shown that CUA-1.1 localizes to the basolateral membrane of the worm intestine under basal conditions. In response to elevated amounts of dietary copper, CUA-1.1 redistributes to lysosome-like gut granules in intestinal cells, likely as a protective measure to sequester potentially toxic excess copper. The other splice variant, CUA-1.2, localizes constitutively to the basolateral membrane irrespective of dietary copper concentration (Chun et al., 2017a). Localization of CUA-1.1 can be perturbed genetically, as loss of *chca-1* decreased distribution of CUA-1.1 to granules, indicative of copper deficiency even in the presence of sufficient dietary copper (Yuan et al., 2018). Surprisingly, ES treatment did not appear to influence the subcellular distribution of CUA-1.1 in the gut (**Figure 3**). This result is intriguing and may suggest an alternative copper uptake pathway exploited by ES that potentially preserves copper in a less toxic form that does not trigger CUA-1.1 re-localization to gut stress granules.

Oral Administration of ES Rescues Neonatal Lethality and Growth Defects in Intestine-specific *Ctr1* Knockout Mice

We next aimed to determine if ES was capable of escorting copper across the polarized intestinal epithelium in mammals.

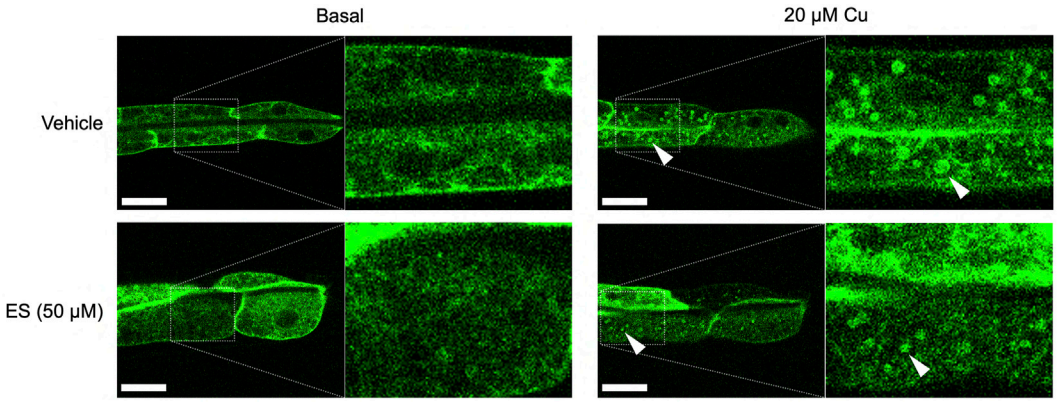

FIGURE 3 | Treatment with ES does not affect subcellular localization of CUA-1 in the intestine. Synchronized BK014 transgenic worms ($P_{vha\text{-}6}$*::CUA-1.1::GFP::unc-54 3′ UTR*) were cultured on NGM agar plates with indicated amounts of $CuCl_2$, vehicle (DMSO) or ES from the L1 stage. *CUA-1.1::GFP* localization in live L4 worms was examined using confocal microscopy. Representative microscope images from three independent replicates are shown; arrowheads indicate CUA-1 localized to gut granules upon copper treatment. Boxed images are enlarged and added as indicated with dotted lines. Scale bar, 20 μm.

Loss of intestinal *Ctr1* in mice leads to profound neonatal defects in copper delivery to peripheral tissues, and results in drastically stunted development with mutants exhibiting 100% lethality within 25 days after birth (Nose et al., 2006). Intestine-specific *Ctr1* knockout mice ($Ctr1^{int/int}$) were administered a 10 mg/kg dose of ES by oral gavage once every 2 days from postnatal day (PND) 7. We found a 35-days survival rate of 100% in ES-treated $Ctr1^{int/int}$ mice, whereas all mutant mice treated with vehicle died between PND 12 and 23 (**Figure 4A**). ES-treated knockout pups showed normal development and weight gain with no apparent difference as compared to vehicle- or ES-treated WT mice, while all vehicle-treated $Ctr1^{int/int}$ pups failed to thrive, lost weight, and began dying around PND 12 (**Figure 4B**). These results suggest that ES can deliver available copper from normal dietary sources—namely, milk from mothers fed a regular chow diet.

To further characterize the intestinal phenotype of ES-rescued $Ctr1^{int/int}$, we isolated IECs from PND 17 mice treated with ES or vehicle, and evaluated the abundance of copper chaperone for superoxide dismutase (CCS), a marker for intracellular copper-availability, as it is known that CCS levels are inversely proportional to cytosolic copper bioavailability (Bertinato and L'Abbé, 2003; Kim et al., 2010). As expected, we observed increased CCS steady-state levels in vehicle-treated $Ctr1^{int/int}$ intestinal cells as compared to levels in cells from control littermates ($Ctr1^{flox/flox}$) treated with vehicle or ES. The increased CCS levels in cells from ES-treated $Ctr1^{int/int}$ were suppressed back to levels observed in $Ctr1^{flox/flox}$ mice (**Figures 4C,D**), indicating that the limited copper availability in the *Ctr1*-deleted enterocytes was normalized by ES gavage. Hyperaccumulation of copper in the IECs observed in $Ctr1^{int/int}$ (Nose et al., 2006) was also rescued in the ES-treated mutants, while ES did not influence overall zinc levels in the intestine (**Figure 4D**) suggesting a copper-specific function for ES. Taken together, our results indicate that oral treatment with ES is capable of escorting copper across a CTR1-deficient polarized enterocyte layer.

DISCUSSION

C. elegans has emerged as a highly amenable model of micronutrient metabolism for metals such as iron, heme-iron, copper, and zinc (Anderson and Leibold, 2014; Sinclair and Hamza, 2015; Dietrich et al., 2017). Our recent studies revealed that CUA-1 is a key intestinal copper exporter in the worm that plays an analogous role to the human P-type ATPase in controlling systemic copper homeostasis to the human P-type ATPases (Chun et al., 2017a; Pierson et al., 2018). Moreover, we found that worms lacking CHCA-1, a CTR1 ortholog, exhibit impaired copper acquisition and profound growth and reproductive defects under copper-limiting conditions, suggesting that the pathway for intestinal copper uptake *via* the conventional CTR1-ATP7A axis is conserved in worms (Wakabayashi et al., 1998; Yuan et al., 2018).

In this study, we show that low concentrations of ES without additional copper supplemented in the media can almost fully rescue the phenotypes caused by either the loss of CHCA-1 or CUA-1 (**Figure 1** and **Figure 2**). We observed that ES is capable of increasing copper accumulation even in the presence of BCS. Considering that ES-Cu^{2+} is much more stable than BCS-Cu^{2+} (Xiao et al., 2008), it is possible that ES binds Cu^{2+} from dietary sources, forms a highly stable and membrane permeable complex, and mediates copper delivery from the intestinal lumen in the form of ES-Cu^{2+}. It is unknown how copper is liberated from the ES-Cu^{2+} complex to be integrated into various cuproproteins, though we do not rule out the possibility that ES is somehow metabolized intracellularly and then copper is released. Future mechanistic studies will be required to answer these questions.

While it is unknown how copper is transported to and utilized by different subcellular compartments after ES facilitates its entry into intestinal cells, our results in the BK015 strain treated with *cua-1* RNAi show that ES treatment can fully rescue the lethality in worms lacking *cua-1* expression across all tissues in the worm, suggesting that *cua-1*-independent copper delivery from the intestine to other tissues can be mediated by ES. These results

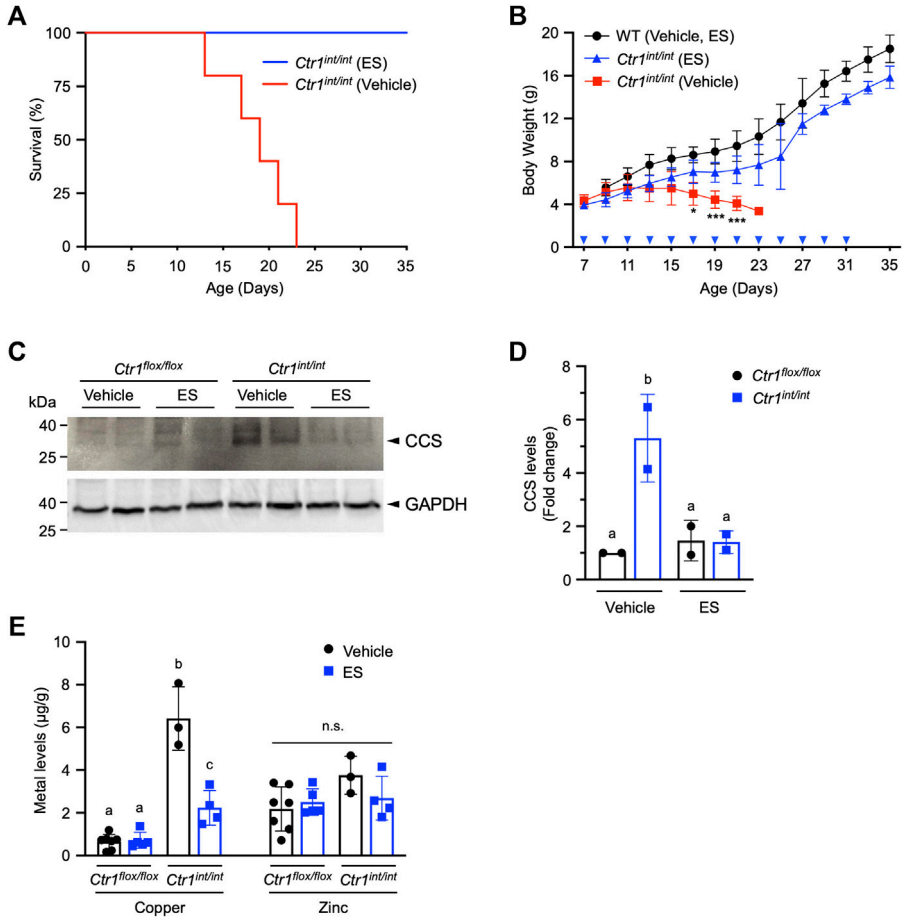

FIGURE 4 | Rescue of *Ctr1*$^{int/int}$ mice with ES by oral gavage. *Ctr1*$^{int/int}$ and control littermates were given ES or vehicle treatment by gavage every 2 days until PND 31. **(A)**, Kaplan-Meier plot showing percent survival of *Ctr1*$^{int/int}$ administered vehicle (red, $n = 5$), or ES (blue, $n = 4$). **(B)**, Body weight (g) of control littermates (*Ctr1*$^{flox/flox}$ or *Ctr1*$^{flox/+}$ referred to as WT), or *Ctr1*$^{int/int}$ treated with vehicle, or ES. Cohorts consisted of WT (Vehicle or ES, $n = 4$), *Ctr1*$^{int/int}$ (Vehicle, n = 5), and *Ctr1*$^{int/int}$ (ES, $n = 7$). No significant difference in growth between WT vehicle and WT ES was found (data not shown) as tested in an ES injection experiment (Guthrie et al., 2020). Asterisk marks indicate significant difference compared to the *Ctr1*$^{int/int}$ vehicle group (two-way ANOVA, Tukey's post hoc test, $^{*}p < 0.05$, $^{***}p < 0.001$). Error bars represent mean ± SD. **(C)**, SDS-PAGE analysis of total extracts of intestinal epithelial cells (IECs) from two representative *Ctr1*$^{flox/flox}$ and *Ctr1*$^{int/int}$ mice (PND 17) 10 days after commencing treatment. CCS levels in IECs were detected by immunoblotting. CCS and GAPDH (used as a loading control) bands are indicated with arrowheads. **(D)**, Quantification of relative CCS expression (normalized by GAPDH) in the enterocytes of the *Ctr1*$^{flox/flox}$ and *Ctr1*$^{int/int}$ mice. Groups with different letters are statistically significantly different from each other at $p < 0.05$ (one-way ANOVA, Sidak post hoc test). Error bars indicate mean ± SD. **(E)**, Copper and zinc levels in *Ctr1*$^{int/int}$ IECs after ES or vehicle administration (**Figure 4C**). Groups with different letters are significantly different from each other at $p = 0.05$. n.s., not significant (one-way ANOVA, Sidak post hoc test). Error bars represent mean ± SD.

indicate that ES can bypass the genetic blockage of intestinal copper absorption and supply copper to circulation and peripheral tissues in *C. elegans*. Additionally, the findings of this study suggest that *C. elegans* can be exploited as an animal model for screening of pharmacological chaperones for cellular copper distribution.

ES-Cu^{2+} administration by subcutaneous injections resulted in substantial rescue of lethal phenotypes in the *mo-br* mouse by restoring critical copper-dependent enzymes such as cytochrome c oxidase in the mitochondria (Guthrie et al., 2020). However, the efficiency of ES-mediated copper delivery to cuproenzymes, particularly in the secretory pathway, seemed to be limited. For example, coat pigmentation, which is dependent on tyrosinase in the secretory compartment that requires ATP7A for its metalation in the Golgi (Petris et al., 2000), was only marginally rescued by ES-Cu^{2+} administration in these experiments (Guthrie et al., 2020). A number of copper dependent enzymes found in the secretory pathway are conserved in *C. elegans*, including tyrosinase (Sendoel et al., 2010), and neuropeptide amidation enzymes (Van Bael et al., 2018; Yuan et al., 2018). Establishing reporter lines for these enzymes would be a first step in exploring and testing subcellular targeting efficiency of structural analogues of ES or new forms of chemical copper ionophores and chaperones in a worm model, ultimately leading to more effective pharmacological treatment of copper deficiency in all tissues and subcellular compartments.

In this study, oral treatment of *Ctr1*$^{int/int}$ mice with ES rescued the lethality of these mutants and, notably, this

rescue occurred in the absence of additional dietary copper. Similar to the *mo-br* mice, *Ctr1*$^{int/int}$ mice exhibit copper deficiency in peripheral tissues due to impaired intestinal copper absorption. These results are directly relevant to long-term therapeutic applications expected in treating disease of copper deficiency including Menkes patients, as oral treatment with ES would minimize invasive procedures. Menkes disease typically presents in the first few months after birth and results in death by 3 years of age. This indicates a high demand for copper during the early developmental stages of mammals (Prohaska and Brokate, 2002) and underscores the critical importance of early and long-term treatments for Menkes patients (Kaler, 2011). Our results in the *cua-1*-depleted worm model suggest the possibility of ATP7A-independent intestinal copper export by ES, and it is worthwhile to further test the efficacy of ES oral administration in mammalian Menkes models. An important follow up question would be whether ES (or an ES-Cu^{2+} complex) could function as an efficient copper delivery agent to the fetus via placental membranes. This question would be readily testable in future studies with genetic mouse models of copper deficiency, including conditional *Atp7a* knockouts (Wang et al., 2012a; Wang et al., 2012b), by feeding ES to pregnant mice.

An interesting observation in ES-treated *Ctr1*$^{int/int}$ mice is that ES rescued the hyperaccumulation of copper in the intestine (**Figure 4**). While it is unknown exactly how *Ctr1*-deleted IECs accumulate elevated levels of copper (Nose et al., 2006), it is possible that copper overaccumulation occurs in vesicular compartments, where CTR1 normally functions to mobilize copper from endosomes to the cytosol in a CTR2-dependent process. Hyperaccumulation of copper also occurs in *Ctr2* knockout fibroblasts and tissues in CTR2 knockout mice (Öhrvik et al., 2013; Öhrvik and Thiele, 2015; Öhrvik et al., 2016). Further studies will be necessary to establish whether ES can be used as a valuable tool for investigating subcellular copper homeostasis, mediated potentially by vesicular copper sequestration (Leary and Ralle, 2020). Taken together, our results from the rescued *chca-1* mutant worm, *Ctr1*$^{int/int}$ mice, and the Menkes worm model provide novel insights into using the copper binding molecule ES or its potential analogs to treat Menkes patients and other copper-deficiency disorders.

EXPERIMENTAL PROCEDURES

Worm Strains, Culture, and RNAi

Bristol N2 was used as the wild-type (WT) *C. elegans* strain. N2 WT, BK014 transgenic worms [$P_{vha\text{-}6}$*::CUA-1.1::GFP::unc-54 3′ UTR*], BK015 [*Pvha-6::CUA-1.1::GFP::unc-54 3′UTR; cua-1(ok904)*] worms, *chca-1 (tm6506 IV)* and their respective WT broodmates were maintained at 20 °C on NGM plates seeded with *E. coli* OP50 or HT115 (DE3) as a food source. Some worm strains were obtained from the *Caenorhabditis* Genetics Center, which is funded by National Institutes of Health Office of Research Infrastructure Programs (P40 OD010440). RNAi bacteria strains against *chca-1* or *cua-1* were used, and bacteria transformed with the empty L4440 vector were used as a negative RNAi control as described previously (Yuan et al., 2018).

Elesclomol Treatment in *C. elegans*

Synchronized L1 larval cultures of WT and *chca-1(tm6506)* mutant worms were cultured on basal media or media containing 100 μM BCS plus 10 μM $CuCl_2$ or various concentrations of ES for ~2.5 days. Worms from each condition were analyzed for time of flight (length), extinction (width), and GFP fluorescence using a COPAS Biosort FP-250 (Union Biometrica) to determine body size and copper content by ICP-MS. To measure brood sizes, N2 worms were exposed to *cua-1* (RNAi) or control (*L4440* vector) from synchronized L1 stage with or without 100 μM BCS treatment, supplemented with vehicle (DMSO) or 5 μM ES. After 4 days, worms under each condition were picked to individual plates in triplicate, allowed to lay eggs, and transferred to fresh plates every 24 h for 3 days. Eggs were incubated overnight to allow hatching and progeny number was determined as the total number of hatched larvae. For the survival assay, BK015 transgenic worms were cultured from the L1 stage on RNAi plates supplemented with either vehicle (DMSO) or 5 μM ES for 4 days, and then scored for survival. Animals were considered dead when no signs of viability (movement, pharyngeal pumping, or response to prodding) were detected. The ES concentration required to observe rescue in different tests reflects technical requirements for each assay—e.g., type of bacterial food source, bacterial culture requirements, and the nature of the genetic background or transgene present in the worm strains.

ICP-MS

Metal content of worms was measured using ICP-MS as described previously (Chun et al., 2017b; Yuan et al., 2018). Values were normalized to the wet weight of worms. Synchronized L1 worms were grown on NGM plates seeded with OP50 supplemented with the indicated amounts of copper, BCS or ES until worms reached the L4 stage. At least three independent biological replicates were analyzed. Copper, and zinc concentrations of mice were measured from nitric acid-digested tissues by ICP-MS as described (Nose et al., 2006). The values were normalized by tissue protein concentration.

Immunofluorescence

BK014 transgenic worms ($P_{vha\text{-}6}$*::CUA-1.1::GFP::unc-54 3' UTR*) were maintained on standard NGM agar plates seeded with OP50 bacteria. Synchronized L1 larvae were cultured on NGM plates with indicated amount of $CuCl_2$, vehicle (DMSO) or ES for 3 days. To visualize live worms, animals were paralyzed in M9 buffer containing 10 mM sodium azide (NaN_3) and mounted on agarose pads. GFP in worms was imaged using an LSM710 confocal microscope (Zeiss).

Elesclomol Gavage in Mice

The intestine-specific *Ctr1* deletion mouse (*Ctr1*$^{int/int}$) was generated by crossing *Ctr1*$^{flox/flox}$ mice with mice expressing Cre recombinase driven by the *Villin*-promoter as described previously (Nose et al., 2006; Chun et al., 2017b). Age-

matched $Ctr1^{flox/+}$ or $Ctr1^{flox/flox}$ siblings not expressing Cre were served as a control group in this study. All animal procedures were performed in accordance with National Institutes of Health Guide and approved by the Institutional Animal Care and Use Committee at the University of Maryland, College Park (protocol #: R-APR-18-14). Starting from postnatal day (PND) 7, $Ctr1^{int/int}$ and control littermates were treated with 10 mg/kg body weight of ES (Selleckchem) or vehicle by gavage every 2 days until PND 31. Mouse body weights were recorded every day from PND 7 to PND 35. Depending on individual mouse weight, an appropriate amount of ES was dissolved in DMSO, and then mixed with 5% methyl cellulose solution (Sigma) to reach a 2% final concentration of ES-DMSO. The vehicle control solution contained 0.5% methyl cellulose solution with 2% DMSO. A subset of mice were dissected at PND 17 for tissue analysis.

Tissue Preparations and Antibodies

The isolation and extraction of intestinal epithelial cells from mice for immunoblot assays and metal measurements have been described previously (Chun et al., 2017b). The anti-CCS antibody (Santa Cruz Biotechnology) and anti-GAPDH antibody (Sigma) were used at 1:1,000 dilution and 1:5,000 dilution, respectively.

Statistical Analysis

Statistical analysis was performed with one-way ANOVA followed by Sidak post hoc test, or two-way ANOVA followed by Tukey's post hoc test, using GraphPad Prism (GraphPad). Differences were considered statistically significant at $p < 0.05$.

DATA AVAILABILITY STATEMENT

All data presented here are contained within the article.

ETHICS STATEMENT

The animal study was reviewed and approved by Institutional Animal Care and Use Committee at the University of Maryland, College Park (protocol #: R-APR-18-14).

AUTHOR CONTRIBUTIONS

SY, TK, and B-EK conceived the study. SY and TK conducted the experiments, analyzed the data, and wrote the primary manuscript with B-EK. All authors reviewed the results and approved the final version of the manuscript.

FUNDING

This work was supported by the National Institutes of Health grant DK110195 (to B-EK). The authors declare that they have no conflicts of interest with the contents of this article.

ACKNOWLEDGMENTS

We thank all Kim laboratory members, in particular, Xuewei Zhao for expert technical assistance. We thank Dr. Kiwon Ok and Dr. Sarah L. J. Michel at the Metallotherapeutics Research Center at the University of Maryland School of Pharmacy for ICP-MS analysis, and thank members of Dr. Iqbal Hamza's laboratory (University of Maryland-College Park) for assistance and expertise in *C. elegans*. We thank Dr. Vishal M. Gohil at the Texas A&M University for critical reading of this manuscript.

REFERENCES

Anderson, C. P., and Leibold, E. A. (2014). Mechanisms of Iron Metabolism in *Caenorhabditis elegans*. *Front. Pharmacol.* 5, 113. doi:10.3389/fphar.2014.00113

Bertinato, J., and L'Abbé, M. R. (2003). Copper Modulates the Degradation of Copper Chaperone for Cu,Zn Superoxide Dismutase by the 26 S Proteosome. *J. Biol. Chem.* 278, 35071–35078. doi:10.1074/jbc.m302242200

Chun, H., Catterton, T., Kim, H., Lee, J., and Kim, B.-E. (2017). Organ-specific Regulation of ATP7A Abundance Is Coordinated with Systemic Copper Homeostasis. *Sci. Rep.* 7, 12001. doi:10.1038/s41598-017-11961-z

Chun, H., Sharma, A. K., Lee, J., Chan, J., Jia, S., and Kim, B.-E. (2017). The Intestinal Copper Exporter CUA-1 Is Required for Systemic Copper Homeostasis in *Caenorhabditis elegans*. *J. Biol. Chem.* 292, 1–14. doi:10.1074/jbc.m116.760876

Dietrich, N., Schneider, D. L., and Kornfeld, K. (2017). A Pathway for Low Zinc Homeostasis that Is Conserved in Animals and Acts in Parallel to the Pathway for High Zinc Homeostasis. *Nucleic Acids Res.* 45, 11658–11672. doi:10.1093/nar/gkx762

Guthrie, L. M., Soma, S., Yuan, S., Silva, A., Zulkifli, M., Snavely, T. C., et al. (2020). Elesclomol Alleviates Menkes Pathology and Mortality by Escorting Cu to Cuproenzymes in Mice. *Science* 368, 620–625. doi:10.1126/science.aaz8899

Kaler, S. G. (2011). ATP7A-related Copper Transport Diseases-Emerging Concepts and Future Trends. *Nat. Rev. Neurol.* 7, 15–29. doi:10.1038/nrneurol.2010.180

Kim, B.-E., Nevitt, T., and Thiele, D. J. (2008). Mechanisms for Copper Acquisition, Distribution and Regulation. *Nat. Chem. Biol.* 4, 176–185. doi:10.1038/nchembio.72

Kim, B.-E., Turski, M. L., Nose, Y., Casad, M., Rockman, H. A., and Thiele, D. J. (2010). Cardiac Copper Deficiency Activates a Systemic Signaling Mechanism that Communicates with the Copper Acquisition and Storage Organs. *Cel Metab.* 11, 353–363. doi:10.1016/j.cmet.2010.04.003

Leary, S. C., and Ralle, M. (2020). Advances in Visualization of Copper in Mammalian Systems Using X-ray Fluorescence Microscopy. *Curr. Opin. Chem. Biol.* 55, 19–25. doi:10.1016/j.cbpa.2019.12.002

Madsen, E. C., and Gitlin, J. D. (2008). Zebrafish Mutants Calamity and Catastrophe Define Critical Pathways of Gene-Nutrient Interactions in Developmental Copper Metabolism. *Plos Genet.* 4, e1000261. doi:10.1371/journal.pgen.1000261

Madsen, E., and Gitlin, J. D. (2007). Copper and Iron Disorders of the Brain. *Annu. Rev. Neurosci.* 30, 317–337. doi:10.1146/annurev.neuro.30.051606.094232

Nose, Y., Kim, B.-E., and Thiele, D. J. (2006). Ctr1 Drives Intestinal Copper Absorption and Is Essential for Growth, Iron Metabolism, and Neonatal Cardiac Function. *Cel Metab.* 4, 235–244. doi:10.1016/j.cmet.2006.08.009

Öhrvik, H., Logeman, B., Turk, B., Reinheckel, T., and Thiele, D. J. (2016). Cathepsin Protease Controls Copper and Cisplatin Accumulation via Cleavage of the Ctr1 Metal-Binding Ectodomain. *J. Biol. Chem.* 291, 13905–13916. doi:10.1074/jbc.M116.731281

Öhrvik, H., Nose, Y., Wood, L. K., Kim, B. E., Gleber, S. C., Ralle, M., et al. (2013). Ctr2 Regulates Biogenesis of a Cleaved Form of Mammalian Ctr1 Metal Transporter Lacking the Copper- and Cisplatin-Binding Ecto-

Domain. *Proc. Natl. Acad. Sci. U S A.* 110, E4279–E4288. doi:10.1073/pnas.1311749110

Öhrvik, H., and Thiele, D. J. (2015). The Role of Ctr1 and Ctr2 in Mammalian Copper Homeostasis and Platinum-Based Chemotherapy. *J. Trace Elem. Med. Biol.* 31, 178–182. doi:10.1016/j.jtemb.2014.03.006

Petris, M. J., Mercer, J. F., Culvenor, J. G., Lockhart, P., Gleeson, P. A., and Camakaris, J. (1996). Ligand-regulated Transport of the Menkes Copper P-type ATPase Efflux Pump from the Golgi Apparatus to the Plasma Membrane: a Novel Mechanism of Regulated Trafficking. *EMBO J.* 15, 6084–6095. doi:10.1002/j.1460-2075.1996.tb00997.x

Petris, M. J., Strausak, D., and Mercer, J. F. (2000). The Menkes Copper Transporter Is Required for the Activation of Tyrosinase. *Hum. Mol. Genet.* 9, 2845–2851. doi:10.1093/hmg/9.19.2845

Pierson, H., Muchenditsi, A., Kim, B.-E., Ralle, M., Zachos, N., Huster, D., et al. (2018). The Function of ATPase Copper Transporter ATP7B in Intestine. *Gastroenterology* 154, 168–180. e165. doi:10.1053/j.gastro.2017.09.019

Prohaska, J. R., and Brokate, B. (2002). The Timing of Perinatal Copper Deficiency in Mice Influences Offspring Survival. *J. Nutr.* 132, 3142–3145. doi:10.1093/jn/131.10.3142

Rossi, L., De Martino, A., Marchese, E., Piccirilli, S., Rotilio, G., and Ciriolo, M. R. (2001). Neurodegeneration in the Animal Model of Menkes' Disease Involves Bcl-2-Linked Apoptosis. *Neuroscience* 103, 181–188. doi:10.1016/s0306-4522(00)00562-5

Sendoel, A., Kohler, I., Fellmann, C., Lowe, S. W., and Hengartner, M. O. (2010). HIF-1 Antagonizes P53-Mediated Apoptosis through a Secreted Neuronal Tyrosinase. *Nature* 465, 577–583. doi:10.1038/nature09141

Sinclair, J., and Hamza, I. (2015). Lessons from Bloodless Worms: Heme Homeostasis in *C. elegans*. *Biometals* 28, 481–489. doi:10.1007/s10534-015-9841-0

Smith, A. D., Logeman, B. L., and Thiele, D. J. (2017). Copper Acquisition and Utilization in Fungi. *Annu. Rev. Microbiol.* 71, 597–623. doi:10.1146/annurev-micro-030117-020444

Soma, S., Latimer, A. J., Chun, H., Vicary, A. C., Timbalia, S. A., Boulet, A., et al. (2018). Elesclomol Restores Mitochondrial Function in Genetic Models of Copper Deficiency. *Proc. Natl. Acad. Sci. USA* 115, 8161–8166. doi:10.1073/pnas.1806296115

Turski, M. L., and Thiele, D. J. (2007). Drosophila Ctr1A Functions as a Copper Transporter Essential for Development. *J. Biol. Chem.* 282, 24017–24026. doi:10.1074/jbc.m703792200

Van Bael, S., Watteyne, J., Boonen, K., De Haes, W., Menschaert, G., Ringstad, N., et al. (2018). Mass Spectrometric Evidence for Neuropeptide-Amidating Enzymes in. *J. Biol. Chem.* 293, 6052–6063. doi:10.1074/jbc.ra117.000731

Wakabayashi, T., Nakamura, N., Sambongi, Y., Wada, Y., Oka, T., and Futai, M. (1998). Identification of the Copper Chaperone, CUC-1, inCaenorhabditis Elegans: Tissue Specific Co-expression with the Copper Transporting ATPase, CUA-1. *FEBS Lett.* 440, 141–146. doi:10.1016/s0014-5793(98)01431-8

Wang, Y., Zhu, S., Hodgkinson, V., Prohaska, J. R., Weisman, G. A., Gitlin, J. D., et al. (2012). Maternofetal and Neonatal Copper Requirements Revealed by Enterocyte-specific Deletion of the Menkes Disease Protein. *Am. J. Physiology-Gastrointestinal Liver Physiol.* 303, G1236–G1244. doi:10.1152/ajpgi.00339.2012

Wang, Y., Zhu, S., Weisman, G. A., Gitlin, J. D., and Petris, M. J. (2012). Conditional Knockout of the Menkes Disease Copper Transporter Demonstrates its Critical Role in Embryogenesis. *PLoS One* 7, e43039. doi:10.1371/journal.pone.0043039

Xiao, Z., Donnelly, P. S., Zimmermann, M., and Wedd, A. G. (2008). Transfer of Copper between Bis(thiosemicarbazone) Ligands and Intracellular Copper-Binding Proteins. Insights into Mechanisms of Copper Uptake and Hypoxia Selectivity. *Inorg. Chem.* 47, 4338–4347. doi:10.1021/ic702440e

Yuan, S., Sharma, A. K., Richart, A., Lee, J., and Kim, B.-E. (2018). CHCA-1 Is a Copper-Regulated CTR1 Homolog Required for normal Development, Copper Accumulation, and Copper-Sensing Behavior in *Caenorhabditis elegans*. *J. Biol. Chem.* 293, 10911–10925. doi:10.1074/jbc.ra118.003503

Conflict of Interest: The authors declare that the research was conducted in the absence of any commercial or financial relationships that could be construed as a potential conflict of interest.

Publisher's Note: All claims expressed in this article are solely those of the authors and do not necessarily represent those of their affiliated organizations, or those of the publisher, the editors and the reviewers. Any product that may be evaluated in this article, or claim that may be made by its manufacturer, is not guaranteed or endorsed by the publisher.

frontiers | Frontiers in Cell and Developmental Biology

ORIGINAL RESEARCH
published: 11 April 2022
doi: 10.3389/fcell.2022.853463

Copper Metabolism in *Naegleria gruberi* and Its Deadly Relative *Naegleria fowleri*

*Kateřina Ženíšková, Maria Grechnikova and Robert Sutak**

Department of Parasitology, Faculty of Science, Charles University, BIOCEV, Vestec, Prague, Czechia

Although copper is an essential nutrient crucial for many biological processes, an excessive concentration can be toxic and lead to cell death. The metabolism of this two-faced metal must be strictly regulated at the cell level. In this study, we investigated copper homeostasis in two related unicellular organisms: nonpathogenic *Naegleria gruberi* and the "brain-eating amoeba" *Naegleria fowleri*. We identified and confirmed the function of their specific copper transporters securing the main pathway of copper acquisition. Adjusting to different environments with varying copper levels during the life cycle of these organisms requires various metabolic adaptations. Using comparative proteomic analyses, measuring oxygen consumption, and enzymatic determination of NADH dehydrogenase, we showed that both amoebas respond to copper deprivation by upregulating the components of the branched electron transport chain: the alternative oxidase and alternative NADH dehydrogenase. Interestingly, analysis of iron acquisition indicated that this system is copper-dependent in *N. gruberi* but not in its pathogenic relative. Importantly, we identified a potential key protein of copper metabolism of *N. gruberi*, the homolog of human DJ-1 protein, which is known to be linked to Parkinson's disease. Altogether, our study reveals the mechanisms underlying copper metabolism in the model amoeba *N. gruberi* and the fatal pathogen *N. fowleri* and highlights the differences between the two amoebas.

Keywords: copper, alternative oxidase, alternative NADH dehydrogenase, *Naegleria gruberi*, *Naegleria fowleri*, DJ-1, CTR copper transporters, electron transport chain

OPEN ACCESS

Edited by:
Kourosh Honarmand Ebrahimi, King's College London, United Kingdom

Reviewed by:
Anastasios D. Tsaousis, University of Kent, United Kingdom
Svetlana Lutsenko, Johns Hopkins Medicine, United States

****Correspondence:***
Robert Sutak
sutak@natur.cuni.cz

Specialty section:
This article was submitted to Cellular Biochemistry, a section of the journal Frontiers in Cell and Developmental Biology

Received: *12 January 2022*
Accepted: *18 March 2022*
Published: *11 April 2022*

Citation:
Ženíšková K, Grechnikova M and Sutak R (2022) Copper Metabolism in Naegleria gruberi and Its Deadly Relative Naegleria fowleri. Front. Cell Dev. Biol. 10:853463. doi: 10.3389/fcell.2022.853463

INTRODUCTION

Transition metals are required in many crucial biological processes of all living organisms. The most abundant redox-active metal in cells is iron, which is followed by other metals such as copper, manganese, cobalt, molybdenum, and nickel (Andreini et al., 2008). Both iron and copper are crucial for the survival of organisms; however, excess concentrations of these metals can be toxic: iron can catalyze the generation of free radicals through the Fenton reaction, causing cellular damage, while copper probably binds to proteins and replaces iron from iron-sulfur cluster-containing proteins, impairing their function and causing iron-induced toxicity (Macomber and Imlay, 2009; Festa and Thiele, 2012; García-Santamarina and Thiele, 2015). On the other hand, copper is a cofactor of at least 30 cuproenzymes with a wide variety of roles, such as electron transport in respiration (cytochrome c oxidase CCOX) or free radical detoxification (superoxide dismutase SOD) (Solomon et al., 2014), and its necessity for biological systems arises from its ability to cycle between two redox states, Cu^{1+} and Cu^{2+}, all of which contribute to

organisms needing to evolve mechanisms to strictly regulate intracellular levels of these potentially harmful metals. Homeostatic mechanisms consist of their uptake, transport, storage, and detoxification pathways. Interestingly, the metabolism of iron and copper are linked, which is best demonstrated by the copper dependence of iron acquisition by the cell, as was shown in yeasts with FET3 multicopper oxidase in the high-affinity iron uptake system (Askwith et al., 1994). The best-described mechanism of copper acquisition involves high-affinity copper transporters named Ctrs. Their function and structure are widely conserved from yeast to humans (Nose et al., 2006; Maryon et al., 2007).

Very little is known about copper transporters in parasitic protists. In *Plasmodium falciparum*, a copper efflux P-ATPase has been identified and partly characterized (Rasoloson et al., 2004), as was a copper-binding protein with sequence features characteristic of copper transporters, including three transmembrane domains: an extracellular copper-binding methionine motif and transmembrane Gx_3G and Mx_3M motifs (Choveaux et al., 2012). Copper transporting ATPases were also identified in trypanosomatid parasites (Isah et al., 2020; Paul et al., 2021). Significantly more research has been performed on copper metabolism in pathogenic yeasts. Ctr homologs responsible for cellular copper uptake were identified in *Candida albicans* (CTR1) (Marvin et al., 2003) and in *Cryptococcus neoformans* (CTR1 and CTR4) (Sun et al., 2014). Importantly, homologs of these proteins are present in the genomes of both amoebas used in our study, *Naegleria gruberi* and *Naegleria fowleri* (Fritz-Laylin et al., 2010; Liechti et al., 2019).

N. gruberi and *N. fowleri* are unicellular organisms living worldwide in freshwater environments (De Jonckheere, 2004; Mull et al., 2013). *N. gruberi* is considered to be the best safe system to study the pathogenic "brain-eating amoeba" *N. fowleri*, which can infect people and cause primary amoebic meningoencephalitis (PAM), a rare but almost always fatal disease (Mungroo et al., 2021). The genomes of these organisms suggest canonical aerobic metabolism, such as the employment of cytochromes and ubiquinone in the respiratory chain, as well as properties of anaerobic metabolism, such as Fe-hydrogenase (Tsaousis et al., 2014), which is typically utilized in metabolic processes of organisms adapted to anaerobic conditions (Fritz-Laylin et al., 2011; Herman et al., 2021). Both amoebas were recently shown to be able to adjust their metabolism to reflect iron availability, downregulating nonessential and predominantly cytosolic iron-dependent pathways and utilizing available iron primarily in mitochondria to maintain essential energy metabolism (Mach et al., 2018; Arbon et al., 2020). In our previous study, we described how *N. fowler*i handles copper toxicity by upregulating a specific copper-exporting ATPase, a key protein of the copper detoxification pathway (Grechnikova et al., 2020). Recent study has found that *Cryptococcus neoformans* is able to sense different Cu environment during infection: high Cu in lungs and low Cu level in brain and is able to adapt its Cu acquisition in these different niches (Sun et al., 2014). Consequently, we focused the current study on the effect of copper deficiency on the metabolism of the brain-eating amoeba as well as its related nonpathogenic model amoeba *N. gruberi*. Herein, we show the role of Ctr homologs identified in both amoebas by functional complementation of mutant yeast lacking high-affinity copper transporters and demonstrate the effect of copper availability on several important components of cell proteomes, iron acquisition, and respiration in both amoebas. We demonstrate that both amoebas can reflect copper-limited conditions by upregulating parts of the respiratory chain to maintain maximal cell respiration. *N. gruberi* adapts to copper-limited conditions by inducing alternative oxidase, similar to the mechanism described in *C. albicans* (Broxton and Culotta, 2016), while *N. fowleri* upregulates alternative NDH-2 dehydrogenase. Moreover, we identified the potential key protein of copper metabolism in *N. gruberi*, the homolog of the DJ-1 protein.

MATERIALS AND METHODS

Identification of *Naegleria* CTRs

Naegleria CTR genes were found by BLAST in the genomes of *N. fowleri* in the AmoebaDB database (Amos et al., 2021) and *N. gruberi* in the JGI PhycoCosm database (Grigoriev et al., 2021) using *Saccharomyces cerevisiae* CTR1 (YPR124 W), CTR2 (YHR175 W), and CTR3 (YHR175 W) gene sequences. Two predicted CTRs of *N. fowleri* (NF0078940, NF0118930) and three predicted CTRs of *N. gruberi* (gene IDs: NAEGRDRAFT_61759, NAEGRDRAFT_61987, and NAEGRDRAFT_62836) were identified.

Functional Complementation Spot Assay of Predicted Ctrs of *N. gruberi* and *N. fowleri*

To synthesize *N. gruberi* and *N. fowleri* cDNA, SuperScript™ III reverse transcriptase (Thermo Fisher Scientific, United States) was used according to the manufacturer's protocol. CTR genes were amplified from cDNA using a Q5 (NEB, United States) and Pfu DNA polymerase mixture (Promega, United States). The resulting products were subcloned into a pUG35 plasmid with a GFP tag (Güldener and Hegemann, http://mips.gsf.de/proj/yeast/info/tools/hegemann/gfp.html) and a pCM189 plasmid (Garí et al., 1997) with a tetracycline-regulatable promotor. The yeast mutant strain ctr1Δ/ctr3Δ (kindly provided by Dennis J. Thiele, Duke University, Durham, North Carolina) was transformed with pCM189 plasmids containing one of the predicted CTRs from *N. fowleri* (NF0078940, NF0118930) or *N. gruberi* (NAEGRDRAFT_61759, NAEGRDRAFT_61987, NAEGRDRAFT_62836). To observe the effect of complementation on phenotype, transformed yeasts were grown overnight in liquid SC-ura medium with 2% glucose (complete synthetic medium without uracil) at 30°C. Cells were diluted to an OD_{600} of 0.2, and 5-µl aliquots of four serial 10-fold dilutions were spotted onto SC-ura plates containing 2% raffinose as a carbon source.

Localization of Ctrs by Fluorescence Microscopy

For protein localization, wild-type (WT) yeast BY4741 cells were transformed with pUG35 containing either the NgCTR or NfCTR gene, and transformants were grown overnight at 30°C in liquid SC-ura medium, washed and resuspended in phosphate-buffered saline (PBS), pipetted onto a microscope slide and mixed with the same volume of 2% agarose. The microscope slide was then covered with a cover slide and sealed. A fluorescent signal was detected using a Leica TCS SP8 WLL SMD confocal microscope (Leica, Germany) with an HC PL APO CS2 63x/1.20 water objective, excited at 488 nm and detected within 498–551 nm by a HyD SMD detector. The PMT detector was used for bright-field imaging. The resulting images were processed by LAS X imaging software (Leica Microsystems, Germany) and ImageJ (Schneider et al., 2012). Yeast transformation was performed according to a previously published protocol (Gietz and Schiestl, 2007).

Amoeba Cultivation

Organisms

a) *N. gruberi* strain NEG-M, which was kindly provided by Lilian Fritz-Laylin (University of Massachusetts Amherst, United States), was grown axenically at 27°C in M7 medium (Fulton, 1974) with the addition of penicillin (100 U/ml) and streptomycin (100 μg/ml) in a 25-cm^2 aerobic cultivation flask.
b) Axenic culture of *N. fowleri* strain HB-1, which was kindly provided by Dr. Hana Peckova (Institute of Parasitology, Biology Center CAS), was maintained at 37°C in 2% Bactocasitone (Difco) medium supplemented with 10% heat-inactivated fetal bovine serum (Thermo Fisher Scientific) with the addition of penicillin (100 U/ml) and streptomycin (100 μg/ml).

Cultivation Conditions

a) For comparative proteomic analysis, oxygen consumption measurements, measurement of the enzyme activity of complex I and NDH-2, and preparation of the samples for SDS–PAGE, copper deprivation was achieved by incubation of cells for 72 h in the presence of 5 μM neocuproine or 25 μM bathocuproinedisulfonic acid disodium salt (BCS), while copper enrichment was achieved by the addition of 25 μM Cu_2SO_4.
b) To examine the effect of copper availability on NgDJ-1 expression by western blot, cells were grown in 25 μM BCS or 1 μM, 25 μM, or 750 μM Cu_2SO_4 for 72 h.
c) The localization of NgDJ-1 was determined by western blotting of crude fractions of *N. gruberi* cultivated without the addition of copper or chelators and by fluorescence microscopy of cells cultivated for 72 h with 100 μM Cu_2SO_4 or 25 μM BCS.
d) To investigate the effect of ROS on NgDJ-1 expression, *N. gruberi* cells were preincubated in 10 μM rotenone or 20 μM PEITEC for 24 h, and cells with no addition of ROS-inducing agents were used as a control.

Crude Fractionation of *N. gruberi* and *N. fowleri* Cells

The grown cells were washed twice in S-M buffer (250 mM Saccharose, 10 mM MOPS, pH 7.2) and disrupted by sonication using SONOPULS ultrasonic homogenizer mini20 (BANDELIN, Germany) with the following settings: amplitude 30%, 1/1 s pulse for 1 min on ice. Disrupted cells were evaluated under a microscope, and sonication was repeated until most of the cells were disrupted. The samples were then centrifuged for 10 min at 1,200 g and 4°C. To obtain the mitochondria-enriched fraction, the supernatant was centrifuged at 14,000 g for 20 min at 4°C. The pellet was used as a mitochondrial-enriched fraction and diluted to the same protein concentration as the supernatant (cytosol-enriched fraction).

The Effect of Different Copper Chelators on the Growth of *N. gruberi* and *N. fowleri*

To investigate the effect of copper deprivation on the growth of *N. gruberi* and *N. fowleri*, the cultures were grown in the presence of copper chelators BCS (concentrations: 25 and 100 μM) and neocuproine (concentrations: 5 and 20 μM). Copper-rich conditions (25 μM Cu_2SO_4) were used as a control. Since BCS binds copper extracellularly and consequently its effect may only be evident after a longer period, we observed the effect of this chelator in long-term growth analysis with a dilution of the cells after 2 days. Each condition was set up in three independent biological replicates with starting culture concentrations of 50 000 cell/ml (*N. gruberi*) and 5,000 cell/ml (*N. fowleri*), and the cell concentration was measured every day by a Cell Counter (Beckman Coulter, United States). The effect of the intracellular copper chelator neocuproine was observed only at one time point: 72 h. Cells were grown in three biological replicates with starting concentrations of 1×10^4 cells/ml (*N. gruberi*) and 4×10^3 cells/ml (*N. fowleri*), and the cell concentration was measured on a Guava easyCyte 8HT flow cytometer (Merck, Germany) after treatment with 2% paraformaldehyde.

ICP–MS Analysis

Cultures of *N. gruberi* and *N. fowleri* were grown in triplicate for each condition, washed three times (1,200 g, 10 min, 4°C) in 10 mM HEPES with 140 mM NaCl buffer, pH 7.2, and pelleted by centrifugation. The pellets were dried at 100°C, digested in 65% HNO_3 in Savillex vials overnight at room temperature, incubated for 2 h at 130°C in Savillex vials (Millipore, United States) and diluted to a final volume of 10 ml in deionized water. The copper concentration was determined by inductively coupled plasma–mass spectrometry (ICP–MS) using iCAP Q ICP–MS (Thermo Fisher Scientific).

LC–MS

N. gruberi and *N. fowleri* cells were grown in biological triplicates for each condition. After incubation, cells were pelleted by centrifugation (1,200 g, 10 min, 4°C) and washed three times with phosphate-buffered saline (PBS). Whole-cell label-free

proteomic analysis followed by the same method as that described in (Mach et al., 2018) was performed by applying nanoflow liquid chromatography (LC) coupled with mass spectrometry (MS). Data were evaluated with MaxQuant software (Cox et al., 2014) using the AmoebaDB *N. fowleri* database downloaded in August 2018 or the *N. gruberi* database (downloaded from UniProt August 2018). Selected proteins (lacking annotation) were manually annotated using HHpred (Zimmermann et al., 2018) or NCBI BLAST (Altschul et al., 1990). The resulting data were further processed by Perseus software (Tyanova et al., 2016). Potential contaminants and reverse hits were filtered out. To evaluate significantly changed proteins at the level of the false discovery rate, Student's t test with Benjamini–Hochberg correction was used. Proteins that were significantly changed and those found in only one condition (in at least two of three replicates) were selected. Proteins identified by only one peptide and proteins with Q-value higher than 0 were excluded from the selection.

RT–qPCR

Naegleria cells were grown in copper-rich and copper-deficient conditions, and control untreated cells were grown for 72 h in quadruplicate. Cells were washed twice with PBS and spun (1,200 g, 4°C, 10 min). Total RNA was isolated using the High Pure RNA Isolation Kit (Roche, Switzerland). The KAPA SYBR® FAST One-Step universal kit (Sigma Aldrich, United States) was used for RT–PCR according to the manufacturer's protocol. RT–PCR was performed on a RotorGene 3000 PCR cycler (Corbett Research, Australia) under the following conditions: 42°C for 30 min (reverse transcription), 95°C for 5 min, and 40 cycles of 95°C for 10 s, 55°C for 20 s, and 72°C for 20 s; for melt-curve analysis, the temperature change was set from 55 to 95°C with a 1°C step and 5 s per step. The abundance of transcripts was calculated after normalization to the endogenous reference gene β-actin.

Obtaining the NgDJ-1 Recombinant Protein for Antibody Preparation

The sequence of NgDJ-1 (XP_002680488.1) was obtained from the UniProt database (in August 2019), and bioinformatic analysis was performed by InterProScan in Geneious Prime® 2019 2.3 (www.geneious.com), including protein domain prediction software such as Phobius (Käll et al., 2004), Pfam (Mistry et al., 2021), PANTHER (Thomas et al., 2003), and SignalP 5.0 (Almagro Armenteros et al., 2019) (see **Supplementary Figure S4**). The NgDJ-1 gene was amplified from cDNA without the transmembrane domain at the N-terminal part of the NgDJ-1 gene (primers: forward 5′-CAC CATATGGTCGAGGCTCAGAATATTGATCAC-3′, reverse 5′-CACGGATCCATTTTGCTTATTCAAGAGCTTGT-3′) and subcloned into the vector pET42b (Merck) containing the C-terminal histidine tag. The protein was expressed in *E. coli* BL21 (DE3) (Merck) induced by 0.5 mM isopropyl β-D-1-thiogalactopyranoside (IPTG, Sigma Aldrich) for 4 h at 37°C. Protein was purified under denaturing conditions according to the manufacturer's protocol using Ni-NTA agarose beads (Qiagen, Germany).

NfNDH-2 and NgDJ-1 Antibody Production

NgDJ-1 and NfNDH-2 polyclonal antibodies were produced by David Biotechnology (Germany) in rabbits. NgDJ-1 antibody was prepared using purified HIS-tagged recombinant protein, while NfNDH-2 was prepared by 3 synthesized immunogenic peptides preselected by David Biotechnology (HDRQVSFAKSIHKPNEKKN, HEDYHYFEGKAIAIDTENQR, DPKSKKILVTDHLKVKGFE). To obtain a more specific signal, the produced antibodies NgDJ-1 and NfNDH-2 were purified by the SulfoLink Immobilization Kit for Proteins (Thermo Fisher Scientific) or the AminoLink Plus Immobilization Kit (Thermo Fisher Scientific), respectively. All purification procedures were performed following the manufacturer's manual.

Sample Preparation for SDS–PAGE, Native PAGE, and Western Blot

Cells were grown under specific conditions for 72 h, washed two times with PBS, pelleted at 1,000 g, 10 min, 4°C, and diluted to equal protein concentration determined by BCA Protein Assay Kit (Sigma Aldrich). Denatured samples (100°C for 5 min) were separated by SDS electrophoresis, blotted onto a nitrocellulose membrane (Amersham Protram 0.2 μm PC, GE Healthcare Life Sciences, United States), and incubated with specific polyclonal antibody at the following concentrations: anti-AOX (Agrisera, Sweden) 1:100, anti-NgDJ-1 1 1:50, and anti-NfNDH-2 1:1,000. HRP-conjugated goat anti-rabbit or anti-mouse antibodies (BioRad, United States) were used as secondary antibodies. Antibodies were detected using Immobilon Forte Western HRP substrate (Merck) on an Amersham Imager 600 (GE Health care Life Sciences, United States).

Crude fractions of *N. gruberi* (Chapter 2.5) used for localization of NgDJ-1 by western blot were prepared the same as SDS samples described above, but crude fractions of *N. fowleri* (Chapter 2.5) used for localization of NfNDH-2 were treated with 1% digitonin (Sigma Aldrich), incubated for 5 min on ice and resuspended in ×5 native sample buffer. The samples were then loaded on a native gel (containing 0.1% Triton TX-100, Sigma Aldrich) and separated by PAGE under native conditions.

Immunofluorescence Microscopy

N. gruberi cells were stained with 100 nM MitoTracker Red CMXRos (Thermo Fisher Scientific) for 30 min in M7 medium in the dark at 27°C. After incubation, the medium was exchanged, and the cells were fixed with 1% formaldehyde for another 30 min. The treated cells were then carefully centrifuged (800 g, 5 min, 24°C), resuspended in PEM (100 mM piperazine-N,N′-bis(2-ethane sulfonic acid), 1 mM ethylene glycol-bis(β-aminoethyl ether)-N,N,N′,N′-tetraacetic acid, and 0.2 mM $MgSO_4$) and transferred onto cover slides. The cell slides were then incubated for 1 h in PEMBALG blocking solution (1% BSA, 0.1% NaN_3, 100 mM L-lysin, 0.5% cold water fish skin gelatin in PEM). The NgDJ-1 protein was visualized by an anti-rat antibody coupled to Alexa Fluor 488 (Thermo Fisher Scientific) (dilution 1:1,000) bound to a custom-made rat polyclonal antibody (dilution 1:100). Slides with stained cells were mounted by Vectashield with DAPI (Vector Laboratories,

United States). The signal was detected by a TCS SP8 WLL SMD confocal microscope (Leica) equipped with an HC PL APO CS2 63x/1.20 oil objective, excited by 509 nm and detected within 526–655 nm by a HyD SMD detector. The PMT detector was used for bright-field imaging and processed as described in Chapter 2.3.

N. fowleri microscopy slides for visualization of NfNDH-2 were prepared as described above except that *N. fowleri* cells were immobilized on slides covered with poly-L-lysine and all the staining, including 10 nM MitoTracker Red CMXRos and primary and secondary antibodies, were completed on slides rather than in a cultivation flask.

Measurements of Oxygen Consumption

N. fowleri and *N. gruberi* cells were grown for 72 h in biological triplicates or tetraplicates, respectively, under copper-depleted and copper-rich conditions, pelleted (1,200 g, 10 min, 4°C), washed twice, and resuspended to the same cell concentration in glucose buffer (50 mM glucose, 0.5 mM $MgCl_2$, 0.3 mM $CaCl_2$, 5.1 μM KH_2PO_4, 3 μM Na_2HPO_4, pH 7.4). The cell concentration was measured on a Guava easyCyte 8HT flow cytometer (Merck). Cell respiration in each sample was measured by detecting oxygen decreases using the Clark-type electrode system Oxygen meter Model 782 (Strathkelvin) in a Mitocell Mt 200 cuvette in a total volume of 700 μl. The whole system was calibrated for 27°C for *N. gruberi* and 37°C for *N. fowleri*. Specific inhibitors of alternative oxidase, salicyl hydroxamic acid (SHAM) at concentrations of 0.5 mM (*N. gruberi*) or 0.2 mM (*N. fowleri*), and an inhibitor of complex IV, KCN, at concentrations of 2.4 mM (*N. gruberi*) or 2.05 mM (*N. fowleri*) were used. The protein concentration of the sample was determined using a BCA kit (Sigma Aldrich).

Complex I and NDH-2 Enzyme Activity of *Naegleria fowleri*

Total NADH dehydrogenase activity was measured by the following protocol. Three biological replicates of *N. fowleri* were cultivated for 72 h in copper-rich or copper-deficient conditions. The cells were spun down, washed with S-M buffer (250 mM saccharose, 10 mM MOPS, pH 7.2), and diluted to the same cell concentration. Next, the cells were treated with 1% digitonin (Sigma Aldrich) for 5 min on ice and added to a reaction mixture containing 100 μM KPi buffer at pH 7.5 and 300 μM NADH. The reaction was started by the addition of 50 μM nonnatural coenzyme Q2 (in 99.9% ethanol, Sigma Aldrich), an analog of Q10. The activity was measured for 5 min at 340 nM wavelength on a Shimadzu UV-2600 UV–VIS spectrophotometer (Shimadzu, Japan) with UV Probe software (Shimadzu).

The activity of alternative NADH dehydrogenase (NDH-2) was estimated as the remaining activity measured in digitonine-treated culture preincubated for 5 min with the inhibitor of Complex I, 75 μM rotenone. The activity of complex I was calculated as the remaining activity after NDH-2 activity subtraction from overall NADH dehydrogenase activity. The protein concentration was determined by a BCA kit (Sigma Aldrich).

Iron Uptake

N. fowleri and *N. gruberi* cells were grown in copper-rich and copper-deficient conditions for 72 h, pelleted (1,200 g, 10 min, 4°C), washed twice, resuspended in glucose-HEPES medium (50 mM glucose, 20 mM HEPES, pH 7.2) and diluted to the same cell concentration of 1×10^6 cells per sample. The cell concentration was estimated by a Guava easyCyte 8HT flow cytometer (Merck). Samples were incubated for 1 h with 1 μM ^{55}Fe-citrate or with 1 μM ^{55}Fe-citrate with the addition of 1 m mM ascorbate to reduce iron to the ferrous form. Uptake was stopped by the addition of 1 mM EDTA, and the cells were then washed three times with glucose-HEPES buffer, diluted to the same protein concentration [using a BCA kit (Sigma Aldrich)] and separated using the Novex Native PAGE Bis-Tris Gel system (4–16%, Invitrogen, United States). The gel was dried for 2 h in a vacuum and autoradiographed by Typhoon FLA 7000 (GE Life Sciences, United States) using a tritium storage phosphor screen (GE Life Sciences).

RESULTS

Identification of Copper Uptake Proteins (Ctrs) of *N. gruberi* and *N. fowleri*

In the genomes of both amoebas, we identified several homologs of copper transporters based on a BLAST search using *S. cerevisiae* CTR1, CTR2, and CTR3. To confirm the copper uptake function of these candidate transporters, we performed a functional complementation assay using copper transporter 1 and copper transporter 3 double knockout yeast strain (ctr1Δ/ctr3Δ). One of the selected Ctrs from each amoeba (NgCTR1, NAEGRDRAFT_61759, and NfCTR1, NF0078940) restored copper transporter function in the yeast mutant and showed typical localization to the yeast plasma membrane (**Figure 1A** and **Figure 1B**). The localization of the other homologs is shown in **Supplementary Figure S1**. To determine whether *N. fowleri* and *N. gruberi* regulate the copper acquisition pathway depending on the availability of the metal at the transcriptional level, as shown in *S. cerevisiae* (Winge et al., 1998), we analyzed the abundance of CTR transcripts by RT–PCR in cells grown under low copper and copper-rich conditions. Our data showed no significant copper-induced changes in the RNA levels of the selected CTR genes (NF0078940, NF0118930, NAEGRDRAFT_61759, NAEGRDRAFT_61987, NAEGRDRAFT_62836) (**Supplementary Figure S2**). This result is not unexpected considering our previous study, where we found that iron starvation-induced changes in *N. fowleri* were mostly posttranslational (Arbon et al., 2020).

Comparative Proteomic Analysis Revealed That ETC Components and NgDJ-1 Are the Most Affected by Copper Deprivation

Since *Naegleria* is not prone to genetic manipulations, we chose whole-cell label-free comparative proteomics to gain complex insight into the metabolic adaptation to copper limitations. To

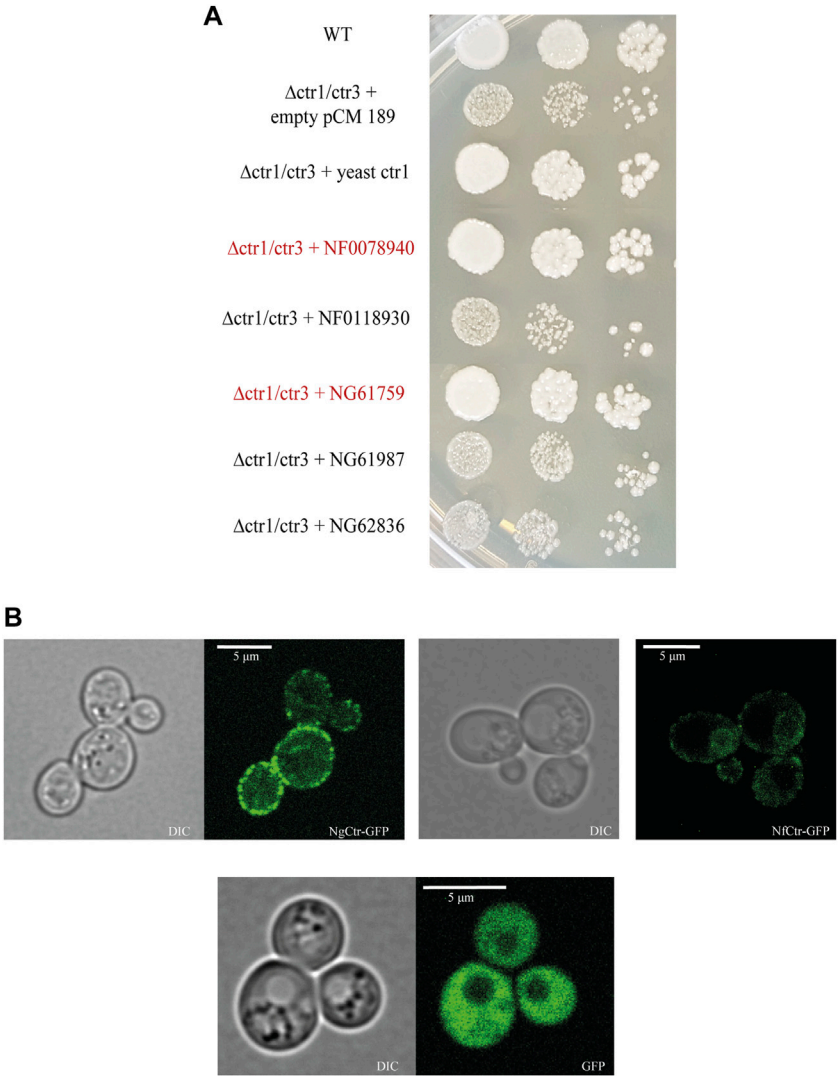

FIGURE 1 | Identification of copper uptake proteins (Ctrs) of *Naegleria gruberi* and *Naegleria fowleri*. **(A)** Functional complementation spot assay of NgCTRs and NfCTRs in Δctr1/ctr3 mutant yeast cells lacking genes for high-affinity copper transporters. Wild-type BY4741 cells transformed with the empty tetracycline-regulated expression vector pCM189 and Δctr1/ctr3 mutant cells transformed with the same plasmid carrying yeast CTR1, NfCTRs (NF0078940, NF0118930) or NgCTRs (NG61759, NG61987, NG62836) were spotted onto synthetic complete medium without uracil with 2% raffinose as the carbon source and grown for 72 h at 30°C. Mutant yeast cells with plasmids containing CTR genes from *N. fowleri* (NF0078940) and *N. gruberi* (NG61759), which functionally complement the missing yeast copper transporters CTR1 and CTR3, are marked in red. **(B)** Localization of NfCtr (NF0078940) and NgCtr (NG61759) by fluorescence microscopy. Wild-type yeast BY4147 expressing copper transporters linked with GFP from *N. gruberi* NgCTR1-GFP (NG61759 + pUG35), *N. fowleri* NfCTR1-GFP (NF0078940 + pUG35), and GFP (empty pUG35 vector).

elucidate the effect of copper deprivation on the viability of *N. gruberi* and *N. fowleri* cells, we cultivated both amoebas for 72 h in the presence of the copper chelators bathocuproinedisulphonic acid (BCS) and neocuproine (Neo). Both chelators are selective for Cu^{+}, and in contrast to the extracellular copper chelator BCS, neocuproine can chelate copper intracellularly.

To determine the amount of copper within the cells grown in the presence of BCS, we analyzed those samples using ICP–MS. **Figure 2A** shows that this extracellular copper chelator causes a significant decrease in copper accumulation compared to control (cells cultivated in presence of 25 μM Cu_2SO_4) after 72 h, while the effect is not further increased using a 10-fold higher concentration. The effect of BCS on copper accumulation was more pronounced in *N. fowleri*, which has a higher overall intracellular amount of copper under control conditions; however, the growth of *N. fowleri*, unlike *N. gruberi*, was not affected by this chelator (**Supplementary Figure S3**). This indicates that *N. fowleri* possesses more efficient copper homeostasis mechanisms than its nonpathogenic relative, and the use of an intracellular chelator is required to observe the physiological response to copper starvation. Based on these results, we decided to perform two proteomic analyses using

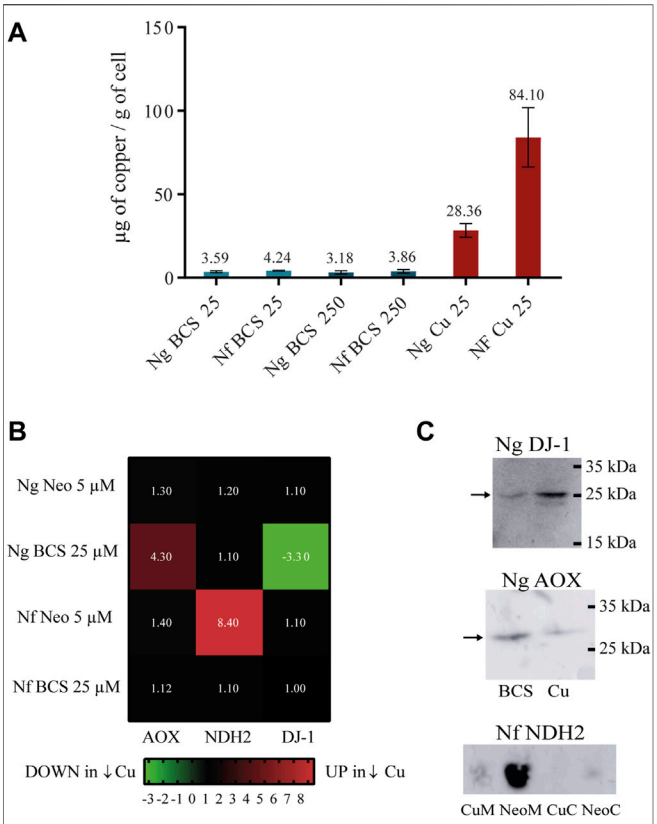

FIGURE 2 | Effect of copper availability on *Naegleria gruberi* and *Naegleria fowleri*. **(A)** Copper contents in *N. gruberi* and *N. fowleri* supplemented with 25 µM Cu_2SO_4, 25 µM BCS, or 250 µM BCS for 72 h. The values represent the mean of copper content of three individual replicates. **(B)** The fold changes of the most relevant proteins in this article are demonstrated on the heatmap; upregulation under copper-limited conditions is indicated by red color and downregulation by green color. The heatmap demonstrates that the chelators have different effects on both amoebas. **(C)** western blot analysis confirming the proteomic results using the specific antibodies antiNgDJ-1, antiNfNDH2, and antiAOX on cell lysates of *N. gruberi* incubated with 25 µM BCS (BCS) or 25 µM Cu_2SO_4 (Cu) and separated by SDS–PAGE and on cytosolic (C) and mitochondrial (M) fractions of *N. fowleri* cells incubated with 25 µM Cu_2SO_4 (Cu) or 5 µM neocuproine (Neo) separated by clear native PAGE.

the cells grown with the addition of 25 µM BCS and the cells grown in 5 µM neocuproine to achieve copper deprivation for both amoebas. To ensure sufficient copper status, the cells cultivated in presence of 25 µM Cu_2SO_4 were used as a control sample for both proteomic analyses. This concentration was used based on our previous work where we elucidated the IC50 of copper being 1 mM for *N. gruberi* and as high as 1.6 mM for *N. fowleri* (Grechnikova et al., 2020).

The list of all proteins that were significantly changed under copper deprivation is presented in **Supplementary Table S1**. In the analysis of the resulting proteomic data, we focused on proteins that are likely to bind copper or are related to copper metabolism, potentially compensating for the lack of copper or being involved in the oxidative stress response or energy metabolism. The selected proteins meeting these criteria are listed in **Table 1**. A heatmap presenting the most relevant proteins identified in this study demonstrates that selected chelators cause different effects on amoebas (**Figure 2B**).

The mitochondrial electron transport chain of *Naegleria gruberi* and *Naegleria fowleri* consists of complexes I, II, and III, two terminal oxidases: alternative oxidase (AOX) and cytochrome c oxidase (complex IV), and an alternative NADH ubiquinone oxidoreductase. Our proteomic analysis revealed that both amoebas responded to copper starvation by upregulating alternative enzymes involved in the electron transport chain. AOX (XP_002681229.1) from *N. gruberi* showed a 4.3-fold upregulation under copper-limited conditions. In contrast to *N. gruberi, N. fowleri* reacted to copper starvation through 8.4-fold upregulation of the protein NF0090420 (partial sequence) identified as nonproton pumping alternative NADH dehydrogenase (NDH-2). The complete sequence of this protein was obtained from genome of *N. fowleri* strain ATCC 30894 (AmoebaDB - FDP41_010952) (**Supplementary Figure S4**).

Additionally, the proteins involved in reactive oxygen species (ROS) detoxification pathways were significantly downregulated in copper-limited *N. gruberi* (thioredoxin reductase and two homologs of glutathione-S-transferase). Furthermore, in both amoebas, we observed significant upregulation in the expression of hemerythrin under copper limitation, a protein that probably plays a role in the defense against oxidative stress in bacteria (Li X. et al., 2015; Ma et al., 2018). Together, these results indicate that copper deprivation in naeglerias may lead to the generation of ROS.

Interestingly, one of the most downregulated proteins (fold change 3.3) of *N. gruberi* in copper-limited conditions was protein XP_002680488.1, which is a homolog of DJ-1 family proteins (**Supplementary Figure S4**). These proteins are thought to perform many functions (Bandyopadhyay and Cookson, 2004; Wei et al., 2007). Some studies on the human homolog of DJ-1 claim its ability to bind copper and serve as a copper chaperone for Cu, Zn superoxide dismutase (Girotto et al., 2014).

The copper-induced changes in protein abundance were also confirmed using western blot analysis with specific antibodies (**Figure 2C**). The localization of NfNDH-2 by fluorescence microscopy to demonstrate the antibody specificity is shown in **Supplementary Figure S5**.

RT qPCR Analysis Revealed That Changes Caused by Copper Deprivation Are Posttranslational

Selected genes encoding copper-regulated proteins (NfNDH-2, NfHemerythrin) were also analyzed by RT qPCR using copper-starved and control cells. Transcript abundance was normalized to the endogenous reference gene β-actin. Analogous to CTRs, no changes in the transcriptional level of these selected genes were observed, suggesting that the proteomic response of both amoebas to copper starvation occurs at the posttranslational level (**Supplementary Figure S2**).

TABLE 1 | Selected *N. gruberi* and *N. fowleri* proteins whose abundance was significantly changed under copper-limited conditions in at least one condition and in one amoeba. Arrows indicate significant upregulation or downregulation, and no arrow sign in proteins with a fold change lower than 1.5 indicates no significant change.

Naegleria gruberi			
Fold Change in BCS	**Fold Change in Neo**	**Accession Number in Database**	**Database Annotation/Manual Annotation**
↑4.3	1.3	XP_002681229.1	AOX
1.1	1.2	XP_002672148.1	NDH-2
↓3.3	1.1	XP_002680488.1	DJ-1
↑2.0	Not Found	XP_002680302.1	Hemerythrin
1.4	↓1.9	XP_002674924.1	Thioredoxin reductase
↓2.2	1.2	XP_002670102.1	Glutathione-S-transferase
↓1.6	1.3	XP_002670607.1	Glutathione-S-transferase III
Naegleria fowleri			
Fold change in BCS	**Fold change in Neo**	**Accession Number in Database**	**Database Annotation/Manual Annotation**
1.1	1.4	NF0004720	AOX
1.1	↑8.4	NF0090420	NDH-2
1	1.1	NF0125230	DJ-1
1.4	↑3.5	NF0127030	Hemerythrin
1.0	1.2	NF0014440	Thioredoxin reductase
1.1	1.3	NF0101120	Glutathione-S-transferase
1.1	Not Found	NF0101840	Glutathione-S-transferase
1.1	1.1	NF0039660	Glutathione-S-transferase

The Activity of NgAOX and NfNADH-2 Reflects Copper Availability

Our proteomic analysis indicated rearrangement of the mitochondrial electron transport chain in both amoebas under copper starvation. To determine the physiological effect of copper availability on respiration, we performed an oxygen consumption assay with amoebas grown in copper-limited conditions. Both organisms possess two terminal oxidases, cytochrome c oxidase (CCOX) and alternative oxidase (AOX), which couple the electron flow from ubiquinol with the reduction of O_2 to H_2O (Cantoni et al., 2020). In contrast with CCOX, AOX does not participate in ATP generation. The activity of NgAOX corresponded to the proteomic results: in copper-limited *N. gruberi,* the activity of AOX was almost twice as high as that in control cells (**Figure 3A**). In *N. fowleri*, copper starvation did not result in the upregulation of alternative oxidase at the protein level, but its activity in neocuproine-treated cells was significantly increased (**Figure 3A**). Interestingly, our results also demonstrate that *N. gruberi* respiration is predominantly mediated by alternative oxidases, whereas *N. fowleri* respires mainly through complex IV (**Figure 3A**).

In addition to the classical rotenone-sensitive NADH dehydrogenase, the electron transport chain of both amoebas additionally contains an alternative rotenone-insensitive NADH dehydrogenase (NDH-2). These enzymes share the same functions, but NDH-2 does not contribute to the generation of the transmembrane proton gradient. The comparative proteomic analysis indicated that *N. fowleri* adapts to copper-deprived conditions by upregulation of NDH-2. The resistance of NDH-2 to rotenone was used to distinguish this enzyme from classical rotenone-sensitive NADH dehydrogenase. When NADH dehydrogenase activity of lysates of control and copper-limited cells were compared, the rotenone-sensitive complex I activity was not affected by copper, while the rotenone-resistant activity was higher in the neocuproine-treated cells than in the control sample. Although we cannot exclude that other enzymes contribute to this activity, considering the proteomic data, we believe that the main enzyme responsible for the measured activity is NfNDH-2 (**Figure 3B**).

Expression of the Mitochondrially Localized Protein NgDJ-1 is Copper-dependent and is Not Induced by ROS Accumulation

One of the most downregulated proteins in copper-deprived *N. gruberi* cells (3.3-fold change downregulation in BCS) is protein XP_002680488.1 (named NgDJ-1 in this article), which shows homology to proteins belonging to the DJ-1/ThiJ/PfpI superfamily (**Supplementary Figure S4**). This superfamily contains functionally and structurally diverse proteins, many of which remain only poorly characterized at the biochemical level (Bandyopadhyay and Cookson, 2004). To confirm the connection between copper availability and NgDJ-1 expression, we performed a western blot analysis of whole-cell lysates of *N. gruberi* grown in copper-deprived conditions as well as in media supplemented with copper at different concentrations (1 μM, 25 μM, and 750 μM). The results demonstrate that the copper-induced expression of DJ-1 observed in our proteomic analysis is even more pronounced when cells are exposed to copper at levels that probably lead to toxicity, indicating a role of this protein in copper metabolism (**Figure 4A**).

The human homolog of DJ-1 has many predicted functions but is mainly annotated as a redox sensor and ROS scavenger (Zhang et al., 2020). Considering this, we analyzed the lysates of

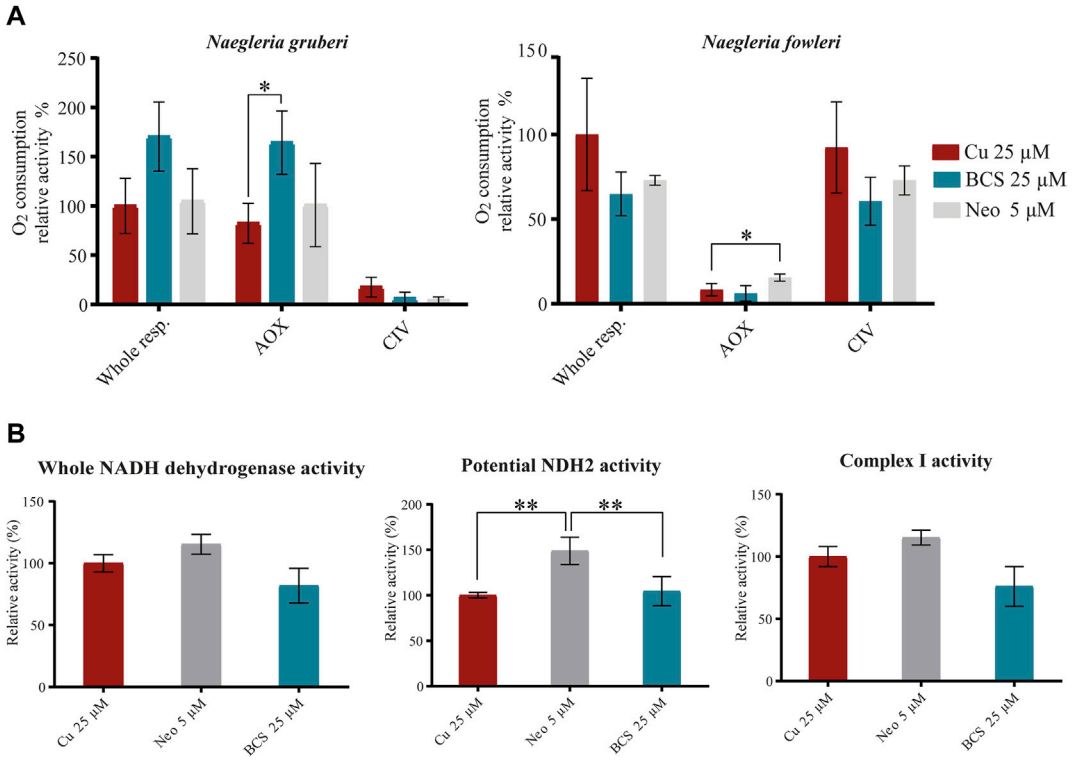

FIGURE 3 | The activity of NgAOX and NfNDH2 reflects the proteomic analysis results. **(A)** Oxygen consumption of NgAOX is increased due to copper deprivation. Oxygen consumption was measured in *N. gruberi* and *N. fowleri* cells incubated for 72 h with 25 M BCS or 5 µM neocuproine, and control cells were supplemented with 25 µM Cu_2SO_4. Specific inhibitors of alternative oxidase (SHAM) and complex IV (KCN) were used to distinguish the activities of these enzymes. For easier interpretation, oxygen consumption activity was calculated as the relative activity, where the whole respiration of control samples (Cu 25 µM) corresponds to 100%. The graphs show the mean of three biological replicates with the standard deviation. To evaluate the statistical confidence, Student's t test was used (* indicates a *p* value ≤0.05). **(B)** The enzyme activity of NfNDH2 is increased under low copper conditions. Spectrophotometric measurement of NADH dehydrogenase activity was measured using nonnatural Q2, the analog of Q10, at 340 nm on *N. fowleri* cells incubated in low or normal copper conditions. The potential NDH2 activity was measured after preincubation of the cells with rotenone. The activity of complex I was calculated by subtracting the potential NDH2 activity from overall NADH dehydrogenase activity. For easier interpretation, the activities are shown as the relative activity (%), and the activities of control cells (Cu 25 µM) correspond to 100%. To evaluate the statistical confidence, Student's t test was used (**indicates a *p* value ≤0.01).

N. gruberi cells exposed for 24 h to two ROS-inducing agents, rotenone and PEITC, by western blot using an NgDJ-1 antibody. Unexpectedly, we observed that treatment with both agents resulted in a decrease in NgDJ-1 expression (**Figure 4B**).

To determine NgDJ-1 cellular localization, we used two different methods: fluorescence microscopy and western blot analysis of crude cell fractions. Both methods revealed mitochondrial localization of NgDJ-1, which is rather unusual for this protein (**Figure 4C**). Predictably, observed molecular weight of DJ-1 on western blots is lower than anticipated (~26 kDa instead of 30 kDa), probably due to cleavage of mitochondrial targeting sequence. More pictures are shown in (**Supplementary Figure S6**).

N. gruberi Iron Uptake is Copper-Regulated

Iron uptake mechanisms in various organisms are frequently interconnected with copper. To determine this connection in both amoebas, we employed blue native electrophoresis analysis allowing visualization of the incorporation of iron radionuclide into cellular protein complexes. In our previous work, we showed that *N. fowleri* prefers to take up the reduced form of iron (Fe^{II}) and that iron acquisition is not induced by iron starvation (Arbon et al., 2020). Here, we show that similarly, the nonpathogenic relative *N. gruberi* preferably acquired a reduced form of iron, indicating a reductive uptake mechanism. Importantly, our results demonstrate that iron uptake is significantly affected by copper availability (**Figure 5A**), suggesting the requirement of copper in some of the iron acquisition system components (e.g., multicopper oxidase). In contrast, iron uptake efficiency in *N. fowleri* remained unaffected by copper deprivation (**Figure 5B**).

DISCUSSION

Copper and host:pathogen Interface

An important host defense process called nutritional immunity occurs at the host-pathogen interface: the host restricts access to essential metals for the pathogen (Hood and Skaar, 2012). Iron sequestration during bacterial infection is well described, and bacterial pathogens have developed a variety of strategies to

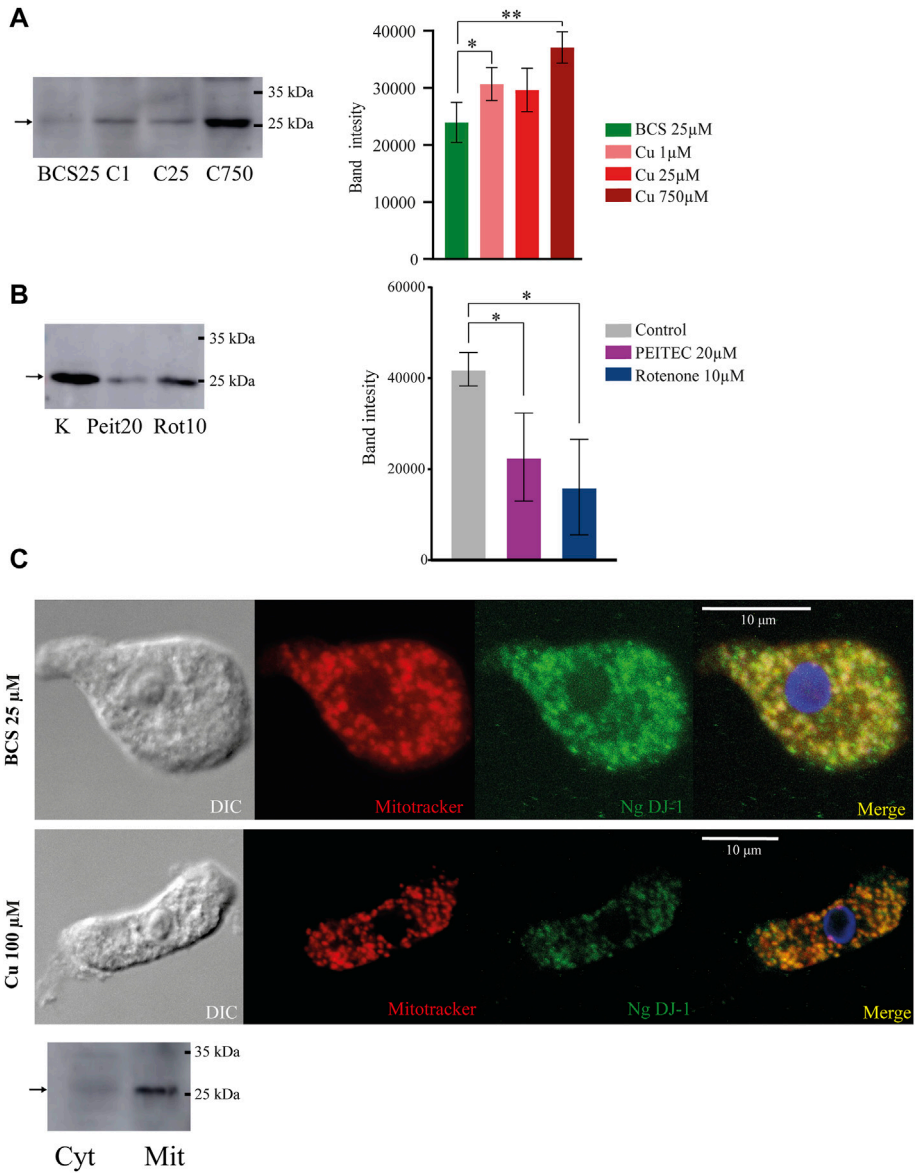

FIGURE 4 | The expression of mitochondrially localized NgDJ-1 is copper-dependent and is not induced by ROS accumulation. **(A)** NgDJ-1 protein expression is copper-dependent. Western blot analysis of whole-cell lysates of cells incubated for 72 h in low or high copper conditions (BCS 25 μM and Cu_2SO_4 1/25/750 μM) using an anti-NgDJ-1 antibody. To compare signal strength in each condition, densitometry of four independent replicates was performed using ImageJ. Changes in signals are demonstrated on the graph showing the mean of the signal with standard deviation error bars (*indicates a *p* value ≤0.05; **indicates a *p* value ≤0.01. **(B)** ROS accumulation does not induce NgDJ-1 expression. Western blot analysis of DJ-1 expression in cells preincubated with the ROS-inducing agents 20 μM PEITC and 10 μM rotenone for 24 h. The control sample (K) was *N. gruberi* without any additions. The graph demonstrates the difference in signal strength in each condition. **(C)** Localization of NgDJ-1 is mitochondrial regardless of copper availability. NgDJ-1 was visualized by immunofluorescence microscopy using a polyclonal antibody (anti-NgDJ-1) on *N. gruberi* cells precultivated with 25 μM BCS and 100 μM Cu_2SO_4 for 72 h. MitoTracker CMXRos (Thermo Fisher) was used for visualization of mitochondria. DIC–differential interference contrast. Mitochondrial localization of NgDJ-1 was also demonstrated by immunoblot detection of cytosolic (Cyt) and mitochondria-enriched (Mit) fractions of *N. gruberi*.

circumvent host-mediated iron limitation (Weinberg, 1975; Posey and Gherardini, 2000; Cassat and Skaar, 2013). In contrast to iron, copper is usually utilized in the opposite manner by host immune cells, which use the toxic properties of this metal to kill pathogens (Festa and Thiele, 2012; Hodgkinson and Petris, 2012; Stafford et al., 2013; Chaturvedi and Henderson, 2014). However, in fungal infections caused by *C. neoformans* and *C. albicans*, the pathogens experience limited copper availability in the host in specific situations. Although host immunity employs the toxic properties of copper in the lungs, which are the main locations of *C. neoformans* infection (Ding et al., 2013), *C. neoformans* tends to disseminate to the brain in immunodeficient hosts, where copper may be restricted. *C. neoformans* adapts to these copper-limited conditions by

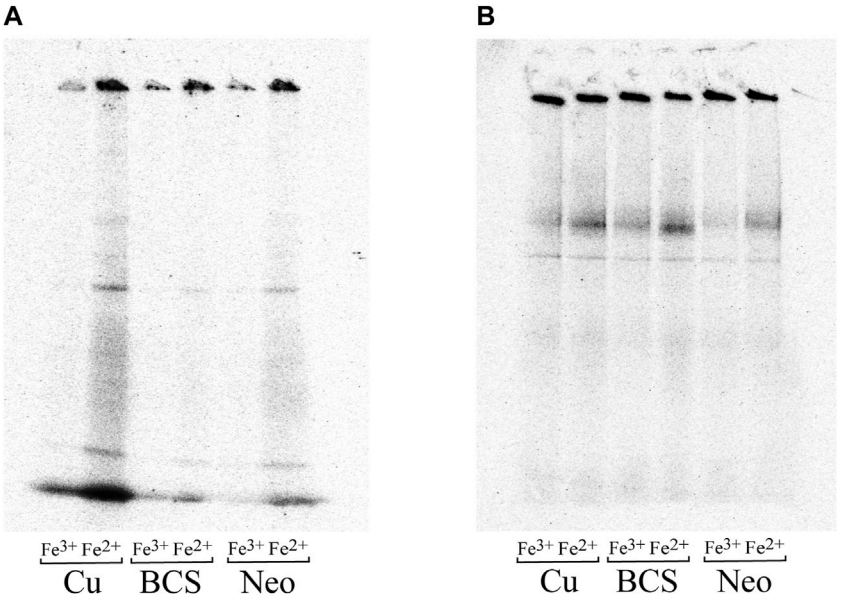

FIGURE 5 | Iron uptake is regulated by copper in *N. gruberi* but not in *N. fowleri*. Ferrous and ferric iron uptake by *N. gruberi* **(A)** and *N. fowleri* **(B)** under copper-rich and copper-deficient conditions. Autoradiography of blue native electrophoresis gels of whole-cell lysates of *N. gruberi* and *N. fowleri* cells incubated with 25 μM BCS (BCS), 5 μM neocuproine (Neo), and 25 μM Cu_2SO_4 (Cu) for 72 h and further incubated with ^{55}Fe(II) (ferrous ascorbate) or ^{55}Fe(III) (ferric citrate) for 1 h.

inducing specific copper uptake transporters (Waterman et al., 2007; Sun et al., 2014). *C. albicans* occupies diverse niches inside the host, but it may disseminate through the bloodstream, and the major location of infection in the murine model is the kidney. In the early stage of kidney infection, copper levels increase briefly, but as the infection progresses, the level of copper drops. *C. albicans* responds to decreasing copper conditions by switching from copper-dependent Cu/Zn SOD to Mn SOD3 and, interestingly, by upregulating alternative oxidase (AOX) to minimize mitochondrial damage and simultaneously maximize COX respiration (Li CX. et al., 2015; Besold et al., 2016; Broxton and Culotta, 2016).

In a recent study, we described how *N. fowleri* handles the toxic properties of copper and identified the key protein of the copper detoxification pathway, a copper-translocating ATPase (Grechnikova et al., 2020). In the present study, we focused on other aspects of copper metabolism and aimed to elucidate the metabolic adaptations of the free-living unicellular organism *N. gruberi* and its pathogenic relative *N. fowleri* to low copper availability.

Copper Acquisition

Our study began with a search for proteins involved in copper acquisition by both amoebas. In eukaryotic cells, the import of copper to the cytoplasm is widely mediated by high-affinity copper transporter (Ctr) localized to the plasma membrane. Ctr is an integral membrane protein conserved from yeast to humans with high specificity for Cu(I) (Zhou and Gitschier, 1997; Kozlowski et al., 2009). In *Saccharomyces cerevisiae*, copper is transported into cells by two high-affinity transporters, CTR1 (Dancis et al., 1994b) and CTR3 (Knight et al., 1996), and a low-affinity copper transporter, CTR2, is responsible for the mobilization of vacuolar copper ions (Rees et al., 2004; Liu et al., 2012). All CTRs of *S. cerevisiae* are regulated by intracellular copper status (Jungmann et al., 1993; Winge et al., 1998). We identified genes encoding potential Ctrs in the genomes of both amoebas, including three genes in *N. gruberi*, and two in *N. fowleri*. Since effective genetic manipulation of these organisms has not been established, we decided to verify copper transport function by expression in yeasts and by functional complementation assay using the ctr1Δ/ctr3Δ mutant yeast strain. One of the proposed CTRs from each amoeba was able to restore copper import function and showed typical localization to the plasma membrane. In contrast to *S. cerevisiae*, neither CTR appears to be regulated by copper starvation at the transcriptional level in *Naegleria*, indicating that the amoebas do not respond to copper starvation at the copper acquisition level or that the regulation is posttranslational.

Branched Mitochondrial ETC

Our proteomic approach to understanding the metabolic adaptations to copper limitation yielded particularly interesting findings: some of the proteins comprising the electron-transporting chain (ETC), the key part of the energy metabolism of a cell, are among the most affected by low copper availability in both amoebas. The ETC of both Naeglerias is branched and, in addition to the classical arrangement of complexes (CI-IV), possesses two nonenergy-conserving components: cyanide insensitive alternative oxidase (AOX) and alternative NADH dehydrogenase (NDH-2), both of which are significantly upregulated in copper-deprived conditions. Branched mitochondrial ETC is also known from plants, fungi, and other

protists, some of which are human pathogens (e.g., *C. albicans*, *C. neoformans*, *Acanthamoeba castellanii*). AOX bypasses complex III and complex IV, but its activity is not coupled to proton translocation; hence, it does not contribute to ATP synthesis. Studies focusing on plants show that two respiration pathways with different energy yields provide the ability to maintain the redox, carbon, and/or energy balance in response to changing demands (Sluse and Jarmuszkiewicz, 1998; Ribas-Carbo et al., 2005; Sieger et al., 2005; Smith et al., 2009; Cvetkovska and Vanlerberghe, 2012; Dahal and Vanlerberghe, 2017). In addition to this function, AOX also decreases the rate of mitochondrial ROS formation (Maxwell et al., 1999; Vishwakarma et al., 2015). In fungi, low copper availability was shown to be connected to impaired respiration (cytochrome c oxidase pathway) (Joseph-Horne et al., 2001), which generally leads to ROS accumulation in the mitochondria; thus, positive regulation of alternative oxidase may compensate for this loss and minimize ROS formation, which was recently demonstrated in *Paracoccidioides brasiliensis* (Petito et al., 2020) and in *C. albicans*, where copper starvation led to mitochondrial SOD1 repression and AOX induction enhanced cytochrome c oxidase activity (Broxton and Culotta, 2016). NDH-2 is a rotenone-insensitive nonproton pumping oxidoreductase that catalyzes a reaction similar to that of complex I, but in contrast to complex I, NDH-2 is not involved in the generation of membrane potential. NDH-2 was identified in plants, fungi, and bacteria as well as in some important parasitic protists, such as *Plasmodium falciparum* and *Toxoplasma gondii* (Marres et al., 1991; Yagi, 1991; Kerscher, 2000; Roberts et al., 2004; Lin et al., 2011). These two members belonging to the phylum Apicomplexa lack genes encoding canonical complex I and possess only homologs of NDH-2 instead (Fry and Beesley, 1991; Gardner et al., 2002; Uyemura et al., 2004). Altogether, NDH-2 is widely distributed in several human pathogens but not in humans themselves; thus, inhibitors of this enzyme could have clinical importance. Several studies have shown that NDH-2 provides a mechanism to remove excessive reducing power to balance the redox state of the cell (Luttik et al., 1998; Overkamp et al., 2000; Melo et al., 2004; Rasmusson et al., 2004). As mentioned above, branched mitochondrial ETC is activated in both studied amoebas upon copper limitation. In addition to AOX, whose activity is increased in both amoebas, NDH-2 is the most upregulated protein in copper-starved *N. fowleri*. Although we cannot conclude the direct consequences of NDH-2 induction for copper starvation in *N. fowleri*, we believe that further studying the exact mechanisms underlying the fascinating maintenance of the delicate balance between ATP production, ROS generation, and redox status in these microorganisms would be exciting.

DJ-1

One of the proteins most affected by copper limitation in *N. gruberi* shows homology to proteins belonging to the DJ-1/ThiJ/PfpI superfamily. Members of this superfamily are present in many organisms from bacteria to humans, and the most studied is the human homolog due to its role in several diseases, such as autosomal recessive early-onset Parkinson's disease (Bonifati et al., 2003). DJ-1 is also suggested to be one of the potential tumor markers and is strongly implicated in the pathogenesis of cancer (Nagakubo et al., 1997; Fan et al., 2015; Yu et al., 2017) and ischemia-reperfusion injury (Wang et al., 2017). Hundreds of publications explore the human homolog of DJ-1 and suggest many diverse functions, with roles as molecular chaperones (Cookson, 2003; Meulener et al., 2005), glyoxalases (Lee et al., 2003), proteases (Chen et al., 2010), and transcriptional regulators (Trempe and Fon, 2013), but the one function connecting these studies is the stress sensor reacting to oxidative stress and protecting cells from ROS (Taira et al., 2004; Inden et al., 2006). Some studies show that cells with a high level of DJ-1 are resistant to oxidative stress and neurotoxins, while lower levels of DJ-1 increase cells' vulnerability to oxidative stress (Inden et al., 2011). Therefore, we assessed the abundance of NgDJ-1 in cells treated with the ROS-inducing agents rotenone and PEITC. However, the expected induction of NgDJ-1 by ROS was not observed; in fact, the protein was downregulated in cells with higher ROS levels.

Human DJ-1 is predominantly localized to the cytoplasm, but it has been reported to be translocated to the mitochondria and nucleus under oxidative stress and to protect cells from oxidative stress-induced cell death (Irrcher et al., 2010; Kim et al., 2012). On the other hand, some studies also show that DJ-1 may be localized to mitochondria even in the absence of oxidative stress, where it directly binds to a subunit of complex I and somehow maintains its activity, since knockdown of DJ-1 in cells decreased complex I activity (Hayashi et al., 2009; Mullett and Hinkle, 2011). A recent study also showed its connection to ATP synthase, where DJ-1 is required for the normal stoichiometry of ATP synthase and to facilitate positioning of the β subunit of ATP synthase to fully close the mitochondrial inner membrane leak (Chen et al., 2019). Interestingly, our results show exclusively mitochondrial localization of NgDJ-1 regardless of copper availability. Only a few studies claim a certain link between copper metabolism and the DJ-1 protein. In 2014, Stefania Girroto and others suggested a putative role of DJ-1 as a copper chaperone for superoxide dismutase (Girotto et al., 2014). Two novel copper-binding sites, one Cu(I) binding site per monomer involving the highly conserved Cys-106 and the second Cu(I) binding site shared between two monomers, were identified, and the kinetics and binding affinity of DJ-1 to copper ions were determined (Girotto et al., 2014). Since the conserved Cys-106 analog is also present in the sequence of NgDJ-1 and the levels of the protein are regulated by copper availability in the amoeba, we may speculate about its role in the copper homeostasis of *N. gruberi*. Because NgDJ-1 is localized only to mitochondria, it may act as a storage site for copper that can be later allocated to complex IV when copper availability is limited, which is somewhat analogous to the case of plastocyanin in *Chlamydomonas* (Kropat et al., 2015). We may also consider the role of this protein as a protein with chelating properties to prevent free copper accumulation, which can cause increased ROS production and lead to impaired respiration. Since the levels of NgDJ-1 are affected by both copper limitation and copper excess, NgDJ-1 may play multiple roles in the amoeba.

Iron Uptake in *N. gruberi*

In our recent work, we showed that *N. fowleri* utilizes a reductive system of iron uptake, as described in the model *S. cerevisiae* (Arbon et al., 2020). This mechanism relies on the extracellular

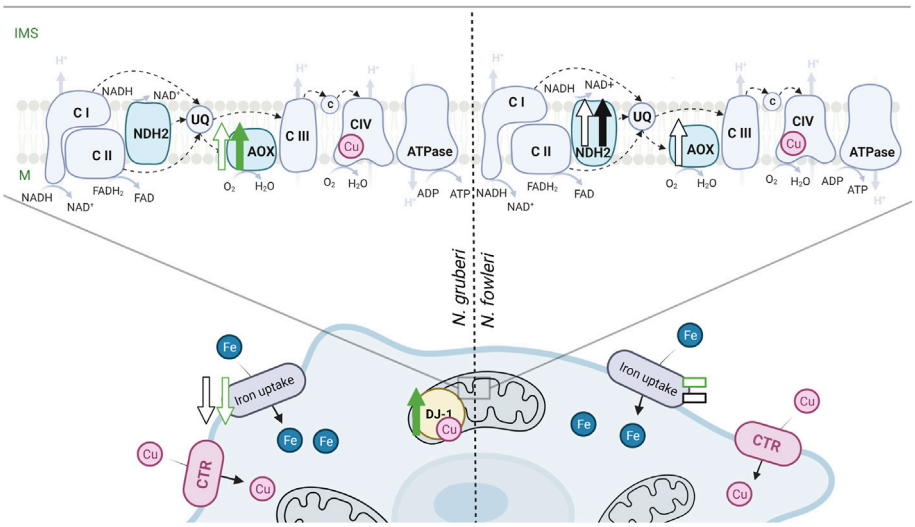

FIGURE 6 | The main effect of copper deprivation on the cellular processes of *N. gruberi* and *N. fowleri*. The green color corresponds to the effect of the copper chelator BCS, and changes caused by neocuproine are depicted in black. Upward pointing arrows represent an increase in copper-deprived conditions, downward pointing arrows denote a decrease in copper-deprived conditions, and dashes indicate no copper-induced changes. Full arrows represent the results from the proteomic analysis, and empty arrows represent the measured activity. Respiration chain complexes are marked by appropriate numbers, UQ–ubichinol/ubichinone, c–cytochrome c. Created with BioRender.com.

reduction of ferric ions from proteins, chelates, or other sources before their import into the cell. In yeast, the high-affinity ferrous-specific iron transport system is composed of multicopper oxidase FET3 and FTR1 permease; thus, copper availability is crucial for maintaining iron homeostasis (Askwith et al., 1994; Kaplan and O'Halloran, 1996; Stearman et al., 1996). Herein, we showed the same preference for the reduced form of iron in *N. gruberi*, but the main and surprising difference is that in contrast to *N. fowleri*, iron uptake efficiency in the nonpathogenic amoeba is decreased in copper-limited conditions, which corresponds to studies on *S. cerevisiae* (Dancis et al., 1994a) and on the model green algae *Chlamydomonas reinhardtii* (Herbik et al., 2002). An interesting question remains whether the pathogenic amoeba employs a copper-independent iron uptake mechanism or prioritizes extremely efficient copper delivery to this system in times of copper deprivation. The second hypothesis is rather unlikely since the *N. fowleri* iron uptake system has been previously shown to not be inducible even by iron starvation (Arbon et al., 2020).

N. gruberi and N. fowleri: So Similar yet so Different. Similarities and Differences

Altogether, our study reveals how *N. gruberi* and *N. fowleri* deal with copper deprivation and highlights the differences between the two amoebas (**Figure 6**). We showed that while both amoebas use Ctr homologs to acquire copper and increase the activity of the branched mitochondrial ETC when copper is limited, their responses to copper limitation differ significantly. Although copper bioavailability limitation in the growth medium results in a more pronounced decrease in the cellular concentration of the metal in *N. fowleri* in comparison to *N. gruberi*, the growth of the pathogen is not affected, and the intracellular copper chelator neocuproine is required to observe a copper-related phenotype. Moreover, even when neocuproine was used to starve the cells for copper, iron uptake efficiency was not affected in *N. fowleri*, unlike *N. gruberi*. To hypothesize whether the particularities in *N. fowleri* copper homeostasis can contribute to its virulence would be an exaggeration, however, one must take into account the fact that copper is an important player in the host-pathogen relationship.

DATA AVAILABILITY STATEMENT

The original contributions presented in the study are included in the article/**Supplementary Material**. The mass spectrometry proteomics data have been deposited to the ProteomeXchange Consortium via the PRIDE (Perez-Riverol et al., 2022) partner repository with the dataset identifier PXD032745, further inquiries can be directed to the corresponding author.

AUTHOR CONTRIBUTIONS

RS, KZ and MG conceived and designed the experiments. KZ, MG performed the experiments. KZ and MG analyzed and interpreted the data. KZ, MG and RS wrote the manuscript. All authors contributed to the article and approved the submitted version.

FUNDING

The project was supported by the Czech Science Foundation (20-28072S), Charles University Grant Agency (343621), CePaViP provided by The European Regional Development Fund and Ministry of Education, Youth and Sports of the Czech Republic (CZ.02.1.01/0.0/0.0/16_019/0000759), the MiCoBion project funded by EU Horizon 2020 (810224), Czech-BioImaging large RI projects (LM2018129 and CZ.02.1.01/0.0/0.0/18_046/0016045, funded by MEYS CR and ERDF), Moore-Simons Project on the Origin of the Eukaryotic Cell (https://doi.org/10.37807/GBMF9738).

ACKNOWLEDGMENTS

Karel Harant and Pavel Talacko from the Laboratory of Mass Spectrometry, Biocev, Charles University, Faculty of Science, where the proteomics and mass spectrometric analyses were performed. Special thanks to Dennis J. Thiele, Ivan Hrdý, Zdeněk Verner and Jan Mach for support and helpful scientific discussions.

SUPPLEMENTARY MATERIAL

The Supplementary Material for this article can be found online at: https://www.frontiersin.org/articles/10.3389/fcell.2022.853463/full#supplementary-material

Supplementary Table 1 | List of whole-cell proteomes of both amoebas under copper-rich and copper-deprived conditions. The list is organized into thirteen sheets containing separately raw data of comparative proteomics results of *N. gruberi* (NG) or *N. fowleri (NF)* cells incubated in 25 μM BCS (BCS) or 5 μM neocuproine (NEO) compared to cells cultured in the presence of 25 μM Cu2SO4 (cu), sheets containing all upregulated (UP) or downregulated (DOWN) proteins under the indicated copper-depleted conditions and the list containing summarized table of significantly changed proteins of both amoebas in both copper-deprived conditions. Upregulated and downregulated proteins were selected and filtered based on the criteria listed in the Methods section.

REFERENCES

Almagro Armenteros, J. J., Tsirigos, K. D., Sønderby, C. K., Petersen, T. N., Winther, O., Brunak, S., et al. (2019). SignalP 5.0 Improves Signal Peptide Predictions Using Deep Neural Networks. *Nat. Biotechnol.* 37, 420–423. doi:10.1038/s41587-019-0036-z

Altschul, S. F., Gish, W., Miller, W., Myers, E. W., and Lipman, D. J. (1990). Basic Local Alignment Search Tool. *J. Mol. Biol.* 215, 403–410. doi:10.1016/s0022-2836(05)80360-2

Amos, B., Aurrecoechea, C., Barba, M., Barreto, A., Basenko, E. Y., Ba˙ Zant, W., et al. (2021). VEuPathDB: The Eukaryotic Pathogen, Vector and Host Bioinformatics Resource center. *Nucleic Acids Res.* 50, D898–D911. doi:10.1093/nar/gkab929

Andreini, C., Bertini, I., Cavallaro, G., Holliday, G. L., and Thornton, J. M. (2008). Metal Ions in Biological Catalysis: From Enzyme Databases to General Principles. *J. Biol. Inorg. Chem.* 13, 1205–1218. doi:10.1007/s00775-008-0404-5

Arbon, D., Ženíšková, K., Mach, J., Grechnikova, M., Malych, R., Talacko, P., et al. (2020). Adaptive Iron Utilization Compensates for the Lack of an Inducible Uptake System in *Naegleria Fowleri* and Represents a Potential Target for Therapeutic Intervention. *Plos Negl. Trop. Dis.* 14, e0007759. doi:10.1371/journal.pntd.0007759

Askwith, C., Eide, D., Van Ho, A., Bernard, P. S., Li, L., Davis-Kaplan, S., et al. (1994). The FET3 Gene of *S. Cerevisiae* Encodes a Multicopper Oxidase Required for Ferrous Iron Uptake. *Cell* 76, 403–410. doi:10.1016/0092-8674(94)90346-8

Bandyopadhyay, S., and Cookson, M. R. (2004). Evolutionary and Functional Relationships within the DJ-1 Superfamily. *BMC Evol. Biol.* 4, 6. doi:10.1186/1471-2148-4-6

Besold, A. N., Culbertson, E. M., and Culotta, V. C. (2016). The Yin and Yang of Copper during Infection. *J. Biol. Inorg. Chem.* 21, 137–144. doi:10.1007/s00775-016-1335-1

Bonifati, V., Rizzu, P., van Baren, M. J., Schaap, O., Breedveld, G. J., Krieger, E., et al. (2003). Mutations in the DJ-1 Gene Associated with Autosomal Recessive Early-Onset Parkinsonism. *Science* 299, 256–259. doi:10.1126/science.1077209

Broxton, C. N., and Culotta, V. C. (2016). An Adaptation to Low Copper in *Candida Albicans* Involving SOD Enzymes and the Alternative Oxidase. *PLoS One* 11, e0168400. doi:10.1371/journal.pone.0168400

Cantoni, D., Osborne, A., Taib, N., Thompson, G., Kazana, E., Edrich, E., et al. (2020). Localization and Functional Characterization of the Alternative Oxidase in *Naegleria*. *bioRxiv*. doi:10.1101/2020.09.26.314807

Cassat, J. E., and Skaar, E. P. (2013). Iron in Infection and Immunity. *Cell Host Microbe* 13, 509–519. doi:10.1016/j.chom.2013.04.010

Chaturvedi, K. S., and Henderson, J. P. (2014). Pathogenic Adaptations to Host-Derived Antibacterial Copper. *Front. Cel. Infect. Microbiol.* 4, 3. doi:10.3389/fcimb.2014.00003

Chen, J., Li, L., and Chin, L.-S. (2010). Parkinson Disease Protein DJ-1 Converts from a Zymogen to a Protease by Carboxyl-Terminal Cleavage. *Hum. Mol. Genet.* 19, 2395–2408. doi:10.1093/hmg/ddq113

Chen, R., Park, H. A., Mnatsakanyan, N., Niu, Y., Licznerski, P., Wu, J., et al. (2019). Parkinson's Disease Protein DJ-1 Regulates ATP Synthase Protein Components to Increase Neuronal Process Outgrowth. *Cell Death Dis* 10 (6), 469. doi:10.1038/s41419-019-1679-x

Choveaux, D. L., Przyborski, J. M., and Goldring, J. P. (2012). A *Plasmodium Falciparum* Copper-Binding Membrane Protein with Copper Transport Motifs. *Malar. J.* 11, 397. doi:10.1186/1475-2875-11-397

Cookson, M. R. (2003). Pathways to Parkinsonism. *Neuron* 37, 7–10. doi:10.1016/s0896-6273(02)01166-2

Cox, J., Hein, M. Y., Luber, C. A., Paron, I., Nagaraj, N., and Mann, M. (2014). Accurate Proteome-Wide Label-Free Quantification by Delayed Normalization and Maximal Peptide Ratio Extraction, Termed MaxLFQ. *Mol. Cel. Proteomics* 13, 2513–2526. doi:10.1074/mcp.m113.031591

Cvetkovska, M., and Vanlerberghe, G. C. (2012). Coordination of a Mitochondrial Superoxide Burst during the Hypersensitive Response to Bacterial Pathogen in *Nicotiana Tabacum*. *Plant Cel Environ.* 35, 1121–1136. doi:10.1111/j.1365-3040.2011.02477.x

Dahal, K., and Vanlerberghe, G. C. (2017). Alternative Oxidase Respiration Maintains Both Mitochondrial and Chloroplast Function during Drought. *New Phytol.* 213, 560–571. doi:10.1111/nph.14169

Dancis, A., Haile, D., Yuan, D. S., and Klausner, R. D. (1994b). The *Saccharomyces Cerevisiae* Copper Transport Protein (Ctr1p). Biochemical Characterization, Regulation by Copper, and Physiologic Role in Copper Uptake. *J. Biol. Chem.* 269, 25660–25667. doi:10.1016/s0021-9258(18)47300-0

Dancis, A., Yuan, D. S., Haile, D., Askwith, C., Eide, D., Moehle, C., et al. (1994a). Molecular Characterization of a Copper Transport Protein in *S. Cerevisiae*: An Unexpected Role for Copper in Iron Transport. *Cell* 76, 393–402. doi:10.1016/0092-8674(94)90345-x

De Jonckheere, J. F. (2004). Molecular Definition and the Ubiquity of Species in the Genus. *Protist* 155, 89–103. doi:10.1078/1434461000167

Ding, C., Festa, R. A., Chen, Y.-L., Espart, A., Palacios, Ò., Espín, J., et al. (2013). *Cryptococcus Neoformans* Copper Detoxification Machinery Is Critical for Fungal Virulence. *Cell Host Microbe* 13, 265–276. doi:10.1016/j.chom.2013.02.002

Fan, J., Yu, H., Lv, Y., and Yin, L. (2015). Diagnostic and Prognostic Value of Serum Thioredoxin and DJ-1 in Non-Small Cell Lung Carcinoma Patients. *Tumor Biol.* 37 (2), 1949–1958. doi:10.1007/s13277-015-3994-x

Festa, R. A., and Thiele, D. J. (2012). Copper at the Front Line of the Host-Pathogen Battle. *Plos Pathog.* 8, e1002887. doi:10.1371/journal.ppat.1002887

Fritz-Laylin, L. K., Ginger, M. L., Walsh, C., Dawson, S. C., and Fulton, C. (2011). The *Naegleria* Genome: A Free-Living Microbial Eukaryote Lends Unique Insights into Core Eukaryotic Cell Biology. *Res. Microbiol.* 162, 607–618. doi:10.1016/j.resmic.2011.03.003

Fritz-Laylin, L. K., Prochnik, S. E., Ginger, M. L., Dacks, J. B., Carpenter, M. L., Field, M. C., et al. (2010). The Genome of *Naegleria Gruberi* Illuminates Early Eukaryotic Versatility. *Cell* 140, 631–642. doi:10.1016/j.cell.2010.01.032

Fry, M., and Beesley, J. E. (1991). Mitochondria of Mammalian *Plasmodium Spp*. *Parasitology* 102 (Pt 1), 17–26. doi:10.1017/s0031182000060297

Fulton, C. (1974). Axenic Cultivation of *Naegleria Gruberi*: Requirement for Methionine. *Exp. Cel Res.* 88, 365–370. doi:10.1016/0014-4827(74)90253-5

García-Santamarina, S., and Thiele, D. J. (2015). Copper at the Fungal Pathogen-Host Axis. *J. Biol. Chem.* 290, 18945–18953. doi:10.1074/jbc.R115.649129

Gardner, M. J., Hall, N., Fung, E., White, O., Berriman, M., Hyman, R. W., et al. (2002). Genome Sequence of the Human Malaria Parasite *Plasmodium Falciparum*. *Nature* 419, 498–511. doi:10.1038/nature01097

Garí, E., Piedrafita, L., Aldea, M., and Herrero, E. (1997). A Set of Vectors with a Tetracycline-Regulatable Promoter System for Modulated Gene Expression in *Saccharomyces Cerevisiae*. *Yeast* 13, 837–848. doi:10.1002/(SICI)1097-0061(199707)13:9<837::AID-YEA145>3.0.CO;2-T

Gietz, R. D., and Schiestl, R. H. (2007). Large-Scale High-Efficiency Yeast Transformation Using the LiAc/SS Carrier DNA/PEG Method. *Nat. Protoc.* 2, 38–41. doi:10.1038/nprot.2007.15

Girotto, S., Cendron, L., Bisaglia, M., Tessari, I., Mammi, S., Zanotti, G., et al. (2014). DJ-1 Is a Copper Chaperone Acting on SOD1 Activation. *J. Biol. Chem.* 289, 10887–10899. doi:10.1074/jbc.m113.535112

Grechnikova, M., Ženíšková, K., Malych, R., Mach, J., and Sutak, R. (2020). Copper Detoxification Machinery of the Brain-Eating Amoeba *Naegleria Fowleri* Involves Copper-Translocating ATPase and the Antioxidant System. *Int. J. Parasitol. Drugs Drug Resist.* 14, 126–135. doi:10.1016/j.ijpddr.2020.10.001

Grigoriev, I. V., Hayes, R. D., Calhoun, S., Kamel, B., Wang, A., Ahrendt, S., et al. (2021). PhycoCosm, a Comparative Algal Genomics Resource. *Nucleic Acids Res.* 49, D1004–D1011. doi:10.1093/nar/gkaa898

Hayashi, T., Ishimori, C., Takahashi-Niki, K., Taira, T., Kim, Y.-C., Maita, H., et al. (2009). DJ-1 Binds to Mitochondrial Complex I and Maintains its Activity. *Biochem. Biophysical Res. Commun.* 390, 667–672. doi:10.1016/j.bbrc.2009.10.025

Herbik, A., Bölling, C., and Buckhout, T. J. (2002). The Involvement of a Multicopper Oxidase in Iron Uptake by the Green Algae *Chlamydomonas Reinhardtii*. *Plant Physiol.* 130, 2039–2048. doi:10.1104/pp.013060

Herman, E. K., Greninger, A., van der Giezen, M., Ginger, M. L., Ramirez-Macias, I., Miller, H. C., et al. (2021). Genomics and Transcriptomics Yields a System-Level View of the Biology of the Pathogen *Naegleria Fowleri*. *BMC Biol.* 19 (1), 142. doi:10.1186/s12915-021-01078-1

Hodgkinson, V., and Petris, M. J. (2012). Copper Homeostasis at the Host-Pathogen Interface. *J. Biol. Chem.* 287, 13549–13555. doi:10.1074/jbc.r111.316406

Hood, M. I., and Skaar, E. P. (2012). Nutritional Immunity: Transition Metals at the Pathogen-Host Interface. *Nat. Rev. Microbiol.* 10, 525–537. doi:10.1038/nrmicro2836

Inden, M., Kitamura, Y., Takahashi, K., Takata, K., Ito, N., Niwa, R., et al. (2011). Protection against Dopaminergic Neurodegeneration in Parkinson's Disease-Model Animals by a Modulator of the Oxidized Form of DJ-1, a Wild-type of Familial Parkinson's Disease-Linked PARK7. *J. Pharmacol. Sci.* 117, 189–203. doi:10.1254/jphs.11151fp

Inden, M., Taira, T., Kitamura, Y., Yanagida, T., Tsuchiya, D., Takata, K., et al. (2006). PARK7 DJ-1 Protects against Degeneration of Nigral Dopaminergic Neurons in Parkinson's Disease Rat Model. *Neurobiol. Dis.* 24, 144–158. doi:10.1016/j.nbd.2006.06.004

Irrcher, I., Aleyasin, H., Seifert, E. L., Hewitt, S. J., Chhabra, S., Phillips, M., et al. (2010). Loss of the Parkinson's Disease-Linked Gene DJ-1 Perturbs Mitochondrial Dynamics. *Hum. Mol. Genet.* 19, 3734–3746. doi:10.1093/hmg/ddq288

Isah, M. B., Goldring, J. P. D., and Coetzer, T. H. T. (2020). Expression and Copper Binding Properties of the N-Terminal Domain of Copper P-type ATPases of African Trypanosomes. *Mol. Biochem. Parasitol.* 235, 111245. doi:10.1016/j.molbiopara.2019.111245

Joseph-Horne, T., Hollomon, D. W., and Wood, P. M. (2001). Fungal Respiration: A Fusion of Standard and Alternative Components. *Biochim. Biophys. Acta - Bioenerg.* 1504, 179–195. doi:10.1016/s0005-2728(00)00251-6

Jungmann, J., Reins, H. A., Lee, J., Romeo, A., Hassett, R., Kosman, D., et al. (1993). MAC1, a Nuclear Regulatory Protein Related to Cu-Dependent Transcription Factors Is Involved in Cu/Fe Utilization and Stress Resistance in Yeast. *EMBO J.* 12, 5051–5056. doi:10.1002/j.1460-2075.1993.tb06198.x

Käll, L., Krogh, A., and Sonnhammer, E. L. L. (2004). A Combined Transmembrane Topology and Signal Peptide Prediction Method. *J. Mol. Biol.* 338, 1027–1036. doi:10.1016/j.jmb.2004.03.016

Kaplan, J., and O'Halloran, T. V. (1996). Iron Metabolism in Eukaryotes-Mars and Venus at it Again. *Science* 271, 1510–1512. doi:10.1126/science.271.5255.1510

Kerscher, S. J. (2000). Diversity and Origin of Alternative NADH:ubiquinone Oxidoreductases. *Biochim. Biophys. Acta - Bioenerg.* 1459, 274–283. doi:10.1016/s0005-2728(00)00162-6

Kim, S.-J., Park, Y.-J., Hwang, I.-Y., Youdim, M. B. H., Park, K.-S., and Oh, Y. J. (2012). Nuclear Translocation of DJ-1 during Oxidative Stress-Induced Neuronal Cell Death. *Free Radic. Biol. Med.* 53, 936–950. doi:10.1016/j.freeradbiomed.2012.05.035

Knight, S. A., Labbé, S., Kwon, L. F., Kosman, D. J., and Thiele, D. J. (1996). A Widespread Transposable Element Masks Expression of a Yeast Copper Transport Gene. *Genes Dev.* 10, 1917–1929. doi:10.1101/gad.10.15.1917

Kozlowski, H., Janicka-Klos, A., Brasun, J., Gaggelli, E., Valensin, D., and Valensin, G. (2009). Copper, Iron, and Zinc Ions Homeostasis and Their Role in Neurodegenerative Disorders (Metal Uptake, Transport, Distribution and Regulation). *Coord. Chem. Rev.* 253, 2665–2685. doi:10.1016/j.ccr.2009.05.011

Kropat, J., Gallaher, S. D., Urzica, E. I., Nakamoto, S. S., Strenkert, D., Tottey, S., et al. (2015). Copper Economy in *Chlamydomonas*: Prioritized Allocation and Reallocation of Copper to Respiration vs. Photosynthesis. *Proc. Natl. Acad. Sci. U.S.A.* 112, 2644–2651. doi:10.1073/pnas.1422492112

Lee, S.-J., Kim, S. J., Kim, I.-K., Ko, J., Jeong, C.-S., Kim, G.-H., et al. (2003). Crystal Structures of Human DJ-1 and *Escherichia coli* Hsp31, Which Share an Evolutionarily Conserved Domain. *J. Biol. Chem.* 278, 44552–44559. doi:10.1074/jbc.m304517200

Li, C. X., Gleason, J. E., Zhang, S. X., Bruno, V. M., Cormack, B. P., and Culotta, V. C. (2015a). *Candida Albicans* Adapts to Host Copper during Infection by Swapping Metal Cofactors for Superoxide Dismutase. *Proc. Natl. Acad. Sci. U. S. A.* 112, E5336–E5342. doi:10.1073/pnas.1513447112

Li, X., Li, J., Hu, X., Huang, L., Xiao, J., Chan, J., et al. (2015b). Differential Roles of the Hemerythrin-Like Proteins of *Mycobacterium Smegmatis* in Hydrogen Peroxide and Erythromycin Susceptibility. *Sci. Rep.* 5, 16130. doi:10.1038/srep16130

Liechti, N., Schürch, N., Bruggmann, R., and Wittwer, M. (2019). Nanopore Sequencing Improves the Draft Genome of the Human Pathogenic Amoeba *Naegleria Fowleri*. *Sci. Rep.* 9, 16040. doi:10.1038/s41598-019-52572-0

Lin, S. S., Gross, U., and Bohne, W. (2011). Two Internal Type II NADH Dehydrogenases of *Toxoplasma Gondii* Are Both Required for Optimal Tachyzoite Growth. *Mol. Microbiol.* 82, 209–221. doi:10.1111/j.1365-2958.2011.07807.x

Liu, L., Qi, J., Yang, Z., Peng, L., and Li, C. (2012). Low-Affinity Copper Transporter CTR2 Is Regulated by Copper-Sensing Transcription Factor Mac1p in *Saccharomyces Cerevisiae*. *Biochem. Biophys. Res. Commun.* 420, 600–604. doi:10.1016/j.bbrc.2012.03.040

Luttik, M. A. H., Overkamp, K. M., Kötter, P., de Vries, S., van Dijken, J. P., and Pronk, J. T. (1998). The *Saccharomyces Cerevisiae* NDE1 and NDE2 Genes Encode Separate Mitochondrial NADH Dehydrogenases Catalyzing the Oxidation of Cytosolic NADH. *J. Biol. Chem.* 273, 24529–24534. doi:10.1074/jbc.273.38.24529

Ma, Z., Strickland, K. T., Cherne, M. D., Sehanobish, E., Rohde, K. H., Self, W. T., et al. (2018). The Rv2633c Protein of *Mycobacterium Tuberculosis* Is a Non-heme Di-iron Catalase with a Possible Role in Defenses against Oxidative Stress. *J. Biol. Chem.* 293, 1590–1595. doi:10.1074/jbc.ra117.000421

Mach, J., Bíla, J., Ženíšková, K., Arbon, D., Malych, R., Glavanakovová, M., et al. (2018). Iron Economy in *Naegleria Gruberi* Reflects its Metabolic Flexibility. *Int. J. Parasitol.* 48 (9-10), 719–727. doi:10.1016/j.ijpara.2018.03.005

Macomber, L., and Imlay, J. A. (2009). The Iron-Sulfur Clusters of Dehydratases Are Primary Intracellular Targets of Copper Toxicity. *Proc. Natl. Acad. Sci. U.S.A.* 106, 8344–8349. doi:10.1073/pnas.0812808106

Marres, C. A. M., Vries, S., and Grivell, L. A. (1991). Isolation and Inactivation of the Nuclear Gene Encoding the Rotenone-Insensitive Internal NADH: Ubiquinone Oxidoreductase of Mitochondria from *Saccharomyces Cerevisiae*. *Eur. J. Biochem.* 195, 857–862. doi:10.1111/j.1432-1033.1991.tb15775.x

Marvin, M. E., Williams, P. H., and Cashmore, A. M. (2003). Tha *Candida Albicans* CTR1 Gene Encodes a Functional Copper Transporter. *Microbiology* 149, 1461–1474. doi:10.1099/mic.0.26172-0

Maryon, E. B., Molloy, S. A., Zimnicka, A. M., and Kaplan, J. H. (2007). Copper Entry into Human Cells: Progress and Unanswered Questions. *Biometals* 20, 355–364. doi:10.1007/s10534-006-9066-3

Maxwell, D. P., Wang, Y., and McIntosh, L. (1999). The Alternative Oxidase Lowers Mitochondrial Reactive Oxygen Production in Plant Cells. *Proc. Natl. Acad. Sci. U.S.A.* 96, 8271–8276. doi:10.1073/pnas.96.14.8271

Melo, A. M. P., Bandeiras, T. M., and Teixeira, M. (2004). New Insights into Type II NAD(P)H:quinone Oxidoreductases. *Microbiol. Mol. Biol. Rev.* 68, 603–616. doi:10.1128/mmbr.68.4.603-616.2004

Meulener, M. C., Graves, C. L., Sampathu, D. M., Armstrong-Gold, C. E., Bonini, N. M., and Giasson, B. I. (2005). DJ-1 Is Present in a Large Molecular Complex in Human Brain Tissue and Interacts with α-synuclein. *J. Neurochem.* 93, 1524–1532. doi:10.1111/j.1471-4159.2005.03145.x

Mistry, J., Chuguransky, S., Williams, L., Qureshi, M., Salazar, G. A., Sonnhammer, E. L. L., et al. (2021). Pfam: The Protein Families Database in 2021. *Nucleic Acids Res.* 49, D412–D419. doi:10.1093/nar/gkaa913

Mull, B. J., Narayanan, J., and Hill, V. R. (2013). Improved Method for the Detection and Quantification of *Naegleria Fowleri* in Water and Sediment Using Immunomagnetic Separation and Real-Time PCR. *J. Parasitol. Res.* 2013, 608367. doi:10.1155/2013/608367

Mullett, S. J., and Hinkle, D. A. (2011). DJ-1 Deficiency in Astrocytes Selectively Enhances Mitochondrial Complex I Inhibitor-Induced Neurotoxicity. *J. Neurochem.* 117, 375–387. doi:10.1111/j.1471-4159.2011.07175.x

Mungroo, M. R., Khan, N. A., Maciver, S., and Siddiqui, R. (2021). Opportunistic Free-Living Amoebal Pathogens. *Pathog. Glob. Health* 49, 1–15. doi:10.1080/21548331.2020.1828888

Nagakubo, D., Taira, T., Kitaura, H., Ikeda, M., Tamai, K., Iguchi-Ariga, S. M. M., et al. (1997). DJ-1, a Novel Oncogene Which Transforms Mouse NIH3T3 Cells in Cooperation Withras. *Biochem. Biophys. Res. Commun.* 231, 509–513. doi:10.1006/bbrc.1997.6132

Nose, Y., Rees, E. M., and Thiele, D. J. (2006). Structure of the Ctr1 Copper trans'PORE'ter Reveals Novel Architecture. *Trends Biochem. Sci.* 31, 604–607. doi:10.1016/j.tibs.2006.09.003

Overkamp, K. M., Bakker, B. M., Kötter, P., van Tuijl, A., de Vries, S., van Dijken, J. P., et al. (2000). *In Vivo* analysis of the Mechanisms for Oxidation of Cytosolic NADH by *Saccharomyces Cerevisiae* Mitochondria. *J. Bacteriol.* 182, 2823–2830. doi:10.1128/jb.182.10.2823-2830.2000

Paul, R., Banerjee, S., Sen, S., Dubey, P., Maji, S., Bachhawat, A. K., et al. (2021). The Novel Leishmanial Copper P-type ATPase Plays a Vital Role in Intracellular Parasite Survival. *J. Biol. Chem.* 298 (2), 101539. doi:10.1016/j.jbc.2021.101539

Perez-Riverol, Y., Bai, J., Bandla, C., García-Seisdedos, D., Hewapathirana, S., Kamatchinathan, S., et al. (2022). The PRIDE Database Resources in 2022: a Hub for Mass Spectrometry-Based Proteomics Evidences. *Nucleic Acids Res.* 50, D543.

Petito, G., de Curcio, J. S., Pereira, M., Bailão, A. M., Paccez, J. D., Tristão, G. B., et al. (2020). Metabolic Adaptation of *Paracoccidioides Brasiliensis* in Response to *In Vitro* Copper Deprivation. *Front. Microbiol.* 11, 1834. doi:10.3389/fmicb.2020.01834

Posey, J. E., and Gherardini, F. C. (2000). Lack of a Role for Iron in the Lyme Disease Pathogen. *Science* 288, 1651–1653. doi:10.1126/science.288.5471.1651

Rasmusson, A. G., Soole, K. L., and Elthon, T. E. (2004). Alternative NAD(P)H Dehydrogenases of Plant Mitochondria. *Annu. Rev. Plant Biol.* 55, 23–39. doi:10.1146/annurev.arplant.55.031903.141720

Rasoloson, D., Shi, L., Chong, C. R., Kafsack, B. F., and Sullivan, D. J. (2004). Copper Pathways in *Plasmodium Falciparum* Infected Erythrocytes Indicate an Efflux Role for the Copper P-ATPase. *Biochem. J.* 381, 803–811. doi:10.1042/bj20040335

Rees, E. M., Lee, J., and Thiele, D. J. (2004). Mobilization of Intracellular Copper Stores by the Ctr2 Vacuolar Copper Transporter. *J. Biol. Chem.* 279, 54221–54229. doi:10.1074/jbc.m411669200

Ribas-Carbo, M., Taylor, N. L., Giles, L., Busquets, S., Finnegan, P. M., Day, D. A., et al. (2005). Effects of Water Stress on Respiration in Soybean Leaves. *Plant Physiol.* 139, 466–473. doi:10.1104/pp.105.065565

Roberts, C. W., Roberts, F., Henriquez, F. L., Akiyoshi, D., Samuel, B. U., Richards, T. A., et al. (2004). Evidence for Mitochondrial-Derived Alternative Oxidase in the Apicomplexan Parasite *Cryptosporidium Parvum*: A Potential Anti-Microbial Agent Target. *Int. J. Parasitol.* 34, 297–308. doi:10.1016/j.ijpara.2003.11.002

Schneider, C. A., Rasband, W. S., and Eliceiri, K. W. (2012). NIH Image to ImageJ: 25 Years of Image Analysis. *Nat. Methods* 9 (7), 671–675. doi:10.1038/nmeth.2089

Sieger, S. M., Kristensen, B. K., Robson, C. A., Amirsadeghi, S., Eng, E. W. Y., Abdel-Mesih, A., et al. (2005). The Role of Alternative Oxidase in Modulating Carbon Use Efficiency and Growth during Macronutrient Stress in Tobacco Cells. *J. Exp. Bot.* 56, 1499–1515. doi:10.1093/jxb/eri146

Sluse, F. E., and Jarmuszkiewicz, W. (1998). Alternative Oxidase in the Branched Mitochondrial Respiratory Network: an Overview on Structure, Function, Regulation, and Role. *Braz. J. Med. Biol. Res.* 31, 733–747. doi:10.1590/s0100-879x1998000600003

Smith, C. A., Melino, V. J., Sweetman, C., and Soole, K. L. (2009). Manipulation of Alternative Oxidase Can Influence Salt Tolerance in *Arabidopsis Thaliana*. *Physiol. Plant* 137, 459–472. doi:10.1111/j.1399-3054.2009.01305.x

Solomon, E. I., Heppner, D. E., Johnston, E. M., Ginsbach, J. W., Cirera, J., Qayyum, M., et al. (2014). Copper Active Sites in Biology. *Chem. Rev.* 114, 3659–3853. doi:10.1021/cr400327t

Stafford, S. L., Bokil, N. J., Achard, M. E., Kapetanovic, R., Schembri, M. A., Mcewan, A. G., et al. (2013). Metal Ions in Macrophage Antimicrobial Pathways: Emerging Roles for Zinc and Copper. *Biosci. Rep.* 33, 541–554. doi:10.1042/BSR20130014

Stearman, R., Yuan, D. S., Yamaguchi-Iwai, Y., Klausner, R. D., and Dancis, A. (1996). A Permease-Oxidase Complex Involved in High-Affinity Iron Uptake in Yeast. *Science* 271, 1552–1557. doi:10.1126/science.271.5255.1552

Sun, T. S., Ju, X., Gao, H. L., Wang, T., Thiele, D. J., Li, J. Y., et al. (2014). Reciprocal Functions of *Cryptococcus Neoformans* Copper Homeostasis Machinery during Pulmonary Infection and Meningoencephalitis. *Nat. Commun.* 5, 5550. doi:10.1038/ncomms6550

Taira, T., Saito, Y., Niki, T., Iguchi-Ariga, S. M. M., Takahashi, K., and Ariga, H. (2004). DJ-1 Has a Role in Antioxidative Stress to Prevent Cell Death. *EMBO Rep.* 5, 213–218. doi:10.1038/sj.embor.7400074

Thomas, P. D., Campbell, M. J., Kejariwal, A., Mi, H., Karlak, B., Daverman, R., et al. (2003). PANTHER: A Library of Protein Families and Subfamilies Indexed by Function. *Genome Res.* 13, 2129–2141. doi:10.1101/gr.772403

Trempe, J.-F., and Fon, E. A. (2013). Structure and Function of Parkin, PINK1, and DJ-1, the Three Musketeers of Neuroprotection. *Front. Neurol.* 4, 38. doi:10.3389/fneur.2013.00038

Tsaousis, A. D., Nývltová, E., Šuták, R., Hrdý, I., and Tachezy, J. (2014). A Nonmitochondrial Hydrogen Production in *Naegleria Gruberi*. *Genome Biol. Evol.* 6, 792–799. doi:10.1093/gbe/evu065

Tyanova, S., Temu, T., Sinitcyn, P., Carlson, A., Hein, M. Y., Geiger, T., et al. (2016). The Perseus Computational Platform for Comprehensive Analysis of (Prote)omics Data. *Nat. Methods* 13, 731–740. doi:10.1038/nmeth.3901

Uyemura, S. A., Luo, S., Vieira, M., Moreno, S. N. J., and Docampo, R. (2004). Oxidative Phosphorylation and Rotenone-Insensitive Malate- and NADH-Quinone Oxidoreductases in *Plasmodium Yoelii* Yoelii Mitochondria *In Situ*. *J. Biol. Chem.* 279, 385–393. doi:10.1074/jbc.m307264200

Vishwakarma, A., Tetali, S. D., Selinski, J., Scheibe, R., and Padmasree, K. (2015). Importance of the Alternative Oxidase (AOX) Pathway in Regulating Cellular Redox and ROS Homeostasis to Optimize Photosynthesis during Restriction of the Cytochrome Oxidase Pathway in *Arabidopsis Thaliana*. *Ann. Bot.* 116, 555–569. doi:10.1093/aob/mcv122

Wang, H., Li, Y.-Y., Qiu, L.-Y., Yan, Y.-F., Liao, Z.-P., and Chen, H.-P. (2017). Involvement of DJ-1 in Ischemic Preconditioning-Induced Delayed Cardioprotection *In Vivo*. *Mol. Med. Rep.* 15, 995–1001. doi:10.3892/mmr.2016.6091

Waterman, S. R., Hacham, M., Hu, G., Zhu, X., Park, Y.-D., Shin, S., et al. (2007). Role of a CUF1/CTR4 Copper Regulatory axis in the Virulence of *Cryptococcus Neoformans*. *J. Clin. Invest.* 117, 794–802. doi:10.1172/jci30006

Wei, Y., Ringe, D., Wilson, M. A., and Ondrechen, M. J. (2007). Identification of Functional Subclasses in the DJ-1 Superfamily Proteins. *PLOS Comput. Biol.* 3, e15. doi:10.1371/journal.pcbi.0030010

Weinberg, E. D. (1975). Nutritional Immunity. Host's Attempt to Withold Iron from Microbial Invaders. *JAMA J. Am. Med. Assoc.* 231, 39–41. doi:10.1001/jama.231.1.39

Winge, D. R., Jensen, L. T., and Srinivasan, C. (1998). Metal-Ion Regulation of Gene Expression in Yeast. *Curr. Opin. Chem. Biol.* 2, 216–221. doi:10.1016/s1367-5931(98)80063-x

Yagi, T. (1991). Bacterial NADH-Quinone Oxidoreductases. *J. Bioenerg. Biomembr.* 23, 211–225. doi:10.1007/bf00762218

Yu, D., Pan, H., Zhang, R., Li, Y., and Nie, X. (2017). Nucleus DJ-1/Park7 Acts as a Favorable Prognostic Factor and Involves Mucin Secretion in Invasive Breast Carcinoma in Chinese Population. *Int. J. Clin. Exp. Med.* 10 (4), 6558–6567.

Zhang, L., Wang, J., Wang, J., Yang, B., He, Q., and Weng, Q. (2020). Role of DJ-1 in Immune and Inflammatory Diseases. *Front. Immunol.* 11, 994. doi:10.3389/fimmu.2020.00994

Zhou, B., and Gitschier, J. (1997). hCTR1: A Human Gene for Copper Uptake Identified by Complementation in Yeast. *Proc. Natl. Acad. Sci. U. S. A.* 94, 7481–7486. doi:10.1073/pnas.94.14.7481

Zimmermann, L., Stephens, A., Nam, S.-Z., Rau, D., Kübler, J., Lozajic, M., et al. (2018). A Completely Reimplemented MPI Bioinformatics Toolkit with a New HHpred Server at its Core. *J. Mol. Biol.* 430, 2237–2243. doi:10.1016/j.jmb.2017.12.007

Conflict of Interest: The authors declare that the research was conducted in the absence of any commercial or financial relationships that could be construed as a potential conflict of interest.

Publisher's Note: All claims expressed in this article are solely those of the authors and do not necessarily represent those of their affiliated organizations, or those of the publisher, the editors and the reviewers. Any product that may be evaluated in this article, or claim that may be made by its manufacturer, is not guaranteed or endorsed by the publisher.

frontiers | Frontiers in Molecular Biosciences

ORIGINAL RESEARCH
published: 11 April 2022
doi: 10.3389/fmolb.2022.863296

Fatty Acid Uptake in Liver Hepatocytes Induces Relocalization and Sequestration of Intracellular Copper

*Nathaniel H. O. Harder, Hannah P. Lee, Valerie J. Flood, Jessica A. San Juan, Skyler K. Gillette and Marie C. Heffern **

Department of Chemistry, University of California, Davis, Davis, CA, United States

Copper is an essential metal micronutrient with biological roles ranging from energy metabolism to cell signaling. Recent studies have shown that copper regulation is altered by fat accumulation in both rodent and cell models with phenotypes consistent with copper deficiency, including the elevated expression of the copper transporter, ATP7B. This study examines the changes in the copper trafficking mechanisms of liver cells exposed to excess fatty acids. Fatty acid uptake was induced in liver hepatocarcinoma cells, HepG2, by treatment with the saturated fatty acid, palmitic acid. Changes in chaperones, transporters, and chelators demonstrate an initial state of copper overload in the cell that over time shifts to a state of copper deficiency. This deficiency is due to sequestration of copper both into the membrane-bound copper protein, hephaestin, and lysosomal units. These changes are independent of changes in copper concentration, supporting perturbations in copper localization at the subcellular level. We hypothesize that fat accumulation triggers an initial copper miscompartmentalization within the cell, due to disruptions in mitochondrial copper balance, which induces a homeostatic response to cytosolic copper overload. This leads the cell to activate copper export and sequestering mechanisms that in turn induces a condition of cytosolic copper deficiency. Taken together, this work provides molecular insights into the previously observed phenotypes in clinical and rodent models linking copper-deficient states to obesity-associated disorders.

Keywords: copper, fatty acid metabolism and signaling, metal homeostasis, metabolic disease, homeostasis

OPEN ACCESS

Edited by:
Peter-Leon Hagedoorn, Delft University of Technology, Netherlands

Reviewed by:
Teresita Padilla-Benavides, Wesleyan University, United States
Francesca Di Sole, Des Moines University, United States

***Correspondence:**
Marie C. Heffern
mcheffern@ucdavis.edu

Specialty section:
This article was submitted to Cellular Biochemistry, a section of the journal Frontiers in Molecular Biosciences

Received: *27 January 2022*
Accepted: *14 March 2022*
Published: *11 April 2022*

Citation:
Harder NHO, Lee HP, Flood VJ, San Juan JA, Gillette SK and Heffern MC (2022) Fatty Acid Uptake in Liver Hepatocytes Induces Relocalization and Sequestration of Intracellular Copper. Front. Mol. Biosci. 9:863296. doi: 10.3389/fmolb.2022.863296

INTRODUCTION

Excess consumption of high-calorie diets rich in fats and sugars are linked to adverse physiological effects, such as increased oxidative stress and inflammation (Joshi-Barve et al., 2007; Klevay, 2011; Statovci et al., 2017; Hieronimus et al., 2019; Perdomo et al., 2019). The increased prevalence of such diets is strongly associated with the rise of metabolic diseases including diabetes and non-alcoholic fatty liver disease (NAFLD) (Cusi, 2009; Lomonaco et al., 2011; Softic et al., 2016; Antonucci et al., 2017). The recent literature suggests that excess macronutrient load may result in disruptions in copper trafficking (Park et al., 2015; Heffern et al., 2016; Song et al., 2018; Harder et al., 2020). The essential metal micronutrient copper serves vital roles in signaling and in enzymatic cofactors for key biological processes ranging from mitochondrial respiration to radical scavenging (Lutsenko, 2010; Nevitt et al., 2012; Ackerman and Chang, 2018). However, due to its redox activity, misregulated copper can also be deleterious *via* increased radical formation and

DNA damage. Thus, copper must be tightly regulated *via* an intricate network of transporters and chaperones to maintain proper levels and control its localization (Lutsenko, 2010; Bost et al., 2016; Lutsenko, 2016). Copper is introduced into cells *via* membrane importers and then trafficked with dedicated chaperones to their directed targets, including metallothioneins, mitochondrial enzymes, and exporter proteins such as ATP7A and ATP7B (Lutsenko et al., 2007; Lutsenko, 2016; Członkowska et al., 2018). The importance of proper copper homeostasis is evidenced in diseases such as Menkes disease and Wilson's disease, deadly disorders resulting from mutations in the copper transporters ATP7A and ATP7B, respectively (Cope-Yokoyama et al., 2010; Członkowska et al., 2018; Horn and Wittung-Stafshede, 2021). These diseases show remarkably similar phenotypes to diseases induced by high-fat and high-sugar diets, insinuating a link between copper- and macronutrient-derived metabolic misregulation.

In addition to its central role in energy metabolism, the liver is the primary organ for maintaining copper balance in the body. The majority of dietary copper is trafficked to the liver for storage, distribution, and utilization (Lutsenko, 2010). It is in this organ that the copper-binding serum protein, ceruloplasmin, is synthesized and metalated (Jiang et al., 2016; Linder, 2016; Linder, 2020). In addition, the liver plays a key role in copper excretion *via* biliary export (Lutsenko, 2016; Linder, 2020). Recent research suggests that dietary fats may affect hepatic copper metabolism. In one study, mice fed high-fat diets showed significant decreases in hepatic copper. In another study, researchers found that human hepatocyte (HepG2) cells exposed to a mixture of palmitic and oleic acids displayed decreases in intracellular copper levels akin to the trends seen in the rodent studies (Arciello et al., 2015; Heffern et al., 2016). The prevailing hypothesis is that changes in copper metabolism are attributed to increased levels of the copper transporter, ATP7B, inducing copper efflux from the cell (Arciello et al., 2015; Heffern et al., 2016). Yet, what instigates alterations to ATP7B, the consequence to intracellular copper pathways, and the interplay with fat consumption and energy metabolism is not well understood.

In this work, we scrutinized how fat accumulation impacts molecular pathways of copper metabolism and sequestration. Our goal was to determine associations between ATP7B expression and cellular copper status in response to fatty acid exposure. We assessed time-dependent changes in gene expression, levels, and localization of major copper proteins in HepG2 cells treated with palmitic acid (PA), a 16:0 saturated fatty acid. At early time points of PA exposure, we identified elevations in upstream regulators of the ATP7B export machinery alongside protein changes typically associated with a cellular state of copper overload. This is accompanied by perturbations in mitochondrial health and mitochondrial copper proteins. Prolonged exposure shifts the cellular state to one resembling copper deficiency at later time points, alongside increased expressions of proteins indicative of lysosomal sequestration and membrane localization of copper. From this data, we propose a scheme wherein fat accumulation induces miscompartmentalization of copper to induce a state resembling cytosolic copper overload, activating sequestration and export of copper from the cytosol, leading to a cytosolic state of copper deficiency.

MATERIALS AND METHODS

Cell Culture and Maintenance

Human hepatocyte carcinoma cells (HepG2) were grown in complete DMEM media (31053036, Thermo Fisher Scientific) with 10% Avantor Seradigm premium grade fetal bovine serum (97068-085, VWR), 1 mM sodium pyruvate (11360070, Thermo Fisher Scientific), 100 IU penicillin and 100 μg/ml streptomycin (MT30002CI, Thermo Fisher Scientific), and 2 mM L-glutamine (25-030-081, Gibco). The cells were subcultured every 2–3 days at 70% confluence. The HepG2 cells were gifted to us from Dr. Patricia Oteiza's laboratory. All experiments were performed on cells between passages 10 and 20. Sterile culturing and assay plates were used for the following experiments. Cells were regularly tested for mycoplasma every 6 months using the MycoAlert assay (LT07-701, Lonza).

General Procedure for Cell Stimulations

HepG2 cells were stimulated with 250 μM PA solution in MEM media (Cremonini and Oteiza, 2018). The stock PA stimulation solution (stock concentration of 8 mM) was prepared by adding sodium palmitate (P9767, MilliporeSigma) to a 10.5% w/w solution of fatty acid-free bovine serum albumin (BP9704100, Thermo Fisher Scientific) in DMEM (31053036, Thermo Fisher Scientific) with 25 mM HEPES (15630-080, Gibco). The solution was stirred for at least 4 h at 50°C until sodium palmitate was completely dissolved. The solution was filtered using a 0.22-μm cellulose acetate filter (976134, Thermo Fisher Scientific) and diluted to a final concentration of 250 μM in MEM (51200038, Thermo Fisher Scientific) solution with 10% Avantor Seradigm premium grade fetal bovine serum (97068-085, VWR), 1 mM sodium pyruvate (11360070, Thermo Fisher Scientific), 100 IU penicillin and 100 μg/ml streptomycin (MT30002CI, Thermo Fisher Scientific), and 2 mM L-glutamine (25-030-081, Gibco). Solutions of $CuCl_2$ were prepared in nanopure water (Millipore) at 200 mM and diluted to 200 μM in the BSA control media. Solutions of bathocuproinedisulfonic acid disodium salt (B1125, MilliporeSigma) were prepared at 20 mM in nanopure water and diluted to 200 μM in BSA control media (10.5% w/w solution of fatty acid-free bovine serum albumin in DMEM and 25 mM HEPES). For each stimulation, HepG2 cells were seeded (see description of experiments below for cell counts) and left to adhere overnight in complete DMEM media. Media were aspirated and cells were then washed once with PBS warmed to 37°C. PBS was aspirated and stimulation media were added to cells, as described for each experiment following.

Cell Viability and Lipid Staining Assays

Cell viability was assessed using an MTS assay (G3582, Promega) at 24 h. HepG2 cells were seeded in a clear-bottom 96-well plate at 10,000 cells per well and stimulated, as described before. The MTS reagent was added and incubated at 37°C for 1 h before detection of absorbance at 490 nm on a plate reader (SpectraMax i3x, Molecular Devices). Oil O Red was used to assess intracellular

fat accumulation within cells plated at 300,000 cells per well in 6-well plates. Cells were stimulated as previously described, washed with PBS, and fixed with 4% paraformaldehyde for 30 min. The Oil O Red stock solution was prepared as 0.5% Oil O Red (NC0961554, Thermo Fisher Scientific) in isopropanol and diluted to 60% in nanopure water fresh for each use. The working Oil O Red solution was filtered before staining for 10 min at room temperature. After staining, cells were washed three times with PBS and then imaged (EVOS Core XL, Thermo Fisher Scientific). To elute dye for quantification, 250 µl of 100% isopropanol was added to stained cells. Cells were then rocked at room temperature for 10 min in isopropanol before transferring 75 µl of the isopropanol solution from each well to a 96-well plate. The absorbance of eluted dye was measured at 540 nm on a plate reader (SpectraMax i3x, Molecular Devices). Statistics were carried out on Prism 9.1 (Graphpad).

Western Blot Analysis

HepG2 cells were plated at 300,000 cells per well in a 6-well plate. Cells were stimulated as described before and then lysed at 1, 6, 12, and 24 h in a RIPA buffer (150 mM NaCl, 1% NP-40, 0.5% sodium deoxycholate, 0.1% SDS, and 50 mM Tris–Cl pH 7.4) with an EDTA-free protease inhibitor (PIA32955, Thermo Fisher Scientific) and a phosphatase inhibitor (4906845001, MilliporeSigma). Lysates were vortexed on ice for 20 min before being cleared by centrifugation at 15,000 × g at 4°C. Lysates were frozen at −20°C prior to protein quantification using the BCA assay (71285-3, Invitrogen), and 20 µg protein was prepared with 2-mercaptoethanol (1610710, Bio-Rad), PBS (Gibco), and LDS sample buffer (NP0007, Invitrogen), according to the manufacturer's protocols, without heating and was loaded into a 4%–12% bis–tris 15-well gel (NW04125BOX, Invitrogen) for probing all proteins, except CCS, Mt2A, and SCO2. To probe CCS, Mt2A, and SCO2, protein solutions were run on a 16% tricine gel (EC66952BOX, Invitrogen). In all cases, gels were run in a MES buffer at 100 V for 1 h and transferred on a low fluorescence PVDF membrane (1704274, Bio-Rad) using a Trans-Blot Turbo Transfer System (Bio-Rad). Membranes were blocked with 5% BSA in TBST (9997S, Cell Signaling Technology) for 1 h at room temperature and incubated with primary antibodies overnight at 4°C. Membranes were washed 3 × 5 min with TBST at room temperature and blotted with secondary antibody in 5% dry milk (31FZ82, Grainger) in TBST. Membranes were washed 3 × 5 min with TBST and submerged in Crescendo HRP substrate solution (Millipore) for 5 min prior to imaging on a ChemiDoc MP Imager (Bio-Rad). Primary antibodies used include anti-ATP7B (ab124973, 1: 2,000 Abcam), anti-CCS (sc-55561, 1:1,000, Santa Cruz Biotechnology), anti-SCO2 (ab113758, 1:1,000, Abcam), anti-β-actin (mouse IgG, sc-47778, 1:5,000 SCBT or rabbit IgG, 4970S, 1:5,000, Cell Signaling Technology), anti-SLC46A3 (NBP1-85054, 1:1,000, Novus Biologicals), anti-Mt2A (PA5-102549, 1:1,000, Invitrogen), and anti-hephaestin (sc-393701,1: 1,000, Santa Cruz Biotechnology). For secondary antibodies, anti-rabbit IgG HRP-conjugated antibody (7074S, 1:2,000, Cell Signaling Technology) was used for SCO2 and ATP7B, anti-mouse IgG HRP-conjugated antibody (7076S, 1:1,000, Cell Signaling Technology) for CCS, and anti-rabbit IgG AlexaFluor 555 (A21428, 1:5,000, Invitrogen) and anti-mouse IgG AlexaFluor 800 (A32789, 1:5,000, Invitrogen) for β-actin. Images were processed using Image Lab software (Bio-Rad). Densitometry analysis was carried out using Image Lab software (Bio-Rad); all analyses were normalized to the baseline condition, BSA at 1 h.

Gene Expression Analysis

HepG2 cells were plated at 300,000 cells per well in a 6-well plate. Cells were then stimulated as described before, and mRNA was isolated at 1, 6, 12, and 24 h using the RNeasy Plus RNA isolation kit (74136, Qiagen). mRNA was quantified using a QuickDrop spectrophotometer (Molecular Devices), and 1,000 ng was added to iScript Reverse Transcription Supermix (1708841, Bio-Rad). A C1000 thermocycler (Bio-Rad) was used for reverse transcription. A total of 0.2 ng cDNA was loaded into a master mix of amplification primer and iQ SYBR green (1708882, Bio-Rad) before amplification, and gene expression was observation using a CFX Connect Real-Time PCR System (Bio-Rad). Data were processed on Microsoft Excel by the $2^{-\Delta\Delta Ct}$ method using β-actin as the housekeeping gene. TBP (TATA binding protein) was used as a secondary housekeeping gene to ensure β-actin was stably expressed over the PA stimulation. Primers for real-time PCR analysis are listed in **Supplementary Table S1**. Statistics were carried out on Prism 9.1 (Graphpad), while a colocalization analysis was carried out on ImageJ (FIJI) using Coloc 2 (Benedict and Zhang, 2017).

Ceruloplasmin Activity and Quantification

Media were collected from qPCR and western blot stimulations for analysis of ceruloplasmin activity and concentration. Collected media were spun at 500 × g for 10 min at room temperature prior to being aliquoted and frozen at −20°C. Undiluted media were assessed for ceruloplasmin concentration by ELISA (EC4201-1, Assaypro), while media for ceruloplasmin ferroxidase activity was diluted to 1:3 in the assay buffer for colorimetric quantification of activity (EIACPLC, Invitrogen). All experiments were run in four independent biological replicates. Statistics were carried out on Prism 9.1 (Graphpad).

Immunofluorescence Imaging

HepG2 cells were plated at 150,000 cells per well on acid-washed and sterilized glass coverslips in a 12-well plate. Cells were stimulated as described before and then washed at 1, 6, 12, and 24 h in cold PBS (Gibco) and fixed for 10 min in 4% paraformaldehyde (AAJ19943K2, Thermo Fisher Scientific). Cells were blocked in 10% BSA and permeabilized with Triton X-100. 1:600 anti-ATP7B (ab124973, Abcam) and 1:600 anti-TGN46 (GTX74290, GeneTex) antibodies were used to stain the copper transporter and trans-Golgi network marker, respectively, and anti-rabbit IgG AlexaFluor 488 (R37116, Invitrogen) and anti-sheep IgG AlexaFluor 647 (A21448, Invitrogen) were used as secondary antibodies to fluorescently label the proteins. A DAPI dye (R37606, Invitrogen) was used to stain the nucleus, and coverslips were sealed to glass slides along with Prolong Gold Antifade Mountant (P36930, Invitrogen). Fixed and mounted cells were imaged using a laser scanning confocal microscope (Olympus FluoView FV1000) using a ×60 oil immersion lens at the UC Davis Molecular and Cellular Biology Light Microscopy Imaging Facility.

Glutathione Oxidation

Oxidized and total glutathione levels were assessed by using the GSH-Glo glutathione assay (V6611, Promega). HepG2 cells were plated at 10,000 cells per well in white 96-well plates. Cells were stimulated for 1, 6, 12, and 24 h before addition of glutathione detection reagents. Oxidized and total glutathione levels were assessed by the bioluminescent signal on the i3x plate reader (Molecular Devices) with an integration of 1,000 ms. Data is expressed as the ratio of oxidized glutathione over total glutathione. Statistics were carried out on Prism 9.1 (Graphpad).

Mitochondrial Membrane Potential

Mitochondrial membrane potential was assessed by using the JC-1 probe assay (ab113850, Abcam). HepG2 cells were plated at 10,000 cells per well in black, clear-bottom 96-well plates. Cells were stimulated for 1, 6, 12, and 24 h before addition of 1 mM JC-1 solution in the corresponding stimulation media. Cells were incubated for 10 min in the dark at 37°C and washed twice with PBS. Stained cells were imaged on the i3x Plate reader (Molecular Devices) with 535 nm excitation and 590 nm emission for aggregates and 475 nm excitation and 530 nm emission for monomers. Statistics were carried out on Prism 9.1 (Graphpad).

Metal Analysis

Metal analysis was performed at the Northwestern University Quantitative Bio-element Imaging Center generously supported by NASA Ames Research Center NNA06CB93G. Total cell pellet and extracellular copper were assessed by inductively-coupled plasma mass spectrometry (Thermo Fisher Scientific iCap Qc ICP-MS). Cells were seeded at 300,000 cells per well and stimulated for 1, 6, 12, and 24 h. Media were collected and spun at 500 × g for 10 min. A total of 250 µL media were added to pre-weighed metal-free 15-ml conical tubes (89049-170, VWR), and 250 µl analytical grade 70% nitric acid (A509P500, Thermo Fisher Scientific) was added to the mixture and left at room temperature for 24 h. Cells were washed two times with cold PBS and digested in 250 µl analytical grade 70% nitric acid. After 24 h of acid digestion, 225 µl of cell lysate was transferred to pre-weighed metal-free 15-ml conical tubes. All samples were diluted to 5 ml with 3% analytical grade nitric acid. Copper and phosphorus were assessed by ICP-MS. Intracellular copper concentration is expressed as the ratio of concentrations of copper over phosphorus, while copper concentration in media samples is expressed as the concentration of copper over the mass of the sample.

RESULTS

Palmitic Acid Alters Copper Transporter Levels With Time Dependence Prompting Copper Export Mechanisms

Previous work showed that high-fat diets perturb hepatic copper metabolism in mice, manifested by an increase in hepatic copper transporter ATP7B (Heffern et al., 2016). Considering the main copper efflux transporter in liver hepatocytes, elevation in ATP7B expression is typically associated with an increased copper export (Lutsenko, 2016; Lutsenko et al., 2007). We first sought to establish whether a hepatocellular model could recapitulate these fat-induced effects on ATP7B expression. HepG2, a human hepatocellular carcinoma cell line, has been extensively used to study metabolic processes at the molecular level; in particular, these cells accumulate fat when treated with fatty acids *via* similar mechanisms as the livers of rodents and human patients given high-fat diets (Joshi-Barve et al., 2007; Arciello et al., 2015; Park et al., 2015; Di Bella et al., 2017). With this precedence, we elected to utilize the well-documented model of treating these cells with sodium palmitate, a sodium salt of PA, for 24 h using bovine serum albumin (BSA) as a carrier and solubilizer (Park et al., 2015; Alsabeeh et al., 2018). Sodium palmitate has been used extensively to model fatty acid exposed livers due to its ability to recapitulate lipid accumulation and steatosis in cells, and as such, it provides a basis to study lipid-induced copper misregulation (Gómez-Lechón et al., 2007; Eynaudi et al., 2021). A 24-h treatment of HepG2 with 250 µM PA indeed resulted in an elevation of ATP7B expression as measured by western blotting (**Figure 1A**; **Supplementary Figure S1A**). This change in ATP7B was accompanied by an increase in lipid droplets as measured by Oil O Red staining (**Supplementary Figure S2A,B**), suggesting that this cell-based model could emulate a similar fat-induced change in copper biology that was previously observed in the mouse models (Heffern et al., 2016). No changes in cell viability were observed under these treatment conditions (**Supplementary Figure S3**). Comparison of metal content of BSA and PA stimulation media showed no difference in copper levels between the two, ensuring that changes in copper metabolism are due to the fatty acid content of the PA treatment (**Supplementary Figure S4**).

With a viable model in hand, we applied this system to assess the time-dependent effects of fat accumulation on copper metabolism. We tracked the time-dependent changes in both ATP7B protein and mRNA levels in cell lysates and cellular lipid content at 1, 6, 12, and 24 h of stimulation with 250 µM PA. Both ATP7B protein levels and gene expression (**Figure 1A**; **Supplementary Figure S1A**), as revealed by western blotting and qPCR analysis, respectively, were elevated with PA treatment relative to the BSA vehicle at all the time points, with the most pronounced changes observed at 12 and 24 h ($p = 0.0015$ and $p = 0.000011$, respectively, for the relative gene expression analysis). The 12-h point at which notable elevation in ATP7B is observed corresponds to the time frame in which elevated fat accumulation is initially observed by Oil O Red staining (**Supplementary Figure S2A,B**), suggesting a possible correlation between intracellular fat stores and copper regulation.

To determine how the ATP7B changes may correlate with cellular copper status, we evaluated the protein and gene expression levels of the copper chaperone of superoxide dismutase 1 (CCS). Copper-deficient states induce the upregulation of CCS, allowing the protein to serve as a marker for the cytosolic copper status (Culotta et al., 1997; Bertinato et al.,

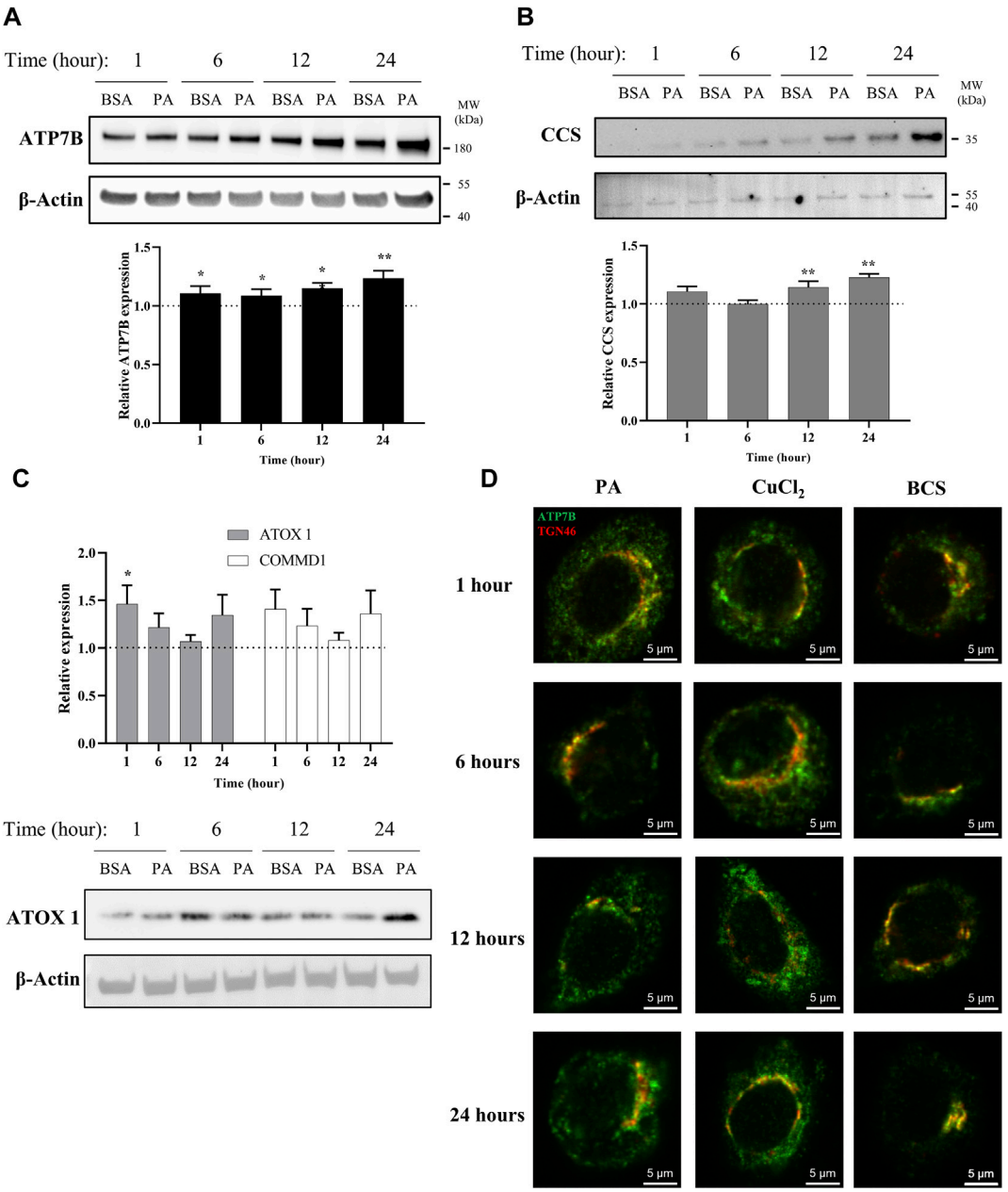

FIGURE 1 | PA induces changes in proteins associated with copper export and induces a subcellular localization of ATP7B that resembles cytosolic copper overload in liver cells. Representative western blot images, densitometry, and gene expression analysis of **(A)** ATP7B (n = 10), **(B)** CCS (n = 9), **(C)** ATOX1 (n = 10), and COMMD1 (n = 10) from lysates collected at different stimulation times with PA. Densitometry is shown in **Supplementary Figures 1A–C**. Gene expression analysis is provided as the levels from PA stimulation relative to BSA stimulation with normalization to β-actin as the housekeeping gene. Mean ± SEM is shown. The Mann–Whitney U test was used to assess significance (*$p < 0.05$, **$p < 0.01$). **(D)** HepG2 cells were stimulated with PA and 200 μM $CuCl_2$ to induce a state of copper overload or 200 μM BCS to induce a state of copper deficiency for 1, 6, 12, and 24 h. Cells were fixed and immunostained, and immunofluorescence imaging was used to capture the subcellular localization of ATP7B (green) and TGN46 (red). Cells were imaged by laser scanning confocal microscopy using a ×60 oil immersion lens. Colocalization is observed by the overlap of signals of ATP7B and TGN46 (yellow).

2003; LassiProhaska and Prohaska, 2012; Brady et al., 2014). A previous work has shown that CCS expression increased in the livers of mice fed with high-fat diets (Heffern et al., 2016). When we stimulated the HepG2 cells with PA, we observed an increase in CCS protein and gene expression levels relative to the vehicle in a similar time-dependent manner to ATP7B, with the most notable increases at 12 and 24 h (p = 0.0040 for 12 h and p = 0.000041 for 24 h for the relative gene expression analysis) (**Figure 1B**; **Supplementary Figure S1B**). This elevation in CCS expression suggests that the PA-induced elevation in

ATP7B is accompanied by the onset of a cytosolic copper-deficient state.

To further understand copper trafficking pathways associated with PA addition, we evaluated the changes in two copper chaperones associated with ATP7B, ATOX1, and COMMD1. ATOX1 acts upstream to ATP7B in the copper export machinery and is responsible for loading copper into ATP7B (Shanmugavel and Wittung-Stafshede, 2019; Zaccak et al., 2020). COMMD1, somewhat elusive in terms of its exact function, is linked to ATP7B both as a possible upstream regulator of ATP7B stability and in supporting the bile-dependent export of copper downstream of interactions with ATP7B and independent of ATOX1 (Gitlins, 1988; Fleming et al., 1991; de Bie et al., 2007; Stewart et al., 2019). Upon PA treatment, both ATOX1 and COMMD1 showed changes in gene expression with similar time-dependent trends to one another but at earlier time points than ATP7B, with initial increases at 1 and 6 h relative to the vehicle, followed by a drop in the expression (albeit still modestly elevated above the vehicle) at 12 h which increases at 24 h (**Figure 1C**; **Supplementary Figure S1C**). The western blot analysis of ATOX1 revealed similar trends between expression and protein levels, with clear increases in PA-stimulated cells at 1 and 24 h. We noted that for ATP7B, CCS, and ATOX1, BSA treatment alone increased their expression over time (**Figures 1A–C**; **Supplementary Figures S1A–C**). Such BSA-dependent changes have not been previously noted in the literature and warrant further exploration beyond this study. Nonetheless, the PA-associated changes occur over this baseline increase with the BSA vehicle. The concomitant changes in these proteins as well as the earlier time points at which they occur support the notion that PA perturbs the copper shuttling machinery upstream of ATP7B.

While classically associated with copper excretion, posttranslational regulation of ATP7B plays a role in altering the cellular localization of the metal as reflected in its subcellular localization, which is modulated by the cellular copper status (Lutsenko et al., 2007; Barnes et al., 2009; Polishchuk et al., 2014). Under copper-deficient conditions, hepatocytic ATP7B localizes to the trans-Golgi network (TGN) where it is presumed to load copper into membrane and serum-derived proteins (Shanmugavel and Wittung-Stafshede, 2019). In contrast, excess cytosolic copper prompts a delocalization of ATP7B from the TGN into dispersed cytosolic vesicles and moves to the cell periphery (Weiss et al., 2008; Barnes et al., 2009; Polishchuk et al., 2014). The delocalization of ATP7B away from the TGN has been associated with the transfer or removal of copper away from the cytosol (Barnes et al., 2009). We thus probed the localization of ATP7B in HepG2 cells treated with PA and compared it to induced copper-overload or copper-deficient conditions, which were achieved by respective treatments with 200 μM $CuCl_2$ or the copper chelator, bathocuproine-disulfonate (BCS). The cells were fixed at 1, 6, 12, and 24 h after treatment and stained for immunofluorescence imaging of ATP7B (green) and TGN46 (red) as a marker for the TGN (**Figure 1D**). As expected, BCS-treated cells exhibited ATP7B localization to the TGN, while ATP7B of $CuCl_2$-treated cells showed dispersed localization away from the TGN. When the same experiment was performed in cells treated with PA, we observed that ATP7B initially localizes to the TGN at the 6-h time point, consistent with the copper-deficient state. However, at 12 and 24 h, ATP7B localized to the cell periphery in a distribution akin to that seen in $CuCl_2$-treated cells, indicating that the observed increase in ATP7B expression may be pointing toward the removal of copper from the cytosol. The colocalization analysis highlighted the similarities between PA- and $CuCl_2$-stimulated cells (**Supplementary Figures S5A–D**) in decreasing TGN/ATP7B colocalization, particularly at the 12-h time point. The similarity between the two treatments suggests that PA induces a cellular response that is observed under copper-overload conditions, despite expressing markers associated with copper deficiency. This data points to a PA-induced shift in copper metabolism that is distinct from changes altering the overall copper levels of the cell as produced by $CuCl_2$ or BCS. Furthermore, the time-dependent changes in ATP7B localization within the cell over the course of the stimulations highlight the plasticity of copper trafficking in the cell in response to fatty acid overload.

Palmitic Acid Sequesters Copper Into the Membrane and Lysosomes

The changes in ATP7B localization point to the ability of PA to induce a removal or sequestration of copper from the cytosol. One of the primary known roles of ATP7B for loading of copper is multi-copper oxidase proteins ceruloplasmin (Cp) and hephaestin (Lutsenko, 2016; Guttmann et al., 2020; Linder, 2020). These homologous multi-copper oxidases are cuproenzymes that contain 6–8 copper atoms per protein. Cp is secreted from the cell and is the most abundant serum copper chaperone, carrying 50%–90% of copper in the blood (Hellman and Gitlin, 2002; Aigner et al., 2008; Linder, 2016). In contrast, hephaestin is anchored to the membrane and presents copper at the cell surface (Vashchenko and MacGillivray, 2013). Both ferroxidases influence iron availability through their copper-dependent ferroxidase activity (Tapryal et al., 2009; Freestone et al., 2016; Jiang et al., 2016). Having observed the PA-induced elevated ATP7B expression and its delocalization from the TGN at 12 and 24 h, we assessed whether these changes were associated with changes in either ferroxidase at these time points. Extracellular Cp concentration and its activity were examined from media taken from the cell supernatant, while cellular hephaestin was assessed by western blotting. No significant differences were observed in either extracellular Cp concentration or copper-dependent extracellular ferroxidase activity upon PA treatment (**Figures 2A,B**). This is reflected in a similar lack of change in total extracellular copper levels in the media and in total cellular copper levels of whole cell pellets, as measured by ICP-MS (**Supplementary Figure S6**). In contrast, we observed an increase in the protein levels of hephaestin at 24 h of stimulation with PA (**Figure 2C**). The concomitant changes in hephaestin, ATP7B, and ATP7B-associated chaperones suggest that PA may induce translocation of copper from the cytosol to the membrane *via* loading into hephaestin, consequently reducing the cytosolic copper content.

Alongside the increases in hephaestin, we investigated other mechanisms involved in the sequestering and redistribution of copper in the cell. Recent research has highlighted SLC46A3 as a

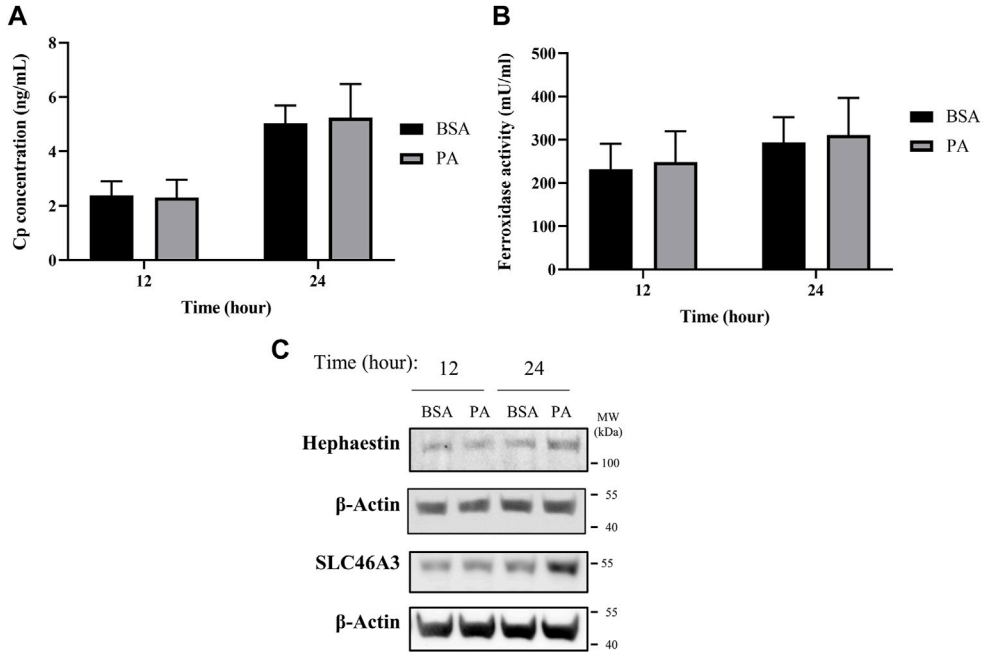

FIGURE 2 | PA does not alter secreted ceruloplasmin (Cp) but induces copper membrane localization and sequestration. **(A)** Cp concentration was measured by ELISA ($n = 4$). **(B)** Copper-dependent ferroxidase activity of Cp in media collected from HepG2 cells treated with PA or BSA for 12 and 24 h ($n = 4$). Mean ± SEM is shown. The Mann–Whitney *U* test was used to assess significance (**$p < 0.01$). **(C)** Representative western blot images of hephaestin and SLC46A3.

protein that is responsible for copper loading into lysosomal units in the liver; as such, we aimed to investigate how SLC46A3 is altered with PA stimulation (Kim et al., 2021). As with hephaestin, PA induces an increase in SLC46A3 protein levels at 24 h of PA stimulation relative to the BSA control (**Figure 2C**). Thus, in addition to the translocation of copper to the membrane, our data also hints at a PA-induced increase in lysosomal copper sequestration. Taken together, the increase of both hephaestin and SLC46A3 expression at 24 h points to a cellular response to PA involving the mobilization of copper away from the cytosol toward the membrane and lysosomal units.

Palmitic Acid Stimulation Perturbs Intracellular Copper Balance and Redox Status

When cytosolic copper levels are perturbed, to counteract oxidative stress and cell damage, the cell utilizes chelators and chaperones to traffic and maintain homeostasis of copper both in terms of overall levels and subcellular distribution (Bertinato et al., 2003; Lutsenko, 2010; Maryon et al., 2013). To this end, we first investigated the effects of PA on metallothionein 2A (Mt2A), a protein implicated in both copper chelation and storage, to establish the cell's copper buffering dynamics with fatty acid accumulation (Bertinato et al., 2003; Kumar et al., 2013; Heffern et al., 2016; Ostrakhovitch et al., 2016). Mt2A levels are initially elevated upon stimulation of PA (**Figures 3A,B**), possibly pointing to an initial state of copper overload. This increase subsides with 6 h of PA stimulation and continues to decrease at 12 h, consistent with depression in cytosolic copper levels. By 24 h, we observed a return to Mt2A levels that is similar to those of the control, implying a level of homeostasis. mRNA expression of Mt2A matches the trends observed by western blot wherein there is an initial increase upon stimulation with PA at 1- ($p = 0.0015$) and 6-h treatments, but it decreases upon extended PA exposure with 12- and 24-($p = 0.023$) h treatments (**Figure 3B**). As a comparison, we assessed Mt2A gene expression with cells treated with 200 μM $CuCl_2$ or 200 μM of the copper chelator BCS. As expected, the addition of $CuCl_2$ increases Mt2A expression, whereas BCS decreases Mt2A expression (**Supplementary Figure S7**). The dynamics of Mt2A suggest that PA treatment initially places the cell's cytosol in a state of copper overload, prompting the cell to remove copper from the cytosol. This reduction in cytosolic copper then prompts a release of copper from Mt2A to restore copper balance.

Intracellular copper levels are integral to maintaining redox balance in the cytosol. Given the perturbation in cytosolic copper homeostasis by PA, we assessed the consequences of the treatment to the cellular oxidative status. We evaluated the expression of Cu,Zn superoxide dismutase (SOD1), a copper-dependent enzyme responsible for scavenging radical and reactive oxygen species (Culotta et al., 1997). SOD1 gene expression increases at 1 ($p = 0.023$), 6, and 24 h of PA stimulation, corroborating previous research relating copper and oxidative stress in liver fat accumulation (**Figure 3B**) (Park et al., 2015; Freedman et al., 1989). We also tracked changes in intracellular glutathione oxidative activity. Glutathione is an intracellular peptide that plays a significant

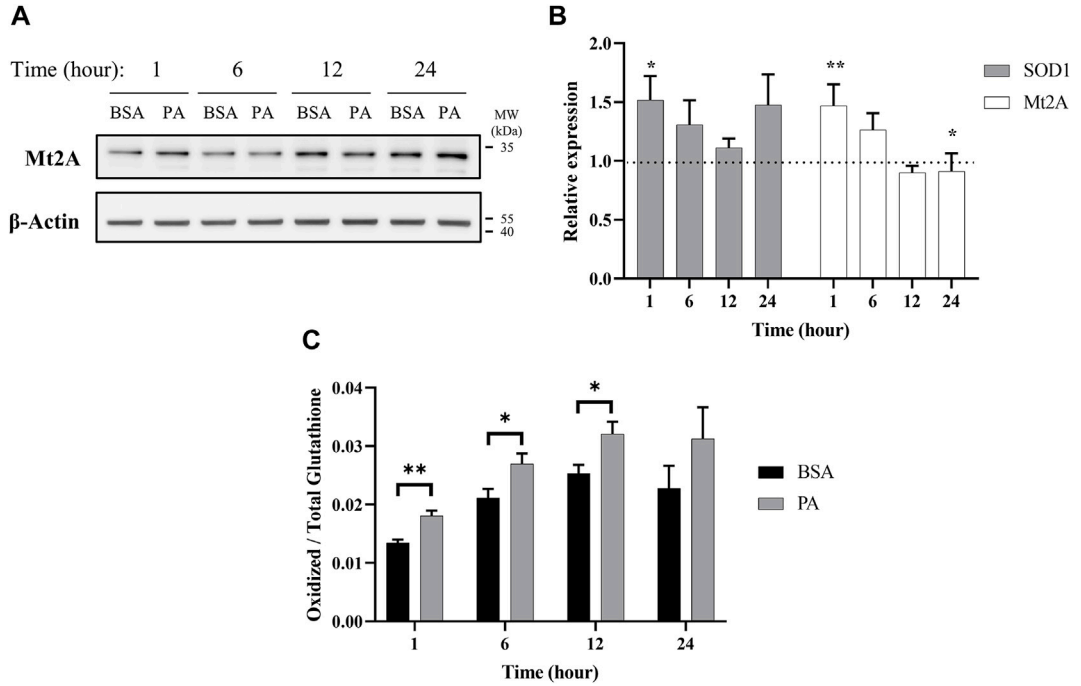

FIGURE 3 | Palmitate stimulations induce changes in cytosolic markers of copper status. Analysis of copper chaperones in the lysates of cells treated with PA or BSA for 1, 6, 12, and 24 h. **(A)** Representative western blot images of Mt2A. **(B)** Gene expression analysis of SOD1 (n = 10) and Mt2A (n = 10) of PA-stimulated cells relative to BSA-stimulated cells at the same time points (normalized to β-actin as the housekeeping gene). The Mann–Whitney U test was used to assess the statistical significance. (*p < 0.05 and **p < 0.01). Mean ± SEM is shown. **(C)** Ratio of oxidized-to-total glutathione in PA-stimulated cells. The unpaired Student's t-test was used to assess significance.

role as an intracellular buffer and maintaining the overall reducing environment of the cytosol due to its free thiols and susceptibility to oxidation by radicals (Gallagher et al., 1973; Freedman et al., 1989; Maryon et al., 2013; Ngamchuea et al., 2016). Alongside its redox control, glutathione is responsible for chelating labile metal pools in the cell to reduce Fenton-like chemistry (Thomas et al., 2009). Upon PA addition, we observed an increase in oxidized glutathione at all the time points, with significant increases at 1 (p = 0.0072), 6 (p = 0.049), and 12 (p = 0.043) h (**Figure 3C**). This may be indicative of either an increase in the overall redox state of the cell, which has been previously observed in fatty acid overload in HepG2 cells, or an increase in the labile copper within the cytoplasm of the cell, or both (Park et al., 2015).

Palmitic Acid Induces Mitochondrial Dysfunction Linked to Cytosolic Copper Overload

Our data points to an initial state of cytosolic copper overload with PA stimulation that the cell compensates for by removing copper from the cytosol. However, as the PA stimulation solution does not contain exogenous copper, the elevation in cytosolic copper may stem from release of copper from intracellular compartments. Excess fat accumulation is strongly associated with disruptions in proper function of the mitochondria, an organelle that plays a critical role in energy processing from fatty acid oxidation to ATP production (Cobine et al., 2006; Softic et al., 2016; Antonucci et al., 2017; Hill et al., 2017). PA-induced mitochondrial fission, that is, the splitting of the organelle, has been proposed as a main contributor to mitochondrial fragmentation and dysfunction (Sergi et al., 2021). As mitochondria contain high levels of copper as the metal plays critical functions in the electron transport chain, we investigated whether mitochondrial fission occurs at early time points of PA stimulation to potentially release copper in the cytosol (Gallagher et al., 1973; Cobine et al., 2006; Leary et al., 2007). We monitored time-dependent changes in the protein FIS1, a marker for mitochondrial fission, in response to PA stimulation (Koch et al., 2005; Swapna Sasi et al., 2020). FIS1 levels are increased at 1 and 24 h with stimulation of PA (**Figure 4A**). The early change in FIS1 levels may thus support a mechanism wherein the excess cytosolic copper originates from release of the metal from mitochondrial fission. In support of the changes in mitochondrial fission, we observe changes in mitochondrial membrane potential. This potential was measured by the JC-1 dye, which aggregates in healthy mitochondria and is monomeric in depolarized membranes, is perturbed by the accumulation of fatty acids in the cell as previously reported (Eynaudi et al., 2021). The changes show a slight increase at 1 h that subsides at 6 h but becomes significantly increased at 12 (p = 0.0109) and 24 h (p = 0.00597), all of which coincides with changes in copper metabolism (**Figure 4B**). Moreover, PA induces changes in COX17, a copper chaperone that facilitates copper transport to

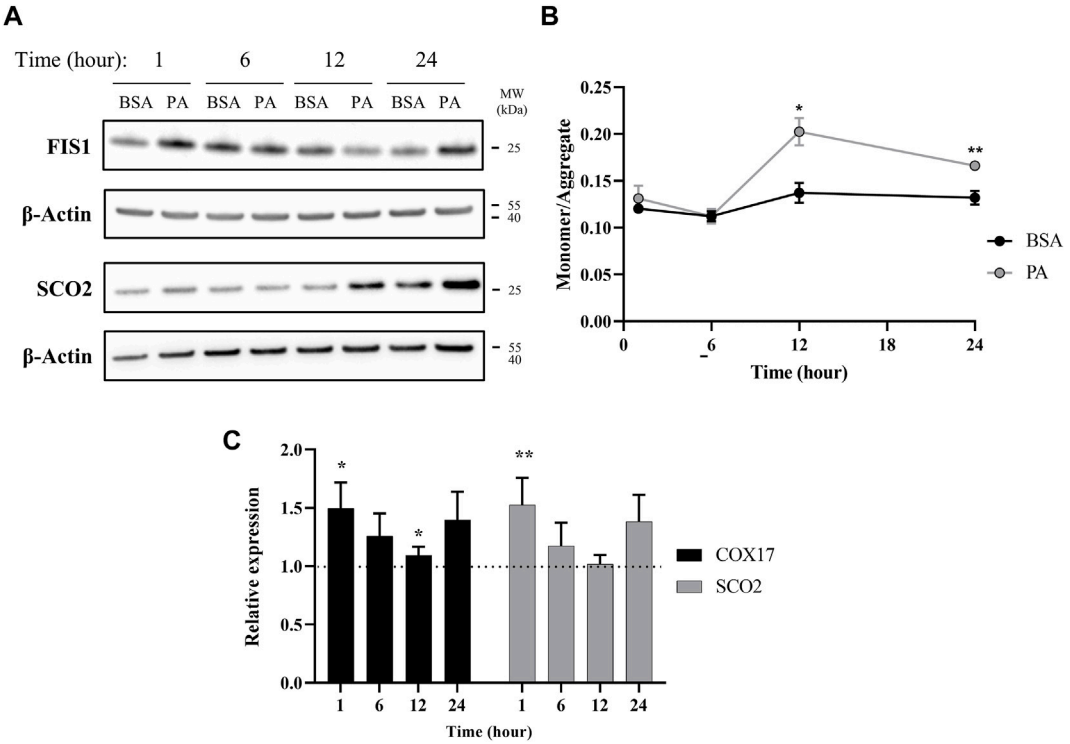

FIGURE 4 | Palmitate stimulations induce changes in mitochondria copper protein regulation. **(A)** Representative western blot images of SCO2 and FIS1 of cells stimulated with BSA or PA. **(B)** Mitochondrial membrane potential was measured using the JC-1 fluorescent dye. Data are shown as monomer/aggregate fluorescence of BSA- and PA-stimulated cells ($n = 4$). Mean ± SEM is shown. The unpaired t-test was used to assess significance (*$p < 0.05$, **$p < 0.01$). **(C)** Gene expression of COX17 and SCO2 with PA-stimulated HepG2 cells relative to BSA-stimulated cells ($n = 10$) with normalization to β-actin as the housekeeping gene. Mean ± SEM is shown. The Mann–Whitney U test was used to assess significance (*$p < 0.05$, **$p < 0.01$).

the mitochondria, and SCO2, a chaperone responsible for copper loading into cytochrome c oxidase in the electron transport chain (Nevitt et al., 2012; Polishchuk et al., 2014; Morrell et al., 2020; Cobine et al., 2021). COX17 and SCO2 gene expression are increased in cells stimulated with PA at all the time points (**Figure 4C**), with notable increases at 1, 6, and 24 h, whereas SCO2 protein levels do not noticeably increase until the 12- and 24-h time points (**Figure 4A**). Similar increases in SCO2 protein and mRNA levels have been previously observed by Arciello et al. (2015) when HepG2 cells are stimulated with 500 μM of a mixed fatty acid (oleic acid and PA) solution. The degree and direction of changes in these genes at the different time points follow a similar trend as the copper proteins ATOX1, COMMD1, and SOD1 expression, corroborating an overall disruption in copper-associated respiration associated with oxidative imbalance. Taken together, the data supports an initial disruption in copper mitochondrial health that may then induce alterations in the copper subcellular localization.

DISCUSSION

Emerging studies on copper metabolism are illuminating its vital roles in energy regulation and nutrient processing. In particular, research is revealing homeostatic perturbations in copper metabolism in relation to obesity-related conditions in rodent models and human physiology (Heffern et al., 2016; Harder et al., 2020; Morrell et al., 2020; Lowe et al., 2017). Previous studies have observed increased expression of ATP7B and hepatic copper deficiency in association with hepatic fat accumulation (Arciello et al., 2015; Heffern et al., 2016). In this study, we profiled the changes in copper trafficking that accompany this change in ATP7B using a cellular model, namely, the stimulation of HepG2 cells with PA. Our observations point to a mechanism wherein fatty acids may induce a response akin to cytosolic copper overload that triggers copper transport mechanisms to subsequently generate a copper-deficient-like state. At shorter time points of stimulation, the cell initially demonstrates an increase in copper trafficking and chaperone proteins associated with copper overload, including the elevated expression of proteins involved in the copper export machinery as well an increase in the levels and expression of Mt2A, a putative copper storage protein. This in turn results in a subsequent shift of markers toward a state of copper deficiency, including downregulation and reduced levels of Mt2A, which may indicate the release of copper stores, an increase in protein levels and gene expression of CCS, and an increase in ATP7B. Overexpression of CCS is an established marker of copper-deficient states and is posited to occur as a means for the cell to redirect the limited available copper toward redox balance

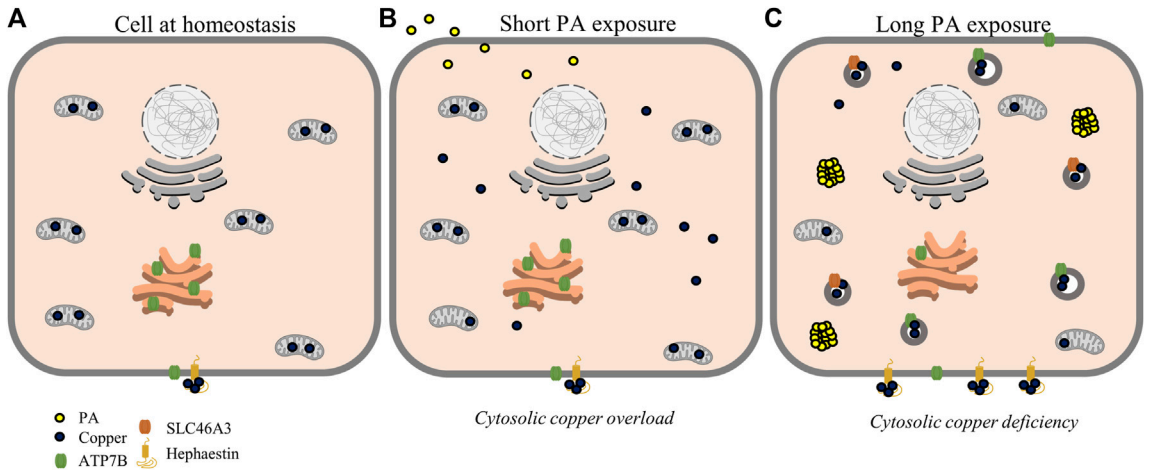

FIGURE 5 | Proposed scheme for possible perturbations of copper homeostasis by PA. At homeostasis **(A)**, copper is mostly sequestered in proteins and organelles with a large concentration in the mitochondria. At short time points of PA exposure **(B)**, cytosolic copper levels are increased alongside mitochondrial dysfunction, leading to a state resembling cytosolic copper overload. With longer PA **(C)**, copper is relocalized toward export by ATP7B and sequestering mechanisms by SLC46A3 and hephaestin resulting in a copper-deficient state.

mechanisms (Freedman et al., 1989; Bertinato et al., 2003; Kumar et al., 2013). Despite the expression of molecular markers of cytosolic copper deficiency at these later time points, the subcellular localization of ATP7B is delocalized from the TGN, a phenotype that is observed in the presence of excess copper (Barnes et al., 2009; Polishchuk et al., 2014). This localization is also accompanied by the increased expression of total ATP7B. While increased ATP7B is typically associated with the activation of copper export, we did not observe changes in total copper concentration of cell pellets nor did we observe increases in extracellular Cp levels or activity. This might suggest that the regulation of ATP7B may instead be functioning toward sequestering or redistributing copper within or at the surface of, rather than exporting the metal from, the cell (Cater et al., 2006; Polishchuk et al., 2014). In support of this hypothesis, we observed an increase in SLC46A3, a protein proposed to play a role in copper loading into lysosomes and potential sequestration (Kim et al., 2021). This membrane protein may be responsible for the changes in cytosolic copper status as copper is redistributed within the cell toward lysosomes. In addition, we observed an increase in protein expression of hephaestin, the membrane-anchored homolog of Cp, supporting a movement of copper to the membrane surface away from the intracellular space (**Figure 5**) (Vashchenko and MacGillivray, 2013; Jiang et al., 2016; Higuchi et al., 2018). In a mouse model of NAFLD, hepatic hephaestin was significantly increased in mice fed a high-fat and high-cholesterol diet (Higuchi et al., 2018). This increase correlates with our observations in HepG2 cells exposed to PA and highlights the relationship of hephaestin and copper redistribution in nutrient overload. While implications of copper loading into the lysosome and hephaestin are not fully understood and require further investigations, their changes may point to a cellular response to either reduce or utilize cytosolic copper (Vashchenko and MacGillivray, 2013; Bacchi et al., 2014; Polishchuk and Polishchuk, 2016). We noted that COMMD1, which has a posited role in biliary copper export, is altered by PA stimulations (de Bie et al., 2005; Shanmugavel and Wittung-Stafshede, 2019; Stewart et al., 2019); however, as HepG2 cells have altered biliary export mechanisms, our model may be limited in its ability to capture this particular trafficking mechanism (Woolbright et al., 2016).

In further investigating potential mechanisms by which PA perturbs cytosolic copper, we identified alterations in mitochondrial copper proteins. Copper plays a critical role in the electron transport chain and is thus tightly regulated within the mitochondria (Joshi-Barve et al., 2007; Arciello et al., 2015; Ruiz et al., 2021). It has even been proposed that the organelle has the ability to store copper within its matrix (Cobine et al., 2006; Lutsenko, 2010; Nevitt et al., 2012). We observed changes in the gene expression of the mitochondrial copper proteins COX17 and SCO2 with PA addition alongside an increase in the mitochondrial fission protein, FIS1, and mitochondrial membrane depolarization. In addition, the time dependence of the changes of the mitochondrial proteins correlate with the increases in Mt2A, denoting a link between PA-induced effects on mitochondrial health and perturbations to cytosolic copper. Our data agrees with published data wherein changes to SCO2 expression were observed alongside fatty acid treatments in cell culture (Arciello et al., 2015). A hypothesis of SCO2-dependent regulation of copper export from the mitochondria may agree with the observed increases in SCO2 protein and point to a loss of mitochondrial copper (Cobine et al., 2021). Mutations and knockout of SCO2 have been implicated in fatty acid processing and insulin resistance in mouse models, further implicating mitochondrial copper dysfunction in fat accumulation (Hill et al., 2017). Our data complements these findings, as we observed increased glutathione oxidation with the PA treatments, which can relate both to altered copper metabolism as well as changes in the overall redox state of the intracellular environment (Freedman et al., 1989; Maryon et al.,

2013). While implications of copper misregulation within the mitochondria are not fully understood, fat overload diseases such as NAFLD have been strongly linked to mitochondrial dysfunction, further connecting such diseases to disruptions in intracellular copper balance (Nassir and Ibdah, 2015; Antonucci et al., 2017). Taken together, our data may point to mitochondrial fission as a potential source for miscompartmentalized copper that triggers subsequent copper shuttling pathways to restore homeostasis. Future studies are required to firmly establish the links between mitochondrial copper regulation and fat accumulation as well as their implications on cell health and disease pathologies.

Diseases that arise alongside fat accumulation are hypothesized to progress in a "multiple-hit" system, with an increase in reactive oxygen species and the accumulation of fat in the liver contributing to disease pathogenesis (Ahmed et al., 2012; Buzzetti et al., 2016; Antonucci et al., 2017). However, the mechanisms behind these phenotypes have yet to be uncovered (Buzzetti et al., 2016; Antonucci et al., 2017; Benedict and Zhang, 2017). As copper can play a role in oxidative stress, the shifts in hepatic copper metabolism that we have observed in response to PA exposure may play a role in the exacerbation of fat-induced cellular stress (Tchounwou et al., 2008; Arnal et al., 2012; Einer et al., 2019). This cytosolic copper overload in turn leads to copper detoxification that appears through export or sequestration as evidenced by increases in SLC46A3 and hephaestin (Barnes et al., 2009; Lutsenko, 2010; Vashchenko and MacGillivray, 2013; Kim et al., 2021). Previous models of copper deficiency demonstrated altered lipid synthesis and metabolism, leading to increased lipid biogenesis and hepatic fat accumulation which could be triggered by the miscompartmenalization of copper observed at later time points (Morrell et al., 2017). This increase in expression of markers of copper deficiency alongside increases in fat accumulation implicates copper misregulation in the process of lipid biogenesis.

From this study, we proposed the following as a mechanism by which copper is misregulated within the liver cell upon PA stimulation (**Figure 5**). Fatty acid stimulation and subsequent uptake initiate a mislocalization of copper, possibly related to mitochondrial dysfunction. This mislocalization triggers an initial cytosolic response similar to copper overload states, initiating export pathways involving ATOX1, COMMD1, and ATP7B to restore copper balance. This results in sequestration and redistribution of copper, likely to the lysosomes and cell membrane, leading to a state of cytosolic copper deficiency corresponding to increases in CCS levels and decreased levels and expression of Mt2A. This copper deficiency may be exacerbated by export induced by overexpression and relocalization of ATP7B.

In conclusion, our studies reveal mechanistic insights into how the cellular copper distribution of hepatocytes is dynamically perturbed by fat accumulation. We suggested that the shift toward copper export or sequestration is due to cells sensing a state of cytosolic copper overload to restore a level of copper homeostasis. This perceived copper overload activates copper export or sequestering pathways, which subsequently induce a state that resembles copper deficiency. We noted that this study is not an exhaustive study of all the proteins that are potentially involved in copper regulation in the cell and focused primarily on regulatory pathways that were established in the literature. Of note, proteins that warrant a deeper study with regard to their function in hepatic copper trafficking and consequent effects of macronutrients such as fatty acids include but are not limited to ATP7A (which recent studies have highlighted as being expressed in the liver) and CUTC (a protein hinted at playing a role in cytosolic copper balance). Nonetheless, the present study provides a starting point to broaden our mechanistic understanding of how macronutrients such as fat can alter the regulation and compartmentalization of micronutrients such as copper within the cell.

DATA AVAILABILITY STATEMENT

The original contributions presented in the study are included in the article/**Supplementary Material**, further inquiries can be directed to the corresponding author.

AUTHOR CONTRIBUTIONS

NH and MH designed the research study; NH, HL, VF, JS, and SG performed the research study; NH and HL analyzed data; and NH, HL, VF, JS, and MH wrote the manuscript with input from all authors.

FUNDING

This work was supported by the NIH MIRA 1R35GM133684-01, the Hartwell Foundation's Individual Biomedical Research Award, and start-up funds from the UC Davis Department of Chemistry. MH is also thankful for the support of the ADVANCE CAMPOS Faculty Scholar Award.

ACKNOWLEDGMENTS

We would like to thank Dr. Michael Paddy for training and assistance on the confocal microscope at the MCB Light Microscopy Imaging Facility at UC Davis. We would like to thank the Northwestern University Quantitative Bio-element Imaging Center for their work in assessing the metal content of cells and media. We would additionally like to thank Dr. Patricia Oteiza and Dr. Eleonora Cremonini of the Nutrition and Environmental Toxicology departments at UC Davis for their support and advice.

SUPPLEMENTARY MATERIAL

The Supplementary Material for this article can be found online at: https://www.frontiersin.org/articles/10.3389/fmolb.2022.863296/full#supplementary-material

REFERENCES

Ackerman, C. M., and Chang, C. J. (2018). Copper Signaling in the Brain and Beyond. *J. Biol. Chem.* 293 (13), 4628–4635. doi:10.1074/jbc.R117.000176

Ahmed, U., Latham, P. S., and Oates, P. S. (2012). Interactions between Hepatic Iron and Lipid Metabolism with Possible Relevance to Steatohepatitis. *World. J. Gastroenterol.* 18, 4651–4658. doi:10.3748/wjg.v18.i34.4651

Aigner, E., Theurl, I., Haufe, H., Seifert, M., Hohla, F., Scharinger, L., et al. (2008). Copper Availability Contributes to Iron Perturbations in Human Nonalcoholic Fatty Liver Disease. *Gastroenterology* 135, 680–688. doi:10.1053/j.gastro.2008.04.007

Alsabeeh, N., Chausse, B., Kakimoto, P. A., Kowaltowski, A. J., and Shirihai, O. (2018). Cell Culture Models of Fatty Acid Overload: Problems and Solutions. *Biochim. Biophys. Acta Mol. Cell Biol. Lipids* 1863, 143–151. doi:10.1016/j.bbalip.2017.11.006

Antonucci, L., Porcu, C., Iannucci, G., Balsano, C., and Barbaro, B. (2017). Non-Alcoholic Fatty Liver Disease and Nutritional Implications: Special Focus on Copper. *Nutrients* 9. doi:10.3390/nu9101137

Arciello, M., Longo, A., Viscomi, C., Capo, C., Angeloni, A., Rossi, L., et al. (2015). Core Domain Mutant Y220C of p53 Protein Has a Key Role in Copper Homeostasis in Case of Free Fatty Acids Overload. *BioMetals* 28, 1017–1029. doi:10.1007/s10534-015-9886-0

Arnal, N., De Alaniz, M. J. T., and Marra, C. A. (2012). Cytotoxic Effects of Copper Overload on Human-Derived Lung and Liver Cells in Culture. *Biochim. Biophys. Acta Gen. Subjects* 1820, 931–939. doi:10.1016/j.bbagen.2012.03.007

Bacchi, M., Berggren, G., Niklas, J., Veinberg, E., Mara, M. W., Shelby, M. L., et al. (2014). Cobaloxime-Based Artificial Hydrogenases. *Inorg. Chem.* 53, 8071–8082. doi:10.1021/ic501014c

Barnes, N., Bartee, M. Y., Braiterman, L., Gupta, A., Ustiyan, V., Zuzel, V., et al. (2009). Cell-specific Trafficking Suggests a New Role for Renal ATP7B in the Intracellular Copper Storage. *Traffic* 10, 767–779. doi:10.1111/j.1600-0854.2009.00901.x

Benedict, M., and Zhang, X. (2017). Non-Alcoholic Fatty Liver Disease: An Expanded Review. *World J. Hepatol.* 9 (16), 715–732. doi:10.4254/wjh.v9.i16.715

Bertinato, J., Iskandar, M., and L'Abbe´, M. R. (2003). Copper Deficiency Induces the Upregulation of the Copper Chaperone for Cu/Zn Superoxide Dismutase in Weanling Male Rats. *J. Nutr.* 133, 28–31. doi:10.1093/jn/133.1.28

Bost, M., Houdart, S., Oberli, M., Kalonji, E., Huneau, J.-F., and Margaritis, I. (2016). Dietary Copper and Human Health: Current Evidence and Unresolved Issues. *J. Trace Elem. Med. Biol.* 35, 107–115. doi:10.1016/j.jtemb.2016.02.006

Brady, D. C., Crowe, M. S., Turski, M. L., Hobbs, G. A., Yao, X., Chaikuad, A., et al. (2014). Copper is Required for Oncogenic BRAF Signalling and Tumorigenesis. *Nature* 509, 492–496. doi:10.1038/nature13180

Buzzetti, E., Pinzani, M., and Tsochatzis, E. A. (2016). The Multiple-Hit Pathogenesis of Non-Alcoholic Fatty Liver Disease (NAFLD). *Metabolism* 65, 1038–1048. doi:10.1016/j.metabol.2015.12.012

Cater, M. A., La Fontaine, S., Shield, K., Deal, Y., and Mercer, J. F. (2006). ATP7B Mediates Vesicular Sequestration of Copper: Insight into Biliary Copper Excretion. *Gastroenterology* 130, 493–506. doi:10.1053/j.gastro.2005.10.054

Cobine, P. A., Pierrel, F., and Winge, D. R. (2006). Copper Trafficking to the Mitochondrion and Assembly of Copper Metalloenzymes. *Biochim. Biophys. Acta.* 1763 (7), 759–772. doi:10.1016/j.bbamcr.2006.03.002

Cobine, P. A., Moore, S. A., and Leary, S. C. (2021). Getting Out what You Put in: Copper in Mitochondria and its Impacts on Human Disease. *Biochim. Biophys. Acta Mol. Cell Res.* 1868, 118867. doi:10.1016/j.bbamcr.2020.118867

Cope-Yokoyama, S., Finegold, M. J., Sturniolo, G. C., Kim, K., Mescoli, C., Rugge, M., et al. (2010). Wilson Disease: Histopathological Correlations with Treatment on Follow-Up Liver Biopsies. *World J. Gastroenterol.* 16, 1487–1494. doi:10.3748/wjg.v16.i12.1487

Cremonini, E., and Oteiza, P. I. (2018). (-)-Epicatechin and its Metabolites Prevent Palmitate-Induced NADPH Oxidase Upregulation, Oxidative Stress and Insulin Resistance in HepG2 Cells. *Arch. Biochem. Biophys.* 646, 55–63. doi:10.1016/j.abb.2018.03.027

Culotta, V. C., Klomp, L. W. J., Strain, J., Casareno, R. L. B., Krems, B., and Gitlin, J. D. (1997). The Copper Chaperone for Superoxide Dismutase. *J. Biol. Chem.* 272, 23469–23472. doi:10.1074/jbc.272.38.23469

Cusi, K. (2009). Role of Insulin Resistance and Lipotoxicity in Non-alcoholic Steatohepatitis. *Clin. Liver Dis.* 13 (4), 545–563. doi:10.1016/j.cld.2009.07.009

Członkowska, A., Litwin, T., Dusek, P., Ferenci, P., Lutsenko, S., Medici, V., et al. (2018). Wilson Disease. *Nat. Rev. Dis. Primers* 4 (1), 21. doi:10.1038/s41572-018-0018-3

de Bie, P., Van De Sluis, B., Klomp, L., and Wijmenga, C. (2005). The Many Faces of the Copper Metabolism Protein MURR1/COMMD1. *J. Hered.* 96 (7), 803–811. doi:10.1093/jhered/esi110

de Bie, P., van de Sluis, B., Burstein, E., van de Berghe, P. V. E., Muller, P., Berger, R., et al. (2007). Distinct Wilson's Disease Mutations in ATP7B are Associated with Enhanced Binding to COMMD1 and Reduced Stability of ATP7B. *Gastroenterology* 133, 1316–1326. doi:10.1053/j.gastro.2007.07.020

Di Bella, L. M., Alampi, R., Biundo, F., Toscano, G., and Felice, M. R. (2017). Copper Chelation and Interleukin-6 Proinflammatory Cytokine Effects on Expression of Different Proteins Involved in Iron Metabolism in HepG2 Cell Line. *BMC Biochem.* 18, 1. doi:10.1186/s12858-017-0076-2

Einer, C., Leitzinger, C., Lichtmannegger, J., Eberhagen, C., Rieder, T., Borchard, S., et al. (2019). A High-Calorie Diet Aggravates Mitochondrial Dysfunction and Triggers Severe Liver Damage in Wilson Disease Rats. *Cell Mol. Gastroenterol. Hepatol.* 7, 571–596. doi:10.1016/j.jcmgh.2018.12.005

Eynaudi, A., Díaz-Castro, F., Bórquez, J. C., Bravo-Sagua, R., Parra, V., and Troncoso, R. (2021). Differential Effects of Oleic and Palmitic Acids on Lipid Droplet-Mitochondria Interaction in the Hepatic Cell Line HepG2. *Front. Nutr.* 8, 901. doi:10.3389/fnut.2021.775382

Fleming, R. E., Whitman, I. P., and Gitlin, J. D. (1991). Induction of Ceruloplasmin Gene Expression in Rat Lung during Inflammation and Hyperoxia. *Am. J. Physiol.* 260, L68–L74. doi:10.1152/ajplung.1991.260.2.L68

Freedman, J. H., Ciriolo$, M. R., and Peisach, J. (1989). The Role of Glutathione in Copper Metabolism and Toxicity. *J. Biol. Chem.* 264 (10), 5598–5605. doi:10.1016/s0021-9258(18)83589-x

Freestone, D., Denoyer, D., Jakab, M., Leigh Ackland, M., Cater, M. A., and Michalczyk, A. (2016). Ceruloplasmin is Regulated by Copper and Lactational Hormones in PMC42-LA Mammary Epithelial Cell Culture Models. *Metallomics* 8, 941–950. doi:10.1039/c6mt00086j

Gallagher, C., Reeve, V. E., and Wright, R. (1973). Copper Deficiency in the Rat Effect on the Ultrastructure of Hepatocytes. *Aust. J. Exp. Biol. Med.* 51, 181–189. doi:10.1038/icb.1973.15

Gitlins, J. D. (1988). Transcriptional Regulation of Ceruloplasmin Gene Expression during Inflammation. *J. Biol. Chem.* 263, 6281–6287. doi:10.1016/s0021-9258(18)68783-6

Gómez-Lechón, M. J., Donato, M. T., Martínez-Romero, A., Jiménez, N., Castell, J. V., and O'Connor, J. E. (2007). A Human Hepatocellular *In Vitro* Model to Investigate Steatosis. *Chem. Biol. Interact* 165, 106–116.

Guttmann, S., Nadzemova, O., Newald, I. Grü., Lenders, M., Brand, E., Zibert, A., et al. (2020). ATP7B Knockout Disturbs Copper and Lipid Metabolism in Caco-2 Cells. *PLoS One* 15 (3), e0230025. doi:10.1371/journal.pone.0230025

Harder, N. H. O., Hieronimus, B., Stanhope, K. L., Shibata, N. M., Lee, V., Nunez, M. V., et al. (2020). Effects of Dietary Glucose and Fructose on Copper, Iron, and Zinc Metabolism Parameters in Humans. *Nutrients* 12, 1–14. doi:10.3390/nu12092581

Heffern, M. C., Park, H. M., Au-Yeung, H. Y., Van de Bittner, G. C., Ackerman, C. M., Stahl, A., et al. (2016). *In Vivo* bioluminescence Imaging Reveals Copper Deficiency in a Murine Model of Nonalcoholic Fatty Liver Disease. *Proc. Natl. Acad. Sci. U.S.A.* 113, 14219–14224. doi:10.1073/pnas.1613628113

Hellman, N. E., and Gitlin, J. D. (2002). Ceruloplasmin Metabolism and Function. *Annu. Rev. Nutr.* 22, 439–458. doi:10.1146/annurev.nutr.22.012502.114457

Hieronimus, B., Griffen, S. C., Keim, N. L., Bremer, A. A., Berglund, L., Nakajima, K., et al. (2019). Effects of Fructose or Glucose on Circulating ApoCIII and Triglyceride and Cholesterol Content of Lipoprotein Subfractions in Humans. *J. Clin. Med.* 8, 913. doi:10.3390/jcm8070913

Higuchi, T., Moriyama, M., Fukushima, A., Matsumura, H., Matsuoka, S., Kanda, T., et al. (2018). Association of mRNA Expression of Iron Metabolism-Associated Genes and Progression of Non-alcoholic Steatohepatitis in Rats. *Oncotarget* 9, 26183–26194. doi:10.18632/oncotarget.25488

Hill, S., Deepa, S. S., Sataranatarajan, K., Premkumar, P., Pulliam, D., Liu, Y., et al. (2017). Sco2 Deficient Mice Develop Increased Adiposity and Insulin Resistance. *Mol. Cell Endocrinol.* 455, 103–114. doi:10.1016/j.mce.2017.03.019

Horn, N., and Wittung-Stafshede, P. (2021). ATP7A-Regulated Enzyme Metalation and Trafficking in the Menkes Disease Puzzle. *Biomedicines* 9. doi:10.3390/biomedicines9040391

Jiang, B., Liu, G., Zheng, J., Chen, M., Maimaitiming, Z., Chen, M., et al. (2016). Hephaestin and Ceruloplasmin Facilitate Iron Metabolism in the Mouse Kidney. *Sci. Rep.* 6, 39470–39511. doi:10.1038/srep39470

Joshi-Barve, S., Barve, S. S., Amancherla, K., Gobejishvili, L., Hill, D., Cave, M., et al. (2007). Palmitic Acid Induces Production of Proinflammatory Cytokine Interleukin-8 from Hepatocytes. *Hepatology* 46, 823–830. doi:10.1002/hep.21752

Kim, J. H., Matsubara, T., Lee, J., Fenollar-Ferrer, C., Han, K., Kim, D., et al. (2021). Lysosomal SLC46A3 Modulates Hepatic Cytosolic Copper Homeostasis. *Nat. Commun.* 12. doi:10.1038/s41467-020-20461-0

Klevay, L. M. (2011). Is the Western Diet Adequate in Copper? *J. Trace Elem. Med. Biol.* 25 (4), 204–212. doi:10.1016/j.jtemb.2011.08.146

Koch, A., Yoon, Y., Bonekamp, N. A., McNiven, M. A., and Schrader, M. (2005). A Role for Fis1 in Both Mitochondrial and Peroxisomal Fission in Mammalian Cells. *Mol. Biol. Cell* 16, 5077–5086. doi:10.1091/mbc.e05-02-0159

Kumar, A., Sharma, A., Duseja, A., Das, A., Dhiman, R. K., Chawla, Y. K., et al. (2013). Patients with Nonalcoholic Fatty Liver Disease (NAFLD) Have Higher Oxidative Stress in Comparison to Chronic Viral Hepatitis. *J. Clin. Exp. Hepatol.* 3, 12–18. doi:10.1016/j.jceh.2012.10.009

LassiProhaska, K. C. J. R., and Prohaska, J. R. (2012). Erythrocyte Copper Chaperone for Superoxide Dismutase Is Increased Following Marginal Copper Deficiency in Adult and Postweanling Mice. *J. Nutr.* 142, 292–297. doi:10.3945/jn.111.150755

Leary, S. C., Cobine, P. A., Kaufman, B. A., Guercin, G.-H., Mattman, A., Palaty, J., et al. (2007). The Human Cytochrome c Oxidase Assembly Factors SCO1 and SCO2 Have Regulatory Roles in the Maintenance of Cellular Copper Homeostasis. *Cell Metab.* 5, 9–20. doi:10.1016/j.cmet.2006.12.001

Linder, M. C. (2020). Copper Homeostasis in Mammals, with Emphasis on Secretion and Excretion. A Review. *Int. J. Mol. Sci.* 21, 1–22. doi:10.3390/ijms21144932

Linder, M. C. (2016). Ceruloplasmin and Other Copper Binding Components of Blood Plasma and Their Functions: an Update. *Metallomics* 8, 887–905. doi:10.1039/c6mt00103c

Lomonaco, R., Chen, J., and Cusi, K. (2011). An Endocrine Perspective of Nonalcoholic Fatty Liver Disease (NAFLD). *Ther. Adv. Endocrinol. Metab.* 2 (5), 211–225. doi:10.1177/2042018811419157

Lowe, J., Taveira-da-Silva, R., and Hilário-Souza, E. (2017). Dissecting Copper Homeostasis in Diabetes Mellitus. *IUBMB Life* 69, 255–262. doi:10.1002/iub.1614

Lutsenko, S., Barnes, N. L., Bartee, M. Y., and Dmitriev, O. Y. (2007). Function and Regulation of Human Copper-Transporting ATPases. *Physiol. Rev.* 87, 1011–1046. doi:10.1152/physrev.00004.2006

Lutsenko, S. (2016). Copper Trafficking to the Secretory Pathway. *Metallomics* 8, 840–852. doi:10.1039/c6mt00176a

Lutsenko, S. (2010). Human Copper Homeostasis: a Network of Interconnected Pathways. *Curr. Opin. Chem. Biol.* 14, 211–217. doi:10.1016/j.cbpa.2010.01.003

Maryon, E. B., Molloy, S. A., and Kaplan, J. H. (2013). Cellular Glutathione Plays a Key Role in Copper Uptake Mediated by Human Copper Transporter 1. *Am. J. Physiol. Cell Physiol.* 304, C768–C779. doi:10.1152/ajpcell.00417.2012

Morrell, A., Tallino, S., Yu, L., and Burkhead, J. L. (2017). The Role of Insufficient Copper in Lipid Synthesis and Fatty-Liver Disease. *IUBMB Life* 69, 263–270. doi:10.1002/iub.1613

Morrell, A., Tripet, B. P., Eilers, B. J., Tegman, M., Thompson, D., Copié, V., et al. (2020). Copper Modulates Sex-specific Fructose Hepatoxicity in Nonalcoholic Fatty Liver Disease (NALFD) Wistar Rat Models. *J. Nutr. Biochem.* 78, 108316. doi:10.1016/j.jnutbio.2019.108316

Nassir, F., and Ibdah, J. A. (2015). Role of Mitochondria in Nonalcoholic Fatty Liver Disease. *Int. J. Mol. Sci.* 15 (5), 8713–8742. doi:10.3390/ijms15058713

Nevitt, T., Öhrvik, H., and Thiele, D. J. (2012). Charting the Travels of Copper in Eukaryotes from Yeast to Mammals. *Biochim. Biophys. Acta Mol. Cell Res.* 1823, 1580–1593. doi:10.1016/j.bbamcr.2012.02.011

Ngamchuea, K., Batchelor-McAuley, C., and Compton, R. G. (2016). The Copper(II)-Catalyzed Oxidation of Glutathione. *Chem. Eur. J.* 22, 15937–15944. doi:10.1002/chem.201603366

Ostrakhovitch, E. A., Song, Y. P., and Cherian, M. G. (2016). Basal and Copper-Induced Expression of Metallothionein Isoform 1,2 and 3 Genes in Epithelial Cancer Cells: The Role of Tumor Suppressor P53. *J. Trace Elem. Med. Biol.* 35, 18–29. doi:10.1016/j.jtemb.2016.01.008

Park, J. Y., Kim, Y., Im, J. A., and Lee, H. (2015). Oligonol Suppresses Lipid Accumulation and Improves Insulin Resistance in a Palmitate-Induced in HepG2 Hepatocytes as a Cellular Steatosis Model. *BMC Complement. Altern. Med.* 15, 185. doi:10.1186/s12906-015-0709-1

Perdomo, C. M., Frühbeck, G., and Escalada, J. (2019). Impact of Nutritional Changes on Nonalcoholic Fatty Liver Disease. *Nutrients* 11. doi:10.3390/nu11030677

Polishchuk, E. V., Concilli, M., Iacobacci, S., Chesi, G., Pastore, N., Piccolo, P., et al. (2014). Wilson Disease Protein ATP7B Utilizes Lysosomal Exocytosis to Maintain Copper Homeostasis. *Develop. Cel* 29, 686–700. doi:10.1016/j.devcel.2014.04.033

Polishchuk, E. V., and Polishchuk, R. S. (2016). The Emerging Role of Lysosomes in Copper Homeostasis. *Metallomics* 8, 853–862. doi:10.1039/c6mt00058d

Ruiz, L. M., Libedinsky, A., and Elorza, A. A. (2021). Role of Copper on Mitochondrial Function and Metabolism. *Front. Mol. Biosci.* 8, 711227. doi:10.3389/fmolb.2021.711227

Sergi, D., Luscombe-Marsh, N., Naumovski, N., Abeywardena, M., and O'Callaghan, N. (2021). Palmitic Acid, But Not Lauric Acid, Induces Metabolic Inflammation, Mitochondrial Fragmentation, and a Drop in Mitochondrial Membrane Potential in Human Primary Myotubes. *Front. Nutr.* 8, 663838. doi:10.3389/fnut.2021.663838

Shanmugavel, K. P., and Wittung-Stafshede, P. (2019). Copper Relay Path through the N-Terminus of Wilson Disease Protein, ATP7B. *Metallomics* 11, 1472–1480. doi:10.1039/c9mt00147f

Softic, S., Cohen, D. E., and Kahn, C. R. (2016). Role of Dietary Fructose and Hepatic *De Novo* Lipogenesis in Fatty Liver Disease. *Dig. Dis. Sci.* 61, 1282–1293. doi:10.1007/s10620-016-4054-0

Song, M., Vos, M. B., and McClain, C. J. (2018). Copper-Fructose Interactions: A Novel Mechanism in the Pathogenesis of NAFLD. *Nutrients* 10 (11), 1815. doi:10.3390/nu10111815

Statovci, D., Aguilera, M., MacSharry, J., and Melgar, S. (2017). The Impact of Western Diet and Nutrients on the Microbiota and Immune Response at Mucosal Interfaces. *Front. Immunol.* 8, 838. doi:10.3389/fimmu.2017.00838

Stewart, D. J., Short, K. K., Maniaci, B. N., and Burkhead, J. L. (2019). COMMD1 and PtdIns(4,5)P2 Interaction Maintain ATP7B Copper Transporter Trafficking Fidelity in HepG2 Cells. *J. Cell Sci.* 132. doi:10.1242/jcs.231753

Swapna Sasi, U. S., Sindhu, G., and Raghu, K. G. (2020). Fructose-palmitate Based High Calorie Induce Steatosis in HepG2 Cells via Mitochondrial Dysfunction: An *In Vitro* Approach. *Toxicol. Vitro* 68, 104952. doi:10.1016/j.tiv.2020.104952

Tapryal, N., Mukhopadhyay, C., Das, D., Fox, P. L., and Mukhopadhyay, C. K. (2009). Reactive Oxygen Species Regulate Ceruloplasmin by a Novel mRNA Decay Mechanism Involving its 3′-Untranslated Region. *J. Biol. Chem.* 284, 1873–1883. doi:10.1074/jbc.m804079200

Tchounwou, P. B., Newsome, C., Williams, J., and Glass, K. (2008). Copper-Induced Cytotoxicity and Transcriptional Activation of Stress Genes in Human Liver Carcinoma (HepG(2)) Cells. *Met. Ions Biol. Med.* 10, 285–290.

Thomas, C., Mackey, M. M., Diaz, A. A., and Cox, D. P. (2009). Hydroxyl Radical is Produced via the Fenton Reaction in Submitochondrial Particles Under Oxidative Stress: Implications for Diseases Associated with Iron Accumulation. *Redox Rep.* 14, 102–108. doi:10.1179/135100009x392566

Vashchenko, G., and MacGillivray, R. T. A. (2013). Multi-Copper Oxidases and Human Iron Metabolism. *Nutrients* 5 (7), 2289–2313. doi:10.3390/nu5072289

Weiss, K. H., Wurz, J., Gotthardt, D., Merle, U., Stremmel, W., and Füllekrug, J. (2008). Localization of the Wilson Disease Protein in Murine Intestine. *J. Anat.* 213, 232–240. doi:10.1111/j.1469-7580.2008.00954.x

Woolbright, B. L., McGill, M. R., Yan, H., and Jaeschke, H. (2016). Bile Acid-Induced Toxicity in HepaRG Cells Recapitulates the Response in Primary Human Hepatocytes. *Basic Clin. Pharmacol. Toxicol.* 118, 160–167. doi:10.1111/bcpt.12449

Zaccak, M., Qasem, Z., Gevorkyan-Airapetov, L., and Ruthstein, S. (2020). An EPR Study on the Interaction between the Cu(I) Metal Binding Domains of ATP7B and the Atox1 Metallochaperone. *Int. J. Mol. Sci.* 21, 1–13. doi:10.3390/ijms21155536

Conflict of Interest: The authors declare that the research was conducted in the absence of any commercial or financial relationships that could be construed as a potential conflict of interest.

Publisher's Note: All claims expressed in this article are solely those of the authors and do not necessarily represent those of their affiliated organizations, or those of the publisher, the editors, and the reviewers. Any product that may be evaluated in this article, or claim that may be made by its manufacturer, is not guaranteed or endorsed by the publisher.

frontiers | Frontiers in Cell and Developmental Biology

ORIGINAL RESEARCH
published: 26 April 2022
doi: 10.3389/fcell.2022.886568

Multiple Poses and Thermodynamics of Ligands Targeting Protein Surfaces: The Case of Furosemide Binding to mitoNEET in Aqueous Solution

Linh Gia Hoang[1,2†], Jonas Goßen[3,4†], Riccardo Capelli[5], Toan T. Nguyen[2], Zhaoxi Sun[6], Ke Zuo[3,7,8], Jörg B. Schulz[1,9], Giulia Rossetti[3,9,10]* and Paolo Carloni[1,2,3]*

[1]INM-11, Forschungszentrum, Jülich, Germany, [2]Key Laboratory for Multiscale Simulations of Complex Systems, VNU University of Science, Vietnam National University, Hanoi, Vietnam, [3]IAS-5/INM-9, Forschungszentrum, Jülich, Germany, [4]Faculty of Mathematics, Computer Science and Natural Sciences, RWTH Aachen University, Aachen, Germany, [5]Department of Applied Science and Technology (DISAT), Politecnico di Torino, Torino, Italy, [6]College of Chemistry and Molecular Engineering, Institute of Theoretical and Computational Chemistry, Peking University, Beijing, China, [7]The Alexander Silberman Institute of Life Science, The Hebrew University of Jerusalem, Edmond J. Safra Campus at Givat Ram, Jerusalem, Israel, [8]Department of Physics, RWTH Aachen University, Aachen, Germany, [9]Department of Neurology, University Hospital Aachen (UKA), RWTH Aachen University, Aachen, Germany, [10]Jülich Supercomputing Centre (JSC), Forschungszentrum, Jülich, Germany

OPEN ACCESS

Edited by:
Kourosh Honarmand Ebrahimi, King's College London, United Kingdom

Reviewed by:
Sergey Samsonov, University of Gdansk, Poland
Huangen Ding, Louisiana State University, United States

***Correspondence:**
Riccardo Capelli
riccardo.capelli@polito.it
Giulia Rossetti
g.rossetti@fz-juelich.de

†These authors have contributed equally to this work and share first authorship

Specialty section:
This article was submitted to Cellular Biochemistry, a section of the journal Frontiers in Cell and Developmental Biology

Received: *28 February 2022*
Accepted: *04 April 2022*
Published: *26 April 2022*

Citation:
Hoang LG, Goßen J, Capelli R, Nguyen TT, Sun Z, Zuo K, Schulz JB, Rossetti G and Carloni P (2022) Multiple Poses and Thermodynamics of Ligands Targeting Protein Surfaces: The Case of Furosemide Binding to mitoNEET in Aqueous Solution. Front. Cell Dev. Biol. 10:886568. doi: 10.3389/fcell.2022.886568

Human NEET proteins, such as NAF-1 and mitoNEET, are homodimeric, redox iron-sulfur proteins characterized by triple cysteine and one histidine-coordinated [2Fe-2S] cluster. They exist in an oxidized and reduced state. Abnormal release of the cluster is implicated in a variety of diseases, including cancer and neurodegeneration. The computer-aided and structure-based design of ligands affecting cluster release is of paramount importance from a pharmaceutical perspective. Unfortunately, experimental structural information so far is limited to only one ligand/protein complex. This is the X-ray structure of furosemide bound to oxidized mitoNEET. Here we employ an enhanced sampling approach, Localized Volume-based Metadynamics, developed by some of us, to identify binding poses of furosemide to human mitoNEET protein in solution. The binding modes show a high variability within the same shallow binding pocket on the protein surface identified in the X-ray structure. Among the different binding conformations, one of them is in agreement with the crystal structure's one. This conformation might have been overstabilized in the latter because of the presence of crystal packing interactions, absent in solution. The calculated binding affinity is compatible with experimental data. Our protocol can be used in a straightforward manner in drug design campaigns targeting this pharmaceutically important family of proteins.

Keywords: NEET proteins, rational drug design, localized volume-based metadynamics, furosemide binding pose and affinity, furosemide, molecular dynamics, [2Fe-2S] cluster

INTRODUCTION

The human NEET [2Fe-2S] homodimeric proteins (such as mitoNEET (Colca et al., 2004; Paddock et al., 2007) and NAF-1 (Conlan et al., 2009)) have emerged as important targets for pharmaceutical intervention, from cancer and diabetes, to metabolic and neurodegenerative diseases (Nechushtai et al., 2020). These proteins are located on the outer membrane of mitochondria and mitochondria

associated membranes, and, in the case of NAF-1, also on the endoplasmic reticulum's membrane. Each subunit features a 3Cys:1His coordinated [2Fe-2S] cluster (**Figure 1**), either in a reduced (Fe(III)-Fe(II)) or oxidized (Fe(III)-Fe(III)) state. In the reduced state, the ferrous ion is located close to the protein surface and bound to the histidine (Dicus et al., 2010) (**Figure 1**). The clusters are reduced and inert in physiological conditions. Oxidation under oxidative stress leads to a cluster-labile oxidized state: the cluster can then be released or transferred to apo-acceptors (Landry and Ding, 2014). Cancer cells may express more human NEET proteins than healthy ones to support their required high level of mitochondrial iron and reactive oxygen species (Darash-Yahana et al., 2016). In contrast, cells undergoing neurodegenerative or metabolic disease express less or no human NEET proteins (Kusminski et al., 2016; Nechushtai et al., 2020). Thus, drugs regulating the [2Fe-2S] cluster stability of human NEET proteins might be able to counteract cell derangement associated with many diseases.

So far, a few ligands targeting mitoNEET (Colca et al., 2004; Paddock et al., 2007) and human NAF-1 (Conlan et al., 2009) have been identified. They have been shown to affect cluster release *in vitro,* and to bind in their cluster binding domain (Geldenhuys et al., 2019; Marjault et al., 2021). Efficient computational protocols predicting poses and affinities of ligands would be of paramount importance to improve the potency of such drug leads. They allow for artificial intelligence-based screening of new compounds, with optimal solubility and selectivity (Adeshina et al., 2020; Gao et al., 2020). In addition, they provide an estimation of ligands affinities for the oxidized human NEET proteins, which is very useful as accurate *in vitro* measurements of such affinities may at times be challenging because of the high liability of the cluster at acidic pH (Zuo et al., 2021).

Docking approaches, currently used in the design of ligands targeting enzymes and receptors binding sites, may encounter difficulties here. Indeed, they do not accurately estimate all the possible interaction and desolvation contributions of ligands targeting proteins which lack well-defined binding pockets (Deng et al., 2015). Thus, docking of small molecules on the flat/shallow binding sites of these proteins may lead to false-positives (Li et al., 2014; Guterres and Im, 2020). This problem can be even more exacerbated in transition metal-based systems (Chen et al., 2007), like the NEET proteins.[1]

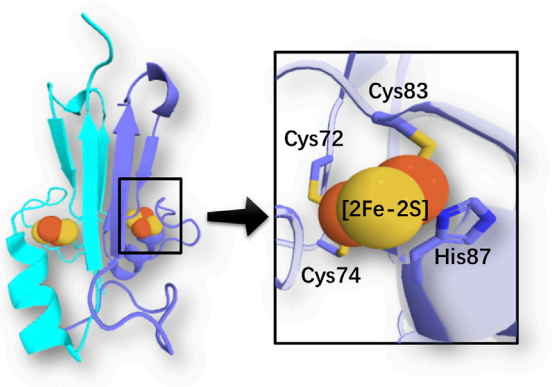

FIGURE 1 | Coordination of an iron-sulfur cluster in a member of the NEET protein family (PDB ID: 2QH7 (Paddock et al., 2007)). Cartoon representation of chain A (light blue) and B (cyan). Sulfur and iron atoms are represented by yellow and orange spheres, respectively.

Both problems were addressed in the past by some of us by 1) developing molecular simulation docking protocols on proteins lacking specific pocket definitions (Kranjc et al., 2009); and 2) by parameterizing both oxidized and reduced NEET [2Fe-2S] clusters for molecular simulations (Pesce et al., 2017; Zuo et al., 2021). Here, by capitalizing on this work, we use a variant of well-tempered metadynamics (WT-MetaD) enhanced sampling simulations (Barducci et al., 2008) to predict the pose and the potency of the ligand targeting mitoNEET. WT-MetaD is an exact method to calculate the free energy of binding as a function of collective variables (CVs) (Barducci et al., 2008). This variant is the so-called Localized Volume-based (LV) MetaD. This approach has already been successfully applied to study ligand binding to proteins with very high computational efficiency (Zhao et al., 2021).

We focus on the furosemide (4-Chloro-2-[(furan-2-ylmethyl) amino]-5-sulfamoylbenzoic acid) molecule (**Chart 1**), which slows down cluster release *in vitro,* and its binding to mitoNEET in the oxidized state (Geldenhuys et al., 2019). This is the only ligand/human NEET protein complex deposited on the protein data bank so far (Geldenhuys et al., 2019). Affinity measurements by radioligand displacement (Geldenhuys et al., 2016) are also available. The X-ray structure shows that the ligand binds in a shallow binding pocket located at the interface between the cluster and the upper part of the monomer (**Figure 2A**). Specifically, the ligand's carboxyl group forms hydrogen bonds (H-bonds) with the iron bound histidine residue (H87) of one subunit and a lysine (K55) from the other (**Figure 2B**). The benzene ring forms hydrophobic interactions with V57, P100, I102, while the furan ring with V70. The NH group forms an intramolecular H-bond with the carboxyl group of the ligand. Finally, the sulfonamide group also forms an H-bond with the protein from the adjacent asymmetric unit (**Figure 2C**).

Our simulations provide a quantitative estimation of the affinity of binding, which is not too dissimilar from experiment. Most importantly, we suggest, based on our calculations, that furosemide can actually bind in several binding poses around the same surface pocket, including the one observed in the crystal structure. The latter may be stabilized by crystal packing interactions in the solid state (**Figure 2C**), as observed before (Marelli et al., 2014). These interactions are absent in water solution (Kranjc et al., 2009; Arif et al., 2011; Geldenhuys et al., 2019).

[1]In spite of these limitations, successful applications of simplified docking approaches such as MAD-28 to mitoNEET/NAF-1 have been reported (Bai et al., 2015). These applications are reported in the SI for furosemide binding to mitoNEET, allowing for a comparison with the free energy calculations performed in this work (**Supplementary Table SI1**).

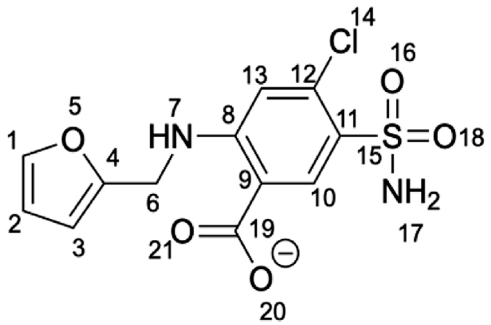

CHART 1 | Structure of furosemide in its most probable protonation state at pH 7.

MATERIALS AND METHODS

System Preparation

The crystal structure of furosemide binding to mitoNEET protein was downloaded from the Protein Data Bank (PDB ID: 6DE9) (Geldenhuys et al., 2019). Maestro (Sastry et al., 2013) (VERSION 2017-2) and GROMACS/2019.4 (Lindahl et al., 2001; Abraham et al., 2019) patched with Plumed 2.5 (Jakalian et al., 2002; Bonomi et al., 2019) were used to perform preparation steps. For protein, water, ions and [2Fe-2S] clusters, we used the AMBER ff99SB-ILDN-DEP (Lindorff-Larsen et al., 2010), TIP3P (Jorgensen et al., 1983), the Åqvist potential (Åqvist, 1990) and force field parameters calculated in our previous work (Pesce et al., 2017), respectively. The ligand was parameterized using the General AMBER Force Field (Wang et al., 2004) obtaining the single-point charges using the semi-empirical AM1-BCC method (Jakalian et al., 2002) generated by the acpype utility script (Sousa da Silva and Vranken, 2012) (**Supplementary Figure SI1**). The system with protein and ligand was solvated in a periodic octahedron box with 28,008 TIP3P (Jorgensen et al., 1983) water molecules. Finally, counterions Na^+ (80) and Cl^- (87) were added to neutralize the system and mimic the physiological salt concentration at 150 mM. The distance from the protein to the edge of the box turned out to be 20 Å or more during the simulations, avoiding self-interaction artifacts.

The bonds were constrained using the LINCS algorithm (Hess et al., 1997). The smooth Particle Mesh Ewald method (Essmann et al., 1995) was used to treat the long-range electrostatic interactions, with a grid spacing value of 1.2 A˚. The cutoff for short-range electrostatic interactions and van der Waals was set to 14 A˚. The temperature and pressure of system (T = 298 K, p = 1 bar) were controlled using the Nose-Hoover thermostat (coupling the system every 0.2 ps with a chain length of 10) (Evans and Holian, 1985) and isotropic Parrinello–Rahman barostat (coupling the system every 0.5 ps with a compressibility of $4.5.10^{-5}$ bar^{-1}) (Parrinello and Rahman, 1981), respectively. The integration step was set to 2 fs.

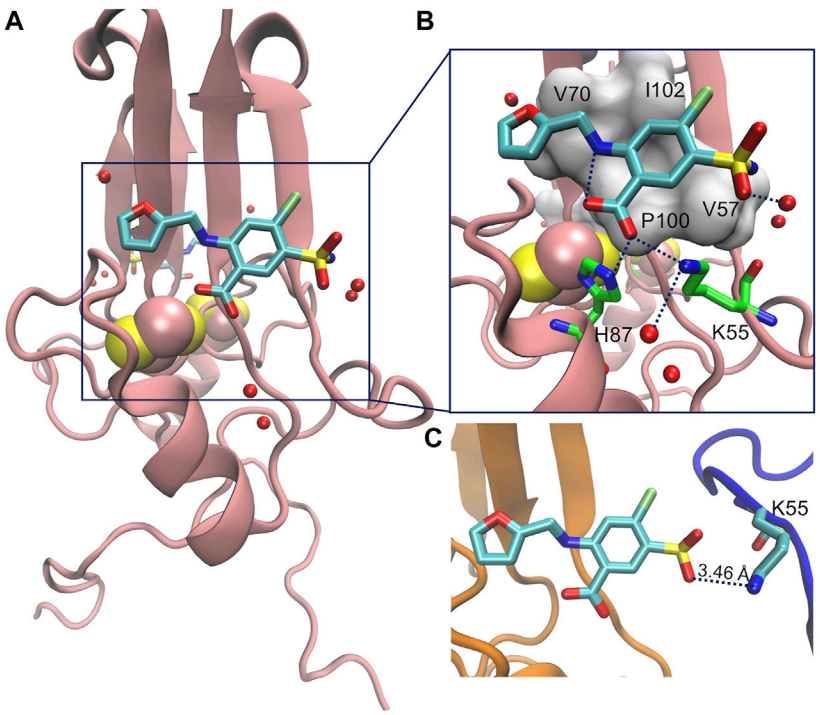

FIGURE 2 | (A) Crystal structure of ligand furosemide binding to mitoNEET protein at pH 7.0. **(B)** Close up showing furosemide-protein H-bonds/salt bridges interactions. **(C)** Interactions of the ligand with the protein image (in blue color) in the crystal.

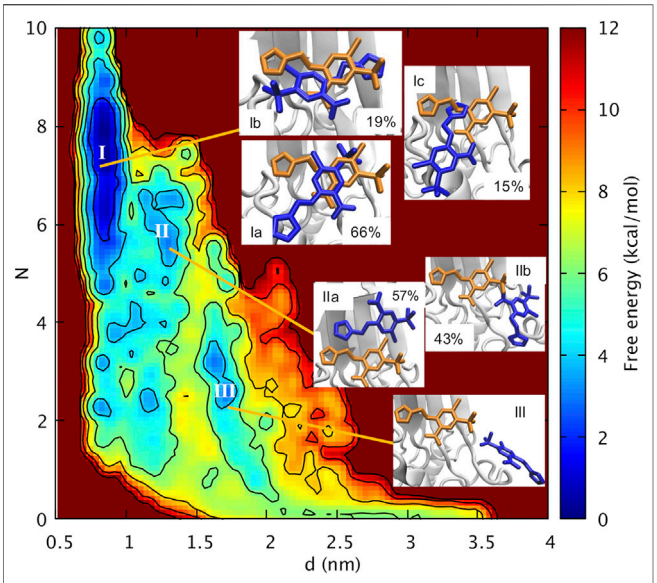

FIGURE 3 | Free energy of furosemide unbinding as a function of the distance between the centers of mass of the furosemide and of the Fe-S cluster (*d*) and the number of H-bonds/salt bridges (*N*).

Molecular Simulations

We performed energy minimization to the system with the steepest descent algorithm, setting the converge criteria to 2.4 kcal mol^{-1} nm^{-1} of the maximum force (Haug et al., 1976). Then, we gradually heated the system in 40 points to 298 K in 1 ns of annealing (**Supplementary Figure SI2**). The system underwent the first 5 ns NVT Molecular Dynamics (MD) at 298 K with a harmonic restraint of 240 kcal mol^{-1} nm^{-2} on both furosemide and protein to maintain the initial experimental conformation. All the bonds were constrained with the LINCS algorithm (Hess et al., 1997). Then, 75 ns NPT MD were performed. Next, the free energy landscape associated with furosemide binding to the protein was investigated by Localized Volume-based Metadynamics (LV-MetaD).

LV-MetaD is a WT-MetaD (Barducci et al., 2008) protocol where a history-dependent potential (called bias) is deposited on three apt collective variables (CVs), *i.e.,* a convenient representation of the reciprocal position of the furosemide with respect to the host protein. To minimize convergence time, the furosemide is constrained in a limited (localized) volume close to the binding pose observed in crystal structure *via* the imposition of a restraining potential. The coordinate system used to represent the furosemide position in the reference frame of the host protein depends on the shape of the restraining potential. Here, we used a parabolic solid volume restraining as in the original implementation of the method (Zhao et al., 2021). The collective variables were: ρ, defined as the distance between the center of mass of the furosemide and the protein, τ, the parameter that defines the parabolic-solid shape of the volume (Zhao et al., 2021), θ, defined as the azimuthal angle of its orthogonal projection on the x-y plane (**Supplementary Figure SI3**). To guarantee a correct sampling for both the bound and the unbound state, we limited the restraining volume (and thus the CVs ranges) to include 1) the binding pose observed in crystal structure, 2) the neighboring regions, and 3) enough volume to observe the ligand being completely solvated (**Supplementary Figure SI4**). The protein-furosemide axis was aligned to the *x*-axis in our system. To avoid artifacts associated with periodic boundary conditions, we applied a restraining bias that kept the protein's center of mass to 10 Å or less from the simulation box center. To avoid unfolding problems due to volume bias, the protein backbone atoms, which are not inside the volume, were restrained to their initial positions so that the overall RMSD was smaller than 3 Å.

We applied the bias potential on the system along the defined CVs, setting the initial height of Gaussian hills to 0.287 kcal/mol and deposited every 1 ps. The Gaussian widths are 1 A˚, 0.04, and pi/8 for ρ, τ, θ, respectively. The bias factor was chosen to be 20. LV-MetaD for 650 ns. The last 100 ns trajectory was used for the reweighting procedure using the Tiwary-Parrinello estimator (Tiwary and Parrinello, 2015). The reweighting procedure allows us to compute the projection of the free energy landscape as a function of apt order parameters that define clearly the bound and unbound states. From this last free energy surface, it is possible to obtain furosemide's binding free energy. In our case, we choose to consider two variables: the distance between the protein and the furosemide centers of mass, and the number of H-bonds between the furosemide and the residues inside the volume, defined using the following switching function:

$$s_{ij} = \frac{1 - \left(\frac{r_{ij} - d_0}{r_0}\right)^n}{1 - \left(\frac{r_{ij} - d_0}{r_0}\right)^m}$$

Here we have $n = 8$ and $m = 12$, d_0 was set to 0 and $r_0 = 2.5$ A˚. The number of H-bonds is $\sum s_{ij}$. To evaluate the errors of the free energy, we used a block average analysis (**Supplementary Figure SI5**). In the lowest energy basin, each pose was equilibrated by 30ns of unbiased MD. MD and LV-MetaD simulations were carried out by GROMACS/2019.4 (Lindahl et al., 2001; Abraham et al., 2019) patched with PLUMED-2.5.2 (Tribello et al., 2014; Bonomi et al., 2019).

RESULTS AND DISCUSSION

The identification of ligand poses on NEET proteins may require approaches that go beyond straightforward molecular docking, as the ligand binds on the protein surface (and not to a binding site), close to a multinuclear iron site. Here we have used enhanced sampling methods to predict poses and affinity of furosemide (**Chart 1**) to the mitoNEET protein, similarly to what done by some of us in the case of a ligand binding to the surface of the prion protein, where the accuracy of our prediction was established by a comparison with NMR data (Kranjc et al., 2009). Our computational protocol profits also from an apt parametrization of the metal cluster recently developed by some of us (Pesce et al., 2017; Zuo et al., 2021).

Our protocol has involved 75 ns of molecular dynamics (MD, **Supplementary Figure SI6**) starting from the X-ray structure of oxidized mitoNEET in complex with furosemide (**Figure 2A**). After a short simulated annealing

procedure, the system was brought to the same conditions as the *in vitro* assays. The MD calculations are followed up by Localized Volume-based Metadynamics (Zhao et al., 2021) enhanced sampling method. These predict the free energy of furosemide unbinding in the canonical ensemble as a function of three apt collective variables (**Supplementary Figure SI3** and Methods for details). The simulations converged after 600 ns (see **Supplementary Figures SI7, SI8**). With the reweighting procedure (Tiwary and Parrinello, 2015), we find it convenient to plot the free energy as a function of the distance d of the centers of mass of the furosemide and of the [2Fe-2S] cluster, as well as the number N of furosemide/protein H-bonds and salt bridges.

Basin **I** is the absolute minimum, lower than about 2 kcal/mol than the local minima **II** and **III.** In **I**, the ligand features three poses with diverse orientations (**Ia-c).** In each pose the ligand is rather close to the cluster (0.77 nm < d < 0.95 nm) and exhibits extensive intramolecular interactions (5 < N < 9, **Figure 3**). This includes the salt bridge between the ligand and Nζ@K55 and the H-bond with Nε@H87 (**Supplementary Table SI2**) (**Figure 4**), present also in the X-ray structure (Geldenhuys et al., 2019). However**,** in **Ia-b,** the salt bridge involves both oxygen atoms and not only one atom as in the X-ray structure (**Figure 2**), and in **Ic,** the furosemide's carboxyl group forms a H-bond with T88 side chain. In all the minima shown here, the carboxy-NH intramolecular H-bond is maintained.

The orientations of the aromatic rings and the interactions of the sulfonamide group with the protein differ from those of the X-ray structure.

In **Ia**, by far the most populated conformer[2], the sulfonamide group forms a water mediated H-bond with Nζ@K68 (**Supplementary Table SI2**), while, as discussed above, it interacts with the protein from the adjacent asymmetric unit in the X-ray structure. The furan ring replaces its hydrophobic interactions with V70, present in the X-ray structure, with those with G85 and T88 (**Supplementary Table SI2**); the benzene ring, while keeping its hydrophobic interactions with P100, I102, replaces the interactions with V57 with those with V70 (**Supplementary Table SI2**). In **Ib**, the furan ring interacts with V57 and I102, while the benzene ring interacts with V70 and P100 and it also forms a π-π stacking interaction with H87 (**Supplementary Table SI2**). The sulfonamide and the carboxyl groups form water-mediated H-bonds with the C83 backbone unit[3] and the T88 side chain, respectively (**Supplementary Table SI2**). In **Ic**, the furan moiety forms hydrophobic contacts I102, V70, P100, the benzene ring is solvent-exposed.

30 ns MD starting from **Ia-c** shows that 1) binding poses **Ib-c** are transient and can interconvert into each other within a few ns (**Supplementary Figure SI9**). 2) **Ia** samples other orientations including the one found in the crystallographic pose (**Supplementary Figure SI10**), and this binding pose reproduces also the experimental electronic density (**Supplementary Figure SI11E**).[4] This variability results from the very shallow binding site as found in the mitoNEET and is already hinted at by challenges in resolving the electron density around the ligand's furan moiety (**Supplementary Figure SI11A**)[5]. The discrepancy between the presence of a unique binding pose and an ensemble of poses (including the X-ray one) in the simulations is attributed here to a packing effect in the crystal. Indeed, in the periodic system (crystal structure), the ligand features a H-bond with K55 of an image protein and this interaction obviously does not present in water solution. We can expect therefore that this interaction stabilizes a specific conformation, following the conformational selection hypothesis (Nussinov et al., 2014), while in water solution an ensemble of conformations may be present.

The free energy of binding/unbinding (7.7 ± 0.8 kcal/mol), from basin **I** to the fully solvated ligand is not too dissimilar from the experimental free energy of binding at the same temperature (5.8 kcal/mol) (**Supplementary Table SI3**).

Basin **II** is located a bit farther from the cluster than **I** (1.1 nm < d < 1.4 nm, **Figure 3**). It forms a smaller number of polar intermolecular interactions (5.2 < N < 6.7). It features two similarly populated poses (**IIa,b, Figure 4**). The H-bond between the carboxyl group and H87 is replaced by a salt bridge with K68 (in **IIa)** or by an H-bond with the solvent (in **IIb).** The salt bridge with K55 is maintained only in **IIb.** In **IIa,** it involves K104. The sulfonamide group forms H-bonds with V57 backbone and N53 in **IIb**. The furan ring forms hydrophobic interactions with V70 (**IIa**) and P54 (**IIb**), while the benzene ring with A59, I102 (**IIa**), V57 side chain (**IIb**). The aromatic rings are more solvent exposed than those in **I.** The higher solvation of the furosemide may account, at least in part, for the higher free energy of this minimum.

Basin **III** is located farther from the cluster than **II** (1.5 nm < d < 1.8 nm). It has lost all the intermolecular interactions in **I-II** (2.3 < N < 3.5, **Figure 3**). The carboxyl group is fully hydrated, while the sulfonamide forms direct and water-mediated H-bonds with V57 as well as a water-mediated H-bond with K55 (**Figure 4**). The aromatic rings have hydrophobic contacts with only P54 and are more solvent-exposed than basin **I** and **II**.

In conclusion, our simulations reproduce the pose of the X-ray structure (**Supplementary Figure SI9B**) and the experimental electronic density (**Supplementary Figure SI11E**), suggesting that this is only one among an ensemble of structures in water solution. The binding free energy values are quantitatively close to the experimental data. Thus, our paper is consistent with the available experimental data.

CONCLUSION

Here, we have investigated furosemide binding to mitoNEET in the oxidized state with the following goals in mind: 1) the comparison with the X-ray structure, which is in the oxidized state (Geldenhuys et al., 2019) and 2) to present an

[2]The populations for **Ia-c** are 66%, 19%, 15%, respectively.

[3]This cysteine is bound to the iron atom close to the solvent.

[4]For a direct comparison between X-ray and basins poses see **Supplementary Figure SI12**.

[5]The populations for **IIa** and **IIb** are 57% and 43%, respectively

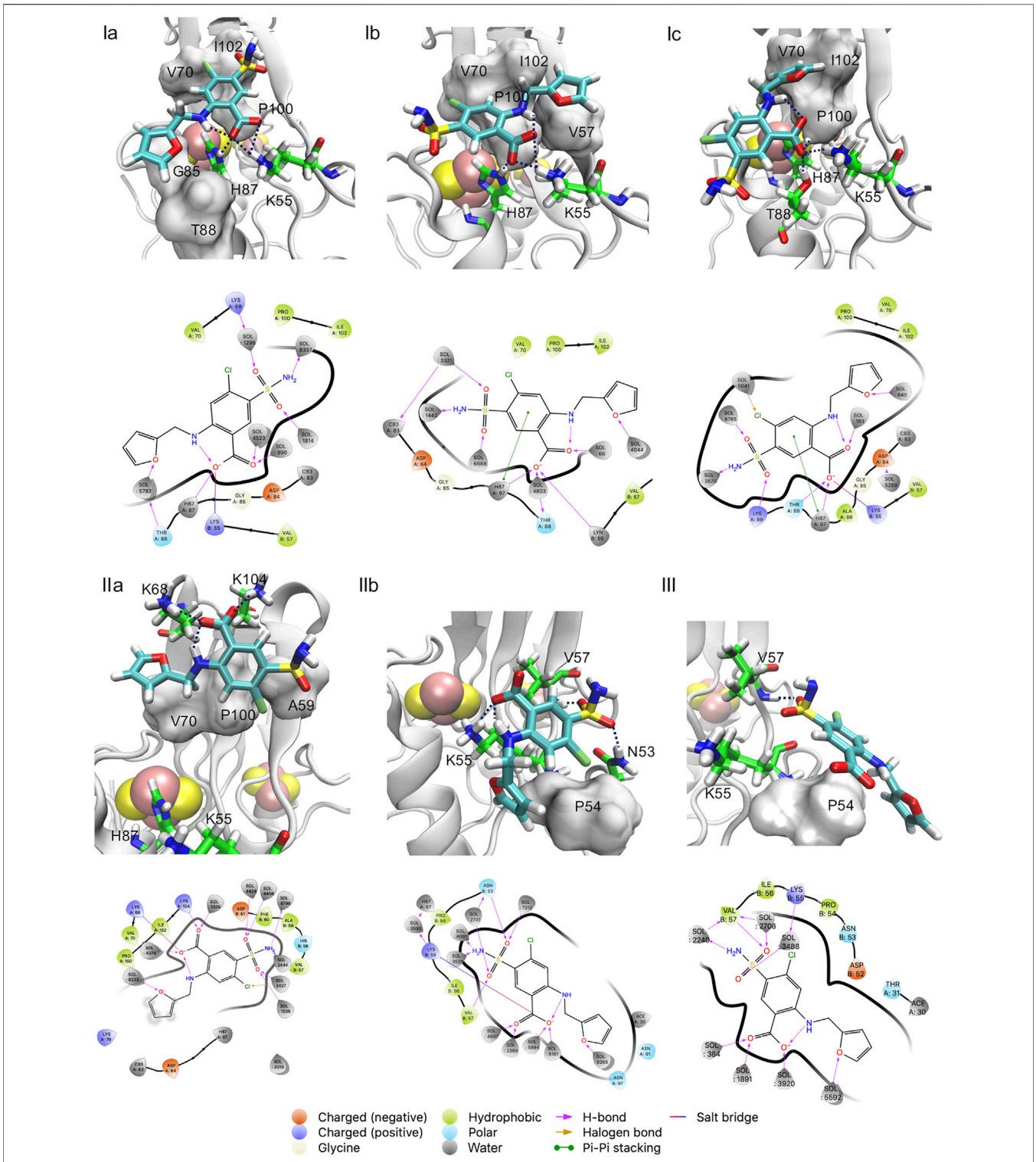

FIGURE 4 | (Ia–c, IIa,b, III) poses of **Figure 2**. Both the 3D structure and the ligand-protein interaction diagram are shown. H-bonds/salt bridges are drawn as dashed lines in the 3D structures.

advanced computational approach able to investigate, for the first time to the best of our knowledge, quantitatively ligand binding to human NEET proteins, a highly important pharmacological target. Our study suggests that the ligand binds to several isoenergetic poses in water solution, including the one emerging from the X-ray structure. The

latter pose is likely to have been selected because of crystal packing interactions. The calculations provide an estimate of the affinity which is fully compatible with that experimentally determined. Driven by the computational findings here, NMR and/or site-directed mutagenesis experiments in the binding regions, such as in those in (Kranjc et al., 2009) and (Zhou et al., 2010) for other ligands bound to protein surfaces, would be additional validations of our calculations.

Our protocol is very general and it emerges as a useful tool to predict binding affinity and multiple poses of ligands targeting human NEET proteins.

DATA AVAILABILITY STATEMENT

The raw data supporting the conclusion of this article will be made available by the authors, without undue reservation.

AUTHOR CONTRIBUTIONS

LH and JG performed the calculations and prepared figures and tables as well as helped in writing the manuscript. RC, PC, TN, ZS, KZ, JS, and GR wrote the paper with input from all authors. JS and PC supervised the project and gave valuable corrections.

FUNDING

PC, GR, and JS acknowledge the Deutsche Forschungsgemeinschaft (DFG) *via* the Research Training Group RTG2416 MultiSenses-MultiScales (368482240/GRK2416). KZ is supported by the Marie Skłodowska-Curie Grant agreement no. 765048. TN and LH are supported partially by the Vietnam National University–Hanoi grant number TXTCN.21.28.

ACKNOWLEDGMENTS

The authors acknowledge many fruitful discussions with Rachel Nechushtai. GR and PC acknowledge the European Union's Horizon 2020 Framework Programme for Research and Innovation under the Specific Grant Agreement No. 945539 (Human Brain Project SGA3).

SUPPLEMENTARY MATERIAL

The Supplementary Material for this article can be found online at: https://www.frontiersin.org/articles/10.3389/fcell.2022.886568/full#supplementary-material

REFERENCES

Abraham, M. J. V. d. S. D., Lindahl, E., and Hess, B. (2019). *GROMACS User Manual Version 2019.4 [Online]*. Available at: http://www.gromacs.org, Accessed 2022).

Adeshina, Y. O., Deeds, E. J., and Karanicolas, J. (2020). Machine Learning Classification Can Reduce False Positives in Structure-Based Virtual Screening. *Proc. Natl. Acad. Sci. U.S.A.* 117 (31), 18477–18488. doi:10.1073/pnas.2000585117

Åqvist, J. (1990). Ion-water Interaction Potentials Derived from Free Energy Perturbation Simulations. *J. Phys. Chem.* 94 (21), 8021–8024. doi:10.1021/j100384a009

Arif, W., Xu, S., Isailovic, D., Geldenhuys, W. J., Carroll, R. T., and Funk, M. O. (2011). Complexes of the Outer Mitochondrial Membrane Protein MitoNEET with Resveratrol-3-Sulfate. *Biochemistry* 50 (25), 5806–5811. doi:10.1021/bi200546s

Bai, F., Morcos, F., Sohn, Y.-S., Darash-Yahana, M., Rezende, C. O., Lipper, C. H., et al. (2015). The Fe-S Cluster-Containing NEET Proteins mitoNEET and NAF-1 as Chemotherapeutic Targets in Breast Cancer. *Proc. Natl. Acad. Sci. U.S.A.* 112(12), 3698–3703. doi:10.1073/pnas.1502960112

Barducci, A., Bussi, G., and Parrinello, M. (2008). Well-Tempered Metadynamics: A Smoothly Converging and Tunable Free-Energy Method. *Phys. Rev. Lett.* 100 (2), 020603. doi:10.1103/PhysRevLett.100.020603

Bonomi, M., Bussi, G., Camilloni, C., Tribello, G. A., Banáš, P., Barducci, A., et al. (2019). Promoting Transparency and Reproducibility in Enhanced Molecular Simulations. *Nat. Methods* 16 (8), 670–673. doi:10.1038/s41592-019-0506-8

Capelli, R., Carloni, P., and Parrinello, M. (2019). Exhaustive Search of Ligand Binding Pathways via Volume-Based Metadynamics. *J. Phys. Chem. Lett.* 10 (12), 3495–3499. doi:10.1021/acs.jpclett.9b01183

Chen, D., Menche, G., Power, T. D., Sower, L., Peterson, J. W., and Schein, C. H. (2007). Accounting for Ligand-Bound Metal Ions in Docking Small Molecules on Adenylyl Cyclase Toxins. *Proteins* 67 (3), 593–605. doi:10.1002/prot.21249

Colca, J. R., McDonald, W. G., Waldon, D. J., Leone, J. W., Lull, J. M., Bannow, C. A., et al. (2004). Identification of a Novel Mitochondrial Protein ("mitoNEET") Cross-Linked Specifically by a Thiazolidinedione Photoprobe. *Am. J. Physiology-Endocrinology Metab.* 286 (2), E252–E260. doi:10.1152/ajpendo.00424.2003

Conlan, A. R., Axelrod, H. L., Cohen, A. E., Abresch, E. C., Zuris, J., Yee, D., et al. (2009). Crystal Structure of Miner1: The Redox-Active 2Fe-2S Protein Causative in Wolfram Syndrome 2. *J. Mol. Biol.* 392 (1), 143–153. doi:10.1016/j.jmb.2009.06.079

Darash-Yahana, M., Pozniak, Y., Lu, M., Sohn, Y.-S., Karmi, O., Tamir, S., et al. (2016). Breast Cancer Tumorigenicity Is Dependent on High Expression Levels of NAF-1 and the Lability of its Fe-S Clusters. *Proc. Natl. Acad. Sci. U.S.A.* 113 (39), 10890–10895. doi:10.1073/pnas.1612736113

Deng, N., Forli, S., He, P., Perryman, A., Wickstrom, L., Vijayan, R. S. K., et al. (2015). Distinguishing Binders from False Positives by Free Energy Calculations: Fragment Screening against the Flap Site of HIV Protease. *J. Phys. Chem. B* 119 (3), 976–988. doi:10.1021/jp506376z

Dicus, M. M., Conlan, A., Nechushtai, R., Jennings, P. A., Paddock, M. L., Britt, R. D., et al. (2010). Binding of Histidine in the (Cys)3(His)1-Coordinated [2Fe–2S] Cluster of Human mitoNEET. *J. Am. Chem. Soc.* 132 (6), 2037–2049. doi:10.1021/ja909359g

Essmann, U., Perera, L., Berkowitz, M. L., Darden, T., Lee, H., and Pedersen, L. G. (1995). A Smooth Particle Mesh Ewald Method. *J. Chem. Phys.* 103 (19), 8577–8593. doi:10.1063/1.470117

Evans, D. J., and Holian, B. L. (1985). The Nose-Hoover Thermostat. *J. Chem. Phys.* 83 (8), 4069–4074. doi:10.1063/1.449071

Gao, D., Chen, Q., Zeng, Y., Jiang, M., and Zhang, Y. (2020). Applications of Machine Learning in Drug Target Discovery. *Cdm* 21 (10), 790–803. doi:10.2174/1567201817999200728142023

Geldenhuys, W. J., Yonutas, H. M., Morris, D. L., Sullivan, P. G., Darvesh, A. S., and Leeper, T. C. (2016). Identification of Small Molecules that Bind to the Mitochondrial Protein mitoNEET. *Bioorg. Med. Chem. Lett.* 26 (21), 5350–5353. doi:10.1016/j.bmcl.2016.09.009

Geldenhuys, W. J., Long, T. E., Saralkar, P., Iwasaki, T., Nuñez, R. A. A., Nair, R. R., et al. (2019). Crystal Structure of the Mitochondrial Protein mitoNEET Bound

to a Benze-Sulfonide Ligand. *Commun. Chem.* 2 (1), 77. doi:10.1038/s42004-019-0172-x

Guterres, H., and Im, W. (2020). Improving Protein-Ligand Docking Results with High-Throughput Molecular Dynamics Simulations. *J. Chem. Inf. Model.* 60 (4), 2189–2198. doi:10.1021/acs.jcim.0c00057

Haug, E. J., Arora, J. S., and Matsui, K. (1976). A Steepest-Descent Method for Optimization of Mechanical Systems. *J. Optim. Theor. Appl.* 19 (3), 401–424. doi:10.1007/bf00941484

Hess, B., Bekker, H., Berendsen, H. J. C., and Fraaije, J. G. E. M. (1997). LINCS: A Linear Constraint Solver for Molecular Simulations. *J. Comput. Chem.* 18 (12), 1463–1472. doi:10.1002/(sici)1096-987x(199709)18:12<1463::aid-jcc4>3.0.co;2-h

Jakalian, A., Jack, D. B., and Bayly, C. I. (2002). Fast, Efficient Generation of High-Quality Atomic Charges. AM1-BCC Model: II. Parameterization and Validation. *J. Comput. Chem.* 23 (16), 1623–1641. doi:10.1002/jcc.10128

Jorgensen, W. L., Chandrasekhar, J., Madura, J. D., Impey, R. W., and Klein, M. L. (1983). Comparison of Simple Potential Functions for Simulating Liquid Water. *J. Chem. Phys.* 79 (2), 926–935. doi:10.1063/1.445869

Kranjc, A., Bongarzone, S., Rossetti, G., Biarnés, X., Cavalli, A., Bolognesi, M. L., et al. (2009). Docking Ligands on Protein Surfaces: The Case Study of Prion Protein. *J. Chem. Theor. Comput.* 5 (9), 2565–2573. doi:10.1021/ct900257t

Kusminski, C. M., Chen, S., Ye, R., Sun, K., Wang, Q. A., Spurgin, S. B., et al. (2016). MitoNEET-Parkin Effects in Pancreatic α- and β-Cells, Cellular Survival, and Intrainsular Cross Talk. *Diabetes* 65 (6), 1534–1555. doi:10.2337/db15-1323

Landry, A. P., and Ding, H. (2014). Redox Control of Human Mitochondrial Outer Membrane Protein MitoNEET [2Fe-2S] Clusters by Biological Thiols and Hydrogen Peroxide. *J. Biol. Chem.* 289 (7), 4307–4315. doi:10.1074/jbc.M113.542050

Li, Y., Han, L., Liu, Z., and Wang, R. (2014). Comparative Assessment of Scoring Functions on an Updated Benchmark: 2. Evaluation Methods and General Results. *J. Chem. Inf. Model.* 54 (6), 1717–1736. doi:10.1021/ci500081m

Limongelli, V., Bonomi, M., and Parrinello, M. (2013). Funnel Metadynamics as Accurate Binding Free-Energy Method. *Proc. Natl. Acad. Sci. U.S.A.* 110 (16), 6358–6363. doi:10.1073/pnas.1303186110

Lindahl, E., Hess, B., and van der Spoel, D. (2001). GROMACS 3.0: a Package for Molecular Simulation and Trajectory Analysis. *J. Mol. Model.* 7 (8), 306–317. doi:10.1007/s008940100045

Lindorff-Larsen, K., Piana, S., Palmo, K., Maragakis, P., Klepeis, J. L., Dror, R. O., et al. (2010). Improved Side-Chain Torsion Potentials for the Amber ff99SB Protein Force Field. *Proteins* 78 (8), 1950–1958. doi:10.1002/prot.22711

Madhavi Sastry, G., Adzhigirey, M., Day, T., Annabhimoju, R., and Sherman, W. (2013). Protein and Ligand Preparation: Parameters, Protocols, and Influence on Virtual Screening Enrichments. *J. Comput. Aided. Mol. Des.* 27 (3), 221–234. doi:10.1007/s10822-013-9644-8

Marelli, U. K., Frank, A. O., Wahl, B., La Pietra, V., Novellino, E., Marinelli, L., et al. (2014). Receptor-Bound Conformation of Cilengitide Better Represented by its Solution-State Structure Than the Solid-State Structure. *Chem. Eur. J.* 20 (44), 14201–14206. doi:10.1002/chem.201403839

Marjault, H.-B., Zuo, K., Mittler, R., Carloni, P., and Nechushtai, R. (2021). "Chapter 21 - NEET Proteins as Novel Drug Targets for Mitochondrial Dysfunction," in *Clinical Bioenergetics*. Editor S. Ostojic (Academic Press), 477–488. doi:10.1016/b978-0-12-819621-2.00021-8

Nechushtai, R., Karmi, O., Zuo, K., Marjault, H.-B., Darash-Yahana, M., Sohn, Y.-S., et al. (2020). The Balancing Act of NEET Proteins: Iron, ROS, Calcium and Metabolism. *Biochim. Biophys. Acta (Bba) - Mol. Cel Res.* 1867 (11), 118805. doi:10.1016/j.bbamcr.2020.118805

Nussinov, R., Ma, B., and Tsai, C.-J. (2014). Multiple Conformational Selection and Induced Fit Events Take Place in Allosteric Propagation. *Biophysical Chem.* 186, 22–30. doi:10.1016/j.bpc.2013.10.002

Paddock, M. L., Wiley, S. E., Axelrod, H. L., Cohen, A. E., Roy, M., Abresch, E. C., et al. (2007). MitoNEET Is a Uniquely Folded 2Fe-2S Outer Mitochondrial Membrane Protein Stabilized by Pioglitazone. *Proc. Natl. Acad. Sci. U.S.A.* 104 (36), 14342–14347. doi:10.1073/pnas.0707189104

Parrinello, M., and Rahman, A. (1981). Polymorphic Transitions in Single Crystals: A New Molecular Dynamics Method. *J. Appl. Phys.* 52 (12), 7182–7190. doi:10.1063/1.328693

Pesce, L., Calandrini, V., Marjault, H.-b., Lipper, C. H., Rossetti, G., Mittler, R., et al. (2017). Molecular Dynamics Simulations of the [2Fe-2S] Cluster-Binding Domain of NEET Proteins Reveal Key Molecular Determinants that Induce Their Cluster Transfer/Release. *J. Phys. Chem. B* 121 (47), 10648–10656. doi:10.1021/acs.jpcb.7b10584

Sousa da Silva, A. W., and Vranken, W. F. (2012). ACPYPE - AnteChamber PYthon Parser interfacE. *BMC Res. Notes* 5 (1), 367. doi:10.1186/1756-0500-5-367

Tiwary, P., and Parrinello, M. (2015). A Time-independent Free Energy Estimator for Metadynamics. *J. Phys. Chem. B* 119 (3), 736–742. doi:10.1021/jp504920s

Tribello, G. A., Bonomi, M., Branduardi, D., Camilloni, C., and Bussi, G. (2014). PLUMED 2: New Feathers for an Old Bird. *Comp. Phys. Commun.* 185 (2), 604–613. doi:10.1016/j.cpc.2013.09.018

Wang, J., Wolf, R. M., Caldwell, J. W., Kollman, P. A., and Case, D. A. (2004). Development and Testing of a General Amber Force Field. *J. Comput. Chem.* 25 (9), 1157–1174. doi:10.1002/jcc.20035

Zhao, Q., Capelli, R., Carloni, P., Lüscher, B., Li, J., and Rossetti, G. (2021). Enhanced Sampling Approach to the Induced-Fit Docking Problem in Protein-Ligand Binding: The Case of Mono-ADP-Ribosylation Hydrolase Inhibitors. *J. Chem. Theor. Comput.* 17 (12), 7899–7911. doi:10.1021/acs.jctc.1c00649

Zhou, T., Lin, J., Feng, Y., and Wang, J. (2010). Binding of Reduced Nicotinamide Adenine Dinucleotide Phosphate Destabilizes the Iron–Sulfur Clusters of Human MitoNEET. *Biochemistry* 49 (44), 9604–9612. doi:10.1021/bi101168c

Zuo, K., Marjault, H.-B., Bren, K. L., Rossetti, G., Nechushtai, R., and Carloni, P. (2021). The Two Redox States of the Human NEET Proteins' [2Fe-2S] Clusters. *J. Biol. Inorg. Chem.* 26 (7), 763–774. doi:10.1007/s00775-021-01890-8

Conflict of Interest: The authors declare that the research was conducted in the absence of any commercial or financial relationships that could be construed as a potential conflict of interest.

Publisher's Note: All claims expressed in this article are solely those of the authors and do not necessarily represent those of their affiliated organizations or those of the publisher, the editors, and the reviewers. Any product that may be evaluated in this article, or claim that may be made by its manufacturer, is not guaranteed or endorsed by the publisher.

frontiers | Frontiers in Cell and Developmental Biology

MINI REVIEW
published: 02 May 2022
doi: 10.3389/fcell.2022.871877

Wilson Disease: Update on Pathophysiology and Treatment

Som Dev[1†], *Robert L. Kruse*[2], *James P. Hamilton*[3] *and Svetlana Lutsenko*[1*†]

[1]Department of Physiology, Johns Hopkins Medical Institutes, Baltimore, MD, United States, [2]Department of Pathology, Brigham and Women's Hospital, Boston, MA, United States, [3]Department of Medicine, Johns Hopkins Medical Institutes, Baltimore, MD, United States

Wilson disease (WD) is a potentially fatal genetic disorder with a broad spectrum of phenotypic presentations. Inactivation of the copper (Cu) transporter ATP7B and Cu overload in tissues, especially in the liver, are established causes of WD. However, neither specific ATP7B mutations nor hepatic Cu levels, alone, explain the diverse clinical presentations of WD. Recently, the new molecular details of WD progression and metabolic signatures of WD phenotypes began to emerge. Studies in WD patients and animal models revealed the contributions of non-parenchymal liver cells and extrahepatic tissues to the liver phenotype, and pointed to dysregulation of nuclear receptors (NR), epigenetic modifications, and mitochondria dysfunction as important hallmarks of WD pathogenesis. This review summarizes recent advances in the characterization of WD pathophysiology and discusses emerging targets for improving WD diagnosis and treatment.

Keywords: copper, liver, Wilson disease, ATP7B, nuclear receptor

OPEN ACCESS

Edited by:
Simone Ciofi Baffoni, University of Florence, Italy

Reviewed by:
Roman Polishchuk, Telethon Institute of Genetics and Medicine (TIGEM), Italy
Rosanna Squitti, San Giovanni di Dio Fatebenefratelli Center (IRCCS), Italy

***Correspondence:**
Svetlana Lutsenko
lutsenkol@jhmi.edu

[†]*These authors have contributed equally to this work*

Specialty section:
This article was submitted to Cellular Biochemistry, a section of the journal Frontiers in Cell and Developmental Biology

Received: *08 February 2022*
Accepted: *30 March 2022*
Published: *02 May 2022*

Citation:
Dev S, Kruse RL, Hamilton JP and Lutsenko S (2022) Wilson Disease: Update on Pathophysiology and Treatment. Front. Cell Dev. Biol. 10:871877. doi: 10.3389/fcell.2022.871877

INTRODUCTION

Wilson disease (WD) is an autosomal-recessive disorder of copper (Cu) metabolism caused by inborn mutations in the Cu(I) transporting ATPase beta polypeptide (ATP7B). Mutations in ATP7B disrupt Cu homeostasis, causing Cu accumulation in the liver and other tissues (Członkowska et al., 2018). Hepatic manifestations of WD range from asymptomatic elevation of hepatic transaminases to fibrosis, cirrhosis, and acute liver failure (Członkowska et al., 2018). Although WD is a monogenic disorder, the time of disease onset and specific presentations vary significantly, which points to existence of modifying factors (Schiefermeier et al., 2000; Ferenci 2014; Ferenci et al., 2019). Variable clinical presentations make the diagnosis, treatment and the mechanistic understanding of WD challenging (Roberts 2018; Stättermayer et al., 2019).

WD has an asymptomatic stage, when hepatic Cu is already elevated, but liver morphology and function are not yet significantly compromised owning to an upregulation of Cu-sequestering metallothioneins and an increased glutathione synthesis. With time, accumulating metabolic and transcriptional changes, oxidation and other posttranslational modifications overwhelm these protective mechanisms, triggering histologic abnormalities, increased autophagy, and diminishing liver function, without further increases in hepatic copper. Down-regulation of hepatic CTR1 and hepatocyte death cause Cu to be diverted from the liver into the circulation, accelerating Cu accumulation in other tissues (Gray et al., 2012) and triggering neurological and psychiatric disturbances (Członkowska et al., 2018). While this sequence of events in WD has long been established, the molecular basis of underlying pathologic changes at each step of the disease are only now emerging; this progress has been accelerated by the availability of several animal models of WD (Reed et al., 2018).

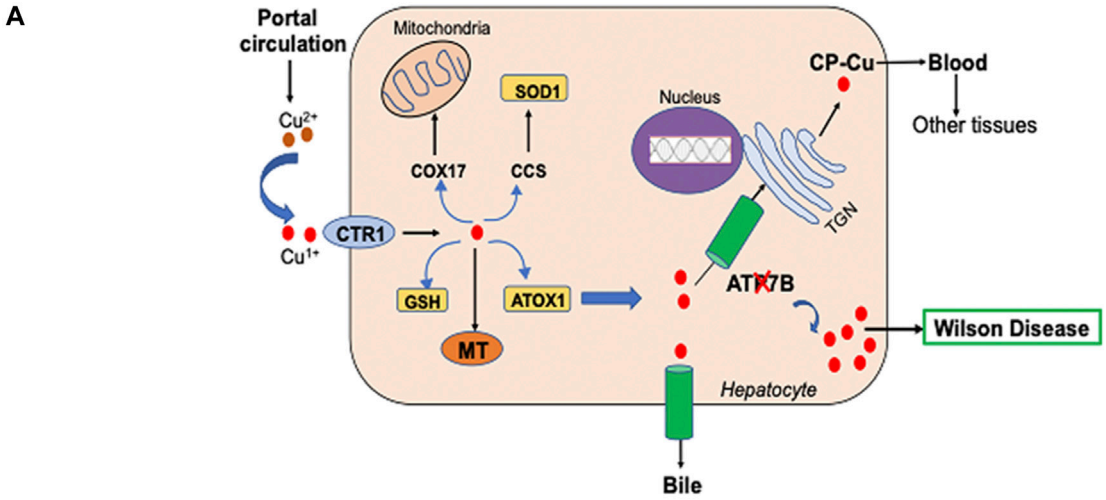

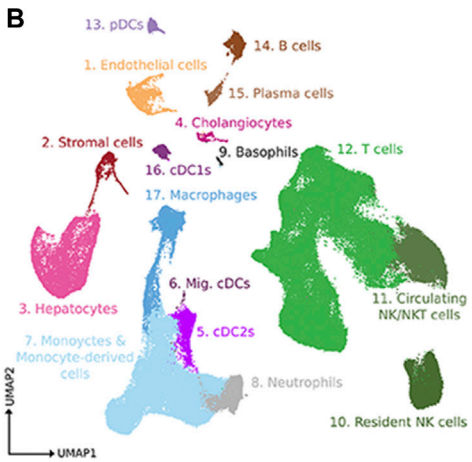

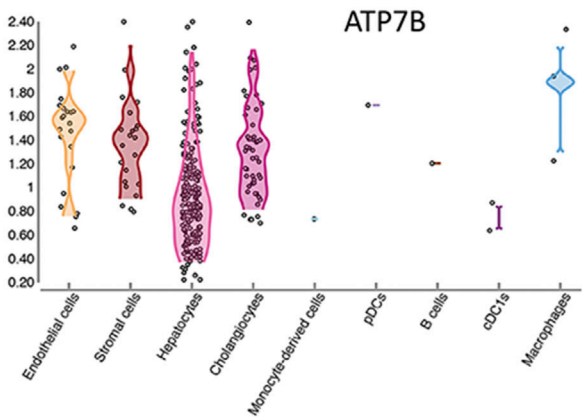

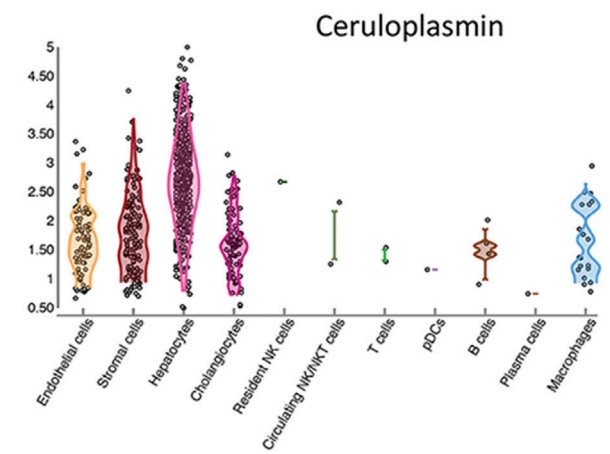

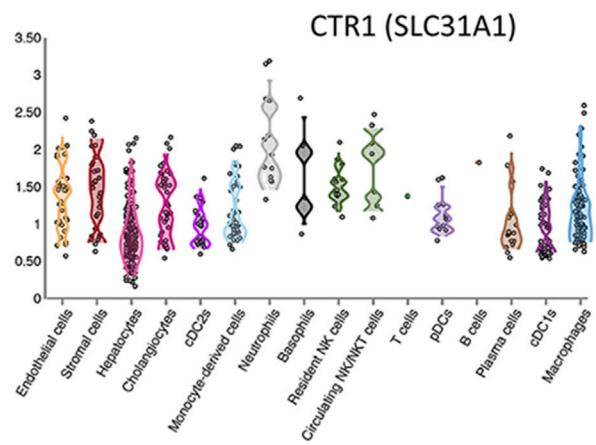

FIGURE 1 | Cu homeostasis in liver **(A)** and Cu-handling proteins in liver cells **(B). (A)** Cu enters liver via portal circulation and transported into liver cells primarily by the high affinity uptake protein, CTR1. Cytosolic Cu chaperones shuttle Cu to specific intracellular targets; CCS transports Cu to SOD1, ATOX1 - to the Cu-transporting ATPase ATP7B. ATP7B transports Cu into the trans-Golgi network (TGN) for incorporation into ceruloplasmin (CP) and to the apical membrane for excretion. Inactivation of ATP7B causes Cu overload, which manifests clinically as WD (ATP7B-ATPase Cu(I) transporting beta polypeptide; CTR1-high affinity Cu uptake protein 1; MT-Metallothionein; GSH-Glutathione, ATOX1-antioxidant protein 1; SOD1-Superoxide dismutase; CCS-Cu Chaperone for SOD, COX17-Cytochrome C oxidase) (Lutsenko 2016; Członkowska et al., 2018). **(B)** Expression of ATP7B, CP and CTR in liver cells. The figure is generated using Liver Cell Atlas (https://www.livercellatlas.org/), which aggregates single cells sequencing data for human and animal livers.

Animal studies demonstrate that multiple cellular compartments (nuclei, mitochondria, lysosomes, autophagosomes) participate in hepatocytes response to Cu overload, and multiple pathways are involved. Inhibition of nuclear receptors (Wooton-Kee et al., 2015; Hamilton et al., 2016; Wooton-Kee et al., 2020), epigenetic modifications (Mordaunt et al., 2018; Mordaunt et al., 2019; Sarode et al., 2021) and mitochondria dysfunction (Roberts et al., 2008; Zischka et al., 2011) have been identified as important hallmarks of the disease. Increased autophagy was observed in $Atp7b^{-/-}$ deficient cells and in the livers of WD patients (Polishchuk et al., 2019). The metabolomic analysis of WD patients' serum suggested existence of distinct metabolic profiles differentiating WD from other liver disorders as well as WD with different phenotypic manifestations (Sarode et al., 2019; Azbukina et al., 2020). The contribution of miRNA and long non-coding RNA to pathogenesis of WD appears likely (Zhang et al., 2021), but remains understudied. Significant gender-related differences in Cu levels, metabolic, and fibroinflammatory changes are observed in human WD and WD mouse models emphasizing the importance of including both sexes in testing new therapeutic approaches (Litwin et al., 2012; Li et al., 2018; Gottlieb et al., 2022). In this review, we summarize recent developments in understanding of WD pathogenesis and progress towards the next generation of diagnostics and therapeutics.

Copper Homeostasis in the Liver

Cu is essential micronutrient for human growth and development, and liver is the major Cu homeostatic organ in humans and animals (Roberts and Sarkar 2008). Cu homeostasis in the liver is maintained by the network of proteins, which include transmembrane Cu transporters (CTR1 and ATP7B), cytosolic Cu carriers (chaperones), Cu storage proteins (metallothioneins) and Cu-requiring enzymes (**Figure 1A**). Several liver enzymes use Cu for their activity: the ferroxidase ceruloplasmin (CP), an abundant Cu-binding protein secreted by hepatocytes into the blood (Linz and Lutsenko 2007), cytochrome c oxidase (mitochondrial respiration), superoxide dismutase 1 (free radical defense), factor VIII (blood clotting) and other less abundant proteins.

ATP7B is central for liver Cu homeostasis. It delivers Cu from the cytosol to CP in the *trans*-Golgi network; and when Cu is elevated, ATP7B traffics towards the apical membrane to facilitate Cu export into the bile. Inactivation of ATP7B disrupts these processes, causing Cu accumulation in the liver and secretion of apo-CP, which is unstable and inactive (Merle et al., 2010; Merle et al., 2009). It is firmly established that ATP7B is expressed in hepatocytes; however, single cell sequencing studies revealed additional information about the Cu-handling machinery of various cells types in the liver. Based on CTR1 expression, hepatocytes, macrophages, cholangiocytes, and stromal cells are the main importers and users of Cu (**Figure 1B**). In addition to hepatocytes, ATP7B is present in cholangiocytes, endothelial, and stromal cells and its expression parallels expression of CP (**Figure 1B**). The ATP7B homologue, ATP7A, which was thought not to be expressed in the liver, has now been found in most cells, including hepatocytes (https://www.livercellatlas.org/). Although ATP7A does not compensate for the loss of ATP7B function, ATP7A can be induced in the liver in response to signaling from other tissues and facilitate Cu export (Kim et al., 2010). The signaling molecule that upregulates hepatic ATP7A remains elusive, but identification of this molecule may be the first step towards de-coppering liver in WD using endogenous means.

Wilson Disease Liver Phenotype is Determined by Copper Misbalance in Different Cell Types in the Liver

Comparison of mice with a global inactivation of Atp7b (as in human WD) and hepatocyte-specific inactivation (Atp7b△Hep) highlighted the contribution of various liver cell types to WD pathogenesis (Muchenditsi et al., 2017; Muchenditsi et al., 2021). The Atp7b△Hep mice accumulate Cu in the liver, produce apo-CP, but show no ballooning (apoptotic) hepatocytes nor inflammation, which are commonly seen in global Atp7b knockouts ($Atp7b^{-/-}$ mice) and in human WD. The only obvious pathology in Atp7b△Hep animals is liver steatosis (Muchenditsi et al., 2017). This finding harmonizes with clinical data showing steatosis to be an early disease manifestation and further suggests that the development of inflammatory responses in WD may depend on the Cu status of non-parenchymal liver cells. Indeed, non-parenchymal liver cells in Atp7b△Hep mice have normal Cu levels in contrast to elevated Cu in non-parenchymal cells in $Atp7b^{-/-}$ mice (Muchenditsi et al., 2017). Proteomics studies show that when Atp7b inactivation is limited to hepatocytes, the liver upregulates proteins involved in redox balance, mitochondria function, amino-acid and lipid metabolism; all of which compensates for functional deficiencies caused by Cu overload (Muchenditsi et al., 2021). This compensatory capacity is lost in $Atp7b^{-/-}$ mice leading to significant metabolic disturbances and activation of energy sensor, AMP kinase (Wooton-Kee et al., 2020). In addition, inactivation of ATP7B in the intestine dysregulates the dietary fat processing and chylomicron assembly and may exacerbate metabolic disturbances in the liver (Pierson et al., 2018). Further studies are needed to better understand the role of non-parenchymal liver cells and extrahepatic tissues in human WD.

Epigenetics and Modifying Factors in Wilson Disease

Lack of strong genotype-to-phenotype correlations in WD reflects the influence of environmental and epigenetic factors. Several genetic modifiers of WD are proposed based on studies of gene allele frequencies in WD patients along with dietary factors that may influence the disease progression (reviewed in (Kieffer and Medici 2017; Medici and Weiss 2017)). In the rat model of WD, high calorie diet accelerated liver failure (Einer et al., 2019), whereas in the mouse model of WD on a similar diet, inflammatory response was diminished in favor of steatosis (Wooton-Kee et al., 2020; Gottlieb et al., 2022). This finding

in mice could be linked to activation of mTORC1 and inhibition of autophagy, and further studies can test this hypothesis. Studies in animals also suggest that natural differences in levels of Cu-chelating metallothioneins MT1/2 may result in different capacities to buffer accumulated Cu and thus modulate liver response to excess Cu (Muchenditsi et al., 2021). In the future, it would be interesting to determine whether the levels of metallothioneins in humans can be used as predictors of the timing of disease onset and progression. ATOX1, COMMD1, and XIAP were shown not to contribute significantly to the WD phenotype (Kieffer and Medici 2017), whereas polymorphisms in PNPLA3, a lipase involved in hepatocyte triglyceride metabolism, were associated with increased hepatic steatosis in WD (Stättermayer et al., 2015). Hydroxysteroid 17-β dehydrogenase polymorphisms in WD appear to have protection against acute liver failure (Pop et al., 2021).

Epigenetic modifications influence gene expression without altering DNA sequences. The best understood epigenetic mechanisms are DNA methylation (Jones 2012) and acetylation (Ganesan et al., 2009). Methylation involves the addition of methyl groups to cytosine bases, typically at CpG sites (Bender 2004) and is mediated by DNA methyltransferases (Okano et al., 1999). Recent studies provide strong evidence for contribution of epigenetics to WD pathogenesis. Aberrant DNA methylation and abnormal 1-carbon metabolism is reported in WD patients and animal models of WD (Medici and LaSalle 2019; Mordaunt et al., 2019). DNA methylation is highly dependent on the availability of the universal methyl donor S-adenosyl-methionine (SAM). Cu inhibits the activity of S-adenosyl-L-homocysteine hydrolase (Li et al., 2007), a key enzyme that regulates the amount of SAM available for methylation, which may in part explain hypomethylation, although the overall mechanism is likely to be more complex. SAM levels are also affected by dietary uptake of folate, vitamin B12, methionine, betaine and choline, as well as genetic variations in enzyme mediating one-carbon metabolism (Niculescu and Zeisel 2002). Dietary supplementation of methyl donor such as betaine (Medici et al., 2013) or choline (Medici et al., 2016) demonstrated that changes in a global DNA methylation status in Atp7b-deficient liver can be reversed.

Studies of DNA methylation in human WD revealed differentially methylated region (DMRs) in liver samples (Mordaunt et al., 2019). The WD-specific DMRs were associated with genes enriched in lipid, folate metabolism and inflammatory response. Genes associated with response to oxidative stress (such as Hif1, Gstp1, and thioredoxin) were differentially methylated in human WD liver (Mordaunt et al., 2018). DNA methylation signatures could be one of the potential biomarkers and/or therapeutic targets.

Histone acetylation (HA) is a dynamic epigenetic modification that regulates transcription, and it is also impaired in murine WD (Sarode et al., 2021). HA is controlled by histone acetyltransferases and deacetylases (Ganesan et al., 2009). A significant decrease in histone deacetylases 4 and 5 (HDAC4/5) is observed in the tx-j mouse model of WD (an inbred mouse strain with a missense mutation in Atp7b) (Sarode et al., 2021). H3ac, H3K9ac, and H3K27ac levels are increased in livers of tx-j mice and supplementing these animals with diets enriched with methyl donors or Cu chelation restored levels of HDAC4/5 (Sarode et al., 2021). These findings may help to understand epigenetic modifications (acetylation and methylation) observed in WD and other liver disorders with similar presentation (Dev and Hamilton 2021).

Nuclear Receptor Dysfunction in Wilson Disease

Nuclear receptors (NR) are ligand dependent transcription factors that regulate gene expression of multiple signaling pathways. Regardless of clinical presentation, hepatic Cu is a hallmark of WD and it causes NR inhibition (Wooton-Kee et al., 2015). Defects in NR signaling alter lipid metabolism in WD patients and Atp7b$^{-/-}$ mice (Wilmarth et al., 2012; Wooton-Kee et al., 2015; Hamilton et al., 2016). Reduced activity of LXR, FXR, RXRα, HNF4α, LRH-1 and PPARα link nuclear receptor dysfunction to WD (Nagasaka et al., 2012; Wooton-Kee et al., 2015; Wooton-Kee et al., 2020). Alterations in NR activity differ at different stages of WD. LXR/RXR was identified as one of the major targets of elevated Cu, especially early in the disease (Hamilton et al., 2016). In the mouse model of WD, LXR is inhibited at 6 weeks after birth, which is an asymptomatic stage of the disease (Hamilton et al., 2016), and other NR receptors become dysregulated as the disease progress (Nagasaka et al., 2012; Wilmarth et al., 2012; Wooton-Kee et al., 2015). Cu does not alter LXR protein levels or blocks its ability to bind substrates. Accordingly, treatment with a LXR agonist (in Atp7b$^{-/-}$ WD mice) prevents injury even in the presence of high Cu (Hamilton et al., 2016). Further studies are needed to determine the contribution of LXR and other NR dysfunction to inflammation and fibrosis, especially in humans. The activity of nuclear receptors in Atp7b$^{-/-}$ liver may reflect a complex interplay of metabolites generated by the Cu-altered enzymes as well as transcriptional activities of NRs *per se*. For example, copper induced oxidative stress and its downstream effect on generation of LXR ligands and antagonists is a possible explanation for downregulation of LXR signaling. Studies with LXR agonists in WD models will better define LXR dependent pathways in WD and may lead to new therapies targeting these pathways (see below).

Available and Emerging Treatments

In WD, phenotypic heterogeneity and lack of unique manifestations can present diagnostic and treatment challenges. Current treatments include Cu chelation, zinc salts, and liver transplantation. Cu chelation is the standard-of care therapy for WD and provides a significant benefit for most patients, especially if initiated early (Czlonkowska et al., 2014). D-penicillamine and Trientine are both approved for use in WD by most regulatory drug agencies, while Tetrathiomolybdate is approved for use in Europe and in a Phase III trial in the United States. Zinc acetate and other zinc salts regulate body Cu balance by presumably decreasing Cu absorption (Czlonkowska et al., 2014). Zinc salts are typically used in pre-symptomatic patients, and as a maintenance drug after chelation. Combination of chelation and zinc salts is common in

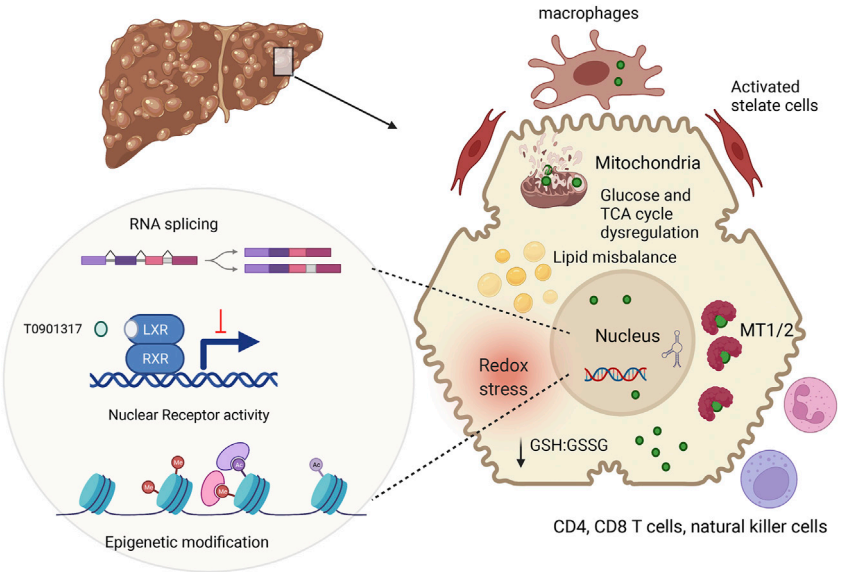

FIGURE 2 | Summary of main pathologic changes in WD liver. ATP7B mutations result in hepatic accumulation of copper (green circle). In the cytosol, Cu is sequestered by metallothioneins (MT1/2), whereas excess Cu causes glutathione oxidation (lower GSH:GSSG ration), contributing to redox stress. Cu elevation in nuclei, alters RNA processing, including splicing (Burkhead et al., 2011) inhibits NR function and induces epigenetic changes. Downstream effects include dysregulation of metabolic profiles in hepatocytes. Hepatocyte injury and possibly Cu accumulation in non-parenchymal cells stimulates immune cells and stellate cells, resulting in inflammation and fibrosis. The figure was generated using BioRender.

clinical practice, but not well studied. Despite proven benefits, current therapies have limitations, including side effects, poor compliance, high cost (up to $300,000 per yer), and potential for neurological decompensation (Merle et al., 2007; Schilsky et al., 2015). A significant percentage of WD patients with primarily neurologic manifestations do not respond well to treatment and these patients are at high risk for deterioration (Mohr and Weiss 2019). Monitoring Cu levels on treatment requires calculation of non-ceruloplasmin bound copper content in serum, which can be challenging. Novel methods of measuring free copper using anion-exchange chromatography coupled to triple quadrupole inductively coupled plasma mass spectroscopy are in development and look very promising (Solovyev et al., 2020).

In WD patients with acute liver failure, liver transplantation remains the only treatment option. Recent studies in the rat model of WD, found that methanobactin, a peptide produced by proteobacterium Methylosinus *trichosporium*, can be successfully used to remove excess Cu from mitochondria, decrease liver histopathology, and prevent liver failure (Lichtmannegger et al., 2016). Mitochondria disfunction is one of the important hallmarks of WD in human and animals (Sternlieb 1968; Roberts et al., 2008; Zischka et al., 2011), and therefore these pre-clinical results are significant. At the same time, developing precise dosing and a treatment regimen may be challenging, because methanobactin has high affinity for Cu and un-intended over-depletion of Cu in the mitochondria may disrupt the respiratory chain and be as harmful as Cu overload. Short-term treatment with subsequent zinc maintenance could be considered. Methanobactin has not yet been studied in humans.

Since dysregulation of nuclear receptors, especially LXR and FXR, contribute significantly to WD phenotype (see above), targeting these receptors, could be an attractive alternative option for patients who do not respond or poorly tolerate Cu chelation. Strong evidence exists that LXR is inhibited in Atp7b$^{-/-}$ liver, and that treatment with the LXR agonist T0901317 significantly delays the pathology onset and improves liver function in mice (Hamilton et al., 2016). However, in pre-clinical studies unrelated to WD, T0901317 was shown to induce hepatic steatosis and hypertriglyceridemia making it unsuitable candidate for treating WD. Further studies are needed to clarify the usefulness of this and/or other LXR agonists for treating human WD.

An exciting potential treatment for WD is delivering a functional ATP7B gene (cDNA) into WD patients. While the premise of gene therapy for WD is straightforward, there are two major hurdles for application to WD. The first consideration is that WD is a systemic disease with ATP7B expression in multiple cell types. While gene therapy vectors can be delivered systemically and enter multiple cell types, the majority of viral vectors and resultant expression resides in the liver (Wang et al., 2019). Thus, current WD gene therapy should primarily be considered a liver-specific correction of the disorder. While this liver-specific expression is a limitation, case reports of liver transplantation reversing neurologic WD suggest that liver-specific expression could be sufficient for some WD patients (Catana and Medici 2012; Poujois et al., 2020). The second consideration is that the cDNA for ATP7B is large (approximately 4.4 kilobases, even without the promoter and

polyA sequences), and when the full-length ATP7B packaged into the most common gene therapy vector, adeno-associated virus (AAV), the production yields of virus are low (Murillo et al., 2016). To address this problem, miniature ATP7B (miniATP7B) was developed by deleting the first four metal binding domains from ATP7B (Leng et al., 2019; Murillo et al., 2019). The miniATP7B was shown *in vitro* to have ATP7B activity (Leng et al., 2019; Murillo et al., 2019); however, precise intracellular regulation is lost when the first 4 metal-binding domains are deleted (Jayakanthan et al., 2017).

The most successful WD gene therapy studies have used AAV vectors in WD mouse models. Using liver-specific promoters, initial studies found that administration of AAV before the onset of liver pathology was effective for partial (Greig et al., 2019) or full disease (Murillo et al., 2016) reversal. Higher doses of AAV are required if liver injury is already present, which would be the case in most WD patients (Murillo et al., 2019), and presence of fibrosis is especially challenging. Concerning the delivery efficiency required to reverse WD, one study found that approximately 20% hepatocyte expression of ATP7B could reverse all markers of WD. It remains unclear whether it is sufficient to correct Atp7b in hepatocytes alone or is correction in non-parenchymal liver cells also needed, and the applicability of this approach in humans.

Two Phase I/II AAV gene therapy trials are currently underway for WD (NCT04537377, Vivet Therapeutics; NCT04884815, Ultragenyx). Translating efficacy of gene therapy in mice to human patients has proved challenging, thus success is not ensured. For example, gene therapy for hemophilia results in a 100-fold loss in gene expression per AAV dose (Nathwani et al., 2006; Nathwani et al., 2011). Thus, significantly higher doses may be required in WD patient trials versus WD mouse models. Another concern is that the liver injury and hepatocyte turnover in WD could lead to dilution of the episomal AAV vector as cells divide, raising uncertainty of how long the AAV therapeutic effect may last. These questions will hopefully be answered once the first data is released from these clinical trials.

An alternative strategy to AAV is ATP7B-carying lentiviruses administered into WD mice during gestation. This method of gene treatment improved liver histology and hepatic Cu content was reduced, but did not uniformly normalize Cu levels and variable ATP7B expression was observed (Roybal et al., 2012). CRISPR-mediated correction could be considered for WD, but the hundreds of different mutations in ATP7B and their often compound heterozygous nature complicate site-specific correction with gene editing (Pöhler et al., 2020).

In conclusion, recent studies in WD patients, murine WD models, and cell lines with inactivated ATP7B have significantly expended and deepened our understanding of WD pathophysiology (**Figure 2**). These new findings suggest that specific biomarkers and improved treatments can eventually be developed for WD with different disease manifestations.

AUTHOR CONTRIBUTIONS

SD, RK, and SL wrote the manuscript; SD, JH and SL edited the final draft.

FUNDING

This work was supported by the National Institute of Health grant R01 DK117396 to SL and JH.

ACKNOWLEDGMENTS

The authors thank Abigael Muchendtsi for useful discussions.

REFERENCES

Azbukina, N. V., Lopachev, A. V., Chistyakov, D. V., Goriainov, S. V., Astakhova, A. A., Poleshuk, V. V., et al. (2020). Oxylipin Profiles in Plasma of Patients with Wilson's Disease. *Metabolites* 10 (6), 222. doi:10.3390/metabo10060222

Bender, J. (2004). DNA Methylation and Epigenetics. *Annu. Rev. Plant Biol.* 55, 41–68. doi:10.1146/annurev.arplant.55.031903.141641

Burkhead, J. L., Ralle, M., Wilmarth, P., David, L., and Lutsenko, S. (2011). Elevated Copper Remodels Hepatic RNA Processing Machinery in the Mouse Model of Wilson's Disease. *J. Mol. Biol.* 406, 44–58. doi:10.1016/j.jmb.2010.12.001

Catana, A. M., and Medici, V. (2012). Liver Transplantation for Wilson Disease. *Wjh* 4, 5–10. doi:10.4254/wjh.v4.i1.5

Członkowska, A., Litwin, T., Dusek, P., Ferenci, P., Lutsenko, S., Medici, V., et al. (2018). Wilson Disease. *Nat. Rev. Dis. Primers* 4, 21. doi:10.1038/s41572-018-0018-3

Czlonkowska, A., Litwin, T., Karlinski, M., Dziezyc, K., Chabik, G., and Czerska, M. (2014). D-penicillamine versus Zinc Sulfate as First-Line Therapy for Wilson's Disease. *Eur. J. Neurol.* 21, 599–606. doi:10.1111/ene.12348

Dev, S., and Hamilton, J. P. (2021). Wilson Disease: Epigenetic Factors Contribute to Genetic Mutations to Affect the Disease. *Cell Mol. Gastroenterol. Hepatol.* 12, 1507–1508. doi:10.1016/j.jcmgh.2021.07.010

Einer, C., Leitzinger, C., Lichtmannegger, J., Eberhagen, C., Rieder, T., Borchard, S., et al. (2019). A High-Calorie Diet Aggravates Mitochondrial Dysfunction and Triggers Severe Liver Damage in Wilson Disease Rats. *Cell Mol. Gastroenterol. Hepatol.* 7, 571–596. doi:10.1016/j.jcmgh.2018.12.005

Ferenci, P. (2014). Phenotype-genotype Correlations in Patients with Wilson's Disease. *Ann. N.Y. Acad. Sci.* 1315, 1–5. doi:10.1111/nyas.12340

Ferenci, P., Stremmel, W., Członkowska, A., Szalay, F., Viveiros, A., Stättermayer, A. F., et al. (2019). Age and Sex but Not ATP7B Genotype Effectively Influence the Clinical Phenotype of Wilson Disease. *Hepatology* 69, 1464–1476. doi:10.1002/hep.30280

Ganesan, A., Nolan, L., Crabb, S., and Packham, G. (2009). Epigenetic Therapy: Histone Acetylation, DNA Methylation and Anti-cancer Drug Discovery. *Ccdt* 9, 963–981. doi:10.2174/156800909790192428

Gottlieb, A., Dev, S., DeVine, L., Gabrielson, K. L., Cole, R. N., Hamilton, J. P., et al. (2022). Hepatic Steatosis in the Mouse Model of Wilson Disease Coincides with a Muted Inflammatory Response. *Am. J. Pathol.* 192, 146–159. doi:10.1016/j.ajpath.2021.09.010

Gray, L. W., Peng, F., Molloy, S. A., Pendyala, V. S., Muchenditsi, A., Muzik, O., et al. (2012). Urinary Copper Elevation in a Mouse Model of Wilson's Disease Is a Regulated Process to Specifically Decrease the Hepatic Copper Load. *PLoS One* 7, e38327. doi:10.1371/journal.pone.0038327

Greig, J. A., Nordin, J. M. L., Smith, M. K., Ashley, S. N., Draper, C., Zhu, Y., et al. (2019). A Gene Therapy Approach to Improve Copper Metabolism and Prevent Liver Damage in a Mouse Model of Wilson Disease. *Hum. Gene Ther. Clin. Development* 30, 29–39. doi:10.1089/humc.2018.219

Hamilton, J. P., Koganti, L., Muchenditsi, A., Pendyala, V. S., Huso, D., Hankin, J., et al. (2016). Activation of Liver X Receptor/retinoid X Receptor Pathway Ameliorates Liver Disease inAtp7B−/−(Wilson Disease) Mice. *Hepatology* 63, 1828–1841. doi:10.1002/hep.28406

Jayakanthan, S., Braiterman, L. T., Hasan, N. M., Unger, V. M., and Lutsenko, S. (2017). Human Copper Transporter ATP7B (Wilson Disease Protein) Forms Stable Dimers *In Vitro* and in Cells. *J. Biol. Chem.* 292, 18760–18774. doi:10.1074/jbc.m117.807263

Jones, P. A. (2012). Functions of DNA Methylation: Islands, Start Sites, Gene Bodies and beyond. *Nat. Rev. Genet.* 13, 484–492. doi:10.1038/nrg3230

Kieffer, D. A., and Medici, V. (2017). Wilson Disease: At the Crossroads between Genetics and Epigenetics-A Review of the Evidence. *Liver Res.* 1, 121–130. doi:10.1016/j.livres.2017.08.003

Kim, B.-E., Turski, M. L., Nose, Y., Casad, M., Rockman, H. A., and Thiele, D. J. (2010). Cardiac Copper Deficiency Activates a Systemic Signaling Mechanism that Communicates with the Copper Acquisition and Storage Organs. *Cel Metab.* 11, 353–363. doi:10.1016/j.cmet.2010.04.003

Leng, Y., Li, P., Zhou, L., Xiao, L., Liu, Y., Zheng, Z., et al. (2019). Long-Term Correction of Copper Metabolism in Wilson's Disease Mice with AAV8 Vector Delivering Truncated ATP7B. *Hum. Gene Ther.* 30, 1494–1504. doi:10.1089/hum.2019.148

Li, M., Li, Y., Chen, J., Wei, W., Pan, X., Liu, J., et al. (2007). Copper Ions Inhibit S-Adenosylhomocysteine Hydrolase by Causing Dissociation of NAD+ Cofactor. *Biochemistry* 46, 11451–11458. doi:10.1021/bi700395d

Li, X., Feng, Z., Tang, W., Yu, X., Qian, Y., Liu, B., et al. (2018). Sex Differences in Clinical Characteristics and Brain MRI Change in Patients with Wilson's Disease in a Chinese Population. *Front. Physiol.* 9, 1429. doi:10.3389/fphys.2018.01429

Lichtmannegger, J., Leitzinger, C., Wimmer, R., Schmitt, S., Schulz, S., Kabiri, Y., et al. (2016). Methanobactin Reverses Acute Liver Failure in a Rat Model of Wilson Disease. *J. Clin. Invest.* 126, 2721–2735. doi:10.1172/jci85226

Linz, R., and Lutsenko, S. (2007). Copper-transporting ATPases ATP7A and ATP7B: Cousins, Not Twins. *J. Bioenerg. Biomembr* 39, 403–407. doi:10.1007/s10863-007-9101-2

Litwin, T., Gromadzka, G., and Członkowska, A. (2012). Gender Differences in Wilson's Disease. *J. Neurol. Sci.* 312, 31–35. doi:10.1016/j.jns.2011.08.028

Lutsenko, S. (2016). Copper Trafficking to the Secretory Pathway. *Metallomics* 8, 840–852. doi:10.1039/c6mt00176a

Medici, V., Kieffer, D. A., Shibata, N. M., Chima, H., Kim, K., Canovas, A., et al. (2016). Wilson Disease: Epigenetic Effects of Choline Supplementation on Phenotype and Clinical Course in a Mouse Model. *Epigenetics* 11, 804–818. doi:10.1080/15592294.2016.1231289

Medici, V., and LaSalle, J. M. (2019). Genetics and Epigenetic Factors of Wilson Disease. *Ann. Transl. Med.* 7, S58. doi:10.21037/atm.2019.01.67

Medici, V., Shibata, N. M., Kharbanda, K. K., LaSalle, J. M., Woods, R., Liu, S., et al. (2013). Wilson's Disease: Changes in Methionine Metabolism and Inflammation Affect Global DNA Methylation in Early Liver Disease. *Hepatology* 57, 555–565. doi:10.1002/hep.26047

Medici, V., and Weiss, K.-H. (2017). Genetic and Environmental Modifiers of Wilson Disease. *Handb Clin. Neurol.* 142, 35–41. doi:10.1016/b978-0-444-63625-6.00004-5

Merle, U., Eisenbach, C., Weiss, K. H., Tuma, S., and Stremmel, W. (2009). Serum Ceruloplasmin Oxidase Activity Is a Sensitive and Highly Specific Diagnostic Marker for Wilson's Disease. *J. Hepatol.* 51, 925–930. doi:10.1016/j.jhep.2009.06.022

Merle, U., Schaefer, M., Ferenci, P., and Stremmel, W. (2007). Clinical Presentation, Diagnosis and Long-Term Outcome of Wilson's Disease: a Cohort Study. *Gut* 56, 115–120. doi:10.1136/gut.2005.087262

Merle, U., Weiss, K. H., Eisenbach, C., Tuma, S., Ferenci, P., and Stremmel, W. (2010). Truncating Mutations in the Wilson Disease Gene ATP7B Are Associated with Very Low Serum Ceruloplasmin Oxidase Activity and an Early Onset of Wilson Disease. *BMC Gastroenterol.* 10, 8. doi:10.1186/1471-230x-10-8

Mohr, I., and Weiss, K. H. (2019). Current Anti-copper Therapies in Management of Wilson Disease. *Ann. Transl. Med.* 7, S69. doi:10.21037/atm.2019.02.48

Mordaunt, C. E., Shibata, N. M., Kieffer, D. A., Czlonkowska, A., Litwin, T., Weiss, K. H., et al. (2018). Epigenetic Changes of the Thioredoxin System in the Tx-J Mouse Model and in Patients with Wilson Disease. *Hum. Mol. Genet.* 27, 3854–3869. doi:10.1093/hmg/ddy262

Mordaunt, C. E., Kieffer, D. A., Shibata, N. M., Członkowska, A., Litwin, T., Weiss, K.-H., et al. (2019). Epigenomic Signatures in Liver and Blood of Wilson Disease Patients Include Hypermethylation of Liver-specific Enhancers. *Epigenetics & Chromatin* 12, 10. doi:10.1186/s13072-019-0255-z

Muchenditsi, A., Talbot, C. C., Jr., Gottlieb, A., Yang, H., Kang, B., Boronina, T., et al. (2021). Systemic Deletion of Atp7b Modifies the Hepatocytes' Response to Copper Overload in the Mouse Models of Wilson Disease. *Sci. Rep.* 11, 5659. doi:10.1038/s41598-021-84894-3

Muchenditsi, A., Yang, H., Hamilton, J. P., Koganti, L., Housseau, F., Aronov, L., et al. (2017). Targeted Inactivation of Copper Transporter Atp7b in Hepatocytes Causes Liver Steatosis and Obesity in Mice. *Am. J. Physiology-Gastrointestinal Liver Physiol.* 313, G39–G49. doi:10.1152/ajpgi.00312.2016

Murillo, O., Moreno, D., Gazquez, C., Barberia, M., Cenzano, I., Navarro, I., et al. (2019). Liver Expression of a MiniATP7B Gene Results in Long-Term Restoration of Copper Homeostasis in a Wilson Disease Model in Mice. *Hepatology* 70, 108–126. doi:10.1002/hep.30535

Murillo, O., Luqui, D. M., Gazquez, C., Martinez-Espartosa, D., Navarro-Blasco, I., Monreal, J. I., et al. (2016). Long-term Metabolic Correction of Wilson's Disease in a Murine Model by Gene Therapy. *J. Hepatol.* 64, 419–426. doi:10.1016/j.jhep.2015.09.014

Nagasaka, H., Miida, T., Inui, A., Inoue, I., Tsukahara, H., Komatsu, H., et al. (2012). Fatty Liver and Anti-oxidant Enzyme Activities along with Peroxisome Proliferator-Activated Receptors γ and α Expressions in the Liver of Wilson's Disease. *Mol. Genet. Metab.* 107, 542–547. doi:10.1016/j.ymgme.2012.08.004

Nathwani, A. C., Gray, J. T., Ng, C. Y. C., Zhou, J., Spence, Y., Waddington, S. N., et al. (2006). Self-complementary Adeno-Associated Virus Vectors Containing a Novel Liver-specific Human Factor IX Expression Cassette Enable Highly Efficient Transduction of Murine and Nonhuman Primate Liver. *Blood* 107, 2653–2661. doi:10.1182/blood-2005-10-4035

Nathwani, A. C., Tuddenham, E. G. D., Rangarajan, S., Rosales, C., McIntosh, J., Linch, D. C., et al. (2011). Adenovirus-associated Virus Vector-Mediated Gene Transfer in Hemophilia B. *N. Engl. J. Med.* 365, 2357–2365. doi:10.1056/nejmoa1108046

Niculescu, M. D., and Zeisel, S. H. (2002). Diet, Methyl Donors and DNA Methylation: Interactions between Dietary Folate, Methionine and Choline. *J. Nutr.* 132, 2333S–2335S. doi:10.1093/jn/132.8.2333s

Okano, M., Bell, D. W., Haber, D. A., and Li, E. (1999). DNA Methyltransferases Dnmt3a and Dnmt3b Are Essential for De Novo Methylation and Mammalian Development. *Cell* 99, 247–257. doi:10.1016/s0092-8674(00)81656-6

Pierson, H., Muchenditsi, A., Kim, B.-E., Ralle, M., Zachos, N., Huster, D., et al. (2018). The Function of ATPase Copper Transporter ATP7B in Intestine. *Gastroenterology* 154, 168–180. e165. doi:10.1053/j.gastro.2017.09.019

Pöhler, M., Guttmann, S., Nadzemova, O., Lenders, M., Brand, E., Zibert, A., et al. (2020). CRISPR/Cas9-mediated Correction of Mutated Copper Transporter ATP7B. *PLoS One* 15, e0239411. doi:10.1371/journal.pone.0239411

Polishchuk, E. V., Merolla, A., Lichtmannegger, J., Romano, A., Indrieri, A., Ilyechova, E. Y., et al. (2019). Activation of Autophagy, Observed in Liver Tissues from Patients with Wilson Disease and from ATP7B-Deficient Animals, Protects Hepatocytes from Copper-Induced Apoptosis. *Gastroenterology* 156, 1173–1189. e1175. doi:10.1053/j.gastro.2018.11.032

Pop, T. L., Grama, A., Stefanescu, A. C., Willheim, C., and Ferenci, P. (2021). Acute Liver Failure with Hemolytic Anemia in Children with Wilson's Disease: Genotype-Phenotype Correlations? *Wjh* 13, 1428–1438. doi:10.4254/wjh.v13.i10.1428

Poujois, A., Sobesky, R., Meissner, W. G., Brunet, A.-S., Broussolle, E., Laurencin, C., et al. (2020). Liver Transplantation as a rescue Therapy for Severe Neurologic Forms of Wilson Disease. *Neurology* 94, e2189–e2202. doi:10.1212/wnl.0000000000009474

Reed, E., Lutsenko, S., and Bandmann, O. (2018). Animal Models of Wilson Disease. *J. Neurochem.* 146, 356–373. doi:10.1111/jnc.14323

Roberts, E. A., Robinson, B. H., and Yang, S. (2008). Mitochondrial Structure and Function in the Untreated Jackson Toxic Milk (Tx-j) Mouse, a Model for Wilson Disease. *Mol. Genet. Metab.* 93, 54–65. doi:10.1016/j.ymgme.2007.08.127

Roberts, E. A., and Sarkar, B. (2008). Liver as a Key Organ in the Supply, Storage, and Excretion of Copper. *Am. J. Clin. Nutr.* 88, 851S–854S. doi:10.1093/ajcn/88.3.851s

Roberts, E. A. (2018). Update on the Diagnosis and Management of Wilson Disease. *Curr. Gastroenterol. Rep.* 20, 56. doi:10.1007/s11894-018-0660-7

Roybal, J. L., Endo, M., Radu, A., Gray, L., Todorow, C. A., Zoltick, P. W., et al. (2012). Early Gestational Gene Transfer with Targeted ATP7B Expression in the Liver Improves Phenotype in a Murine Model of Wilson's Disease. *Gene Ther.* 19, 1085–1094. doi:10.1038/gt.2011.186

Sarode, G. V., Kim, K., Kieffer, D. A., Shibata, N. M., Litwin, T., Czlonkowska, A., et al. (2019). Metabolomics Profiles of Patients with Wilson Disease Reveal a Distinct Metabolic Signature. *Metabolomics* 15, 43. doi:10.1007/s11306-019-1505-6

Sarode, G. V., Neier, K., Shibata, N. M., Shen, Y., Goncharov, D. A., Goncharova, E. A., et al. (2021). Wilson Disease: Intersecting DNA Methylation and Histone Acetylation Regulation of Gene Expression in a Mouse Model of Hepatic Copper Accumulation. *Cell Mol. Gastroenterol. Hepatol.* 12, 1457–1477. doi:10.1016/j.jcmgh.2021.05.020

Schiefermeier, M., Kollegger, H., Madl, C., Polli, C., Oder, W., Kuhn, H., et al. (2000). The Impact of Apolipoprotein E Genotypes on Age at Onset of Symptoms and Phenotypic Expression in Wilson's Disease. *Brain* 123, 585–590. doi:10.1093/brain/123.3.585

Schilsky, M. L., Roberts, E. A., Hahn, S., and Askari, F. (2015). Costly Choices for Treating Wilson's Disease. *Hepatology* 61, 1106–1108. doi:10.1002/hep.27663

Solovyev, N., Ala, A., Schilsky, M., Mills, C., Willis, K., and Harrington, C. F. (2020). Biomedical Copper Speciation in Relation to Wilson's Disease Using strong Anion Exchange Chromatography Coupled to Triple Quadrupole Inductively Coupled Plasma Mass Spectrometry. *Analytica Chim. Acta* 1098, 27–36. doi:10.1016/j.aca.2019.11.033

Stättermayer, A. F., Entenmann, A., Gschwantler, M., Zoller, H., Hofer, H., and Ferenci, P. (2019). The Dilemma to Diagnose Wilson Disease by Genetic Testing Alone. *Eur. J. Clin. Invest.* 49, e13147. doi:10.1111/eci.13147

Stättermayer, A. F., Traussnigg, S., Dienes, H.-P., Aigner, E., Stauber, R., Lackner, K., et al. (2015). Hepatic Steatosis in Wilson Disease - Role of Copper and PNPLA3 Mutations. *J. Hepatol.* 63, 156–163. doi:10.1016/j.jhep.2015.01.034

Sternlieb, I. (1968). Mitochondrial and Fatty Changes in Hepatocytes of Patients with Wilson's Disease. *Gastroenterology* 55, 354–367. doi:10.1016/s0016-5085(19)34045-4

Wang, D., Tai, P. W. L., and Gao, G. (2019). Adeno-associated Virus Vector as a Platform for Gene Therapy Delivery. *Nat. Rev. Drug Discov.* 18, 358–378. doi:10.1038/s41573-019-0012-9

Wilmarth, P. A., Short, K. K., Fiehn, O., Lutsenko, S., David, L. L., and Burkhead, J. L. (2012). A Systems Approach Implicates Nuclear Receptor Targeting in the Atp7b−/− Mouse Model of Wilson's Disease. *Metallomics* 4, 660–668. doi:10.1039/c2mt20017a

Wooton-Kee, C. R., Jain, A. K., Wagner, M., Grusak, M. A., Finegold, M. J., Lutsenko, S., et al. (2015). Elevated Copper Impairs Hepatic Nuclear Receptor Function in Wilson's Disease. *J. Clin. Invest.* 125, 3449–3460. doi:10.1172/jci78991

Wooton-Kee, C. R., Robertson, M., Zhou, Y., Dong, B., Sun, Z., Kim, K. H., et al. (2020). Metabolic Dysregulation in the Atp7b −/− Wilson's Disease Mouse Model. *Proc. Natl. Acad. Sci. U.S.A.* 117, 2076–2083. doi:10.1073/pnas.1914267117

Zhang, J., Ma, Y., Xie, D., Bao, Y., Yang, W., Wang, H., et al. (2021). Differentially Expressed lncRNAs in Liver Tissues of TX Mice with Hepatolenticular Degeneration. *Sci. Rep.* 11, 1377. doi:10.1038/s41598-020-80635-0

Zischka, H., Lichtmannegger, J., Schmitt, S., Jägemann, N., Schulz, S., Wartini, D., et al. (2011). Liver Mitochondrial Membrane Crosslinking and Destruction in a Rat Model of Wilson Disease. *J. Clin. Invest.* 121, 1508–1518. doi:10.1172/jci45401

Conflict of Interest: The authors declare that the research was conducted in the absence of any commercial or financial relationships that could be construed as a potential conflict of interest.

Publisher's Note: All claims expressed in this article are solely those of the authors and do not necessarily represent those of their affiliated organizations, or those of the publisher, the editors and the reviewers. Any product that may be evaluated in this article, or claim that may be made by its manufacturer, is not guaranteed or endorsed by the publisher.

frontiers | Frontiers in Molecular Biosciences

ORIGINAL RESEARCH
published: 05 May 2022
doi: 10.3389/fmolb.2022.897621

Multinuclear Metal-Binding Ability of the N-Terminal Region of Human Copper Transporter Ctr1: Dependence Upon pH and Metal Oxidation State

Maria Incoronata Nardella[1], *Mariagrazia Fortino*[2], *Alessandra Barbanente*[1], *Giovanni Natile*[1], *Adriana Pietropaolo*[2] *and Fabio Arnesano*[1]*

[1]Department of Chemistry, University of Bari Aldo Moro, Bari, Italy, [2]Dipartimento di Scienze Della Salute, University of Catanzaro, Catanzaro, Italy

OPEN ACCESS

Edited by:
Simone Ciofi Baffoni,
University of Florence, Italy

Reviewed by:
David Huffman,
Western Michigan University, United States
Nicola d'Amelio,
University of Picardie Jules Verne, France

***Correspondence:**
Fabio Arnesano
fabio.arnesano@uniba.it

Specialty section:
This article was submitted to Cellular Biochemistry, a section of the journal Frontiers in Molecular Biosciences

Received: 16 March 2022
Accepted: 20 April 2022
Published: 05 May 2022

Citation:
Nardella MI, Fortino M, Barbanente A, Natile G, Pietropaolo A and Arnesano F (2022) Multinuclear Metal-Binding Ability of the N-Terminal Region of Human Copper Transporter Ctr1: Dependence Upon pH and Metal Oxidation State. Front. Mol. Biosci. 9:897621. doi: 10.3389/fmolb.2022.897621

The 14mer peptide corresponding to the N-terminal region of human copper transporter Ctr1 was used to investigate the intricate mechanism of metal binding to this plasma membrane permease responsible for copper import in eukaryotic cells. The peptide contains a high-affinity ATCUN Cu(II)/Ni(II)-selective motif, a methionine-only MxMxxM Cu(I)/Ag(I)-selective motif and a double histidine HH(M) motif, which can bind both Cu(II) and Cu(I)/Ag(I) ions. Using a combination of NMR spectroscopy and electrospray mass spectrometry, clear evidence was gained that the Ctr1 peptide, at neutral pH, can bind one or two metal ions in the same or different oxidation states. Addition of ascorbate to a neutral solution containing $Ctr1_{1\text{-}14}$ and Cu(II) in 1:1 ratio does not cause an appreciable reduction of Cu(II) to Cu(I), which is indicative of a tight binding of Cu(II) to the ATCUN motif. However, by lowering the pH to 3.5, the Cu(II) ion detaches from the peptide and becomes susceptible to reduction to Cu(I) by ascorbate. It is noteworthy that at low pH, unlike Cu(II), Cu(I) stably binds to methionines of the peptide. This redox reaction could take place in the lumen of acidic organelles after Ctr1 internalization. Unlike $Ctr1_{1\text{-}14}$-Cu(II), bimetallic $Ctr1_{1\text{-}14}$-2Cu(II) is susceptible to partial reduction by ascorbate at neutral pH, which is indicative of a lower binding affinity of the second Cu(II) ion. The reduced copper remains bound to the peptide, most likely to the HH(M) motif. By lowering the pH to 3.5, Cu(I) shifts from HH(M) to methionine-only coordination, an indication that only the pH-insensitive methionine motif is competent for metal binding at low pH. The easy interconversion of monovalent cations between different coordination modes was supported by DFT calculations.

Keywords: Ctr1, copper, silver, metal transport, redox processes, NMR specroscopy, mass spectrometry, DFT calculations

INTRODUCTION

An elaborate machinery controls the numerous metal ions circulating in the blood and stored in the cells of living organisms. The intracellular concentration of these metal ions is finely regulated because, despite their beneficial effects, they are potentially toxic (particularly those redox active) and can participate in aberrant reactions.

In the case of copper (Cu), the metal participates in various cellular metabolic processes, such as oxidative phosphorylation (Hu et al., 1977; Tsukihara et al., 1995), formation of connective tissue (Kagan and Li, 2003), iron metabolism (Dancis et al., 1994), maturation of neuropeptides (Prigge et al., 2000), detoxification of free radicals (Baker et al., 2017), pigmentation (Matoba et al., 2006), etc. To sustain copper demand, while minimizing the risk of toxic side effects, is critically important for cell viability. For this reason the homeostasis of Cu(I) is finely controlled by a complex protein system, which keeps the metal ion protein-bound while it is delivered to the various intracellular compartments, so preventing the toxic effects stemming from intracellular accumulation of unbound Cu(I) species (O'Halloran and Culotta, 2000; Huffman and O'Halloran, 2001; Field et al., 2002; Boal and Rosenzweig, 2009; Robinson and Winge, 2010; Nevitt et al., 2012; Palumaa, 2013; Lutsenko, 2021). The copper transporter 1 (Ctr1) is a protein essential for copper transport across the plasma membrane (Dancis et al., 1994; Lee et al., 2001). Human Ctr1 (hCtr1) is a membrane protein of approximately 28 kDa and made of 190 amino acids, which features three transmembrane α-helices, a C-terminal domain of 15 amino acids and a long N-terminal extracellular domain (ectodomain) of 67 amino acids (Zhou and Gitschier, 1997; Pope et al., 2012). The exact mechanism by which copper enters the cell is not entirely elucidated, however experimental evidence indicates that three units of Ctr1 are associated to form a pore acting as an ion channel (De Feo et al., 2009; Ren et al., 2019). The localization of Ctr1 is controlled by the intra and extra-cellular copper concentration. An increase in the extracellular concentration of copper induces endocytosis of Ctr1, so reducing the transit of the metal ion across the membrane (Petris et al., 2003; Guo et al., 2004; Van Den Berghe et al., 2007). Conversely, a decrease in copper concentration restores the Ctr1 level at the plasma membrane (Molloy and Kaplan, 2009; Clifford et al., 2016). Proteins homologous to Ctr1 transport selectively the Cu(I) ions, while in the extracellular environment the metal is present mainly in the oxidized Cu(II) form. Therefore, the intervention of reducing agents or enzymes capable of transforming Cu(II) into Cu(I) is required before the metal can be transported into the cytosol. In the case of yeast *S. cerevisiae*, two selective reductases for copper and iron are present (Fre1 and Fre2) (Hassett and Kosman, 1995; Georgatsou et al., 1997). In humans, there is a family of proteins, called STEAP, capable of reducing the two metal ions and facilitate their acquisition by cells (Ohgami et al., 2006; Oosterheert et al., 2018). An alternative, simplified, copper reduction model has also been proposed. It is based on the observation that the N-terminal end of hCtr1 is able to bind and reduce Cu(II) to Cu(I) using ascorbate, and to stabilize Cu(I) thanks to the presence of histidine (His) and methionine (Met) motifs in monomeric (Pushie et al., 2015) or multimeric (Galler et al., 2020) arrangements. The binding of Cu(I) to hCtr1 induces a conformational change, which promotes the interaction of the ectodomain with the cell membrane and may represent the initial step of the Cu(I) uptake process (Yang et al., 2019).

In the present study, we investigated the metal binding properties of a 14mer peptide corresponding to the first 14 amino acids of the N-terminal region of human Ctr1 ($Ctr1_{1-14}$). The peptide contains the amino acid motifs essential for the acquisition of copper from the extracellular environment. The initial H_2N-X_2-His motif (known as the ATCUN motif) is also found in human serum albumin (HSA) and is selective for Cu(II) and Ni(II) (Bossak et al., 2018; Gonzalez et al., 2018). Cu(II) binds to this site in a square planar coordination geometry involving four nitrogen atoms (4N): the free NH_2 terminus, a histidine residue in the third position and the two intervening amidic nitrogens (Santoro et al., 2018).

In the N-terminal region, both hCtr1 and yeast Ctr1 (yCtr1) exhibit Met-rich motifs MxM and MxxM, able to bind Cu(I) (Jiang et al., 2005; Rubino et al., 2010). Furthermore, hCtr1, unlike yCtr1, contains also histidine-rich motifs that have been implicated in the acquisition of Cu(II) and Cu(I) in mammals (Haas et al., 2011). In particular, quite close to the N-terminal end of hCtr1 there is a bis-His (HH) motif (Himes et al., 2007; Shearer and Szalai, 2008) flanked by a Met (the HHM motif) capable of binding and stabilizing Cu(I) (Pushie et al., 2015). The contiguous presence of ATCUN and HHM motifs suggests a possible interaction with copper in both oxidation states (Haas et al., 2011; Pushie et al., 2015).

Based on the above consideration, we deemed it appropriate to investigate the interaction of $Ctr1_{1-14}$ with copper in both oxidation states and also with the redox-inactive Ag(I) ion, as a Cu(I) mimic. Moreover, since the endosomal compartment where hCtr1 is internalized is acidic, the investigation was carried on at different pH values (from neutral to highly acidic).

MATERIALS AND METHODS

The 14mer $Ctr1_{1-14}$ peptide (sequence MDHSHHMGMSYMDS, MM: 1665.85 Da; pI: 5.68) was purchased from Genscript Biotech (Piscataway, New Jersey, United States) and used without further purification.

Nuclear Magnetic Resonance (NMR) Spectroscopy

NMR samples were prepared by dissolving $Ctr1_{1-14}$ in phosphate buffer (Pi, 25 mM, pH = 7 or 3.5) or in 2-(N-morpholino) ethanesulfonic acid (MES, 10 mM, pH = 7) at 250 μM concentration. NMR titrations were performed by gradually adding $CuSO_4$ or $AgNO_3$ dissolved in pure water to the apopeptide solution, directly in the NMR tube. 1D ^{1}H NMR spectra were recorded at 298 K on a Bruker Avance 300 Ultrashield spectrometer equipped with a double resonance broad-band probe with Z-Gradient. 1D ^{1}H NMR spectra were

acquired with a relaxation delay of 1.5 s, 256 scans, 32K data points and a spectral width of 16 ppm. ^{1}H chemical shifts were referenced to trimethylsilylpropanoic acid (TSP, δ_{1H} = 0.0 ppm).

Electrospray Ionization Mass Spectrometry (ESI-MS)

Solutions of $Ctr1_{1-14}$ (200 μM) and its adducts with Cu(II) and Ag(I), at different metal:peptide ratios, were prepared in NH_4OAc (20 mM) at 25 °C. Aliquots of these samples were diluted with buffer to a final concentration of 20 μM and directly infused into the mass spectrometer, an Agilent 6530 Accurate-Mass Quadruple Time-of-Flight (Q-TOF) system equipped with an electrospray interface. Ionization was achieved in the positive or negative ion mode by application of 4.0 kV at the entrance of the capillary; the pressure of the nebulizer gas was 20 psi. The drying gas was heated to 325 °C and introduced at a flow rate of 10 μL/min. Full-scan mass spectra were recorded in the mass/charge (*m/z*) range of 50–3,000. Isotopic distributions were calculated with the program Molecular Weight Calculator (https://omics.pnl.gov/software/molecular-weight-calculator).

Modeling Calculations

The initial coordinates of the $Ctr1_{1-14}$ peptide were obtained using the CHIMERA software (Pettersen et al., 2004). The coordinates were energy minimized through the Steepest Descent Algorithm and equilibrated with 9 ns of standard molecular dynamics at 300 K using the amber99SB force field (Ivani et al., 2016) and the TIP3P potential (Jorgensen et al., 1983) for water molecules, within the GROMACS MD code - version 2020.2 (Abraham and van der Spoel, 2020). Parallel Bias Metadynamics (PBMetaD) (Pfaendtner and Bonomi, 2015) simulations were subsequently performed using the GROMACS MD code - version 2020.2 (Abraham and van der Spoel, 2020) in the NVT ensemble, using the gyration radius as collective variable. Gaussians with initial height equal to 1.2 kJ/mol and width of 0.2 nm were deposited with a bias factor equal to 20. The total time of the simulation was 45 ns.

The three highly populated conformers were extracted from the PBMetaD trajectory through cluster analysis using the method of Daura and van Gunsteren (Daura et al., 1999) and were used as starting coordination geometries. The coordination models of $Ctr1_{1-14}$ with Ag(I) were built considering the residues from Met1 to Met12 and capping the side chains of Asp2, Ser4, Ser10, Tyr11, Asp13 and Ser14 with hydrogen atoms to reduce the computational cost and maintain simulation accuracy. The derived coordinates were optimized at *ab initio* level, within the Density Functional Theory (DFT) framework by using the PBE functional, suitable for this type of systems (Ernzerhof and Perdew, 1998) and the DGDZVP basis sets (Godbout et al., 1992) with Gaussian16 (Frisch et al., 2016) suite of quantum chemical programs. The use of double-zeta DGDZVP basis set allows to combine a high computational speed and a high accuracy for the study of large systems (Siiskonen and Priimagi, 2017).

RESULTS

Analysis of $Ctr1_{1-14}$ at Neutral and Acidic pH

The $Ctr1_{1-14}$ apopeptide was initially characterized by electrospray ionization mass spectrometry (ESI-MS) to verify its identity and degree of purity. The ESI-MS spectrum carried out in NH_4OAc shows two main signals with *m/z* ratios of 833.3012 and 555.8680, associated to the doubly and triply charged species, respectively (**Supplementary Figure S1**; **Table 1**).

Subsequently, a 1D ^{1}H NMR spectrum of the apopeptide was recorded in 10 mM MES at pH 7.0 (**Supplementary Figure S2**) and in 25 mM Pi buffer at pH 7.0 and 3.5 (**Figure 1**). The main spectral changes between neutral and acidic pH were observed in the region of amides and aromatic protons. While the strong degenerate signal assigned to the ε-CH_3 methyl protons of the four Met residues and the two signals of Tyr phenyl ring were nearly insensitive to the pH variation; in contrast, the signals of the His imidazole ring were highly perturbed. This result is in agreement with the protonation of imidazole nitrogen (pKa ~6) in the pH range from 7.0 to 3.5, and suggests that metal ions may prefer different coordination modes depending upon the neutral or acidic environment in which the protein is placed.

Structural models of *apo*$Ctr1_{1-14}$ were obtained through Parallel Bias Metadynamics (PBMetaD) (Pfaendtner and Bonomi, 2015) simulations. The main clusters of conformers extracted from the PBMetaD trajectory, representing three possible metal coordination networks, are highlighted in **Figure 2**. The first cluster is characterized by a close proximity of Met7, Met9 and Met12 and represents a population of 84% (**Figure 2A**). The second cluster features a network of residues involving His5, Met7 and Met12 and is 10% populated (**Figure 2B**). Finally, the third cluster features a close proximity of His5, His6 and Met7 and represents a population of 6% (**Figure 2C**). In the last cluster, a β-turn component of the secondary structure was found between His6 and Met7 residues.

Interaction of $Ctr1_{1-14}$ With Cu(II) Ions

The interaction between Cu(II) and $Ctr1_{1-14}$ was investigated via NMR by treating the peptide solution (250 μM) with increasing aliquots of a solution of $CuSO_4$, up to 1 eq of Cu(II), both in 25 mM Pi and in 10 mM MES buffers at pH 7.0 (**Figure 3**). In Pi, the Cu(II) ion binds to $Ctr1_{1-14}$ and, given its paramagnetic nature, determines the broadening of the ^{1}H NMR signals, in particular those of the His ring which show the greatest relative reduction in intensity. Moreover, the addition of Cu(II) produces only a negligible dipolar hyperfine (pseudocontact) shift, which is consistent with a type-II Cu(II) site (ATCUN) having modest magnetic susceptibility anisotropy (Arnesano et al., 2005). In MES, the broadening of the peptide signals was larger than that observed in the titration carried out in Pi buffer. This can be explained with the poorer coordinating ability of MES with respect to phosphate, which makes more Cu(II) available for binding to the peptide.

The interaction between Cu(II) and the peptide was also monitored by ESI-MS. Two signals were observed at 864.7583

TABLE 1 | Stoichiometry of $Ctr1_{1-14}$ complexes with Cu(II) and Ag(I) ions observed by ESI-MS.

Ions	Experimental *m/z* [a]	Calculated *m/z* [a]	ΔDa	Error (ppm)
apo$Ctr1_{1-14}$				
$[Ctr1_{1-14} + 2H]^{2+}$	833.3012	833.2998	0.0014	2
$[Ctr1_{1-14} + 3H]^{3+}$	555.8680	555.8692	−0.0012	−2
$Ctr1_{1-14}$-Cu(II)				
$[Ctr1_{1-14} + Cu(II)]^{2+}$	864.7583	864.7618	−0.0035	−4
$[Ctr1_{1-14} + Cu(II) + H]^{3+}$	576.8399	576.8438	−0.0039	−7
$Ctr1_{1-14}$-2Cu(II)				
$[Ctr1_{1-14} + 2Cu(II) - 2H]^{2+}$	895.2160	895.2238	−0.0078	−9
$[Ctr1_{1-14} + 2Cu(II) - H]^{3+}$	597.1451	597.1518	−0.0067	−11
$Ctr1_{1-14}$-Ag(I)				
$[Ctr1_{1-14} + Ag(I) + H]^{2+}$	887.2496	887.2485	0.0011	1
$[Ctr1_{1-14} + Ag(I) + 2H]^{3+}$	591.8346	591.8349	−0.0003	−1
$Ctr1_{1-14}$-2Ag(I)				
$[Ctr1_{1-14} + 2Ag(I)]^{2+}$	940.1882	940.1971	-0.0089	−9
$[Ctr1_{1-14} + 2Ag(I) + H]^{3+}$	627.1270	627.1340	−0.0070	−11
$Ctr1_{1-14}$-Ag(I),Cu(II)				
$[Ctr1_{1-14} + Ag(I) + Cu(II) - H]^{2+}$	917.6949	917.7104	−0.0155	−17
$[Ctr1_{1-14} + Ag(I) + Cu(II)]^{3+}$	612.1314	612.1429	−0.0115	−19

[a]*The reported* m/z *ratios are referred to the prevailing isotopologue in the isotope pattern.*

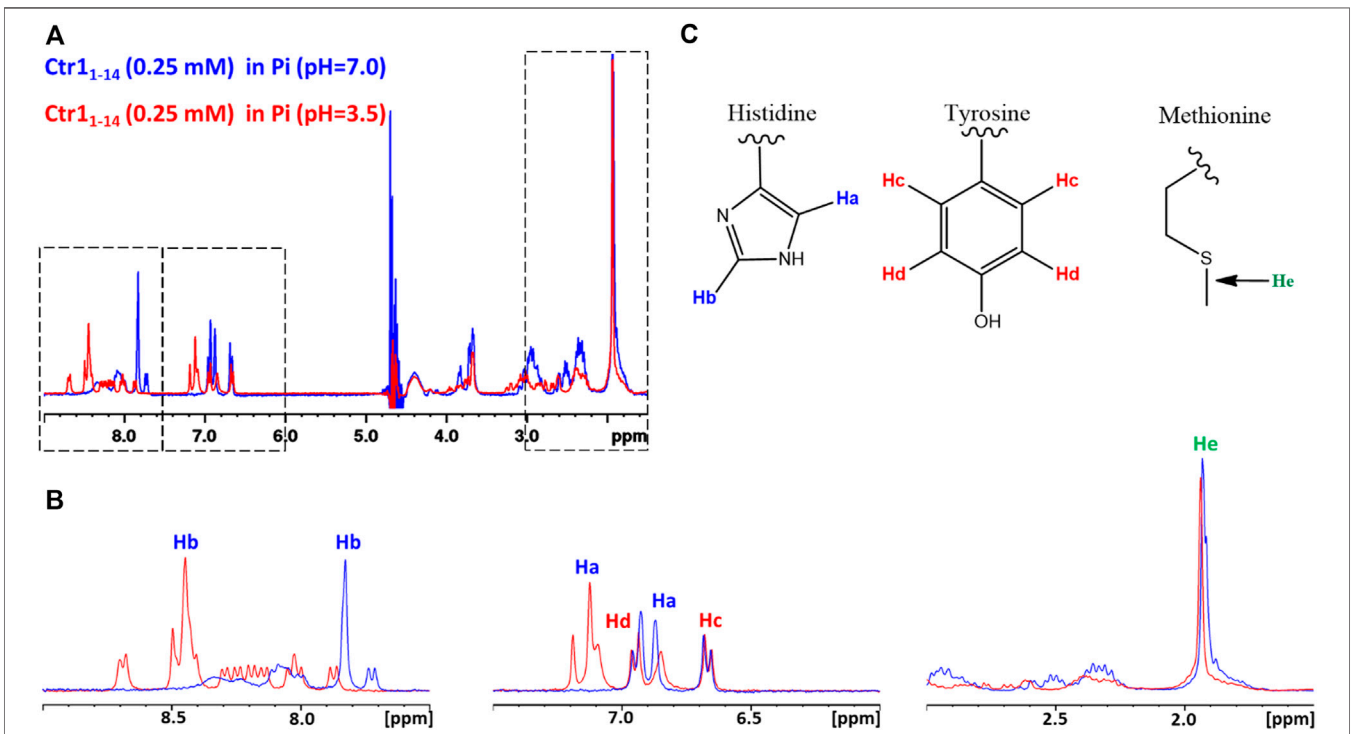

FIGURE 1 | (A) Superposition of 1D ^{1}H NMR spectra of $Ctr1_{1-14}$ in 25 mM Pi buffer at pH 7.0 (*blue contours*) and 3.5 (*red contours*). The regions enclosed in *dashed boxes* are expanded in **(B)**. The proton assignment scheme is shown in **(C)** where the structure of aminoacid side chains is reported.

and 576.8399 m/*z*, corresponding to the adduct $Ctr1_{1-14}$-Cu(II) having 2+ and 3 + overall charge, respectively (**Figures 4A, B**). The addition of Cu(II) beyond one equivalent leads to the almost complete disappearance of the NMR signals, however the ESI-MS spectra indicate the binding of a second Cu(II) ion to the peptide, as deduced from the appearance of two signals at 895.2160 and 597.1451 m/*z* (2+ and 3 + charged $Ctr1_{1-14}$-2Cu(II) adduct) with the predicted isotopic distribution pattern (**Figures 4C, D**). The relative abundance of $Ctr1_{1-14}$ species (apopeptide and metal adducts) based on ESI-MS peak intensity at different Cu(II):peptide ratios is reported in panel E of **Figure 4**.

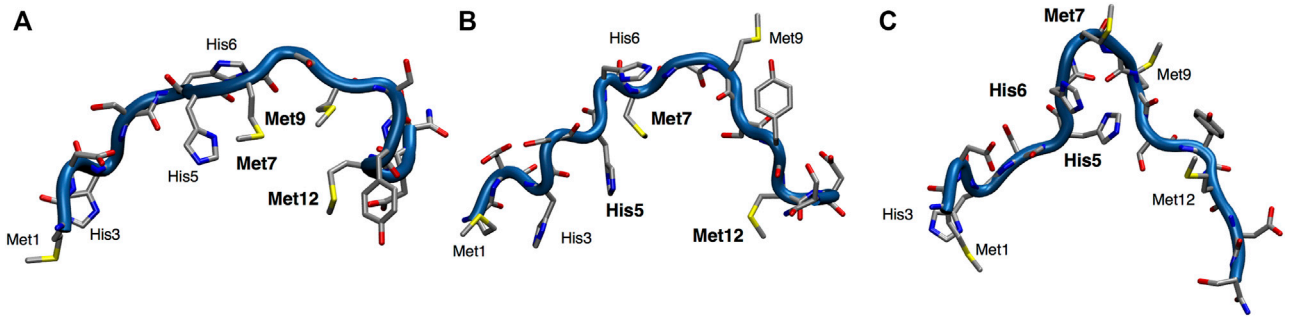

FIGURE 2 | Representation of the three main clusters **(A–C)** extracted from the PBMetaD simulation trajectory. Oxygen is shown in red, nitrogen in blue, carbon in gray and sulfur in yellow.

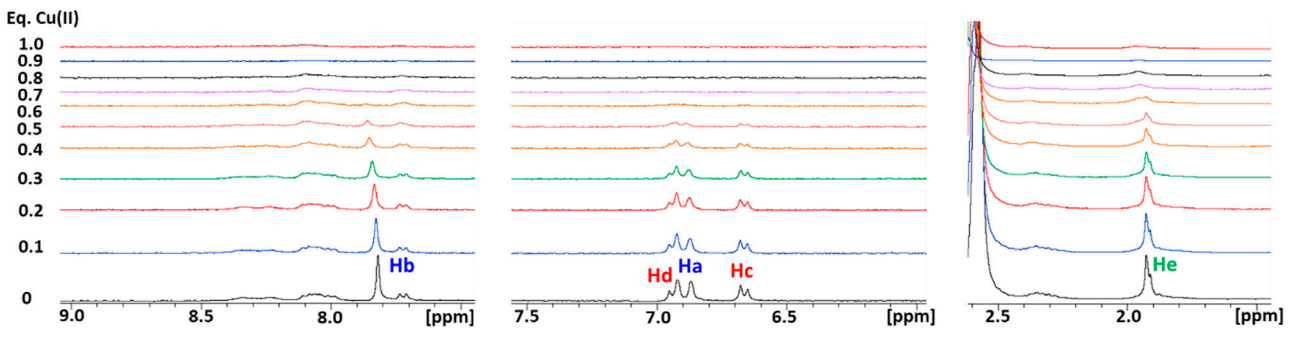

FIGURE 3 | Overlay of three regions of 1D ^{1}H NMR spectra of $Ctr1_{1-14}$ in 10 mM MES (pH 7) at different Cu(II):peptide ratios. Proton assignment scheme as shown in **Figure 1C**.

Interaction of $Ctr1_{1-14}$ With Ag(I) Ions

As a next step, the interaction of $Ctr1_{1-14}$ with redox-stable Ag(I), as a mimic of Cu(I), was investigated via NMR. Thus, a peptide solution (250 μM) was treated with increasing aliquots of $AgNO_3$ both in Pi buffer (25 mM) and in MES (10 mM) at pH 7.0. NMR is more informative in the present case given the diamagnetic nature of the metal ion. Ag(I) was found to perturb the signals of His and Met, indicating the involvement of both types of residues in Ag(I) coordination. In particular, the methyl signals of methionines underwent a downfield shift with respect to the apopeptide and a splitting into four peaks, indicating chemical inequivalence of ε-CH_3 groups. Similarly to Cu(II), also in this case a greater variation of chemical shifts was observed in MES buffer than in Pi. Chemical shift changes were complete after addition of 2 eq of Ag(I) to the peptide (**Figure 5**). Consistently, the ESI-MS spectra indicated the binding of one and two Ag(I) ions, giving rise to two pairs of signals at 887.2496 and 591.8346 m/*z* and at 940.1882 and 627.1270 m/*z*, respectively (in each pair the first signal belongs to the 2 + fragment and the second to the 3 + fragment; **Figures 6A–E**).

To model the putative metal binding site(s), the Ag(I) ion was coordinated to the network topologies calculated for the apopeptide (see above), and the metal-bound coordinates were optimized at the Density Functional Theory (DFT) level using PBE as density functional (Ernzerhof and Perdew, 1998) and DGDZVP as basis sets (Godbout et al., 1992). The DFT optimized structures of $Ctr1_{1-14}$ coordinated to Ag(I) are reported in **Figure 7** and the coordination distances are listed in **Table 2**.

Model 1 shows a quasi-trigonal geometry around the Ag(I) ion which involves the sulfur atoms of Met7 and Met12 and the carbonyl of Met7, with a predicted hydrogen bond involving the amide proton and the sulfur atom of Met9 (it can be noted that this model alone could account for different chemical shifts for all methionine methyls). In Model 2, Ag(I) has a pseudo-tetrahedral geometry involving the Nε2 of His5, the sulfur atom of Met12 and the two carbonyl groups of Ser10 and Tyr11. Model 3 is compatible with a quasi-tetrahedral geometry around the Ag(I) ion involving the Nε2 of His5 and His6, the sulfur atom of Met7 and the carbonyl group of His6. In Model 4, Ag(I) has a pseudo-linear coordination geometry involving Nε2 of His5 and His6, eventually bent by the hydrogen bonds between the imidazole ring proton HNδ1 of His6 and the sulfur atom of Met7 and between HNδ1 of His5 and the carbonyl oxygen of Ser10.

The calculated total energy differences are reported in **Table 3** and indicate that Model 1 is the lowest in energy, followed by Model 2 and Model 3 with energy differences of 0.47 and 0.82 kcal/mol, respectively. These small energy differences are easily accessible owing to thermal effects at room temperature and suggest a possible interconversion between different

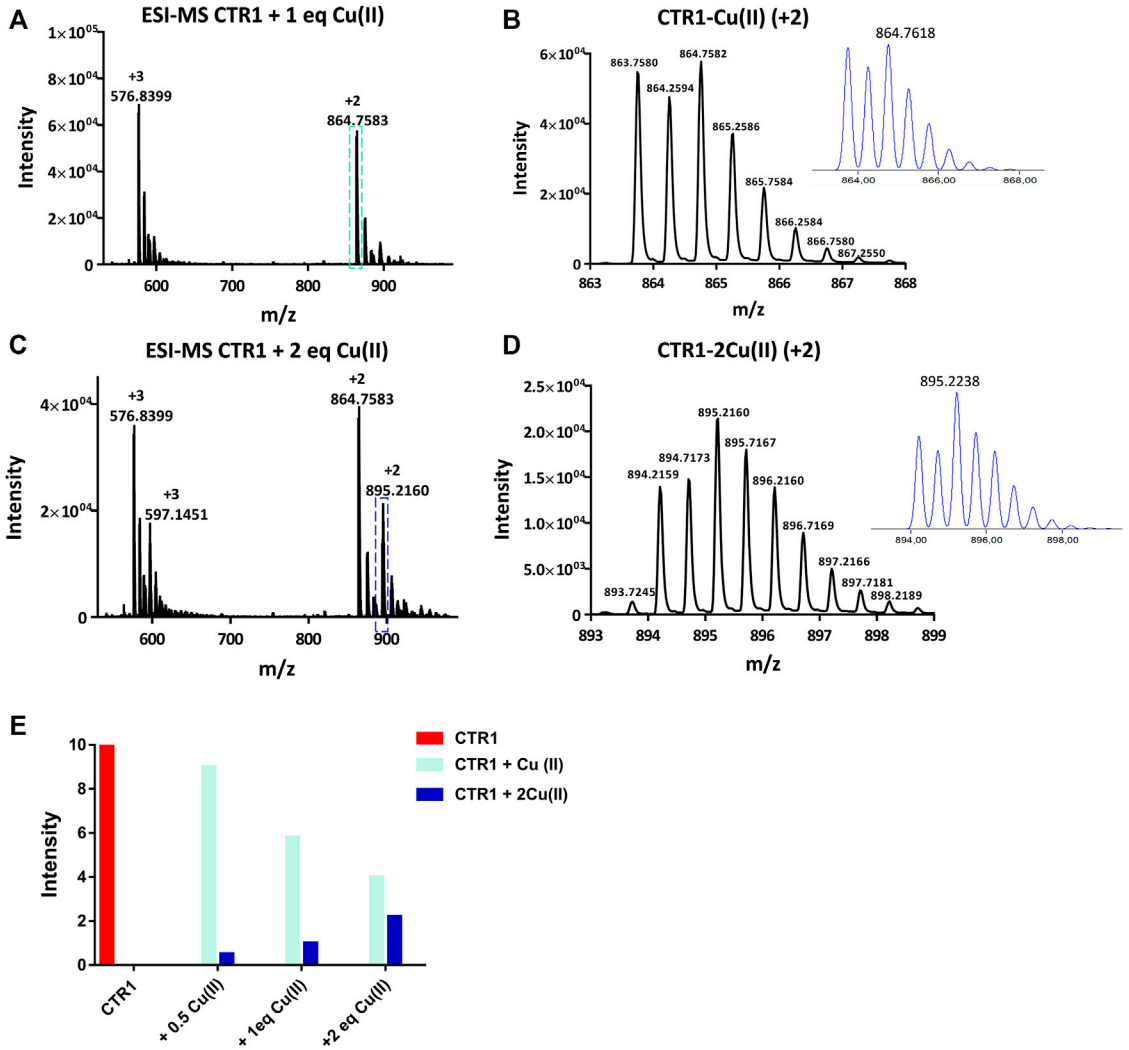

FIGURE 4 | ESI-MS spectra of $Ctr1_{1-14}$ treated with 1 and 2 eq of $CuSO_4$ **(A,C)**and magnification of the doubly charged peaks (*cyan and blue dashed boxes*) displayed in **(B,D)**, respectively; the insets show the calculated isotopic distributions. **(E)** Intensity of doubly charged ESI-MS peaks of different $Ctr1_{1-14}$ species as a function of Cu(II):peptide ratio.

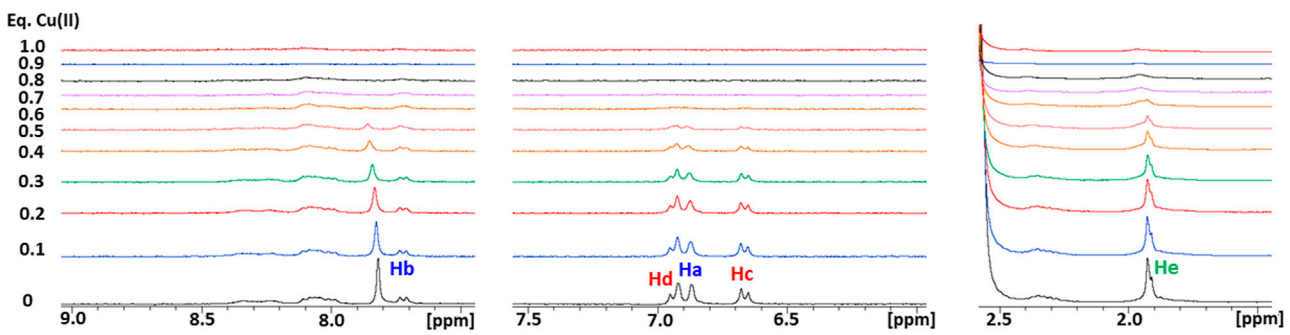

FIGURE 5 | Overlay of three regions of 1D ^{1}H NMR spectra of $Ctr1_{1-14}$ in 10 mM MES (pH 7) at different Ag(I):peptide ratios. Proton assignment scheme as shown in **Figure 1C**.

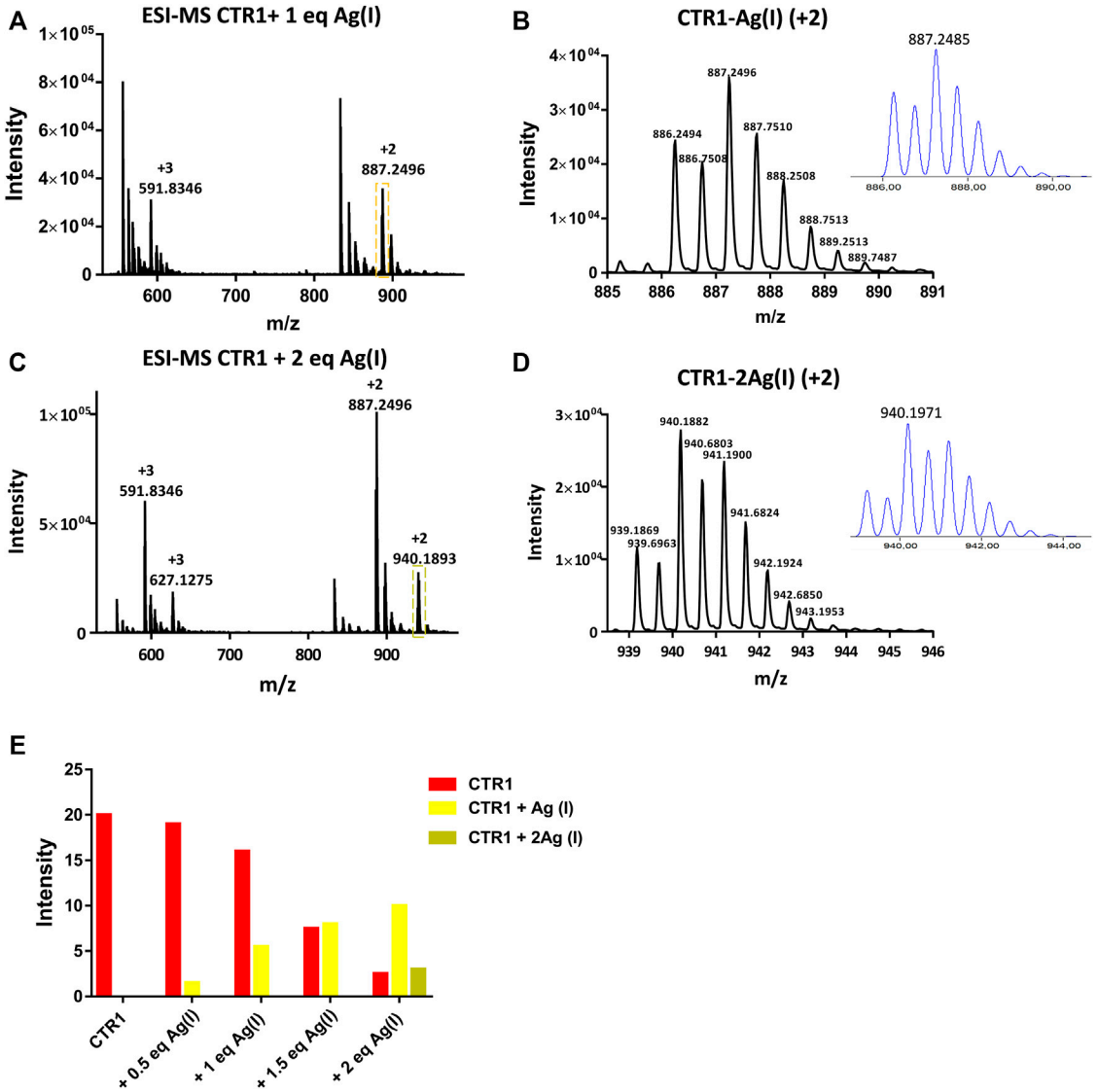

FIGURE 6 | ESI-MS spectra of $Ctr1_{1-14}$ treated with 1 and 2 eq of $AgNO_3$ **(A,C)** and magnification of the doubly charged peaks (*yellow and green dashed boxes*) displayed in **(B,D)**, respectively; the insets show the calculated isotopic distributions. **(E)** Intensity of doubly charged ESI-MS peaks of different $Ctr1_{1-14}$ species as a function of Ag(I):peptide ratio.

coordination modes. Model 4 is predicted to be the highest in energy (ΔE = +6.33 kcal/mol).

Simultaneous Binding of Cu(II) and Ag(I) to $Ctr1_{1-14}$

Given the presence of multiple metal binding sites in $Ctr1_{1-14}$, the possible interaction of the peptide with both Cu(II) and Ag(I) was investigated.

Addition of Cu(II) to a solution of $Ctr1_{1-14}$ containing 1 eq of Ag(I) in MES (pH 7.0), was found to cause a widespread broadening of the 1D ^{1}H NMR signals; however, at sub-stoichiometric Cu(II) addition a shift to lower fields of the methyl signals of methionines could be detected (**Figure 8**). Since, apart from broadening, Cu(II) alone did not cause any significant shift of apopeptide peaks (see **Figure 3**), the downfield shift of the ε-CH_3 signals could indicate a further shift of Ag(I) coordination towards the methionines caused by the interaction of Cu(II) with histidines, whose signals undergo the largest line broadening due to the paramagnetic effect of Cu(II). It is concluded that $Ctr1_{1-14}$ can accommodate a Cu(II) (ATCUN site) and an Ag(I) ion. On the basis of the different Ag(I) coordination models discussed above and displayed in **Figure 7**, it can be proposed that the conformer with Met-only coordination (Model 1 in **Figure 7A**), which was already found to be the most favored in the interaction with the free peptide, can become even more populated after addition of Cu(II).

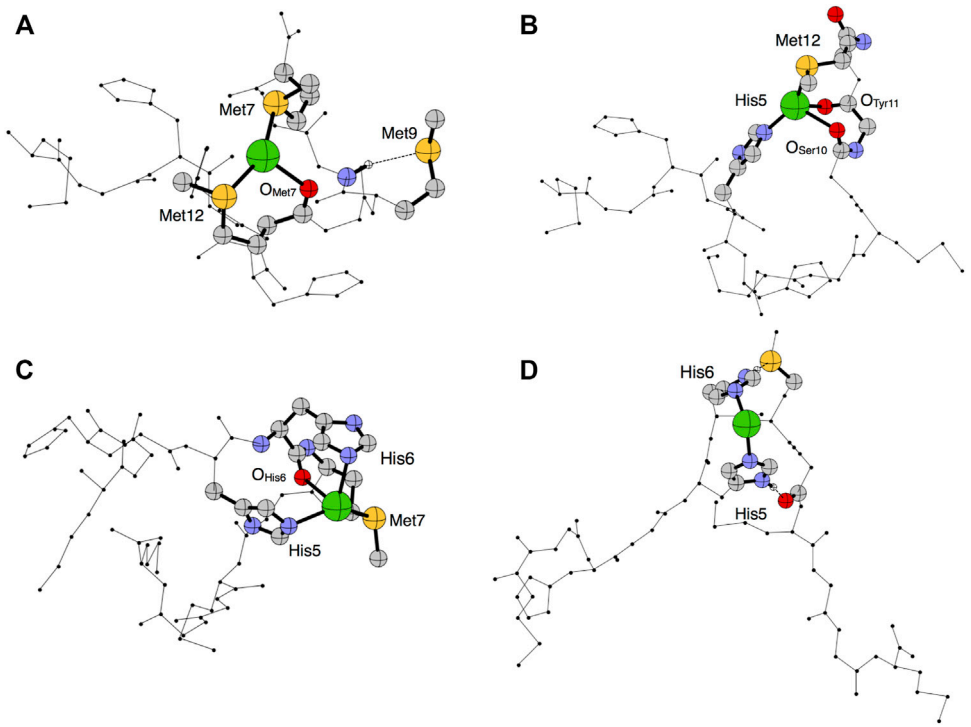

FIGURE 7 | Optimized structural models 1–4 **(A–D)** predicted in the PBE/DGDZVP framework for Ag(I)-Ctr1$_{1-14}$. The silver ion is shown in green, oxygen in red, nitrogen in blue, carbon in gray and sulfur in yellow.

TABLE 2 | Coordination parameters derived from the optimized coordinates in gas phase. Distances are reported interatomic distances (in Angstroms) and angles (in degrees) are defined by the atom names (peptide residues are indicated in brackets).

Distances (Å)				**Angles (°)**			
Model 1							
(Met7) Sδ-Ag(I)	**(Met12) Sδ-Ag(I)**	**(Met7) O-Ag(I)**		**(Met7)Sδ-Ag(I)-(Met12)Sδ**	**(Met7)Sδ-Ag(I)-(Met7)O**	**(Met12)Sδ-Ag(I)-(Met7)O**	
2.57	2.58	2.43		153.7	98.1	105.1	
Model 2							
(His5) Nε2-Ag(I)	**(Met12) Sδ-Ag(I)**	**(Ser10) O-Ag(I)**	**(Tyr11) O-Ag(I)**	**(His5)Nε2-Ag(I)-(Met12)Sδ**	**(His5)Nε2-Ag(I)-(Ser10)O**	**(Met12)Sδ-Ag(I)-(Tyr11)O**	**(Ser10)O-Ag(I)-(Tyr11)O**
2.27	2.57	2.58	2.53	149.7	112.1	110.3	72.4
Model 3							
(His5) Nε2-Ag(I)	**(His6) Nε2-Ag(I)**	**(Met7) Sδ-Ag(I)**	**(His6) O-Ag(I)**	**(His5)Nε2-Ag(I)-(His6)Nε2**	**(His6)Nε2-Ag(I)-(Met7)Sδ**	**(Met7)Sδ-Ag(I)-(His6)O**	**(His6)O-Ag(I)-(His5)Nε2-**
2.34	2.45	2.66	2.94	121.5	107.1	82.8	74.9
Model 4							
(His5) Nε2-Ag(I)	**(His6) Nε2-Ag(I)**			**(His5)Nε2-Ag(I)-(His6)Nε2**			
2.26	2.27			115.0			

TABLE 3 | PBE/DGDZVP relative energies computed for all investigated models in gas phase.

	|ΔE|(kcal/mol)
Model 1	0.00
Model 2	0.47
Model 3	0.82
Model 4	6.33

The formation of a heterobimetallic complex of Ctr1$_{1-14}$ with Cu(II) and Ag(I) was confirmed by the ESI-MS spectrum recorded in NH_4OAc, which shows, after addition of 1 eq of $CuSO_4$ to the solution of Ctr1$_{1-14}$ containing 1 eq of $AgNO_3$ in MES (pH 7.0), a pair of signals at 917.6949 and 612.1314 m/*z* (2+ and 3 + fragments, respectively), corresponding to the adduct of Ctr1$_{1-14}$ with both Ag(I) and Cu(II), as also confirmed by the full agreement between the experimental and the theoretical isotopic

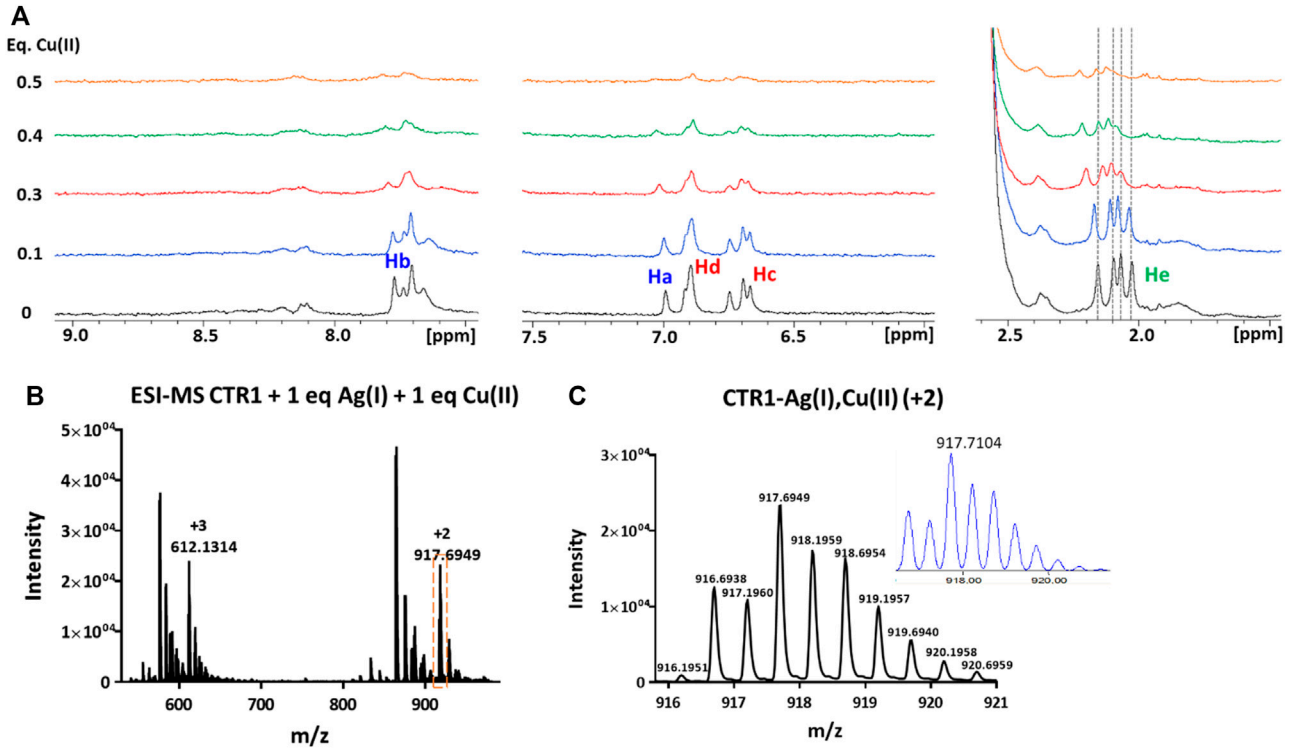

FIGURE 8 | (A) Overlay of three regions of 1D ^{1}H NMR spectra of $Ctr1_{1-14}$ containing 1 eq of Ag(I) in 10 mM MES (pH 7) treated with Cu(II) at different copper: peptide ratios; the dashed lines indicate the positions of the four methyl signals of methionines (He) before addition of Cu(II). Proton assignment scheme as shown in **Figure 1C**. **(B)** ESI-MS spectra of $Ctr1_{1-14}$ after treatment with 1 eq of $AgNO_3$ and 1 eq of $CuSO_4$ and **(C)** magnification of the doubly charged peak (*orange dashed box in B*); the inset shows the calculated isotope distribution.

distribution patterns (**Figure 8**). A similar result was obtained when the order of salt addition was reversed (addition of $AgNO_3$ to a solution of $Ctr1_{1-14}$ containing 1 eq of $CuSO_4$).

Interaction of $Ctr1_{1-14}$ With Metal Ions at Low pH

In accord with the species distribution diagram of the Cu(II) complexes with $Ctr1_{1-14}$, indicating that the affinity of Cu(II) for the peptide drops at low pH due to α-NH_2 and His protonation (Magrì et al., 2022), the NMR spectra of $Ctr1_{1-14}$ containing 1 eq of Cu(II) in 25 mM Pi buffer show almost complete recovery of the free peptide signals when the pH is lowered from 7.0 to 3.5 (**Figure 9A**). The ESI-MS spectra at low pH of a solution of $Ctr1_{1-14}$ containing 1 eq of $CuSO_4$ confirmed that the Cu(II) ion is detached and only the apopeptide is present (**Supplementary Figure S3**).

Unlike Cu(II), Ag(I) remains coordinated to $Ctr1_{1-14}$ also at low pH. This was shown by titration of *apo*$Ctr1_{1-14}$ with $AgNO_3$ in Pi buffer at pH 3.5. In this acidic environment, Ag(I) addition causes shift and splitting of the ε-CH_3 signals of methionines, while the His signals remain unperturbed, consistent with the imidazole nitrogens remaining protonated. It was observed also a distinct shift of the tyrosine ring protons (Hc), which may reflect the formation of a macrochelate (including Tyr11) consequent to the binding of Ag(I) to methionines (**Figure 9C**). The binding of Ag(I) to the peptide at acidic pH was confirmed by the ESI-MS experiment performed on a solution of $Ctr1_{1-14}$ containing 1 eq of $AgNO_3$ at pH 3.5. The observation of the pair of signals at 887.2496 and 591.8346 m/z indicates the presence of the $Ctr1_{1-14}$-Ag(I) adduct (2+ and 3+ charged fragments, respectively; **Supplementary Figure S3**).

Susceptibility of Cu(II) to Undergo Reduction by Ascorbate

Addition of ascorbate to a neutral solution containing Cu(II) and $Ctr1_{1-14}$ in 1:1 ratio does not cause an appreciable reduction of Cu(II) to Cu(I); in contrast, under acidic conditions (pH 3.5), Cu(II) can be fully reduced by addition of a stoichiometric amount of ascorbate. The formation of Cu(I), consequent to the addition of ascorbate, causes a splitting of the initially degenerate signals of the four ε-CH_3 groups of methionines (all resonating at ~1.95 ppm in *apo*$Ctr1_{1-14}$ both under neutral and acidic conditions) into three peaks that are shifted to lower field and integrate for 3, 6, and 3H, respectively. Furthermore, the proton signals of the imidazoles do not undergo any change upon addition of ascorbate, indicating that His residues are not involved in Cu(I) binding at low pH. It can be concluded that, at pH 3.5, the formed Cu(I) ion coordinates to the sulfur atoms of methionines, as already observed for Ag(I).

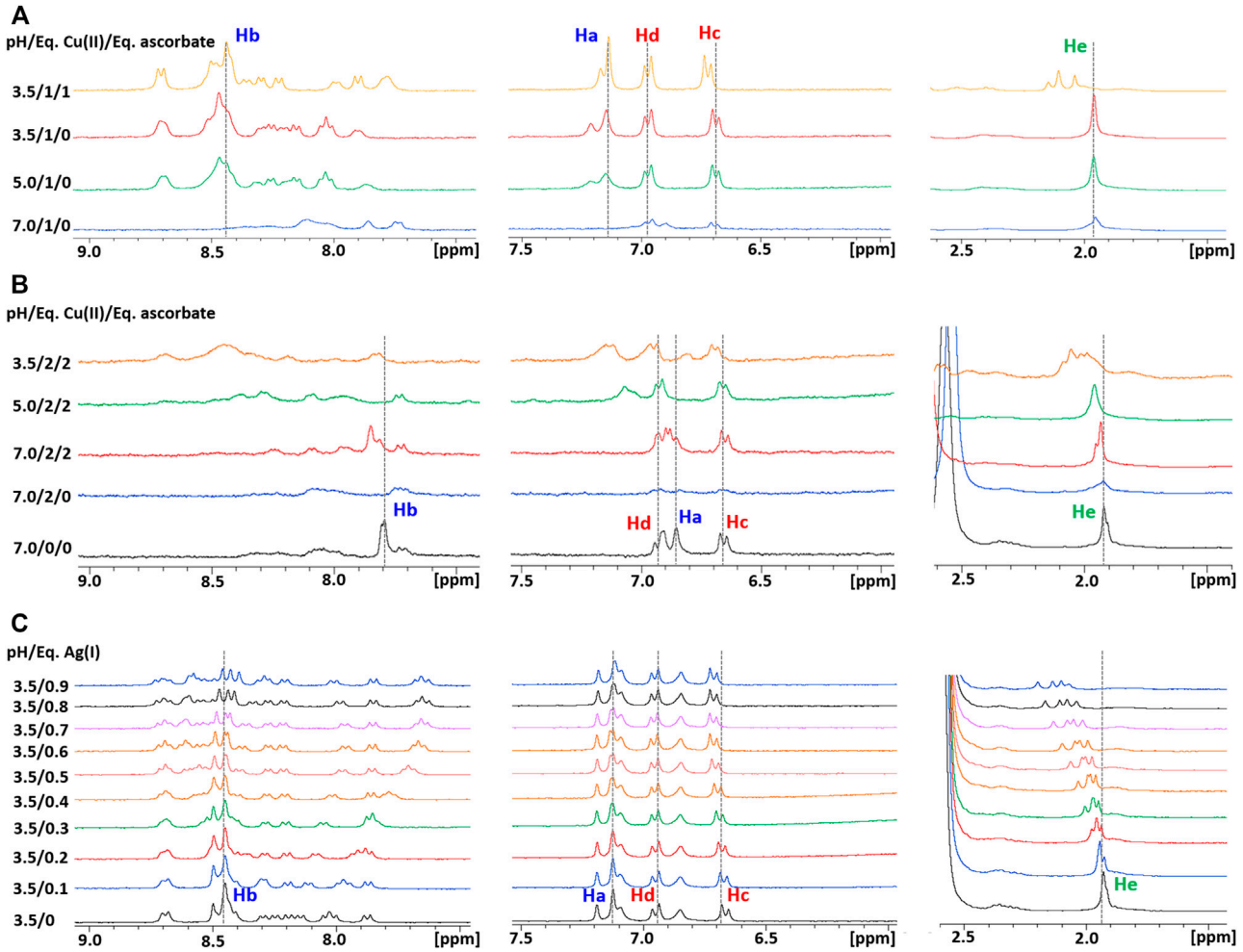

FIGURE 9 | (A) Overlay of three regions of 1D ^{1}H NMR spectra of Ctr1$_{1-14}$ containing 1 eq of Cu(II) in 25 mM Pi buffer at different pH values, with or without ascorbate; the dashed lines indicate the positions of the corresponding proton signals at pH 3.5 in the absence of ascorbate. **(B)** Overlay of three regions of 1D ^{1}H NMR spectra of Ctr1$_{1-14}$ containing 2 eq of Cu(II) in 10 mM MES at different pH values, with or without ascorbate; the dashed lines indicate the positions of the corresponding proton signals at pH 7.0 in the absence of Cu(II). **(C)** Overlay of three regions of 1D ^{1}H NMR spectra of Ctr1$_{1-14}$ in 25 mM Pi buffer (pH 3.5) at different Ag(I):peptide ratios; the dashed lines indicate the positions of the corresponding proton signals in the absence of Ag(I).

In a final experiment, Ctr1$_{1-14}$ was loaded with two equivalents of Cu(II) ions in MES at pH 7.0 and then treated with ascorbate. In this case, ascorbate was able to reduce some Cu(II) to Cu(I), even at neutral pH, causing a partial recovery in intensity of the NMR peaks, which showed a downfield shift of His aromatic signals not observed in the solution of Ctr1$_{1-14}$ containing 1 eq of Cu(II) at pH 7.0. When the pH was lowered from 7.0 to 3.5, the ε-CH_3 signals of Met residues underwent a downfield shift indicative of Cu(I) switching from His to Met coordination (**Figure 9B**). It can be concluded that the second Cu(II) is more loosely bound to the peptide and can be reduced to Cu(I) by ascorbate at neutral pH and the formed monovalent copper ion coordinates to histidines at neutral pH and to methionines at low pH.

Concerning similarities and differences between Cu(I) and Ag(I) binding to Ctr1$_{1-14}$, information can be drawn from the following observations. At pH 3.5, comparison between the ^{1}H NMR spectra of 1:1 complexes of Ctr1$_{1-14}$ with Cu(I) and Ag(I) (top spectra of **Figures 9A, C**) indicates a more pronounced downfield shift of methionine-methyl signals in the case of Ag(I) with respect to Cu(I). At neutral pH, the comparison between the spectra of Ctr1$_{1-14}$ with Cu(I) and Ag(I) (middle spectra of **Figure 9B**; **Figure 5**) suggests that while Cu(I) preferentially binds to the bis-His motif, Ag(I) binds also to Met residues. Both observations are consistent with the softer character of Ag(I), which causes this metal ion to prefer coordination to sulfur over nitrogen.

CONCLUSION

The present investigation highlights the ability of the first 14 residues of hCtr1 to host both divalent and monovalent metal ions and to form, beyond monometallic species, also

bimetallic complexes, such as $Ctr1_{1-14}$-2Cu(II) and $Ctr1_{1-14}$-2Ag(I).

Regarding the relative affinity of Cu(II) and Ag(I) ions for the peptide under neutral conditions, the ESI-MS peak intensity diagrams (**Figure 4E**; **Figure 6E**) indicate that, while the apopeptide peaks disappear after addition of 1 eq of Cu(II), the apopeptide is still the prevailing species after addition of 1 eq of Ag(I). Although, in general, the intensity of the ESI-MS peaks cannot be taken as a measure of the abundance of species in solution, in the present case the observed trend in intensities of the ESI-MS peaks parallels the relative abundances observed in a potentiometric investigation of $Ctr1_{1-14}$ solutions treated with either Cu(II) or Ag(I) ions (Magrì et al., 2022). Moreover, the results are in agreement with isothermal calorimetry data for the titration with Cu(II) or Ag(I) of the entire hCtr1 ectodomain ($Ctr1_{1-55}$) (Du et al., 2013).

By lowering the pH, the Cu(II) ion detaches from the peptide; in contrast the Ag(I) complex can survive in acidic conditions (pH 3.5), but shifts from histidines to methionine-only coordination.

Addition of ascorbate to a neutral solution containing Cu(II) and $Ctr1_{1-14}$ in 1:1 ratio does not cause an appreciable reduction of Cu(II) to Cu(I), indicating a tight binding of Cu(II) to the peptide at the ATCUN site. However, by lowering the pH to 3.5, the Cu(II) detaches from the peptide (as discussed above) and becomes susceptible to reduction to Cu(I) by ascorbate. It is noteworthy that, unlike Cu(II), Cu(I) remains coordinated to the peptide (NMR shift and splitting of the methyls of methionines), possibly by adopting a ligand coordination similar to that observed for Ag(I) at low pH and involving only Met residues (Ag(I) mode of coordination also supported by DFT calculations; **Figure 7**).

As stated above, $Ctr1_{1-14}$ can also bind two Cu(II) ions, but these Cu(II) ions proved to have different susceptibility to reduction by ascorbate at neutral pH. Therefore, addition of ascorbate to $Ctr1_{1-14}$-2Cu(II) at pH 7.0 causes a partial recovery in intensity of the NMR signals (otherwise heavily broadened by paramagnetic Cu(II)) accompanied by an evident shift of His signals (as compared to the apopeptide) with only a slight variation of Met signals, which is indicative of Cu(I) binding to the HH(M) site. By lowering the pH to 3.5, all Met signals undergo a downfield shift, in accord with Cu(I) shifting from HH(M) to Met-only coordination (and the detachment of the Cu(II) ion). This pH-regulated ligand switching is similar to that previously observed for the lumenal HM loop of ATP7A, a human Cu(I)-transporting ATPase that shuttles between the Golgi organelle and the plasma membrane (Kline et al., 2016).

That at neutral pH the N-terminal region of hCtr1 can simultaneously host a Cu(II) and a Cu(I) ion at different sites is also supported by the observation that a heterobimetallic complex ($Ctr1_{1-14}$-Cu(II),Ag(I)) can be obtained by addition of Ag(I) (a mimic of Cu(I)) to a solution of $Ctr1_{1-14}$ already loaded with Cu(II). Interestingly, the same product is obtained by addition of Cu(II) to a solution of $Ctr1_{1-14}$ loaded with Ag(I).

DATA AVAILABILITY STATEMENT

The original contributions presented in the study are included in the article/**Supplementary Material**, further inquiries can be directed to the corresponding author.

AUTHOR CONTRIBUTIONS

FA, GN, and AP planned the experiments and the calculations. MN, AB, and FA performed the experiments. MF and AP performed the calculations. MN, AB, FA, MF, and AP analyzed the data. MN, FA, GN, and AP wrote the manuscript.

FUNDING

This work was supported by the Italian Ministero dell'Istruzione, dell'Università e della Ricerca (Project "ICHEMFLY" PRIN 2017WBZFHL).

ACKNOWLEDGMENTS

The authors thank the Universities of Bari, Catania and Catanzaro for support, and the Consorzio Interuniversitario di Ricerca in Chimica dei Metalli nei Sistemi Biologici (CIRCMSB). We thank Tony Laera for his valuable contribution in sample preparation and NMR spectra analysis.

SUPPLEMENTARY MATERIAL

The Supplementary Material for this article can be found online at: https://www.frontiersin.org/articles/10.3389/fmolb.2022.897621/full#supplementary-material

REFERENCES

Abraham, L., and van der Spoel, H. (2020). *GROMACS 2020.2 Source Code*. Version 2020.2. Geneve, Switzerland: CERN Data Center.

Arnesano, F., Banci, L., and Piccioli, M. (2005). NMR Structures of Paramagnetic Metalloproteins. *Quart. Rev. Biophys.* 38, 167–219. doi:10.1017/S0033583506004161

Baker, Z. N., Cobine, P. A., and Leary, S. C. (2017). The Mitochondrion: A Central Architect of Copper Homeostasis. *Metallomics* 9, 1501–1512. doi:10.1039/c7mt00221a

Boal, A. K., and Rosenzweig, A. C. (2009). Structural Biology of Copper Trafficking. *Chem. Rev.* 109, 4760–4779. doi:10.1021/cr900104z

Bossak, K., Drew, S. C., Stefaniak, E., Płonka, D., Bonna, A., and Bal, W. (2018). The Cu(II) Affinity of the N-Terminus of Human Copper Transporter CTR1: Comparison of Human and Mouse Sequences. *J. Inorg. Biochem.* 182, 230–237. doi:10.1016/j.jinorgbio.2018.01.011

Clifford, R. J., Maryon, E. B., and Kaplan, J. H. (2016). Dynamic Internalization and Recycling of a Metal Ion Transporter: Cu Homeostasis and hCTR1, the Human Cu Uptake System. *J. Cell Sci.* 129, 1711–1721. doi:10.1242/jcs.173351

Dancis, A., Yuan, D. S., Haile, D., Askwith, C., Eide, D., Moehle, C., et al. (1994). Molecular Characterization of a Copper Transport Protein in *S. cerevisiae*: An

Unexpected Role for Copper in Iron Transport. *Cell* 76, 393–402. doi:10.1016/0092-8674(94)90345-X

Daura, X., Gademann, K., Jaun, B., Seebach, D., van Gunsteren, W. F., and Mark, A. E. (1999). Peptide Folding: When Simulation Meets Experiment. *Angew. Chem. Int. Ed.* 38, 236–240. doi:10.1002/(sici)1521-3773(19990115)38:1/2<236::aid-anie236>3.0.co;2-m

De Feo, C. J., Aller, S. G., Siluvai, G. S., Blackburn, N. J., and Unger, V. M. (2009). Three-dimensional Structure of the Human Copper Transporter hCTR1. *Proc. Natl. Acad. Sci. U.S.A.* 106, 4237–4242. doi:10.1073/pnas.0810286106

Du, X., Li, H., Wang, X., Liu, Q., Ni, J., and Sun, H. (2013). Kinetics and Thermodynamics of Metal Binding to the N-Terminus of a Human Copper Transporter, hCTR1. *Chem. Commun.* 49, 9134. doi:10.1039/c3cc45360j

Ernzerhof, M., and Perdew, J. P. (1998). Generalized Gradient Approximation to the Angle- and System-Averaged Exchange Hole. *J. Chem. Phys.* 109, 3313–3320. doi:10.1063/1.476928

Field, L. S., Luk, E., and Culotta, V. C. (2002). Copper Chaperones: Personal Escorts for Metal Ions. *J. Bioenerg. Biomembr.* 34, 373–379. doi:10.1023/a:1021202119942

Frisch, M. J., Trucks, G. W., Schlegel, H. B., Scuseria, G. E., Robb, M. A., Cheeseman, J. R., et al. (2016). *Gaussian 16, Revision C.01*. Wallingford CT: Gaussian, Inc.,

Galler, T., Lebrun, V., Raibaut, L., Faller, P., and Wezynfeld, N. E. (2020). How Trimerization of CTR1 N-Terminal Model Peptides Tunes Cu-Binding and Redox-Chemistry. *Chem. Commun.* 56, 12194–12197. doi:10.1039/D0CC04693K

Georgatsou, E., Mavrogiannis, L. A., Fragiadakis, G. S., and Alexandraki, D. (1997). The Yeast Fre1p/Fre2p Cupric Reductases Facilitate Copper Uptake and Are Regulated by the Copper-Modulated Mac1p Activator. *J. Biol. Chem.* 272, 13786–13792. doi:10.1074/jbc.272.21.13786

Godbout, N., Salahub, D. R., Andzelm, J., and Wimmer, E. (1992). Optimization of Gaussian-type Basis Sets for Local Spin Density Functional Calculations. Part I. Boron through Neon, Optimization Technique and Validation. *Can. J. Chem.* 70, 560–571. doi:10.1139/v92-079

Gonzalez, P., Bossak, K., Stefaniak, E., Hureau, C., Raibaut, L., Bal, W., et al. (2018). N-Terminal Cu-Binding Motifs (Xxx-Zzz-His, Xxx-His) and Their Derivatives: Chemistry, Biology and Medicinal Applications. *Chem. Eur. J.* 24, 8029–8041. doi:10.1002/chem.201705398

Guo, Y., Smith, K., Lee, J., Thiele, D. J., and Petris, M. J. (2004). Identification of Methionine-Rich Clusters That Regulate Copper-Stimulated Endocytosis of the Human Ctr1 Copper Transporter. *J. Biol. Chem.* 279, 17428–17433. doi:10.1074/jbc.M401493200

Haas, K. L., Putterman, A. B., White, D. R., Thiele, D. J., and Franz, K. J. (2011). Model Peptides Provide New Insights into the Role of Histidine Residues as Potential Ligands in Human Cellular Copper Acquisition via Ctr1. *J. Am. Chem. Soc.* 133, 4427–4437. doi:10.1021/ja108890c

Hassett, R., and Kosman, D. J. (1995). Evidence for Cu(II) Reduction as a Component of Copper Uptake by *Saccharomyces cerevisiae*. *J. Biol. Chem.* 270, 128–134. doi:10.1074/jbc.270.1.128

Himes, R. A., Park, G. Y., Barry, A. N., Blackburn, N. J., and Karlin, K. D. (2007). Synthesis and X-Ray Absorption Spectroscopy Structural Studies of Cu(I) Complexes of HistidylHistidine Peptides: The Predominance of Linear 2-coordinate Geometry. *J. Am. Chem. Soc.* 129, 5352–5353. doi:10.1021/ja0708013

Hu, V. W., Chan, S. I., and Brown, G. S. (1977). X-ray Absorption Edge Studies on Oxidized and Reduced Cytochrome C Oxidase. *Proc. Natl. Acad. Sci. U.S.A.* 74, 3821–3825. doi:10.1073/pnas.74.9.3821

Huffman, D. L., and O'Halloran, T. V. (2001). Function, Structure, and Mechanism of Intracellular Copper Trafficking Proteins. *Annu. Rev. Biochem.* 70, 677–701. doi:10.1146/annurev.biochem.70.1.677

Ivani, I., Dans, P. D., Noy, A., Pérez, A., Faustino, I., Hospital, A., et al. (2016). Parmbsc1: a Refined Force Field for DNA Simulations. *Nat. Methods* 13, 55–58. doi:10.1038/nmeth.3658

Jiang, J., Nadas, I. A., Kim, M. A., and Franz, K. J. (2005). A Mets Motif Peptide Found in Copper Transport Proteins Selectively Binds Cu(I) with Methionine-Only Coordination. *Inorg. Chem.* 44, 9787–9794. doi:10.1021/ic051180m

Jorgensen, W. L., Chandrasekhar, J., Madura, J. D., Impey, R. W., and Klein, M. L. (1983). Comparison of Simple Potential Functions for Simulating Liquid Water. *J. Chem. Phys.* 79, 926–935. doi:10.1063/1.445869

Kagan, H. M., and Li, W. (2003). Lysyl Oxidase: Properties, Specificity, and Biological Roles inside and outside of the Cell. *J. Cell. Biochem.* 88, 660–672. doi:10.1002/jcb.10413

Kline, C. D., Gambill, B. F., Mayfield, M., Lutsenko, S., and Blackburn, N. J. (2016). pH-Regulated Metal–Ligand Switching in the HM Loop of ATP7A: a New Paradigm for Metal Transfer Chemistry. *Metallomics* 8, 729–733. doi:10.1039/C6MT00062B

Lee, J., Prohaska, J. R., and Thiele, D. J. (2001). Essential Role for Mammalian Copper Transporter Ctr1 in Copper Homeostasis and Embryonic Development. *Proc. Natl. Acad. Sci. U.S.A.* 98, 6842–6847. doi:10.1073/pnas.111058698

Lutsenko, S. (2021). Dynamic and Cell-Specific Transport Networks for Intracellular Copper Ions. *J. Cell Sci.* 134, jcs240523. doi:10.1242/jcs.240523

Magrì, A., Tabbì, G., Naletova, I., Attanasio, F., Arena, G., and Rizzarelli, E. (2022). A Deeper Insight in Metal Binding to the hCtr1 N-Terminus Fragment: Affinity, Speciation and Binding Mode of Binuclear Cu2+ and Mononuclear Ag+ Complex Species. *Ijms* 23, 2929. doi:10.3390/ijms23062929

Matoba, Y., Kumagai, T., Yamamoto, A., Yoshitsu, H., and Sugiyama, M. (2006). Crystallographic Evidence that the Dinuclear Copper Center of Tyrosinase Is Flexible during Catalysis. *J. Biol. Chem.* 281, 8981–8990. doi:10.1074/jbc.M509785200

Molloy, S. A., and Kaplan, J. H. (2009). Copper-dependent Recycling of hCTR1, the Human High Affinity Copper Transporter. *J. Biol. Chem.* 284, 29704–29713. doi:10.1074/jbc.M109.000166

Nevitt, T., Öhrvik, H., and Thiele, D. J. (2012). Charting the Travels of Copper in Eukaryotes from Yeast to Mammals. *Biochim. Biophys. Acta (BBA) - Mol. Cell Res.* 1823, 1580–1593. doi:10.1016/j.bbamcr.2012.02.011

O'Halloran, T. V., and Culotta, V. C. (2000). Metallochaperones, an Intracellular Shuttle Service for Metal Ions. *J. Biol. Chem.* 275, 25057–25060. doi:10.1074/jbc.R000006200

Ohgami, R. S., Campagna, D. R., McDonald, A., and Fleming, M. D. (2006). The Steap Proteins Are Metalloreductases. *Blood* 108, 1388–1394. doi:10.1182/blood-2006-02-003681

Oosterheert, W., van Bezouwen, L. S., Rodenburg, R. N. P., Granneman, J., Förster, F., Mattevi, A., et al. (2018). Cryo-EM Structures of Human STEAP4 Reveal Mechanism of Iron(III) Reduction. *Nat. Commun.* 9, 4337. doi:10.1038/s41467-018-06817-7

Palumaa, P. (2013). Copper Chaperones. The Concept of Conformational Control in the Metabolism of Copper. *FEBS Lett.* 587, 1902–1910. doi:10.1016/j.febslet.2013.05.019

Petris, M. J., Smith, K., Lee, J., and Thiele, D. J. (2003). Copper-stimulated Endocytosis and Degradation of the Human Copper Transporter, hCtr1. *J. Biol. Chem.* 278, 9639–9646. doi:10.1074/jbc.M209455200

Pettersen, E. F., Goddard, T. D., Huang, C. C., Couch, G. S., Greenblatt, D. M., Meng, E. C., et al. (2004). UCSF Chimera?A Visualization System for Exploratory Research and Analysis. *J. Comput. Chem.* 25, 1605–1612. doi:10.1002/jcc.20084

Pfaendtner, J., and Bonomi, M. (2015). Efficient Sampling of High-Dimensional Free-Energy Landscapes with Parallel Bias Metadynamics. *J. Chem. Theory Comput.* 11, 5062–5067. doi:10.1021/acs.jctc.5b00846

Pope, C. R., Flores, A. G., Kaplan, J. H., and Unger, V. M. (2012). Structure and Function of Copper Uptake Transporters. *Curr. Top. Membrin.* 69, 97–112. doi:10.1016/B978-0-12-394390-3.00004-5

Prigge, S. T., Mains, R. E., Eipper, B. A., and Amzel* **, L. M. (2000). New Insights into Copper Monooxygenases and Peptide Amidation: Structure, Mechanism and Function. *Cell. Mol. Life Sci.* 57, 1236–1259. doi:10.1007/PL00000763

Pushie, M. J., Shaw, K., Franz, K. J., Shearer, J., and Haas, K. L. (2015). Model Peptide Studies Reveal a Mixed Histidine-Methionine Cu(I) Binding Site at the N-Terminus of Human Copper Transporter 1. *Inorg. Chem.* 54, 8544–8551. doi:10.1021/acs.inorgchem.5b01162

Ren, F., Logeman, B. L., Zhang, X., Liu, Y., Thiele, D. J., and Yuan, P. (2019). X-ray Structures of the High-Affinity Copper Transporter Ctr1. *Nat. Commun.* 10, 1386. doi:10.1038/s41467-019-09376-7

Robinson, N. J., and Winge, D. R. (2010). Copper Metallochaperones. *Annu. Rev. Biochem.* 79, 537–562. doi:10.1146/annurev-biochem-030409-143539

Rubino, J. T., Riggs-Gelasco, P., and Franz, K. J. (2010). Methionine Motifs of Copper Transport Proteins Provide General and Flexible Thioether-Only

Binding Sites for Cu(I) and Ag(I). *J. Biol. Inorg. Chem.* 15, 1033–1049. doi:10.1007/s00775-010-0663-9

Santoro, A., Walke, G., Vileno, B., Kulkarni, P. P., Raibaut, L., and Faller, P. (2018). Low Catalytic Activity of the Cu(II)-binding Motif (Xxx-Zzz-His; ATCUN) in Reactive Oxygen Species Production and Inhibition by the Cu(i)-Chelator BCS. *Chem. Commun.* 54, 11945–11948. doi:10.1039/c8cc06040a

Shearer, J., and Szalai, V. A. (2008). The Amyloid-β Peptide of Alzheimer's Disease Binds Cu 1 in a Linear Bis-His Coordination Environment: Insight into a Possible Neuroprotective Mechanism for the Amyloid-β Peptide. *J. Am. Chem. Soc.* 130, 17826–17835. doi:10.1021/ja805940m

Siiskonen, A., and Priimagi, A. (2017). Benchmarking DFT Methods with Small Basis Sets for the Calculation of Halogen-Bond Strengths. *J. Mol. Model.*. 23, 50. doi:10.1007/s00894-017-3212-4

Tsukihara, T., Aoyama, H., Yamashita, E., Tomizaki, T., Yamaguchi, H., Shinzawa-Itoh, K., et al. (1995). Structures of Metal Sites of Oxidized Bovine Heart Cytochrome C Oxidase at 2.8 Å. *Science* 269, 1069–1074. doi:10.1126/science.7652554

Van Den Berghe, P. V. E., Folmer, D. E., Malingré, H. E. M., Van Beurden, E., Klomp, A. E. M., Van De Sluis, B., et al. (2007). Human Copper Transporter 2 Is Localized in Late Endosomes and Lysosomes and Facilitates Cellular Copper Uptake. *Biochem. J.* 407, 49–59. doi:10.1042/BJ20070705

Yang, Y., Zhu, Y., Hu, H., Cheng, L., Liu, M., Ma, G., et al. (2019). Cuprous Binding Promotes Interaction of Copper Transport Protein hCTR1 with Cell Membranes. *Chem. Commun.* 55, 11107–11110. doi:10.1039/C9CC04859F

Zhou, B., and Gitschier, J. (1997). hCTR1: A Human Gene for Copper Uptake Identified by Complementation in Yeast. *Proc. Natl. Acad. Sci. U.S.A.* 94, 7481–7486. doi:10.1073/pnas.94.14.7481

Conflict of Interest: The authors declare that the research was conducted in the absence of any commercial or financial relationships that could be construed as a potential conflict of interest.

Publisher's Note: All claims expressed in this article are solely those of the authors and do not necessarily represent those of their affiliated organizations, or those of the publisher, the editors and the reviewers. Any product that may be evaluated in this article, or claim that may be made by its manufacturer, is not guaranteed or endorsed by the publisher.

frontiers | Frontiers in Cell and Developmental Biology

ORIGINAL RESEARCH
published: 17 June 2022
doi: 10.3389/fcell.2022.925457

Mapping of the sGC Stimulator BAY 41-2272 Binding Site on H-NOX Domain and Its Regulation by the Redox State of the Heme

*Garyfallia I. Makrynitsa[1], Aikaterini I. Argyriou[1], Aikaterini A. Zompra[1], Konstantinos Salagiannis[2], Vassiliki Vazoura[2], Andreas Papapetropoulos[3], Stavros Topouzis[2] and Georgios A. Spyroulias[1]**

[1]Department of Pharmacy, University of Patras, Patras, Greece, [2]Laboratory of Molecular Pharmacology, Department of Pharmacy, University of Patras, Patras, Greece, [3]Laboratory of Pharmacology, Faculty of Pharmacy, National and Kapodistrian University of Athens, Athens, Greece

OPEN ACCESS

Edited by:
Simone Ciofi Baffoni,
University of Florence, Italy

Reviewed by:
Peep Palumaa,
Tallinn University of Technology, Estonia
Ricardo O. Louro,
Universidade Nova de Lisboa, Portugal
Mario Piccioli,
University of Florence, Italy

***Correspondence:**
Georgios A. Spyroulias
G.A.Spyroulias@upatras.gr

Specialty section:
This article was submitted to Cellular Biochemistry, a section of the journal Frontiers in Cell and Developmental Biology

Received: 21 April 2022
Accepted: 27 May 2022
Published: 17 June 2022

Citation:
Makrynitsa GI, Argyriou AI, Zompra AA, Salagiannis K, Vazoura V, Papapetropoulos A, Topouzis S and Spyroulias GA (2022) Mapping of the sGC Stimulator BAY 41-2272 Binding Site on H-NOX Domain and Its Regulation by the Redox State of the Heme. Front. Cell Dev. Biol. 10:925457. doi: 10.3389/fcell.2022.925457

Soluble guanylate cyclase (sGC) is the main receptor of nitric oxide (NO) and by converting GTP to cGMP regulates numerous biological processes. The β1 subunit of the most abundant, α1β1 heterodimer, harbors an N-terminal domain called H-NOX, responsible for heme and NO binding and thus sGC activation. Dysfunction of the NO/sGC/cGMP axis is causally associated with pathological states such as heart failure and pulmonary hypertension. Enhancement of sGC enzymatic function can be effected by a class of drugs called sGC "stimulators," which depend on reduced heme and synergize with low NO concentrations. Until recently, our knowledge about the binding mode of stimulators relied on low resolution cryo-EM structures of human sGC in complex with known stimulators, while information about the mode of synergy with NO is still limited. Herein, we couple NMR spectroscopy using the H-NOX domain of the *Nostoc* sp. cyanobacterium with cGMP determinations in aortic smooth muscle cells (A7r5) to study the impact of the redox state of the heme on the binding of the sGC stimulator BAY 41-2272 to the *Ns* H-NOX domain and on the catalytic function of the sGC. BAY 41-2272 binds on the surface of H-NOX with low affinity and this binding is enhanced by low NO concentrations. Subsequent titration of the heme oxidant ODQ, fails to modify the conformation of H-NOX or elicit loss of the heme, despite its oxidation. Treatment of A7r5 cells with ODQ following the addition of BAY 41-2272 and an NO donor can still inhibit cGMP synthesis. Overall, we describe an analysis in real time of the interaction of the sGC stimulator, BAY 41-2272, with the *Ns* H-NOX, map the amino acids that mediate this interaction and provide evidence to explain the characteristic synergy of BAY 41-2272 with NO. We also propose that ODQ can still oxidize the heme in the H-NOX/NO complex and inhibit sGC activity, even though the heme remains associated with H-NOX. These data provide a more-in-depth understanding of the molecular mode of action of sGC stimulators and can lead to an optimized design and development of novel sGC agonists.

Keywords: BAY 41-2272, nitric-oxide (NO), NMR spectroscopy, soluble guanylate cyclase (sGC), H-NOX domain, cGMP (cyclic GMP)

INTRODUCTION

The nitric oxide/cyclic guanosine monophosphate (NO/cGMP) signaling pathway plays a pivotal role in numerous physiological processes, such as the establishment of a healthy homeostasis for the cardiovascular system. Hence, its impaired function has been linked to several diseases, such as pulmonary arterial hypertension (PAH), heart failure, chronic kidney disease and erectile dysfunction (Sandner et al., 2021). The physiological "receptor" of NO is the enzyme soluble guanylate cyclase (sGC), which converts GTP to cGMP (Derbyshire and Marletta, 2009; Papapetropoulos et al., 2015).

sGC is a heterodimer formed by one α and one β subunit, each with two variants, $\alpha1\beta1$ being the most common and best described isoform found in mammals. Each subunit consists of four distinct domains: an N-terminal H-NOX (heme-nitric oxide/oxygen binding) domain, a Per/Arnt/Sim (PAS) domain, followed by a coiled-coil region and the C-terminal catalytic domain. A prosthetic heme group binds on the H-NOX domain of the $\beta1$ subunit *via* a covalent bond with the residue His105. The corresponding domain of $\alpha1$ subunit is not able to bind heme and does not exhibit the features of the H-NOX protein (Derbyshire and Marletta, 2012). NO binds to the H-NOX heme-associated iron, arising electronic, dynamic and conformational changes transmitted to the catalytic domain and eliciting the activation of the sGC (Underbakke et al., 2014; Kang et al., 2019).

Impaired sGC activity can result from either heme oxidation and subsequent loss from sGC (followed by sGC degradation) or from low NO bioavailability. Both lead to dysfunction of the NO/cGMP pathway and the development of pathological conditions (Stasch et al., 2006; Sandner et al., 2021).

In the past 20 years, two classes of therapeutic molecules have been synthesized as agonists of the sGC, to be added to the old class of NO donors: NO- and heme-independent "activators" and NO-independent "stimulators" that require a reduced heme moiety is essential for their action on sGC. Activators associate with the oxidized or heme-free sGC, by occupying the same cavity with the heme and restoring the proper function of the enzyme as well as stabilizing it (Evgenov et al., 2006). Om the other hand, although stimulator molecules increase the activity of sGC in an NO-independent manner, they are also able to strongly synergize with low NO levels, a characteristic important for their therapeutic success. So far, two stimulators have been approved by the FDA: Riociguat (trade name: Adempas), to treat forms of pulmonary arterial hypertension (PAH) (Mittendorf et al., 2009; Stasch and Evgenov, 2013; Khaybullina et al., 2014) and Vericiguat (trade name: Verquvo) for reduced ejection fraction heart failure (Follmann et al., 2017; Armstrong et al., 2018). Recently, two cryoEM structures of sGC in complex with NO and either of two stimulators, Riociguat (PDB ID: 7D9R) and YC-1 (PDB ID: 7D9S) at a resolution of 3.70 Å and 3.90 Å respectively, suggested that the binding site of Riociguat and YC-1 is located between the H-NOX domain and the two coiled-coil domains (Liu et al., 2021). BAY 41-2272 is a potent sGC stimulator which can increase sGC activity by 400-fold in synergy with NO and based on preclinical evidence (Straub et al., 2001; Dunkern et al., 2007), it could be used for treatment of pulmonary fibrosis. Despite the years of studying the biochemistry and the pharmacology of the sGC stimulators, little is known about their exact mechanism of action and how NO can modulate their activity. Additionally, static Cryo-EM studies offer little knowledge about the atomic-level conformational and dynamical changes coupled with sGC's activation by a stimulator.

In the present study, we use as a model the recombinant H-NOX domain from the *Nostoc* sp. cyanobacterium (*Ns* H-NOX) and apply NMR spectroscopy to probe the binding behavior of the sGC stimulator BAY 41-2272, in the absence of any external ligand besides the heme prosthetic group. Additionally, we exploit the unique potential of NMR to simultaneously probe conformational changes, weak binding events and changes in the electronic and coordination state of the heme and to identify the link between the redox state of the heme and the synergistic action of the stimulators with NO. Moreover, we provide functional evidence by cell-based assays to determine the impact of the heme oxidation state on the ability of BAY 41-2272 to stimulate the sGC holoenzyme.

MATERIALS AND METHODS

Materials

All chemicals for bacterial cultures and the protein sample preparation were from Applichem. DEA-NONOate and 5-aminolevulinic acid (hydrochloride) were purchased by Cayman chemicals and used for as NO-donor and precursor of heme's biosynthesis respectively. 1H-[1,2,4]oxadiazolo[4,3-a] quinoxalin-1-one (ODQ) (Cayman chemicals) were used as a heme-oxidizing. The sGC stimulator BAY 41-2272 was kindly provided by BAYER AG. Non-selective PDE inhibitor (isobutyl-methyl-xanthine, IBMX) and sodium nitroprusside (SNP, NO donor in cell-based assays) were purchased by Applichem. Cyclic GMP Elisa kit and micro BCA protein assay kit were purchased by Cayman chemicals and Thermo Fisher Scientific respectively.

Protein Sample Preparation

The experimental protocol for the expression, purification and NMR sample preparation of the *Ns* H-NOX C139A variant (residues M1-D183) has been reported previously (Alexandropoulos et al., 2016). Protein concentration of the ^{15}N-labeled sample for NMR titration experiments was 0.5 and 0.8 mM for the titration experiment with NO and BAY 41-2272 respectively.

NMR Spectroscopy

All NMR experiments acquired on a Bruker Avance III HD four channel 700 MHz NMR spectrometer at 298 K, equipped with TCI 5 mm 1H/13C/15N/D-gradient probe while ^{19}F NMR spectra were acquired on a Bruker Avance III HD 600 MHz NMR spectrometer equipped with BBFO probe. All data sets were processed with Topspin 3.5 software and analyzed with CARA (Keller, 2004). Backbone and side chain assignment of the heme-bound *Ns* H-NOX domain has been reported in previous study (BMRB ID: 26048) (Alexandropoulos et al., 2016).

^{19}F NMR spectra were acquired with 512 scans, 1 s recycle delay and acquisition time of 0.4893355 s.

NMR Titration Experiments

To monitor the behavior of the individual amino acids of the ^{15}N-labeled *Ns* H-NOX in the presence of BAY 41-2272, we calculated the changes of their chemical shifts in ^{1}H–^{15}N HSQC spectra during the NMR titration experiment. The unlabeled ligand (stock: 100 mM) was added in 9 steps in order to reach excess in the protein sample. Chemical shift perturbation (CSP) values were calculated using the **Eq. 1**.

$$\Delta\delta_{ppm} = \sqrt{(\Delta\delta_{HN})^2 + \left(\frac{\Delta\delta_N}{5}\right)^2} \quad (1)$$

The threshold was defined by calculating the standard deviation σ and then multiplying the value by 3 (Williamson, 2013). The same approach was applied to examine the interaction of BAY 41-2272 in the presence of NO, by preparing firstly the *Ns* H-NOX/NO through NMR driven titration experiments. For the residues with significant perturbations, their CSPs were plotted as a function of BAY 41-2272 concentration and fitted into the **Eq. 2** (Williamson, 2013).

$$\Delta\delta_{ppm} = \Delta\delta_{max}\left\{ ([P]_t + [L]_t + K_D) - \left[([P]_t + [L]_t + K_D)^2 - 4[P]_t + [L]_t \right]^{1/2} \right\} \Big/ 2[P]_t \quad (2)$$

where $\Delta\delta_{max}$ is the maximum shift change on saturation, $[P]_t$ is the total concentration of the protein and $[L]_t$ is the total concentration of the ligand.

UV-Vis Measurements

All the measurements were carried out on Q5000 microvolume spectrophotometer (Quawell) at room temperature with sample volume 2 µl and measurement path 0.2 mm. The spectra were recorded from the proteins in a solution of 50 mM potassium phosphate and 30 mM NaCl (pH: 7).

Cell-Based cGMP Determination

A7r5 rat aortic smooth muscle cells (RAoSM) (ATCC, Rockville, MD, United States) were cultured in 48-well clusters in DMEM growth media (GibcoTM), supplemented with 10% Fetal Bovine Serum (GibcoTM) and 1% Penicillin/Streptomycin (Biosera).

At confluence, cells were serum-starved for 2 h in media containing 0.1% BSA and were then pre-exposed for 5 min to the non-selective phosphodiesterase (PDE) inhibitor isobutyl-methyl-xanthine (IBMX, 1 mM). Then, they were treated with the sGC stimulator BAY 41-2272 at 10 µM or a combination of the heme-dependent NO donor sodium nitroprusside (SNP at 100 µM) and BAY 41-2272, for 15 min. Some of the cells that received the BAY compound or the BAY/SNP combination were also treated with the heme-oxidizing compound 1H-[1,2,4] oxadiazolo[4,3-a]quinoxalin-1-one (ODQ) (at 10 µM) or its vehicle control (DMSO), either 20 min before the addition of IBMX (and hence before the sGC agonists) or 2 min after the addition of the agonist(s).

Cellular cGMP content was assessed as previously described (Argyriou et al., 2021), by collecting the extracts with HCl 0.1 M, which were analyzed by a commercial ELISA kit according to the manufacturer's instructions. The cGMP levels in each well were normalized for the respective total protein determined by a Micro BCA Protein assay kit.

RESULTS

BAY 41-2272 Binds Weakly to the *Nostoc* sp. H-NOX Domain

For the NMR experiments, the H-NOX domain from cyanobacterium *Nostoc* sp. (*Ns* H-NOX) was used as model. H-NOX domains are well-conserved among different organisms, sharing common structural features. *Ns* H-NOX shares 33.86% sequence identity with *Hs* sGC β1-subunit H-NOX: 17 out of 27 amino acids that form the heme cavity are identical, making it the most extensively characterized among the H-NOX family domains (Makrynitsa et al., 2019; Wittenborn and Marletta, 2021).

Initially, we investigated the binding behaviour of the sGC stimulator BAY 41-2272, through NMR-driven titration experiments. Overall, during the interaction, 13 residues were found in the fast-exchange regime on the NMR time-scale and displayed CSP values above threshold (**Figures 1A,B**, **2A**). Mapping these residues on the 3D structure of the *Ns* H-NOX (PDB ID: 4IAM) (Kumar et al., 2013), shows that the amino acids affected mainly lie on the α_3 and α_4 α-helices as well as on the loop connecting α_2-α_3 and α_3-α_4 α-helices, are distributed on the surface of the protein and delineate a binding site juxtaposed to the heme moiety (**Figures 1B**, **2A**). Residues defining the binding surface are conserved in other bacterial H-NOX domains (Makrynitsa et al., 2019) as well as in the β1 H-NOX domain (**Supplementary Figure S1A**), making it likely that they also play a role in the interaction of BAY 41-2272 with the sGC β1 H-NOX. Moreover, when these results are compared to the reported cryoEM structure of sGC in complex with NO and Riociguat (Liu et al., 2021), it is evident that the residues participating in the binding of the drug are the same in both cases, strengthening the evidence that BAY 41-2272 and related stimulators bind to a conserved pocket in the H-NOX domain (**Supplementary Figure S1B**).

CSP values of all 16 perturbed residues were plotted against the BAY 41-2272 concentration, yielding the binding constant (K_D) for each residue (**Figure 1C**; **Supplementary Table S1**). Values of the K_D are very similar to the corresponding ones for *Shewanella woodyi* (*Sw*), indicating that BAY 41-2272 exhibit the same affinity towards *Ns* H-NOX domain as the IWP-051 to *Sw* H-NOX (Wales et al., 2018). It is observed a low affinity interaction (~mM) between *Ns* H-NOX domain BAY 41-2272. However, the stoichiometry of the binding cannot be calculated

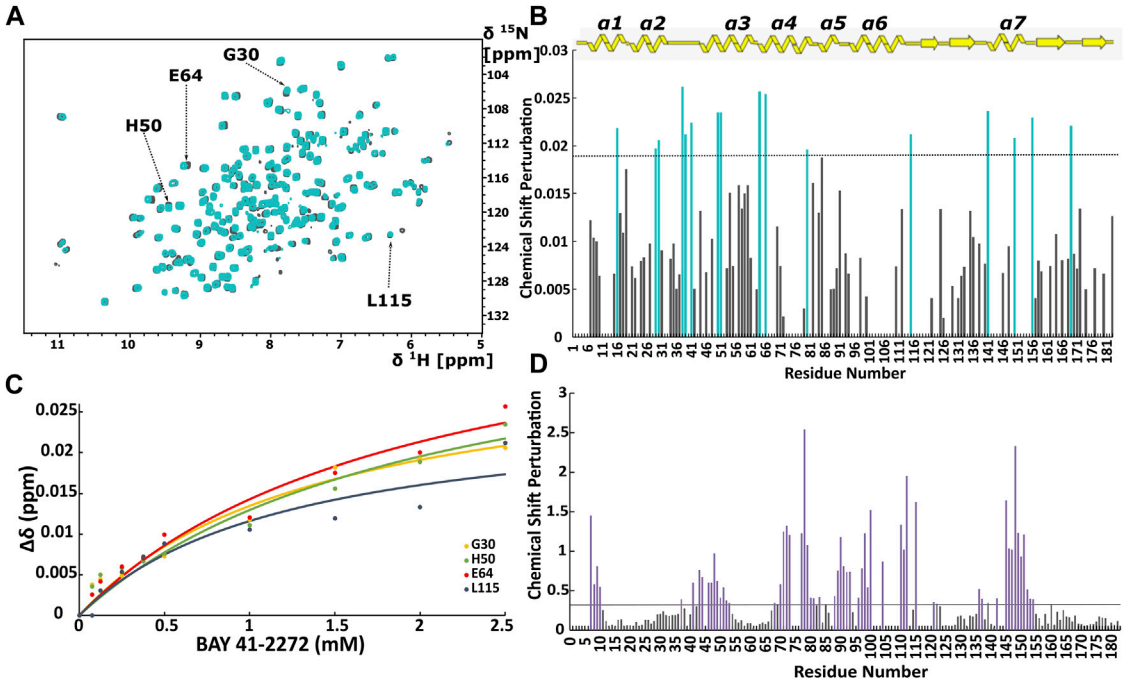

FIGURE 1 | (A) Overlay of ^{1}H-^{15}N HSQC spectra of the *Ns* H-NOX domain in heme-bound state (grey) and BAY 41-2272 bound state (cyan). **(B)** Top panel: Secondary structure of X-ray structure of *Ns* H-NOX. CSP in response to BAY 41-2272 binding with threshold value 0.0188. **(C)** Plot of CSP versus BAY 41-2272 concentration; data fitted against **Eq. 2**. Cyan bars represent the residues with higher CSP than the threshold **(D)** CSP in response to BAY 58-2667 binding with threshold value 0.33. Purple bars indicate the residues with CSP value above the threshold after BAY 58-2667 addition (Argyriou et al., 2021).

because the titration experiment was performed up to 1:5. In fact, according to CSP data, BAY 41-2272 interacts with *Ns* H-NOX domain *via* one specific site on the protein surface, while the cryoEM structure of the sGC in complex with another stimulator (Riociguat) indicate a single binding site (Liu et al., 2021). Therefore, it is speculated that *Ns* H-NOX domain binds one molecule of BAY 41-2272.

Mapping of the residues with a CSP value above the threshold on the X-ray structure of *Ns* H-NOX domain under 6atm of Xenon (PDB ID: 3TFA) (Winter et al., 2011), revealed that the binding site of the BAY 41-2272 is located near the Xe atoms in juxtaposition with the two tunnels that are thought to allow the flux of NO (**Figure 2B**). This system of tunnels behaves as a "pathway" for NO diffusion, while mutations of these residues which result to blockade of the channels can affect the NO-sensing ability of sGC (Winter et al., 2011). The binding site of BAY 41-2272 suggests that BAY 41-2272 may serve as a block to these tunnels and prevent the escape of the NO.

When we compare the present data with those probing the interaction of *Ns* H-NOX with sGC activators (Argyriou et al., 2021) (**Figure 1D**), we can observe several major differences. Activators of sGC (BAY 58-2667 and BAY 60-2770) form very stable complexes with the *Ns* H-NOX domain, reducing considerably the dynamic properties of the protein and they interact mainly with H-NOX residues around the heme cavity, since they replace the heme by occupying the same space (**Supplementary Figure S2**). Furthermore, BAY 41-2272 exhibits much lower CSP values than those seen with BAY 58-2267, implying that the interaction of BAY 41-2272 with the *Ns* H-NOX domain is considerably weaker than that of BAY 58-2267, and implicates a completely different site of the protein, which is located on the protein surface.

Nitric Oxide Facilitates H-NOX Domain's Interaction With BAY 41-2272

Because stimulators are able to trigger sGC's function in a heme-dependent manner and strongly synergize with NO (Follmann et al., 2013; Breitenstein et al., 2016), we performed NMR titration experiments of *Ns* H-NOX domain with BAY 41-2272 in the presence of NO. We prepared an *Ns* H-NOX/NO complex by adding 0.7 mM of the NO donor DEA-NONOate and then added excess BAY 41-2272, at a protein-ligand ratio of 1:4. By a look at the ^{1}H-^{15}N HSQC NMR spectrum we can see the formation of a new *Ns* H-NOX domain complex, containing the heme group as well as two extra ligands, NO and BAY 41-2272 (**Figure 3B**). This NMR spectrum is very different compared to the spectra of the *Ns* H-NOX in the reference state (without any extra ligand besides the heme) and to the *Ns* H-NOX/NO complex (**Figures 3A,C,D**), yielding that low concentration of NO may increase the binding affinity of the BAY 41-2272. Unfortunately, due to the low stability of the H-NOX/NO/BAY complex, acquisition of 3D NMR spectra for the backbone assignment was not feasible. To gain more detailed insight into the interaction of *Ns* H-NOX with

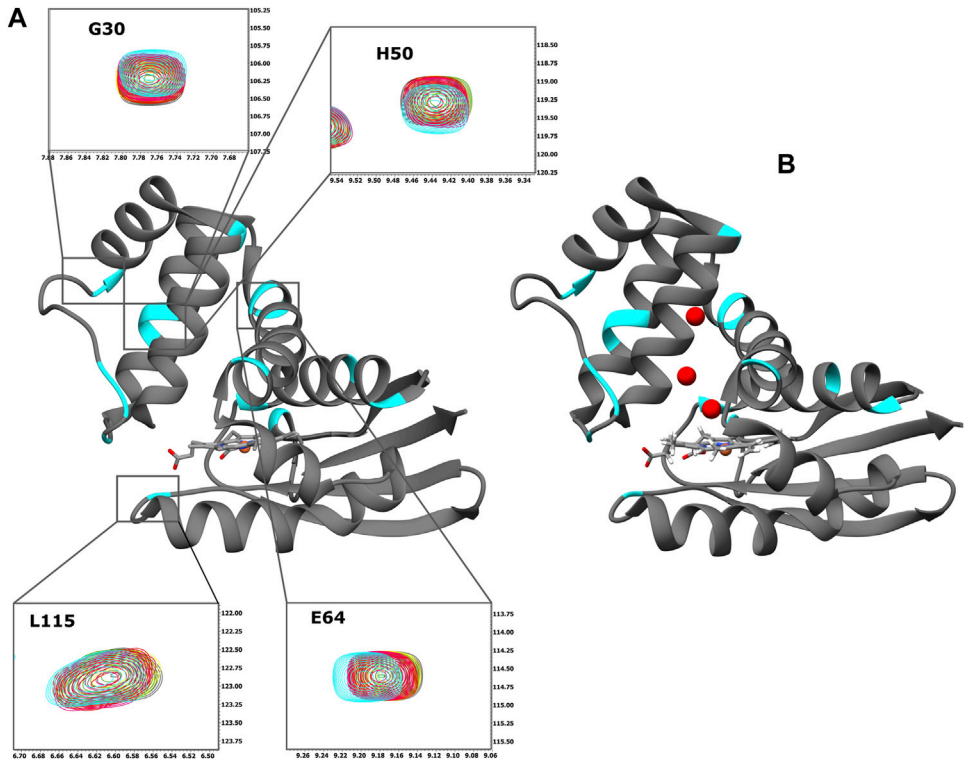

FIGURE 2 | (A) Ribbon representation of the X-ray structure of *Ns* H-NOX domain (PDB ID: 4IAM) (Kumar et al., 2013). The residues with CSP above the threshold are mapped on the surface (cyan). Expansion of the selected HSQC regions. Overlay of HSQC spectra of *Ns* H-NOX 27 with increasing concentration of BAY 41-2272: 0 mM (grey), 0.125 mM (yellow), 0.25 mM (green), 0.5 mM (red), 1 mM (magenta), and 2,5 mM (cyan). **(B)** Ribbon representation of the X-ray structure of *Ns* H-NOX domain under 6atm of xenon gas (PDB ID: 3TFA) (Winter et al., 2011). The residues with CSP above the threshold are mapped on the surface (cyan). Ribbon representation was generated using UCSF Chimera software (Pettersen et al., 2004).

BAY 41-2272 in the presence of NO, and in order to confirm that the changes in the ^{1}H-^{15}N HSQC are indeed a consequence of the interaction with BAY 41-2272, we performed ^{19}F-NMR analysis. Overlay of the two spectra, the first resulting from the addition of BAY 41-2272 alone and the second after the interaction of BAY 41-2272 with the *Ns* H-NOX/NO complex, shows a clear change on the chemical shift of the one fluorine atom of BAY 41-2272 (**Figure 4**) indicating that the new complex indeed results from the interaction with the BAY 41-2272 and cannot be attributed simply to a more effective interaction of the *Ns* H-NOX domain with the NO forming a more stable H-NOX/NO complex.

To test whether NO has an impact on the weak binding of BAY 41-2272, we titrated DEA-NONOate (final concentration 0.6 mM), at a ratio of 1:1 (protein/DEA), into the *Ns* H-NOX/BAY 41-2272 complex. The ^{1}H-^{15}N HSQC spectrum (**Figures 3E,F**) is different than the spectrum of *Ns* H-NOX/NO/BAY 41-2272 complex and shows that NO still interacts with *Ns* H-NOX independently of BAY 41-2272 suggesting that the action of NO excels the action of BAY 41-2272. Therefore, the weak binding of the stimulator cannot be enhanced by the subsequent addition of the NO, but is strengthened only if NO has previously formed a complex with the *Ns* H-NOX domain, as observed by UV-vis and NMR spectroscopies.

Heme's Oxidation State Regulates the Binding of BAY 41-2272

The redox state of the heme moiety of *Ns* H-NOX domain was monitored by UV-vis. *Ns* H-NOX with the heme moiety in a reduced unliganded state (i.e., in the absence of NO), has a characteristic Soret band at 428 nm (**Figure 5A**). On the other hand, *Ns* H-NOX after addition of 0.7 mM DEA-NONOate exhibits a Soret band at 412 nm (**Figure 5B**), corresponding to an intermediate state consisting mainly of 6-coordinated Fe(II)-NO complex which is inactive, while 1.3 mM DEA-NONOate results in the formation of the final state of the NO complex with 5-coordinated Fe(II)-NO and a Soret band near 407 nm. Addition of BAY 41-2272 to the 6-coordinated NO complex causes a shift of the Soret band from 412 to 404 nm (**Figure 5D**). This value, therefore, is much closer to the value of the 5-coordinated Fe(II)-NO complex, in good agreement with published evidence (Ma et al., 2007; Tsai et al., 2010) (**Figure 5C**). Electronic absorption spectra indicate that BAY 41-2242 manages to

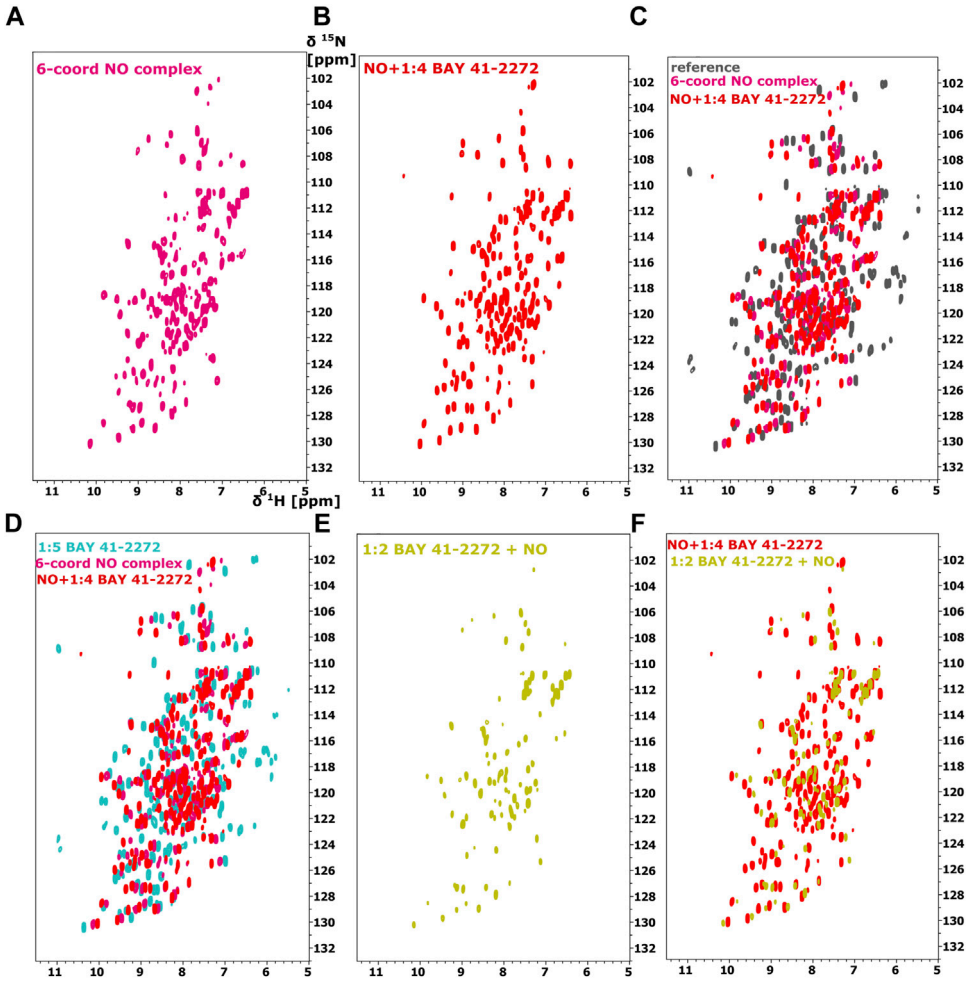

FIGURE 3 | ^{1}H-^{15}N HSQC spectra of the *Ns* H-NOX domain **(A)** in 6-coordinated NO-bound state (magenta), **(B)** with NO and 1:4 BAY 41-2272 (red), **(C)** Overlay of ^{1}H-^{15}N HSQC of *Ns* H-NOX domain (reference-grey) with NO (magenta) and NO/1:4 BAY 41-2272 (red). **(D)** Overlay of ^{1}H-^{15}N HSQC spectra of *Ns* H-NOX domain with 1:5 BAY 41-2272 (cyan), NO (magenta) and NO/1:4 BAY 41-2272 (red), **(E)** ^{1}H-^{15}N HSQC spectra of the *Ns* H-NOX domain with 1:2 BAY 41-2272 and NO (yellow), **(F)** Overlay of ^{1}H-^{15}N HSQC spectra of *Ns* H-NOX domain with NO/1:4 BAY 41-2272 (red) and 1:2 BAY 41-2272/NO (yellow).

lead the *Ns* H-NOX/NO complex to the active, a 5-coordinated state, even at low NO concentrations. Taken together, the NMR and electronic absorption spectra indicate that in the presence of NO, BAY 41-2272 exhibits a different type of interaction with the *Ns* H-NOX domain, imposing possibly greater conformational changes while it also impacts the heme's environment and iron's electronic structure. Similar behavior has been previously observed with the prototype sGC stimulator, YC-1: addition of YC-1 to the previously formed sGC-CO complex affected the electronic absorption spectra of the complex by shifting the Soret peak from 424 to 420 nm (Kharitonov et al., 1999).

BAY 41-22 Prevents Loss of the Heme Group by Subsequent Addition of ODQ

It is now well accepted that reduced heme is necessary for the sGC-stimulating activity of stimulator-type molecules, as the oxidation of heme abolishes their activity (Stasch and Hobbs, 2009). To test the effect of heme's oxidation after the interaction of H-NOX with BAY 41-2272, we titrated excess of the sGC inhibitor, the heme oxidant ODQ, to the *Ns* H-NOX domain and then to the complex of *Ns* H-NOX with NO and BAY 41-2272.

The ^{1}H-^{15}N HSQC spectrum of *Ns* H-NOX domain, after addition of ODQ at a protein-ODQ ratio of 1:0.5, reveals that several peaks are missing. Mapping these peaks on the X-ray structure of *Ns* H-NOX domain (**Supplementary Figure S3**), shows that most of these peaks are located around the heme cavity, implying that ODQ is able to oxidize the heme and affect its environment even in such a low ratio. Increasing the protein-ODQ ratio to 1:3 changes completely the NMR spectrum, causing a disappearance of almost all the peaks, compatible to an unfolding of the protein (**Figure 6A**), with simultaneously oxidation of the heme (**Figure 6D**).

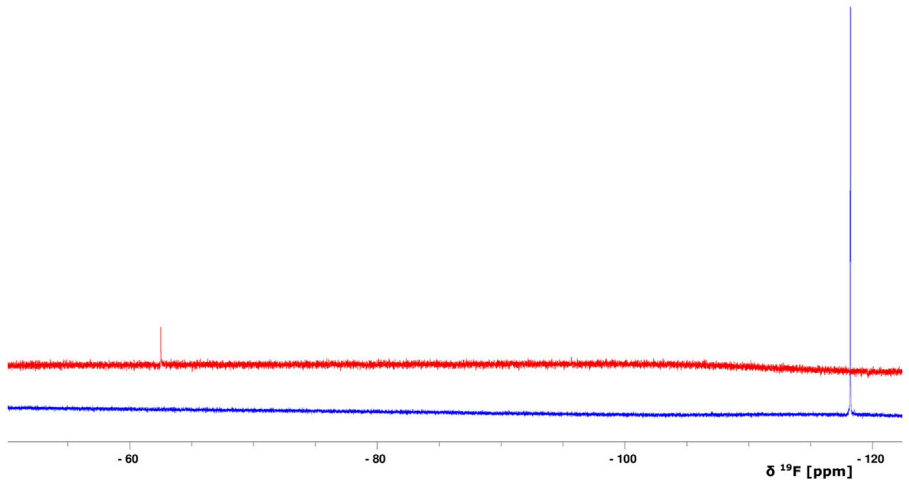

FIGURE 4 | Overlay of 1D ^{19}F NMR spectra of BAY 41-2272 (only the compound, no protein is added) (blue) and after the interaction with the complex *Ns* H-NOX/NO (red). The S/N ratio of the two spectra is different due to the intensity scale of the red one which is set *2.

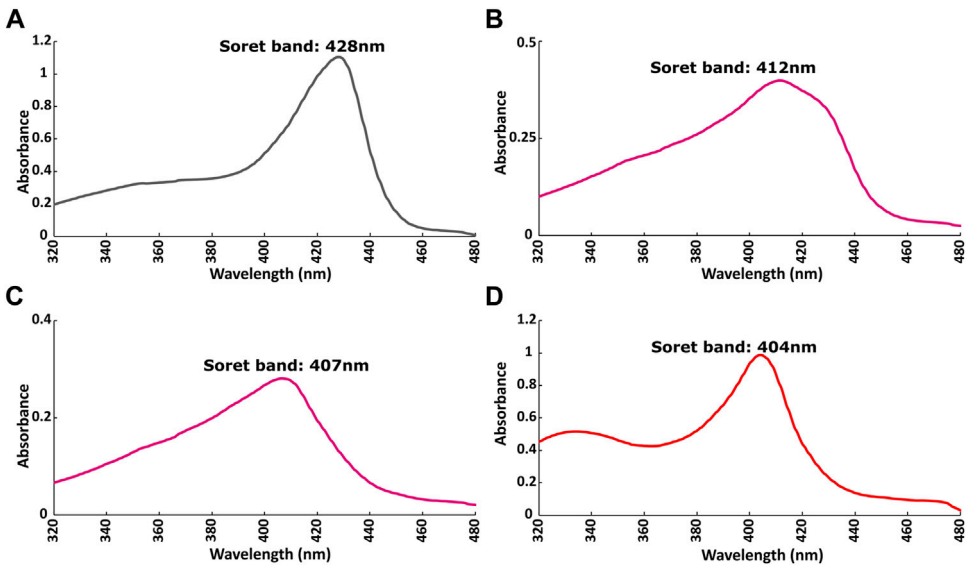

FIGURE 5 | Electronic absorption spectra of *Ns* H-NOX domain **(A)** before and **(B)** after adding 0.7 mM DEA-NONOate or **(C)** 1.5 mM DEA-NONOate and **(D)** after adding 1:4 BAY 41-2272 in the presence of 0.7 mM DEA-NONOate.

Surprisingly, ODQ exhibits a different behavior towards the complex of *Ns* H-NOX with NO/BAY 41-2272. Unexpectedly, addition of ODQ did not alter the ^{1}H-^{15}N HSQC spectrum (**Figures 6B,C**), suggesting that ODQ does not cause any detectable conformational changes. However, we can observe a small but distinct shift of the Soret band from 404 to 405nm, while the absorbance is significantly lower after the addition of ODQ (from 0.9844 to 0.6395) (**Figure 6E**), implying loss of the heme's amount. These data suggest that ODQ is still able to oxidize the H-NOX-bound heme but that the binding BAY 41-2252 prevents the loss of the heme moiety and therefore allowing the *Ns* H-NOX domain to retain its structure.

Varying the Timing of Heme Oxidation: Effect the sGC Catalytic Function

The synergy of sGC stimulators such as BAY 41-2272 with NO and its dependence on the presence of heme are well-described characteristics (Friebe et al., 2020). In A7r5 RAoSM cells, which naturally express the soluble guanylate cyclase (sGC) $\alpha1\beta1$ isoenzyme (Holt et al., 2016), BAY 41-2272 is capable of

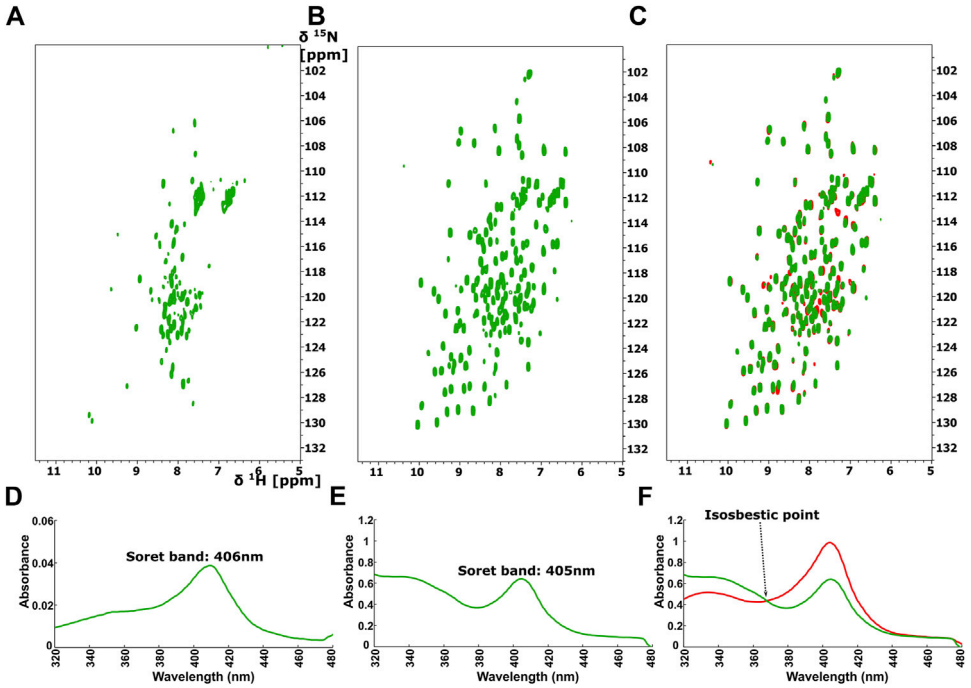

FIGURE 6 | ^{1}H-^{15}N HSQC after addition of ODQ with ration 1:1 to **(A)** the *Ns* H-NOX and to **(B)** the *Ns* H-NOX/NO/BAY 41-2272. **(C)** Overlay of ^{1}H-^{15}N HSQC spectra of the *Ns* H-NOX/NO/BAY 41-2272 complex before (red) and after ODQ addition (green). Electronic absorption spectra of **(D)** *Ns* H-NOX domain after addition of ODQ with ratio 1:1 and **(E)** *Ns* HNOX/NO/BAY 41-2272 after adding ODQ **(F)** Overlay of UV-vis spectra of Ns H-NOX/NO/BAY 41-2272 complex before (red) and after addition of ODQ (green) with isosbestic point at 368 nm.

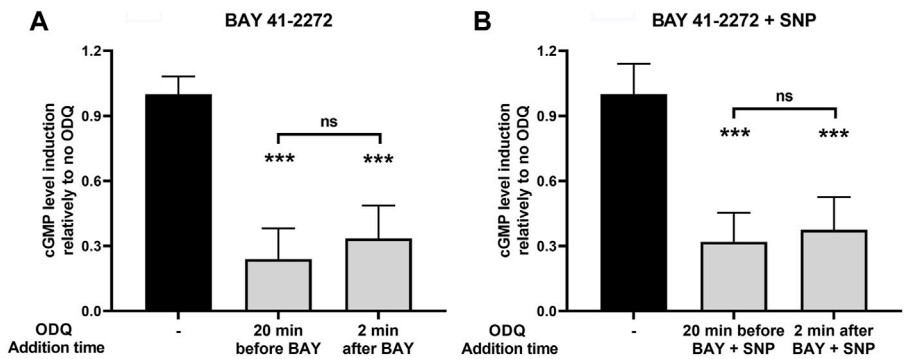

FIGURE 7 | The effects of ODQ after sGC activation by **(A)** the sGC stimulator BAY 41-2272 (10 μM) alone or **(B)** in combination with the NO donor SNP (100 μM), in A7r5 rat aortic smooth muscle cells. The heme oxidant ODQ (10 μM) or its vehicle (DMSO) was added either 20 min before or 2 min after the sGC agonists. 15 min after the exposure to the agonists, cell extracts were taken, analyzed for cGMP content and normalized for total protein. Data are expressed as means ± STDEV of $n = 4$ determinations, obtained in two independent experiments. p values were determined by 2-tailed Student's t-test. **(A)**. The effect of BAY 41-2272 in the absence of ODQ was taken as 1.0. ***: $p < 0.001$ relative to BAY 41-2272 treatment in the absence of ODQ. **(B)**. The effect of BAY 41-2272 + SNP in the absence of ODQ was taken as 1.0. ***: $p < 0.001$ relative to BAY 41-2272 + SNP treatment in the absence of ODQ.

increasing cGMP levels by itself and synergizes with the NO donor sodium nitroprusside (SNP) (**Supplementary Figure S4**), indicating that our assay system works as expected based on the stimulator's mechanism of action (Adderley et al., 2012).

Most *in vitro* studies on the role of heme on sGC function are focused on examining the role of prior heme oxidation (and loss from H-NOX) on the effectiveness of heme-dependent sGC agonists (Morbidelli et al., 2010; Chen et al., 2020). We attempted to address the NMR-based results shown above by testing whether an oxidant such as ODQ can interfere with the sGC stimulatory activity, after the BAY/sGC β1 complex has been allowed to form. To do so, we added the oxidant ODQ 2 min after BAY 41-2272 addition and compared its effect side-by-side with the increases in cGMP formation obtained when cells were

pretreated with ODQ 20 min before BAY 41-2272. Our results indicate that ODQ is capable of significantly reducing the effect of BAY 41-2272 to a similar extent when added either prior to (↓ 76% ± 14%) or after (↓ 67% ± 15%) the sGC agonist (**Figure 7A**).

Furthermore, we addressed the same question using sGC activation caused by the combination of BAY 41-2272 and SNP. Similarly, we observed that ODQ treatment 2 min after co-stimulation with BAY 41-2272 + SNP was able to reduce cGMP levels (↓ 63% ± 15%), i.e., to a similar extent to that obtained with ODQ pretreatment (↓ 68% ± 13%) (**Figure 7B**).

DISCUSSION

The study of the interaction of the sGC stimulators with the H-NOX domain allows us to determine in unprecedented detail the molecular mode of interaction of this class of drugs with H-NOX, by providing insights into 1) the affinity of binding, 2) the H-NOX residues involved and 3) how the formation of an active complex consisting of the H-NOX domain and the stimulator compound can be impacted by the redox-state of the heme and the addition of NO.

The available cryo-EM structures of sGC with a stimulator (Riociguat or YC-1), although quite informative, are characterized by low resolution. For the first time, we monitored how BAY 41-2272 interacts with the H-NOX domain with and without the synergistic presence of NO, in real-time, by solution NMR. Our NMR data reveal that BAY 41-2272 interacts rather weakly with a specific site of the H-NOX domain in the absence of NO. The amino acids participating in the interaction are located mainly on the surface of the protein, so they are not part of the heme cavity. The interaction surface includes regions of the α_3 and α_4 α-helices as well as the loop connecting α_2-α_3 and α_3-α_4 helices. Importantly, these residues are close to the tunnels permitting the flux of diatomic gas agonists inside the protein where they elicit its stimulation. Our findings suggest that BAY 41-2272 may act as a gatekeeper at this tunnel network to prevent the gas molecules to diffuse outside the protein, thus potentiating their effect.

BAY 41-2272 exhibits a strikingly different binding behaviour compared to that of the activator BAY 58-2667. While BAY 41-2272 interacts weakly on the surface of the *Ns* H-NOX domain juxtaposed to the heme cavity, BAY 58-2667 occupies the heme cavity and affects mainly regions close to heme located on the α5, α6, and α7 helices, forming a new, very stable complex and erasing completely the dynamic properties of the system (Argyriou et al., 2021). The different interaction mode of stimulators and activators may therefore justify the different impact they have on the activation of the sGC enzyme.

So far, there is no X-ray structure available for the H-NOX/BAY 41-2272 complex, probably due to the compound's weak binding, with a K_D that we determined is at the mM range. However, in the presence of NO, BAY 41-2272 exhibits a quite different binding behaviour: its binding is significantly enhanced, compatible with its strong synergistic action with NO. Our cell-based assays show that BAY 41-2272 stimulates sGC activity almost 15-fold above baseline, while BAY 41-2272 along with SNP (NO donor) can activate the enzyme by 80-fold (**Supplementary Figure S2**). The K_D we determined for the interaction of BAY 41-2272 with the *Ns* H-NOX is somewhat higher compared to that observed for the interaction of the stimulator IWP-051 with the H-NOX domain from *Shewanella woodyi* in the presence of carbon monoxide (K_D = 1.9 mM) (Wales et al., 2018). We conclude that stimulators of sGC tend to interact weakly with the H-NOX domain of various organisms and use similar protein residues. These findings along with the information derived from the 3D structures of sGC, strongly imply that in spite of the presence of the other sGC domains (PAS, CC, CD), the H-NOX domain and the associated heme play a pivotal role in the stimulation of the enzyme's activity as the primary sensor of both NO and stimulator molecules. This conclusion is further supported by the NMR and UV-visible data presented here which illustrate the synergistic action between NO and stimulators, clearly implicating the H-NOX domain as the main drug target for the regulation of sGC activity, whether it is manifested as impairment or enhancement (Liu et al., 2021).

NO plays a critical role, with the exact mechanism of this interaction still not entirely elucidated. Superimposition of the free and NO-bound *Ns* H-NOX domains shows no significant alterations regarding the overall arrangement (Makrynitsa et al., 2019), suggesting that the H-NOX-mediated activation of sGC may be driven by protein dynamics and redox changes, rather than large conformational changes of the H-NOX domain itself. This, of course, cannot exclude changes in the orientation of the sGC domains or even domain rearrangements, for example, if the stimulator binds on the interface of H-NOX with other sGC domains. Furthermore, the binding of BAY 41-2272 may be enhanced by NO thanks to changes in the redox state of the heme induced by NO. The results presented herein indicate that the *Ns* H-NOX domain forms a folded 6-coordinated Fe(II)-NO complex with a characteristic Soret band at 412 nm. BAY 41-2272 favours the transition of the previous complex to the 5-coordinated Fe(II)-NO complex with a Soret band at 405 nm, even without excess amount of NO. In contrast, the interaction with NO is not appreciably affected by the presence of BAY 41-2272, since NO alone can form a complex with the *Ns* H-NOX domain. In essence, the action of BAY 41-2272 is enabled and potentiated by NO and not *vice versa*. Cooperation of BAY 41-2272 with NO results in the formation of a unique complex with the *Ns* H-NOX domain, where the Fe of the heme adopts a different electronic structure, either through redox switch or through the differentiation of the coordination geometry, which coincides with a fully active state of the protein. BAY 41-2272, therefore, allows the *Ns* H-NOX domain to reach more easily and efficiently the fully active state with low NO concentrations. Our findings along with our previous results (Argyriou et al., 2021) put forth the paramount importance of the oxidation state of the heme for the effective action of sGC agonists and provide a possible mechanism of action for stimulators.

Furthermore, NMR results reveal that the complex *Ns* H-NOX/NO/BAY 41-2272 is overall insensitive to the action of ODQ, a selective and irreversible inhibitor of sGC. Taken together with the observation of an isosbestic point at 369 nm (**Figure 6F**), these results indicate that the ODQ may convert the

ferrous heme/NO complex to a new complex with oxidized heme, without any intermediate state. This particular complex exhibits the same conformation with the *Ns* H-NOX/NO/BAY 41-2272 complex but with the exception of the oxidized heme. Our interpretation is that BAY 41-2272 may trap the oxidized heme and unbound NO inside the protein, securing the conformation of the *Ns* H-NOX domain and hindering the exit of the oxidized heme.

Our cell-based assays show that, when sGC activation is assayed in cells that carry the mammalian holoenzyme, the prior formation of a heme/NO/BAY 41-2272 complex still allows ODQ to reach in, oxidize the heme and thus interfere with sGC activation. Similar results (K. Salagiannis, unpublished observations) were obtained by allowing more time (10 min) for the complex of sGC and stimulators (SNP + BAY) to form before ODQ addition. These observations are compatible with our structural NMR results where the *Ns* H-NOX/NO/BAY 41-2272 complex appears to maintain its conformation despite the action of ODQ, since the ferric heme remains associated with the protein but without any NO molecules bound.

In the present work, we point out the crucial role of the reduced heme for the proper function of the sGC enzyme during the stimulation by NO and BAY 41-2272. ODQ manages to inhibit the sGC-driven cGMP formation by oxidizing the heme while simultaneously BAY 41-2272 protects the conformation of the H-NOX domain. Hence, we are led to conclude that the catalytic activity of sGC may not be guaranteed by the simple presence of heme in the H-NOX cavity, but that its coordination state and relation to the attached Fe or the stereochemistry of the Fe-heme association may play a paramount role.

Overall, we describe an analysis in real time of the interaction of the sGC stimulator, BAY 41-2272, with the recombinant *Ns* H-NOX, map the amino acids on the protein surface that mediate this interaction and provide evidence to explain the characteristic synergy of BAY 41-2272 with NO: prior association of NO with the heme plays a permissive role in BAY's association, while the presence of BAY 41-2272, in return, allows *Ns* H-NOX to be sensitive to low NO levels, by establishing a fully reduced heme prosthetic group and thus maximal sGC activity.

DATA AVAILABILITY STATEMENT

The original contributions presented in the study are included in the article/**Supplementary Material**, further inquiries can be directed to the corresponding author.

AUTHOR CONTRIBUTIONS

GM: Methodology, Investigation, Resources, Writing. AA: Methodology, Investigation, Resources, Writing. AZ Resources, Funding acquisition. KS: Methodology, Investigation, Resources, Writing. VV: Methodology, Investigation. AP: Conceptualization. ST: Conceptualization, Investigation, Supervision, Funding acquisition, Writing. GS: Conceptualization, Methodology, Supervision, Funding acquisition, Investigation, Writing.

FUNDING

We acknowledge support of this work by the project "INSPIRED-The National Research Infrastructures on Integrated Structural Biology, Drug Screening Efforts and Drug target functional characterization" (MIS 5002550) which is implemented under the Action "Reinforcement of the Research and Innovation Infrastructure," funded by the Operational Programme "Competitiveness, Entrepreneurship and Innovation" (NSRF, 2014-2020) and co-financed by Greece and the European Union (European Regional Development Fund). Aikaterini Zompra acknowledges the received funding from the Hellenic Foundation for Research and Innovation (HFRI) and the General Secretariat for Research and Technology (GSRT), under grant agreement No. (938) for this project. EU FP7 REGPOT CT-2011-285950—"SEE-DRUG" project is acknowledged for the purchase of UPAT's 700 MHz NMR equipment.

ACKNOWLEDGMENTS

We are indebted to Dr. Peter Sandner (BAYER AG, Wuppertal, Germany) for the generous gift of BAY 41-2272. We also acknowledge the Instrumental Analysis Laboratory of University of Patras for the use of AVANCE III, 600 MHz for the acquisition of the ^{19}F 1D spectra.

SUPPLEMENTARY MATERIAL

The Supplementary Material for this article can be found online at: https://www.frontiersin.org/articles/10.3389/fcell.2022.925457/full#supplementary-material

REFERENCES

Adderley, S. P., Joshi, C. N., Martin, D. N., and Tulis, D. A. (2012). Phosphodiesterases Regulate BAY 41-2272-Induced VASP Phosphorylation in Vascular Smooth Muscle Cells. *Front. Pharmacol.* 3, 10. doi:10.3389/FPHAR.2012.00010

Alexandropoulos, I. I., Argyriou, A. I., Marousis, K. D., Topouzis, S., Papapetropoulos, A., and Spyroulias, G. A. (2016). 1H, 13C, 15N Backbone and Side-Chain Resonance Assignment of Nostoc Sp. C139A Variant of the Heme-Nitric Oxide/oxygen Binding (H-NOX) Domain. *Biomol. NMR Assign.* 10 (2), 395–400. doi:10.1007/s12104-016-9707-6

Argyriou, A. I., Makrynitsa, G. I., Dalkas, G., Georgopoulou, D. A., Salagiannis, K., Vazoura, V., et al. (2021). Replacement of Heme by Soluble Guanylate Cyclase (sGC) Activators Abolishes Heme-Nitric Oxide/oxygen (H-NOX) Domain Structural Plasticity. *Curr. Res. Struct. Biol.* 3, 324–336. doi:10.1016/J.CRSTBI.2021.11.003

Armstrong, P. W., Roessig, L., Patel, M. J., Anstrom, K. J., Butler, J., Voors, A. A., et al. (2018). A Multicenter, Randomized, Double-Blind, Placebo-Controlled Trial of the Efficacy and Safety of the Oral Soluble Guanylate Cyclase Stimulator. *JACC Heart Fail.* 6 (2), 96–104. doi:10.1016/J.JCHF.2017.08.013

Breitenstein, S., Roessig, L., Sandner, P., and Lewis, K. S. (2016). "Novel sGC Stimulators and sGC Activators for the Treatment of Heart Failure," in *Heart Failure* (Heidelberg, Germany: Springer), 225–247. doi:10.1007/164_2016_100

Chen, P.-J., Kuo, L.-M., Wu, Y.-H., Chang, Y.-C., Lai, K.-H., and Hwang, T.-L. (2020). BAY 41-2272 Attenuates CTGF Expression via sGC/cGMP-independent Pathway in TGFβ1-Activated Hepatic Stellate Cells. *Biomedicines* 8 (9), 330. doi:10.3390/BIOMEDICINES8090330

Derbyshire, E. R., and Marletta, M. A. (2009). Biochemistry of Soluble Guanylate Cyclase. *Handb. Exp. Pharmacol.* 191, 17–31. doi:10.1007/978-3-540-68964-5_2

Derbyshire, E. R., and Marletta, M. A. (2012). Structure and Regulation of Soluble Guanylate Cyclase. *Annu. Rev. Biochem.* 81 (1), 533–559. doi:10.1146/annurev-biochem-050410-100030

Dunkern, T. R., Feurstein, D., Rossi, G. A., Sabatini, F., and Hatzelmann, A. (2007). Inhibition of TGF-β Induced Lung Fibroblast to Myofibroblast Conversion by Phosphodiesterase Inhibiting Drugs and Activators of Soluble Guanylyl Cyclase. *Eur. J. Pharmacol.* 572 (1), 12–22. doi:10.1016/J.EJPHAR.2007.06.036

Evgenov, O. V., Pacher, P., Schmidt, P. M., Haskó, G., Schmidt, H. H. H. W., and Stasch, J.-P. (2006). NO-independent Stimulators and Activators of Soluble Guanylate Cyclase: Discovery and Therapeutic Potential. *Nat. Rev. Drug Discov.* 5 (9), 755–768. doi:10.1038/nrd2038

Follmann, M., Ackerstaff, J., Redlich, G., Wunder, F., Lang, D., Kern, A., et al. (2017). Discovery of the Soluble Guanylate Cyclase Stimulator Vericiguat (BAY 1021189) for the Treatment of Chronic Heart Failure. *J. Med. Chem.* 60 (12), 5146–5161. doi:10.1021/acs.jmedchem.7b00449

Follmann, M., Griebenow, N., Hahn, M. G., Hartung, I., Mais, F.-J., Mittendorf, J., et al. (2013). The Chemistry and Biology of Soluble Guanylate Cyclase Stimulators and Activators. *Angew. Chem. Int. Ed.* 52 (36), 9442–9462. doi:10.1002/ANIE.201302588

Friebe, A., Sandner, P., and Schmidtko, A. (2020). cGMP: a Unique 2nd Messenger Molecule - Recent Developments in cGMP Research and Development. *Schmiedeb. Arch. Pharmacol.* 393 (2), 287–302. doi:10.1007/s00210-019-01779-z

Holt, A. W., Martin, D. N., Shaver, P. R., Adderley, S. P., Stone, J. D., Joshi, C. N., et al. (2016). Soluble Guanylyl Cyclase-Activated Cyclic GMP-dependent Protein Kinase Inhibits Arterial Smooth Muscle Cell Migration Independent of VASP-Serine 239 Phosphorylation. *Cell. Signal.* 28 (9), 1364–1379. doi:10.1016/J.CELLSIG.2016.06.012

Kang, Y., Liu, R., Wu, J.-X., and Chen, L. (2019). Structural Insights into the Mechanism of Human Soluble Guanylate Cyclase. *Nature* 574 (7777), 206–210. doi:10.1038/s41586-019-1584-6

Keller, R. (2004). *The Computer Aided Resonance Assignment Tutorial*. Germany: CANTINA Verlag.

Kharitonov, V. G., Sharma, V. S., Magde, D., and Koesling, D. (1999). Kinetics and Equilibria of Soluble Guanylate Cyclase Ligation by CO: Effect of YC-1. *Biochemistry* 38 (33), 10699–10706. doi:10.1021/BI990277F

Khaybullina, D., Patel, A., and Zerilli, T. (2014). Riociguat (Adempas): a Novel Agent for the Treatment of Pulmonary Arterial Hypertension and Chronic Thromboembolic Pulmonary Hypertension. *Pharm. Ther.* 39 (11), 749. Available at: /pmc/articles/PMC4218670/[Accessed July 30, 2021].

Kumar, V., Martin, F., Hahn, M. G., Schaefer, M., Stamler, J. S., Stasch, J.-P., et al. (2013). Insights into BAY 60-2770 Activation and S-Nitrosylation-Dependent Desensitization of Soluble Guanylyl Cyclase via Crystal Structures of Homologous Nostoc H-NOX Domain Complexes. *Biochemistry* 52 (20), 3601–3608. doi:10.1021/bi301657w

Liu, R., Kang, Y., and Chen, L. (2021). Activation Mechanism of Human Soluble Guanylate Cyclase by Stimulators and Activators. *Nat. Commun.* 12 (1), 1–10. doi:10.1038/s41467-021-25617-0

Ma, X., Sayed, N., Beuve, A., and Van Den Akker, F. (2007). NO and CO Differentially Activate Soluble Guanylyl Cyclase via a Heme Pivot-Bend Mechanism. *EMBO J.* 26 (2), 578–588. doi:10.1038/sj.emboj.7601521

Makrynitsa, G. I., Zompra, A. A., Argyriou, A. I., Spyroulias, G. A., and Topouzis, S. (2019). Therapeutic Targeting of the Soluble Guanylate Cyclase. *Cmc* 26 (15), 2730–2747. doi:10.2174/0929867326666190108095851

Mittendorf, J., Weigand, S., Alonso-Alija, C., Bischoff, E., Feurer, A., Gerisch, M., et al. (2009). Discovery of Riociguat (BAY 63-2521): A Potent, Oral Stimulator of Soluble Guanylate Cyclase for the Treatment of Pulmonary Hypertension. *ChemMedChem* 4 (5), 853–865. doi:10.1002/cmdc.200900014

Morbidelli, L., Pyriochou, A., Filippi, S., Vasileiadis, I., Roussos, C., Zhou, Z., et al. (2010). The Soluble Guanylyl Cyclase Inhibitor NS-2028 Reduces Vascular Endothelial Growth Factor-Induced Angiogenesis and Permeability. *Am. J. Physiology-Regulatory, Integr. Comp. Physiology* 298 (3), R824–R832. doi:10.1152/AJPREGU.00222.2009

Papapetropoulos, A., Hobbs, A. J., and Topouzis, S. (2015). Extending the Translational Potential of Targeting NO/cGMP-regulated Pathways in the CVS. *Br. J. Pharmacol.* 172 (6), 1397–1414. doi:10.1111/bph.12980

Pettersen, E. F., Goddard, T. D., Huang, C. C., Couch, G. S., Greenblatt, D. M., Meng, E. C., et al. (2004). UCSF Chimera?A Visualization System for Exploratory Research and Analysis. *J. Comput. Chem.* 25 (13), 1605–1612. doi:10.1002/JCC.20084

Sandner, P., Zimmer, D. P., Milne, G. T., Follmann, M., Hobbs, A., and Stasch, J.-P. (2018). Soluble Guanylate Cyclase Stimulators and Activators. *Handb. Exp. Pharmacol.* 264, 355–394. doi:10.1007/164_2018_197

Stasch, J.-P., and Evgenov, O. V. (2013). Soluble Guanylate Cyclase Stimulators in Pulmonary Hypertension. *Handb. Exp. Pharmacol.* 218, 279–313. doi:10.1007/978-3-642-38664-0_1210.1007/978-3-662-45805-1_12

Stasch, J.-P., and Hobbs, A. J. (2009). NO-independent, Haem-dependent Soluble Guanylate Cyclase Stimulators. *Handb. Exp. Pharmacol.* 191 (191), 277–308. doi:10.1007/978-3-540-68964-5_13

Stasch, J.-P., Schmidt, P. M., Nedvetsky, P. I., Nedvetskaya, T. Y., H.S., A. K., Meurer, S., et al. (2006). Targeting the Heme-Oxidized Nitric Oxide Receptor for Selective Vasodilatation of Diseased Blood Vessels. *J. Clin. Invest.* 116 (9), 2552–2561. doi:10.1172/JCI28371

Straub, A., Stasch, J.-P., Alonso-Alija, C., Benet-Buchholz, J., Ducke, B., Feurer, A., et al. (2001). NO-independent Stimulators of Soluble Guanylate Cyclase. *Bioorg. Med. Chem. Lett.* 11 (6), 781–784. doi:10.1016/S0960-894X(01)00073-7

Tsai, A.-L., Berka, V., Martin, F., Ma, X., Van Den Akker, F., Fabian, M., et al. (2010). Is Nostoc H-NOX a NO Sensor or Redox Switch? *Biochemistry* 49 (31), 6587–6599. doi:10.1021/BI1002234

Underbakke, E. S., Iavarone, A. T., Chalmers, M. J., Pascal, B. D., Novick, S., Griffin, P. R., et al. (2014). Nitric Oxide-Induced Conformational Changes in Soluble Guanylate Cyclase. *Structure* 22 (4), 602–611. doi:10.1016/j.str.2014.01.008

Wales, J. A., Chen, C.-Y., Breci, L., Weichsel, A., Bernier, S. G., Sheppeck, J. E., et al. (2018). Discovery of Stimulator Binding to a Conserved Pocket in the Heme Domain of Soluble Guanylyl Cyclase. *J. Biol. Chem.* 293 (5), 1850–1864. doi:10.1074/JBC.RA117.000457

Williamson, M. P. (2013). Using Chemical Shift Perturbation to Characterise Ligand Binding. *Prog. Nucl. Magnetic Reson. Spectrosc.* 73, 1–16. doi:10.1016/j.pnmrs.2013.02.001

Winter, M. B., Herzik, M. A., Kuriyan, J., and Marletta, M. A. (2011). Tunnels Modulate Ligand Flux in a Heme Nitric Oxide/oxygen Binding (H-NOX) Domain. *Proc. Natl. Acad. Sci. U.S.A.* 108 (43), E881–E889. doi:10.1073/pnas.1114038108

Wittenborn, E. C., and Marletta, M. A. (2021). Structural Perspectives on the Mechanism of Soluble Guanylate Cyclase Activation. *Ijms* 22 (11), 5439. doi:10.3390/ijms22115439

Conflict of Interest: The authors declare that the research was conducted in the absence of any commercial or financial relationships that could be construed as a potential conflict of interest.

Publisher's Note: All claims expressed in this article are solely those of the authors and do not necessarily represent those of their affiliated organizations, or those of the publisher, the editors and the reviewers. Any product that may be evaluated in this article, or claim that may be made by its manufacturer, is not guaranteed or endorsed by the publisher.

frontiers | Frontiers in Cell and Developmental Biology

ORIGINAL RESEARCH
published: 11 July 2022
doi: 10.3389/fcell.2022.895433

ZIP11 Regulates Nuclear Zinc Homeostasis in HeLa Cells and Is Required for Proliferation and Establishment of the Carcinogenic Phenotype

*Monserrat Olea-Flores[1,2], Julia Kan[1], Alyssa Carlson[1†], Sabriya A. Syed[2], Cat McCann[1], Varsha Mondal[1], Cecily Szady[3], Heather M. Ricker[3], Amy McQueen[1], Juan G. Navea[3], Leslie A. Caromile[4] and Teresita Padilla-Benavides[1]**

[1]Department of Molecular Biology and Biochemistry, Wesleyan University, Middletown, CT, United States, [2]Department of Biochemistry and Molecular Biotechnology, University of Massachusetts Chan Medical School, Worcester, MA, United States, [3]Department of Chemistry, Skidmore College, Saratoga Springs, NY, United States, [4]Department of Cell Biology, Center for Vascular Biology, UCONN Health-Center, Farmington, CT, United States

OPEN ACCESS

Edited by:
Peter-Leon Hagedoorn,
Delft University of Technology,
Netherlands

Reviewed by:
Jian Hu,
Michigan State University,
United States
Sangyong Choi,
University of Connecticut,
United States
Kourosh Honarmand Ebrahimi,
King's College London,
United Kingdom

***Correspondence:**
Teresita Padilla-Benavides
tpadillabena@wesleyan.edu

†Present address:
Alyssa Carlson,
Tisch Multiple Sclerosis Research Center of New York, New York, NY, United States

Specialty section:
This article was submitted to Cellular Biochemistry, a section of the journal Frontiers in Cell and Developmental Biology

Received: 13 March 2022
Accepted: 13 June 2022
Published: 11 July 2022

Citation:
Olea-Flores M, Kan J, Carlson A, Syed SA, McCann C, Mondal V, Szady C, Ricker HM, McQueen A, Navea JG, Caromile LA and Padilla-Benavides T (2022) ZIP11 Regulates Nuclear Zinc Homeostasis in HeLa Cells and Is Required for Proliferation and Establishment of the Carcinogenic Phenotype. Front. Cell Dev. Biol. 10:895433. doi: 10.3389/fcell.2022.895433

Zinc (Zn) is an essential trace element that plays a key role in several biological processes, including transcription, signaling, and catalysis. A subcellular network of transporters ensures adequate distribution of Zn to facilitate homeostasis. Among these are a family of importers, the Zrt/Irt-like proteins (ZIP), which consists of 14 members (ZIP1-ZIP14) that mobilize Zn from the extracellular domain and organelles into the cytosol. Expression of these transporters varies among tissues and during developmental stages, and their distribution at various cellular locations is essential for defining the net cellular Zn transport. Normally, the ion is bound to proteins or sequestered in organelles and vesicles. However, though research has focused on Zn internalization in mammalian cells, little is known about Zn mobilization within organelles, including within the nuclei under both normal and pathological conditions. Analyses from stomach and colon tissues isolated from mouse suggested that ZIP11 is the only ZIP transporter localized to the nucleus of mammalian cells, yet no clear cellular role has been attributed to this protein. We hypothesized that ZIP11 is essential to maintaining nuclear Zn homeostasis in mammalian cells. To test this, we utilized HeLa cells, as research in humans correlated elevated expression of ZIP11 with poor prognosis in cervical cancer patients. We stably knocked down ZIP11 in HeLa cancer cells and investigated the effect of Zn dysregulation *in vitro*. Our data show that ZIP11 knockdown (KD) reduced HeLa cells proliferation due to nuclear accumulation of Zn. RNA-seq analyses revealed that genes related to angiogenesis, apoptosis, mRNA metabolism, and signaling pathways are dysregulated. Although the KD cells undergoing nuclear Zn stress can activate the homeostasis response by MTF1 and MT1, the RNA-seq analyses showed that only ZIP14 (an importer expressed on the plasma membrane and endocytic vesicles) is mildly induced, which may explain the sensitivity to elevated levels of extracellular Zn. Consequently, ZIP11 KD HeLa cells have impaired migration, invasive properties and decreased mitochondrial potential. Furthermore, KD of ZIP11 delayed cell

cycle progression and rendered an enhanced senescent state in HeLa cells, pointing to a novel mechanism whereby maintenance of nuclear Zn homeostasis is essential for cancer progression.

Keywords: ZIP11, zinc transport, cell cycle, senescence, gene expression, MTF1, cervical cancer cells

INTRODUCTION

Zinc (Zn) is among the most abundant trace elements essential for life. As a micronutrient, Zn is involved in many biological processes, such as cell signaling, transcriptional modulation, and as a catalytic cofactor and structural component of several proteins (Reviewed by (Wu and Wu, 1987; Kambe et al., 2015)). Under physiological conditions, Zn is present in a non-redox active form as a divalent cation (Zn^{2+}). Zn homeostasis plays a key role in human health, as Zn deficiencies have been identified as leading causes of diverse diseases. Patients lacking this ion may present skin abnormalities, hypogonadism, anemia, growth delays, alopecia, chronic inflammation, as well as deficiencies in immune, hepatic, and mental functions (Vallee and Falchuk, 1993; Hambidge, 2000; Maret and Sandstead, 2006; Devirgiliis et al., 2007; Takeda and Tamano, 2009; Sandstead, 2013). On the other hand, excess Zn is toxic and may disrupt the cellular acquisition of other micronutrients, such as copper (Cu) (Ogiso et al., 1979; Fischer et al., 1981; Broun et al., 1990). Total cellular Zn concentrations are typically in or below the micromolar range (Palmiter and Findley, 1995; Krezel and Maret, 2006; Colvin et al., 2008; Paskavitz et al., 2018; Gordon et al., 2019a; Gordon et al., 2019b; Tavera-Montañez et al., 2019). In general, 50% of subcellular Zn is located in the cytoplasm, 30–40% in the nucleus, and approximately 10% in the plasma membrane (Thiers and Vallee, 1957; Haase and Rink, 2014). However, Zn distribution may change depending on the developmental stage of the cells in a lineage-specific manner (Gordon et al., 2019a). The levels of labile, or "free," Zn in the cytosol are low, ranging from picomolar and low nanomolar concentrations, as it is normally bound to proteins and sequestered into organelles and vesicles (Tavera-Montañez et al., 2019; Gordon et al., 2019a; Gordon et al., 2019b; Outten and O'Halloran, 2001; Qin et al., 2011; Vinkenborg et al., 2009; Sensi et al., 1997). To maintain low levels and adequate subcellular distribution of the ion, cells have developed complex systems to maintain Zn homeostasis.

Two families of Zn transporters mobilize Zn between the extracellular milieu, the cytoplasm, and the organelles (Dufner-Beattie et al., 2003a; Eide, 2006; Kambe et al., 2014; Kambe et al., 2015). The Zn transporter family (also named ZnT, solute-linked carrier 30, or SLC30) mediates cellular Zn export, while the Zrt- and Irt-like proteins (also named ZIP, solute-linked carrier 39, or SLC39) mediate cellular Zn import. ZnTs and ZIPs are transmembrane proteins with six or eight predicted transmembrane (TM) domains, respectively (Dufner-Beattie et al., 2003a; Kambe et al., 2015). Mammalian cells express nine ZnT (1–8, 10) exporters and 14 ZIP importers (1–14), but their contributions to Zn physiology continue to be largely understudied. These transporters maintain cytosolic Zn pools by mobilizing the ion from the extracellular space and intracellular compartments, as they are differentially distributed based on the cellular demands for Zn and stage of life (Lichten and Cousins, 2009; Jeong and Eide, 2013). The majority of ZIP transporters have a dynamic localization to the cell membrane, as their expression, internalization, and degradation is dependent on the levels of the ion (Chowanadisai et al., 2013; Weaver et al., 2007; Hojyo et al., 2011; Dufner-Beattie et al., 2003b; Kelleher and Lönnerdal, 2003; Liuzzi et al., 2004; Liu et al., 2008; Lichten et al., 2011; Gaither and Eide, 2000; Wang et al., 2004; Huang and Kirschke, 2007; Mao et al., 2007; Taylor et al., 2005). Though they mainly mobilize Zn, ZIP importers can also transport iron (Fe) (Liuzzi et al., 2006; Gao et al., 2008; Jenkitkasemwong et al., 2015), manganese (Mn), and cadmium (Cd) (Girijashanker et al., 2008; Fujishiro et al., 2012; Jenkitkasemwong et al., 2012; Gordon et al., 2019b).

To date, the only crystal structure available for a ZIP transporter is from the bacteria *Bordetella bronchiseptica* (BbZIP), which was obtained in the presence of Cd^{2+} (Zhang et al., 2017). BbZIP structure shows eight TM helices that are proposed to form a tight bundle. TM2, TM4, TM5, and TM7 constitute an inner bundle surrounded by the remaining TMs (Zhang et al., 2017). The BbZIP TM2 contains a 36 amino acid-long domain with a kink associated with a conserved proline (P110) (Zhang et al., 2017). TM4 and TM5 are also bent due to the presence of two proline residues in the metal-binding sites (MBS (Zhang et al., 2017)). BbZIP was found to have a novel symmetric structure. The first three TMs, TM1-TM3, are symmetrically related with the last three, TM6-TM8, by a pseudo-two-fold axis, which was defined to be almost parallel to the proposed membrane plane. Further, TM4 and TM5 also seem to be symmetrically related by the same axis, however these two segments appear to be fitted-in by the other two named 3-TM repeats (Zhang et al., 2017). This previously unrecognized architecture was defined as an unusual 3+2+3TM structure (Zhang et al., 2017). Crystallization of BbZIP in the presence of $CdCl_2$ allowed for the identification of four Cd^{2+}-binding sites and revealed that the amino- and carboxy-termini both face the extracellular domain (Zhang et al., 2017). This novel structural data support previous hydrophobicity plot predictions that suggested that ZIP transporters have eight TM helices with extracellular amino- and carboxy-terminal domains (Lichten and Cousins, 2009; Jeong and Eide, 2013).

To transport Zn, ZIP importers are proposed to form homodimers (Lin et al., 2010; Bin et al., 2011). Biochemical characterization and overexpression analyses have demonstrated that the apparent K_m ranges from hundreds of nM to approximately 20 μM (Gaither and Eide, 2000; Gaither and Eide, 2001a; Dufner-Beattie et al., 2003a; Wang et al., 2004; Liu

et al., 2008; Pinilla-Tenas et al., 2011; Antala and Dempski, 2012; Dempski, 2012). Although the mechanism of Zn transport is not fully understood, early biochemical analyses of BbZIP suggested that Zn transport occurs in a channel-like, non-saturable electrogenic manner (Lin et al., 2010), and that phosphorylation by casein kinase 2 may also activate transport (Taylor et al., 2012). BbZIP crystallization points to a putative mechanism of Zn transport that may apply to other members of the ZIP family. Essentially, two conserved metal-binding residues, D113 and D305, seem to be necessary to recruit the metal to the transporter (Zhang et al., 2017). A conserved serine (S106) located at the bottom of the entrance cavity seems to be required to guide the ion into the transport pathway, while A102 was proposed to be a pore-lining residue at the extracellular side (Zhang et al., 2017). An inward-open conformation of the transporter can be stabilized by substrate binding at the binuclear metal center, which is in the middle of the transport pathway. Then the ion may be released to the cytoplasm through a "chain" of metal-binding residues (H177, E276, H275, and D144) and a histidine-rich loop that connects TM3 and TM4 (Zhang et al., 2017). These weak Zn-binding sites are located at the exit cavity and were named as a "metal sink," proposed to facilitate metal release from the binuclear metal center (Zhang et al., 2017). Zn release is thought to occur due to the effect of repulsive electrostatic forces between the MBS and/or the removal of geometric constraints in the rearrangement of the TMs to form an open channel at the extracellular side of the membrane which may be blocked by conserved hydrophobic residues (M99 and A102 on TM2, L200 and I204 on TM5, and M269 on TM7) as the transporter opens to the cytosol (Zhang et al., 2017).

ZIP transporters are classified into subfamilies I, II, LIV-1, and GufA according to their sequence similarities (Taylor, 2000; Gaither and Eide, 2001b; Taylor and Nicholson, 2003; Yu et al., 2013; Hu, 2021). These transporters localize to specific cellular compartments and are regulated depending on cellular needs and stage of development or disease (Reviewed by (Kambe et al., 2015)). However, there is still a gap in our knowledge on the specific functions of some members of the family, such as ZIP11. This transporter was classified as a member of the GufA subfamily of ZIP proteins. The *ZIP11* gene contains several metal responsive elements (MRE), which are targets of the classic Metal Regulatory Transcription Factor 1 (MTF1) that enable *ZIP11* expression to respond to metal levels (Martin et al., 2013; Yu et al., 2013). However, it seems that this transporter is not largely induced by MTF1 upon increase in Zn levels, as are other transporters. In mice, a modest increase in *Zip11* mRNA expression was detected in the intestine and other organs (e.g. spleen) of animals exposed to acute oral Zn exposure (Yu et al., 2013). Thus, it was proposed that ZIP11 is not required to maintain the net quota of cellular Zn, and rather instead helps to maintain appropriate subcellular distribution of the ion. Gene expression analyses showed that the murine *Zip11* (*mZip11*) is highly expressed in the testes, stomach, ileum, and cecum, with a lower level of expression detected in the liver, duodenum, jejunum, and colon (Martin et al., 2013; Yu et al., 2013). Martin and coworkers (Martin et al., 2013) showed that within the murine gastrointestinal tract, ZIP11 is modestly downregulated by Zn deficiency in the stomach. This data showed that Zn deficiency may trigger the absorption of Z from the colon by ZIP4 rather than by ZIP11 (Martin et al., 2013).

Overexpression analyses determined that HEK cells expressing *mZip11-Flag* had elevated Zn content compared to controls. Moreover, incubation of cells expressing *mZip11-Flag* in the presence of Zn led to cell death after 2 days, while supplementation with the chelator N,N,N′N′-tetrakis (–) [2-pyridylmethyl]-ethylenediamine (TPEN) favored cell growth (Yu et al., 2013). Knockdown (KD) experiments in Raw264.7 cells consistently showed a decrease in cellular Zn levels, strengthening the hypothesis that mZip11 is a Zn importer (Yu et al., 2013). However, experiments using MDCK cells expressing the *mZip11-Flag* construct determined that the transporter may also mobilize Cu (Yu et al., 2013). Murine models have demonstrated that *Zip11* expression in different tissues have differential responses to Zn acquired from the diet (Martin et al., 2013; Yu et al., 2013). At the cellular level, ZIP11 is proposed to be localized to the nucleus and Golgi apparatus (Kelleher et al., 2012; Martin et al., 2013). Despite this evidence, the physiological and cellular functions of ZIP11 have not been established.

Emerging evidence has shown that ZIP transporters are associated with the development of various types of cancer. In the particular case of ZIP11, early gene association analyses using genome-wide association study (GWAS) datasets coupled with analyses of tumors for somatic change of *ZIP11* gene variants, and patient survival from data in The Cancer Genome Atlas (TCGA) showed that the variant (rs8081059) was significantly associated with increased risk of renal cell carcinoma, while four other variants (rs11871756, rs11077654, rs9913017, and rs4969054) were significantly associated with bladder cancer risk. These variants were located within predicted transcribed or enhancer regions. Moreover, out of 253 bladder cancer patients reported in TCGA, two had tumors that contained deleterious missense mutations in *ZIP11*. These data led to the identification of *ZIP11* as a contributor to bladder cancer (Wu et al., 2015). A recent study of patients with pancreatic adenocarcinoma (PAAD) showed that patients present with decreased serum Zn levels. Analysis of TCGA and the Genotype-Tissue Expression (GTEx) databases showed a correlation between high expression of *ZIP11* and poor prognosis in PAAD patients (Zhu et al., 2021). Gene expression analyses showed that *ZIP11* is upregulated in PAAD tumors compared to normal pancreatic controls (Zhu et al., 2021). KD of *ZIP11* in Capan-1 pancreatic cancer cells impaired cell proliferation associated with a decreased activation of ERK1/2 pathway (Zhu et al., 2021). A transcriptome analysis focused on colorectal cancer (CRC) and breast cancer samples showed that *ZIP11* is also upregulated in these patients (Barresi et al., 2018). Conversely, a negative correlation between *ZIP11* expression and glioma grades was described. A study involving 74 glioma tissue samples showed that low expression of *ZIP11* in gliomas correlated with grades III and IV tumors, while higher expression of the transporter correlated with grade I and II tumors (Kang et al., 2015). In this context, the data suggest that ZIP11 is a potential contributor

to the development of "low grade" tumors that do not spread out of the brain, but instead grow into the normal brain tissue. However, despite this evidence, there is no information on the mechanism or detailed biological function of ZIP11 in the onset and progression of brain or other types of cancer.

In this study, we characterized the contributions of ZIP11 in maintaining cell proliferation *via* regulating Zn levels in the nuclei of HeLa cells. We reduced the expression of *ZIP11* in HeLa cells using two short hairpin RNA (shRNA) against the *SLC39A11* gene and then assessed the proliferation capabilities and Zn accumulation in whole, cytosolic, and nuclear fractions. We then treated with increasing concentrations of $ZnSO_4$ and tested for metal resistance. Our data show that decreased ZIP11 expression impaired growth under normal culture conditions and increased the sensitivity of the cells due to Zn accumulation in the nuclei. RNA-seq analyses showed that the Notch pathway is downregulated in cells lacking *ZIP11*. RNA-seq and qPCR analyses revealed that the expression of cell cycle related genes was altered. For instance, we found that genes related to cell growth, such as Cyclin Dependent Kinase 20 (*CDK20*), is downregulated. On the other hand, genes implicated in the negative control of cell growth and division, such as Cyclin Dependent Kinase Inhibitor 2C (*CDKN2C*) and the Protein Phosphatase 2 Catalytic Subunit Alpha (*PPP2CA*), are induced. These analyses also showed that some DNA repair and senescence associated genes, as well as some apoptotic and genes related to epithelial mesenchymal transition (EMT), are downregulated, suggesting that the impaired growth may be due to the induction of a senescent state in the cells. Expression of exogenous wild type (WT) ZIP11 rescues the proliferation defect, restores nuclear Zn levels, and ameliorates the metal resistance phenotype observed in *ZIP11* KD HeLa cells. Interestingly, overexpression of ZIP11 in WT HeLa cells enhanced cell growth and resistance to higher levels of Zn in the media, while maintaining similar levels of the metal in cytosol and nuclei, compared to controls. Functional analyses of cancer cell migration and invasion phenotypes demonstrated that ZIP11 KD decreases the mobility and invasive capabilities of HeLa cells. As expected, ZIP11 reconstitution experiments restored these metastasis-associated properties, while overexpression of ZIP11 enhanced these phenotypes. Finally, ZIP11 KD cells have a significant decrease in mitochondrial potential and elevated β-galactosidase activity, which may also be a reflection of the dormant, or senescent, state (Chapman et al., 2019) and other metabolic deficiencies. We conclude that ZIP11 is required to maintain nuclear levels of Zn to enable proper gene expression and proliferation in HeLa cells by impairing the machinery associated with DNA damage and maintaining the cells in a senescent state. This nuclear Zn dyshomeostasis is reflected in defective metastatic properties, making ZIP11 a new potential target for further investigation using *in vivo* models and anti-cancer drug development.

MATERIALS AND METHODS

Database Searches

We queried the publicly available database cBioPortal for Cancer Genomics, (https://www.cbioportal.org/), for SNPs within the coding region of *ZIP11* in patients with either cervical or ovarian cancer. To determine if the ZIP11 coding SNPs A234P and P243S had individual biological consequences, we queried the publicly available consensus classifier PredictSNP1 (https://loschmidt.chemi.muni.cz/predictsnp1/ (Bendl et al., 2014)). To evaluate the effects of A234P and P243S (alone or in combination) on the ZIP11 protein structure, we incorporated the SNPs into a published model of ZIP11 (AF-Q8N1S5-F1) using the PyMol Molecular Graphics System version 2.4.1 (https://pymol.org; Schrödinger, LLC). To investigate the predicted consequences that A234P and P243S might have on ZIP11s protein structure, we queried the publicly available PredictProtein algorithm (https://predictprotein.org/ (Rost et al., 2004)). To verify if the HeLa cell line was appropriate for our studies, we queried the interactive HeLa Spatial Proteome Database (http://mapofthecell.biochem.mpg.de/index.html) (Itzhak et al., 2016). To determine if wild type HeLa cells contained either the A234P or the P243S mutation within the ZIP11 gene within of its genome, we queried the Broad Institutes DEPMAP Portal (https://depmap.org/portal/cell_line/HELA_CERVIX?tab=mutation). The https://www.ncbi.nlm.nih.gov/gene?Db=gene&Cmd=DetailsSearch&Term=201266 website was used to identify the number of ZIP11 isoforms that may be present in cells.

Cell Culture

HeLa and HEK293T cells were obtained from American Type Culture Collection (ATCC, Manassas, VA, United States) and cultured in DMEM media (Sigma-Aldrich, St Louis, MO, United States) supplemented with 10% fetal bovine serum (FBS) and 1% antibiotics (penicillin G/Streptomycin, Gibco, Waltham, MA, United States) in a humidified atmosphere containing 5% CO_2 at 37°C.

Plasmids and Lentivirus Production

Mission plasmids encoding for two different shRNA against human *ZIP11* and the control scrambled (Scr) construct with a puromycin resistance cassette were obtained from Sigma (**Supplementary Table S1**). The mammalian gene expression lentiviral vector pLV[Exp]-EGFP/Neo-EF1A encoding hSLC39A11 or empty vectors with a neomycin resistance cassette were purchased from Vector Builder. Plasmids were isolated with the ZymoPURE™ II maxiprep plasmid system (Zymo Research, Irvine, CA, United States) following the manufacturer's instructions. shRNA (15 μg) and the packing vectors pLP1 (15 μg), pLP2 (6 μg), pSVGV (3 μg) were transfected using lipofectamine 2000 (Thermo Fisher, Waltham, MA, United States) into HEK293T cells for lentiviral production. After 24 and 48 h, the supernatant containing viral particles were collected and filtered using a 0.22 μm syringe filter (Millipore Sigma, Burlington, MA, United States). HeLa cells were transduced with lentivirus in the presence of 8 mg/ml polybrene and selected with 4 μg/ml puromycin (Invitrogen, Waltham, MA, United States) or 2 mg/ml geneticin. After selection, the cells were maintained with 1 μg/ml of puromycin or 200 μg/ml of geneticin as needed.

Antibodies

The rabbit anti-ZIP11 (PA5-20679), antibody was from Thermo Fisher. The mouse anti-lamin A/C (SC376248) and anti-tubulin (TU-02; SC8035) were from Santa Cruz Biotechnologies (Dallas, TX, United States). The rabbit anti-GAPDH (A19056) and anti-MTF1 (custom made against the residues 520–630 from the human protein) were from Abclonal Technologies (Woburn, MA, United States). The rabbit anti-Caspase-3 antibody was from Cell Signaling Technologies (9662). The mouse anti-Golgin-97 (A21270) and the secondary HRP-conjugated anti-mouse and anti-rabbit antibodies were from Invitrogen (31,430 and 31,460, respectively). The fluorescent goat anti-rabbit Alexa-488 secondary antibody was from Thermo Fisher (A-11008).

Western Blot Analyses

Protein samples from HeLa cells (WT, Scr control, *ZIP11*-KD, and cells transduced with the empty or ZIP11-containing pLV [Exp]-EGFP/Neo-EF1A vectors) were solubilized with RIPA buffer (10 mM piperazine-N,N-bis(2-ethanesulfonic acid), pH 7.4, 150 mM NaCl, 2 mM ethylenediamine-tetraacetic acid (EDTA), 1% Triton X-100, 0.5% sodium deoxycholate and 10% glycerol) supplemented with protease inhibitor cocktail (Thermo Fisher). Protein content was quantified by Bradford assay (Bradford, 1976). Samples (20 μg) were separated by SDS-PAGE and electrotransferred to PVDF membranes (Millipore Sigma). The proteins of interest were detected using the primary antibodies anti-ZIP11 and anti-GAPDH as a loading control. The membranes were then incubated with species-specific secondary antibodies coupled to horseradish peroxidase. Chemiluminescent detection was performed using high sensitivity Tanon reagents (Abclonal Technologies).

Confocal Microscopy

Monolayers of HeLa cells were fixed overnight in 10% formalin-PBS at 4°C. Samples were washed with PBS, permeabilized with 0.2% Triton X-100 in PBS for 15 min, incubated for 1 h at RT in blocking solution (PBS, 0.2% Triton X-100, 3% FBS), and incubated overnight with anti-ZIP11 and anti-Golgin 97 antibodies in blocking buffer at 4°C. The next day, the cells were incubated for 3 h with fluorescent goat anti-rabbit Alexa-594 and anti-mouse Alexa-633 secondary antibodies in blocking solution for at RT and 30 min with DAPI. Microscopy and image processing were performed using a Leica SP8 Confocal Microscope and the Leica Application Suite X (Leica Microsystems Inc., Buffalo Grove, IL, United States).

Cell Proliferation Assays

HeLa and HeK293T cells were seeded at 1×10^4 cells/cm^2 and samples were collected 24, 48, 72, and 96 h after plating. Increasing concentrations of $ZnSO_4$ (0–200 μM) were added to the cell cultures as indicated in the figures and figure legends. The cells were trypsinized, washed three times with PBS, and counted using a Cellometer Spectrum (Nexcelcom Biosciences, Lawrence, MA, United States). To determine cell viability, HeLa cells were collected at 72 h after plating and stained with 0.4% Trypan Blue (Sigma) diluted in PBS for 5 min at RT. Cell number and viability were determined using the Cellometer Spectrum, and data were analyzed with FCS Express 7 software (*De Novo* Software).

Metal Content Analysis

Three independent biological replicates of HeLa cells stably expressing the shRNA or the pLV[Exp]-EGFP/Neo-EF1A encoding hSLC39A11 or empty vectors were seeded at 1×10^4 cells/cm^2 and allowed to proliferate for 48 h. Then the cells were rinsed three times with ice-cold PBS without Ca^{2+} and Mg^{2+} (Gibco). Subcellular fractionation was performed following the Rapid, Efficient, and Practical nuclear and cytoplasmic separation method (Suzuki et al., 2010; Gordon et al., 2019a; Tavera-Montañez et al., 2019). Briefly, cells were scraped and transferred to a 1.5-ml microcentrifuge tube. Cells were centrifuged for 10 s at 13,000 × *g* and the supernatant was discarded. The samples were resuspended in 400 ml of ice-cold PBS containing 0.1% NP40 (Sigma-Aldrich) and 50 μl of the cell suspension were collected as the whole cell fraction. The remaining 350 μl were used to obtain nuclear and cytosolic fractions by disrupting the cells by pipetting using a 1-ml pipette tip. Cell suspension was centrifuged for another 10 s and the supernatant was collected as the cytosolic fraction. The nuclear pellet was washed twice in 1 ml of ice-cold PBS containing 0.1% NP40 and centrifuged for additional 10 s. The supernatant was removed, and the pellet was resuspended in 100 μl of PBS. Nuclear integrity was verified by light microscopy. All samples were sonicated at medium intensity for 5 min in 30 s on 30 s off cycles. Protein was quantified by the Bradford method (Bradford, 1976). Purity of cytosolic and nuclear fractions used to determine metal levels was verified by western blot using an anti-Tubulin and anti-Lamin A/C antibodies.

The comparative analysis of ultra-trace (<1 ppm) Zn concentrations from each sample was determined using a method adapted from previously described protocols (Paskavitz et al., 2018; Gordon et al., 2019a; Tavera-Montañez et al., 2019). Here, Zn measurements were carried out using a PerkinElmer AAnalyst 800 atomic absorption spectrometer (AAS) with a zinc hollow cathode lamp as the radiation source. The AAS was equipped with a graphite furnace (GF-AAS) with UltraClean THGA® graphite tubes (PerkinElmer, Waltham, MA, United States). This technique allowed accurate ultra-trace zinc analysis in low volume samples, where dilution was limited by the low initial concentration of Zn in the samples (Paskavitz et al., 2018; Gordon et al., 2019a). In a typical analysis, a known mass of the sample was digested in concentrated nitric acid using single-stage digestion (Paskavitz et al., 2018; Gordon et al., 2019a; Tavera-Montañez et al., 2019). The resulting solution was analyzed for Zn *via* AAS with measurements carried out at least in triplicates. Contamination was avoided by using analytical grade reagents and 18 MΩ purified water. All analytical glassware was acid washed overnight in 10% (v/v) hydrochloric acid and rinsed with 18 MΩ purified water before use (Paskavitz et al., 2018; Gordon et al., 2019a; Tavera-Montañez et al., 2019; Kim et al., 2020). Zn standard solutions were prepared from 1000 mg/L (Sigma-Aldrich) to determine the limits of detection and obtain a calibration curve for the method. The limit of detection for Zn, calculated as three times the standard deviation of the intercept (3σ), was 0.05 ppb, with a limit of linearity at 2.5 ppb. Zn content on each sample was normalized to the initial protein content in each sample.

RNA-Seq and Data Analysis

Total RNA from HeLa cells transduced with Scr or one of two shRNA against *ZIP11* was isolated using TRIzol and frozen at −80°C until analysis. Independent replicates for each sample were evaluated for quality and concentration at the Molecular Biology Core Lab at the University of Massachusetts Chan Medical School. Quality Control-approved samples were submitted to BGI Genomics for library preparation and sequencing. Libraries were sequenced using the BGISEQ-500 platform and reads were filtered to remove adaptor-polluted, low quality and high content of unknown base reads. About 99% of the raw reads were identified as clean reads (~65 M). The resulting reads were mapped onto the reference human genome (hg38) using HISAT (Kim et al., 2015). Transcripts were reconstructed using StringTie (Pertea et al., 2015), and novel transcripts were identified using Cufflinks (Trapnell et al., 2010) and combined and mapped to the hg38 reference transcriptome using Bowtie2 (Langmead and Salzberg, 2012). Gene expression levels were calculated using RSEM (Li and Dewey, 2011). DEseq2 (Love et al., 2014) and PoissonDis (Audic and Claverie, 1997) algorithms were used to identify differentially expressed genes (DEG). Gene Ontology (GO) analysis was performed on DEGs to cluster genes into function-based categories.

RT-qPCR Gene Expression Analysis

RNA was purified from three independent biological replicates of proliferating HeLa cells (Scr control and KDs) with TRIzol (Invitrogen) following the manufacturer's instructions. cDNA synthesis was performed with 500 ng of RNA as template, random primers, and SuperScript III reverse transcriptase (Invitrogen) following the manufacturer's protocol. Quantitative RT-PCR was performed with Fast SYBR green master mix on the ABI StepOne Plus Sequence Detection System (Applied Biosystems) using the primers listed in **Supplementary Table S2**, and the delta threshold cycle value (ΔC_T) (Livak and Schmittgen, 2001) was calculated for each gene and represented the difference between the C_T value of the gene of interest and that of the control gene, *GAPDH*.

Wound Healing Assay

Cells were grown until confluence on 24 well plates in DMEM supplemented with 10% FBS and antibiotics. Cells were starved for 24 h in DMEM without FBS and cell proliferation was inhibited by treating the cells with Cytosine β-D-Arabinofuranoside (AraC) for 2 h. The monolayers were then scratch-wounded using a sterile 200 µl pipette tip and suspended cells were washed away with PBS twice. The progress of cell migration into the wound was monitored every 24 h until wound closure using the ×10 objective of an Echo Rebel Microscope as previously described (Lacombe et al., 2021). The bottom of the plate was marked for reference, and the same field of the monolayers was photographed immediately after performing the wound (time = 0 h) and at different time points after performing the scratch, as indicated in the figures. Area migrated by the cells was quantified using FIJI software, version 1.44p (Schindelin et al., 2012).

Matrigel Invasion Assay

Matrigel invasion assay was performed following the Transwell chamber method as described (Olea-Flores et al., 2019). Briefly, BioCoat® Matrigel® Invasion Chambers with 8.0 µm PET membrane placed in 6-well Plates were used to seed cells that were previously treated for 2 h with 10 µM AraC to inhibit cell proliferation. The cells were plated at 1.25×10^5 cells/ml in 2 ml of serum-free medium on the top chamber, as recommended by the manufacturer. The lower chamber of the Transwell contained 2.5 ml of advanced DMEM supplemented with 10% FCS. Cells were incubated for 24 h at 37°C in a 5% CO_2 atmosphere. Following incubation, cells and Matrigel on the upper surface of the Transwell membrane were gently removed with cotton swabs. Invading cells on the lower surface of the membrane were washed and fixed with methanol for 5 min and stained with 0.1% crystal violet diluted in PBS. Images from 10 fields of three independent biological replicates were taken and used for cell quantification using FIJI software, version 1.44p (Schindelin et al., 2012). The invasion index was calculated as the ratio between number of cells of *ZIP11* KD cells, KDs reconstituted with EV or *ZIP11*, or WT overexpressing the EV or *ZIP11* and the number of WT control cells.

Cell Cycle Analyses

HeLa cells (1×10^6 cells) were arrested in mitosis with 50 ng/ml nocodazole (Kaida et al., 2011) for 16 h and released by washing with PBS and cultured with medium with 10% FBS for an additional 24 h. Timepoints were collected as indicated in the figure legend. Cell cycle analysis was performed using a standard propidium iodide (PI)-based cell cycle assay. Briefly, cells were trypsinized, washed three times with PBS, and fixed by slowly adding 200 µl of ice-cold 70% ethanol and incubated overnight at 4°C. Cells were washed with PBS, and the pellet was resuspended in 50 µl PBS containing 100 µg/ml RNAse A and 0.1% Triton X-100 and incubated at 37°C for 30 min. Finally, the cells were incubated with 40 µg/ml PI staining solution at 37°C for 40 min and analyzed in a Cellometer Spectrum instrument. Data were analyzed with FCS Express 7 software.

Senescence Assay

We used CellEvent™ Senescence Green Flow Cytometry Assay Kit following manufacturer's instructions (Thermo Fisher). Briefly, HeLa cells (WT, Scr control, *ZIP11* KD, and cells transduced with the empty or *ZIP11*-containing pLV[Exp]-EGFP/Neo-EF1A vectors) were seeded at 1×10^6 cells/cm^2 and maintained on DMEM media supplemented with 10% FBS for 48 h. We treated wild type HeLa cells with 5 mM Palbociclib (Sigma-Aldrich) as a positive control for senescence, as suggested by the manufacturer. HeLa cells were trypsinized, washed and resuspended in PBS and fixed in 4% paraformaldehyde for 10 min at room temperature. The cells suspension was stained with the CellEvent™ Senescence Green Probe (1/500) in CellEvent™ Senescence Buffer for 90 min in a 37°C incubator with no CO_2. Cells were washed in PBS containing 1% BSA, and finally resuspended in PBS. Fluorescence intensity of β-gal was measured by Spectrum Cellometer (Nexcelom Biosciences) by setting the filter excitation at 530/30 nm filter. Data was analyzed with FCS Express 7 (*De Novo* Software).

Mitochondrial Membrane Potential

Changes in mitochondrial membrane potential produced by *ZIP11* KD in HeLa cells were determined with the tetramethylrhodamine ethyl ester (TMRE)-Mitochondrial Membrane Potential Assay Kit (Abcam, Cambridge, MA, United States) following the manufacturer's protocol. Briefly, proliferating cells were supplemented with 200 nM TMRE and incubated in the dark for 10 min at 37°C. The cells were then trypsinized and washed three times with PBS. Fluorescence intensity of TMRE was measured by Spectrum Cellometer (Nexcelom Biosciences, Lawrence, MA, United States) by setting the filter excitation at 502 nm and emission at 595 nm, as previously reported (Angireddy et al., 2020; Chowdhury et al., 2020; Lacombe et al., 2021). Data was analyzed with FCS Express 7 (*De Novo* Software).

Statistical Analysis

Statistical analyses were performed using Kaleidagraph (Version 4.1). Statistical significance was determined using *t*-test where $p < 0.05$ was considered to be statistically significant.

RESULTS

ZIP11 Plays a Role in the Progression of Cervical and Ovarian Cancer

A closer look to the TCGA database showed that of 1321 cases reported in the TCGA database for *ZIP11* (SLC39A11) mutations, 61% have been found in females and 39% in males. The higher incidence of mutations for *ZIP11* gene occurs in patients presenting uterine corpus endometrial carcinoma (**Supplementary Figure S1A**). In terms of loss of function or decrease expression of the *ZIP11* gene esophageal cancer patients represent the most affected population (8% of the patients), while for gain of function or increased expression of *ZIP11*, impacts primarily ovarian cysteous adenocarcinoma (almost 30% of the patients), followed by breast invasive carcinoma (approximately 22% of the individual; **Supplementary Figure S1B**). Between 10 and 15% of the patients presenting lung squamous cell carcinoma, bladder urothelial carcinoma, esophageal carcinoma, uterine corpus endometrial and cervical squamous cell and endocervical carcinomas are also among the groups presenting increased expression of *ZIP11* (**Supplementary Figure S1C**).

Patients of cervical and ovarian cancers represent the groups with larger numbers in *ZIP11* mutations, however mutations on this gene are not considered to be a prognostic marker of the disease (**Figure 1** and **Supplementary Figure S1** and **Supplementary Table S3**). Therefore, we looked closely into genotypes and phenotypes observed in these populations. Analysis of 2344 samples from 2330 patients found in seven publicly available cervical and ovarian cancer studies (https://www.cbioportal.org/) confirmed that *ZIP11* had an alteration frequency of 2–3%, within the genome, with the majority of the genes being amplified or mutated rather than deleted (**Figure 1A**). Further structural analysis of these datasets revealed two unique missense mutations within the *ZIP11* coding region, A26S and A234P, while another two mutations, P243S and A89V, correlated with the two known coding SNPs rs763797008 and rs202154945 (**Figure 1B**). Although the effect of an individual SNP is generally minor, some variants do affect gene expression or the function of the translated proteins (Risch and Merikangas, 1996; Collins et al., 1997). Therefore, the effect of combinations of functionally relevant SNPs may synergistically contribute to increased disease progression. Compared to individual SNPs, multiple SNPs can be either more or less deleterious. Multiple SNPs on the same gene have been found to contribute or be linked to various genetic diseases (Rafi et al., 2003; Kamphans et al., 2013). To determine if these SNPs had biological consequences, we used PredictSNP (Bendl et al., 2014), a publicly available consensus classifier for disease related amino acid mutations. Results showed that both A234P and P243S had deleterious biological consequences (**Figure 1C**). The limitation of the PredictSNP model is that it can only predict the consequence of one SNP, not multiple. We knew that some of the patients in these data sets were positive for both A234P and P243S mutations. Therefore, using PyMol Molecular Graphics System, we used the predicted structure of ZIP11 (PDB AF-Q8N1S5-F1) to construct a model that contained the two deleterious SNPs and compared this to the wild type structure. The model indicated SNP induced structural variations within the substrate binding region that possibly could affect the function of the protein (**Figures 1D,E**). To show exactly where the SNPs affected ZIP11 structure and what could be the predicted consequences; we used the publicly available PredictProtein algorithm. PredictProtein searches public sequence databases, creates alignments, and predicts aspects of protein structure and function (Rost et al., 2004). These *in silico* analyses suggested that substitutions in A234P and P243S may result in an increase in substrate accessibility (**Figure 1F**). Since these residues are facing away from the transmembrane metal binding site, these mutations may potentially affect the interactions between surrounding transmembrane helices. However, further biochemical characterization is needed to clarify this point. Finally, using the Human Protein Atlas (https://www.proteinatlas.org/) we constructed a Kaplan-Meier survival curve using a cervical cancer data set containing 291 patients. The survival curve demonstrated that patients with high *ZIP11* RNA expression within their cervical cancer tumors had a 63% chance of surviving over 5 years, while those with low *ZIP11* RNA had a 72% survival rate (**Figure 1G** and **Supplementary Table S3**). This trend in survival suggests that ZIP11 expression may correlate with the progression of cervical cancer, although the information provided by the database does not specify whether these patients harbor the indicated SNPs.

ZIP11 has been proposed to be a transporter that mobilizes Zn from the nucleus and Golgi into the cytosol (Kambe et al., 2015). However, overexpression studies in early characterization of RAW264.7 cells, which are monocyte/macrophage-like cells suggested a potential role mobilizing extracellular Zn into the cytosol (Yu et al., 2013). To verify if the HeLa cell line was an appropriate model for our studies of ZIP11 in the context of nuclear transport, we used the interactive HeLa Spatial Proteome Database (http://mapofthecell.biochem.mpg.de/index.html) to

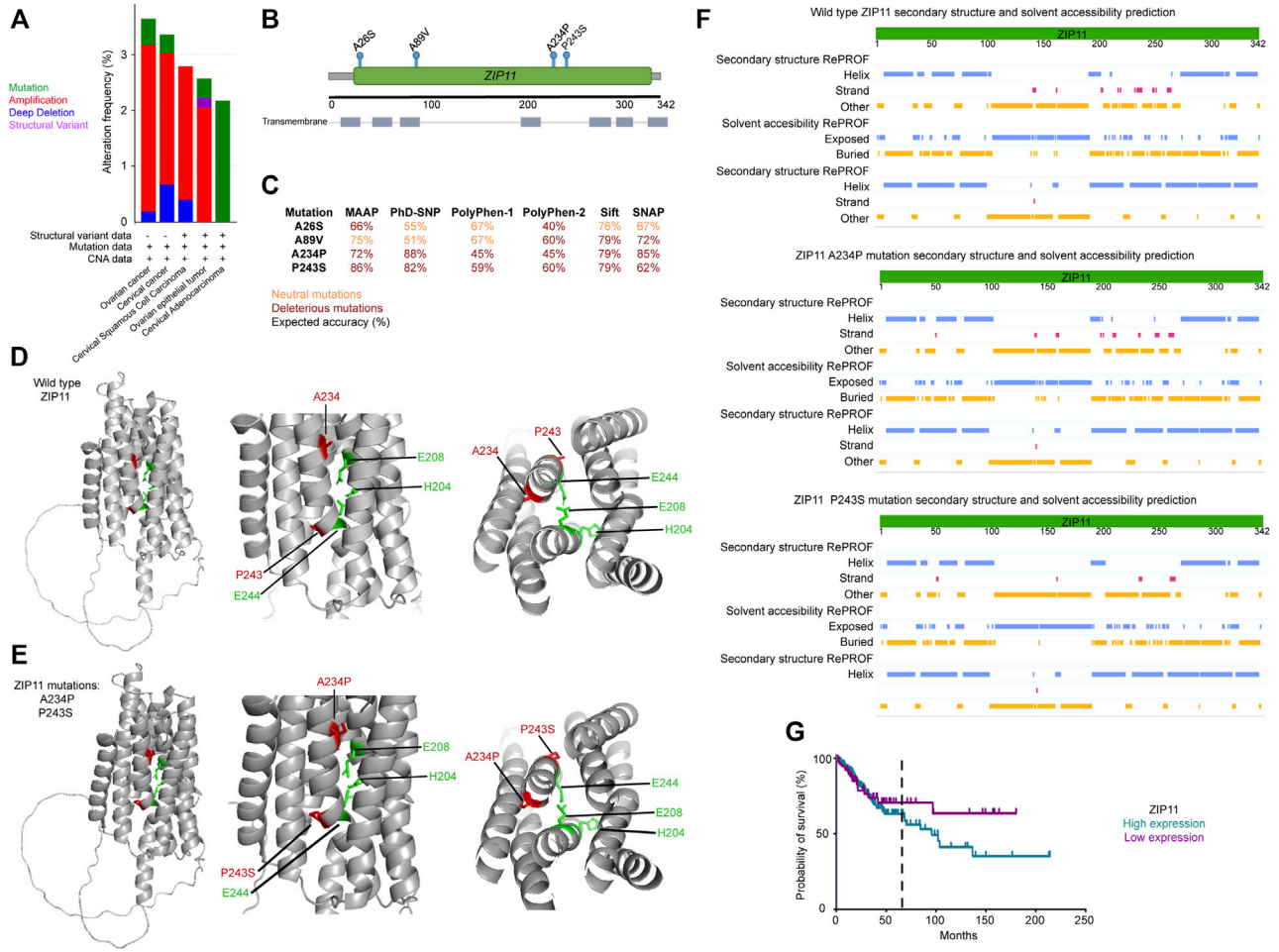

FIGURE 1 | ZIP11 role in the progression of cervical and ovarian cancer. **(A)** Analysis of 2344 samples from 2330 patients found in seven publicly available cervical and ovarian cancer studies (https://www.cbioportal.org/) confirmed that ZIP11 had an alteration frequency of 2–3%, within the genome. **(B)** Schematic of ZIP11 and SNP locations (green) within the ZIP11 protein and transmembrane domains (gray). **(C)** PredictSNP analysis of *ZIP11* SNPs in cervical and ovarian cancer (red = deleterious; orange = neutral mutations). Representative model of wild type ZIP11 **(D)** and ZIP11 containing two deleterious SNPs (A234P and P243S, **(E)** within the substrate binging region. **(F)** *In silico* modeling with PredictProtein calculated that ZIP11 may have increased substrate accessibility when the two deleterious SNPs (A234P and P243S) are introduced. **(G)** Kaplan-Meier survival curve using a cervical cancer data set containing 291 patients. Five-year survival indicated by black, vertical, dashed line. The statistical information for the comparison of survival curves can be found in **Supplementary Table S3**.

understand the cellular localization of ZIP11. The HeLa Spatial Proteome Database provides subcellular localization information for 8,700 proteins from HeLa cells. It indicates how a queried protein is distributed over the nucleus, cytosol, and organelles of the HeLa cells using a cross-validation of a 1,000-member organelle marker set resulting in a median prediction accuracy of >94% (Itzhak et al., 2016). Principal components analysis of six Dynamic Organellar Maps of ZIP11 generated by the HeLa Spatial Proteome interactive (**Supplementary Figures S2A–F**) database revealed that ZIP11 is present in both the nucleus and some organelle compartments of HeLa cells in roughly equal numbers and is also present in the cytosol (p = 0.0269 when comparing nucleus to cytosol; (**Supplementary Figure S2G**). Finally, using the DEPMAP portal, we confirmed that the wild type HeLa cell line does not harbor either the A234P or the P243S mutation in the ZIP11 gene within its genome (https://depmap.org/portal/cell_line/HELA_CERVIX?tab=mutation). Taken together, the HeLa cell line was determined to be an appropriate model for our studies of ZIP11 in the context of nuclear transport.

ZIP11 Expression Is Required for Proliferation in HeLa Cells

Considering that cervical cancer patients are amongst the higher incident population of individuals with mutations in *ZIP11*, we chose HeLa cervical carcinoma cells as a model to investigate the contributions of this transporter to the cancer phenotype. ZIP11 has been proposed to localize in the nuclei and Golgi, and confocal microscopy analyses of WT cells shows that ZIP11 is primarily located in the perinuclear/nuclear region of the cells and partially colocalized with the Golgi marker Golgin-97 vesicles

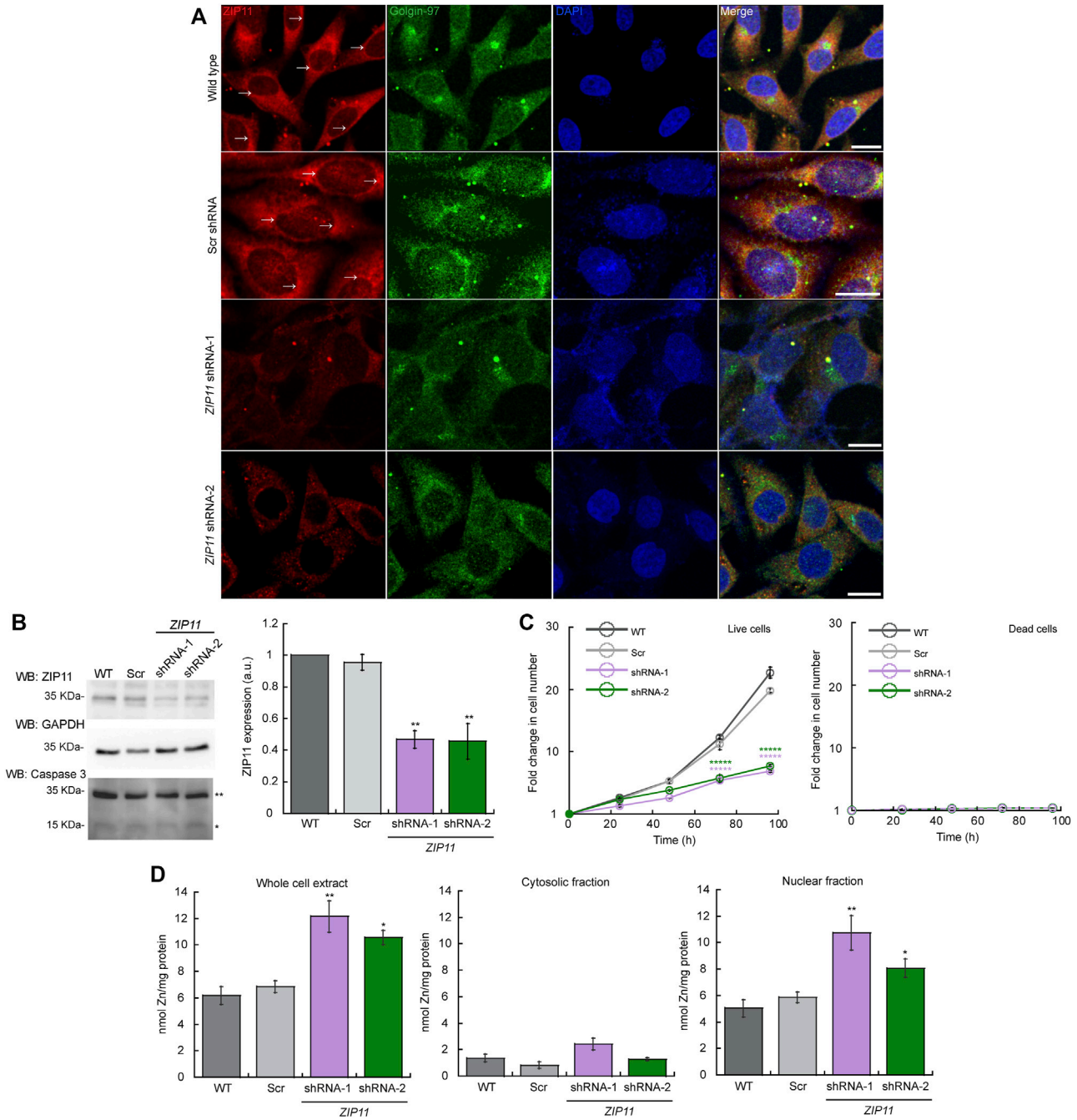

FIGURE 2 | ZIP11 is required for proliferation of HeLa cells and regulates nuclear levels of Zn. **(A)** Representative confocal images showing a perinuclear and cytosolic punctuated pattern of expression of ZIP11 (red) in wild type and scramble (Scr) shRNA transduced HeLa cells. Confocal images of HeLa cells transduced with *ZIP11* shRNA-1 and shRNA-2 show a decrease in the staining around the nucleus and vesicles. shRNA1 and shRNA2 targets the CDS and UTR regions of *ZIP11*, respectively. The anti-Golgi-97 antibody (green) was used as a marker of Golgi apparatus and nuclei was stained with DAPI (blue). Bar = 10 μm. **(B)** Representative immunoblot (left) and quantification (right) of *ZIP11* levels of the 35 KDa (isoform 1) in HeLa proliferating cells for 72 h. *See* **Supplementary Figure S3** for the data of the rest of isoforms. Immunoblots against GAPDH were used as loading controls. Samples were compared to the corresponding wild type sample. An anti-caspase 3 antibody was used to detect cell death in HeLa cells proliferating for 72 h; single asterisk (*) indicate cleaved caspase 3 and double asterisks (**) indicate the full inactive pro-caspase 3 form. **(C)** Cell counting assay of proliferating WT, and cells transduced with scrambled shRNA (shRNA Scr), or *ZIP11* shRNAs. Data represent the fold change in number of live and dead cells as determined by Trypan blue assay. **(D)** Zn levels in proliferating HeLa cells. Wild type and cells stably expressing Scr, shRNA-1 or shRNA-2 against *ZIP11* were allowed to grow for 48 h and subcellular fractions were obtained using the REAP protocol. Whole cell (left) cytosolic (middle) and nuclear (right) Zn content determined by AAS (Suzuki et al., 2010; Gordon et al., 2019a; Tavera-Montañez et al., 2019). For all samples, data are the mean ± SE of three independent biological replicates. $^{*}p < 0.05$; $^{**}p < 0.01$; $^{*****}p < 0.00001$.

(**Figure 2A**). Furthermore, we performed confocal microscopy analyses of ZIP11 and the endoplasmic reticulum (ER) marker calnexin and detected minimal colocalization between these proteins, suggesting no strong association of ZIP11 with the ER on HeLa cells (**Supplementary Figure S3**).

To test the biological role of ZIP11 in the proliferation of HeLa cells, we reduced the expression of the transporter using two different shRNA clones, one which targeted the coding sequence (sh-1) and the other the UTR region (sh-2). Confocal microscopy (**Figure 2A**), and western blot and densitometric analyses of three independent biological replicates (**Figure 2B**) showed the decreased expression of *ZIP11* following this strategy and confirms the specificity of the ZIP11 antibody. According to the https://www.ncbi.nlm.nih.gov/gene?Db=gene&Cmd=DetailsSearch&Term=201266 website, there are 16 known isoforms of the ZIP11 protein expressed in human cells that range from 20 to 36 KDa (**Supplementary Figure S3**). Analyses of the complete membrane showed that the selected antibody likely recognize some of these variants of ZIP11 (**Supplementary Figure S3**). The specific roles of these isoforms are beyond the scope of this work; however we can detect a reduction on their expression with the two shRNAs used in this study. Two higher MW bands are present on the gel. We believe these are non-specific targets in western blot analyses, as quantification of the individual bands/clusters of bands indicates these species are not reduced by the ZIP11 shRNAs whereas the ZIP11 isoforms are reduced by the shRNAs. We focused on the 35 KDa isoform (X1) for our study as it is one of the most common forms expressed in human cells.

Upon reduction of the expression of ZIP11, we detected a significant decrease in the proliferation rate of KD cells (**Figure 2C** left panel). Trypan blue analyses determined that there is no increase in cell death in *ZIP11* KD cells during the experiment (**Figure 2C** right panel), which was verified by western blot analyses against caspase 3 of proliferating HeLa cells at a representative time point of 72 h (**Figure 2B**). We also tested the effect of *ZIP11* KD in the non-carcinogenic cell line HEK273T, isolated from human embryonic kidneys. We observed that upon KD of the transporter there are no significant changes in the proliferation of these cells (**Supplementary Figure S2**). The contrasting results of the effect of *ZIP11* KD on the proliferation rate observed between HeLa and HEK cells suggest that the biological role of the transporter may be dependent on the cellular context and may be a distinctive feature across cell types and tissues.

Therefore, we focused our studies in HeLa cells, as we observed the most dramatic phenotype associated to *ZIP11* KD in this cell line. Considering the location of the transporter, we evaluated the effect of ZIP11 KD on metal accumulation in whole cell extract, cytosolic and nuclear fractions of HeLa cells (**Figure 2D** left, middle and right panels, respectively). ZIP11 has been implicated in nuclear transport of Zn because its expression is dependent on Zn levels; however, *ZIP11* does not exhibit drastic changes upon cellular exposure to this metal, as other metalloprotective genes (Martin et al., 2013; Yu et al., 2013). Therefore, to understand how partial loss of ZIP11 affects accumulation of Zn, we used AAS to measure total metal levels in proliferating HeLa cells (**Figure 2D**). WT and cells transfected with scrambled (Scr) shRNA showed similar content of Zn in whole cell extracts, with Zn mainly located in the nucleus. Importantly, a significant increase in whole cell levels of Zn was observed in the two *ZIP11* KD cell lines with the metal accumulated primarily in the nuclei (**Figure 2D**), suggesting that reduced expression of this transporter impairs the mobilization of the ion from the nucleus to the cytosol. **Supplementary Figure S6** shows a representative western blot of the purity of the cytosolic and nuclear fractions used in the metal content analyses. Tubulin was used as a marker of cytosol and Lamin A/C was used as marker of the nuclear fractions.

We then analyzed the effect of Zn stress on the growth of HeLa cells KD for ZIP11 (**Figure 3**). To this end, cells were cultured in the presence of increasing concentrations of $ZnSO_4$, and counting assays were performed over 5 days. We found that the KD cells had a decrease in proliferation at 75 μM $ZnSO_4$ (**Figure 3C**) compared to non-treated KD and control cells, which were sensitive to higher concentrations of the metal (200 μM; **Figures 3D,E**). These data suggest that ZIP11 may be a regulator of proliferation in HeLa cells by mediating nuclear Zn homeostasis, by potentially mediating appropriate gene expression. However, we cannot overrule alternative mechanisms that lead to a different pathway where *ZIP11* KD also influences the levels of Zn in Golgi and potentially other subcellular organelles which have not been isolated yet, to produce this deleterious effect.

Effect of *ZIP11* KD in HeLa Cells Transcriptome

We performed RNA-seq to investigate global changes in gene expression in proliferating HeLa cells transduced with either the Scr or the two different *ZIP11* shRNAs. The sequenced libraries from the samples had approximately 92M total reads, where the average mapping ratio with the gene is 85.28%. The unique matched reads are shown in **Supplementary Table S4**. Reads were mapped to the human genome (GRCh38/hg38) and gene expression levels were determined. Differentially expressed genes that were significant in both replicates for each shRNA were considered for analysis (log_2FoldChange>1 and <−1). Replicate samples for scramble and *ZIP11* shRNA resulted in Pearson coefficients of >0.94 for each comparison of replicates (**Supplementary Table S4**). Each *ZIP11* KD affected the expression of a similar number of genes, however, there are noticeable differences (**Figures 4A–C**). shRNA-1 affected a total of 4433 genes, of which 2136 were upregulated and 2297 were downregulated (**Figure 4A**), and shRNA-2 affected 5121 genes in total, with 2645 genes upregulated and 2476 downregulated (**Figure 4B**). Both shRNAs shared 2292 differentially expressed genes (DEG) compared to gene expression in the control cells (**Supplementary Table S4** and **Figure 4C**). To identify function-based categories, we performed gene ontology (GO) analysis on DEG that were significant in both replicates for both shRNAs. The complete results are listed in **Supplementary Table S4**. The top 10 significant categories of down-regulated and up-regulated genes shared by both KD cells are shown in **Figures 4D,E**. The top ranked categories of down-regulated genes included regulation of cell migration involved in angiogenesis, metabolism of dicarboxylic acid, regulation of smooth muscle proliferation, and Notch signaling pathway (**Figure 4D** and **Supplementary Table S4**). RNA processing

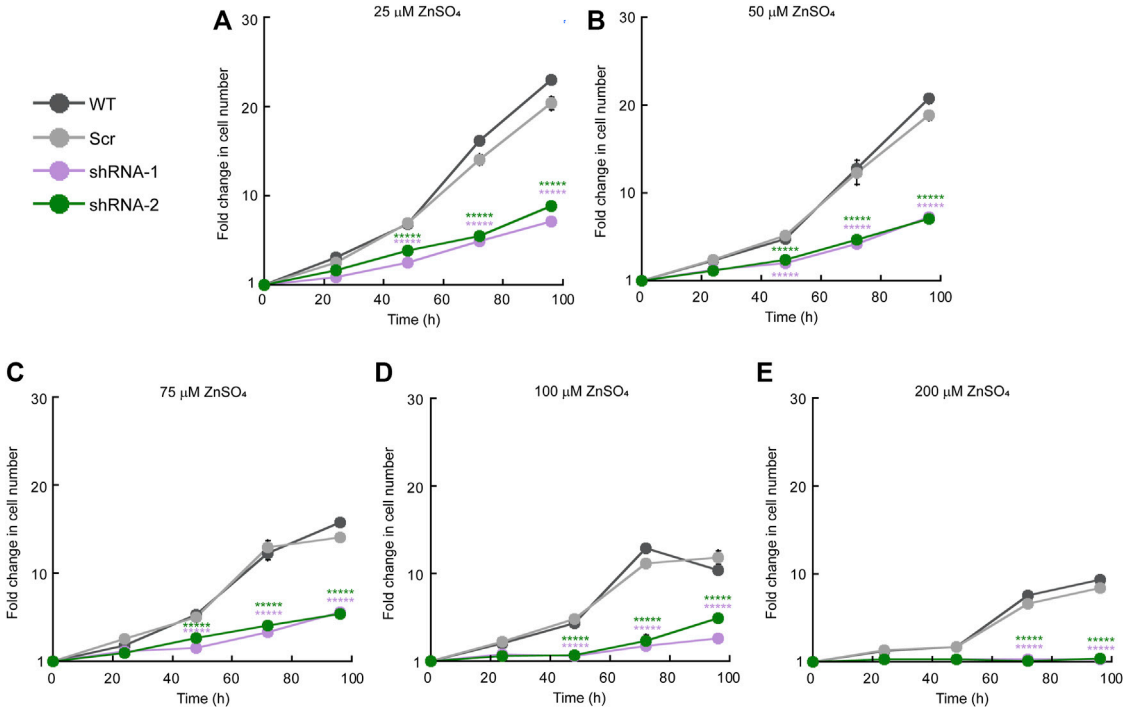

FIGURE 3 | *ZIP11* knockdown results in elevated sensitivity to Zn in HeLa cells. Cell counting assay of proliferating WT, and cells transduced with scrambled shRNA (shRNA Scr), or *ZIP11* shRNAs cultured for 96 h with increasing concentrations of $ZnSO_4$. **(A)** 25 μM. **(B)** 50 μM. **(C)** 75 μM. **(D)** 100 μM. **(E)** 200 μM. Cells were seeded at 1×10^4 cells/cm^2 and the growth for each clone and timepoint was normalized to the seeding density. The data represents the mean ± SE for three independent experiments. *****$p < 0.00001$.

and metabolism were the most remarkable up-regulated categories followed by regulation of cell cycle, but genes involved in the regulation of DNA transcription and termination were also upregulated (**Figure 4E** and **Supplementary Table S4**). A close analysis of genes related to cell growth, DNA repair, senescence, apoptosis, and EMT suggested important changes that may explain the impaired proliferation phenotype and different shapes observed in both KD strains. Some of these genes were validated by qPCR analyses. For instance, the expression of the cell cycle regulatory gene *CDK20* is decreased (**Figure 4F** and **Supplementary Table S4**), and genes related to EMT (*LOXL3* and *FUZ*; **Supplementary Table S4**) are downregulated as well. Interestingly, we found changes in the expression of senescence associated genes, however, these behaved slightly different in both shRNA KD strains. In addition, genes implicated in the negative control of cell growth and division, such as *CDKN2C* and *PPP2CA*, were upregulated (**Figure 4F**). Genes implicated in senescence (*CDKNA* (*p21*) (Pospelova et al., 2009; Noren Hooten and Evans, 2017)) were also upregulated in both cell lines partially depleted for *ZIP11* (**Supplementary Figure S7A** and **Supplementary Table S4**). Additional senescence genes (i.e. *CXCL1*, *CXCL2*, *CSF2*, and *ANKRD1*) presented a small increase in HeLa cells transduced with shRNA2, with minor changes in shRNA1 cells (**Supplementary Table S4**).

Changes were also detected in the expression of the metalloprotective transcription factor, MTF1, and the target gene *METALLOTHIONEIN*, *MT1A* (**Supplementary Figures S7B,C** and **Supplementary Table S4**). However, the RNA-seq analyses showed that the members of the network of Zn exporters and importers, *ZnTs1-8,10* and *ZIPs1-13*, do not present any significant changes in their expression (**Supplementary Table S4**). Only the gene encoding *ZIP14* has a significant and consistent decrease in its expression in both KD HeLa cells. The data suggest that the cells are unable to cope with the nuclear Zn stress produced by the KD of ZIP11, and potentially the impaired growth may be due to a senescent state and decrease in cell cycle progression rate induced by nuclear Zn dysregulation. Distinctive GO categories between shRNA-1 and shRNA-2 are shown in **Supplementary Figure S8**.

Expression of Exogenous ZIP11 Rescues the Proliferation Defect, Restores Nuclear Zn Levels, and Confers Resistance to Elevated Levels of the Metal

To determine whether the lack of ZIP11 and increase in nuclear Zn levels are responsible for the growth defect observed in KD cells, we reintroduced the *ZIP11* gene using a standard protocol of viral transduction and generated clones stably expressing the protein

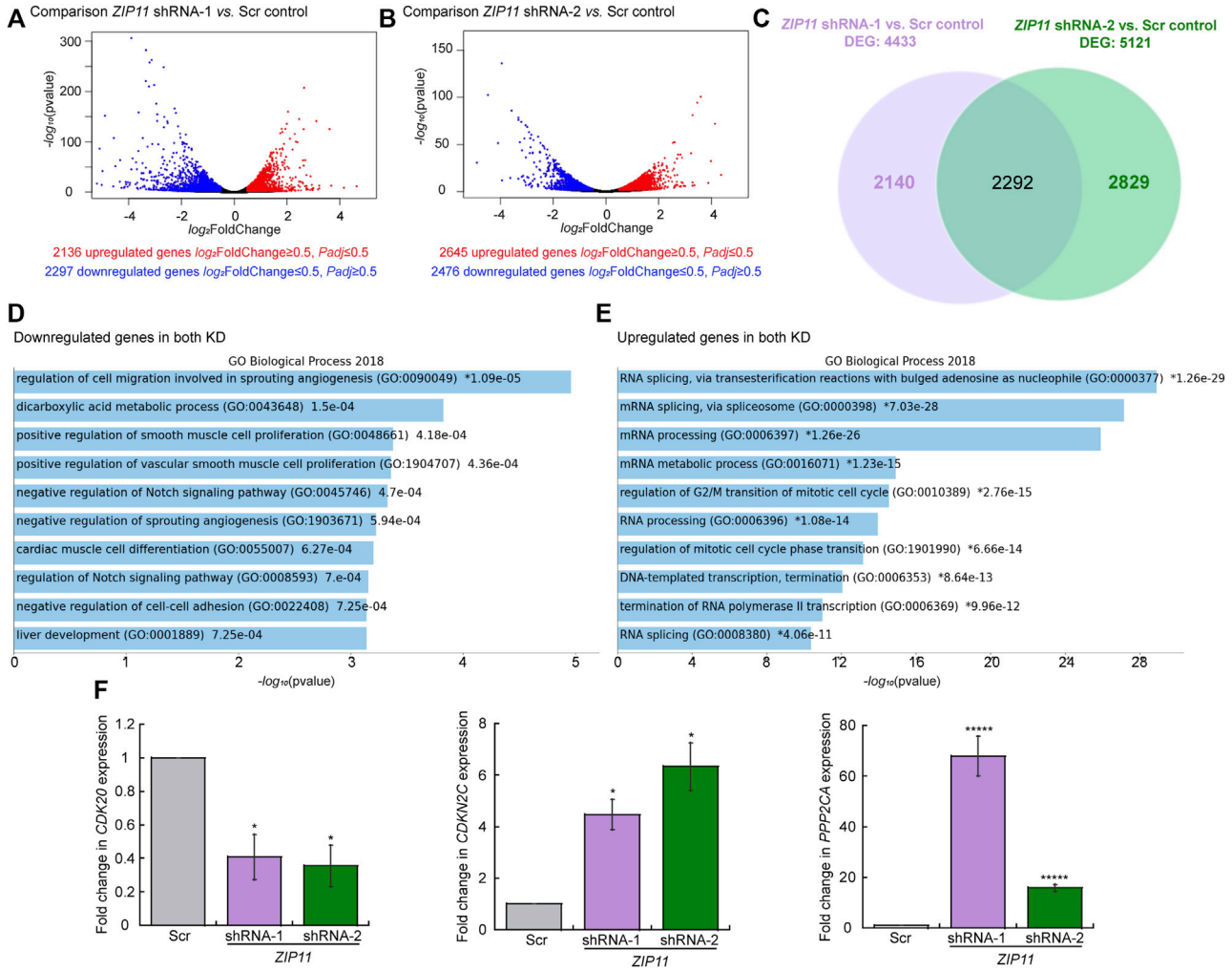

FIGURE 4 | Changes in gene expression dependent on *ZIP11* knockdown in HeLa cells. Volcano plots displaying differentially expressed genes between Scr control and *ZIP11* KD with shRNA1 **(A)** or*shRNA2* **(B)** in HeLa cells. The *y*-axis corresponds to the mean log10 expression levels (*p* values). The red and blue dots represent the up- and down-regulated transcripts in *ZIP11* KD (false-discovery rate [FDR] of <0.05), respectively. The gray dots represent the expression levels of transcripts that did not reach statistical significance (FDR of >0.05). **(C)** Venn diagram showing the overlapping DEG between the two shRNAs used to KD *ZIP11*. GO term analysis of down-regulated **(D)** or up-regulate **(E)** genes consistent in both KD of *ZIP11* in HeLa cells. Cut-off was set at 2.0 of the –log(adjusted *p* value). *See* **Supplementary Table S4** for the complete list of genes and individual GO terms detected for each shRNA using Panther. **(F)** Steady state mRNA levels determined by qRT-PCR of representative downregulated (*CDK20*) and up-regulated (*CDKN2C* and *PPP2CA*) genes selected from the RNA-seq analyses which are associated to cell cycle progression and apoptosis. Data are the mean ± SE for three independent experiments. *$p < 0.05$, *****$p < 0.00001$.

(**Figure 5**). Cells transduced with an empty vector (EV) were used as controls. For the reconstitution experiments, we used cells expressing the shRNA-2 for *ZIP11* KD, as this shRNA recognizes the UTR of the transporter gene. Expression of exogenous ZIP11 was confirmed by immunoblot (**Figure 5A**). Consistent with our RNA-Seq and gene expression profiles, under normal metal conditions, the expression of MTF1 protein was elevated in cells KD for ZIP11 and restored to basal levels in cells expressing exogenous *ZIP11* gene (**Figure 5A**). The proliferation defect detected in *ZIP11* KD cells was rescued upon expression of WT ZIP11 as shown by cell counting assays (**Figure 5B**). Confocal microscopy analyses showed an increase in the staining of ZIP11 in a perinuclear and cytosolic punctuated pattern upon reintroducing the gene to the KD cells (**Figure 5C**). Importantly, the cells expressing ZIP11 also presented a concentration of nuclear Zn similar to the levels of control cells (**Figure 5D** By contrast, the cells transduced with the EV maintained the proliferation defect, reduced levels of the protein in the perinuclear area and maintained elevated levels of the metal in the nucleus (**Figures 5B–D**). We then asked whether reintroduction of the gene would also restore cell resistance to extracellular Zn stress. The cells were grown under increasing concentrations of $ZnSO_4$ and proliferation was determined by cell counting assays. **Figures 5E–I** show that cells expressing the recombinant transporter are less sensitive to Zn stress and can grow at a rate similar to control cells. As expected, the cells transduced with EV were sensitive to extracellular Zn

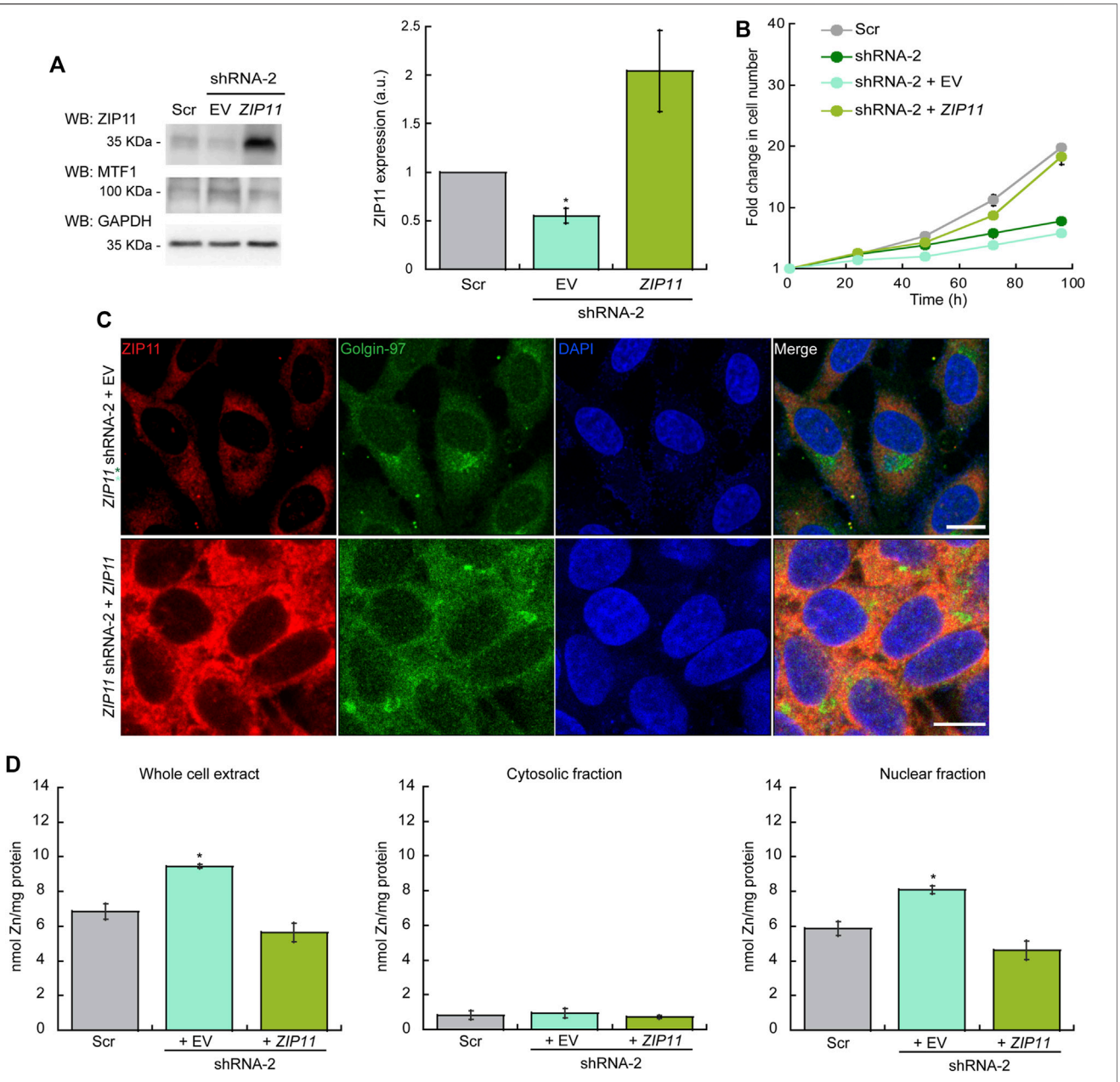

FIGURE 5 | (Continued).

stress as non-transduced cells. Thus, the data supports a role for ZIP11 in maintaining nuclear Zn homeostasis.

Overexpression of Exogenous ZIP11 Exacerbates the Growth of HeLa Cells and Provides Elevated Resistance to External Zn Stress

To further understand the effect of ZIP11 in the proliferation and metal resistance of HeLa cells, we performed overexpression experiments where WT cells were transduced with and stably expressed either the *ZIP11* gene or the EV as a control (**Figure 6**). Evaluation of ZIP11 by western blot shows that cells transduced with the vector encoding the *ZIP11* gene expressed a significantly larger amount of the transporter compared to non-transduced EV-infected control cells (**Figure 6A**). In this case, the levels of MTF1 protein remained constant in the three cell lines tested (**Figure 6A**). Cell proliferation assays revealed that overexpression of *ZIP11* in WT cells enhanced proliferation (**Figure 6B**). Confocal microscopy analyses showed an increased perinuclear and cytosolic punctuated staining for ZIP11 (**Figure 6C**), similar to the observed pattern of reconstitution experiments (**Figure 5C**), though the total, cytosolic, and nuclear

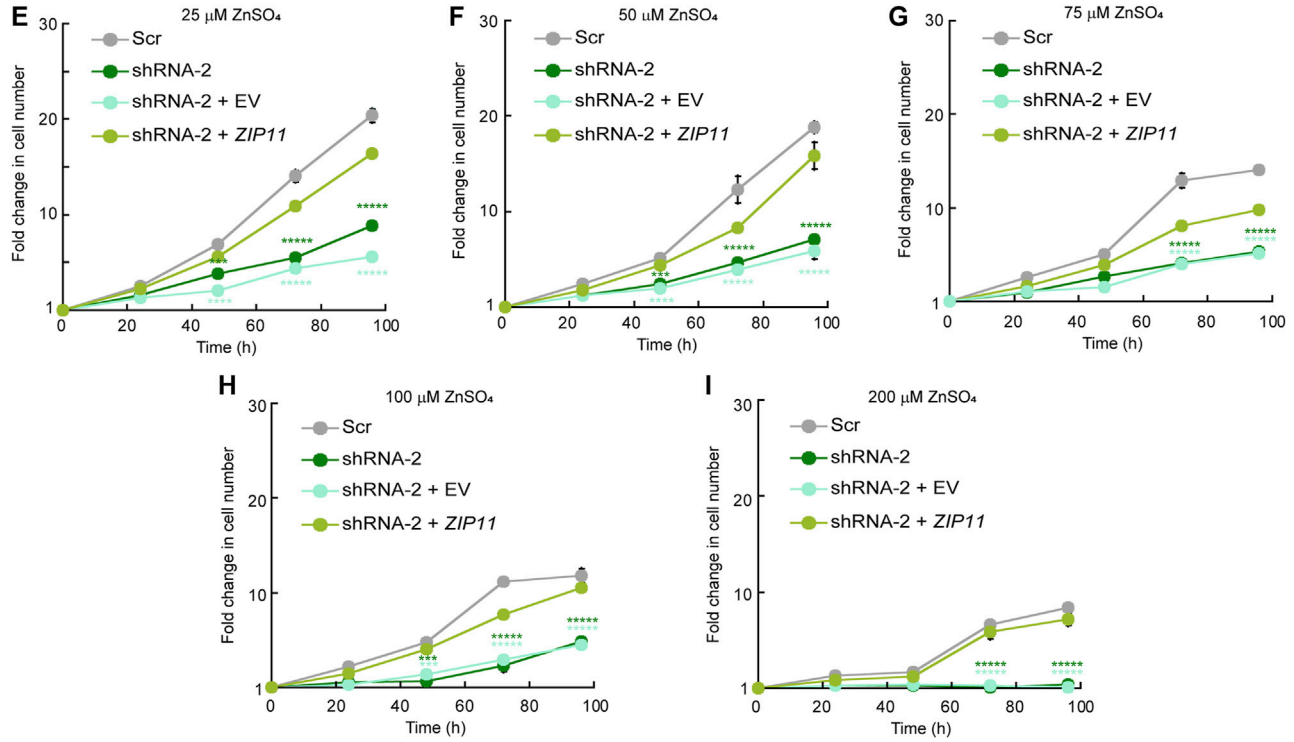

FIGURE 5 | Reintroducing *ZIP11* in HeLa cells restores growth, nuclear Zn levels and resistance to elevated levels of Zn. **(A)** Representative immunoblot (left) and quantification (right) of *ZIP11* levels in HeLa proliferating cells. The cells expressing the shRNA2 against *ZIP11* targeting the UTR region of *ZIP11* were used for reconstitution of phenotypes experiments. Immunoblots against MTF1 shows increased expression of its metalloprotective transcription factor in ZIP11 KD cells. GAPDH was used as loading controls. **(B)** Cell counting assay of proliferating cells transduced with scrambled shRNA (shRNA Scr), or *ZIP11* shRNA-2 expressing exogenous ZIP11 or empty vector (EV). **(C)** Representative confocal micrographies of ZIP11 (red) and Golgin-97 (green) showing the enhanced expression and perinuclear and vesicular distribution of ZIP11 in HeLa cells KD for *ZIP11* (shRNA-2) and stably expressing ZIP11 or the empty vector (EV). Nuclei was stained with DAPI. Bar = 10 μm. **(D)** Distribution of the Zn levels in proliferating HeLa cells. Cells stably expressing Scr, and shRNA-2 against ZIP11 reconstituted with ZIP11 or the empty vector were allowed to grow for 48 h and subcellular fractions were obtained using the REAP protocol. Whole cell (left) cytosolic (middle) and nuclear (right) Zn content determined by AAS (Itzhak et al., 2016; Gordon et al., 2019a; Tavera-Montañez et al., 2019). **(E–I)** Analyses of Zn resistance upon reintroduction of the *ZIP11* gene. Cell counting assay of proliferating cells transduced with scrambled shRNA (shRNA Scr), *ZIP11* shRNA2 expressing the transporter gene or an empty vector, cultured for 96 h with increasing concentrations of ZnSO4. **(E)** 25 μM. **(F)** 50 μM. **(G)** 75 μM. **(H)** 100 μM. **(I)** 200 μM. The data represents the mean ± SE for three independent experiments. *****$p < 0.00001$.For all samples, data are the mean ± SE of three independent biological replicates. *$p < 0.05$; **$p < 0.01$; *****$p < 0.00001$.

levels of Zn remained stable and similar to control cells (**Figure 6C**). Importantly, the cells overexpressing ZIP11 were significantly more resistant to elevated levels of Zn (up to 200 μM) supplemented in the culture media than control cells (**Figures 6D–H**). The data corroborates a function for ZIP11 in maintaining nuclear Zn homeostasis to enable appropriate gene regulation and cell growth.

ZIP11 KD Impairs the Migration and Invasive Properties of HeLa Cells

Cancer cells have several hallmarks and biological functions that promote EMT and metastasis. Thus far, we have evidence showing that ZIP11 is required for the growth of HeLa cells. Therefore, we utilized two functional assays to assess the contributions of ZIP11 to the carcinogenic phenotype of these cells. First, we performed a wound-healing assay, wherein a confluent cell monolayer is scratched and the time and extent of cell migration to close the wound was determined. **Figure 7** shows a time course of representative light microscopy images of the wound-healing assay for WT HeLa cells, cells transduced with Scr, shRNA-1, and shRNA-2, and cells reconstituted and overexpressing *ZIP11* and the EV. Time 0 h indicates the moment when the wound is performed, and subsequent pictures are representative of subsequent time points (taken every 24 h) where the cells were monitored to determine the time needed for the wound to close (**Figure 7A**). Quantification of the area migrated over time showed that the rate of migration of *ZIP11* KD cells into the wound was reduced compared to Scr controls (**Figure 7B**). This deficient migration phenotype was reverted by reintroducing the exogenous *ZIP11* gene into the KD cells (**Figure 7C**), and was enhanced in WT cells overexpressing ZIP11, as these cells fully covered the wound 1 day earlier than the rest of the cells (**Figure 7D**). Thus, directional migration induced by a wound closure is impaired with ZIP11 KD and conversely enhanced by ZIP11 overexpression.

To further investigate the functional consequences of decreasing the expression of ZIP11 in HeLa cells, we also studied their invasive

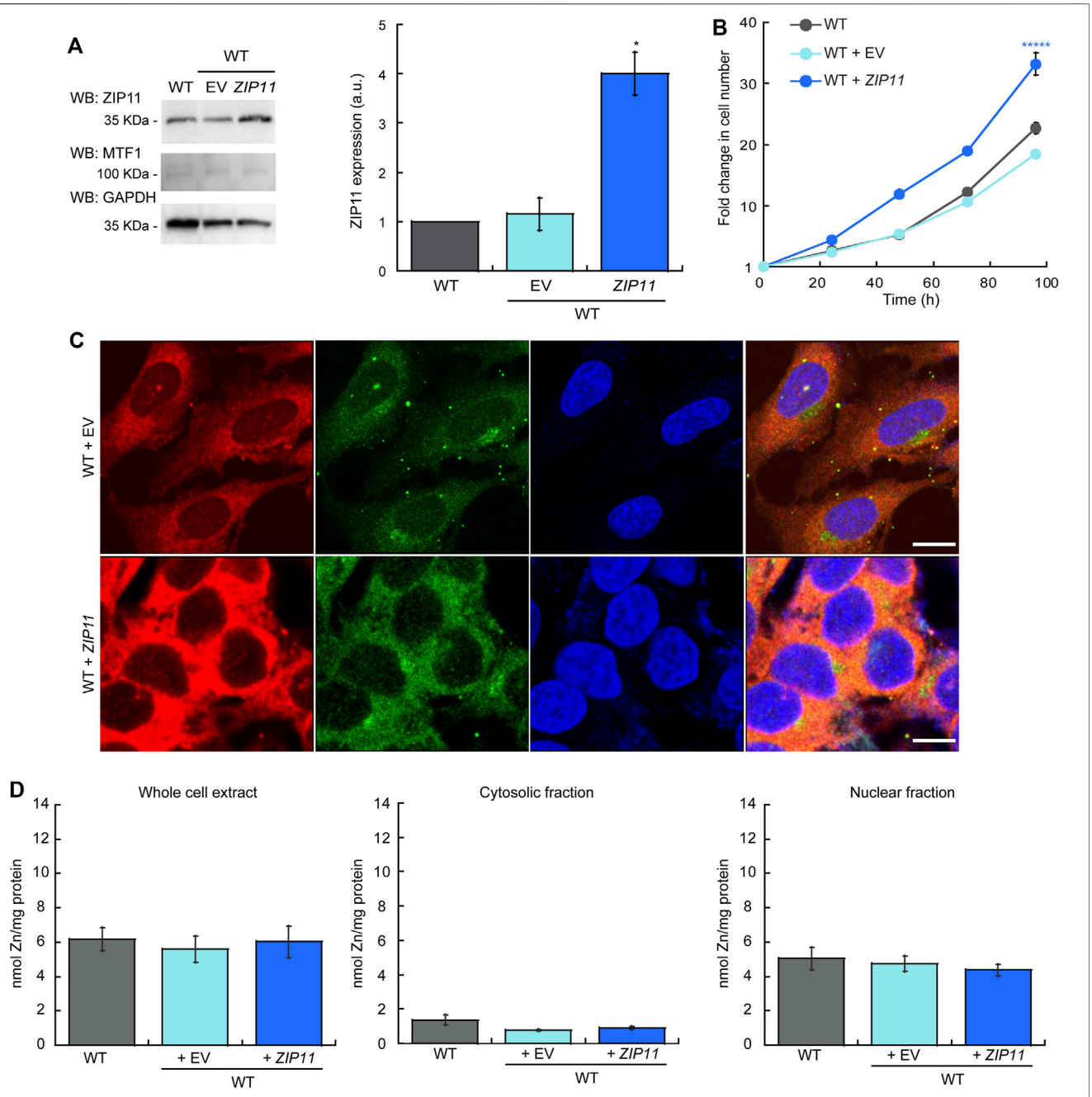

FIGURE 6 | (Continued).

properties through Matrigel, a basement membrane extract. In this experiment, cells were seeded on the top of a polycarbonate membrane with 8 µm pores covered with Matrigel. This model allows invasive cells to cross and invade the opposite side of the membrane, which are then fixed and stained (**Figure 8**). To prevent cell proliferation, the cells were pre-treated with AraC before performing the invasion assays (Olea-Flores et al., 2019; Lacombe et al., 2021). Consistent with the migration results, we found that after 24 h of culture the *ZIP11* KD cells were unable to cross the matrix and the membrane, while control cells could colonize the other side of the membrane (**Figure 8A**). As expected, reconstitution of *ZIP11* gene in the shRNA-2 KD cells recovered the invasive phenotype (**Figure 8B**), and overexpression of the transporter in WT cells exacerbated the effect (**Figure 8C**). On average, the cells overexpressing *ZIP11* had a 3.5-fold increase in number of cells migrating across the Matrigel and the membrane

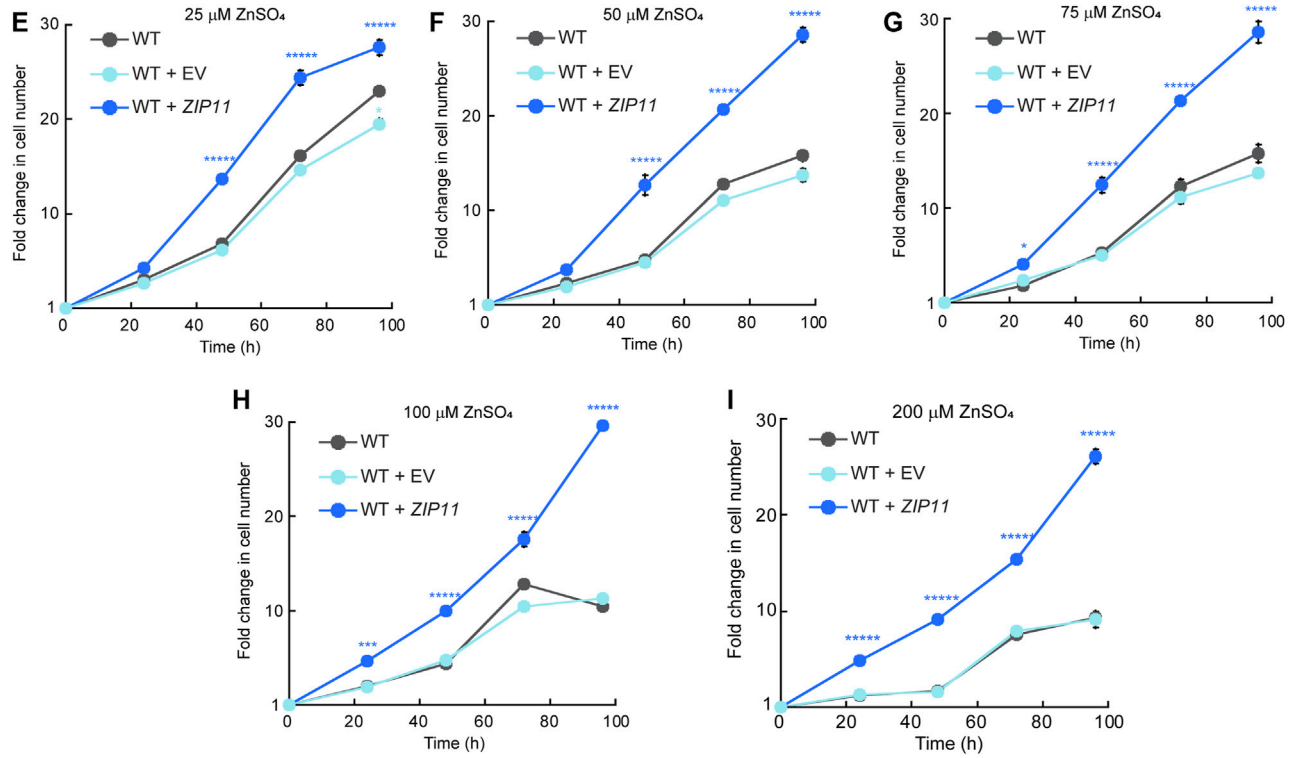

FIGURE 6 | Overexpression of *ZIP11* in WT HeLa enhances growth and resistance to elevated levels of Zn. **(A)** Representative immunoblot (left) and quantification (right) of *ZIP11* levels in HeLa proliferating cells. WT cells were transduced with a plasmid encoding the ZIP11 gene or the empty vector as control. Immunoblots against MTF1 shows no changes in the expression of the metalloprotective transcription factor in WT HeLa cells overexpressing ZIP11. Immunoblot against GAPDH was used as loading control. **(B)** Cell counting assay of proliferating cells WT HeLa cells expressing exogenous ZIP11 or empty vectors. **(C)** Representative confocal micrographies of ZIP11 (red) and Golgin-97 (green) showing the enhanced expression and perinuclear and vesicular distribution of ZIP11 in wild type HeLa cells stably expressing ZIP11 or the empty vector (EV). Nuclei was stained with DAPI. Bar = 10 μm. **(D)** Wild type cells stably expressing ZIP11 or the empty vector were allowed to grow for 48 h and subcellular fractions were obtained using the REAP protocol. Whole cell (left) cytosolic (middle) and nuclear (right) Zn content determined by AAS (Itzhak et al., 2016; Gordon et al., 2019a; Tavera-Montañez et al., 2019). **(E–I)** Analyses of Zn resistance in cells overexpression of the *ZIP11* gene. Cell counting assay of proliferating cells transduced with the *ZIP11* gene or an empty vector, cultured for 96 h with increasing concentrations of ZnSO4. **(E)** 25 μM. **(F)** 50 μM. **(G)** 75 μM. **(H)** 100 μM. **(I)** 200 μM. The data represents the mean ± SE for three independent experiments. For all samples, data are the mean ± SE of three independent biological replicates. $^{*}p < 0.05$; $^{*****}p < 0.00001$.

pores compared to the control cells. Together, these data indicate that the transporter, and potentially nuclear Zn homeostasis, are important players in the development of the migratory and invasive phenotype in cancer cells. The fact that *ZIP11* KD cells have impaired migration and invasion of the Matrigel supports the idea of a potential dormancy or senescent state triggered by nuclear Zn dysregulation. Conversely, the increase in migration and invasion through Matrigel when ZIP11 is overexpressed supports the idea of a role for this transporter in promoting aggressive cancer phenotypes observed in cervical cancer patients (**Figure 1** and **Supplementary Figure S1**).

Alterations in Cell Cycle Progression and in Functional Senescence Markers Reflect a Potential Senescent State of the Cells KD for *ZIP11*

Increasing evidence points to a correlation between DNA damage, cellular senescence, and mitochondrial dysfunction as hallmarks of aging and the onset of various age-related pathologies, such as cancer (Reviewed by (Chapman et al., 2019; Gudmundsrud et al., 2021)). To better understand the growth defect and decreased mobility and invasion properties of HeLa cells KD for *ZIP11,* we tested for changes in cell cycle progression and metabolic changes of the senescence marker β-galactosidase and mitochondrial membrane potential. Our data show that ZIP11 contributes to proliferation and to re-entry into the cell cycle following release from a nocodazole-induced mitotic block, as KD HeLa cells present a delayed progression of the cycle and accumulate in sub G0 after 24 h of arrest (**Figure 9A**). The arrest in sub G0 phase was rescued by reintroduction of exogenous *ZIP11* into the KD cells. Consistent with the enhanced proliferation effect observed in wild type HeLa cells overexpressing the transporter, we detected a small but significant increase of cells in S phase compared to control cells that were largely in G0/G1 stage (**Figure 9B**). This data suggests that ZIP11 contributes, at least in part, to successful transition through cell cycle, which is also

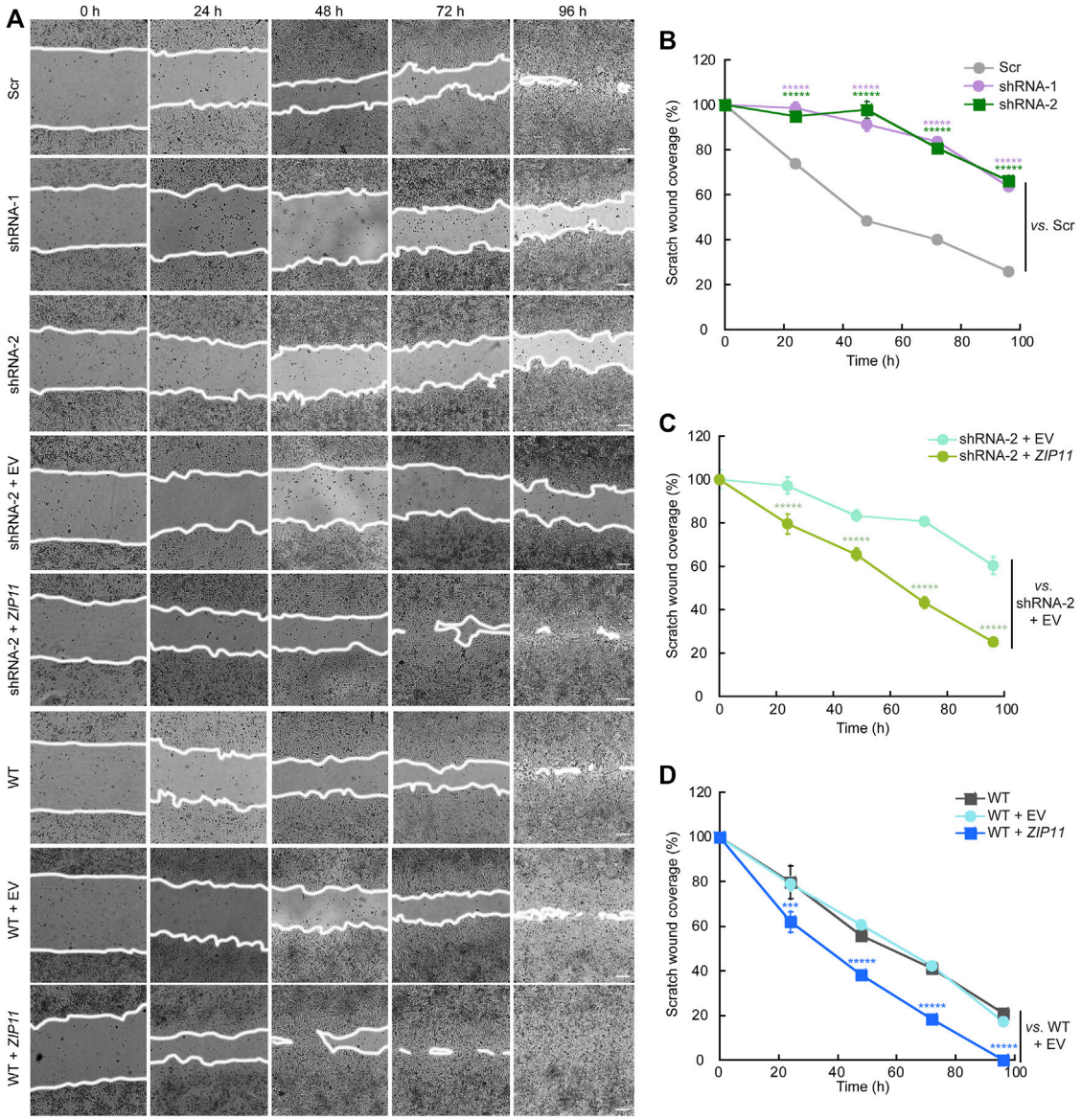

FIGURE 7 | *ZIP11* is required for directional migration of HeLA cells. **(A)** Representative light microscopy images of the wound healing assay of HeLA cells in which *ZIP11* was KD or overexpressed. Time 0 represents confluent monolayer wounds at 0 h and wounds were monitored until the monolayers of WT cells overexpressing *ZIP11* became fully closed 96 h after scratching the monolayer. Images are representative of three independent biological replicates. Scale bar: 100 μm. **(B–D)** Quantification of the area of migration over time shown in **(A)**. **(B)** HeLa cells expressing Scr and both shRNAs against *ZIP11*. **(C)** Data for the reconstitution of phenotype of *ZIP11* KD cells. **(D)** Migration data of non-transduced WT HeLa cells and those overexpressing ZIP11 or the empty vector (EV). Data represents the means ± SE of three independent biological replicates imaged. *****$p < 0.00001$ relative to the samples indicated in the plot.

consistent with the gene expression changes shown in our RNA-seq analyses.

To further provide insight into whether *ZIP11* KD induces a dormant or senescent state in the cells, we performed a classic functional assay of β-galactosidase activity to evaluate senescence in cells. The CellEvent Senescence Green assay relies on a fluorescent probe that contains two galactoside fractions which are targets for β-galactosidase (β-gal), a marker for senescent cells. The activation of the hydrolase activity of β-gal occurs in lysosomes under acidic pH and converts β-galactosides into monosaccharides which remains in the cell and emit a fluorescent signal. **Figure 10A** shows that *ZIP11* KD cells present an increase in the activation of β-gal which is similar to senescent control cells, which was reverted by reintroducing the transporter. Interestingly, a small but not significant decrease in β-gal activity was detected for wild type HeLa cells overexpressing ZIP11 (**Figure 10B**). Finally, we investigated the mitochondrial potential of HeLa cells KD and overexpressing ZIP11 using a TMRE assay as a proxy measure of their metabolic state. TMRE is a positively-charged,

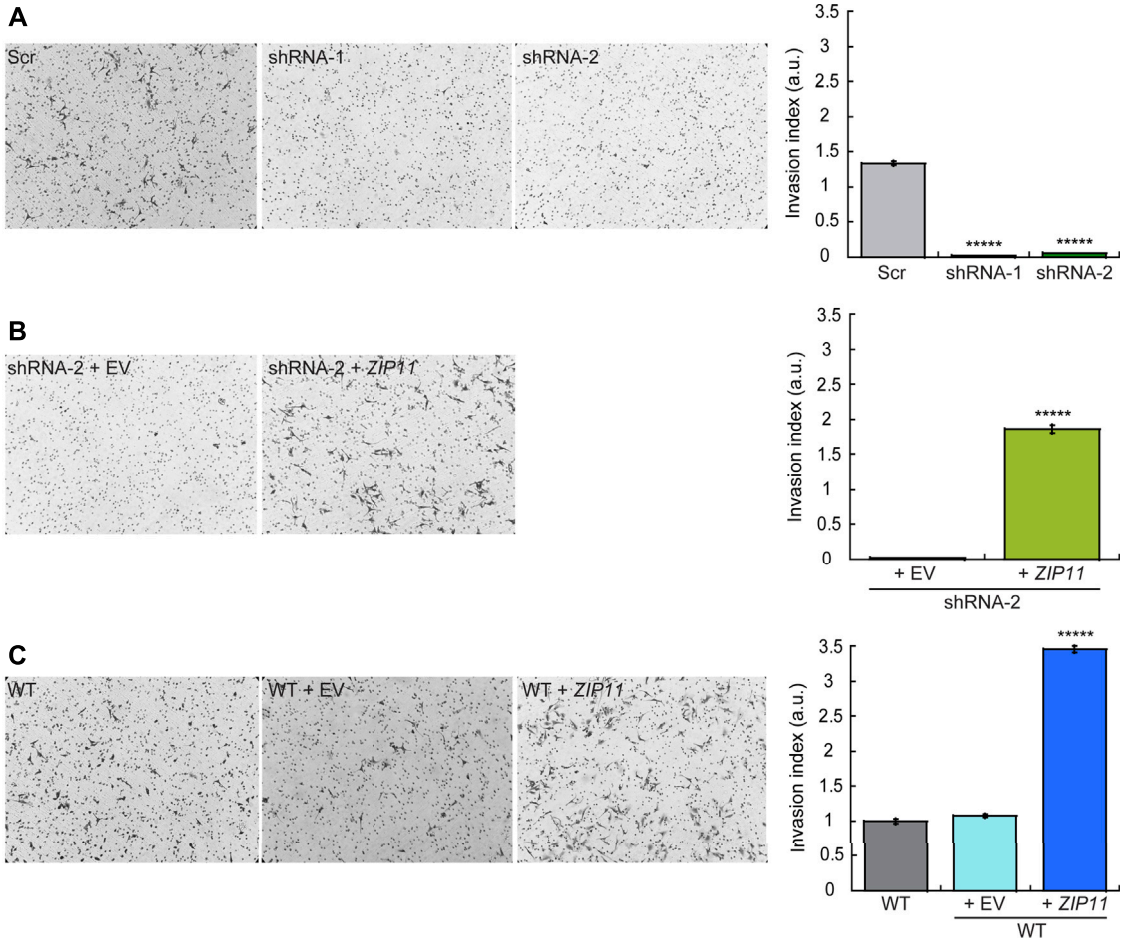

FIGURE 8 | ZIP11 is required for HeLa cells invasion through Matrigel. Representative light microscopy images (left panels) and quantification (right panels) of Matrigel invasion assay at 24 h for HeLa cells in which ZIP11 was KD **(A)**, reconstituted in the shRNA2 strain **(B),** or overexpressed in WT cells **(C)**. The data show the means ± SE of three independent biological replicates imaged and are expressed as the percentage of invading cells compared to the control shown in the plots. *****$p <$ 0.00001.

permeable dye that enters the cells and accumulates in active mitochondria, as this organelle presents a relatively high negative charge. When cells have depolarized or their mitochondria are inactive, a decrease in mitochondrial membrane potential consequently impairs the internalization of the TMRE dye. The data show that HeLa cells partially depleted of ZIP11 have a significant decrease in the incorporation of TMRE into the mitochondria compared to control cells, as indicated by a decrease in the intensity of the fluorescent signal of TMRE (**Figure 10C**). This decrease in mitochondrial function and potential can be restored upon reintroduction of the *ZIP11* gene, but not when the cells are transduced with the EV plasmid (**Figure 10C**). No significant changes were detected in TMRE incorporation into the mitochondria of WT cells overexpressing the ZIP11 transporter (**Figure 10D**). Together, the data suggest that nuclear control of Zn homeostasis by ZIP11 contributes to cell cycle progression and establishment of carcinogenic properties in HeLa cells.

DISCUSSION

Cancer development and progression encompasses metabolic changes that rely on the bioavailability of transition metals, like Zn, to promote cell growth and development of metastatic properties. In this work, we provide evidence that ZIP11 is a Zn transporter is located in the perinuclear area and in small vesicles partially associated to Golgi that may contribute to the maintenance of metal homeostasis in the nuclei. We determined the functional significance of ZIP11 expression by decreasing the levels of this transporter using a stable shRNA KD strategy in proliferating HeLa cells. We found that dysregulation of nuclear Zn levels produced by the ZIP11 KD resulted in a delay in cell cycle progression and a potential senescent state in the cells that may be related to DNA damage, as suggested by the alterations in expression of cell cycle and some senescence genes (Pospelova et al., 2009). RNA-Seq analyses also showed that angiogenic, EMT-related, and apoptotic genes were dysregulated. In terms of expression of additional Zn

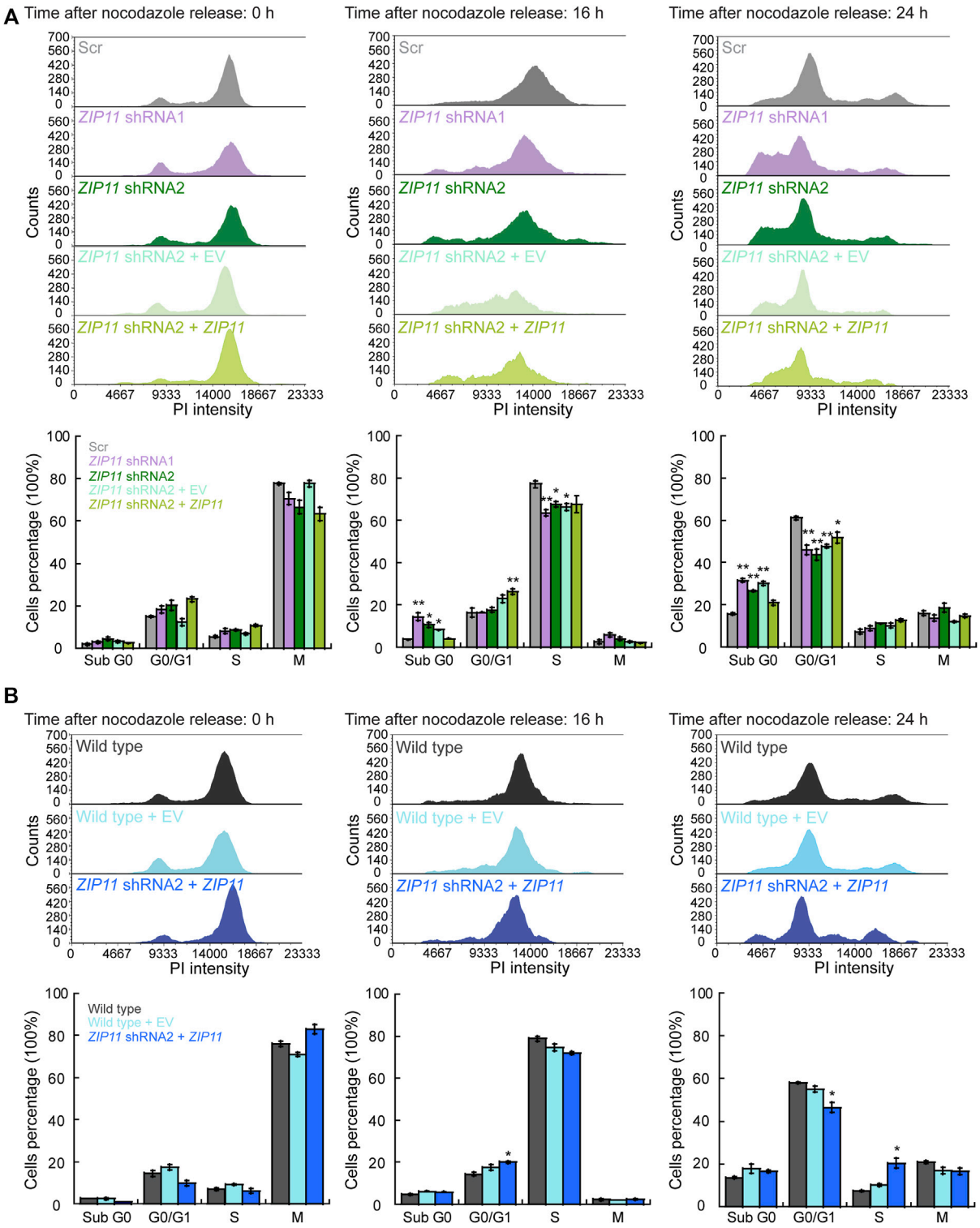

FIGURE 9 | Knockdown of ZIP11 alters cell cycle progression. Representative histograms of cell cycle progression (top panels) and percentage of cells in each cell cycle phase (bottom panel). **(A)** HeLa cells transduced with Scr, *ZIP11* shRNA1 or shRNA2 and reconstituted with an empty vector or *ZIP11* gene. **(B)** Wild type HeLa cells transduced with an empty vector or overexpressing *ZIP11*. Plots show cells arrested in mitosis with nocodazole at the time of release (0 h), and after 16 and 24 h post-release. The data are representative of three independent biological experiments. $^{*}p < 0.05$; $^{**}p < 0.01$.

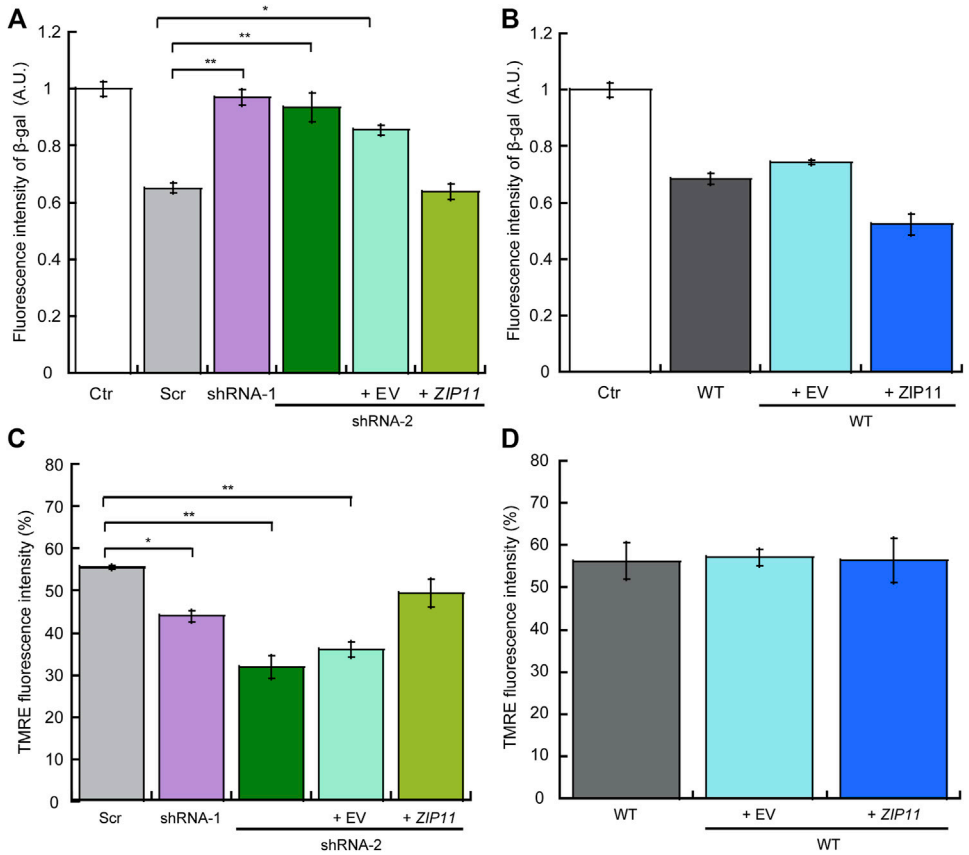

FIGURE 10 | Knockdown of ZIP11 induces a senescent state which correlates with decreased mitochondrial potential in HeLa cells. Detection of cellular senescence *via* activation of β-galactosidase hydrolysis, a marker for senescent cells, in Scr, *ZIP11* KD cells and reconstituted with exogenous *ZIP11* **(A)** or wild type cells over expressing the transporter **(B)**. WT HeLa cells treated with 5 mM Palbociclib were used as a positive control for senescence (Ctr). Data was normalized to Palbociclib treated cells. Mitochondrial membrane potential was measured by staining cells KD for ZIP11, reconstituted **(C)** or overexpressing **(D)** the exogenous gene with 200 nM TMRE and the percentage of fluorescence intensity of three independent biological replicates was plotted. Data show means ± SE of three independent biological replicates imaged. $^{*}p < 0.05$, $^{**}p < 0.01$ relative to control.

transporters, ZIPs and ZNTs, we detected no significant changes on their gene expression, which suggested that ZIP11 KD cells fail to compensate for the nuclear metal stress induced by ZIP11 malfunction. In the context of cancer patients, altered levels of Zn have been considered an indicator of tumor burden and disease progression (Prasad and Kucuk, 2002; Prasad et al., 2009). Zn defects promote the expression of the tumor suppressor p53 and affect the DNA binding capacity of several transcription factors, including p53, the nuclear factor κB (NFκB), and AP-1 in various models of cancer (Ho and Ames, 2002; Yan et al., 2008; Ho and Song, 2009). Zn is also proposed to repress tumor growth by decreasing angiogenesis, and by promoting the expression of inflammatory cytokines and apoptotic genes in cancer cells (Boehm et al., 1998; Prasad et al., 2009). Studies in murine models demonstrated that Zn treatment increases resistance against tumor growth and decreases the occurrence of spontaneous lung tumors in mice undergoing anti-carcinogenic therapies (Singh et al., 1992; Satoh et al., 1993). Consistent with these findings, Zn deficiency in rats enhances the proliferation and expression of cell cycle markers and promotes development of tumors derived from esophageal cells stimulated with the tumorigenic agent N-nitrosomethylbezylamine. This effect can be reduced by dietary Zn supplementation by inducing apoptosis (Wangu et al., 1996). Although existing evidence supports an anti-cancer role for Zn, there is still lack of understanding of the direct and indirect mechanisms by which Zn impacts cancer cells biology.

ZIP11 KD cells not only accumulated nuclear Zn and failed to proliferate, but also showed a decrease in migration and invasive properties, as well as a reduction in mitochondrial membrane potential, and increased β-gal activity, which supports the hypothesis of a potential senescent state (Passos et al., 2006; Passos and von Zglinicki, 2012; Gudmundsrud et al., 2021). These phenotypes were reverted by reintroducing the WT transporter into the *ZIP11* KD cells. Consistent with these data, enhanced proliferation, migration, and invasive features were detected in WT HeLa cells overexpressing ZIP11. Interestingly, the levels of nuclear Zn in cells overexpressing the transporter were similar to those in WT control cells. This phenotype can be partially explained by the fact that no free Zn is found in the nucleus,

and that nuclear Zn-binding proteins may have higher affinity to the ion and require the metal for proper function. Therefore, it is plausible that these proteins will not release the Zn even if the transporter expression increase. Importantly, confocal microscopy analyses showed elevated levels of ZIP11 in cytosolic vesicles, and some partially associated to Golgi. It is plausible that additional components of such vesicles contribute to the enhanced carcinogenic phenotype observed in cells overexpressing the transporters. The nature of such vesicles, their constituents and biological relevance remain to be characterized. Taken together, these data indicate that ZIP11 is essential for the proliferation and development of carcinogenic properties of the cervical cancer model, HeLa cells. This transporter may play a relevant role in the regulation of gene expression in the HeLa cell cancer model, which is in agreement with the correlation of a deleterious effect observed in cervical cancer patients that present elevated levels of ZIP11.

It is well known that senescence is a biological process that occurs in response to various stress stimuli under normal and pathological conditions. For instance, senescence can occur as a consequence of oncogene activation, chromatin and nuclear alterations, and oxidative stress (Kuilman et al., 2010). Senescence was also proposed to be a process that prevents cell replication when DNA damage occurs, and it is an efficient way to prevent cancer development and tumor progression (Campisi, 2001a; Campisi, 2001b). Interestingly, Zn has been shown to have a positive effect on DNA repair, which would prevent cancer development derived from DNA damage (Reviewed by (Yildiz et al., 2019)). Senescence is also known to suppress cancer by stopping the growth of pre-malignant cells, and it has been shown to be an important component for wound healing as well (Demaria et al., 2014). Experiments using a murine model in which senescent cells can be visualized and removed showed that senescent fibroblasts and endothelial cells appear very early in response to a cutaneous wound and promote the healing of the wound *via* the platelet-derived growth factor AA pathway (Demaria et al., 2014). From our observations in *ZIP11* KD HeLa cells, we proposed that the potential senescent phenotype resulting from nuclear Zn dysbalance impairs malignant cell mobilization. This rationale may also apply to the phenotype observed in the migratory properties of the model presented here. In conclusion, we propose a novel mechanism whereby elevated levels of Zn in the nuclei of cells lacking *ZIP11* is a contributing stress factor that impairs cell growth and other events associated with cancer cell biology (migration and invasion) by inducing a senescent state. This work highlights the importance of ZIP11, an understudied metal transporter, in cancer development and progression, and provides a foundation for future mechanistic and drug development studies that may target ZIP11 in patients affected by this disease.

DATA AVAILABILITY STATEMENT

The datasets presented in this study can be found in online repositories. The names of the repository/repositories and accession number(s) can be found in the article/ **Supplementary Material**. RNA-seq datasets are available at GEO. The accession number is: GSE198411

AUTHOR CONTRIBUTIONS

TP-B conceived and designed the research; MO-F, JK, AC, CS, CM, HR, AM, JN, and TP-B performed experiments and compiled data; MO-F, JK, SS, CM, VM, AM, JN, LC, and TP-B analyzed data; TP-B and LC prepared figures and tables; TP-B drafted the manuscript; all authors edited and revised the manuscript; all authors approved the final version of the manuscript.

FUNDING

This work was funded by Wesleyan University institutional funds and by NIH grant R01AR077578 to TP-B.

ACKNOWLEDGMENTS

The authors are thankful to Anthony N. Imbalzano, Jose Argüello and Jeffrey Gilarde for their critical comments and technical assistance on this manuscript.

SUPPLEMENTARY MATERIAL

The Supplementary Material for this article can be found online at: https://www.frontiersin.org/articles/10.3389/fcell.2022.895433/full#supplementary-material

REFERENCES

Angireddy, R., Chowdhury, A. R., Zielonka, J., Ruthel, G., Kalyanaraman, B., and Avadhani, N. G. (2020). Alcohol-induced CYP2E1, Mitochondrial Dynamics and Retrograde Signaling in Human Hepatic 3D Organoids. *Free Radic. Biol. Med.* 159, 1–14. doi:10.1016/j.freeradbiomed.2020.06.030

Antala, S., and Dempski, R. E. (2012). The Human ZIP4 Transporter Has Two Distinct Binding Affinities and Mediates Transport of Multiple Transition Metals. *Biochemistry* 51, 963–973. doi:10.1021/bi201553p

Audic, S., and Claverie, J.-M. (1997). The Significance of Digital Gene Expression Profiles. *Genome Res.* 7, 986–995. doi:10.1101/gr.7.10.986

Barresi, V., Valenti, G., Spampinato, G., Musso, N., Castorina, S., Rizzarelli, E., et al. (2018). Transcriptome Analysis Reveals an Altered Expression Profile of Zinc Transporters in Colorectal Cancer. *J. Cell Biochem.* 119, 9707–9719. doi:10.1002/jcb.27285

Bendl, J., Stourac, J., Salanda, O., Pavelka, A., Wieben, E. D., Zendulka, J., et al. (2014). PredictSNP: Robust and Accurate Consensus Classifier for Prediction of Disease-Related Mutations. *PLoS Comput. Biol.* 10, e1003440. doi:10.1371/journal.pcbi.1003440

Bin, B.-H., Fukada, T., Hosaka, T., Yamasaki, S., Ohashi, W., Hojyo, S., et al. (2011). Biochemical Characterization of Human ZIP13 Protein. *J. Biol. Chem.* 286, 40255–40265. doi:10.1074/jbc.m111.256784

Boehm, T., O'Reilly, M. S. M., Keough, K., Shiloach, J., Shapiro, R., and Folkman, J. (1998). Zinc-binding of Endostatin Is Essential for its Antiangiogenic Activity. *Biochem. biophysical Res. Commun.* 252, 190–194. doi:10.1006/bbrc.1998.9617

Bradford, M. M. (1976). A Rapid and Sensitive Method for the Quantitation of Microgram Quantities of Protein Utilizing the Principle of Protein-Dye Binding. *Anal. Biochem.* 72, 248–254. doi:10.1016/0003-2697(76)90527-3

Broun, E. R., Greist, A., Tricot, G., and Hoffman, R. (1990). Excessive Zinc Ingestion. *Jama* 264, 1441–1443. doi:10.1001/jama.1990.03450110087033

Campisi, J. (2001). Cellular Senescence as a Tumor-Suppressor Mechanism. *Trends Cell Biol.* 11, S27–S31. doi:10.1016/s0962-8924(01)82148-6

Campisi, J. (2001). Cellular Senescence, Aging and Cancer. *TheScientificWorldJournal* 1, 65. doi:10.1100/tsw.2001.23.106

Chapman, J., Fielder, E., and Passos, J. F. (2019). Mitochondrial Dysfunction and Cell Senescence: Deciphering a Complex Relationship. *FEBS Lett.* 593, 1566–1579. doi:10.1002/1873-3468.13498

Chowanadisai, W., Graham, D. M., Keen, C. L., Rucker, R. B., and Messerli, M. A. (2013). Neurulation and Neurite Extension Require the Zinc Transporter ZIP12 (Slc39a12). *Proc. Natl. Acad. Sci. U.S.A.* 110, 9903–9908. doi:10.1073/pnas.1222142110

Chowdhury, A. R., Zielonka, J., Kalyanaraman, B., Hartley, R. C., Murphy, M. P., and Avadhani, N. G. (2020). Mitochondria-targeted Paraquat and Metformin Mediate ROS Production to Induce Multiple Pathways of Retrograde Signaling: A Dose-dependent Phenomenon. *Redox Biol.* 36, 101606. doi:10.1016/j.redox.2020.101606

Collins, F. S., Guyer, M. S., and Chakravarti, A. (1997). Variations on a Theme: Cataloging Human DNA Sequence Variation. *Science* 278, 1580–1581. doi:10.1126/science.278.5343.1580

Colvin, R. A., Bush, A. I., Volitakis, I., Fontaine, C. P., Thomas, D., Kikuchi, K., et al. (2008). Insights into Zn2+homeostasis in Neurons from Experimental and Modeling Studies. *Am. J. Physiology-Cell Physiology* 294, C726–C742. doi:10.1152/ajpcell.00541.2007

Demaria, M., Ohtani, N., Youssef, S. A., Rodier, F., Toussaint, W., Mitchell, J. R., et al. (2014). An Essential Role for Senescent Cells in Optimal Wound Healing through Secretion of PDGF-AA. *Dev. cell* 31, 722–733. doi:10.1016/j.devcel.2014.11.012

Dempski, R. E. (2012). The Cation Selectivity of the ZIP Transporters. *Curr. Top. Membr.* 69, 221–245. doi:10.1016/b978-0-12-394390-3.00009-4

Devirgiliis, C., Zalewski, P. D., Perozzi, G., and Murgia, C. (2007). Zinc Fluxes and Zinc Transporter Genes in Chronic Diseases. *Mutat. Research/Fundamental Mol. Mech. Mutagen.* 622, 84–93. doi:10.1016/j.mrfmmm.2007.01.013

Dufner-Beattie, J., Langmade, S. J., Wang, F., Eide, D., and Andrews, G. K. (2003). Structure, Function, and Regulation of a Subfamily of Mouse Zinc Transporter Genes. *J. Biol. Chem.* 278, 50142–50150. doi:10.1074/jbc.m304163200

Dufner-Beattie, J., Wang, F., Kuo, Y.-M., Gitschier, J., Eide, D., and Andrews, G. K. (2003). The Acrodermatitis Enteropathica Gene ZIP4 Encodes a Tissue-specific, Zinc-Regulated Zinc Transporter in Mice. *J. Biol. Chem.* 278, 33474–33481. doi:10.1074/jbc.m305000200

Eide, D. J. (2006). Zinc Transporters and the Cellular Trafficking of Zinc. *Biochimica Biophysica Acta (BBA) - Mol. Cell Res.* 1763, 711–722. doi:10.1016/j.bbamcr.2006.03.005

Fischer, P. W., Giroux, A., and L'Abbé, M. R. (1981). The Effect of Dietary Zinc on Intestinal Copper Absorption. *Am. J. Clin. Nutr.* 34, 1670–1675. doi:10.1093/ajcn/34.9.1670

Fujishiro, H., Yano, Y., Takada, Y., Tanihara, M., and Himeno, S. (2012). Roles of ZIP8, ZIP14, and DMT1 in Transport of Cadmium and Manganese in Mouse Kidney Proximal Tubule Cells. *Metallomics* 4, 700–708. doi:10.1039/c2mt20024d

Gaither, L. A., and Eide, D. J. (2001). Eukaryotic Zinc Transporters and Their Regulation. *Biometals* 14, 251–270. doi:10.1023/a:1012988914300

Gaither, L. A., and Eide, D. J. (2000). Functional Expression of the Human hZIP2 Zinc Transporter. *J. Biol. Chem.* 275, 5560–5564. doi:10.1074/jbc.275.8.5560

Gaither, L. A., and Eide, D. J. (2001). The Human ZIP1 Transporter Mediates Zinc Uptake in Human K562 Erythroleukemia Cells. *J. Biol. Chem.* 276, 22258–22264. doi:10.1074/jbc.m101772200

Gao, J., Zhao, N., Knutson, M. D., and Enns, C. A. (2008). The Hereditary Hemochromatosis Protein, HFE, Inhibits Iron Uptake via Down-Regulation of Zip14 in HepG2 Cells. *J. Biol. Chem.* 283, 21462–21468. doi:10.1074/jbc.m803150200

Girijashanker, K., He, L., Soleimani, M., Reed, J. M., Li, H., Liu, Z., et al. (2008). Slc39a14 Gene Encodes ZIP14, a Metal/bicarbonate Symporter: Similarities to the ZIP8 Transporter. *Mol. Pharmacol.* 73, 1413–1423. doi:10.1124/mol.107.043588

Gordon, S. J. V., Fenker, D. E., Vest, K. E., and Padilla-Benavides, T. (2019). Manganese Influx and Expression of ZIP8 Is Essential in Primary Myoblasts and Contributes to Activation of SOD_2. *Metallomics* 11 (6), 1140–1153. doi:10.1039/c8mt00348c

Gordon, S. J. V., Xiao, Y., Paskavitz, A. L., Navarro-Tito, N., Navea, J. G., and Padilla-Benavides, T. (2019). Atomic Absorbance Spectroscopy to Measure Intracellular Zinc Pools in Mammalian Cells. *J. Vis. Exp.* 1, 1. doi:10.3791/59519

Gudmundsrud, R., Skjånes, T. H., Gilmour, B. C., Caponio, D., Lautrup, S., and Fang, E. F. (2021). Crosstalk Among DNA Damage, Mitochondrial Dysfunction, Impaired Mitophagy, Stem Cell Attrition, and Senescence in the Accelerated Ageing Disorder Werner Syndrome. *Cytogenet Genome Res.* 161, 297–304. doi:10.1159/000516386

Haase, H., and Rink, L. (2014). Zinc Signals and Immune Function. *Biofactors* 40, 27–40. doi:10.1002/biof.1114

Hambidge, M. (2000). Human Zinc Deficiency. *J. Nutr.* 130, 1344S–1349S. doi:10.1093/jn/130.5.1344s

Ho, E., and Ames, B. N. (2002). Low Intracellular Zinc Induces Oxidative DNA Damage, Disrupts P53, NFκB, and AP1 DNA Binding, and Affects DNA Repair in a Rat Glioma Cell Line. *Proc. Natl. Acad. Sci. U.S.A.* 99, 16770–16775. doi:10.1073/pnas.222679399

Ho, E., and Song, Y. (2009). Zinc and Prostatic Cancer. *Curr. Opin. Clin. Nutr. Metabolic Care* 12, 640–645. doi:10.1097/mco.0b013e32833106ee

Hojyo, S., Fukada, T., Shimoda, S., Ohashi, W., Bin, B.-H., Koseki, H., et al. (2011). The Zinc Transporter SLC39A14/ZIP14 Controls G-Protein Coupled Receptor-Mediated Signaling Required for Systemic Growth. *PloS one* 6, e18059. doi:10.1371/journal.pone.0018059

Hu, J. (2021). Toward Unzipping the ZIP Metal Transporters: Structure, Evolution, and Implications on Drug Discovery against Cancer. *Febs J.* 288, 5805–5825. doi:10.1111/febs.15658

Huang, L., and Kirschke, C. P. (2007). A Di-leucine Sorting Signal in ZIP1 (SLC39A1) Mediates Endocytosis of the Protein. *FEBS J.* 274, 3986–3997. doi:10.1111/j.1742-4658.2007.05933.x

Itzhak, D. N., Tyanova, S., Cox, J., and Borner, G. H. (2016). Global, Quantitative and Dynamic Mapping of Protein Subcellular Localization. *eLife* 5, 1. doi:10.7554/eLife.16950

Jenkitkasemwong, S., Wang, C.-Y., Coffey, R., Zhang, W., Chan, A., Biel, T., et al. (2015). SLC39A14 Is Required for the Development of Hepatocellular Iron Overload in Murine Models of Hereditary Hemochromatosis. *Cell metab.* 22, 138–150. doi:10.1016/j.cmet.2015.05.002

Jenkitkasemwong, S., Wang, C.-Y., Mackenzie, B., and Knutson, M. D. (2012). Physiologic Implications of Metal-Ion Transport by ZIP14 and ZIP8. *Biometals* 25, 643–655. doi:10.1007/s10534-012-9526-x

Jeong, J., and Eide, D. J. (2013). The SLC39 Family of Zinc Transporters. *Mol. aspects Med.* 34, 612–619. doi:10.1016/j.mam.2012.05.011

Kaida, A., Sawai, N., Sakaguchi, K., and Miura, M. (2011). Fluorescence Kinetics in HeLa Cells after Treatment with Cell Cycle Arrest Inducers Visualized with Fucci (Fluorescent Ubiquitination-Based Cell Cycle Indicator). *Cell. Biol. Int.* 35, 359–363. doi:10.1042/cbi20100643

Kambe, T., Hashimoto, A., and Fujimoto, S. (2014). Current Understanding of ZIP and ZnT Zinc Transporters in Human Health and Diseases. *Cell. Mol. Life Sci.* 71, 3281–3295. doi:10.1007/s00018-014-1617-0

Kambe, T., Tsuji, T., Hashimoto, A., and Itsumura, N. (2015). The Physiological, Biochemical, and Molecular Roles of Zinc Transporters in Zinc Homeostasis and Metabolism. *Physiol. Rev.* 95, 749–784. doi:10.1152/physrev.00035.2014

Kamphans, T., Sabri P Fau - Zhu, N., Zhu N Fau - Heinrich, V., Heinrich V Fau - Mundlos, S., Mundlos S Fau - Robinson, P. N., Robinson Pn Fau - Parkhomchuk, D., et al. (2013). Filtering for Compound Heterozygous Sequence Variants in Non-consanguineous Pedigrees. *Plos One* 8 (8), e70151. doi:10.1371/journal.pone.0070151

Kang, X., Chen, R., Zhang, J., Li, G., Dai, P.-G., Chen, C., et al. (2015). Expression Profile Analysis of Zinc Transporters (ZIP4, ZIP9, ZIP11, ZnT9) in Gliomas and Their Correlation with IDH1 Mutation Status. *Asian Pac. J. Cancer Prev.* 16, 3355–3360. doi:10.7314/apjcp.2015.16.8.3355

Kelleher, S. L., and Lönnerdal, B. (2003). Zn Transporter Levels and Localization Change throughout Lactation in Rat Mammary Gland and Are Regulated by Zn in Mammary Cells. *J. Nutr.* 133, 3378–3385. doi:10.1093/jn/133.11.3378

Kelleher, S. L., Velasquez, V., Croxford, T. P., McCormick, N. H., Lopez, V., and MacDavid, J. (2012). Mapping the Zinc-Transporting System in Mammary Cells: Molecular Analysis Reveals a Phenotype-dependent Zinc-Transporting Network during Lactation. *J. Cell. Physiol.* 227, 1761–1770. doi:10.1002/jcp.22900

Kim, D., Langmead, B., and Salzberg, S. L. (2015). HISAT: a Fast Spliced Aligner with Low Memory Requirements. *Nat. Methods* 12, 357–360. doi:10.1038/nmeth.3317

Kim, D., Xiao, Y., Karchere-Sun, R., Richmond, E., Ricker, H. M., Leonardi, A., et al. (2020). Atmospheric Processing of Anthropogenic Combustion Particles: Effects of Acid Media and Solar Flux on the Iron Mobility from Fly Ash. *ACS Earth Space Chem.* 4, 750–761. doi:10.1021/acsearthspacechem.0c00057

Krezel, A., and Maret, W. (2006). Zinc-buffering Capacity of a Eukaryotic Cell at Physiological pZn. *J. Biol. Inorg. Chem.* 11, 1049–1062. doi:10.1007/s00775-006-0150-5

Kuilman, T., Michaloglou, C., Mooi, W. J., and Peeper, D. S. (2010). The Essence of Senescence: Figure 1. *Genes Dev.* 24, 2463–2479. doi:10.1101/gad.1971610

Lacombe, M.-L., Lamarche, F., De Wever, O., Padilla-Benavides, T., Carlson, A., Khan, I., et al. (2021). The Mitochondrially-Localized Nucleoside Diphosphate Kinase D (NME4) Is a Novel Metastasis Suppressor. *BMC Biol.* 19, 228. doi:10.1186/s12915-021-01155-5

Langmead, B., and Salzberg, S. L. (2012). Fast Gapped-Read Alignment with Bowtie 2. *Nat. Methods* 9, 357–359. doi:10.1038/nmeth.1923

Li, B., and Dewey, C. N. (2011). RSEM: Accurate Transcript Quantification from RNA-Seq Data with or without a Reference Genome. *BMC Bioinforma.* 12, 323. doi:10.1186/1471-2105-12-323

Lichten, L. A., and Cousins, R. J. (2009). Mammalian Zinc Transporters: Nutritional and Physiologic Regulation. *Annu. Rev. Nutr.* 29, 153–176. doi:10.1146/annurev-nutr-033009-083312

Lichten, L. A., Ryu, M.-S., Guo, L., Embury, J., and Cousins, R. J. (2011). MTF-1-mediated Repression of the Zinc Transporter Zip10 Is Alleviated by Zinc Restriction. *PloS one* 6, e21526. doi:10.1371/journal.pone.0021526

Lin, W., Chai, J., Love, J., and Fu, D. (2010). Selective Electrodiffusion of Zinc Ions in a Zrt-, Irt-like Protein, ZIPB*. *J. Biol. Chem.* 285, 39013–39020. doi:10.1074/jbc.m110.180620

Liu, Z., Li, H., Soleimani, M., Girijashanker, K., Reed, J. M., He, L., et al. (2008). Cd2+ versus Zn2+ Uptake by the ZIP8 HCO3--dependent Symporter: Kinetics, Electrogenicity and Trafficking. *Biochem. biophysical Res. Commun.* 365, 814–820. doi:10.1016/j.bbrc.2007.11.067

Liuzzi, J. P., Aydemir, F., Nam, H., Knutson, M. D., and Cousins, R. J. (2006). Zip14 (Slc39a14) Mediates Non-transferrin-bound Iron Uptake into Cells. *Proc. Natl. Acad. Sci. U.S.A.* 103, 13612–13617. doi:10.1073/pnas.0606424103

Liuzzi, J. P., Bobo, J. A., Lichten, L. A., Samuelson, D. A., and Cousins, R. J. (2004). Responsive Transporter Genes within the Murine Intestinal-Pancreatic axis Form a Basis of Zinc Homeostasis. *Proc. Natl. Acad. Sci. U.S.A.* 101, 14355–14360. doi:10.1073/pnas.0406216101

Livak, K. J., and Schmittgen, T. D. (2001). Analysis of Relative Gene Expression Data Using Real-Time Quantitative PCR and the 2−ΔΔCT Method. *Methods* 25, 402–408. doi:10.1006/meth.2001.1262

Love, M. I., Huber, W., and Anders, S. (2014). Moderated Estimation of Fold Change and Dispersion for RNA-Seq Data with DESeq2. *Genome Biol.* 15, 550. doi:10.1186/s13059-014-0550-8

Mao, X., Kim, B.-E., Wang, F., Eide, D. J., and Petris, M. J. (2007). A Histidine-Rich Cluster Mediates the Ubiquitination and Degradation of the Human Zinc Transporter, hZIP4, and Protects against Zinc Cytotoxicity. *J. Biol. Chem.* 282, 6992–7000. doi:10.1074/jbc.m610552200

Maret, W., and Sandstead, H. H. (2006). Zinc Requirements and the Risks and Benefits of Zinc Supplementation. *J. Trace Elem. Med. Biol.* 20, 3–18. doi:10.1016/j.jtemb.2006.01.006

Martin, A. B., Aydemir, T. B., Guthrie, G. J., Samuelson, D. A., Chang, S.-M., and Cousins, R. J. (2013). Gastric and Colonic Zinc Transporter ZIP11 (Slc39a11) in Mice Responds to Dietary Zinc and Exhibits Nuclear Localization. *J. Nutr.* 143, 1882–1888. doi:10.3945/jn.113.184457

Noren Hooten, N., and Evans, M. K. (2017). Techniques to Induce and Quantify Cellular Senescence. *J. Vis. Exp.* 1, 55533. doi:10.3791/55533

Ogiso, T., Ogawa, N., and Miura, T. (1979). Inhibitory Effect of High Dietary Zinc on Copper Absorption in Rats. II. Binding of Copper and Zinc to Cytosol Proteins in the Intestinal Mucosa. *Chem. Pharm. Bull.* 27, 515–521. doi:10.1248/cpb.27.515

Olea-Flores, M., Zuñiga-Eulogio, M., Tacuba-Saavedra, A., Bueno-Salgado, M., Sánchez-Carvajal, A., Vargas-Santiago, Y., et al. (2019). Leptin Promotes Expression of EMT-Related Transcription Factors and Invasion in a Src and FAK-dependent Pathway in MCF10A Mammary Epithelial Cells. *Cells* 8, 1133. doi:10.3390/cells8101133

Outten, C. E., and O'Halloran, a. T. V. (2001). Femtomolar Sensitivity of Metalloregulatory Proteins Controlling Zinc Homeostasis. *Science* 292, 2488–2492. doi:10.1126/science.1060331

Palmiter, R. D., and Findley, S. D. (1995). Cloning and Functional Characterization of a Mammalian Zinc Transporter that Confers Resistance to Zinc. *EMBO J.* 14, 639–649. doi:10.1002/j.1460-2075.1995.tb07042.x

Paskavitz, A. L., Quintana, J., Cangussu, D., Tavera-Montañez, C., Xiao, Y., Ortiz-Miranda, S., et al. (2018). Differential Expression of Zinc Transporters Accompanies the Differentiation of C2C12 Myoblasts. *J. Trace Elem. Med. Biol.* 49, 27–34. doi:10.1016/j.jtemb.2018.04.024

Passos, J. F., and von Zglinicki, T. (2012). Mitochondrial Dysfunction and Cell Senescence - Skin Deep into Mammalian Aging. *Aging* 4, 74–75. doi:10.18632/aging.100432

Passos, J. F., Zglinicki, T. v., and Saretzki, G. (2006). Mitochondrial Dysfunction and Cell Senescence: Cause or Consequence? *Rejuvenation Res.* 9, 64–68. doi:10.1089/rej.2006.9.64

Pertea, M., Pertea, G. M., Antonescu, C. M., Chang, T.-C., Mendell, J. T., and Salzberg, S. L. (2015). StringTie Enables Improved Reconstruction of a Transcriptome from RNA-Seq Reads. *Nat. Biotechnol.* 33, 290–295. doi:10.1038/nbt.3122

Pinilla-Tenas, J. J., Sparkman, B. K., Shawki, A., Illing, A. C., Mitchell, C. J., Zhao, N., et al. (2011). Zip14 Is a Complex Broad-Scope Metal-Ion Transporter Whose Functional Properties Support Roles in the Cellular Uptake of Zinc and Nontransferrin-Bound Iron. *Am. J. Physiology-Cell PhysiologyCell physiology* 301, C862–C871. doi:10.1152/ajpcell.00479.2010

Pospelova, T. V., Demidenko, Z. N., Bukreeva, E. I., Pospelov, V. A., Gudkov, A. V., and Blagosklonny, M. V. (2009). Pseudo-DNA Damage Response in Senescent Cells. *Cell Cycle* 8, 4112–4118. doi:10.4161/cc.8.24.10215

Prasad, A. S., Beck, F. W. J., Snell, D. C., and Kucuk, O. (2009). Zinc in Cancer Prevention. *Nutr. cancer* 61, 879–887. doi:10.1080/01635580903285122

Prasad, A. S., and Kucuk, O. (2002). Zinc in Cancer Prevention. *Cancer Metastasis Rev.* 21, 291–295. doi:10.1023/a:1021215111729

Qin, Y., Dittmer, P. J., Park, J. G., Jansen, K. B., and Palmer, A. E. (2011). Measuring Steady-State and Dynamic Endoplasmic Reticulum and Golgi Zn 2+ with Genetically Encoded Sensors. *Proc. Natl. Acad. Sci. U.S.A.* 108, 7351–7356. doi:10.1073/pnas.1015686108

Rafi, M. A., Coppola S Fau - Liu, S. L., Liu Sl Fau - Rao, H. Z., Rao Hz Fau - Wenger, D. A., and Wenger, D. A. (2003). Disease-causing Mutations in Cis with the Common Arylsulfatase A Pseudodeficiency Allele Compound the Difficulties in Accurately Identifying Patients and Carriers of Metachromatic Leukodystrophy. *Mol. Genet. Metab.* 79 (2), 83–90. doi:10.1016/s1096-7192(03)00076-3

Risch, N., and Merikangas, K. (1996). The Future of Genetic Studies of Complex Human Diseases. *Science* 273, 1516–1517. doi:10.1126/science.273.5281.1516

Rost, B., Yachdav, G., and Liu, J. (2004). The PredictProtein Server. *Nucleic Acids Res.* 32, W321–W326. doi:10.1093/nar/gkh377

Sandstead, H. H. (2013). Human Zinc Deficiency: Discovery to Initial Translation. *Adv. Nutr.* 4, 76–81. doi:10.3945/an.112.003186

Satoh, M., Kondo, Y., Mita, M., Nakagawa, I., Naganuma, A., and Imura, N. (1993). Prevention of Carcinogenicity of Anticancer Drugs by Metallothionein Induction. *Cancer Res.* 53, 4767–4768.

Schindelin, J., Arganda-Carreras, I., Frise, E., Kaynig, V., Longair, M., Pietzsch, T., et al. (2012). Fiji: an Open-Source Platform for Biological-Image Analysis. *Nat. Methods* 9, 676–682. doi:10.1038/nmeth.2019

Sensi, S. L., Canzoniero, L. M. T., Yu, S. P., Ying, H. S., Koh, J.-Y., Kerchner, G. A., et al. (1997). Measurement of Intracellular Free Zinc in Living Cortical Neurons: Routes of Entry. *J. Neurosci.* 17, 9554–9564. doi:10.1523/jneurosci.17-24-09554.1997

Singh, K. P., Zaidi, S. I. A., Raisuddin, S., Saxena, A. K., Murthy, R. C., and Ray, P. K. (1992). Effect of Zinc on Immune Functions and Host Resistance against Infection and Tumor Challenge. *Immunopharmacol. Immunotoxicol.* 14, 813–840. doi:10.3109/08923979209009237

Suzuki, K., Bose, P., Leong-Quong, R. Y., Fujita, D. J., and Riabowol, K. (2010). REAP: A Two Minute Cell Fractionation Method. *BMC Res. Notes* 3, 294. doi:10.1186/1756-0500-3-294

Takeda, A., and Tamano, H. (2009). Insight into Zinc Signaling from Dietary Zinc Deficiency. *Brain Res. Rev.* 62, 33–44. doi:10.1016/j.brainresrev.2009.09.003

Tavera-Montañez, C., Hainer, S. J., Cangussu, D., Gordon, S. J. V., Xiao, Y., Reyes-Gutierrez, P., et al. (2019). The Classic Metal-Sensing Transcription Factor MTF1 Promotes Myogenesis in Response to Copper. *Faseb J.* 33, 14556–14574. doi:10.1096/fj.201901606R

Taylor, K. M., Hiscox, S., Nicholson, R. I., Hogstrand, C., and Kille, P. (2012). Protein Kinase CK2 Triggers Cytosolic Zinc Signaling Pathways by Phosphorylation of Zinc Channel ZIP7. *Sci. Signal* 5, ra11. doi:10.1126/scisignal.2002585

Taylor, K. M. (2000). LIV-1 Breast Cancer Protein Belongs to New Family of Histidine-Rich Membrane Proteins with Potential to Control Intracellular Zn 2+ Homeostasis. *IUBMB Life (International Union Biochem. Mol. Biol. Life)* 49, 249–253. doi:10.1080/15216540050033087

Taylor, K. M., Morgan, H. E., Johnson, A., and Nicholson, R. I. (2005). Structure-function Analysis of a Novel Member of the LIV-1 Subfamily of Zinc Transporters, ZIP14. *FEBS Lett.* 579, 427–432. doi:10.1016/j.febslet.2004.12.006

Taylor, K. M., and Nicholson, R. I. (2003). The LZT Proteins; the LIV-1 Subfamily of Zinc Transporters. *Biochimica Biophysica Acta (BBA) - Biomembr.* 1611, 16–30. doi:10.1016/s0005-2736(03)00048-8

Thiers, R. E., and Vallee, B. L. (1957). Distribution of Metals in Subcellular Fractions of Rat Liver. *J. Biol. Chem.* 226, 911–920. doi:10.1016/s0021-9258(18)70877-6

Trapnell, C., Williams, B. A., Pertea, G., Mortazavi, A., Kwan, G., van Baren, M. J., et al. (2010). Transcript Assembly and Quantification by RNA-Seq Reveals Unannotated Transcripts and Isoform Switching during Cell Differentiation. *Nat. Biotechnol.* 28, 511–515. doi:10.1038/nbt.1621

Vallee, B. L., and Falchuk, K. H. (1993). The Biochemical Basis of Zinc Physiology. *Physiol. Rev.* 73, 79–118. doi:10.1152/physrev.1993.73.1.79

Vinkenborg, J. L., Nicolson, T. J., Bellomo, E. A., Koay, M. S., Rutter, G. A., and Merkx, M. (2009). Genetically Encoded FRET Sensors to Monitor Intracellular Zn2+ Homeostasis. *Nat. Methods* 6, 737–740. doi:10.1038/nmeth.1368

Wang, F., Kim, B.-E., Petris, M. J., and Eide, D. J. (2004). The Mammalian Zip5 Protein Is a Zinc Transporter that Localizes to the Basolateral Surface of Polarized Cells. *J. Biol. Chem.* 279, 51433–51441. doi:10.1074/jbc.m408361200

Wangu, Q.-S., Sabourin, C. L. K., Wang, H., and Stoner, G. D. (1996). Overexpression of Cyclin D1 and Cyclin E in N-Nitrosomethylbezylamine-Induced Rat Esophageal Tumorigenesis. *Carcinogenesis* 17, 1583–1588. doi:10.1093/carcin/17.8.1583

Weaver, B. P., Dufner-Beattie, J., Kambe, T., and Andrews, G. K. (2007). Novel Zinc-Responsive Post-transcriptional Mechanisms Reciprocally Regulate Expression of the Mouse Slc39a4 and Slc39a5 Zinc Transporters (Zip4 and Zip5). *Biol. Chem.* 388, 1301–1312. doi:10.1515/bc.2007.149

Wu, F. Y. H., and Wu, C. W. (1987). Zinc in DNA Replication and Transcription. *Annu. Rev. Nutr.* 7, 251–272. doi:10.1146/annurev.nu.07.070187.001343

Wu, L., Chaffee, K. G., Parker, A. S., Sicotte, H., and Petersen, G. M. (2015). Zinc Transporter Genes and Urological Cancers: Integrated Analysis Suggests a Role for ZIP11 in Bladder Cancer. *Tumor Biol.* 36, 7431–7437. doi:10.1007/s13277-015-3459-2

Yan, M., Song, Y., Wong, C. P., Hardin, K., and Ho, E. (2008). Zinc Deficiency Alters DNA Damage Response Genes in Normal Human Prostate Epithelial Cells. *J. Nutr.* 138, 667–673. doi:10.1093/jn/138.4.667

Yildiz, A., Kaya, Y., and Tanriverdi, O. (2019). Effect of the Interaction between Selenium and Zinc on DNA Repair in Association with Cancer Prevention. *J. Cancer Prev.* 24, 146–154. doi:10.15430/jcp.2019.24.3.146

Yu, Y., Wu, A., Zhang, Z., Yan, G., Zhang, F., Zhang, L., et al. (2013). Characterization of the GufA Subfamily Member SLC39A11/Zip11 as a Zinc Transporter. *J. Nutr. Biochem.* 24, 1697–1708. doi:10.1016/j.jnutbio.2013.02.010

Zhang, T., Liu, J., Fellner, M., Zhang, C., Sui, D., and Hu, J. (2017). Crystal Structures of a ZIP Zinc Transporter Reveal a Binuclear Metal Center in the Transport Pathway. *Sci. Adv.* 3, e1700344. doi:10.1126/sciadv.1700344

Zhu, B., Huo, R., Zhi, Q., Zhan, M., Chen, X., and Hua, Z.-C. (2021). Increased Expression of Zinc Transporter ZIP4, ZIP11, ZnT1, and ZnT6 Predicts Poor Prognosis in Pancreatic Cancer. *J. Trace Elem. Med. Biol.* 65, 126734. doi:10.1016/j.jtemb.2021.126734

Conflict of Interest: The authors declare that the research was conducted in the absence of any commercial or financial relationships that could be construed as a potential conflict of interest.

The reviewer SC declared a shared affiliation with the author LAC to the handling editor at the time of review.

Publisher's Note: All claims expressed in this article are solely those of the authors and do not necessarily represent those of their affiliated organizations, or those of the publisher, the editors and the reviewers. Any product that may be evaluated in this article, or claim that may be made by its manufacturer, is not guaranteed or endorsed by the publisher.

frontiers | Frontiers in Cell and Developmental Biology

TYPE Brief Research Report
PUBLISHED 05 September 2022
DOI 10.3389/fcell.2022.916114

OPEN ACCESS

EDITED BY
Kourosh Honarmand Ebrahimi,
King's College London, United Kingdom

REVIEWED BY
Patrick Eichenberger,
New York University, United States
Kimihiro Abe,
National Institute of Infectious Diseases (NIID), Japan

*CORRESPONDENCE
Christopher Dennison,
christopher.dennison@ncl.ac.uk

SPECIALTY SECTION
This article was submitted to Cellular Biochemistry, a section of the journal Frontiers in Cell and Developmental Biology

RECEIVED 08 April 2022
ACCEPTED 26 July 2022
PUBLISHED 05 September 2022

CITATION
Lee J, Dalton RA and Dennison C (2022), Copper delivery to an endospore coat protein of Bacillus subtilis.
Front. Cell Dev. Biol. 10:916114.
doi: 10.3389/fcell.2022.916114

Copper delivery to an endospore coat protein of *Bacillus subtilis*

Jaeick Lee, Rosemary A. Dalton and Christopher Dennison*

Biosciences Institute, Newcastle University, Newcastle Upon Tyne, United Kingdom

A family of cytosolic copper (Cu) storage proteins (the Csps) bind large quantities of Cu(I) via their Cys-lined four-helix bundles, and the majority are cytosolic (Csp3s). The presence of Csp3s in many bacteria appears inconsistent with the current dogma that bacteria, unlike eukaryotes, have evolved not to maintain intracellular pools of Cu due to its potential toxicity. Sporulation in *Bacillus subtilis* has been used to investigate if a Csp3 binds Cu(I) in the cytosol for a target enzyme. The activity of the Cu-requiring endospore multi-Cu oxidase *Bs*CotA (a laccase) increases under Cu-replete conditions in wild type *B. subtilis*. In the strain lacking *Bs*Csp3 lower *Bs*CotA activity is observed and is unaffected by Cu levels. *Bs*Csp3 loaded with Cu(I) readily activates apo-*Bs*CotA *in vitro*. Experiments with a high affinity Cu(I) chelator demonstrate that Cu(I) transfer from Cu(I)-*Bs*Csp3 must occur via an associative mechanism. *Bs*Csp3 and *Bs*CotA are both upregulated during late sporulation. We hypothesise that *Bs*Csp3 acquires cuprous ions in the cytosol of *B. subtilis* for *Bs*CotA.

KEYWORDS

copper, copper storage, bacterial copper homeostasis, bacterial laccases, sporulation, *Bacillus subtilis*

Introduction

Copper (Cu) is essential for most organisms, but use of this metal ion is associated with significant risks due to its potential toxicity. The availability of Cu is regulated by the presence of high-affinity sites in both eukaryotes (Rae et al., 1999) and prokaryotes (Changela et al., 2003). Therefore, all intracellular Cu(I) is tightly bound to either proteins or small molecules, i.e. there is no 'free' Cu(I) (Rae et al., 1999; Changela et al., 2003; Festa and Thiele 2011). Import, cytosolic handling, trafficking to different locations, and storage of Cu have all been characterised in eukaryotic cells (Festa and Thiele 2011). In bacteria, some of these processes are either not thought to occur, or are not yet fully understood. For example, the plasma membrane protein CcoG, which reduces Cu(II) to the preferred intracellular oxidation state [Cu(I)] has only recently been identified in bacteria as a cytochrome oxidase (COX) assembly factor (Marckmann et al., 2019). The reduction of Cu(II) prior to import into eukaryotic cells has been known to happen for many years (Hassett and Kosman 1995; Festa and Thiele 2011). Excess Cu(I) is removed from the cytosol by probably the best-studied component of bacterial Cu homeostasis (homologues are present in eukaryotes); a Cu-transporting P-type ATPase (CopA), which can be assisted by the cytosolic Cu metallochaperone CopZ (Figure 1A) (Rensing et al., 2000;

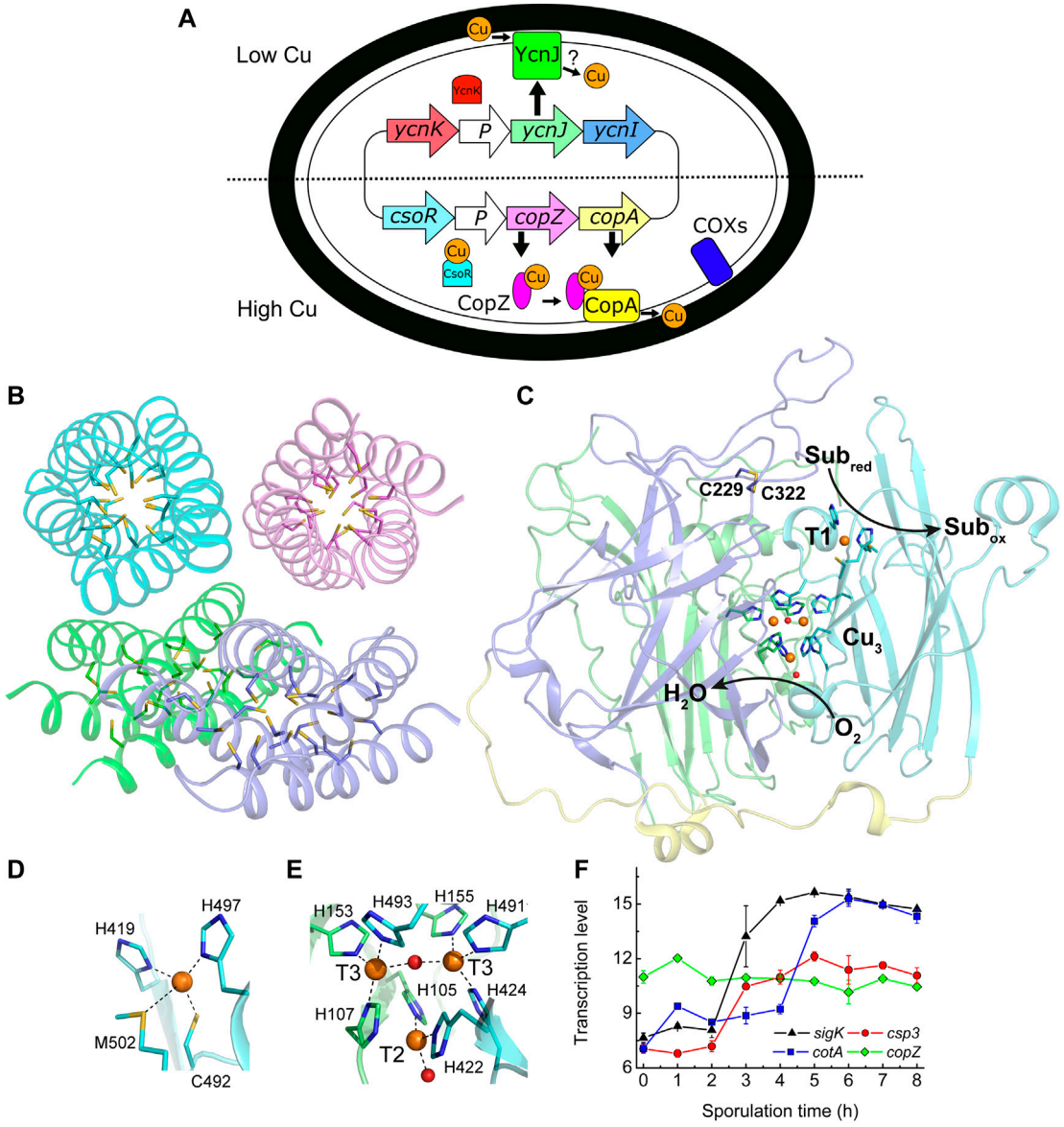

FIGURE 1
Copper handling, a cytosolic Cu(I) storage protein, a Cu-requiring enzyme, and their transcription during sporulation in *B. subtilis*. **(A)** An overview of Cu homeostasis in *B. subtilis* including Cu (orange circles, oxidation state undefined) export by CopA and CopZ (regulated by CsoR) (Smaldone and Helmann 2007), and import by YcnJ (regulated by YcnK) (Chillappagari et al., 2009; Hirooka et al., 2012). YcnI is membrane bound and binds Cu(II) *in vitro*, but its role in Cu homeostasis is unclear (Damle et al., 2021). The only currently known Cu-requiring enzymes in vegetative *B. subtilis* cells are two cytochrome oxidases (COXs) located on the plasma membrane (Lauraeus et al., 1991). **(B)** The crystal structure of Cu(I)-free *Bs*Csp3 (PDB: 5FIG), a tetramer of four-helix bundles each with 19 Cys residues pointing into their cores enabling the binding of up to ~20 Cu(I) ions per monomer (Vita et al., 2016). **(C)** The crystal structure of the endospore multi-Cu oxidase (a laccase) *Bs*CotA (PDB: 1GSK, Enguita et al., 2003) with domains 1, 2, and 3 coloured green, slate and cyan, respectively (the linking regions are yellow). Substrates are oxidized (Sub_{red} to Sub_{ox}) at the T1 Cu centre with electrons passed to the T2/T3 trinuclear (Cu_3) cluster where oxygen is reduced to water. Also highlighted is the disulfide bond between Cys229 and Cys322. Detailed views of the T1 Cu site **(D)** and the Cu_3 cluster **(E)** are shown. The side chains of coordinating residues are represented as sticks, Cu ions as orange spheres and the oxygen atoms of water (bound to the T2 Cu) and hydroxide (bridging the T3 Cu ions) ligands as red spheres in **(C–E)**. **(F)** Transcription profiles (Nicolas et al., 2012) of the *sigK* (σ^K, which facilitates expression of outer and inner spore coat proteins, black triangles), *csp3* (red circles), *cotA* (blue squares) and *copZ* (green diamonds) genes during sporulation.

Solioz et al., 2010; Festa and Thiele 2011; Rensing and McDevitt 2013; Meydan et al., 2017). The toxicity of Cu can involve Cu(I) binding in place of the native metal in cytosolic iron-sulfur (Fe-S) cluster-containing proteins (Macomber and Imlay 2009), and Cu catalyses ROS formation (Solioz et al., 2010; Festa and Thiele 2011; Rensing and McDevitt 2013). The intracellular damage that

Cu causes, and the current dearth of intracellular Cu-requiring enzymes (Ridge et al., 2008), has resulted in a prevailing view that bacteria have evolved not to use this metal ion in the cytosol (Ridge et al., 2008; Rensing and McDevitt 2013). However, there is no *a priori* reason why bacteria, like eukaryotes, cannot utilise Cu in this compartment if mechanisms are available to enable its safe handling, i.e., by ensuring tight chelation and specific delivery. The presence of cytosolic Cu storage proteins (Csps) that bind large quantities of Cu(I) with high affinity (Vita et al., 2015; Vita et al., 2016; Dennison et al., 2018; Lee and Dennison 2019) provide a possible route for intracellular Cu use in bacteria.

The Csps were first identified in Gram-negative bacteria that oxidize methane (Vita et al., 2015). These methanotrophs can possess different Csp homologues, all having many Cys residues lining the cores of their four-helix bundles that enable the binding of a large number of Cu(I) ions (Vita et al., 2015; Vita et al., 2016; Dennison et al., 2018). A Csp exported from the cytosol (Csp1) stores up to 52 Cu(I) ions per tetramer for the particulate (membrane-bound) methane monooxygenase (pMMO) in the model methanotroph *Methylosinus trichosporium* OB3b (*Mt*Csp1) (Vita et al., 2015). *Mt*Csp1 is upregulated at the Cu concentrations required for methane oxidation by pMMO in switchover methanotrophs (Gu and Semrau 2017), which uses a soluble Fe MMO when Cu is limiting (DiSpirito et al., 2016). However, a cytosolic Csp homologue (*Mt*Csp3) is not upregulated with pMMO in *M. trichosporium* OB3b (Gu and Semrau 2017).

The Gram-positive bacterium *Bacillus subtilis* is an ideal model system for investigating the role of a Csp3 as its Cu homeostasis system is well characterised (Figure 1A) (Radford et al., 2003; Smaldone and Helmann 2007; Chillappagari et al., 2009; Ma et al., 2009; Solioz et al., 2010; Hirooka et al., 2012; Damle et al., 2021). This includes the *copZA* operon (Cu efflux machinery, *vide supra*) and its Cu-sensing repressor CsoR (Radford et al., 2003; Smaldone and Helmann 2007; Ma et al., 2009; Solioz et al., 2010). The membrane protein YcnJ is upregulated under Cu-limiting conditions, controlled by the suggested repressor YcnK (Chillappagari et al., 2009; Hirooka et al., 2012), and has been proposed to play a role in Cu acquisition (Figure 1A). The gene for the membrane-anchored YcnI is part of the same (*ycnKJI*) operon and is also thought to be regulated by YcnK (Hirooka et al., 2012). The soluble domain of YcnI binds Cu(II) *in vitro*, and this protein has been suggested to function as a Cu metallochaperone (Damle et al., 2021. Cytosolic Cu(I) could be safely stored by the *B. subtilis* Csp3 homologue (YhjQ, herein *Bs*Csp3) whose core is lined with 19 Cys residues (Figure 1B), enabling the binding of ~80 Cu(I) ions per tetramer *in vitro* (Vita et al., 2016).

Only two families of Cu enzymes are currently known to be present in *B. subtilis*; two COXs (one without the Cu_A site in subunit II), located on the plasma membrane (Figure 1A) and the multi-Cu oxidase (MCO; a laccase) *Bs*CotA (Lauraeus et al., 1991; Hullo et al., 2001; Martins et al., 2002; Enguita et al., 2003). Assembly of the COXs, including their acquisition of Cu has been extensively studied (for example von Wachenfeldt et al., 2021). *Bs*CotA is an outer spore-coat (endospore) enzyme (McKenney et al., 2013) that possesses the typical type 1 (T1), 2 (T2) and 3 (T3) Cu sites of an MCO (Enguita et al., 2003), which are all involved in the catalytic cycle (see Figures 1C–E). *Bs*CotA produces a melanin-like pigment thought to provide spores with protection against hydrogen peroxide and UV light (Hullo et al., 2001; McKenney et al., 2013). This enzyme is upregulated during the latter stages of sporulation, as is *Bs*Csp3 (Figure 1F) (Nicolas et al., 2012).

Herein we demonstrate that, despite previous preliminary work from our laboratory (Vita et al., 2016), *Bs*Csp3 does not provide resistance to toxicity caused by elevated Cu levels in *B. subtilis*. We have therefore tested the hypothesis that *Bs*Csp3 binds Cu(I) ions in the cytosol for a Cu-requiring enzyme by investigating the effect of gene deletion on the activity of *Bs*CotA in spores grown under Cu limiting and replete conditions. The data obtained indicate a role for *Bs*Csp3 in ensuring maximum *Bs*CotA activity. The ability of Cu(I)-*Bs*Csp3 to activate apo-*Bs*CotA has been confirmed *in vitro*. A model for how *Bs*CotA is loaded with Cu during sporulation is proposed. This is the first example showing an enzyme acquiring Cu(I) in the cytosol of a bacterium, as well as identifying the protein from which the metal ion is obtained.

Results

*Bs*Csp3 is not required in combating Cu toxicity in *B. subtilis*

The presence of *Bs*Csp3 with a high capacity for Cu(I) in the cytosol of *B. subtilis* (Vita et al., 2015; Vita et al., 2016; Dennison et al., 2018) would suggest a role in helping to prevent the issues associated with excess Cu (Macomber and Imlay 2009; Lee and Dennison 2019). The toxicity of Cu to bacteria is highlighted by how increasing Cu concentrations limited the growth of wild type (WT) *B. subtilis* in LB medium (Supplementary Figure S1). At ≥1.5 mM Cu cells started to grow more slowly, with a very small increase in the absorbance/OD observed only after more than 6 h at 2 mM added Cu, coinciding with elevated intracellular Cu concentrations (Supplementary Figure S2). Very similar growth and Cu accumulation results were obtained (Supplementary Figures S1, S2) for the *B. subtilis* strain (Δ*csp3*) lacking the *csp3* gene (*yhjQ*). The growth studies reported herein demonstrate that *Bs*Csp3 is not solely required in helping prevent the harmful effects of elevated Cu levels on *B. subtilis* (more details are provided in the legend to Supplementary Figure S1). Therefore, the protein apparently does not have a function like the eukaryotic cytosolic Cys-rich metallothioneins (Festa and Thiele 2011).

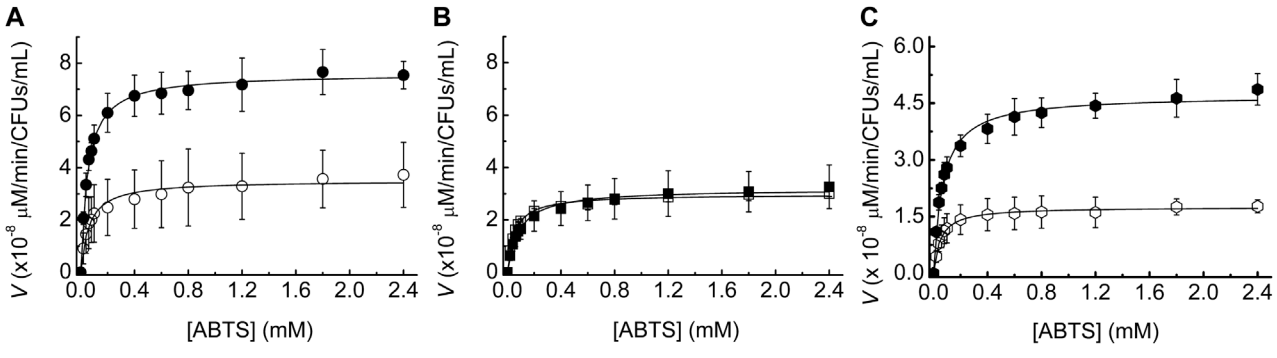

D

B. subtilis strain	Cu (µM)	IPTG	V_{max} (×10^{-8} µM/min/CFUs/mL)	K_M (µM)
WT	0	No	3.53 ± 1.21	58.1 ± 5.00
	50		7.59 ± 0.83	51.5 ± 1.60
Δ*csp3*	0	No	2.98 ± 0.21	52.8 ± 1.40
	50		3.32 ± 0.68	79.4 ± 3.90
Complemented Δ*csp3*	0	Added	1.76 ± 0.34	54.2 ± 2.60
	50		4.71 ± 0.44	64.6 ± 2.60

FIGURE 2
The influence of Cu levels and *Bs*Csp3 on *Bs*CotA activity in *B. subtilis* spores. Michaelis-Menten plots of *Bs*CotA activity for heated purified spores from WT **(A)**, Δ*csp3* **(B)**, and the complemented Δ*csp3* **(C)** strains. Spores **(A,B)** were produced in DSM plus no (open symbols) and 50 µM (black filled symbols) added $Cu(NO_3)_2$. For the complemented Δ*csp3* strain **(C)** sporulation was carried out in the presence of 1 mM IPTG with either no (open symbols) or 50 µM (black filled symbols) added $Cu(NO_3)_2$. Plots from which the initial rates for WT and Δ*csp3 B. subtilis* spores were obtained are shown in Supplementary Figure S3. Kinetics measurements were made in 100 mM citrate-phosphate buffer pH 4.0 at 37°C using three different sets of spores (averages and standard deviations are shown). **(D)** The V_{max} and K_M values obtained from the fits of the data in **(A–C)** to the Michaelis-Menten equation. The K_M values for the oxidation of ABTS by *Bs*CotA in spores are all in the range of those reported for purified enzyme (Martins et al., 2002; Durão et al., 2008; Fernandes et al., 2011).

Using sporulation to determine the function of *Bs*Csp3

*Bs*CotA, along with the two COXs (whose Cu acquisition is well-characterised, von Wachenfeldt et al., 2021), are the only known Cu-requiring enzymes present in spores. The *csp3* and *cotA* genes are both upregulated (Nicolas et al., 2012) at similar stages during sporulation (Figure 1F). We have therefore studied whether *Bs*Csp3 is involved in Cu(I) supply to *Bs*CotA. This enzyme binds four Cu ions (Figures 1C–E), which are required to enable oxidation of the laccase substrate 2,2′-azino-bis(3-ethylbenzothiazoline-6-sulfonic acid) (ABTS) *in vitro* and in spores (Martins et al., 2002). We have used the oxidation of ABTS to assess the relative amounts of Cu-*Bs*CotA in *B. subtilis* spores (Figure 2). For WT *B. subtilis* spores, the ability to oxidise ABTS increased approximately two-fold when 50 µM Cu is added to Difco sporulation medium (DSM) (Figures 2A,D, Supplementary Figures S3A,B). This indicated that unless supplemented, DSM does not contain sufficient Cu (the Cu concentration in DSM without any added Cu is ~0.4 µM) to allow all of the *Bs*CotA produced during sporulation to be active.

The *Bs*CotA activity of Δ*csp3 B. subtilis* spores grown in DSM without added Cu was similar to that for WT spores produced under the same conditions (Figures 2B,D, Supplementary Figures S3C,D). However, unlike for WT *B. subtilis*, supplementing DSM with Cu during sporulation had no effect on *Bs*CotA activity for the Δ*csp3* strain. These results indicate that *Bs*Csp3 plays a role in Cu acquisition by *Bs*CotA during sporulation, particularly under Cu-replete conditions. Some *Bs*CotA activity remained for Δ*csp3 B. subtilis* spores, and an alternative mechanism of Cu acquisition by *Bs*CotA must exist, which could also be responsible for the activity observed in the WT strain under Cu-limiting conditions.

To confirm that *Bs*Csp3 is involved in Cu(I) supply to *Bs*CotA, the Δ*csp3* strain was complemented by introducing the *csp3* gene at a different location (the *amyE* locus), which can be induced by isopropyl β-D-thiogalactopyranoside (IPTG). The highest *Bs*CotA activity was obtained for spores of this strain grown in the presence of IPTG and Cu (Figures 2C,D). Under these conditions, activity was almost three-fold greater than without their addition, similar to the increase for WT *B. subtilis* spores under Cu-replete conditions (Figures 2A,D).

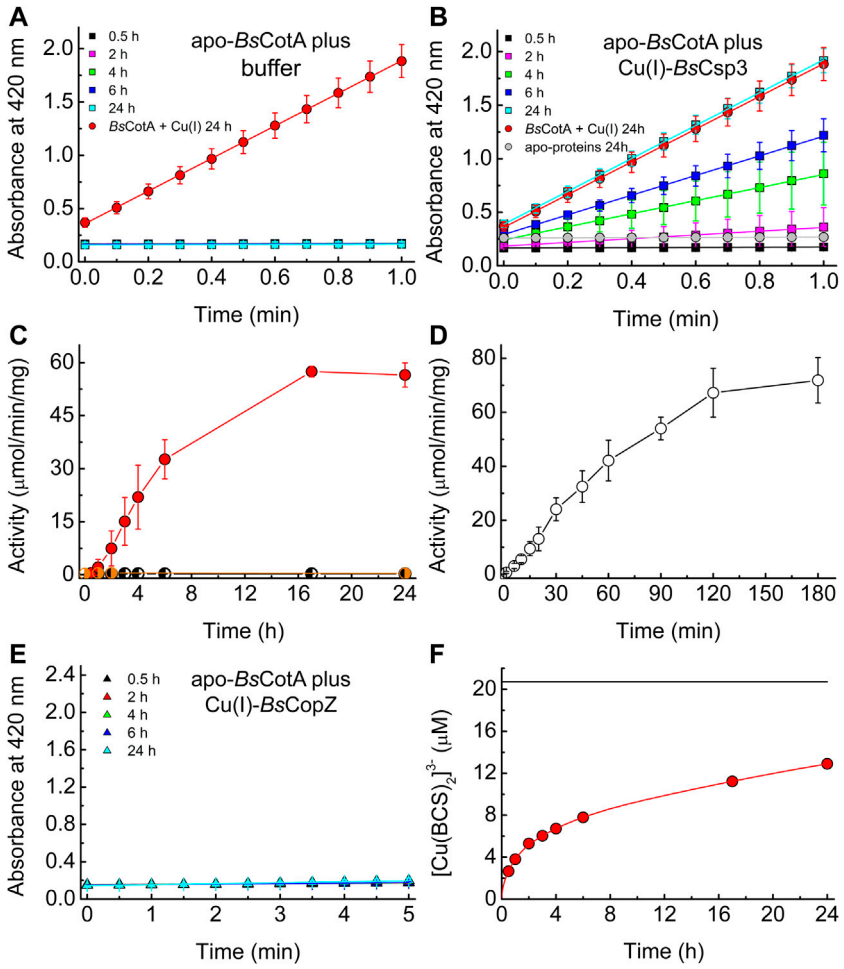

FIGURE 3
The activation of apo-*Bs*CotA by Cu(I)-*Bs*Csp3 and associative Cu(I) transfer. Plots of absorbance at 420 nm against time for the reaction with 2.4 mM ABTS (at 37°C) of mixtures of apo-*Bs*CotA incubated with buffer **(A)** and Cu(I)-*Bs*Csp3 **(B)** for up to 24 h. Also shown is the data obtained when apo-*Bs*CotA was incubated with Cu(I) (red circles in A and B) and apo-*Bs*Csp3 (grey circles in B) for 24 h. Mixtures were incubated under anaerobic conditions (apart from the reaction with apo-*Bs*Csp3) in 20 mM 4-(2-hydroxyethyl)piperazine-1-ethanesulfonic acid (HEPES) pH 7.5 plus 200 mM NaCl (the buffer used in **A**), and *Bs*CotA activity was measured in 100 mM citrate-phosphate buffer pH 4.0. **(C)** Plots of activity against incubation time of apo-*Bs*CotA plus buffer alone (half-black circles), Cu(I)-*Bs*Csp3 (red circles), and apo-*Bs*Csp3 (half-grey circles) for up to 24 h (very similar values to those at 24 h were measured at 48 h for buffer and Cu(I)-*Bs*Csp3). In **(D)** are activity data obtained when apo-*Bs*CotA with the Cys229-Cys322 disulfide bond reduced, was mixed with Cu(I)-*Bs*Csp3 for up to 180 min. **(E)** Plots of absorbance at 420 nm against time for the reaction with 2.4 mM ABTS (at 37°C) of apo-*Bs*CotA incubated with Cu(I)-*Bs*CopZ for up to 24 h (there was also no sign of activity after 48 h). All activity data are averages from three to six independent experiments (apart from apo-*Bs*CotA plus apo-*Bs*Csp3) with error bars showing standard deviations. **(F)** A plot of $[Cu(BCS)_2]^{3-}$ concentration against time for *Bs*Csp3 (1.08 µM) plus 18.0 equivalents of Cu(I) mixed with 2.5 mM BCS (red line) carried out in the same buffer as that used in **(A–E)** under anaerobic conditions. The data at 0.5, 1, 2, 3, 4, 6, 17, and 24 h, which correspond to times at which *Bs*CotA activity was measured **(C)**, are shown by red circles. The black line indicates the outcome of the same experiment but with 6.64 M guanidine-HCl present in the buffer. The Cu(I)-protein unfolds resulting in much faster removal of cuprous ions, giving the end point for the reaction (the value shown was obtained after 2 h). The average percentage removal compared to that for unfolded samples, and the standard deviations, from three independent experiments are listed in Supplementary Table S1.

The activation of Cu-free-*Bs*CotA by Cu(I)-*Bs*Csp3 *in vitro*

The above data support the hypothesis that *Bs*Csp3 binds Cu(I) in the cytosol under Cu-replete conditions, which is used to metallate *Bs*CotA. The ability of Cu(I)-*Bs*Csp3 to activate apo (Cu-free)-*Bs*CotA was therefore studied *in vitro* (Figures 3A–D). Apo-*Bs*CotA is inactive (Figures 3A,C), whilst the addition of Cu produces enzyme that rapidly oxidises ABTS (for example see Figure 3A and Martins et al., 2002). Cu(I)-*Bs*Csp3 readily activates apo-*Bs*CotA (Figures 3B,C), giving similar reactivity to enzyme plus Cu(I) at 24 h (Figure 3B). This is consistent with Cu(I) transfer from Cu(I)-*Bs*Csp3 to apo-*Bs*CotA (apo-*Bs*Csp3 does not activate apo-*Bs*CotA, see Figures 3B,C),

and >50% activation is achieved in 6 h (Figure 3C). The number of free thiols in this form of *Bs*CotA, which possess four Cys residues, was routinely determined to be ~2, consistent with the Cys229-Cys322 disulfide bond being present in the overexpressed enzyme purified from *E. coli* (Enguita et al., 2003). Reduction of the protein with dithiothreitol (DTT) resulted in ~3.5 free thiols and thus cleavage of the Cys229-Cys322 disulfide. Reduced apo-*Bs*CotA reacts much more rapidly with Cu(I)-*Bs*Csp3 and >50% activation is achieved in just over 45 min (Figure 3D). Inactive apo-*Bs*CotA was found to contain no detectable Cu (<0.2 equivalents) by atomic absorption spectrometry (AAS). After transfer, 4.11 ± 0.75 ($n = 4$) equivalents were bound, and when measured the absorbance values at 600 and 330 nm were consistent with full occupancy of the T1 and T3 sites with Cu(II), respectively (Durão et al., 2008). Another cytosolic Cu(I)-binding protein with a well-established role in Cu homeostasis (delivering Cu(I) to *Bs*CopA, Radford et al., 2003) and a similar Cu(I) affinity (~10^{17} M^{-1} at pH 7.5) to *Bs*Csp3 (Badarau and Dennison 2011a; Vita et al., 2016) is *Bs*CopZ (see Figure 1A). After incubation of apo-*Bs*CotA with Cu(I)-*Bs*CopZ for 24 h almost no activity is observed (Figure 3E), indicating Cu(I) transfer does not occur. A large excess of bathocuproine disulfonate (BCS) removes only ~60% of Cu(I) from *Bs*Csp3 in 24 h (Figure 3F; Supplementary Table S1). The slow kinetics for this reaction demonstrates that Cu(I) does not freely dissociate from *Bs*Csp3, otherwise the $[Cu(BCS)_2]^{3-}$ complex would rapidly form. We therefore assume associative mechanisms for the reactions of Cu(I)-*Bs*Csp3 with BCS and also with apo-*Bs*CotA, with the partners interacting prior to Cu(I) transfer.

Discussion

In this study we have demonstrated that *Bs*Csp3 binds cytosolic Cu(I) and plays a role in supplying Cu(I) to the Cu-requiring enzyme *Bs*CotA during sporulation (Figure 2). This is not the only mechanism available to load *Bs*CotA with Cu as some activity is observed in Δ*csp3 B. subtilis*. A possibility we considered was that the cytosolic Cu metallochaperone *Bs*CopZ, as well as transferring Cu(I) to *Bs*CopA (Figure 1A), may supply cuprous ions to *Bs*CotA. The *in vitro* studies reported here show that despite the similar Cu(I) affinity to *Bs*Csp3 (Badarau and Dennison 2011a; Vita et al., 2016), Cu(I)-*Bs*CopZ cannot activate apo-*Bs*CotA (Figure 3E), consistent with *Bs*CopZ not being upregulated during sporulation (Figure 1F). Furthermore, *Bs*CotA activity in Δ*csp3 B. subtilis* spores is unaffected when the Cu concentration is higher, conditions which would increase *Bs*CopZ expression. A similar level of activity is determined for WT spores without supplementing DSM with Cu, conditions under which *Bs*CopZ will not be upregulated. Collectively, these data exclude a potential role for *Bs*CopZ in activating *Bs*CotA. The source(s) of Cu(I) for activating *Bs*CotA in the absence of *Bs*Csp3, and also at lower intracellular concentrations of the metal ion, remain(s) to be established. Regardless, the lack of activation of apo-*Bs*CotA by Cu(I)-*Bs*CopZ *in vitro* highlights the specificity of activation by Cu(I)-*Bs*Csp3. This is essential in a cell as it ensures Cu(I) is delivered to where it is needed, as observed for other Cu-homeostasis proteins (Pufahl et al., 1997; Rae et al., 1999; Schmidt et al., 1999; Lamb et al., 2001; Banci et al., 2006; Banci et al. 2010; Banci et al. 2011; Sala et al., 2019).

The high Cu(I) affinity (Vita et al., 2016) of *Bs*Csp3 (1.5 × 10^{17} M^{-1}), and the slow formation of $[Cu(BCS)_2]^{3-}$ when BCS is added to protein fully loaded with Cu(I) (Figure 3F), indicates the transfer of cuprous ions from Cu(I)-*Bs*Csp3 to apo-*Bs*CotA has to occur via an associative mechanism (unassisted Cu(I) off-rates for *Bs*Csp3 can be estimated to be ~10^{-9} s^{-1}, Dennison et al., 2018). This is consistent with the requirement for no intracellular 'free' Cu(I). For the acquisition of such tightly bound Cu(I) to be possible, metalation must take place once *Bs*CotA has at least partially folded so the sites where Cu is required have formed. The T1 Cu site is closest to the surface, with its His497 ligand solvent exposed, and is ~12.5–15.5 Å from the Cu_3 cluster (Figure 1C). Therefore, *Bs*Csp3 association at more than one location may be required to metalate all of the sites in folded *Bs*CotA. Published Cu(I) affinities of T1 Cu sites (Badarau and Dennison 2011b; North and Wilcox 2019) are (2.1–4.0) × 10^{17} M^{-1}, similar to the average Cu(I) affinity of *Bs*Csp3 (Vita et al., 2016). Although Cu(I) affinities are not available for the Cu_3 cluster, Cu(I) transfer from the storage protein to the enzyme should not be hindered thermodynamically (Banci et al., 2010; Badarau and Dennison 2011b). To facilitate access to the more buried Cu_3 cluster (required for activity) the protein may need to be partially unfolded. The MCO CueO from *E. coli* undergoes a transition from an 'open' non-metallated folded form with accessible Cu sites, to a more 'closed' conformation after Cu has bound (Strolle et al., 2016). *Bs*CotA has a disulfide bond between Cys229 and Cys322 (Figure 1C) that is ~12–13 Å from the T1 Cu site and 17–23 Å from the Cu_3 cluster (Enguita et al., 2003). Only two of the four Cys residues are reactive in *Bs*CotA overexpressed and purified from *E. coli* (see Materials and Methods) and this form of the enzyme possesses the Cys229-Cys322 disulfide. *In vitro* activation is significantly faster in the absence of the disulfide (Figures 3C,D), and the formation of this bond in *Bs*CotA may be linked to Cu(I) binding *in vivo* (*vide infra*). This is consistent with previous studies that found an increase in the rate of Cu(II) binding when this disulfide was removed (Fernandes et al., 2011), but with limited influence on overall structure and stability.

*Bs*Csp3 and *Bs*CotA expression are regulated by sigma factor K (SigK or σ^K), which is produced after the forespore has been engulfed by the mother cell (Figure 4). It appears the *csp3* gene constitutes an operon with *yhjR*, an inner spore coat protein (Hosan et al., 2006) also regulated by SigK (Eichenberger et al., 2004) and co-expressed with Csp3 (Nicolas et al., 2012). Upregulation of the *csp3* gene happens prior to *cotA* (Figure 1F), which would allow *Bs*Csp3 to acquire Cu(I) before production of the enzyme requiring the metal. We propose that Cu(I) is transferred to *Bs*CotA before it localizes to the spore coat. If Cu(I) acquisition occurs once *Bs*CotA

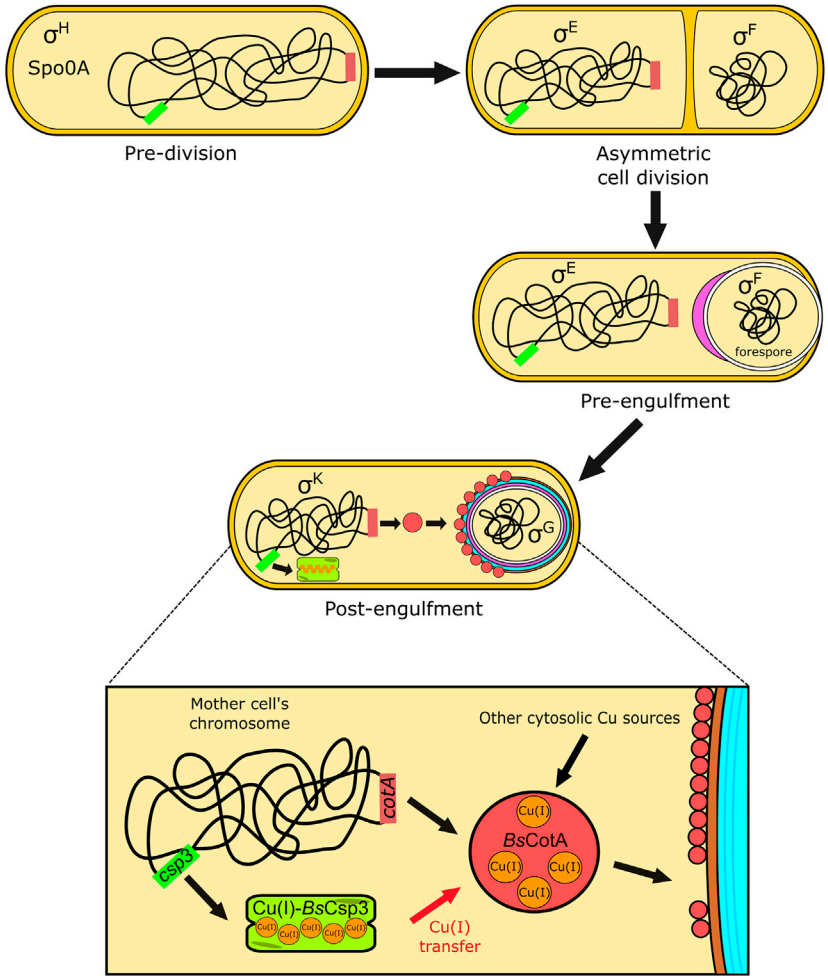

FIGURE 4
The proposed role of *Bs*Csp3 in Cu(I) acquisition by *Bs*CotA during sporulation in *B. subtilis*. The transcription factor Spo0A, along with σ^H, initiates sporulation. A septum asymmetrically divides the cell into the forespore and mother cell, with σ^E and σ^F, respectively, activated within these. The mother cell begins engulfment of the forespore and σ^E directs gene expression and initiation of spore coat (purple) formation. The expression of *Bs*Csp3 and *Bs*CotA now begins, promoted by σ^K (see Figure 1F) and coat assembly continues. We propose that *Bs*Csp3 acquires Cu(I) during this stage of sporulation, which is transferred to *Bs*CotA prior to insertion of the Cu-enzyme into the spore coat.

is part of the spore coat it is possible that YhjR plays a role in assisting this process. As discussed, *Bs*CotA activation by Cu(I)-*Bs*Csp3 *in vitro* is significantly faster in the absence of the Cys229-Cys322 disulfide, indicating that Cu(I) is acquired prior to the formation of this bond *in vivo*. Currently, there is only one known example of Cu acquisition by an enzyme from a partner protein in the cytosol. This is the eukaryotic Cu,Zn-superoxide dismutase (SOD1), which obtains Cu(I) from the Cu metallochaperone CCS (Rae et al., 1999; Schmidt et al., 1999; Lamb et al., 2001; Banci et al., 2010; Banci et al., 2011; Sala et al., 2019; Culotta et al., 1997; Wong et al., 2000). After many years of study, the activation of SOD1 by CCS is now fully understood and has been found to be linked to the formation of an essential disulfide bond in SOD1.

Added importance to understanding the correct metalation of *Bs*CotA is provided by the observation that melanin production interferes with the phagocytosis of pathogenic yeast, and is required to allow survival in macrophages (Eisenman and Casadevall 2012). The related pigment made by Cu-loaded *Bs*CotA is important for spore survival (Hullo et al., 2001; McKenney et al., 2013), and this may include within a host. *Bacillus* spores, and particularly those from *B. cereus*, cause food poisoning and are a common contaminant in a range of foods (Soni et al., 2016; Jessberger et al., 2020). The development of more effective inactivation approaches requires a better understanding of enzymes such as CotA that help protect spores. This includes establishing how they acquire essential cofactors including Cu ions.

Materials and methods

WT *B. subtilis* and the strain with the *csp3* gene deleted

WT *B. subtilis* 168 (genotype: *trpC2*) and the strain with the *yhjQ* gene deleted (genotype: *trpC2 ΔyhjQ::erm*, referred to herein as Δ*csp3*) strains were obtained from the *Bacillus* Genetic Stock Centre (BGSC) library (BGSCID 1A1 and BKE10600, respectively). These strains were checked by PCR (Supplementary Figures S4A,B, S5A; Supplementary Table S2). The disrupted *csp3* gene was amplified by PCR using genomic DNA from the Δ*csp3* strain with primers that hybridise ~300 bp upstream and downstream of this region (Supplementary Figures S4B, S5A; Supplementary Table S2). The resulting fragment was sequenced with primers designed to hybridise ~20 bp from the ends of the PCR product (Supplementary Table S2) and matches that of the erythromycin resistance gene.

Growth curves for WT and Δ*csp3 B. subtilis* at increasing Cu concentrations

To test the influence of Cu on WT and Δ*csp3* strains, cultures were grown (agitation at 250 rpm) in LB medium at 37°C overnight, diluted 100-fold in LB and LB plus added $Cu(NO_3)_2$ (0.5–2.0 mM). The absorbance at 600 nm was measured at regular intervals for up to 12 h, and also after 24 h. Cells (~35 ml) were collected and washed, including with buffer plus 10 mM ethylenediaminetetraacetic acid (EDTA) (Lee and Dennison 2019), and digested in 200 µl of 65% HNO_3 (Ultrapur) for up to 3 days at room temperature. These mixtures were centrifuged at 12,000 g for 10 min, diluted in MilliQ water to give a final HNO_3 concentration of 2% and analysed for Cu by AAS. The Cu concentration in the stock solution used for these studies was regularly determined by AAS, as described previously (Lee and Dennison 2019).

The construction of the Δ*csp3 B. subtilis* strain complemented with *csp3*

To insert the *csp3* gene plus its ribosome binding site (RBS) into the *amyE* locus of the Δ*csp3* strain, a region including an additional 28 bp at the 5′ end was amplified from WT *B. subtilis* 168 genomic DNA by PCR using primers; rbs_BsCsp3-F and rbs_BsCsp3-R (Supplementary Figures S4A, S5A; Supplementary Table S2). The product was cloned into pGEM-T (Promega) and the resulting *rbs_csp3* fragment sub-cloned into pDR111, which possesses the IPTG-inducible $P_{hyerspank}$ promoter (Quisel et al., 2001; Britton at al. 2002), using HindIII and NheI to generate pDR111_rbs_csp3. To obtain a strain possessing an IPTG-inducible copy of the *csp3* gene (*trpC2 ΔyhjQ::erm amyE::*$P_{hyspank}$*-rbs_yhjQ*, called complemented Δ*csp3* herein), Δ*csp3 B. subtilis* was transformed with pDR111_rbs_csp3. Selection was achieved using spectinomycin (50 µg/ml) and successful integration into the chromosomal *amyE* (α-amylase) gene identified by growing on LB agar containing 1% starch and staining with iodine (Engman et al., 2012). Insertion of the *csp3* gene was determined as described above (Supplementary Figures S4C, S5B; Supplementary Table S2), with the location and size of the fragment incorporated confirmed by PCR using the primers pDR111_int-F and pDR111_int-R (Supplementary Figures S4C, S5B; Supplementary Table S2).

The production of *B. subtilis* spores

WT, Δ*csp3* and complemented Δ*csp3* strains were grown overnight (agitation at 250 rpm) in 20 ml of DSM. Cultures were diluted 50-fold into 200 ml of DSM in a single 1 L Erlenmeyer flask and grown until the absorbance at 580 nm reached ~0.5. This culture was split into four 50 ml cultures, each in a 250 ml Erlenmeyer flask, and 50 µM $Cu(NO_3)_2$ and 1 mM IPTG added when required. The cultures were grown (agitation at 250 rpm) for 48 h at 37°C and absorbance values at 580 nm measured at regular intervals. To purify spores (Tavares et al., 2013) cultures were centrifuged (4°C) for 10 min at 5,000 g, pellets re-suspended in 50 mM tris(hydroxymethyl)aminomethane (Tris) pH 7.2 plus 50 µg/ml lysozyme and incubated at 37°C for 1 h. After incubation and further centrifugation (4°C) for 10 min at 5,000 g, pellets were washed once in sterile MilliQ water and centrifuged. The pellets were re-suspended in 0.05% SDS by vortexing, centrifuged (4°C) for 10 min at 5,000 g and subsequently washed three times with sterile MilliQ water and stored at 4°C. The purity was checked by determining the colony-forming units (CFUs) of spore stocks that were unheated and those heated at 65°C for 1 h prior to growth on LB plates overnight at 37°C, and was typically >75%. As well as strains, spores used for kinetic experiments were verified by PCR (for example, Supplementary Figure S5) after germination in LB overnight at 37°C, using the primers listed in Supplementary Table S2.

*Bs*CotA activity of purified spores

For kinetic measurements of *Bs*CotA activity, purified spores from the WT, Δ*csp3* and complemented Δ*csp3* strains were diluted with MilliQ water to give an absorbance at 580 nm of ~1.2 (measured accurately), and heated at 65°C for 1 h prior to use. To determine the CFUs/ml for this suspension a 5×10^5-fold dilution in LB was plated (100 µl) onto LB agar, incubated at 37°C overnight and colonies counted. An aliquot of the heat-treated spore suspension (100 µl) was added to 900 µl of 100 mM citrate-phosphate buffer pH 4.0 plus 0.1–2.4 mM ABTS, and the absorbance at 420 nm (ε = 35,000 $M^{-1}cm^{-1}$) measured for

5 min at 37°C (Supplementary Figure S3). A control using 100 µl of buffer was also measured and showed no change in absorbance at 420 nm. The initial velocity (V_0; typically reported in units of µM/min/CFUs/mL) was calculated, and plots of V_0 against ABTS concentration (Figure 2) were fit to the Michaelis-Menten equation to determine V_{max} (the maximum rate) and K_M (the Michaelis constant). Comparing V_{max} values calculated based on the absorbance at 580 nm of the heat-treated spore suspension, rather than using CFUs/mL, has no significant influence on the outcome of the study, but generally produces data with larger errors.

Cloning and purification of *Bs*CotA

The *cotA* gene was amplified from *B. subtilis* genomic DNA using primers CotA_1F and CotA_1R listed in Supplementary Table S2, and cloned into pGEM-T. After removing the NdeI site in the gene by QuickChange site-directed mutagenesis (with primers CotA_2F and CotA_2R, Supplementary Table S2), the product was excised with NdeI and BamHI and re-cloned into pET11a. *Bs*CotA was overexpressed in *E. coli* BL21 (DE3) (100 µM IPTG) grown at 20°C for 24 h. The protein was purified using a modified version of a published procedure (Martins et al., 2002). Cells from 0.5 to 2.0 L of culture were resuspended in 20 mM Tris pH 8.5, sonicated and centrifuged at 40,000 g for 30 min. The supernatant was diluted five-fold in 20 mM Tris pH 8.5 (sometimes plus 1 mM EDTA) and loaded onto a HiTrap Q HP column (1 or 5 ml) equilibrated in the same buffer. Proteins were eluted with a linear NaCl gradient (0–500 mM, total volume 50–200 ml) and fractions analysed using 18% SDS-PAGE. *Bs*CotA-containing fractions were diluted with 20 mM Tris pH 7.6 (sometimes plus 1 mM EDTA) and loaded onto a HiTrap SP HP column (5 ml) and eluted with a linear NaCl gradient (0–500 mM, total volume, 200 ml). In some cases the *Bs*CotA-containing fractions were heated at 70 °C for 30 min [*Bs*CotA is a highly thermostable enzyme (Martins et al., 2002)], centrifuged at 40,000 g for 30 min, and the supernatant exchanged into 20 mM 4-(2-hydroxyethyl) piperazine-1-ethanesulfonic acid (HEPES) pH 7.5 plus 200 mM NaCl for further purification on a Superdex 75 10/300 GL gel-filtration column. Purified *Bs*CotA had no detectable Cu (<0.2 equivalents) associated with it when analysed by AAS (Vita et al., 2015; Vita et al., 2016), and showed minimal ABTS oxidation activity (<0.3 µmol/min/mg).

Purification of *Bs*CopZ and sample preparation

*Bs*CopZ was purified as described previously (Vita et al., 2016) and contains a small amount of bound Zn(II). Samples were therefore incubated with >10 equivalents of EDTA for 1 h and exchanged with 20 mM HEPES pH 7.5 plus 200 mM NaCl. The resulting protein had no Zn(II) associated with it and was reduced with DTT under anaerobic conditions and desalted as described previously (Vita et al., 2015; Vita et al., 2016).

Analysing the Activation of Recombinant apo-*Bs*CotA by Cu(I)-*Bs*Csp3 and Cu(I)-*Bs*CopZ

*Bs*Csp3 plus ~18 equivalents of Cu(I) was prepared by adding the appropriate amount of a buffered solution of Cu(I) in an anaerobic chamber (Belle Technology, O_2 << 2 ppm) to apo-protein in 20 mM HEPES pH 7.5 plus 200 mM NaCl, quantified using the 5,5′-dithiobis (2-nitrobenzoic acid) (DTNB) assay carried out in the presence of ~6.0 M guanidine hydrochloride (Vita et al., 2015; Vita et al., 2016). Apo-*Bs*CotA was quantified using the absorbance at 280 nm (ε value of 84,739 $M^{-1}cm^{-1}$, Durão et al., 2008) and the number of free thiols determined with the DTNB assay (Vita et al., 2016). To reduce the Cys229-Cys322 disulfide (see Figure 1C), apo-*Bs*CotA was incubated overnight in the anaerobic chamber with a 100-fold excess of DTT. The protein was desalted twice on a PD10 column and quantified from the absorbance at 280 nm, with thiols measured using the DTNB assay. Fully-reduced *Bs*CopZ was also quantified using the DTNB assay and loaded with ~0.8 equivalents of Cu(I) under anaerobic conditions. Cu(I)-*Bs*Csp3 [~3 µM binding ~49–55 µM Cu(I)] was mixed with ~1.1–1.3 µM of either as-isolated or reduced apo-*Bs*CotA, requiring ~4.4–5.2 µM Cu(I) to occupy all four Cu sites. Control experiments in which apo-*Bs*CotA was incubated with a similar concentration (~49–55 µM) of either Cu(I) or Cu(II) were also analyzed, as was a mixture of apo-*Bs*CotA (1.1 µM) plus apo-*Bs*Csp3 (3.1 µM). Cu(I)-*Bs*CopZ [~50–53 µM binding ~40–42 µM Cu(I)] was separately added to ~1 µM apo-*Bs*CotA, requiring ~4 µM Cu(I) to fill all Cu sites. Mixtures were incubated at room temperature in the anaerobic chamber (some experiments with Cu(II) were performed in air as was the reaction between the two apo-proteins) for up to 48 h. To measure activity, 10 µl of each mixture was added to 990 µl of aerated 100 mM citrate-phosphate buffer pH 4.0 plus 2.4 mM ABTS, and the absorbance at 420 nm measured for up to 5 min at 37°C (Figures 3A,B,E). A similar concentration of apo-*Bs*CotA was also incubated anaerobically with just buffer (20 mM HEPES pH 7.5 plus 200 mM NaCl) and the lack of activity is clear (Figures 3A,D).

After some transfer experiments with reduced apo-*Bs*CotA plus Cu(I)-*Bs*Csp3 mixtures were loaded onto a 1 ml HiTrap SP HP column and eluted with a linear NaCl gradient (0–1 M, total volume 12 ml). Fractions containing *Bs*CotA were combined, concentrated and a UV/Vis spectrum measured. This not only enabled protein quantification from the absorbance at 280 nm, but allowed Cu(II) occupancies of the T1 and T3 sites to be estimated from the absorbance at 600 (ε = 3,870 $M^{-1}cm^{-1}$) and 330 (ε = 3,639 $M^{-1}cm^{-1}$) nm, respectively (Durão et al., 2008).

The total Cu content of *Bs*CotA after transfer was measured using AAS (Vita et al., 2015; Vita et al., 2016).

The removal of Cu(I) by BCS (~2.5 mM) was analysed for the Cu(I)-*Bs*Csp3 [~0.8–1.2 μM plus ~18 equivalents of Cu(I)] samples used for activity experiments, both in the absence (folded *Bs*Csp3) and presence (unfolding conditions) of guanidine-HCl (6.64 M) (Vita et al., 2015; Vita et al., 2016). The absorbance increase at 483 nm due to formation of $[Cu(BCS)_2]^{3-}$ (ε = 12,500 $M^{-1}cm^{-1}$) (Badarau and Dennison 2011a) was measured over time at 22°C in 20 mM HEPES pH 7.5 plus 200 mM NaCl (Figure 3F).

Data availability statement

The raw data supporting the conclusions of this article will be made available by the authors, without undue reservation.

Author contributions

CD and JL conceived the project and designed the experiments. JL and RD performed the experiments and analysed data with help from CD. CD wrote the manuscript with help from JL and RD.

Funding

The Biotechnology and Biological Sciences Research Council (BBSRC) funded CD (grant BB/K008439/1) and RD (DTP grant BB/M011186/1). JL was partly supported by an Overseas Research Scholarship (ORS) award from Newcastle University.

Acknowledgments

We thank Prof. Heath Murray for help generating *B. subtilis* mutant strains, Dr. Mark Harrison for cloning the *cotA* gene and Dr. Gianpiero Landolfi for purifying *Bs*CopZ.

Conflict of interest

The authors declare that the research was conducted in the absence of any commercial or financial relationships that could be construed as a potential conflict of interest.

Publisher's note

All claims expressed in this article are solely those of the authors and do not necessarily represent those of their affiliated organizations, or those of the publisher, the editors and the reviewers. Any product that may be evaluated in this article, or claim that may be made by its manufacturer, is not guaranteed or endorsed by the publisher.

Supplementary material

The Supplementary Material for this article can be found online at: https://www.frontiersin.org/articles/10.3389/fcell.2022.916114/full#supplementary-material

References

Badarau, A., and Dennison, C. (2011a). Copper trafficking mechanism of CXXC-containing domains: Insight from the pH dependence of their Cu(I) affinities. *J. Am. Chem. Soc.* 133, 2983–2988. doi:10.1021/ja1091547

Badarau, A., and Dennison, C. (2011b). Thermodynamics of copper and zinc distribution in the cyanobacterium *Synechocystis* PCC 6803. *Proc. Natl. Acad. Sci. U. S. A.* 108, 13007–13012. doi:10.1073/pnas.1101448108

Banci, L., Bertini, I., Cantini, F., Felli, I. C., Gonnelli, L., Hadjiliadis, N., et al. (2006). The Atx1-Ccc2 complex is a metal-mediated protein-protein interaction. *Nat. Chem. Biol.* 2, 367–368. doi:10.1038/nchembio797

Banci, L., Bertini, I., Cantini, F., Kozyreva, T., Massagni, C., Palumaa, P., et al. (2011). Human superoxide dismutase 1 (hSOD1) maturation through interaction with human copper chaperone for SOD1 (hCCS). *Proc. Natl. Acad. Sci. U. S. A.* 109, 13555–13560. doi:10.1073/pnas.1207493109

Banci, L., Bertini, I., Ciofi-Baffoni, S., Kozyreva, T., Zovo, K., and Palumaa, P. (2010). Affinity gradients drive copper to cellular destinations. *Nature* 465, 645–648. doi:10.1038/nature09018

Britton, R. A., Eichenberger, P., Gonzalez-Pastor, J. E., Fawcett, P., Monson, R., Losick, R., et al. (2002). Genome-wide analysis of the stationary-phase sigma factor (sigma-H) regulon of *Bacillus subtilis*. *J. Bacteriol.* 184, 4881–4890. doi:10.1128/JB.184.17.4881-4890.2002

Changela, A., Chen, K., Xue, Y., Holschen, J., O'Halloran, T. V., and Mondragón, A. (2003). Molecular basis of metal-ion selectivity and zeptomolar sensitivity by CueR. *Science* 301, 1383–1387. doi:10.1126/science.1085950

Chillappagari, S., Miethke, M., Trip, H., Kuipers, O. P., and Marahiel, M. M. (2009). Copper acquisition is mediated by YcnJ and regulated by YcnK and CsoR in *Bacillus subtilis*. *J. Bacteriol.* 191, 2362–2370. doi:10.1128/JB.01616-08

Culotta, V. C., Klomp, L. W., Strain, J., Casareno, R. L., Krems, B., and Gitlin, J. D. (1997). The copper chaperone for superoxide dismutase. *J. Biol. Chem.* 272, 23469–23472. doi:10.1074/jbc.272.38.23469

Damle, M. S., Singh, A. N., Peters, S. C., Szalai, V. A., and Fisher, O. S. (2021). The YcnI protein from Bacillus subtilis contains a copper-binding domain. *J. Biol. Chem.* 297, 101078. doi:10.1016/j.jbc.2021.101078

Dennison, C., David, S., and Lee, J. (2018). Bacterial copper storage proteins. *J. Biol. Chem.* 293, 4616–4627. doi:10.1074/jbc.TM117.000180

DiSpirito, A. A., Semrau, J. D., Murrell, J. C., Gallagher, W. H., Dennison, C., and Vuilleumier, S. (2016). Methanobactin and the link between copper and bacterial methane oxidation. *Microbiol. Mol. Biol. Rev.* 80, 387–409. doi:10.1128/MMBR.00058-15

Durão, P., Chen, Z., Fernandes, A. T., Hilderbrandt, P., Murgida, D. H., Todorovic, S., et al. (2008). Copper incorporation into recombinant CotA laccase from *Bacillus subtilis*: Characterisation of fully copper loaded enzymes. *J. Biol. Inorg. Chem.* 13, 183–193. doi:10.1007/s00775-007-0312-0

Eichenberger, P., Fujita, M., Jensen, S. T., Conlon, E. M., Rudner, D. Z., Wang, S. T., et al. (2004). The program of gene transcription for a single differentiating cell type during sporulation in *Bacillus subtilis*. *PLoS Biol.* 2, e328. doi:10.1371/journal.pbio.0020328

Eisenman, H. C., and Casadevall, A. (2012). Synthesis and assembly of fungal melanin. *Appl. Microbiol. Biotechnol.* 93, 931–940. doi:10.1007/s00253-011-3777-2

Engman, J., Rogstam, A., Frees, D., Ingmer, H., and von Wachenfeldt, C. (2012). The YjbH adaptor protein enhances proteolysis of the transcriptional regulator Spx in *Staphylococcus aureus*. *J. Bacteriol.* 194, 1186–1194. doi:10.1128/JB.06414-11

Enguita, F. J., Martins, L. O., Henriques, A. O., and Carrondo, M. A. (2003). Crystal structure of a bacterial endospore coat component. *J. Biol. Chem.* 278, 19416–19425. doi:10.1074/jbc.M301251200

Fernandes, A. T., Pereira, M. M., Silva, C. S., Lindley, P. F., Bento, I., Pinho Melo, E., et al. (2011). The removal of a disulfide bridge in CotA-laccs changes the slower motion dynamics involved in copper binding but has no effect on the thermodynamic stability. *J. Biol. Inorg. Chem.* 16, 641–651. doi:10.1007/s00775-011-0768-9

Festa, R. A., and Thiele, D. J. (2011). Copper: An essential metal in biology. *Curr. Biol.* 21, R877–R883. doi:10.1016/j.cub.2011.09.040

Gu, W., and Semrau, J. D. (2017). Copper and cerium-regulated gene expression in *Methylosinus trichosporium* OB3b. *Appl. Microbiol. Biotechnol.* 101, 8499–8516. doi:10.1007/s00253-017-8572-2

Hassett, R., and Kosman, D. J. (1995). Evidence for Cu(II) reduction as a component of copper uptake by *Saccharomyces cerevisiae*. *J. Biol. Chem.* 270, 128–134. doi:10.1074/jbc.270.1.128

Hirooka, K., Edahiro, T., Kimura, K., and Fujita, Y. (2012). Direct and indirect regulation of the *ycnKJI* operon involved in copper uptake through two transcriptional respresors, YcnK and CsoR, in *Bacillus subtilis*. *J. Bacteriol.* 194, 5675–5687. doi:10.1128/JB.00919-12

Hosan, K., Marlene, H., Paul, G., Derrell, C. M., Michele, M. O., Rong, W., et al. (2006). The *Bacillus subtilis* spore coat protein interaction network. *Mol. Microbiol.* 59, 487–502. doi:10.1111/j.1365-2958.2005.04968.x

Hullo, M. F., Moszer, I., Danchin, A., and Martin-Verstraete, I. (2001). CotA of *Bacillus subtilis* is a copper-dependent laccase. *J. Bacteriol.* 183, 5426–5430. doi:10.1128/JB.183.18.5426-5430.2001

Jessberger, N., Dietrich, R., Granum, P. E., and Märtlbauer, E. (2020). The *Bacillus cereus* food infection as multifactorial process. *Toxins* 12, 701. doi:10.3390/toxins12110701

Lamb, A. L., Torres, A. S., O'Halloran, T. V., and Rosenzweig, A. C. (2001). Heterodimeric structure of superoxide dismutase in complex with its metallochaperone. *Nat. Struct. Biol.* 8, 751–755. doi:10.1038/nsb0901-751

Lauraeus, M., Haltia, T., Saraste, M., and Wikström, M. (1991). *Bacillus subtilis* expresses two kinds of haem-A-containing terminal oxidases. *Eur. J. Biochem.* 197, 699–705. doi:10.1111/j.1432-1033.1991.tb15961.x

Lee, J., and Dennison, C. (2019). Cytosolic copper binding by a bacterial storage protein and interplay with copper efflux. *Int. J. Mol. Sci.* 20, 4144. doi:10.3390/ijms20174144

Ma, Z., Cowart, D. M., Scott, R. A., and Giedroc, D. P. (2009). Molecular insights into the metal selectivity of the copper(I)-sensing repressor CsoR from *Bacillus subtilis*. *Biochemistry* 48, 3325–3334. doi:10.1021/bi900115w

Macomber, L., and Imlay, J. A. (2009). The iron-sulfur clusters of dehydratases are primary intracellular targets of copper toxicity. *Proc. Natl. Acad. Sci. U. S. A.* 106, 8344–8349. doi:10.1073/pnas.0812808106

Marckmann, D., Trasnea, P. I., Schimpf, J., Winterstein, C., Andrei, A., Schmoller, S., et al. (2019). The cbb_3-type cytochrome oxidase assembly factor CcoG is a widely distributed cupric reductase. *Proc. Natl. Acad. Sci. U. S. A.* 116, 21166–21175. doi:10.1073/pnas.1913803116

Martins, L. O., Soares, C. M., Pereira, M. M., Teixeira, M., Costa, T., Jones, G. H., et al. (2002). Molecular and biochemical characterisation of a highly stable bacterial laccase that occurs as a structural component of the *Bacillus subtilis* endospore coat. *J. Biol. Chem.* 277, 18849–18859. doi:10.1074/jbc.M200827200

McKenney, P. T., Driks, A., and Eichenberger, P. (2013). The *Bacillus subtilis* endospore: Assembly and functions of the multilayered coat. *Nat. Rev. Microbiol.* 11, 33–44. doi:10.1038/nrmicro2921

Meydan, S., Klepacki, D., Karthikeyan, S., Margus, T., Thomas, P., Jones, J. E., et al. (2017). Programmed ribosomal frameshifting generates a copper transporter and a copper chaperone from the same gene. *Mol. Cell.* 65, 207–219. doi:10.1016/j.molcel.2016.12.008

Nicolas, P., Mäder, U., Dervyn, E., Rochat, T., Leduc, A., Pigeonneau, N., et al. (2012). Condition-dependent transcriptome reveals high-level regulatory architecture in *Bacillus subtilis*. *Science* 335, 1103–1106. doi:10.1126/science.1206848

North, M. L., and Wilcox, D. E. (2019). Shift from entropic Cu^{2+} binding to enthaplic Cu^{1+} binding determines the reduction thermodynamics of blue copper proteins. *J. Am. Chem. Soc.* 141, 14329–14339. doi:10.1021/jacs.9b06836

Pufahl, R. A., Singer, C. P., Peariso, K. L., Lin, S. J., Schmidt, P. J., Fahrni, C. J., et al. (1997). Metal ion chaperone function of the soluble Cu(I) receptor Atx1. *Science* 278, 853–856. doi:10.1126/science.278.5339.853

Quisel, J. D., Burkholder, W. F., and Grossman, A. D. (2001). *In vivo* effects of sporulation kinases on mutant Spo0A proteins in *Bacillus subtilis*. *J. Bacteriol.* 183, 6573–6578. doi:10.1128/JB.183.22.6573-6578.2001

Radford, D. S., Kihlken, M. A., Borrelly, G. P. M., Harwood, C. R., Le Brun, N. E., and Cavet, J. S. (2003). CopZ from *Bacillus subtilis* interacts *in vivo* with a copper exporting CPx-type ATPase CopA. *FEMS Microbiol. Lett.* 220, 105–112. doi:10.1016/S0378-1097(03)00095-8

Rae, T. D., Schmidt, P. J., Pufahl, R. A., Culotta, V. C., and O'Halloran, T. V. (1999). Undetectable intracellular free copper: The requirement for a copper chaperone for superoxide dismutase. *Science* 284, 805–808. doi:10.1126/science.284.5415.805

Rensing, C., Fan, B., Sharma, R., Mitra, B., and Rosen, B. P. (2000). CopA: An *Escherichia coli* Cu(I)-translocating P-type ATPase. *Proc. Natl. Acad. Sci. U. S. A.* 97, 652–656. doi:10.1073/pnas.97.2.652(

Rensing, C., and McDevitt, S. F. (2013). The copper metallome in prokaryotic cells. *Metall. Ions Life Sci.* 12, 417–450. doi:10.1007/978-94-007-5561-1_12

Ridge, P. G., Zhang, Y., and Gladyshev, V. N. (2008). Comparative genomic analyses of copper transporters and cuproproteomes reveal evolutionary dynamics of copper utilization and its link to oxygen. *PLoS One* 3, e1378. doi:10.1371/journal.pone.0001378

Sala, F. A., Wright, G. S. A., Antonyuk, S. V., Garratt, R. C., and Hasnain, S. S. (2019). Molecular recognition and maturation of SOD1 by its evolutionary destabilised cognate chaperone hCCS. *PLoS Biol.* 17, e3000141. doi:10.1371/journal.pbio.3000141

Schmidt, P. J., Rae, T. D., Pufahl, R. A., Hamma, T., Strain, J., O'Halloran, T. V., et al. (1999). Multiple protein domains contribute to the action of the copper chaperone for superoxide dismutase. *J. Biol. Chem.* 274, 23719–23725. doi:10.1074/jbc.274.34.23719

Smaldone, G. T., and Helmann, J. D. (2007). CsoR regulates the copper efflux operon *copZA* in *Bacillus subtilis*. *Microbiology* 153, 4123–4128. doi:10.1099/mic.0.2007/011742-0

Solioz, M., Abicht, H. K., Mermod, M., and Mancini, S. (2010). Response of Gram-positive bacteria to copper stress. *J. Biol. Inorg. Chem.* 15, 3–14. doi:10.1007/s00775-009-0588-3

Soni, A., Oey, I., Silcock, P., and Bremer, P. (2016). *Bacillus* spores in the food industry: A review on resistance and response to novel inactivation technologies. *Comp. Rev. Food Sci. Food Saf.* 15, 1139–1148. doi:10.1111/1541–4337.12231

Strolle, P., Hou, B., and Brüser, T. (2016). The Tat substrate CueO is transported in an incomplete folding state. *J. Biol. Chem.* 291, 13520–13528. doi:10.1074/jbc.M116.729103

Tavares, M. B., Souza, R. D., Luiz, W. B., Cavalcante, R. C. M., Casaroli, C., Martins, E. G., et al. (2013). *Bacillus subtilis* endospores at high purity and recovery yields: Optimization of growth conditions and purification method. *Curr. Microbiol.* 66, 279–285. doi:10.1007/s00284-012-0269-2

Vita, N., Landolfi, G., Baslé, A., Platsaki, S., Lee, J., Waldron, K. J., et al. (2016). Bacterial cytosolic proteins with a high capacity for Cu(I) that protects against copper toxicity. *Sci. Rep.* 6, 39065. doi:10.1038/srep39065

Vita, N., Platsaki, S., Baslé, A., Allen, S. J., Paterson, N. G., Crombie, A. T., et al. (2015). A four-helix bundle stores copper for methane oxidation. *Nature* 525, 140–143. doi:10.1038/nature14854

von Wachenfeldt, C., Hallgren, J., and Hederstedt, L. (2021). YtkA (CtaK) and YozB (CtaM) function in the biogenesis of cytochrome *c* oxidase in *Bacillus subtilis*. *Mol. Microbiol.* 116, 184–199. doi:10.1111/mmi.14701

Wong, P. C., Waggoner, D., Subramaniam, J. R., Tessarollo, L., Bartnikas, T. B., Culotta, V. C., et al. (2000). Copper chaperone for superoxide dismutase is essential to active mammalian Cu/Zn superoxide dismutase. *Proc. Natl. Acad. Sci. U. S. A.* 97, 2886–2891. doi:10.1073/pnas.040461197

frontiers | Frontiers in Molecular Biosciences

TYPE Opinion
PUBLISHED 21 October 2022
DOI 10.3389/fmolb.2022.1032220

OPEN ACCESS

EDITED BY
Marie-Pierre Golinelli,
UPR2301 Institut de Chimie des Substances Naturelles (ICSN CNRS), France

REVIEWED BY
Teresita Padilla-Benavides,
Wesleyan University, United States
Soumi Ghosh,
Massachusetts Institute of Technology, United States

*CORRESPONDENCE
Kourosh H. Ebrahimi,
Kourosh.ebrahimi@kcl.ac.uk

SPECIALTY SECTION
This article was submitted to Cellular Biochemistry, a section of the journal Frontiers in Molecular Biosciences

RECEIVED 30 August 2022
ACCEPTED 07 October 2022
PUBLISHED 21 October 2022

CITATION
Ji Y, Wei L, Da A, Stark H, Hagedoorn P-L, Ciofi-Baffoni S, Cowley SA, Louro RO, Todorovic S, Mroginski MA, Nicolet Y, Roessler MM, Le Brun NE, Piccioli M, James WS, Hagen WR and Ebrahimi KH (2022), Radical-SAM dependent nucleotide dehydratase (SAND), rectification of the names of an ancient iron-sulfur enzyme using NC-IUBMB recommendations. *Front. Mol. Biosci.* 9:1032220. doi: 10.3389/fmolb.2022.1032220

Radical-SAM dependent nucleotide dehydratase (SAND), rectification of the names of an ancient iron-sulfur enzyme using NC-IUBMB recommendations

Yuxuan Ji[1], Li Wei[1], Anqi Da[1], Holger Stark[2], Peter-Leon Hagedoorn[3], Simone Ciofi-Baffoni[4], Sally A. Cowley[5], Ricardo O. Louro[6], Smilja Todorovic[6], Maria Andrea Mroginski[7], Yvain Nicolet[8], Maxie M. Roessler[9], Nick E. Le Brun[10], Mario Piccioli[4], William S. James[5], Wilfred R. Hagen[3] and Kourosh H. Ebrahimi[1]*

[1]Institute of Pharmaceutical Science, King's College London, London, United Kingdom, [2]Institute for Pharmaceutical and Medicinal Chemistry, Heinrich-Heine-University Düsseldorf, Duesseldorf, Germany, [3]Department of Biotechnology, Delft University of Technology, Delft, Netherlands, [4]Magnetic Resonance Center (CERM), University of Florence and Consorzio Interuniversitario Risonanze Magnetiche di Metalloproteine (CIRMMP), Florence, and Department of Chemistry, University of Florence, Florence, Italy, [5]Sir William Dunn School of Pathology, University of Oxford, Oxford, United Kingdom, [6]Instituto de Tecnologia Química e Biológica António Xavier, Universidade Nova de Lisboa, Av. da República–EAN, Oeiras, Portugal, [7]Institute of Chemistry, Technische Universität Berlin, Berlin, Germany, [8]Université Grenoble Alpes, Grenoble, France, [9]Department of Chemistry, Molecular Sciences Research Hub, Imperial College London, London, United Kingdom, [10]Centre for Molecular and Structural Biochemistry, School of Chemistry, University of East Anglia, Norwich, United Kingdom

KEYWORDS

antiviral, innate immun system, dehydratase, nucleotide analogue, iron-sulfur [FeS] cluster

Main text

In 1789, the influential French chemist Antoine-Laurent Lavoisier described his view of science and its langague in his book *Traité élémentaire de chimie*. According to the Robert Kerr's translation it states (Lavoisier, 1790): "*As ideas are preserved and communicated by means of words, it necessarily follows that we cannot improve the language of any science without at the same time improving the science itself; neither can we, on the other hand, improve a science without improving the language or nomenclature which belongs to it.*" This view reminds us of Confucius's earlier doctrine, the rectification of names (Steinkraus, 1980; Lau, 2000). Confucius believed that rectification of names is imperative. He explained (Steinkraus, 1980; Lau, 2000): "*If language is incorrect, then what is said does not concord with what was meant, what is to be done cannot be affected. If what is to be done cannot be affected, then rites and music will not flourish. If rites and music do not flourish, then mutilations and lesser punishments will go astray. And if mutilations and lesser punishments go astray, then the people have nowhere to put hand or foot. Therefore the gentleman uses only such language as is proper for speech, and only speaks of what it would be proper to carry into effect. The gentleman in what*

he says leaves nothing to mere chance." Inspired by these views, we make the analogy that the progress of science and the language used to describe it are two entangled electrons. This entanglement highlights the importance of introducing systemic names for enzymes using EC classification and the ever-growing problem of protein names (McDonald and Tipton, 2021). Here, we tackle one specific case of iron-sulfur ([FeS]) enzymes. We show that the language used to describe a conserved [FeS] enzyme of the innate immune system, i.e., viperin or RSAD2, is now inadequate and disentangled from its science. We discuss that the enzyme has cellular functions beyond its antiviral activity and that eukaryotic and prokaryotic enzymes catalyse the same chemical reactions. To prevent bias towards antiviral activity while studying various biochemical activities of the enzyme and using scientifically incorrect terms like "prokaryotic viperins," we rectify the language describing the enzyme. Based on NC-IUBMB recommendations, we introduce the nomenclature S-adenosylmethionine (SAM) dependent Nucleotide Dehydratase (SAND).

Firstly, considering the progress in understanding the biology of the enzyme in humans (Figure 1), the name "viperin" is no longer adequate and should be avoided. In 1997, Hua Z., et al. found that in response to human cytomegalovirus infection, the mRNA level of a novel protein was elevated in human cells (Zhu et al., 1997). The gene related to this mRNA was named cytomegalovirus-induced human gene-5 (cig-5). In 2001, Chin and Cresswell showed that interferons (IFNs) induce the expression of the protein product of cig-5 (Chin and Cresswell, 2001). This induction restricted the replication of human cytomegalovirus, and the protein was localised to the cytoplasmic face of the endoplasmic reticulum (ER) (Chin and Cresswell, 2001). Because, at the time, nothing was known about the chemistry of the enzyme, an abbreviation based on the cellular localisation and antiviral activity was introduced, "viperin" (virus inhibitory protein, endoplasmic reticulum-associated, interferon-inducible) (Chin and Cresswell, 2001). Subsequent studies showed that the expression of the protein affects the life-cycle of many RNA and DNA viruses, including Influenza (Wang et al., 2007), HIV-1 (Nasr et al., 2012), Hepatitis C (Wang et al., 2012; Ghosh et al., 2020), Zika (Van der Hoek et al., 2017; Panayiotou et al., 2018), and tick-borne encephalitis (Panayiotou et al., 2018), among others. However, for each virus, different mechanisms were proposed (Figure 1A). For example, the enzyme affects lipid rafts (lipid microdomains on the cellular membrane and enriched in cholesterol and sphingolipids (Ripa et al., 2021)) and inhibits influenza virus (Wang et al., 2007) or HIV-1 (Nasr et al., 2012) release. In the case of the Hepatitis C virus, viperin expression appears to interfere with the binding of the viral nonstructural protein NS5A with host hVAP22 (Wang et al., 2012) or promotes proteasomal-dependent degradation of viral NS5A (Ghosh et al., 2020). In the case of Zika and tick-borne encephalitis viruses, the enzyme appears to induce proteasomal degradation of the viral nonstructural protein NS3 (Panayiotou et al., 2018). Finally, in the case of tick-borne encephalitis virus and Dengue virus type-2, the enzyme restricts viral RNA reproduction (Helbig et al., 2013; Upadhyay et al., 2014).

Despite the established antiviral activity, many studies have reported biological functions inconsistent with or unrelated to the biology defined by the nomenclature "viperin". Cresswell and colleagues showed that the enzyme localises to lipid droplets (Hinson and Cresswell, 2009) and enhances human

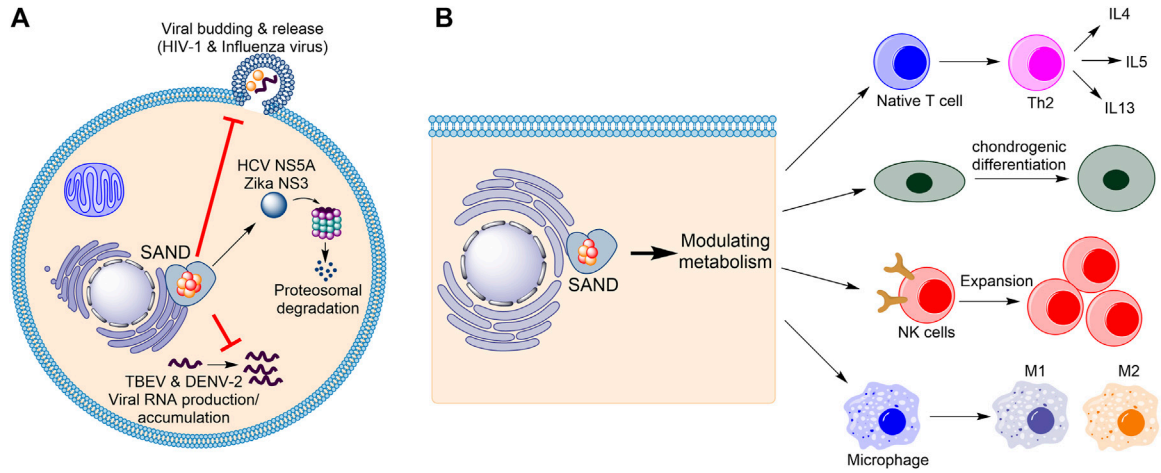

FIGURE 1
Human SAND has functions beyond its antiviral activity. **(A)** Various mechanisms of antiviral activity are proposed for human SAND. **(B)** Expression of SAND affects the function and differentiation of various types of cells. HCV, hepatitis C virus; TBEV, tick-born encephalitis virus; DENV-2, Dengue type-2 virus; NK, natural killer; IL, interleukin.

cytomegalovirus infection (Seo et al., 2011). In addition to interferons, lipopolysaccharides were found to induce protein expression (Olofsson et al., 2005). The proposal of multiple mechanisms of antiviral activity prompted us to postulate that the protein's enzymatic activity regulates metabolism to affect various cellular processes causing broad-spectrum antiviral activity (Ebrahimi, 2018) (Figure 1B). This effect of the enzyme on metabolism suggests a cellular function beyond its antiviral activity. Indeed, many studies corroborate this proposal and demonstrate that human SAND has a role in modulating metabolism, regulating the activity/maturation of the immune cells, and inducing the expression of immune genes (Figure 1B). For example, the activity of SAND modulates central carbon metabolism (Ebrahimi et al., 2020c), regulates thermogenesis in adipose tissues (Eom et al., 2019), inhibits thiolase activity of the trifunctional enzyme complex (a mitochondrial enzyme complex with three activities: enoyl-CoA hydratase, 3-hydroxyacyl-CoA dehydrogenase, and 3-ketoacyl-CoA thiolase) (Dumbrepatil et al., 2020), and modulates cholesterol metabolism (Tang et al., 2016; Grunkemeyer et al., 2021). It is required for optimal T helper two cell response (Qiu et al., 2009) and chondrogenic differentiation *via* CXCL10 protein secretion (Steinbusch et al., 2019). It has a role in the innate system (Ebrahimi et al., 2022) and modules immune cell function and maturation e.g., expansion of natural killer cells (Wiedemann et al., 2020), dendritic cell maturation (Jang et al., 2018), B cell hyperactivity (Zhu et al., 2021), and polarisation of macrophages (Eom et al., 2018). Additionally, the enzyme's expression induces the expression of many immune genes (Zhang et al., 2014).

Secondly, the nomenclature RSAD2 should be revised to fully describe the chemistry of the enzyme relevant to its biological function. By 2010, it became clear that human SAND has a CxxxCxxC motif coordinating a [4Fe-4S] cluster, similar to many members of the radical S-adenosylmethionine (SAM) enzymes (Duschene and Broderick, 2010; Shaveta et al., 2010). As a result, the HUGO Gene Nomenclature Committee suggested the name RSAD2 (radical-SAM domain containing 2) around this time. This name can be easily confused with another radical-SAM enzyme of unknown function (RSAD1), and it only partially describes the SAM-dependent chemistry of the enzyme. In 2017, the structure of mouse SAND was solved (Fenwick et al., 2017), confirming that it is a radical-SAM enzyme. It was shown that the cytosolic iron-sulfur biogenesis machinery is required to deliver and insert the [4Fe-4S] cluster into the enzyme (Upadhyay et al., 2017). The expression of human SAND in *E. coli* changed the cells' morphology, suggesting the enzyme's substrate is a metabolite common between eukaryotic and prokaryotic cells (Nelp et al., 2017), and initial structural studies proposed that the substrate is a nucleotide (Fenwick et al., 2017). Subsequently, it was revealed that eukaryotic SAND could catalyse the dehydration of CTP or UTP to 3′-deoxy-3′, 4′-didehydro (ddh) analogues (Figure 2A) (Fenwick et al., 2020). In human macrophages, the enzyme was found to produce ddhCTP (Gizzi et al., 2018; Ebrahimi et al., 2020b). This novel nucleotide analogue metabolite may act as a chain-terminator to inhibit viral replication (IC_{50} values $\geq$ 20 mM) (Gizzi et al., 2018). Subsequent studies revealed that the expression of SAND and synthesis of ddhCTP in HEK293 cells affects the cellular nucleotide pool and mitochondrial function (Ebrahimi et al., 2020a). The enzyme in macrophages modulates central carbon metabolism potentially by inhibiting the NAD^+-dependent activity of the glycolytic enzyme GAPDH (Ebrahimi et al., 2020c) (Figure 2A). This function requires the radical-SAM domain to produce ddhCTP since this nucleotide analogue inhibits the NAD^+-dependent activity of GAPDH *in vitro* (Ebrahimi et al., 2020c). This immunometabolism function of ddhCTP may regulate the immune response in various ways (Ebrahimi et al., 2021, Ebrahimi et al., 2022). Consistently, studies have shown that the expression of the enzyme indeed primes the immune response (Zhang et al., 2014).

Finally, the use of the outdated nomenclature "viperin" can introduce scientifically incorrect terms such as "prokaryotic viperin." Before 2017 little was done to isolate fungal and microbial SANDs and characterise the chemical reaction catalysed by them. In 2017, a thermostable fungal SAND from *Thielavia terrestris* was isolated and characterised (Ebrahimi et al., 2017). It was hypothesised that the fungal enzyme produces antiviral natural products and is a suitable candidate for the biotechnological production of antiviral lead molecules. The fungal SAND has promiscuous activity and catalyses the dehydration of diverse nucleoside triphosphates (NTPs), e.g., CTP, UTP, and 5-bromo-UTP, to their ddh analogues *via* a mechanism requiring the transfer of an electron and a proton (Figure 2B) (Ebrahimi et al., 2020b). Next, a number of other groups characterised some microbial enzymes and showed that they catalyse dehydration of various NTPs to their ddh analogues (Bernheim et al., 2021; Lachowicz et al., 2021) (Figure 2C). While the cellular function of these microbial proteins is not fully understood, the chemical reaction catalysed by SANDs can inhibit the activity of phage T7 RNA polymerase in *E. coli* (Bernheim et al., 2021). These findings suggest that the enzyme might have a cellular function and act as an antimicrobial/antiviral defence system. The fungal enzyme was named TtRSAD2 (Ebrahimi et al., 2020b) due to the lack of a proper name, and studies with bacterial enzymes (Bernheim et al., 2021) introduced a new nomenclature, i.e., "prokaryotic viperin," to describe prokaryotic enzymes producing ddh analogues with antiviral activity (Bernheim et al., 2021; Wein and Sorek, 2022). The term "prokaryotic viperin" is not fit for purpose because it implies that bacteria and archaea have endoplasmic reticulum, and interferons activate their immune system. This assertion questions our fundamental understanding of biology, i.e., prokaryotes do not have an endoplasmic reticulum and interferon-mediated antiviral response.

A growing number of investigators are studying this new class of enzymes across all domains of life (Figure 2D). Consequently, different nomenclatures like RSAD2, viperin, prokaryotic viperin, or viperin-like enzymes are being used by various investigators, including us, to describe eukaryotic or microbial enzymes. As discussed above, none of the existing nomenclatures accurately

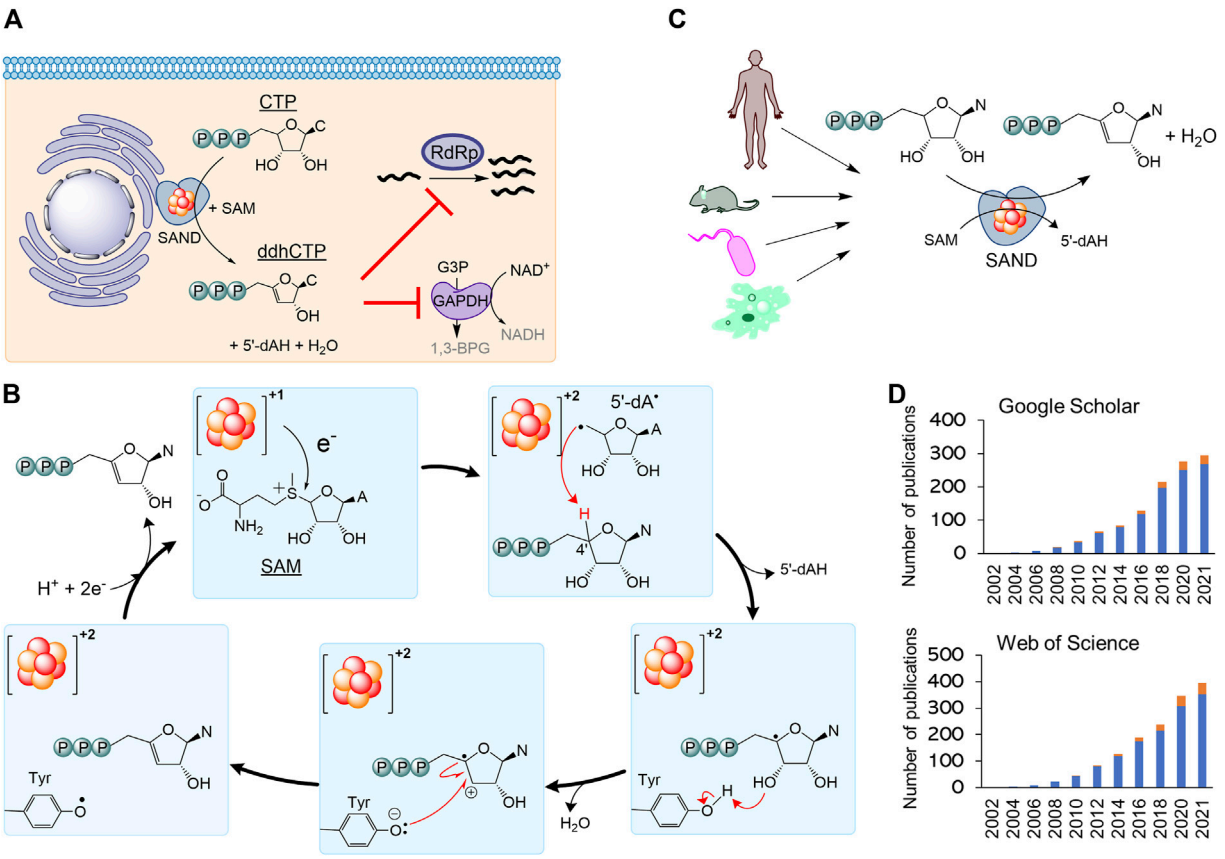

FIGURE 2
The nomenclature SAND (SAM-dependent Nucleotide Dehydratase) defines chemistry relevant to biology across all domains of life. **(A)** SAND produces the nucleoside triphosphate analogue ddhCTP in humans. ddhCTP modulates metabolism affecting cell function and restricting viral replication. **(B)** The proposed mechanism of dehydration of nucleoside triphosphates by SAND. The mechanism shows the transfer of a proton and an electron from a conserved tyrosine. Alternatively, it is possible that proton transfer occurs *via* another amino acid residue. It is not clear if the transfer of proton and electron occurs simultaneously (proton-coupled electron transfer). **(C)** SANDs from various organisms produce diverse ddh analogues. **(D)** An increasing number of investigators study SANDs. The data were obtained from a search of nomenclature viperin and RSAD2 in the title of articles. Google Scholar (scholar.google.com) and Web of Science search engines were used. N, nucleobase; C, cytosine; A, adenine; 5′-dAH, 5′-deoxyadenosine, 5′-dA·, 5′-deoxyadenosyl radical.

describe the cellular function or chemistry in prokaryotes or eukaryotes. Additionally, using various terminologies for enzymes performing the same chemical reaction is confusing. Hence, we strongly suggest the classification of the enzyme as a nucleoside triphosphate dehydratase (NTPD, EC 4.2.1) and the nomenclature SAND describing the SAM-dependent chemistry across all domains of life. This classification and abbreviation to rectify the naming of an ancient iron-sulfur enzyme should help the increasing number of investigators studying the cellular function or biotechnological application of these enzymes and the discovery of new enzymes performing novel chemistries.

Author contributions

KE conceived the idea and wrote the manuscript together with all the other authors.

Acknowledgments

All authors acknowledge the support from the European Cooperation in Science and Technology (COST) Action CA21115.

Conflict of interest

The authors declare that the research was conducted in the absence of any commercial or financial relationships that could be construed as a potential conflict of interest.

Publisher's note

All claims expressed in this article are solely those of the authors and do not necessarily represent those of their affiliated organizations, or those of the publisher, the editors and the reviewers. Any product that may be evaluated in this article, or claim that may be made by its manufacturer, is not guaranteed or endorsed by the publisher.

Supplementary Material

The Supplementary Material for this article can be found online at: https://www.frontiersin.org/articles/10.3389/fmolb.2022.1032220/full#supplementary-material

References

Bernheim, A., Millman, A., Ofir, G., Meitav, G., Avraham, C., Shomar, H., et al. (2021). Prokaryotic viperins produce diverse antiviral molecules. *Nature* 589, 120–124. doi:10.1038/s41586-020-2762-2

Chin, K.-C., and Cresswell, P. (2001). Viperin (cig5), an IFN-inducible antiviral protein directly induced by human cytomegalovirus. *Proc. Natl. Acad. Sci. U. S. A.* 98, 15125–15130. doi:10.1073/pnas.011593298

Dumbrepatil, A. B., Zegalia, K. A., Sajja, K., Kennedy, R. T., and Marsh, E. N. G. (2020). Targeting viperin to the mitochondrion inhibits the thiolase activity of the trifunctional enzyme complex. *J. Biol. Chem.* 295, 2839–2849. doi:10.1074/jbc.RA119.011526

Duschene, K. S., and Broderick, J. B. (2010). The antiviral protein viperin is a radical SAM enzyme. *FEBS Lett.* 584, 1263–1267. doi:10.1016/j.febslet.2010.02.041

Ebrahimi, K. H. (2018). A unifying view of the broad-spectrum antiviral activity of RSAD2 (viperin) based on its radical-SAM chemistry. *Metallomics* 10, 539–552. doi:10.1039/C7MT00341B

Ebrahimi, K. H., Carr, S. B., McCullagh, J., Wickens, J., Rees, N. H., Cantley, J., et al. (2017). The radical-SAM enzyme Viperin scatalyses reductive addition of a 5′-deoxyadenosyl radical to UDP-glucose *in vitro*. *FEBS Lett.* 591, 2394–2405.

Ebrahimi, K. H., Diofi, S., Hagedoorn, P. L., Nicolet, Y., Le Brun, N. E., Hagen, W. R., et al. (2022). Iron-sulphur clusters as inhibitors and catalysts of viral replication. *Nat. Chem.* 14, 253–266.

Ebrahimi, K. H., Gilbert-Jaramillo, J., James, W. S., and McCullagh, J. S. O. (2021). Interferon-stimulated gene products as regulators of central carbon metabolism. *FEBS J.* 288, 3715–3726. doi:10.1111/febs.15625

Ebrahimi, K. H., Howie, D., Rowbotham, J., McCullagh, J., Armstrong, F., and James, W. S. (2020a). Viperin, through its radical-SAM activity, depletes cellular nucleotide pools and interferes with mitochondrial metabolism to inhibit viral replication. *FEBS Lett.* 594, 1624–1630. doi:10.1002/1873-3468.13761

Ebrahimi, K. H., Rowbotham, J., McCullagh, J., and James, W. S. (2020b). Mechanism of diol dehydration by a promiscuous radical-SAM enzyme homologue of the antiviral enzyme viperin (RSAD2). *ChemBioChem* 21, 1605–1612. doi:10.1002/cbic.201900776

Ebrahimi, K. H., Vowles, J., Browne, C., McCullagh, J., and James, W. S. (2020c). ddhCTP produced by the radical-SAM activity of RSAD2 (viperin) inhibits the NAD+-dependent activity of enzymes to modulate metabolism. *FEBS Lett.* 594, 1631–1644. doi:10.1002/1873-3468.13778

Eom, J., Kim, J. J., Yoon, S. G., Jeong, H., Son, S., Lee, J. B., et al. (2019). Intrinsic expression of viperin regulates thermogenesis in adipose tissues. *Proc. Natl. Acad. Sci. U. S. A.* 116, 17419–17428. doi:10.1073/pnas.1904480116

Eom, J., Yoo, J., Kim, J. J., Lee, J. B., Choi, W., Park, C. G., et al. (2018). Viperin deficiency promotes polarization of macrophages and secretion of M1 and M2 cytokines. *Immune Netw.* 18, e32. doi:10.4110/in.2018.18.e32

Fenwick, M. K., Li, Y., Cresswell, P., Modis, Y., and Ealick, S. E. (2017). Structural studies of viperin, an antiviral radical SAM enzyme. *Proc. Natl. Acad. Sci. U. S. A.* 114, 6806–6811. doi:10.1073/pnas.1705402114

Fenwick, M. K., Su, D., Dong, M., Lin, H., and Ealick, S. E. (2020). Structural basis of the substrate selectivity of viperin. *Biochemistry* 59, 652–662. doi:10.1021/acs.biochem.9b00741

Ghosh, S., Patel, A. M., Grunkemeyer, T. J., Dumbrepatil, A. B., Zegalia, K. A., Kennedy, R. T., et al. (2020). Interactions between viperin, vesicle-associated membrane protein A and Hepatitis C virus protein NS5A modulate viperin activity and NS5A degradation. *Biochemistry* 59, 780–789. doi:10.1021/acs.biochem.9b01090

Gizzi, A. S., Grove, T. L., Arnold, J. J., Jose, J., Jangra, R. K., Garforth, S. J., et al. (2018). A naturally occurring antiviral ribonucleotide encoded by the human genome. *Nature* 558, 610–614. doi:10.1038/s41586-018-0238-4

Grunkemeyer, T. J., Ghosh, S., Patel, A. M., Sajja, K., Windak, J., Basrur, V., et al. (2021). The antiviral enzyme viperin inhibits cholesterol biosynthesis. *J. Biol. Chem.* 297, 100824. doi:10.1016/j.jbc.2021.100824

Helbig, K. J., Carr, J. M., Calvert, J. K., Wati, S., Clarke, J. N., Nicholase, S. E., et al. (2013). Viperin is induced following Dengue virus type-2 (DENV-2) infection and has anti-viral actions requiring the C-terminal end of viperin. *PLoS Negl. Trop. Dis.* 7, e2178. doi:10.1371/journal.pntd.0002178

Hinson, E. R., and Cresswell, P. (2009). The antiviral protein, viperin, localizes to lipid droplets via its N-terminal amphipathic alpha-helix. *Proc. Natl. Acad. Sci. U. S. A.* 106, 20452–20457. doi:10.1073/pnas.0911679106

Jang, J.-S., Lee, J.-H., Jung, N.-C., Choi, S.-Y., Park, S.-Y., Yoo, J.-Y., et al. (2018). Rsad2 is necessary for mouse dendritic cell maturation via the IRF7-mediated signaling pathway. *Cell. Death Dis.* 9, 823. doi:10.1038/s41419-018-0889-y

Lachowicz, J. C., Gizzi, A. S., Almo, S. C., and Grove, T. L. (2021). Structural insight into the substrate scope of viperin and viperin-like enzymes from three domains of life. *Biochemistry* 60, 2116–2129. doi:10.1021/acs.biochem.0c00958

Lau, D. C. (2000). Confucius: The analects.

Lavoisier, A. L. (1790). Elements of chemistry.

McDonald, A. G., and Tipton, K. F. (2021). Enzyme nomenclature and classification: The state of the art. *FEBS J.* doi:10.1111/febs.16274

Nasr, N., Maddocks, S., Turville, S. G., Harman, A. N., Woolger, N., Helbig, K. J., et al. (2012). HIV-1 infection of human macrophages directly induces viperin which inhibits viral production. *Blood* `20, 778–788. doi:10.1182/blood-2012-01-407395

Nelp, M. T., Young, A. P., Stepanski, B. M., and Bandarian, V. (2017). Human viperin causes radical SAM-dependent elongation of *Escherichia coli*, hinting at its physiological role. *Biochemistry* 56, 3874–3876. doi:10.1021/acs.biochem.7b00608

Olofsson, P. S., Jatta, K., Wagsater, D., Gredmark, S., Hedin, U., Paulsson-Berne, G., et al. (2005). The antiviral cytomegalovirus inducible gene 5/viperin is expressed in atherosclerosis and regulated by proinflammatory agents. *Arterioscler. Thromb. Vasc. Biol.* 25, e113–e116. doi:10.1161/01.ATV.0000170130.85334.38

Panayiotou, C., Lindqvist, R., Kurhade, C., Vonderstein, K., Pasto, J., Edlund, K., et al. (2018). Viperin restricts Zika virus and tick-borne encephalitis virus replication by targeting NS3 for proteasomal degradation. *J. Virol.* 92, 020544–e2117. doi:10.1128/JVI.02054-17

Qiu, L.-Q., Cresswell, P., and Chin, K.-C. (2009). Viperin is required for optimal Th2 responses and T-cell receptor-mediated activation of NF-kappaB and AP-1. *Blood* 113, 3520–3529. doi:10.1182/blood-2008-07-171942

Ripa, I., Andreu, S., López-Guerrero, J. A., and Bello-Morales, R. (2021). Membrane rafts: Portals for viral entry. *Front. Microbiol.* 12, 631274. doi:10.3389/fmicb.2021.631274

Seo, J.-Y., Yaneva, R., Hinson, E. R., and Cresswell, P. (2011). Human cytomegalovirus directly induces the antiviral protein viperin to enhance infectivity. *Sci. (80-.)* 332, 1093–1097. doi:10.1126/science.1202007

Shaveta, G., Shi, J., Chow, V. T. K., and Song, J. (2010). Structural characterization reveals that viperin is a radical S-adenosyl-L-methionine (SAM) enzyme. *Biochem. Biophys. Res. Commun.* 391, 1390–1395. doi:10.1016/j.bbrc.2009.12.070

Steinbusch, M. M. F., Caron, M. M. J., Surtel, D. A. M., van den Akker, G. G. H., van Dijk, P. J., Friedrich, F., et al. (2019). The antiviral protein viperin regulates chondrogenic differentiation via CXCL10 protein secretion. *J. Biol. Chem.* 294, 5121–5136. doi:10.1074/jbc.RA119.007356

Steinkraus, W. E. (1980). Socrates, Confucius, and the rectification of names. *Philos. East West* 30, 261–264. doi:10.2307/1398850

Tang, H.-B., Lu, Z.-L., Wei, X.-K., Zhong, T.-Z., Ouyang, L.-X., Luo, Y., et al. (2016). Viperin inhibits rabies virus replication via reduced cholesterol and sphingomyelin and is regulated upstream by TLR4. *Sci. Rep.* 6, 30529. doi:10.1038/srep30529

Upadhyay, A. S., Stehling, O., Panayiotou, C., Rosser, R., Lill, R., and Overby, A. K. (2017). Cellular requirements for iron-sulfur cluster insertion into the antiviral radical SAM protein viperin. *J. Biol. Chem.* 292, 13879–13889. doi:10.1074/jbc.M117.780122

Upadhyay, A. S., Vonderstein, K., Pichlmair, A., Stehling, O., Bennett, K. I., Dobler, G., et al. (2014). Viperin is an iron–sulfur protein that inhibits genomesynthesis of tick-borne encephalitis virus via radical SAM domain activity. *Cell. Microbiol.* 16, 834–848. doi:10.1111/cmi.12241

Van der Hoek, K. H., Eyre, N. S., Shue, B., Khantisitthiporn, O., Glab-Ampi, K., Carr, J. M., et al. (2017). Viperin is an important host restriction factor in control of Zika virus infection. *Sci. Rep.* 7, 4475. doi:10.1038/s41598-017-04138-1

Wang, S., Wu, X., Pan, T., Song, W., Wang, Y., Zhang, F., et al. (2012). Viperin inhibits hepatitis C virus replication by interfering with binding of NS5A to host protein hVAP-33. *J. Gen. Virol.* 93, 83–92. doi:10.1099/vir.0.033860-0

Wang, X., Hinson, E. R., and Cresswell, P. (2007). The interferon-inducible protein viperin inhibits influenza virus release by perturbing lipid rafts. *Cell. Host Microbe* 2, 96–105. doi:10.1016/j.chom.2007.06.009

Wein, T., and Sorek, R. (2022). Bacterial origins of human cell-autonomous innate immune mechanisms. *Nat. Rev. Immunol.* 22, 629–638. doi:10.1038/s41577-022-00705-4

Wiedemann, G. M., Geary, C. D., Lau, C. M., and Sun, J. C. (2020). Cutting edge: STAT1-Mediated epigenetic control of Rsad2 promotes clonal expansion of antiviral NK cells. *J. Immunol.* 205, 21–25. doi:10.4049/jimmunol.2000086

Zhang, B., Zhang, J., Xiao, Z. Z., and Sun, L. (2014). Rock bream (*Oplegnathus fasciatus*) viperin is a virus-responsive protein that modulates innate immunity and promotes resistance against megalocytivirus infection. *Dev. Comp. Immunol.* 45, 35–42. doi:10.1016/j.dci.2014.02.001

Zhu, H., Cong, J.-P., and Shenk, T. (1997). Use of differential display analysis to assess the effect of human cytomegalovirus infection on the accumulation of cellular RNAs: Induction of interferon-responsive RNAs. *Proc. Natl. Acad. Sci. U. S. A.* 94, 13985–13990. doi:10.1073/pnas.94.25.13985

Zhu, H., Zheng, J., Zhou, Y., Wu, T., and Zhu, T. (2021). Knockdown of RSAD2 attenuates B cell hyperactivity in patients with primary Sjögren's syndrome (pSS) via suppressing NF-κb signaling pathway. *Mol. Cell. Biochem.* 476, 2029–2037. doi:10.1007/s11010-021-04070-z

Frontiers in
Cell and Developmental Biology

Explores the fundamental biological processes of life, covering intracellular and extracellular dynamics.

The world's most cited developmental biology journal, advancing our understanding of the fundamental processes of life. It explores a wide spectrum of cell and developmental biology, covering intracellular and extracellular dynamics.

Discover the latest Research Topics

See more →

Frontiers

Avenue du Tribunal-Fédéral 34
1005 Lausanne, Switzerland
frontiersin.org

Contact us

+41 (0)21 510 17 00
frontiersin.org/about/contact